



**Junior Scientist Conference  
2006**

**PROCEEDINGS**

April 19th - 21st 2006  
Vienna University of Technology



Bank Austria  
Creditanstalt

[www.tuwien.ac.at/jsc06](http://www.tuwien.ac.at/jsc06)

**Proceedings of the  
Junior Scientist Conference 2006**

---



# **Proceedings of the Junior Scientist Conference 2006**

---

**Vienna University of Technology  
Vienna, Austria  
April 2006**

Edited by  
Wilfried Elmenreich and Hans Kaiser

The views and opinions expressed in all the papers of this book are the author's personal ones.

The copyright of the individual papers belongs to the authors. Copies cannot be reproduced for commercial profit.

Cover page design: Bettina Neunteufl

©2006, Copyright protected.

ISBN 3-902463-05-8

Printed in Austria.

# Table of Contents

<b>Welcome Message from Peter Skalicky</b>	<b>xv</b>
<b>Welcome Message from Hans K. Kaiser</b>	<b>xvii</b>
<b>Conference Organizers</b>	<b>xix</b>
<b>1 Information and Communication Technology</b>	<b>1</b>
Kalman Filter in Geodesy <i>Sonja Bogatin, Dušan Kogoj and Karl Foppe</i> . . . . .	3
Effective transmission over AWGN channel using Turbo codes <i>Lubomír Čopjan and Stanislav Marchevský</i> . . . . .	5
The Steepest Descent Method Used for Indirect Frequency <i>Jakub Džubera and Aleš Prokeš</i> . . . . .	7
Structuring Architectural Services in the DECOS Integrated Architecture <i>Christian El Salloum and Hermann Kopetz</i> . . . . .	9
A Remote and Transparent Approach for the Test and Diagnosis of Automotive Networks <i>Eric Armengaud and Andreas Steininger</i> . . . . .	11
Peak to Average Power Ratio Reduction in M-modification of MC-CDMA <i>Zbyněk Fedra and Vladimír Šebesta</i> . . . . .	13
Security in Building Automation <i>Wolfgang Granzer and Wolfgang Kastner</i> . . . . .	15
The least risk path for outdoor and indoor areas <i>Eva Grum and Andrew Frank</i> . . . . .	17
Simulation and Optimization of CSO and CTB in Cable Television <i>Ondřej Hála and Václav Říčný</i> . . . . .	19

Deterministic and stochastic constituent analysis of diurnal and semi-diurnal coordinate variations in European permanent GPS network <i>Michal Hřčka and Ján Hefty</i> . . . . .	21
Implementation of an FPGA-Based Hardware Fault Injector <i>Thomas Handl and Andreas Steininger</i> . . . . .	23
Application for Solving Direct and Inverse Kinematic task <i>Eubomír Jasenovec and Ján Jadlovský</i> . . . . .	25
Optimization of CAL Gates for an FPGA Architecture <i>Marcus Jeitler and Martin Delvai</i> . . . . .	27
Implications of Automation for Manufacturing Industries of Less Developed Countries: Force-Field Analysis <i>Gebremeskel Kahsay, Peter Herbert Osanna and Numan Muhammet Durakbasa</i> . . . . .	29
Systematic Automated Testing of Safety-Critical Applications in the Automotive Domain <i>Susanne Kandl and Raimund Kirner</i> . . . . .	31
The Smart Car - a distributed controlled autonomous robot <i>Gernot Klingler, Alexander Kößler and Wilfried Elmenreich</i> . . . . .	33
Automatic solution evaluation during a practical examination <i>Alexander Kößler and Wilfried Elmenreich</i> . . . . .	35
A Fourier Transform 3D-Model for Wave Propagation in Layered Orthotropic Media <i>Felix Kramer and Holger Waubke</i> . . . . .	37
Power Equivalent Gaussian Beam for Terrestrial Optical Wireless Link Power Budget <i>Petr Krivak and Otakar Wilfert</i> . . . . .	39
A Portable Real-Time Communication System for Embedded Systems with Heterogeneous Hardware <i>Stefan Krywult and Wilfried Elmenreich</i> . . . . .	41
Procedures of Detection and Removal of Blotches on Scanned Optical Sound Tracks using MatLab <i>Andy Kuiper and Milan Sigmund</i> . . . . .	43
Forward Error Correction Coding Schemes in Ultra Wideband Communications <i>Vishwas Lakkundi and Roman Marsalek</i> . . . . .	45

Construction of a Fault-Tolerant Wireless Communication Topology Using Distributed Agreement <i>Heinrich Moser and Ulrich Schmid</i> . . . . .	47
Software Tool CESim for Graphical Design, Simulation and Analysis of C/E Petri Nets <i>Petr Novosad and Milan Češka</i> . . . . .	49
Security Protocols: Analysis and Design <i>Pavel Ocenasek and Miroslav Sveda</i> . . . . .	51
Meta-Modelling in Tool Support for Time-Triggered Application Development <i>Christian Paukovits and Wilfried Elmenreich</i> . . . . .	53
Validation Framework for Advanced Maintenance Strategies <i>Harald Paulitsch and Hermann Kopetz</i> . . . . .	55
Detection of Impulses form the Respose of a Scintillation Detector <i>Ondřej Pirochta and Aleš Prokeš</i> . . . . .	57
A versatile networked embedded platform for KNX/EIB <i>Fritz Praus and Wolfgang Kastner</i> . . . . .	59
A Graph-Based Approach to Optical Flow Estimation <i>Christoph Rhemann, Michael Bleyer and Margrit Gelautz</i> . . . . .	61
Design Comprehension of Time-Triggered Real-Time Systems <i>Bernhard Rumpler and Hermann Kopetz</i> . . . . .	63
UMTS Network Modelling – Interference Impact to Signal Quality <i>Zdeněk Růžička and Stanislav Hanus</i> . . . . .	65
Extended Confidence-Weighted Averaging in Sensor Fusion <i>Angela Schörgendorfer and Wilfried Elmenreich</i> . . . . .	67
Numerical Simulations of Electrical Characteristics of Piezoceramic Sensor <i>Petr Sedlak, Jiri Majzner, Jan Havranek and Josef Sikula</i> . . . . .	69
Black-Box Modelling of Microwave Amplifiers for Linearization <i>Daniel Silveira and Gottfried Magerl</i> . . . . .	71
Time-Triggered Ethernet <i>Klaus Steinhammer and Hermann Kopetz</i> . . . . .	73
Efficient Position-based Communication in Wireless Ad-hoc Networks <i>Hannes Stratil and Ulrich Schmid</i> . . . . .	75
Time-Multiplexed Multiple Constant Multiplication <i>Peter Tummeltshammer and Andreas Steininger</i> . . . . .	77

Sandbox Geography	
<i>Florian A. Twaroch and Andrew U. Frank</i> . . . . .	79
Implementing an Active Noise Reduction Solution on a FPGA	
<i>Christian Varga and Andreas Steininger</i> . . . . .	81
Simulating Distributed Real-Time Systems	
<i>Daniel Albeseder and Josef Widder</i> . . . . .	83
Analysis of the Influence of Background Traffic on FTP Traffic	
<i>Anna Shklyaeva and Vit Novotny</i> . . . . .	85
Area-Efficient Dual-Port Memory Architecture for Multi-Core Processors	
<i>Hassan Bajwa and Xinghao Chen</i> . . . . .	87
Multilayer Adhesive Bonding Under Hot Air Stream	
<i>Daniela Andrijasevic, Werner Brenner and Johann Nikolics</i> . . . . .	89
Quantum-Mechanical designed Terahertz Laser	
<i>Alexander Benz, Gernot Fasching, Karl Unterrainer, Reinhard Zobl,</i> <i>Aaron Maxwell Andrews, Tomas Roch, Werner Schrenk and Gottfried</i> <i>Strasser</i> . . . . .	91
High-level Modeling, Analysis and Verification on Programmable Hardware Design	
<i>Aleš Smrčka</i> . . . . .	93
Signal Detection with Needle and Segmental Ionization Detector	
<i>Pavel Cernoch and Josef Jirak</i> . . . . .	95
Automation of Microassembly Process in the SEM Chamber with a Novel Protective Covering Plate	
<i>Aleksandra Cvetanovic, Werner Brenner and Helmut Detter</i> . . . . .	97
<b>2 Material Sciences</b>	<b>99</b>
Rubber ferrite composites containing strontium hexaferrite	
<i>Denisa Bellušová, Eva Ůrögiová, Ivan Hudec and Gabriela Kyselá</i> . . . . .	101
Ofloxacin-Releasing biodegradable chitosan microspheres	
<i>Silvia Bubeníková, Lucia Vodná, Igor Lacík and Dušan Bakoš</i> . . . . .	103
Formation of Crosslinked Inorganic-Organic Polymers as Matrices for the In Situ Preparation of Lanthanide Oxide Nanoparticles	
<i>Claudia Feldgitscher and Guido Kickelbick</i> . . . . .	105
Application Of Electrochemical Method In The Study of Corrosion Properties of System Fe Powder / Metal Coating	
<i>Zuzana Feckova and Ladislav Lux</i> . . . . .	107

A New Optical Set-up of a Reflective Holographic Confocal Microscope <i>Zdeněk Foret</i> . . . . .	109
Influence of Electrical and Thermal Ageing on the Course of Complex Permittivity of Thermikanit <i>Martin Frk and Rostislav Stráník</i> . . . . .	111
Magnetic and Superconducting Properties of HoNi <sub>2</sub> B <sub>2</sub> C Single Crystal <i>René Fuger and Harald W. Weber</i> . . . . .	113
Binuclear Copper(II) Complexes as Building Blocks for the Synthesis of Inorganic-Organic Nanocomposites <i>Fatmir Hamza and Guido Kickelbick</i> . . . . .	115
The Structure and Mechanical Properties of ADI in Dependence on Heat Treatment Conditions <i>Klára Hanzlíková, Stanislav Věchet and Jan Kohout</i> . . . . .	117
Investigation of an atmospheric-pressure radio-frequency capacitive plasma jet <i>Stefan Haslinger, Johannes Hell and Johann Laimer</i> . . . . .	119
1/f noise in submicron MOSFETs <i>Jan Havranek and Petr Sedlak</i> . . . . .	121
Nonlinear Spectroscopy of Metallic and Rock Samples <i>Stepan Hefner, Josef Sikula and Martin Blaha</i> . . . . .	123
Local probe magnetisation measurements of high temperature superconductors <i>Florian Hengstberger and Harald W. Weber</i> . . . . .	125
Edge Isolation of the Silicon Solar Cells - an Etching Paste Approach <i>Jiri Hladik, Radim Barinka and Ivan Szendiuch</i> . . . . .	127
Fabrication of Cellular Ceramic Structures by Gelcasting and Rapid Prototyping <i>Johannes Homa and Jürgen Stampfl</i> . . . . .	129
Structuring Methods Capable of Building 3D Parts with feature resolutions from 50 $\mu\text{m}$ to 100 nm <i>Robert Inführ, Christina Fritscher, Volker Schmidt, Ladislav Kuna, Robert Liska, Helga Lichtenegger and Jürgen Stampfl</i> . . . . .	131
Hybrid Inorganic-Organic Materials by Coordinative Linkage between Polymers and Metal Alkoxides <i>Sorin Ivanovici and Guido Kickelbick</i> . . . . .	133
Copper matrix composites with multi-wall carbon nanotubes <i>Thomas Janhsen and Christian Edtmaier</i> . . . . .	135

Influence of filler particle size on structure and properties of polypropylene/clay composites <i>Daniela Klimová, Viera Khunová and Pavol Lukáč</i> . . . . .	137
New Approach to Electrochemical Sensor Electrodes Construction <i>Kateřina Klosová, Radim Hrdý and Jaromír Hubálek</i> . . . . .	139
The Supercapacitors of Double Layer Type <i>Martin Kocian and Jiří Vondrák</i> . . . . .	141
Materials from renewable resources used in rubber mixtures <i>Zuzana Kramárova, Peter Bugaj, Jozef Feranc, Miroslav Ďuračka, Eugen Špírk, Peter Šuri, Anton Karvaš, Ivan Chodák and Pavol Alexy</i> . . . . .	143
Hybrid Electrochromic Cells Employing Sol-Gel and Polymeric I <sup>3</sup> -/I <sup>-</sup> Redox Electrolytes <i>Ondřej Krejza and Jiří Vondrák</i> . . . . .	145
Conservation of Historical Papers with Chitosan <i>Katarína Kunovská and Ludmila Černáková</i> . . . . .	147
FIB EDX Tomography – 3D Characterization of Al-Si eutectics <i>Fernando Adrián Lasagni and Hans Peter Degischer</i> . . . . .	149
Laser Interference Metallurgy – New Surface properties through advanced microstructure design <i>Andrés Lasagni and Frank Mücklich</i> . . . . .	151
Silica-Based Capillary Monoliths. New Stationary Phases for Liquid Chromatography <i>Stefan Laschober and Erwin Rosenberg</i> . . . . .	153
Preparation And Properties Of Electrochromic Device <i>Michal Macalik and Marie Sedlarikova</i> . . . . .	155
Rheological, Morphological and Mechanical Properties of Polycaprolactone - Thermoplastic Starch Blends <i>Anna Nahálková, Peter Bugaj, Veronika Fuleová and Pavol Alexy</i> . . . . .	157
Excessive Grinding and its Effect on Egeing of Calciumsulphate $\alpha$ -Hemihydrate <i>Ivo Ostradecky and Marcela Fridrichova</i> . . . . .	159
Three Dimensional Micromechanics Finite Element Model for Shape Memory Alloys Based on Return Mapping <i>Andrej Pukšič and Franc Kosel</i> . . . . .	161

Preparation of Lanthanide Oxide Nanoparticles from Microemulsions and by Controlled Precipitation <i>Christoph Rill and Guido Kickelbick</i> . . . . .	163
Ordered arrays of metallic nanoparticles for nanoelectronics <i>Jana Röschlová, Martin Weis, Marek Vančo, Drahoslav Barančok Ján Vajda and Július Cirák</i> . . . . .	165
Synthesis and Properties of Copolyamides from $\epsilon$ -Caprolactam and Nylon Salts <i>Jozef Ryba, Michal Krištofič, Iveta Vassová and Mária Dulíková</i> . . . . .	167
Photonic Crystal Cavities for Quantum Cascade Lasers <i>Stephan Schartner, Sebastian Golka, Max Austerer, Christan Pflügl, Werner Schrenk and Gottfried Strasser</i> . . . . .	169
Nano-patterning and growth of self-assembled nano-structures <i>Matthias Schramböck, Aaron Maxwell Andrews, Tomas Roch, Werner Schrenk, A. Lugstein and Gottfried Strasser</i> . . . . .	171
Biophotopolymers for Rapid Prototyping of Cellular Bone Replacement Materials <i>Monika Schuster, Claudia Turecek, Bertrand Kaiser, Franz Varga, Jürgen Stampfl and Robert Liska</i> . . . . .	173
Improvement of Grout for Prestressed Tendons <i>Marijana Serdar, Irina Stipanovic and Dubravka Bjegovic</i> . . . . .	175
Electronic and Magnetic Structure of Spintronics Materials from ab-initio Bandstructure Calculations <i>Martin Sieberer and Peter Mohn</i> . . . . .	177
Polyamide Fibers Filled by Inorganic Nanoparticles Boehmite: Mechanical and Thermal Properties <i>Lubica Škrovanová, Eberhard Borsig, Jens Erler and Ralf Muelhaupt</i> . . . . .	179
Influence of ferromagnetic fillers on properties of rubber blends <i>Eva Ürögiová, Denisa Bellušová and Ivan Hudec</i> . . . . .	181
Structure of Lyocell Fibres and its Influence on the Fibre Properties <i>Ksenija Varga, Mohammad Abu Rous, Elisabeth Ingolic and K. Christian Schuster</i> . . . . .	183
Collagen/Hyaluronic Acid Membranes For Tissue Engineering <i>Lucia Vodná, Silvia Bubeníková and Dušan Bakoš</i> . . . . .	185
Order in low-dimensional systems: the Langmuir film study. <i>Martin Weis, Marek Vančo, Jana Röschlová, Július Cirák and Drahoslav Barančok and Ján Vajda</i> . . . . .	187

Simulation of Interstitial Element Redistribution and Phase Profile in Dissimilar Welds of Creep-Resistant Steels <i>Bronislav Zlámal and Rudolf Foret</i> . . . . .	189
Metal-Semiconductor Contact Modeling and Transport Characteristics Detectors of Radiation Based on the CdTe <i>Alexey Andreev and Jiri Zajacek</i> . . . . .	191
Zinc Oxide Crystal Growth by Molten fluxes <i>Chun-Min Feng and Glen Kowach</i> . . . . .	193
Ultrasonic Characterization of Microstructure for High Purity Metals <i>Fei Zeng and Feng-Bao Lin</i> . . . . .	195
Two-dimensional Micro- and Nanoparticle Monolayer Films <i>Carlos A. Silvera Batista and Ilona Kretzschmar</i> . . . . .	197
Bubble and Droplet Motion in a Yield-Stress Fluid <i>John Paul Bir Singh and Morton M. Denn</i> . . . . .	199
Orientation Transitions in Dispersed Liquid Crystalline Droplets <i>Rajesh Goyal and Morton M. Denn</i> . . . . .	201
Raman Imaging and spectroscopy of individual carbon nanotubes <i>Li Zhang and Zhonghua Yu</i> . . . . .	203
Numerical Modeling of the Performance of a Silicon-on-Insulator Based High-Temperature-Resistance Pressure Sensor <i>Xiaojun Wang and Feng-Bao Lin</i> . . . . .	205
Non-Linear Oscillatory Crystallization in the Formation of Rhythmic Bands in the Palisades Sill, New Jersey <i>Karin A. Block and Jeffrey C. Steiner</i> . . . . .	207
Viscoelastic Behaviour of Plasticized Poly(3-hydroxy butyrate) <i>Andreas Hähndel and Hans-Joachim Radusch</i> . . . . .	209
MBE-grown $Zn_xCd_{(1-x)}Se/Zn_{x'}Cd_{y'}Mg_{(1-x'-y')}Se$ multi-quantum wells for intersubband devices <i>Hong Lu and Maria C. Tamargo</i> . . . . .	211
<b>3 Environmental Sciences</b>	<b>213</b>
Delignification of Atmospheric Aerosol Sample <i>Rui Andrade, Alexandre Caseiro, Casimiro Pio, Anne Kasper-Giebl, Heidi Bauer and Hans Puxbaum</i> . . . . .	215

Sustainable Energy Production in Microbial Fuel Cells <i>Susanne Beisteiner, Sonja Hein and Alexandra Wolfsberger and Peter Holubar</i> . . . . .	217
Odour and Corrosion Problems in Pressure Sewers <i>Fátima Bertrán de Lis, Ernis Saracevic and Norbert Matsché</i> . . . . .	219
Development of a Simulation Method to predict Ultraviolet Disinfection Reactor Performance and Comparison to Biodosimetric Measurements <i>Christoph Buchner, Christoph Reichl and Norbert Vana</i> . . . . .	221
Contribution of wood burning to PM10 in Austria <i>Alexandre Caseiro, Casimiro Pio, Anne Kasper-Giebl, Heidi Bauer and Hans Puxbaum</i> . . . . .	223
Selective Separation of Carbon Dioxide for Biogas Upgrading <i>Helmut Feichtner, Alexander Reichhold and Hermann Hofbauer</i> . . . . .	225
Designing Tomorrow's Energy Supply: Polygeneration of Transportation Fuels, Power and Heat from Biomass <i>Stefan Fürnsinn and Hermann Hofbauer</i> . . . . .	227
Seasonal Variation of Trace Metals in the PM10 Fraction at Three Sampling Sites in the City of Vienna <i>Markus Handler, Hannes Zbiral, Hans Puxbaum and Andreas Limbeck</i> . . . . .	229
Hydraulic Design of Single Stones in Biocorridor <i>Lea Hašková and Jozef Kamenský</i> . . . . .	231
The Possibility of Utilization of Permeable Reactive Barriers for Remediation of Contaminated Groundwater <i>Mária Heželová, Ladislav Lux and Daniela Kladeková</i> . . . . .	233
Using of Genetic Algorithms for Assessment of the Directing Discharge of Water from Reservoir <i>Lubomír Jaroš and Miloš Starý</i> . . . . .	235
New technology for processing of fly ashes <i>Veronika Kalova and Rostislav Drochytka</i> . . . . .	237
Fluid dynamic and reaction modelling of the combustion reactor in a Dual Fluidized Bed biomass-steam gasification system <i>Priyanka Kaushal and Hermann Hofbauer</i> . . . . .	239
Analysis Of Humic Like Substances in Airborne Particulate Matter (< 10 $\mu$ m) from Sampling Sites in Austria and Selected Source Samples <i>Barbara Klatzer, Heidi Bauer and Hans Puxbaum</i> . . . . .	241

Three Cities Intercomparison of n-Alkanes and Polyaromatic Hydrocarbons in the Atmospheric Aerosols <i>Petra Kotianová, Hans Puxbaum, Heidi Bauer and Gabriel Čík</i> . . . . .	243
Optimisation of Sampling Design Programmes and Calibration of Water Distribution Models by Genetic Algorithms <i>Daniel Kozelj and Franci Steinman</i> . . . . .	245
Multi-criteria optimization as a support by the rehabilitation planning of the water mains <i>Tomas Kucera and Ladislav Tuhovcak</i> . . . . .	247
Decision Support for the Rehabilitation Planning of the Sewer Network <i>Stanislav Malanik and Petr Hlavinec</i> . . . . .	249
Possibilities of waste raw materials – fly ash in special application in civil engineering <i>Pavla Matulova, Gabriela Michalcova and Rostislav Drochytka</i> . . . . .	251
Mitigation of Energy Loss and CO2 Emission from the Building Stock <i>Martin Mohapl and Petr Lizal</i> . . . . .	253
New Materials in Old Buildings – The Problem of Heat Flow and Vapour Diffusion through Walls (Facades) <i>Iva Muraj and Jasenka Bertol-Vrček</i> . . . . .	255
Ecodesign Decision Boxes for Environmentally Sound Product Development <i>Hesamedin Ostad Ahmad Ghorabi and Wolfgang Wimmer</i> . . . . .	257
Photoacoustic Monitoring of CO2 in Biogas Matrix Using a Quantum Cascade Laser <i>Wolfgang Ritter and Bernhard Lendl</i> . . . . .	259
Soil Conservation and Flood Protection in Loucka River Watershed <i>Aleksandra Sala and Miroslav Dumbrovský</i> . . . . .	261
Use of organomineral complex at remediation of contaminated soil <i>Zuzana Sejkova, Marianna Skokanová and Katarina Dercová</i> . . . . .	263
Life Cycle Assessment – Case Study of Aluminium Production <i>Lenka Sencakova, Lucia Gdovicinova and Edita Vircikova</i> . . . . .	265
Toxicity of low-chlorinated phenols and pentachlorophenol (PCP) <i>Marianna Skokanová, Zuzana Sejkova and Katarina Dercová</i> . . . . .	267
Applications of the Data-Driven Modelling Techniques in Hydrology <i>Luka Stravs and Mitja Brilly</i> . . . . .	269

Life Cycle Assessment, Total Quality Management and Intelligent Metrology to support disassembly, recycling and re-use of parts from used electronic products <i>Halima Tahirova, Peter Herbert Osanna and Numan Muhammet Durakbasa</i>	271
Giant Phospholipid Vesicles as a Possible Diagnostic System for the Study of Protein Interaction with Membranes <i>Jasna Urbanija and Veronika Kralj-Iglič</i>	273
Investigations at Industrial Wastewater Treatment Plants in Nicaragua <i>Ulrike Wegracht, Vanessa Parravicini and Helmut Kroiss</i>	275
Development of an Online Tool for the Simulation of the Anaerobic Digestion Process <i>Alexandra Wolfsberger, Susanne Beisteiner and Peter Holubar</i>	277
Meanings in Urban Public Landscapes <i>Burcu Yigit Turan and Richard Stiles</i>	279
Interactions of Halide Ions with Aqueous Ammonia under Ultraviolet Irradiation with Low Pressure Mercury Lamps <i>Yvette Beckles and Vasil Diyamandoglu</i>	281
The role of reduced sulfur species in the degradation of thiometon and disulfoton in stimulated coastal environments <i>Qiu Gan and Urs Jans</i>	283
Characterization of Biomass Burning: Fourier Transform Infrared Analysis of North American Woods and Vegetation Combustion Products <i>Diomaris Padilla and Jeffrey C. Steiner</i>	285
Multi-scale Modeling of H <sub>2</sub> Storage in Clathrates <i>Prasad Yedlapalli and Jae W. Lee</i>	287
Amplification of Small Electric Fields in Neurons; Implications for Environmental Risks <i>Thomas Radman, Lucas Parra and Marom Bikson</i>	289
Developing a Remotely Sensed Rainfall Retrieval Algorithm using Multi-Spectral Information <i>Cecilia Hernandez, Shayesteh Mahani and Reza Khanbilvardi</i>	291
Multi-Spectral Remotely Sensed Snowfall Rate Estimation <i>Yajaira Mejia, Shayesteh Mahani and Reza Khanbilvardi</i>	293
Concentration and chiral signatures of chlordanes in surficial sediments from Long Island Sound <i>Lijia Yang, Xiqing Li, Youxian Wu, Michael Melcer, Pengfei Zhang and Urs Jans</i>	295

Analysis of Polar Organic Compounds in Aerosols <i>Barbara Rollinger, Heidi Bauer, Petra Kotianová, Christoph Schmidl, Yo Abe and Hans Puxbaum</i> . . . . .	297
---	-----

**4 Science and Technology** **299**

Finite Mixture Model Diagnostics Using the Parametric Bootstrap <i>Bettina Grün and Friedrich Leisch</i> . . . . .	301
---	-----

Electrophysiological Monitoring of Membrane Capacitance Changes in Cell-Attached Mammalian Lactotrophs <i>Jernej Jorgačevski, Matjaž Stenovec, Marko Kreft and Robert Zorec</i> . . .	303
--	-----

Methods from SPM family <i>Jaroslav Kala</i> . . . . .	305
---	-----

Constructional and Architectural Analysis of Great Moravian Masonry Buildings <i>Lubor Kalousek and Milan Vlček</i> . . . . .	307
--	-----

Integrated map of construction processes <i>Peter Kozák</i> . . . . .	309
--	-----

Quantum cascade laser dynamics probed by broad-band Terahertz pulses <i>Josef Kröll and Karl Unterrainer</i> . . . . .	311
---	-----

CO <sub>2</sub> Separation by Chemical Looping Combustion – Modelling Results <i>Markus Luisser and Hermann Hofbauer</i> . . . . .	313
---	-----

Propagation of High Power Laser Pulses through Hollow Core Photonic Band Gap Fiber <i>Filip Orban, Heinrich Kofler, Andrey B. Fedotov, Aleksey M. Zheltikov and Ernst Wintner</i> . . . . .	315
--	-----

Voltammetry of immobilised microparticles-characteristics of different powder materials electrodisolution <i>Lubomir Pikna and Ladislav Lux</i> . . . . .	317
--	-----

A Two-dimensional Mathematical Hydraulic Model of a Hydro Power Structures Operation <i>Tanja Prešeren and Franci Steinman</i> . . . . .	319
---	-----

Readiness for Adoption of eInvoicing Service <i>Kornélia Pupáková</i> . . . . .	321
--	-----

Hyperpolarized xenon in 4.7 T NMR system <i>Jan Rychnovský, Zdeněk Buchta, Karel Bartušek and Josef Lazar</i> . . . . .	323
--	-----

Measurement infiltration in terrain on no-saturated streaming waters <i>Radovana Sedlackova and Miroslav Dumbrovský</i> . . . . .	325
Secondary Frequency Standard for Experimental Satellite <i>Jiri Spacek and Miroslav Kasal</i> . . . . .	327
High performance concrete bridge supersructure composed of precast girders and cast-in-situ slab <i>Karel Tesař and Jiří Stráský</i> . . . . .	329
Erbium Laser Decontamination of Dental Titanium Implants <i>Ariej Yousif, Martin Strassl and Ernst Wintner</i> . . . . .	331
Simulation of indoor climate of a dwelling heated by convection and radiation <i>Ondřej Šikula and Günter Gebauer</i> . . . . .	333
Hyperglycemia Induced Adenosine Tri-phosphate Depletion and Endothelial Cell Dysfunction <i>Stewart Russell and David Rumschitzki</i> . . . . .	335
Retinal Vascular Permeability in Diabetes <i>Sandra V. Lopez and John M. Tarbell</i> . . . . .	337
In vitro study of LDL transport through endothelial monolayers under convec- tive conditions <i>Limary Cancel, Andrew Fitting and John Tarbell</i> . . . . .	339
The Effect of Chronic Hypertension on the Filtration Properties of Intact and Denuded Vessels <i>Tieuvi Nguyen and David Rumschitzki</i> . . . . .	341
Time-sliced imaging and Monte Carlo simulation study of ex vivo cancerous and normal breast tissues <i>M. Alrubaiee, M. Xu, S. K. Gayen and R. R. Alfano</i> . . . . .	343
Partial Characterization of Blm10p, an Activator of the Nuclear 20S Core Proteasome, that Functions in the Relief of Oxidative Stress in <i>Saccha- romyces cerevisiae</i> <i>Leah D. Pride and Carol Wood Moore</i> . . . . .	345
Hall effect induced by microwave field in two dimensional electron gas with static vortex: A semi-classical approach <i>Hsuan-Yeh Chang and David Schmeltzer</i> . . . . .	347
Surface Enhance Raman Spectroscopy (SERS) as Sensing Method for Bio- molecules on MBE-Grown Quantum Dots <i>Richard Livingstone and John Lombardi</i> . . . . .	351

Calculated proton uptake on anaerobic reduction of cytochrome c oxidase and  
quinol oxidase using MCCE  
*Jun Zhang and Yifan Song and Marilyn Gunner* . . . . . 353

**Author's Index** . . . . . **355**

# Welcome Message from Peter Skalicky

By surfing in Wikipedia one finds the following definition: “*The scientific community consists of the total body of scientists, its relationships and interactions.*” And further: “*Communication between the members is established by disseminating research work and hypotheses through articles in peer reviewed journals, or by attending conferences where new research is presented and ideas are exchanged and discussed.*” So in fact - aside from publications - conferences are the core opportunity for young scientists to become part of their community, present their research, make contacts and make themselves a name.



Foto: © Petra Spiola

The Junior Scientists Conference at the Vienna University of Technology (TU Wien) is specially designed to make it easier for young researchers to enter this arena. So it is my pleasure to wish all of you good luck and a good start for the presentation of your posters and for getting into contact with each other.

The Junior Scientists Conference is also a good example for the collaboration within the heart of Europe. Aside from our friends from New York where the first conference took place, there are - among others - participants from the Czech Republic, Slovakia, Hungary, Croatia and Slovenia. We have great expectations for these new and prospective members of the European Community. The Central European Region - in short: Centrope - is a political commitment to overcome former borders. One promising way to reach this goal is the intensive collaboration between scientists.

*Peter Skalicky*  
*Rector at Vienna University of Technology*



# Welcome Message from Hans K. Kaiser

The idea for such a Junior Scientist Conference originated in the discussions between a delegation from the City College of New York and members of the TU Wien during the visit of our American colleagues to Vienna, headed by president Gregory Williams, in 2004. The aim of such a conference is to give young researchers a first possibility to present the results of their scientific work to a wider audience. In the centre of such a conference is the presentation of posters by young scientists. The first conference in this series took place in New York in March 2005. TU Wien is happy to organize now this second event in a - hopefully - long series of similar conferences to come.



Foto: © Petra Spiola

There was a call for scientific contributions in all fields of Science and Technology both on Master- and Phd-level. Preference was given to posters from the area of Environmental Sciences, Information and Communication Technology and Material Sciences. We are very pleased that the announcement of our conference was well received both by universities in our neighbouring countries and our friends from the City College of New York. So we are proudly welcoming more than 170 young researchers from nine different countries. At the heart of the conference in Vienna will be the poster session. Around this main event there will be three mini-conferences in the area of Environmental Sciences, Material Sciences and Information and Communication Technology. Within the conference we are organizing a best poster award: one for posters on the Master-level and one on Phd-level.

We wish all participants an exciting time in Vienna and a successful conference at the Vienna University of Technology.

*Hans K. Kaiser*

*Vice Rector for Academic Affairs at Vienna University of Technology*



# Conference Organizers

## Conference Chairman

**Hans K. Kaiser** Vice Rector for Academic Affairs at TU Vienna

## Scientific Program Committee

**Gerald Badurek** Dean of the Faculty of Physics, TU Vienna

**Wolfgang Binder** Institute of Applied Synthetic Chemistry, TU Vienna

**Martin Delvai** Institute of Computer Engineering, TU Vienna

**Josef Eberhardsteiner** Institute for Mechanics of Materials and Structures, TU Vienna

**Wilfried Elmenreich** Institute of Computer Engineering, TU Vienna

**Bernard Favre-Bulle** Automation and Control Institute, TU Vienna

**Stefan Filipp** Atomic Institute of the Austrian Universities

**Johannes Fröhlich** Dean of the Faculty of Technical Chemistry, TU Vienna

**Peter Gärtner** Institute of Applied Synthetic Chemistry, TU Vienna

**Bruno Grösel** Dean of the Faculty of Mechanical and Industrial Engineering, TU Vienna

**Gerhard Jambrich** Automation and Control Institute, TU Vienna

**Johann Litzka** Institute for Road Construction and Maintenance, TU Vienna

**Norbert Matsché** Inst. f. Water Quality, Resources and Waste Management, TU Vienna

**Irene Reichl** TU Vienna

**Helmut Springer** Institute of Mechanics and Mechatronics, TU Vienna

## Administrative Support

**Monika Petutschnig** Assistent to the Vice Rector

**Werner Sommer** Assistent to the Rectorate

**Melanie Wagner** Secretary to the Vice Rectorate



# **Symposium 1**

## **Information and Communication Technology**



# Kalman Filter in Geodesy

Evaluation of linear Kalman Filter processing terrestrial geodetic observations of kinematical system, using known trajectory

Sonja Bogatin, Dušan Kogoj, Karl Foppe\*  
Faculty for civil and geodetic engineering  
University in Ljubljana  
Ljubljana, Slovenia  
Email: [sbogatin@fgg.uni-lj.si](mailto:sbogatin@fgg.uni-lj.si)

\* Technical University Munich, Chair for Geodesy, Arcisstr.21, Munich, Germany

**Abstract** — *The main objective of the contribution is to introduce the efficiency of the linear Kalman filter as an alternative method for estimation of kinematical process observed with electronic tachymeter. The efficiency of the linear Kalman filter is controlled using a known reference trajectory.*

## I. INTRODUCTION

Nowadays ‘geodetic deformation analysis’ means geodetic analysis of dynamic and kinematic processes, which means incorporating the influencing factors and time dependence. Models describing the deformation as a function of time, i.e. velocity, acceleration etc., are called kinematical models. From the instruments point of view modern geodetic terrestrial instruments allow capturing kinematical process with high frequency of measurements.

With proper kinematical deformation model the system state and its accuracy are definable in real time, with time delays taken into account. Because no redundant observations are available for the time point, the classical geodetic adjustment can not be used. Instead, the filter methods have to be applied. Kalman filter represents a method of advanced geodetic analysis of dynamic and kinematic processes.

## II. KALMAN FILTER MODEL

The Kalman filter is a set of mathematical equations that provides a computational (recursive) solution of the least-squares method. It gives the answer to the most frequent engineering question: how can we get the best estimate of the system state from the noisy measurements. We assume that the discrete random kinematical process to be estimated can be modeled with two main Kalman filter equations:

$$\mathbf{x}_{k+1} = \mathbf{A} \cdot \mathbf{x}_k + \mathbf{w}_k \dots \text{process equation} \quad (1)$$

$$\mathbf{z}_k = \mathbf{H} \cdot \mathbf{x}_k + \mathbf{v}_k \dots \text{measurement equation.} \quad (2)$$

With the assumption of a-priori system state estimate at some point of time, we now seek to use the current measurement to improve the a-prior estimate. The

main object of deriving the Kalman filter is to get equations for computing a-posteriori estimate  $\hat{\mathbf{x}}_k$  as a linear combination of a-priori estimate  $\hat{\mathbf{x}}_k^-$  and a weighted difference between true  $\mathbf{z}_k$  and predicted measurements  $\mathbf{H} \cdot \hat{\mathbf{x}}_k^-$ :

$$\hat{\mathbf{x}}_k = \hat{\mathbf{x}}_k^- + \mathbf{K} \cdot (\mathbf{z}_k - \mathbf{H} \cdot \hat{\mathbf{x}}_k^-). \quad (3)$$

The weighted difference between true and predicted measurements performs improvement of the estimation or measurement correction. The Kalman filter iteratively corrects the Kalman gain  $\mathbf{K}$  (weight) so that the estimation of the state vector tends towards an optimal solution.

## III. DISCRETE LINEAR KALMAN FILTER ALGORITHM FOR THREE-DIMENSIONAL TRACKING PROBLEM

When working with practical problems involving discrete data, particularly evaluating them in real time, it is important that the used method is computationally feasible as well as mathematically correct. The evaluation of the three-dimensional discrete linear Kalman filter model for different input information and kinematical properties was made on the straight test trajectory at the geodetic laboratory of the Technical University Munich. The observations - horizontal angles, slope distances and zenith distances - were carried out with a terrestrial surveying instrument – the *TCRA1101plus* electronic tachymeter from *Leica Geosystems* in fast tracking mode. On the trolley, the 360°-reflector was used. The object is to estimate horizontal position of the moving trolley with Kalman filter. The Kalman filter equations were performed according to the problem after [2].

The first criterion for filter efficiency is the convergence of covariance matrix  $\mathbf{P}_k$  trace and accordingly the convergence of standard deviations of system states components. But this criterion can be used just as inner confidence, because the divergence can

occur when the error covariance matrix becomes unjustifiably small compared with the actual error in the estimate [3]. To estimate the actual quality of filtering, another method which will give the comparison with true state has to be defined. The perpendicular distance of filtered values  $(x_n, y_n)$ , from the reference trajectory  $(x_{ref}, y_{ref})$ , is used as a performance figure merit, which is defined as

$$f_{f_i} = \sqrt{(x_{ref_i} - x_{filt_i})^2 + (y_{ref_i} - y_{filt_i})^2} \quad (4)$$

and compared with distance of measured position  $(x_m, y_m)$  from the reference trajectory:

$$f_{m_i} = \sqrt{(x_{ref_i} - x_{m_i})^2 + (y_{ref_i} - y_{m_i})^2} \quad (5)$$

for each time step  $t_i$ .

#### IV. NUMERICAL RESULTS AND CONCLUSIONS

As a predefined desired position accuracy the value of 1 cm was taken. The question was: is the used model sophisticated enough and which a-priori information has to be used to reach predetermined accuracy after filtering. From the numerical results it was concluded that the main problem to perform Kalman filter is defining process noise. In the figure 1 the filtering for best process noise covariance matrix is given.

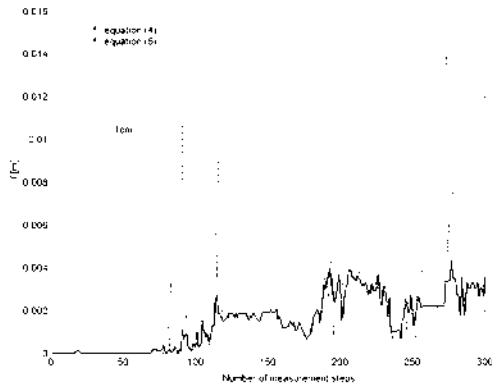


Figure 1: Perpendicular distance from reference trajectory

For this value of process noise the convergence of process noise covariance matrix trace is reached. Accordingly also standard deviations of position components converge. The standard deviations for horizontal position are  $s_x = 2$  mm and  $s_y = 5$  mm.

In this work the Kalman filter was implemented for kinematical measurements with electronic tachymeter for the first time. The conclusions are:

- The position accuracy of tachymeters from TPS1100 *Leica Geosystems* series for kinematical measurements is up to few centimetres and depends on the velocity of moving object.
- The model is appropriate for evaluating kinematical observations only when sufficient a-priori information is known.

In future work linearized and adaptive Kalman filter will be developed and researched. The capabilities of tachymeters from new TPS1200 series for kinematical processes should be analysed. Because the convergence of covariance matrix is not sufficient merit of filter efficiency other statistical merits should be incorporated to get convenient estimation of filtering when the reference trajectory is not known.

#### ACKNOWLEDGMENTS

I would like to thank prof. Thomas A. Wunderlich, dr. Karl Foppe, Peter Wasmeier and Thomas Schäfer at Chair for Geodesy, Technical University Munich, and dr. Werner W. Stempfhuber from *Leica Geosystems* for their help and advice during my stay in Munich. I would like to thank DAAD for their financial support.

#### REFERENCES

- [1] S. Bogatin, K. Foppe, Th. A. Wunderlich, P. Wasmeier, Th. Schäfer. Evaluation of linear Kalman filtering for TPS observations using known trajectory. In review.
- [2] R. G. Brown, P. Y. C. Hwang. Introduction to random signals and applied Kalman filtering. John Wiley & Sons, 2<sup>nd</sup> edition, 1992.
- [3] H. W. Sorenson. Least-squares estimation: from Gauss to Kalman. Reprinted for IEEE Spectrum, vol.7, pages 63-68, 1970.
- [4] W. V. Stempfhuber. Ein integritätswahrendes Messsystem für kinematische Anwendungen. Dissertaton. Fakultät für Bau- und Vermessungswesen, TUM, 2004.
- [5] W. Welsch, O. Heunecke, H. Kuhlmann. Handbuch Ingenieurgeodäsie – Auswertung geodätischer Überwachungsmessungen. Herbert Wichmann Verlag, Heidelberg, 2000.

# Effective transmission over AWGN channel using Turbo codes

Lubomír Čopjan and Stanislav Marchevský (Faculty Mentor)  
Department of Electronics and Multimedia Communications  
Technical university of Košice  
Košice, Slovak Republic

Email: [lubomir.copjan@tuke.sk](mailto:lubomir.copjan@tuke.sk), [stanislav.marchevsky@tuke.sk](mailto:stanislav.marchevsky@tuke.sk)

**Abstract** — In this paper, powerful Forward error correction technique, called Turbo codes, is described. Experimental results with five different  $E_b/N_0$  values, made in Matlab and the System View environment, will show, how useful this method is, when transmitted signal is corrupted by AWGN noise.

## I. INTRODUCTION

Transmitted signals are in real communication channels corrupted by noise. To reduce this problem, many correction techniques were invented. In 1993 Berrou and Glaviueux proposed the form of parallel concatenated codes, called Turbo codes, which allow reliable transmission of information at rates near the Shannon limit. Nowadays, they are used in many applications, as digital video broadcasting, or space telemetry.

## II. AWGN CHANNEL

The most common noise in real channels is Additive White Gaussian Noise (AWGN).

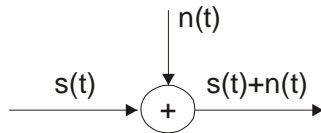


Figure 1: Corruption of the signal

As the Figure 1 depicted, to the transmitted signal  $s(t)$ , the AWGN noise is added. This noise has Gaussian (Normal) distribution with a variate  $x$ , mean  $\mu$  and variance  $\sigma^2$  and is described by Equation (1) [1][2][5].

$$P(x) = \frac{1}{\sigma\sqrt{2\pi}} \exp\left(-\frac{(x-\mu)^2}{2\sigma^2}\right) \quad (1)$$

## III. TURBO ENCODING

In the classical Turbo codes theory, for encoding information bit sequence, two Recursive Systematic Convolutional (RSC) encoders are used. They are usually identical. Each RSC encoder produces parity bits. The interleaver, which is used before for the second encoder, as shows Figure 2., ensures the permutation of the sequence of input bits. It is also possible to use puncturing and so not all parity bits are sent to the channel. Encoding is frame oriented [3].

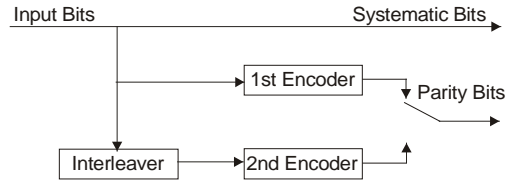


Figure 2: Turbo encoder

## IV. PRINCIPLE OF ITERATIVE DECODING

Because of the Turbo codes encoder consists of two RSC encoders, the decoder composes of two soft input/output decision decoders, as shows Figure 3. Each decoder has three inputs: systematic bits  $x$ , one half of parity bits  $y$  and a priori information  $\lambda$ . The aim of both decoders is to produce a posteriori probabilities for all input samples. Of them, extrinsic information are computed and used as a priori probability (APP) in the next iteration (in the first iteration is not for the first decoder available). These probabilities are used to reduce bit error rate (BER) ratio and so improve results in the next iteration. There are two well-known methods to obtain these APP's, Viterbi algorithm and Maximum A Posteriori (MAP) algorithm. Experiments showed that the second one has better performance. To reduce its complexity, log-MAP modification was created to compute log-likelihood ratio, which is defined as:

$$\Lambda(b_k) = \log \left[ \frac{P[b_k = 1 | r(t)]}{P[b_k = 0 | r(t)]} \right] \quad (2)$$

where  $r(t)$  describes corrupted signal  $s(t)$  and  $b_k$  denotes the input bit [4].

Deinterleaver insures a reverses process to interleaver.

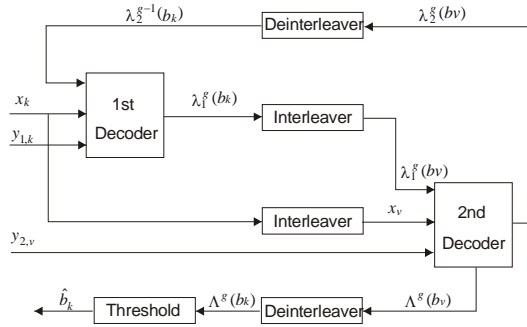


Figure 3: Iterative Turbo Decoder

Very important is a number of iterations. The iterative process continues in this manner until further iterations yield little or no significant improvement. After the last iteration, hard decision on the information bits is made. Generally written:

$$\hat{b}_k = \begin{cases} 0 \dots \Lambda(b_k) < 0 \\ 1 \dots \Lambda(b_k) \geq 0 \end{cases} \quad (3)$$

## V. EXPERIMENTAL RESULTS

In this section, our simulation results from Matlab and System View environment are presented. For encoding block of the 10.000 bits, we used identical RSC encoders and pseudo-random interleaver. Encoded samples, transmitted with five different  $E_b/N_0$  values, were damaged by Gaussian noise. On the Figure 4., simulation results after 6 iterations of Turbo decoding are depicted.

## VI. CONCLUSION

There is currently a significant interest in Turbo codes. They became a part of many standards (for example CDMA2000). They are very interesting for multiuser communication systems, like CDMA, where are used for interference cancellation and show very good performance. My future research will be focused on adaptive multiuser detection algorithms for CDMA systems, especially on "blind" algorithms, which don't need a training sequence to estimate some important parameters of the environment. To improve performances of these systems,

Turbo codes for a forward error correction will be exploited.

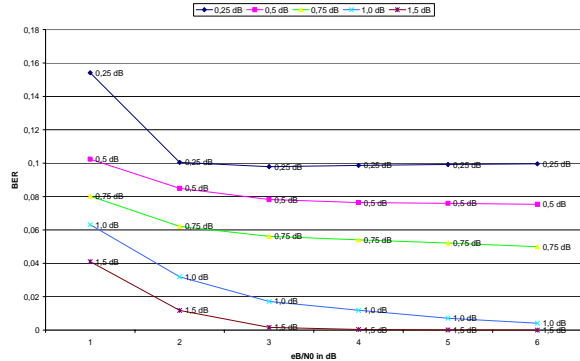


Figure 4: Experimental results

## ACKNOWLEDGMENTS

The work presented in this paper was supported by Grant of Ministry of Education and Academy of Science of Slovak republic VEGA under Grant No. 1/1057/04.

## REFERENCES

- [1] L. Doboš, J. Dúha, S. Marchevský and V. Wieser. Mobilné rádiové siete. Vydavateľstvo Žilinskej univerzity EDIS, Žilina, Slovak Republic, 1<sup>st</sup> edition, 2002.
- [2] V. Wieser. Adaptation Methods in Mobile Communications Networks. Advances in Electrical and Electronic Engineering, Žilinská univerzita, Vol. 2/2003, pages 27-31, Žilina, Slovak Republic, 2003.
- [3] C. Berrou, A. Glavieux and P. Thitimajshima. Near Shannon limit error-correcting coding and decoding: Turbo Codes. In Proceedings of the IEEE International Conference on Communications, number 2, pages 1064-1070, Geneva, Switzerland, May 1993.
- [4] B. Sklar. A primer on turbo code concepts. IEEE Communications Magazine, Vol.35, no. 12, pages 94-102, December 1997.
- [5] I. Baroňák and P. Kvačkaj. Submission to CAC. Communications, Scietific Letters of the University of Žilina, volume 6, pages 80-83, Žilina, Slovak Republic, April 2004.

# The Steepest Descent Method Used for Indirect Frequency Estimation

Jakub Džubera and Dr. Aleš Prokeš  
 Dept. of Radio Electronics, FEEC  
 Brno University of Technology  
 Brno, Czech Republic

Email: xdzube00@stud.feec.vutbr.cz, prokes@feec.vutbr.cz

**Abstract** — This contribution is focused on an indirect estimation of carrier frequency offset which is used in carrier recovery process. The carrier frequency offset is estimated from the received signal to be eliminated. Then an accurate carrier waveform is synthesized. It is used for correct demodulation. The steepest descent optimization method is chosen for the estimation process. It is implemented in Matlab as a dual phase locked loop system and examined. The time dependencies of phase offset estimates and recovered message signal are the results of simulation.

## I. INTRODUCTION

The three main channel parameters required by the most receivers for the correct signal demodulation are the carrier frequency, the carrier phase (which is not need for non-coherent demodulation), and the symbol timing of the received signal. The carrier frequency of the received signal may differ from the carrier frequency of transmitter. The main goal is to estimate the exact carrier frequency from the received signal and to synthesize new carrier frequency waveform which can be used for demodulation. Optimization methods based on the steepest descent approach can be successfully utilized.

## II. SYSTEM MODEL

Dual PLL (*Phase Locked Loop*) system [2] presented at the Figure 1 is used for this research and for the Matlab implementation. This system provides the carrier phase estimation which can be used for the carrier frequency offset elimination thanks to a very close connection between the signal's frequency and its phase. The system is based on an optimization of a particular cost function which can be derived from a signal's representation in an input of a receiver [2]:

$$F(\theta) = \frac{1}{2} \text{LPF}\{r(kT_s) \cos(4\pi f_c kT_s + 2\theta)\} \quad (1)$$

where LPF symbolizes low pass filtering,  $r(kT_s)$  symbolizes the received signal,  $T_s$  is a sampling pe-

riod,  $f_c$  and  $\theta$  are the carrier frequency and phase, respectively.

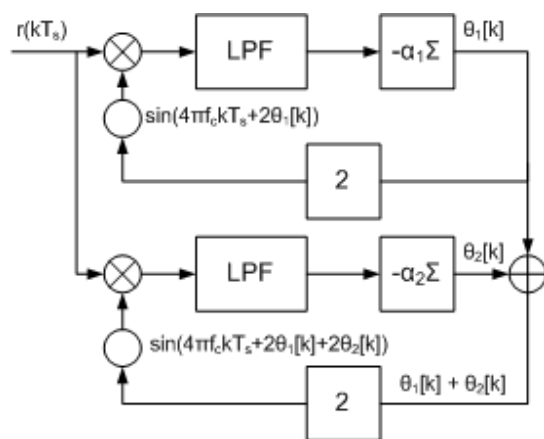


Figure 1: Dual PLL system used in model

The gradient method called ‘Steepest Descent’ is suitable and can be applied to solve this carrier offset estimation problem. The  $F(\theta)$  cost function needs to be maximized while the derivation with respect to  $\theta$  is applied. The derivation leads to the adaptive elements which are described by following formulas:

$$\begin{aligned} \theta_1[k+1] &= \theta_1[k] - \alpha_1 \text{LPF}\{r(kT_s) \sin(4\pi f_c kT_s + 2\theta_1[k])\} \\ \theta_2[k+1] &= \theta_2[k] - \alpha_2 \text{LPF}\{r(kT_s) \sin(4\pi f_c kT_s + 2\theta_1[k] + 2\theta_2[k])\} \end{aligned} \quad (2)$$

where  $\theta_1$  and  $\theta_2$  are the estimated phase elements and  $\alpha_1$  and  $\alpha_2$  are the iterative stepsizes.

## III. IMPLEMENTATION AND SIMULATION

The equations (2) above are suitable for Matlab implementation and they create a core of a system simulating receiver performance. The simulation model processes an  $N$ -level square binary message signal which is modulated using ASK modulation and particular carrier frequency. The receiver section pre-processes the received signal by squaring and filtering with a bandpass filter with a centre frequency of  $2f_c$ . The carrier frequency of the local

oscillator is set to be different from the carrier frequency of the received signal to simulate a frequency offset. Figure 2 shows the estimated phase offsets  $\theta_1$  and  $\theta_2$  which results in a frequency offset elimination. These estimated phase offsets are used in following operation for synthesis of a carrier frequency used in demodulation process.

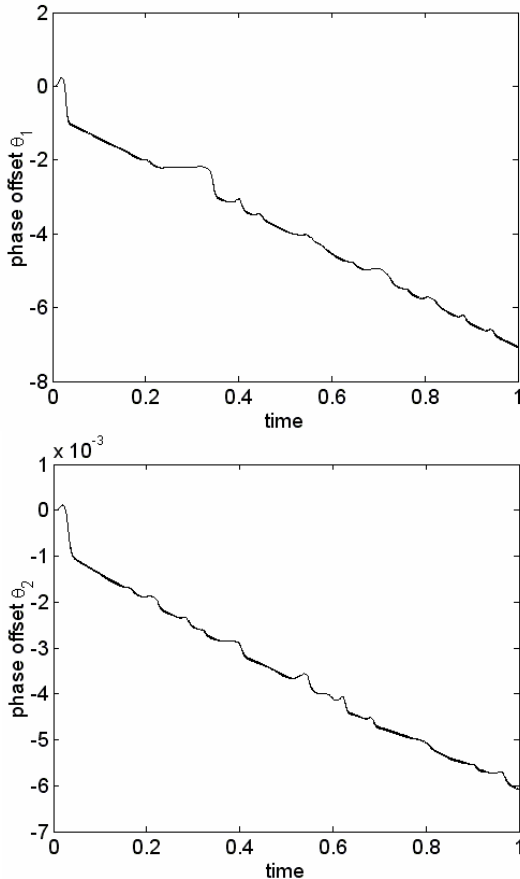


Figure 2: Phase offset  $\theta_1$  (top) of the top loop and  $\theta_2$  (bottom) of the bottom loop

Figure 3 shows a comparison of the original message signal and the recovered message signal when the synthesized carrier is applied. A slight time shift is observable. The ratio between the carrier frequency of the received signal and the local oscillator was set to 1.001. The ‘unknown’ received signal phase was set to  $-0.25\pi$  and the iterative stepsizes  $\alpha_1$  and  $\alpha_2$  to  $5 \cdot 10^{-6}$  and  $5 \cdot 10^{-9}$ , respectively. The initial phase offsets  $\theta_1(0)$  and  $\theta_2(0)$  were set to 0.

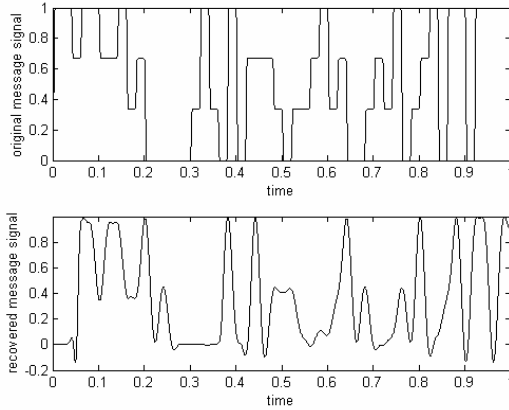


Figure 3: Original (top), recovered (bottom) signal

#### IV. CONCLUSIONS

The examined PLL system is very reliable and provides accurate synthesis of both the carrier frequency and phase. The main disadvantage is its sensitivity to initial setting and the setting of stepsizes  $\alpha_1$  and  $\alpha_2$ . High stepsize values lead to inaccurate phase estimation and incorrect demodulation. Reversely, extremely small values are ineffective and slow down the estimation process. It was found out that for the rough phase estimation the top PLL is sufficient. The following work is focused on examining the system performance when affected by noise. The comparison with a different optimization method will be done. The Newton’s method was chosen.

#### ACKNOWLEDGMENTS

This work has been supported by the doctoral project of the GACR (Czech Science Foundation) No. 102/03/H109 „Methods, Structures and Components of Electronic Wireless Communication“ and with the support of the research plan MSM0021630513 „Electronic Communications Systems and Technologies of New Generation“.

#### REFERENCES

- [1] T. F. Wong, T. M. Lok. Theory of Digital Communication. University of Florida 2004.
- [2] C. R. Johnson, A. W. Sethares. Telecommunication Breakdown. Upper Saddle River, Prentice Hall 2003.
- [3] W. H. Tranter, K. S. Shanmugan, T. S. Rappaport, K. L. Kosbar. Principles of Communication System Simulations with Wireless Applications. 1st ed, New Jersey, Prentice Hall 2004.

# Structuring Architectural Services in the DECOS Integrated Architecture

Christian El Salloum and Hermann Kopetz (Faculty Mentor)  
Institute of Computer Engineering, Vienna University of Technology  
Email: [salloum@vmars.tuwien.ac.at](mailto:salloum@vmars.tuwien.ac.at)

**Abstract** — “Integrated” systems are characterized by the integration of multiple application subsystems within a single distributed computer system. A central issue in the DECOS integrated architecture is the provision of standardized, validated and certified architectural services that facilitate the development of distributed real-time applications. We propose a layered model that supports the provision of a scalable and configurable set of architectural services for mixed-criticality subsystems. In order to show the feasibility of our approach, a prototype implementation of a DECOS cluster was developed.

## I. BACKGROUND

Distributed real-time systems are increasingly being used for control safety-critical functions in automotive, aerospace and space applications for civil or military purposes. Examples are steer-by-wire, fly-by-wire, missile guidance systems and many other control systems.

At present, the design of large and complex safety-critical systems often follows a “federated” design philosophy, where each application subsystem has its own dedicated distributed computer system. Federated systems have been preferred for ultra-dependable applications since the inherent separation of application subsystems simplifies fault-isolation and complexity management.

Contrary to a federated system an “integrated” system is characterized by the integration of multiple application subsystems within a single distributed computer system [1]. Since different application subsystems share the available hardware resources (computational nodes and the communication network) the total number of required nodes and communication resources can be significantly reduced compared to the federated approach (modern luxury cars incorporate up to 75 Electronic Control Units (ECUs) [2]).

The objective of the European IST project DECOS (IST-511764) is to devise an integrated architecture that provides a framework for integrating multiple application subsystems within a single distributed computer system while retaining the fault-isolation, fault-containment and complexity-management benefits of a federated system [1].

## II. PROBLEM STATEMENT

The DECOS architecture [1] offers a framework for the development of distributed embedded real-time systems integrating multiple subsystems with different levels of criticality and different requirements concerning the underlying platform.

A central issue in the DECOS integrated architecture is the provision of standardized, validated and certified architectural services that facilitate the development of distributed real-time applications. The problem on which we focus in this work is how to structure these services

and how to provide them to the applications. Figure 1

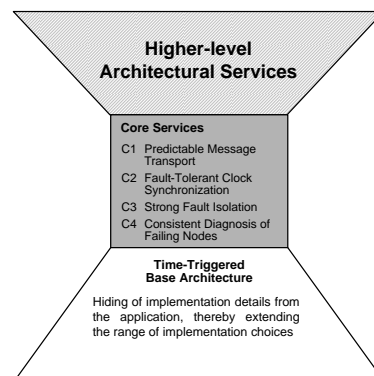


Figure 1: DECOS Architecture

depicts the hierarchical structure of the DECOS architecture. The architecture is based on a minimal set of *core services*. The core services include predictable time-triggered message transport, fault tolerant clock synchronization, strong fault isolation, and consistent diagnosis of failing nodes. Any architecture that provides these core services can be used as a base architecture for the DECOS integrated distributed architecture. An example of a suitable base architecture is the Time-Triggered Architecture (TTA) [3].

Based on the core services, higher-level architectural services should be realized. Since the DECOS architecture is intended to be used in multiple heterogeneous application domains where each domain has its own specific demands, a *diverse, configurable, scalable, and open* set of architectural services has to be provided. Openness means in this sense, that third party developers should be allowed to add additional domain-specific services to the architecture. Since freely added services can not always be assumed to be free from software faults, error containment with respect to architectural services is a key issue.

In the following chapter we propose a layered model for higher-level architectural services that supports the open integration of additional services without compromising the dependability of already existing services.

## III. PROPOSED MODEL

The proposed approach divides the set of architectural services into two distinct layers: A stable and trusted set of *Generic High-level Services*, and based on these services an extensible and open set of *Domain Specific Services* (see Figure 2).

### A. GENERIC HIGH-LEVEL SERVICES

In the DECOS architecture, the application services of the integrated system that are provided at controlled object interfaces are divided into a set of nearly-

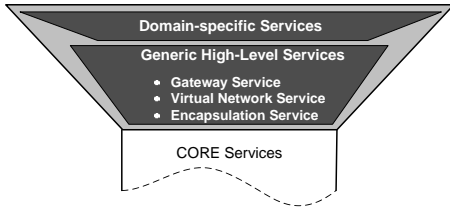


Figure 2: Architectural Services

independent Distributed Application Subsystems (DASs) where each DAS provides a distinct functionality (e.g. a brake-by-wire DAS or a multimedia DAS in a car). Each DAS is further decomposed into smaller units called *jobs* which are the basic unit of distribution and the Fault Containment Regions (FCRs) for software faults [1].

The *generic high-level services* encompass a set of services that support a DAS-centric design flow. Among the generic high-level services are the *encapsulation service* that establishes so-called *partitions*, where each partition functions as an encapsulated execution environment for a single job (establishes an FCR for software faults) and the *virtual network services* [4] which realize encapsulated communication infrastructures for single DASs. The generic high-level services are provided via the so called *Platform Interface (PI)* to the jobs of a DAS (figure 3).

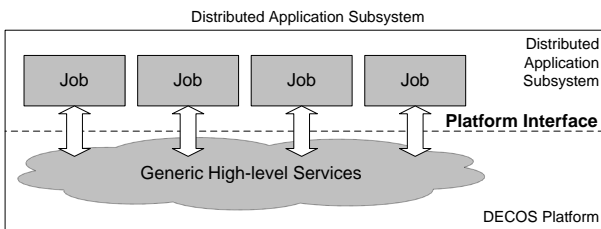


Figure 3: Platform Interface

## B. DOMAIN-SPECIFIC SERVICES

In order to provide a simple and stable baseline for application development only a small set of selected services is provided natively via the PI. For many applications these services will be sufficient, but in some cases (e.g. incorporation of legacy systems) they might have to be extended or refined. Such domain-specific services are realized on top of the PI in a dedicated layer within the application job. We call this layer the *application middleware* and its interface the *Application Programming Interface (API)* (see Figure 4).

In contrast to the PI the API is not considered to be a single stable interface. Each application middleware provides its own specific set of services, and thus has its own dedicated API which may conform to an existing open or proprietary standard (e.g. TCP/IP or CAN [5]). The concept of the job-internal application middleware enables the addition and the removal of domain-specific services without changing the PI or the underlying platform.

By placing the application middleware within the job, the domain-specific services become part of the job's fault-containment region. This leads to an architecture where a given application middleware can be certified according to the criticality level that is sufficient for the DASs in which it will be actually used, and does not have to be certified according to the highest criticality level

within the system.

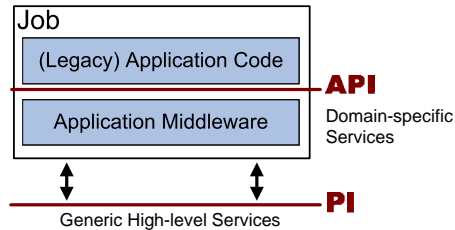


Figure 4: PI versus API

## IV. RESULTS AND IMPLEMENTATION

We have proposed a layered model that supports the provision of a scalable and configurable set of architectural services for mixed-criticality subsystems in an integrated architecture. On the basis of a generic and stable platform interface, domain-specific services can be freely added by third party developers by means of a specific application middleware. The architecture enforces error containment in a way that the impact of a design fault in a given domain-specific service is restricted to distributed application subsystems that incorporate the corresponding application middleware realizing that service.

In order to show the feasibility of our approach, a prototype implementation of a DECOS cluster was developed [6].

## REFERENCES

- [1] H. Kopetz, R. Obermaisser, P. Peti, and N. Suri. From a federated to an integrated architecture for dependable embedded real-time systems. Technical Report 22, Technische Universität Wien, Institut für Technische Informatik, Treitlstr. 1-3/182-1, 1040 Vienna, Austria, 2004.
- [2] A. Deicke. The electrical/electronic diagnostic concept of the new 7 series. In *Convergence International Congress & Exposition On Transportation Electronics*, Detroit, USA, October 2002.
- [3] H. Kopetz and G. Bauer. The time-triggered architecture. *IEEE Special Issue on Modeling and Design of Embedded Software*, January 2003.
- [4] R. Obermaisser, P. Peti, and H. Kopetz. Virtual networks in an integrated time-triggered architecture. In *Proceedings of the 10th IEEE International Workshop on Object-oriented Real-time Dependable Systems (WORDS2005)*, pages 241–253, Sedona, Arizona, February 2005.
- [5] CAN Specification, Version 2.0. Robert Bosch GmbH, Stuttgart, Germany, 1991.
- [6] B. Huber, P. Peti, R. Obermaisser, and C. El Salloum. Using RTAI/LXRT for partitioning in a prototype implementation of the DECOS architecture. In *Proceedings of the Third International Workshop on Intelligent Solutions in Embedded Systems*, pages 3–16, 2005.

# A Remote and Transparent Approach for the Test and Diagnosis of Automotive Networks

Eric Armengaud and Andreas Steininger (Faculty Mentor)  
Vienna University of Technology  
Embedded Computing Systems Group E182-2  
Treitlstr. 3, A-1040 Vienna  
{armengaud, steininger}@ecs.tuwien.ac.at

**Abstract** — *The aggressive competition that occurs in the automotive domain leads to a high demand for improvements on the car manufacturers. Nowadays, most of the innovations emanate from electronics and the use of communication networks. While this new system architecture decreases costs and enables the development of new functionalities, it hardly requires high dependability since the consequences in case of failure might be catastrophic. To that aim, accurate testing – both during the development phases and during field operation – is required. It is the aim of this work to present an approach for testing time-triggered communication services such as the FlexRay protocol (a) transparently to the system architecture and (b) transparently to the system operation.*

## I. INTRODUCTION

Over 20% of the costs of a high-end car are caused by the price of electronics [1], and this percentage increases rapidly. Point-to-point wiring, for the connection between sensors, controllers and actuators, is reaching its limitations and is being replaced by bus systems such as CAN, LIN, MOST or FlexRay. The usage of bus systems does not only reduce the overall costs, but also improves system reliability and makes local information globally available, thus inspiring various additional services. Such services are convenience features (e.g., electrical window control), engine control (e.g. fuel injection), and safety-critical systems such as "X-by-Wire". Some of these applications require high dependability since human life or health are directly concerned. Hence, systematic test campaigns are necessary to guarantee the required reliability. The ExTraCT<sup>1</sup> project is dedicated to the development of a novel method to enable the transparent testing of the communication network. This paper provides an overview of the project's topic and presents our approach and the research results attained so far. The next section discusses the challenges of testing automotive networks. Then, Section 3 presents our transparent approach, and finally the results attained so far are summarized in Section 4.

<sup>1</sup>The ExTraCT-project received support from the Austrian FIT-IT Embedded Systems initiative, funded by the Austrian Ministry for Traffic, Innovation and Technology (BMVIT) and managed by the Austrian Research Promotion Agency (FFG) under grant 810834. See <http://www.ecs.tuwien.ac.at/~armengaud>

## II. CHALLENGES

Today's automotive applications are typically implemented as complex distributed systems with several tens of electronic control units. Testing such distributed systems is especially complex due to *the state explosion*, which results from the concurrent process operation and reinforced by the fact that each new input combination might lead to a new program execution path. A second reason is *the presence of race conditions* [2] and the difficulty to observe the system without adding a probe effect. Moreover, *the real-time nature* of the system and the presence of timing constraints gives a new dimension to the test operations. Correctness, in the context of real-time systems, not only depends on the logical results of the computations but also on the time when these results are produced [3]. Finally, *the lack of test support* due to the high degree of system integration increases furthermore the complexity [4].

It is the aim of this work to present a novel framework for the transparent tests of the FlexRay protocol [5]. *Transparent*, in our case, describes two attributes. First, transparent in the sense of non-intrusive, means to keep the nodes unmodified and consequently do not change their behavior neither in the value domain nor in the time domain. Second, transparent in terms of system operation, to enable continuous service delivery during test execution, and therefore avoid system interruption while testing.

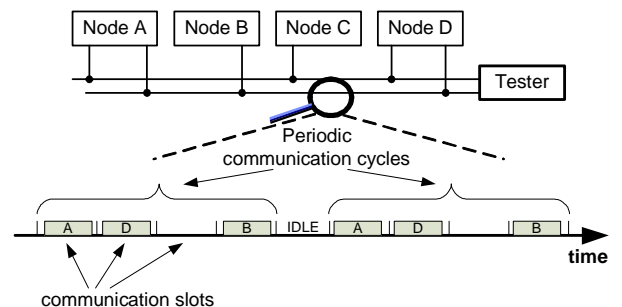


Figure 1: System architecture

### III. THE TRANSPARENT APPROACH

Our approach is based on the TDMA scheme implemented in time-triggered protocols [6] such as FlexRay. This medium access scheme defines time windows (communication slots), which are uniquely assigned to the nodes for message transmission within a periodic communication cycle (see Figure 1). The involved nodes require periodic synchronization to correct local clock drifts and agree on a unified view of time.

The basic idea of our approach is to send test frames to influence the nodes' clock correction mechanisms and forces them to follow a non conventional but still correct progress. For that, a tester node is connected to the bus as illustrated in Figure 1. The transmission time of the messages generated by the node(s) under test can be analyzed to check whether their local clock correction mechanism was affected by the test frames – which signifies that the test frames were correctly received – or not. This approach is based on the fact that erroneous frames are disregarded by the clock synchronization algorithms.

### IV. RESULTS AND FUTURE WORK

The main results so far are the publication of the presented concepts [7] and the submission of a new remote diagnosis approach. Furthermore, first tests have been run on a prototype to validate our approach. During this experiment, we have considered a cluster consisting of two nodes with a communication cycle length of  $3000\mu\text{s}$ . In addition a tester generated two stimulus messages with the aim to drive the cycle length down to  $2998\mu\text{s}$ . All messages were fault free except for communication cycles 1930 to 1940 during which both stimulus messages exhibit header CRC errors. Figure 2 pictures the cycle length of the four frames over time. As expected, the test cluster integrated to the existing network traffic, and stayed synchronous during the whole experiment. Furthermore, the faulty frames lead to a reaction of the nodes under test but did not crash the communication. The errors contained in these messages were correctly detected (thus providing evidence for the proper operation of the CRC checker) and discarded from the internal clock correction computation.

The principal benefit of this approach is its transparency, both in terms of architecture (non-intrusive) and system operation (concurrent execution). The non-intrusiveness, first, is reached by the exploitation of the existing loop-back from the clock correction in TDMA schemes. The nodes building the cluster under test have not been modified during this experiment. Second, this simple experiment illustrated the transparency for the system. Indeed, the additional frames generated by the carrier were ignored by the application, and the two frames originally building the communication were

transmitted without any disturbance. Consequently, the system under test delivered its expected services while the test performed in a real environment.

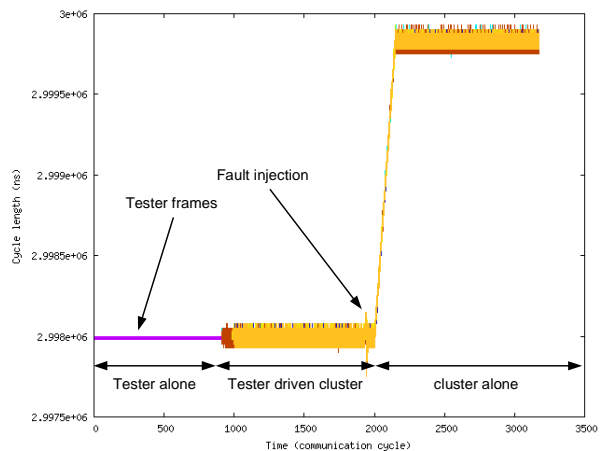


Figure 2: Preliminary experiment

Future work will be directed towards the evaluation of the transparency for the system (has this stimulus any influences on the system dependability or performance?). Furthermore, the achievable test coverage and the need to couple with other test methods have to be examined.

### REFERENCES

- [1] G. Leen, D. Heffernan, and A. Dunne. Digital Networks in the Automotive Vehicle. *Computing & Control Engineering Journal*, 10(6):257–266, 1999.
- [2] Charles E. McDowell and David P. Helmbold. Debugging Concurrent Programs. *ACM Comput. Surv.*, 21(4):593–622, 1989.
- [3] Hermann Kopetz. *Real-Time Systems: Design Principles for Distributed Embedded Applications*. Kluwer Academic Publishers, Norwell, MA, USA, 1997.
- [4] W. Schütz. Fundamental Issues in Testing Distributed Real-Time Systems. *Real Time System Journal*, 7(2):129–157, 1994.
- [5] Flexray Communications Systems – Protocol Specification Version 2.1. FlexRay Consortium, 2005.
- [6] Hermann Kopetz and Günther Bauer. The Time-Triggered Architecture. *Proceedings of the IEEE*, 91(1):112 – 126, January 2003.
- [7] Eric Armengaud. ExTraCT: A New Approach for the Transparent Test of Time-Triggered Communication Services. In *Proceedings of ITG 2006 (to appear)*, March 2006.

# Peak to Average Power Ratio Reduction in M-modification of MC-CDMA

Zbyněk Fedra and Vladimír Šebesta (Faculty Mentor)

Dept. of Radio Electronics, FEEC

Brno University of Technology

Brno, Czech Republic

Email: xfedra01@stud.feec.vutbr.cz

**Abstract** — This paper describes the new PAPR (peak to average power ratio) reduction approach in MC-CDMA (multicarrier code division multiple access) system (in so called M-modification). The spreading sequence introduces coherence among subcarriers. This is used for chip position formatting to PAPR minimization. The optimization method is used to get best chip interleaving sequence (namely Genetic Algorithm (GA)). The complementary cumulative distribution function (CCDF) of PAPR for original and optimized approach is introduced.

## I. INTRODUCTION

Multicarrier code division multiple access (MC-CDMA) combines orthogonal frequency division multiplexing (OFDM) with code division multiple access (CDMA) [1]. Resulted system has advantage in frequency diversity and multiple access capability. The systems based on OFDM suffer by high PAPR (peak to average power ratio) [2]. Numerous methods for PAPR reduction exist for OFDM and can be used for MC-CDMA, but usage of spreading code gives other possibilities to PAPR reduction.

## II. SYSTEM MODEL

The basic transmitter structure is similar to OFDM. Different symbols are transmitted on the subcarriers in OFDM, but MC-CDMA transmits same symbol on several subcarriers. Each subcarrier transmits part of the spreaded symbol (called chip). Let the number of subcarriers ( $N_c$ ) is equal to spreading code ( $c$ ) length. Then one user signal can be written as:

$$x^l(t) = \frac{1}{N_c} \sum_{n=0}^{N_c-1} b^l c_n^l e^{j2\pi f_n t}, \quad 0 \leq t \leq T_s, \quad (1)$$

where  $x^l(t)$  is  $l$ -th user signal,  $b^l$  is data symbol of  $l$ -th user,  $c_n^l$  is  $n$ -th chip of  $l$ -th user and  $f_n$  is frequency of  $n$ -th subcarrier (Figure. 1). Spreading code length has not necessarily to be equal to the number of all subcarriers. Some modifications are presented in [3] for complexity reduction and flexible system design. The M-modification [3] of MC-CDMA is considered. One user (uplink) and Walsh sequences with spreading factor of

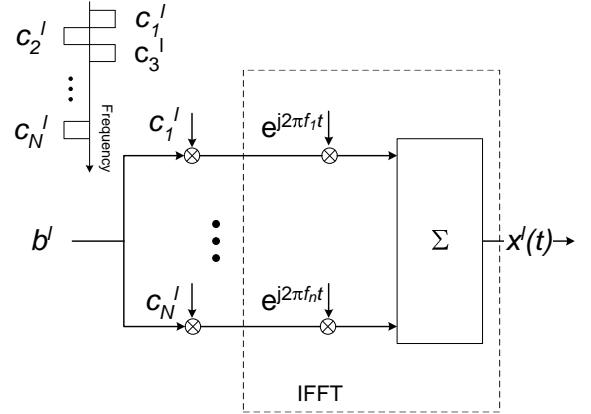


Figure 1: MC-CDMA model.

four are used for 48 data subcarriers BPSK modulated. 64 IFFT inputs are formatted according to Figure 2. After spreading, chips are sorted (Figure 3) to IFFT input.

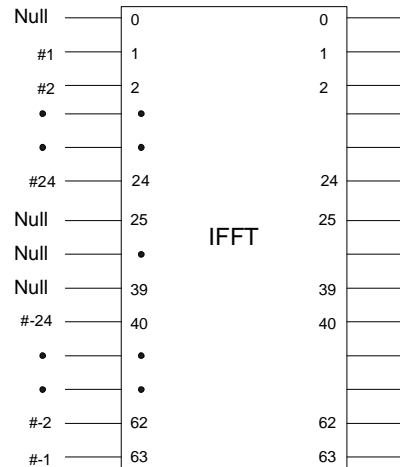


Figure 2: Block of IFFT.

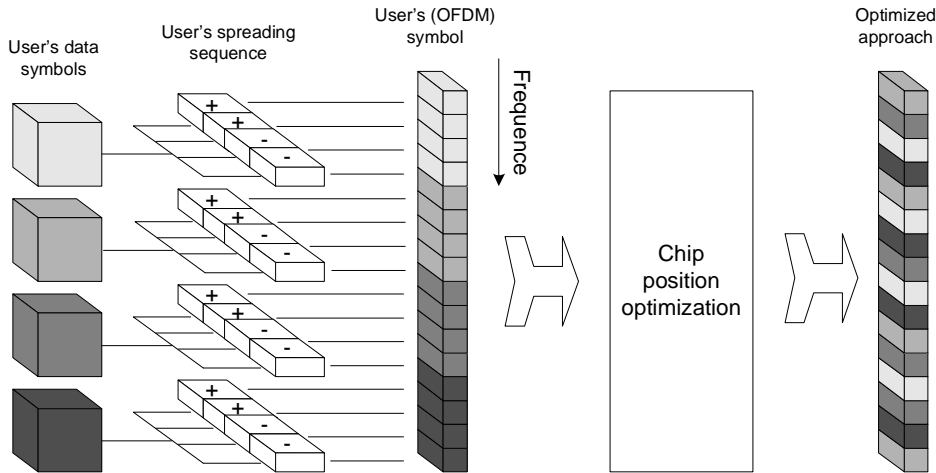


Figure 3: M-modification of MC-CDMA and its optimization.

The new approach is coming-out from chip sorting. The optimal (in case of PAPR minimization) chip interleaving pattern is searched.

### III. OPTIMIZATION AND RESULTS

There exist  $1,24 \times 10^{61}$  combinations for 48 data subcarriers. Genetic algorithm (GA) was used for PAPR optimization. The mean PAPR for all spreading sequences and all combinations of data bits is used as criterion. The result of GA is scrambled sequence for chip mapping. The Figure 4 shows complementary cumulative distribution function of PAPR for original and M-modification

and for optimized approach. The peak PAPR (with low probability) remains, but for example the probability that  $PAPR > 8\text{dB}$  is about 70% for original and less than 10% for optimized approach.

### IV. CONCLUSION

This PAPR reduction can be used for uplink in M-modification MC-CDMA. Realization of this approach can be made by interleaving (not classical matrix, but by the rule), where all users in system have the same interleaving pattern to preserve orthogonality among the users. The main advantage of this approach is small complexity (only modified interleaving), no performance degradation and no side information.

### ACKNOWLEDGMENTS

This work has been prepared as the part of the solution of the Grant Agency of Czech Republic grants no. 102/03/H109 and 102/04/0557 and with support of the research plan MSM 0021630513.

### REFERENCES

- [1] S. Hara and R. Prasad. Overview of multicarrier CDMA. *IEEE Communication Magazine*, 35(12), 1997.
- [2] L. Hanzo, M. Münster, B. J. Choi, and T. Keller. *OFDM and MC-CDMA for Broadband Multi-User Communications, WLANs and Broadcasting*. John Wiley & Sons, 2003.
- [3] K. Fazel and S. Kaiser. *Multi-Carrier and Spread Spectrum Systems*. John Wiley & Sons, 2003.

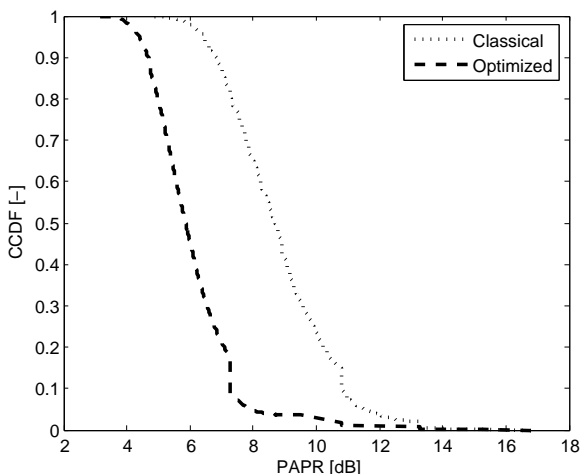


Figure 4: CCDF of PAPR for classical and optimized M-modification

# Security in Building Automation

Wolfgang Granzer and Wolfgang Kastner  
Institute of Computer Aided Automation, Automation Systems Group  
Vienna University of Technology  
Vienna, Austria  
Email: {wgranzer, k}@auto.tuwien.ac.at

**Abstract** — *Nowadays, a tighter integration of formerly dedicated stand-alone building automation systems (BAS) is desirable. Since extending BAS towards new application areas increases the demands on the BAS architecture, available BAS solutions are not suitable anymore.*

*In this paper, a security architecture for KNX/EIB called EIBsec is described. This extension supports mechanisms that guarantee data integrity, confidentiality and freshness as well as authentication. Using these services, secure process data and management communication can be provided. Additionally, other important issues such as key management and distribution are also addressed.*

## I. INTRODUCTION

Building Automation Systems (BAS) aim at improving control, monitoring and administration of technical building subsystems and interaction among devices typically found in buildings. The core BAS application area is environmental control with the traditional service types lighting/daylighting and Heating, Ventilation and Air conditioning (HVAC) systems.

Extending BAS towards new application areas allows improvements in building control and cost reductions. Furthermore, management and configuration of an integrated BAS becomes easier, since a variety of different management solutions can be replaced by a single tool. Obviously, the demands on a more sophisticated BAS controlling different subsystems increase. This is especially true for the integration of security critical applications (e.g. access control and security alarm systems). They force the underlying control system to be reliable and robust against malicious manipulations (security attacks) to fulfil their purpose. To provide a secure environment for security critical applications, the control system itself must integrate mechanisms which provide an effective and efficient protection against such security attacks. Thus, in a networked BAS, the control network protocol has a key role in providing the required protection.

## II. SECURITY DEMANDS

To begin with, it is necessary to protect the exchanged process data (secure process data communication) as well as prevent unauthorised use of the management services which are used for configuration and maintenance purposes (secure management communication). For these types of secure communication, two essential elements are required.

On the one hand an authentication mechanism is necessary, verifying the claimed identities of the communication partners. On the other hand, a secure transmission channel is necessary to protect the transmission of data between authenticated participants against malicious interference. The main objectives of such a secure transmission channel are data confidentiality, data integrity and data freshness (see [1]). This secure channel can be accomplished by cryptographic algorithms, making use of keys. To prevent unintended disclosure of keys, a sophisticated key management facility is necessary which must offer the opportunity to generate and distribute the necessary keys in a secure manner.

Since networked BAS can consist of hundreds or even thousands of devices, scalability of the implemented mechanisms is also essential. Finally, a dedicated update mechanism that allows distributing software patches in an easy and secure manner is often desirable.

## III. STATE OF THE ART

In the building automation domain, many different solutions exist. In previous work (see [1]), the security aspects of three popular BAS (LONWorks [2], BACnet [3] and KNX/EIB [4]) were analysed revealing that neither LONWorks nor KNX/EIB support the necessary mechanisms to satisfy the above mentioned requirements. The integrated security concepts are very rudimentary and not suitable for the use in security critical environments. Additionally, services that provide data confidentiality as well as a sophisticated key management facility are missing.

The security architecture of BACnet is more advanced. However, the used cryptographic algorithm is obsolete and therefore it should be replaced by a modern one. Additionally, the BACnet protocol must be improved to avoid certain security flaws.

Due to the fact that KNX/EIB does not support the required mechanisms, further development is badly required. At the TU Munich, a secure communication protocol called Secure EIB (SEIB) was developed (see [5]). This security extension provides data confidentiality, integrity and freshness for process data communication. It is based on the SNEP protocol which is part of the Secure Protocol for Sensor Networks called SPINS (see [6]). As mentioned in [1], there is still a variety of problems which remain unsolved (e.g. unprotected management communication, rudimentary key management).

#### IV. SECURE EXTENSION TO KNX/EIB: EIBSEC

Regarding the limited usability of KNX/EIB and SEIB in security critical environments, the development of a KNX/EIB security extension called EIBsec is currently in progress. To satisfy the above mentioned requirements, EIBsec supports the following mechanisms:

- Data confidentiality, integrity and freshness
- Authentication of both communication participants
- Protection of management and process data communication
- Sophisticated key management (including mechanisms to revoke keys and to limit the lifetime)
- Mechanisms for initial key distribution

##### A. TOPOLOGY

A KNX/EIB network is divided into network segments which are arranged in a three-level tree structure. In our approach, the functionality of the EIBsec specific components is distributed across this tree structure. Each network segment contains a special device called Advanced Coupler Unit (ACU) (see Figure 1).

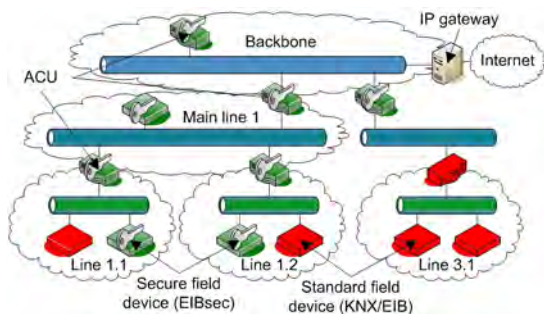


Figure 1: Topology of EIBsec

Such an ACU performs the EIBsec specific tasks. The distributed solution avoids introducing a single point of failure. If an ACU is successfully attacked or fails, isolation will keep the rest of the network operable. Another benefit is that it can help to minimize the consequences of Denial-of-Service (DoS) attacks. If the ACU detects a DoS attack in its network segment, it will be able to isolate the affected segment and prevent an interference of other network segments. Another important feature of EIBsec is compatibility to standard KNX/EIB technology. Since the frame format of SEIB is used, the header information necessary for routing messages is transmitted in plaintext. Hence, KNX/EIB devices not supporting EIBsec are still able to route these messages.

##### B. SECURE DATA TRANSMISSION

To protect transmission data against malicious attacks, an encryption algorithm is necessary. Since the used embedded microcontrollers have limited resources (process-

ing power and memory), the symmetric Advanced Encryption Standard (AES) (see [7]) was chosen. The required keys are managed using a key server infrastructure. Since EIBsec uses a distributed solution, the functionality of this key server is implemented by the different ACUs. Therefore, each network segment has its own key server instance. Secure management communication is performed using sessions. To establish a session, a so called session key must be retrieved from the corresponding ACU. Using this key, it is possible to communicate through a secure point-to-point channel. In KNX/EIB the exchange of process data is performed via group communication. To protect this group communication, the transmitted process data is encrypted using a so called group key. This group key can be retrieved from the corresponding ACU. A detailed description of EIBsec is presented in [8].

##### V. CONCLUSION AND FUTURE WORK

With the integration of these security mechanisms, KNX/EIB is no longer limited to the use in non security critical environments. In addition to this basic security architecture, advanced security services like a secure update mechanism and an advanced DoS prevention (including an intrusion detection system) have to be further investigated. Wireless solutions will also be subject of future research, since they are getting more and more popular in the building automation domain.

##### REFERENCES

- [1] W. Granzer. Security in Networked Building Automation Systems. Master's thesis, Vienna University of Technology, Institute of Computer Aided Automation, Automation Systems Group, 2005.
- [2] Control Network Protocol Specification. ANSI/EIA/CEA 709.1, 1999.
- [3] BACnet – A Data Communication Protocol for Building Automation and Control Networks. ANSI/ASHRAE 135, 2004.
- [4] Konnex Association, Brussels. *KNX Handbook 1.1 and KNX Standard Extensions*, 2004.
- [5] G. Westermeir. *Diversitäre Zugangs- und Sicherheitsmechanismen angewendet in automatisierten Gebäuden*. PhD thesis, TU Munich, 2004.
- [6] A. Perrig, R. Szewczyk, J.D. Tygar, V. Wen, and D.E. Culler. SPINS: Security Protocols for Sensor Networks. In *Proc. 7th Annual International Conference on Mobile Computing and Networking (MobiCom)*, pages 189–199, July 2001.
- [7] Advanced Encryption Standard (AES). FIPS PUB 197, National Institute of Standards and Technology, 2001.
- [8] W. Granzer, W. Kastner, G. Neugschwandtner, and F. Praus. Security in Networked Building Automation Systems, January 2006. Submitted to 6th IEEE International Workshop on Factory Communication Systems (WFCS).

# The least risk path for outdoor and indoor areas

Eva Grum and Andrew Frank (Faculty Mentor)  
Institute for Geoinformation and Cartography  
Technical University of Vienna

Email: [grum@geoinfo.tuwien.ac.at](mailto:grum@geoinfo.tuwien.ac.at) and [frank@geoinfo.tuwien.ac.at](mailto:frank@geoinfo.tuwien.ac.at)

**Abstract** — *Way finding is an important topic in the literature and in every day life. How to find the way from a starting point to a destination? How to find the shortest way? An example for trivial usage is to find the next physician in case of illness. The priority is to reach the office. One possibility would be to use the shortest way [1] that depends only on the length of the path. Another possibility is to search for the simplest way [2] that has as few turns as possible. Another approach would be to minimize the effects of wrong decisions along the path. Describing such a path is the goal of my thesis.*

## I. INTRODUCTION

In my thesis, risk is meant to be the risk of getting lost. The user is at risk on every path because mistakes can occur every time and everywhere. There is also the possibility that the explanation of the route is not precise enough or there are road works that block the path or that there are differences between the mental map, that is, a person's perception of the world [3], of the explainer, and the reality.

The least risk path is the path from a starting point to a destination where the risk of getting lost is as small as possible, even if the user makes wrong decisions. All possibilities of making mistakes are included in this path. The intention of my thesis is to define, formalize, and test an algorithm to find the least risk path.

At the moment a business traveler who arrives at the station is taking a taxi to the building where a meeting takes place. In some cases it would not be necessary to use a taxi. If the destination is nearby it takes often more time to take the car than to walk. Cars have to follow road signs as one way or are not allowed to pass pedestrian roads and parks. The business traveler has no knowledge about the area and the taxi driver will not change this. This can cause a trip that is longer than it should be. Way finding does not end at the entrance of buildings if pedestrians are involved. After entering the building the traveler is searching for a porter to ask for the floor of the meeting place. In some buildings there are maps near the lift to help orientating in the indoor area.

For finding the way from the station to the office where a meeting takes place the user would need a system that can navigate him through the outdoor area and the indoor area.

## II. THE RISK VALUE OF DECISION POINTS

While working on the NAVIO project I read about the shortest path [1] and the simplest path [2]. I asked myself whether there is also a least risk path. The first result was the formula for calculating a risk value of a path in the two-dimensional outdoor area.

The formula for finding the least risk path must include a risk value of decision points and a cost value for street segments [4]. Decision points are in this case the crossings where the user has to make decisions. The risk value of a decision point is two times the number of wrong choices divided by the number of possible choices. A street segment is the distance between two decision points. The value of a street segment depends on the length of this segment. The reason for taking the length of wrong choices two times is that I assume that the user recognizes at a decision point if he is right or wrong. If he is wrong he goes back the same way he came along until he reaches the last decision point where he was sure that he was still right. Equation (1) shows the formula.

$r_d$  = risk value of a decision point in a 2D area (outdoor area)

$l_i$  = length of the paths in 2D (same level) that is wrong

$n$  = degree of nodes

$$r_d = \frac{2 * \sum_{i=1}^{n-1} l_i}{n} \quad (1)$$

## III. THE RISK VALUE OF THE WHOLE PATH

The result of the sum of the risk values of the decision points and the sum of the values of the street segments must be added. The total result is the risk value of the whole path. The total calcula-

tion shows that the risk value of the least risk path is smaller than the risk values of the shortest path and the simplest path. The least risk path is a little bit longer than the shortest path and has one more turn than the simplest path.

#### IV. THE RISK VALUE IN 3D

The second part of my work in the NAVIO project is to extend this risk value of a path for the *three-dimensional* indoor area. Therefore I had to think about how to add the height to the formula for the risk value for the outdoor navigation.

A challenge was that the height must be weighted because there is a difference in moving uphill, downhill, or on the same level. The standard assumption for uphill is 300 meters and for downhill 500 meters per hour. Going uphill is more exhausting than going downhill or moving on the same level. Thus the relation between the same level and uphill is 1:17 and the same level and downhill 1:10. I had to add this standard assumption to the formula of the risk value of decision points to get an available result.

$r_{d3}$  = risk value of a decision point in a 3D area (indoor area)

$h$  = assumed mean value of the height difference between two floors (3,5 meters)

$h_m$  = height multiplier makes height differences comparable to horizontal distances

$$r_{d3} = \frac{2 * \sum_{i=1}^{n-1} l_i + 2 * \sum_{i=1}^{n-1} h * h_m}{n} \quad (2)$$

For getting a valid formula for the whole building, shown in equation (2), I assume a mean value of 3 meters of room height and 0,5 meters for the thickness of the ceiling. Therefore the difference between two floors is 3,5 meters. This is used to translate floor levels into height meters for having constant values for the formula.

#### V. THE COMBINATION

For a combined outdoor and indoor navigation the system that is used for it must be able to change between locating the position via satellite and locating via sensors. To reach a positioning of the user in the outdoor area with sensors would also be a possibility but is not feasible at the moment.

The functionality of such a navigation system depends on the method of data collection. Sensor

technology is highly developed but not adequate for solving the problem of the data collection. The reason is that for a city like Vienna thousands of sensors would have to be installed. Satellite positioning and connecting the accurate position with a digital map would be another possibility. There is a problem that in cities with high buildings the reception of the required number of satellites for getting the accurate position can not be given at every point. For pedestrian navigation it is essential to identify the position of the user with high accuracy which means that the deviation should not be more than 3 meters for the outdoor areas and about 1 meter for the indoor areas. Reason for this accuracy is that if the accuracy is not as high as is defined in the last sentence the system can be responsible for a mistake the user makes. Especially for the indoor navigation a precise positioning is necessary.

#### VI. CONCLUSION

The risk we are dealing with in this case is defined as the risk of getting lost on a path. Mistakes can happen and lead to make detours. But these detours are included in the formula and finally the user reaches the destination with as least risk as possible.

#### REFERENCES

- [1] Dijkstra, E.W. "A Note on Two Problems in Connection with Graphs." *Numerische Mathematik*, no. 1 (1959): 269-71
- [2] Duckham, M., Kulik, L. "Simplest Path: Automated Route Selection for Navigation." Paper presented at the COSIT 2003, Kartause Ittingen, Switzerland 2003.
- [3] Rosenberg, Matt T. *Mental Maps 2005*, cited. Available from <http://geography.about.com/cs/culturalgeography/a/mentalmaps.htm>.
- [4] Grum, E. "Danger of Getting Lost: Optimize a Path to Minimize Risk." Paper presented at the CORP 2005 & Geomultimedia05, Vienna, Austria, Feb. 22-25 2005 2005.

# Simulation and Optimization of CSO and CTB in Cable Television

Ondřej Hála and Prof. Václav Říčný  
Dept. of Radio Electronics, FEEC  
Brno University of Technology  
Brno, Czech Republic

Email: xhalao00@stud.feec.vutbr.cz, ricny@feec.vutbr.cz

**Abstract** — *One of the main disadvantages of CATV is nonlinear dependence of output signals on input signals of active equipments. The paper describes intermodulation products simulation, calculation of the ratio of the carrier frequency of picture level to intermodulation products accumulation and optimization of the input signal level for attainment of optimal carrier picture level to intermodulation products accumulation ratio value and deals with influence of broadband amplifier for transmission of more TV channels and calculation of intermodulation products in MATLAB program.*

## I. INTRODUCTION

Maximum TV signal output level of the active equipment (band amplifiers, modulators of master station, broadband amplifiers) in the cable TV networks is limited by nonlinear distortion. Nonlinear distortion is caused by nonlinear dependence of output signals on input signals of these active equipments and increases with input signal level. For low-level signals, distortion is insignificant but it becomes undesirable at higher-level signals.

The largest part of TV signal power is situated in the narrow frequency band of the carrier frequency of the picture. If more harmonic frequencies are transmitted into the broadband active equipment, a lot of intermodulation products arise as a result of nonlinear distortion. The parameter for representation of accumulation of intermodulation products effect was introduced as the ratio of the carrier frequency of the picture level to intermodulation products accumulation of the second order – C/CSO (CSO - *Composite Second Order*) and as the ratio of the carrier frequency of the picture level to intermodulation products accumulation of the third order – C/CTB (CTB - *Composite Triple Beat*).

## II. SYSTEM MODEL

It is possible to assess the influence of nonlinear transmission characteristic for synchronous broadcasting of more TV signals by means transmission of more harmonic signals, which correspond with car-

rier frequencies and active equipment with universal transmission characteristic. Then the output signal will have infinite number of members, which are created by a single harmonic signal or by interaction of more harmonic signals. The transmission characteristic of the system is given by:

$$e_{out} = A \cdot e_{in} + B \cdot e_{in}^2 + C \cdot e_{in}^3 + \dots, \quad (1)$$

$$e_{in} = \sum_{i=1}^n E_i \cdot \cos(2\pi \cdot f_i t), \quad (2)$$

where A,B,C,D... are coefficients of transmission function,  $f_i$  is the frequency of individual harmonic signals (the carrier frequencies of pictures) and  $f_i < f_{i+1} < f_{i+n}$  hold and  $n$  the number of input harmonic signals.

The components of identical frequency can develop from different expressions of transmission function. Every component of the output signal, which is represented by such an expression, is a product of nonlinear distortion. If the component -  $\omega_i$  has a single member it is considered as a harmonic product and if the component -  $\omega_i$  has more members it is then an intermodulation product.

It is possible to simplify the formula for transmission characteristic of active equipment according to the formula:

$$e_{out} = k_1 \cdot e_{in} + k_2 \cdot e_{in}^2 + k_3 \cdot e_{in}^3, \quad (3)$$

where  $k$  is a real positive or negative constant after simplification.

A multispectral component arises at the amplifier output with transmission characteristic according to equation (3) after substitution of equation (2) in equation (3) and mathematical modifications.

A model of broadband amplifier and its influence on transmission of more TV channels, clustering in one broadband direct channel, was made in Matlab. Saleh's model of amplifier [5] and a simplified transmission characteristic of active equipment were used for the broadband amplifier model in Matlab.

The simplified transmission characteristic of active equipment is given by the formula (3) and (2).

### III. SIMULATION

More signals in frequencies of system PAL D, K were fed into the model amplifier input. A lot of intermodulation products develop from mutual interactions in the amplifier output. The simplified model of amplifier makes simulation of the most important intermodulation products possible namely products of the second order and the third order which is sufficient. Values of CSO and CTB are obtained through simulation, and subsequently parameter values of the ratio of the carrier frequency of picture level to accumulation of intermodulation products of the second order –  $C/CSO$  and of the third order –  $C/CTB$  (figure 1a) are determined.

A frequency spectrum of broadband channel after transmission through broadband amplifier with nonlinear transmission characteristic is displayed in Figure 1.

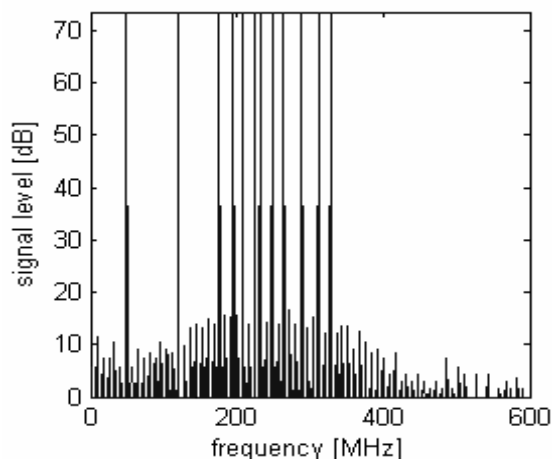


Figure 1: Output signal of broadband amplifier

The ratio of the carrier frequency of picture level to intermodulation products accumulation is dependent on the change in output signals level of the active equipment. So it is dependent on input signals value and amplification. The program for optimization of input signals level was made in Matlab, so as to obtain an optimum value of the ratio of the carrier frequency of picture level to intermodulation products accumulation. The gradient method of the steepest decline was applied for optimization [6]. The result is the biggest input signal level value, so that the value of the ratio of the carrier frequency of picture level to intermodulation products accumulation will not be less than 57dB. For example the result of

optimization for 12 carrier frequencies is displayed in Figure 2.

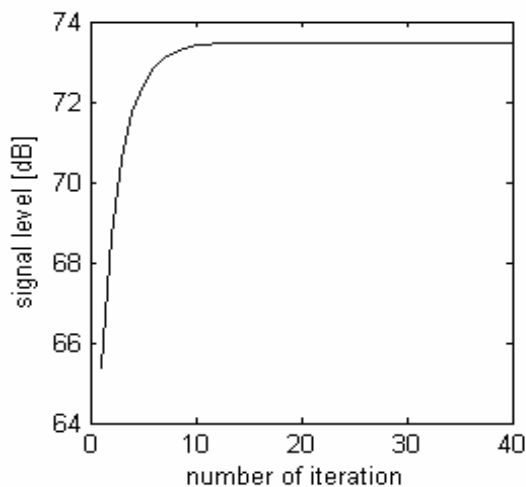


Figure 2: Optimization of input signal level

### IV. CONCLUSIONS

An influence of TV input signal level on value of the ratio of the carrier frequency of picture level to intermodulation products accumulation is examined and optimized in this article.

### ACKNOWLEDGMENTS

This work has been supported by the doctoral project of the GACR (Czech Science Foundation) No. 102/03/H109 „Methods, Structures and Components of Electronic Wireless Communication“ and with the support of the research plan MSM0021630513 „Electronic Communications Systems and Technologies of New Generation“.

### REFERENCES

- [1] S. Dianiška. Siete káblovej televízie – Parametre a štruktúry. SAKT, 2001.
- [2] W. Ciciora, et al. Modern Cable Television Technology. Morgan Kaufmann publishers, 2004.
- [3] V. Žalud. Moderní radioelektronika. BEN, 2000.
- [4] V. Říčný. Televizní kabelové rozvody. FEEC Brno University of Technology, 2001.
- [5] W. H. Tranter, et al. Principles of Communication Systems with Wireless Applications. Prentice Hall, 2004.
- [6] P. E. Gill, et al. Practical Optimization. Academic Press, 1997.

# Deterministic and stochastic constituent analysis of diurnal and semi-diurnal coordinate variations in European permanent GPS network

Michal Hřčka and Ján Hefty (Faculty Mentor)  
Department of Theoretical Geodesy  
Faculty of Civil Engineering, Slovak University of Technology  
Bratislava, Slovak republic  
Email: {hrcka, hefty}@svf.stuba.sk

**Abstract** — *Regular analysis of permanent GPS network covering almost the whole European continent performed at Slovak University of Technology in Bratislava allows to detect small short-periodic oscillations of site coordinates. We analyze one-year interval of station time series comprising of coordinates evaluated from 4-hour observing samples. The variations of horizontal coordinates and ellipsoidal height with amplitudes from 0.5 to 2.0 mm are observed at majority of analyzed sites. After elimination of these deterministic signals still residual diurnal oscillations of stochastic character can be observed in the coordinate series. They are detected at majority of analyzed stations by means of ARMA process modeling.*

## I. INTRODUCTION

In 2002 was the Department of Theoretical Geodesy at Slovak University of Technology accepted as one of the EPN (The European Reference Frame (EUREF) Permanent Network) Local Analysis Center (LAC SUT).

For the regular processing is used Bernese GPS software 4.2. The analysis procedure follows the rules applied for EUREF permanent network analysis. The theoretical tidal effects affecting the site coordinates are consistently modelled according to IERS Conventions [3]. Outputs from the EPN processing are the daily station coordinates obtained from 24-hours observing intervals and their covariance matrix, which are merged in weekly solutions.

The additional alternative data processing performed at SUT is resulting to coordinates obtained from observations from shorter intervals covering separate 4-hours observing spans.

All the network solutions are referenced to International Terrestrial Reference Frame 2000 (ITRF 2000) through one site strongly constrained - the Borowiec (BOR1) station in Poland. This method of network referencing means, that all network station variations are relative to BOR1 station.

## II. TIME SERIES FROM EPN SUBNETWORK

In this paper we analyze the 4-hour interval solutions of EPN subnetwork covering the period from Oct. 1, 2003 to Sept. 29, 2004. We will present results obtained for selected subset of analyzed EPN stations, namely GOPE, HELG, KOSG, ORID, SULP, STAS and TUBO. The choice of these stations is motivated by the fact, that their series are continuous and the stations are situated in various regions of the continent.

The resulting station time series are formed by geocentric coordinates  $X, Y, Z$ . These time series were examined for outliers and missing parts were interpolated. Length of the time series is one year and is comprised of 2190 observations – 4-hour interval coordinates. In the next step, the geocentric coordinates  $X, Y, Z$  are transformed to local system  $n, e, v$  [2], where axis  $n$  is directed to the north, axis  $e$  to the east and  $v$  to the local vertical.

## III. DETERMINISTIC CONSTITUENTS IN STATION COORDINATES SERIES

Deterministic constituents of  $n, e, v$  time series are expressed usually by means of additive decomposition. The additive model has the form

$$Y_t = T_t + S_t + C_t + E_t \quad (1)$$

where  $Y$  is one of the  $n, e, v$  constituents,  $T$  is trend,  $S$  is seasonal component,  $C$  is periodic component and  $E$  is residual component. The subscript  $t$  is used for expressing the time dependence of observations and the modeled components.

The trend component is expressed by linear regression in the form

$$T_t = \alpha + \beta t \quad (2)$$

where  $\alpha, \beta$  are regression coefficients.

Significant periods of  $n, e, v$  series are determined after elimination of linear trend by spectral analysis method, which uses for Fourier transformation the estimates of autocovariance function. Exam-

ple of spectra of  $n$  coordinate time serie for station GOPE is given in Figure 1.

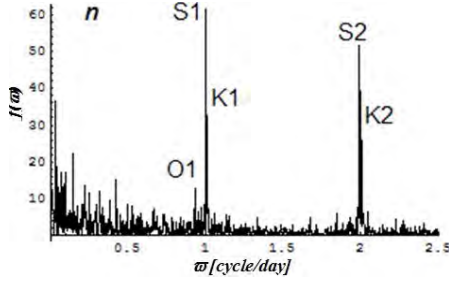


Figure 1: Spectra of coordinate time serie

The most significant terms are with seasonal frequencies (annual and semi-annual), and tidal frequencies: diurnal ( $O_1$ ,  $P_1$ ,  $S_1$ ,  $K_1$ ) and semi-diurnal ( $M_2$ ,  $S_2$ ,  $K_2$ ). The periods of observed tidal waves are given in Table 1.

Tidal waves band	Wave	Period $P_i$ [hours]
Semi-diurnal	$M_2$	12.420 601
	$S_2$	12.000 000
	$K_2$	11.967 234
Diurnal	$O_1$	25.819 320
	$P_1$	24.132 120
	$S_1$	24.000 000
	$K_1$	23.934 469

Table 1: Periods of observed tidal waves

Seasonal components model has the form

$$S_t = \sum_{i=1}^2 \left( a_i \sin\left(\frac{2\pi t}{P_i}\right) + b_i \cos\left(\frac{2\pi t}{P_i}\right) \right) \quad (3)$$

and the periodic tidal components are

$$C_t = \sum_{i=3}^9 \left( a_i \sin\left(\frac{2\pi t}{P_i}\right) + b_i \cos\left(\frac{2\pi t}{P_i}\right) \right) \quad (4)$$

where  $a_i$ ,  $b_i$  are regression coefficients,  $P_i$  are annual, semi-annual, diurnal and semi-diurnal periods. Each harmonic component has amplitude  $A$  and phase  $\phi$

$$A_i = \sqrt{a_i^2 + b_i^2}, \quad \tan \phi_i = \frac{a_i}{b_i} \quad (5)$$

Parameters of (2, 3, 4), namely  $\alpha$ ,  $\beta$ ,  $a_i$ ,  $b_i$  are estimated for each of the  $n$ ,  $e$ ,  $v$ , time series for all 7 examined stations.

The periodic variations of horizontal coordinates and ellipsoidal height with amplitudes from 0.5 to 2.0 mm are observed at majority of analyzed sites. They can be assigned mainly to unmodeled solid Earth and ocean tides, polar motion effects and satellite orbits biases. Some of the terms like  $O_1$  and  $P_1$  have generally amplitude less than 0.5 mm for majority of stations. The amplitudes of  $K_1$  and  $K_2$  are very different at the various analyzed sites and reach up to 3 mm.

## IV. STOCHASTIC CONSTITUENTS

After elimination of deterministic signals still residual diurnal oscillations of stochastic character can be observed in the station coordinate series. To describe the stochastic constituents we will use the Box-Jenkins methodology [1]. We expect that coordinates observations are not mutually independent but they are correlated in time. Considering this, the value  $E_t$  of a time series free from systematic influences might be expressed by equation

$$E_t = \varphi_1 E_{t-1} + \varphi_2 E_{t-2} + \dots + \varphi_p E_{t-p} + \tilde{N}_t \quad (6)$$

where  $\varphi_1, \dots, \varphi_p$  are auto-regressive (AR) coefficients (deterministic part) and  $\tilde{N}_t$  is stochastic part or

Moving-average (MA) part. MA part is expressed by

$$\tilde{N}_t = N_t + \Theta_1 N_{t-1} + \dots + \Theta_q N_{t-q} \quad (7)$$

where  $\Theta_1, \dots, \Theta_q$  are MA coefficients. The series  $\{N_t\}$  is white noise with zero mean value and constant variance  $D\{N_t\} = \sigma^2$ .

The set of AR and MA coefficients defines the ARMA(p, q) process, p and q being orders of AR and MA constituents, respectively.

All the series exhibit similar behavior with significant values of 6th both the AR and MA coefficients. As the time series are sampled in 4-hours intervals, this phenomenon corresponds to 24-hour periodicity. The exactly 24-hour periodic terms were eliminated by introducing the  $S_1$  terms. The significant 6th AR and MA terms are due to variations with variable period oscillating around 24-hours. We suppose that these signals have origin in perturbing effect resulting from atmosphere refraction variations, site monumentation movements, multipath effects and other relevant phenomena with no strict periodic character but with diurnal variability.

## ACKNOWLEDGMENTS

This work was supported by grant No. 1/1033/04 of the Grant Agency of Slovak Republic VEGA.

## REFERENCES

- [1] Box, G., Jenkins, G.: Time Series Analysis – Forecasting and Control. Holden Day, San Francisco, Cambridge, London, Amsterdam, 1970.
- [2] Hefty, J., Husár, L.: Satellite geodesy – Global Positioning System. Bratislava, Slovak University of Technology, 2003, 186 pp. (in Slovak).
- [3] McCarthy D. (ed.): IERS Conventions (1996). IERS Technical Note 21. Paris, Central Bureau of IERS, Observatoire de Paris Verlag, Augsburg, Germany, 1st edition, January 2002, 1996.

# Implementation of an FPGA-Based Hardware Fault Injector

Thomas Handl and Andreas Steininger (Faculty Mentor)

Embedded Computing Systems Group E182/2

Vienna University of Technology

Vienna, Austria

Email: {handl, steininger}@ecs.tuwien.ac.at

**Abstract** — *Fault injection (FI) plays a key role in the assessment of fault tolerance mechanisms of digital systems. It artificially increases the rate of fault occurrences, thus allowing a more comprehensive study of the fault effect which finally improves the quality of the results obtained.*

*However, problems related to accessibility of internal nodes of a chip or SoC make it difficult to conduct such experiments. It is claimed that the most suitable location for placing an FI tool is directly on-chip. Other approaches (i.e. simulation) often tend to use levels of abstraction inadequate for dependability evaluation.*

*This paper presents an FPGA-based hardware FI toolset we developed in order to address exactly this problem.*

## I. MOTIVATION

The ever increasing potential of modern digital systems directly leads to a massive increase in size, complexity and error-proneness. As a consequence, reliability [1], availability, security and safety (among others) can not be guaranteed only by means of elaborate design methodologies, fault avoidance techniques or other methods of quality assurance.

This fact leads to an emerging demand for methods and techniques to validate the criteria an application has to fulfill. Basically, two methods are viable: (i) theoretical analysis and (ii) experimental evaluation. Because of the causality of operation, theoretical analysis (e.g. model checking, [2]) seems to be especially suitable for the analysis of computer systems. In practice, this approach fails due to the above mentioned complexity of these systems, making an experimental approach like fault injection ([3], [4]) more promising and attractive.

## II. FAULT INJECTION

FI is a methodology to (i) increase the rate of faults a system is subjected to and (ii) to – depending on the method used – exactly choose where inside the system the faults will be activated. Each of the available methods is associated with a certain class of faults depending on the system level accessible.

*Simulation* can be done at any level, from transistors up to gate level or even system level. The results obtained strongly depend on the quality of the model and its level of abstraction.

*Software FI* is located at a rather high system level and can be done at runtime or at compile time. It mainly focuses on code corruption or code modification and is therefore of limited value when exact fault locations are demanded. On the other hand, there is no need for any hardware modifications.

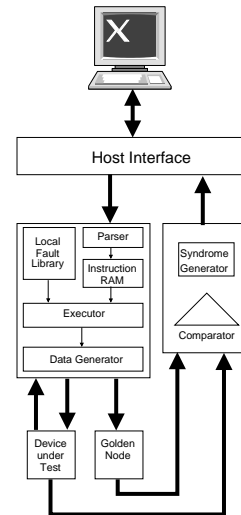


Figure 1: The structure of **FIDYCO**

Finally, *hardware FI* is capable of directly inserting faults into a system's circuitry or into its pins. At pin level, usually additional programmable logic is used to introduce errors on signals. Within a system, heavy ions can cause *Single Event Upsets* (SEUs), electromagnetic or electrostatic disturbances can be generated as well as power supply disturbances, and even lasers are used to inject faults. With additional logic and, provided the device under test is available as VHDL description or in a similar form, any node even within the circuit can be reached. This is the approach we took in our implementation.

## III. FIDYCO

This work focuses on the implementation of a highly flexible, scalable hardware FI environment called **FIDYCO** (*Flexible on-chip fault Injection for run-time Dependability validation with target specific COmmand language*). In contrast to existing tools ([3], [4]), it should be more easily adaptable to the devices to be tested and should exhibit powerful yet flexible means to introduce faults into the tested object.

### A. GENERAL STRUCTURE

The discussed FI environment constitutes a modular system basically consisting of the device under test, a reference node (golden node), a host interface, an evaluation unit and the FI unit itself. Figure 1 shows this architecture.

The host interface, an RS-232 UART, has two main functions: (i) receiving configuration information and FI programs generated by the user from the host PC, and



# Application for solving direct and inverse kinematic task

Lubomír Jasenovec, Ján Jadlovský ( Supervisor )  
 Department of Cybernetics and Artificial Intelligence  
 Technical University of Košice  
 Košice, Slovakia  
 Email: lubomir.jasenovec@tuke.sk

**Abstract** — This paper describes application that solve direct and inverse kinematic task. Main goal of this work is to create application for control of robotic manipulation system.

Two methods will be used to solve inverse kinematic task that calculate joint positions depending on position and orientation of end-effector for use in this application. Methods are based on inverse Jacobian matrix and optimization. Results obtained from Matlab simulation will be presented.

Result of this work is a client-server application that can solve inverse kinematic task for robotic manipulation system and provide 3D simulation, offline and online programming of robotic system.

## I. ROBOTIC MANIPULATION SYSTEM

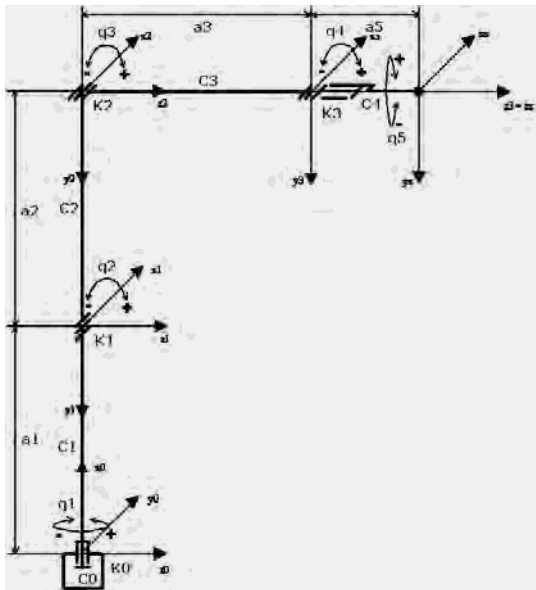


Figure 1: Kinematic structure of 5DOF robotic arm

Robotic system consists from 3 robotic arms, 3 belt conveyors and 3 rotary tables that are driven by step motors. Kinematic structure of all of robotic arms is shown at Figure 1. [1] Direct control of all step motors is performed by single-chip microcomputer control system that is connected to the local com-

puter through the RS-232 interface and data for its behavior are obtained from described PC application.

## II. METHODS USED FOR SOLVING INVERSE KINEMATIC TASK

Two numeric methods for solving inverse kinematic task are used in this application.

Direct kinematic task solves equation

$$X = f(Q) \quad (1)$$

where  $X$  is position and orientation of end point of robotic arm and  $Q$  is vector of joint positions. Inverse kinematic solves equation inverse to equation (1), thus

$$Q = f^{-1}(X) \quad (2)$$

In general, numeric methods for solving of inverse kinematic task are cyclically calculating change of vector  $Q$  dependent on change of  $X$ . End of iteration is given by minimum of some criteria function.

### A. INVERSE JACOBIAN

Method based on inverse Jacobian is used only for simple solve of inverse kinematic task. This method is fast, but it need a good starting point.

Inverse Jacobian based algorithm has 7 steps [1]:

1. computing of actual position and orientation  $X_i$  according to equation (1)
2. computing of Jacobian  $J(Q_i)$  for actual joint position  $Q_i$  according to

$$J = df / dQ \quad (3)$$

3. inverse of Jacobian  $J^{-1}$
4. difference between actual and desired position  $dX_i$

5. computing of new joint position according to

$$Q_{i+1} = Q_i + dQ_i J^{-1} dX_i \quad (4)$$

6. next step  $i = i + 1$

7.  $Q_i$  is solution and algorithm ends, if  $dX_i < e$ , where  $e$  is toleration, back to step 1 otherwise

Figure 2 shows iteration of this algorithm. Figures 2 and 3 are obtained from Matlab simulation

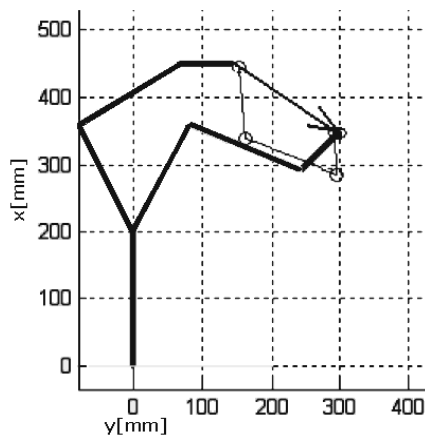


Figure 2 : Iteration of inverse Jacobian method

### B. OPTIMIZATION

Second, optimization method is used for automatic trajectory generation. Optimization method find local extreme of some criteria function which indicate optimal solution. Benefit of this method is that it can reach approximate solution even though target is out of workspace. This feature can be used in trajectory generation, because each step in iteration process can be used like one point in multipoint trajectory [1].

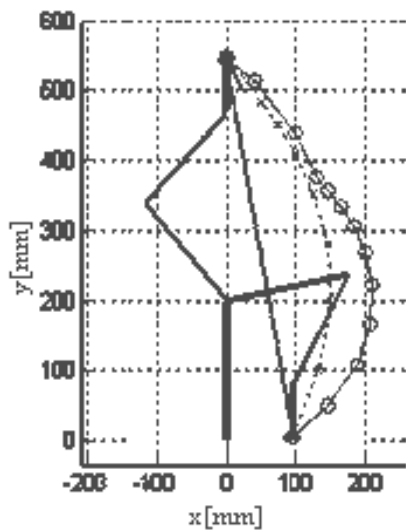


Figure 3: Trajectory generated by optimization method

There are two differences between this and previous algorithm. First, equation (4) changes to

$$Q_{i+1} = Q_i + c dQ_i J^T dX_i \quad (5)$$

where  $c$  is constant between 0 and 1. Effect of use constant  $c$  is that error of iteration step is smaller and generated trajectory is smoother. Second difference is

that algorithm ends when  $dX_i < dX_{i+1}$  which correspond to local extreme of criteria function.

Example of trajectory generated by this algorithm is at Figure 3.

### III. APPLICATION STRUCTURE

Client-server application is designed and programmed. Client side of application is designed as an application for local control that use server for all calculations and store data model of robotic system.

Client-server architecture is chosen in order to use the server side of application in network control system as a computing block for solving of direct and inverse kinematic task. Server side offers computing more models together too.

Client side of application is designed as an application for local control that uses server for calculations and only stores data necessary to control the robotic plant. 3D visualization of plant model is simultaneously provided. In online mode control data are sent to single-chip microcomputer control system.

Structure of whole application is on Figure 4.

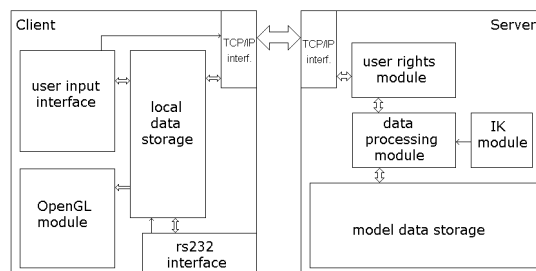


Figure 4: Application structure

### CONCLUSIONS

Client-server application that control robotic system is created. Server side solve direct and inverse kinematic task and stores model data, client side visualize real model and can send data to robotic manipulation system. Client also can simulate robotic system without real system connected.

### REFERENCES

- [1] L. Jasenovc. Solving direct and inverse kinematic task on PC, MS. thesis, Technical University of Košice, Department of Cybernetics and Artificial Intelligence, Košice, Slovakia, 2005.

# Optimization of CAL Gates for an FPGA Architecture

Marcus Jeitler and Martin Delvai (Faculty Mentor)  
 Embedded Computing Systems Group 182/2  
 Vienna University of Technology  
 Vienna, Austria

Email: e0125561@student.tuwien.ac.at, delvai@ecs.tuwien.ac.at

**Abstract** — *Implementing asynchronous circuits for an FPGA architecture is a sophisticated task because on the one hand the resulting design should be delay insensitive but on the other hand the additional overhead should be kept minimal. Based on the research of the Embedded Computing Systems Group this master thesis tries to give a guideline for efficiently implementing asynchronous and delay-insensitive circuits. By investigating different approaches and explaining their pros and cons the reader should get a better understanding of the key features of asynchronous logic and of how to implement them efficiently.*

## I. INTRODUCTION

Over the last years it has become apparent that the synchronous design could be reaching its limits in the near future. Ever increasing clock cycles in conjunction with the increase of chip size places a synchronous solution in jeopardy, which can only be maintained through considerable hardware efforts. The development of a *global cycle distribution network* quickly evolves into a complex process which cannot be addressed simply by attempting miniaturization. Instead of solving all problems in the *time domain*, asynchronous designs are based on solutions in the *information domain* or on *hybrids* of both possibilities. Some implementations use synchronous components which are triggered by a local clock signal while others develop a special signal encoding and use highly sophisticated components for that purpose. The latter solution was developed at the Institute of Computer Engineering and published as *Code Alternation Logic (CAL)* by Mr. M. Delvai [1] and Mr. W. Huber [2]. In the course of their PhD theses the asynchronous processor *ASPEAR* was developed for the *FPGA* platform. This processor was proven to be delay-insensitive and offers the same functionality as its synchronous counterpart *SPEAR*. Figure 1 shows a block diagram of the *SPEAR* processor.

## II. CODE ALTERNATION LOGIC

The *Code Alternation Logic* is based on the *dual rail encoding* scheme which uses two signal lines for representing a single logic state. Therefore both Boolean states (HIGH and LOW) are represented by two different *CAL* encodings which are called the phase of the signal and differ from each other by a single bit. Table 1 shows the appropriate coding scheme.

Within a data stream consecutive bits are encoded in a different phase which allows the *CAL* gates to identify when new data is ready, even in the absence of a

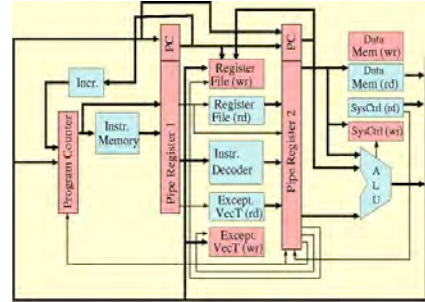


Figure 1: SPEAR Architecture

log.state	code $\varphi_0$	code $\varphi_1$
"LO"	(a,b) = (0,0)	(a,b) = (0,1)
"HI"	(a,b) = (1,1)	(a,b) = (1,0)

Table 1: Coding Scheme

clock cycle. To ensure a secure data flow every *CAL* gate must hold its actual state until all inputs are in the same phase and the new piece of data is ready to propagate. This additional memory element which is also required by combinatorial gates and the extra signal lines for the Dual Rail Encoding result in much larger circuits: the first prototype of *ASPEAR* was approximately ten times larger than its synchronous counterpart. The increase in size can be understood, if we consider a simple *CAL AND* gate. Table 2 shows the logic table of a *CAL AND* gate. The hold entries represent the *Hold states* of the gate

Z		E1			
		h	l	H	L
E2	h	h	l	hold	hold
	l	h	l	hold	hold
	H	hold	hold	H	L
	L	hold	hold	H	L

Table 2: Truth Table of a 2-input AND in CAL

where the input signals E1 and E2 are in different phases. Therefore the gate outputs the last value until the phase of E1 and E2 are equal again - representing new stable data. All other outputs are built by a simple AND function (Za) and adding the corresponding bit (Zb) for the phase regarding Za. The task of this thesis consists of optimiz-

ing CAL gates and, as a result, creating a more attractive basis for asynchronous designs. The development of optimized, generic logic gates are the key to the reduction of the circuit's size. These optimized gates are the building blocks of larger systems. *FPGA* should be used as target devices for the optimization procedure. The smallest programmable blocks of our target *FPGA* are *Logic Elements (LE)*. They are basically built upon a *Look Up Table (LUT)* and a *Register*. Figure 2 shows the structure of a *Logic Unit* [3].

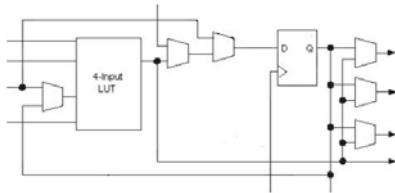


Figure 2: Structure of a Logic Unit

Thus the main challenge is to find an optimal mapping of *CAL* gates to the *LE* structure, maintaining at the same time the delay insensitivity of the resulting circuits. Table 3 shows the major differences between the existing solution and my approach.

	Trigger	Memory	Delay-Insensitivity
Existing approach	phase of each rail	RS-Latch	guaranteed
Improved approach	phase alignment	D-Flip-Flop	timing assumption

Table 3: Major differences between implementations

### III. RESULTS

Depending on the *FPGA* type used the best result achieved is an AND-gate requiring 3 *LE* and 2 registers, which are packed into these elements. Nevertheless, all circuits tend to behave more or less *delay-sensitive* because the usage of synchronous memory elements introduces an additional timing constraint between the Flip-Flops data inputs and the trigger signal. Figure 3 shows a schematic diagram of such an optimized generic *CAL* Gate. Although *CAL* defines the data and phase bit as

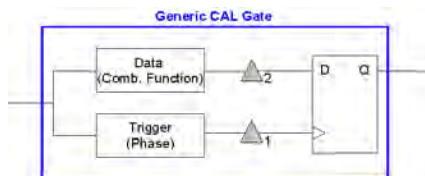


Figure 3: Schematic Diagram of an Optimized Generic *CAL* Gate

an *atomic unit* on the one hand there is a need for splitting them up (into "Data", "Phase") in order to build a smaller circuit but on the other hand this approach becomes *delay-sensitive* on the structural level. Therefore  $\Delta 1$  has to be the largest delay so that the "Data" lines are stable before the Flip-Flops update its values. Moreover, the trigger is derived by phase alignment. Thus, if both rails change at the exact same moment no edge will be generated and the system will not update and miss valid data. The solution to address this problem is to use the phase itself as a trigger. A variation of the former approach generates the trigger by comparing the phase of the input signals against the phase of the output signals. Thus, the usage of synchronous memory elements implies the necessity of a *feedback loop* and requires that the output signals are in a well defined state, especially after reset. Although the design becomes delay-insensitive the number of wired connections increases dramatically because all gates - even combinational ones - require a global reset line to operate correctly. It seems that every attempt to exploit the features of the underlying hardware violates the basic concept of *CAL* and requires additional logic to avoid *timing constraints*. Therefore it appears that the existing approach using RS-Latches is the best solution for the *FPGA* prototyping platform. Further research will investigate an *ASPEAR* implementation using the 3 *LE* AND/OR-gate and testing the *Phased Logic* approach<sup>1</sup> [4] with the *SPEAR* processor. Finally these results will be compared to the existing implementation of the *ASPEAR*.

### REFERENCES

- [1] M. Delvai. *Design of an Asynchronous Processor Based on Code Alternation Logic - Treatment of Non-Linear Data Paths*. PhD thesis, Technische Universitt Wien, January 2005.
- [2] W. Huber. *Design of Asynchronous Processor Based on Code Alternation Logic - Exploration of Delay Insensitivity*. PhD thesis, Technische Universitt Wien, January 2005.
- [3] Altera. <http://www.altera.com>.
- [4] James C. Harden D. H. Lindner. Phased logic: Supporting the synchronous design paradigm with delay-insensitive circuitry. *IEEE Transactions on Computers*, 45(9):1031–1044, September 1997.
- [5] J. McAuley. Dynamic asynchronous logic for high-speed cmos systems. *IEEE Journal of Solid-State Circuits*, 3(27):382–388, March 1992.
- [6] J. McAuley. Four state asynchronous architectures. *IEEE Transactions on Computers*, 2(41):129–142, February 1992.
- [7] J. Sparsø. *Principles of Asynchronous Circuit Design. A System Perspective*. Kluwer Academic Publishers, 2001.

<sup>1</sup>The Phased Logic approach provides the means for directly generating a clockless netlist out of a clocked one.

# Implications of Automation for Manufacturing Industries of Less Developed Countries: Force-Field Analysis

Gebremeskel Kahsay, P.H.Osanna and N.M.Durakbasa

Institute of Production Engineering  
Department of Interchangeable Manufacturing and Industrial Metrology  
Vienna University of Technology  
A-1040 Wien, Austria  
Email: gere94@yahoo.com, [osanna@mail.ift.tuwien.ac.at](mailto:osanna@mail.ift.tuwien.ac.at)

## Abstract

*The threat for manufacturing industries of less developed countries is that, they have to compete in the market with the highly sophisticated and multi-millionaire industries of the developed world, which is highly difficult if not impossible. Therefore, the primary purpose of this paper is to identify some of the important factors that would promote or inhibit investment on industrial automation in LDCs in general and Ethiopia particularly. Using Force-field analysis technique; quality and productivity, globalization, safety and employee motivation are found as driving forces while limited capital, lack of knowledge, lack of competent management and trained manpower, lack of government commitment and infrastructure are found as restraining forces. Working towards the use of a modified Multi-Functions Integrated Factory (MFIF) model is proposed to minimize the effect of the restraining forces.*

*Keywords: LDCs, Driving forces, Restraining forces, Automation, Force-field Analysis (FFA), Multi-Functions Integrated Factory (MFIF) model.*

## INTRODUCTION

Present day manufacturing systems are very complex. They are widely supported by recent achievements in computer technology and very often are highly automated. Obviously, automation is playing a major role in the effort to produce better, faster and cheaper products along side manufacturing business models and systems in conjunction with quality initiatives, tools and techniques. Manufacturing industry plays an important role in the economic development of most countries,

however, least developing countries remains far behind achieving this benefit for many reasons among which are scarcity of skills and low level of technology.

Automation or industrial automation is the use of computers to control industrial automation machinery and processes, replacing human operators [1]. Automation on the factory level can be categorized into hard and soft technology [2]. Hard technologies are hardware (and associated software) based technologies such as FMS, CAD and CAM, while, soft technologies on the other hand are techniques such statistical quality control (SQC/SPC), just-in-time production (JIT), total quality management (TQM) and manufacturing resource planning (MRPII).

Even though such facilities and infrastructures are basic requirements for most industries in the developed world, it is rear to see such facilities in manufacturing industries of least developing countries. The author's of this paper had the opportunity to look in to the facilities of about 30 industries in Ethiopia, one of the least of developing nations. It was only one metal and textile industry that was found equipped partly with the facilities mentioned above, whilst, most of the engineering faculties are equipped with the hard technologies and working on research towards introduction of the soft aspects.

Studies have shown that the successful implementation of automation can help to alleviate the typical problems exists in manufacturing industries of LDCs, which include underutilization of capacity, poor quality, high scrap, long lead time and long down time. If implemented properly, there is no question on the gains such as increased productivity, improved quality, reduced down time and waste as well as increased safety. The question is whether companies are rich enough to invest on

such infrastructures to exceed their competitors on the global market, particularly manufacturing industries of less developed countries, unlike in the developed world, in which most simple manipulation activities has been replaced with machines and technical systems, they have abundant and cheap work force who can work simple manipulation activities, but have scarce of skilled and responsible personnel for decision making, where penalties for wrong decisions are extremely high in the era of automation.

Introduction of automation demands more investment both in terms of cash and knowledge so, initiatives must be based on objective analysis of the companies' internal and external environment. A review of the literature on implementation of automation shows that most of the studies reflect experiences of industries of developed countries. Therefore, the primary purpose of this paper is to identify the factors that would influence the success of automation in LDCs in general and Ethiopian industries in particular and propose an idea for alleviating the challenges. Using Force-field analysis technique, the paper highlights some of the important factors that would promote or inhibit the success of automation.

Force-field analysis is a method borrowed from the mechanical engineering discipline known as free-body diagrams. Free-body diagrams are drawn to help the engineer identify all the forces surrounding and acting on a body. The objective is to ascertain the forces leading to an equilibrium state for the body [3]. Force-field analysis helps the team or managers understand the forces that keep things the way they are. Some of the forces are "drivers" that move the system towards a desired goal. Other forces are "restrainers" that prevent the desired movement and may even cause movement away from the goal. Once the drivers and restrainers are known, the team can design an action plan which will 1) reduce the forces restraining progress and 2) increase the forces which lead to movement in the desired direction.

Multi-Functions Integrated Factory (MFIF) model is initiated with the aim to provide cost-effective, agile and optimum ways to produce customer-driven Multi-Function Products [4].

The paper is organized in such a way that section two discusses the methodology while section three and four discusses characteristic features of LDCs and the factors that are likely to promote or inhibit implementation of automation respectively and at

last recommendations and concluding remarks are discussed.

## REFERENCES

- [1] <http://www.robots.com/article-0000.htm>
- [2] [http://www.cherry.gatech.edu/mod/pubs/proceed3/c5\\_swam.pdf](http://www.cherry.gatech.edu/mod/pubs/proceed3/c5_swam.pdf)
- [3] Thomas Pyzdek (2003), "The Six Sigma Handbook", McGraw-Hill.
- [4] Osanna P.H., Si, L., Multi-Functions Integrated Factory – MFIF – a model of the future enterprises. Conference proceedings: Internet Device Builder Conference, Sta. Clara, May 2000.
- [5] Dale H. Besterfield *et al* (2003), Total Quality Management, Prentice Hall.
- [6] <http://www.britannica.com/eb/article-24865>
- [7] David M. Anderson (1997), Agile Product Development for mass customization, IRWIN professional publishing.
- [8] Roger Hannam (1997), Computer Integrated Manufacturing: from concepts to realization, Addison Wesley Longman Limited.
- [9] Visionary manufacturing Challenges for 2020, National academy of sciences, national academic press, 1998.

# Systematic Automated Testing of Safety-Critical Applications in the Automotive Domain

Susanne Kandl and Raimund Kirner (Faculty Mentor)  
Institute of Computer Engineering  
Vienna University of Technology  
Vienna, Austria

Email: susanne, raimund@vmars.tuwien.ac.at

**Abstract** — Due to the increasing usage of control systems in cars (e.g., ESP, steer-by-wire, brake-by-wire), the fact that more and more applications are also classified as safety-critical, for instance according to the safety standard IEC 61508 [1], and the increasing complexity of software, there is a strong need to improve the testing processes within the automotive domain to ensure the quality of the developed systems. We introduce the development of a testing framework using formal methods. The test cases are automatically derived from a model of the system under test based on the requirements defined in the system specification. This is done by means of model checking. Also the evaluation of the testing results is automated to meet test quality criteria, e.g., coverage metrics.

## I. MODEL-BASED TESTING

Our testing framework is based on the concepts of model-based testing [2]. In *model-based testing* the test cases are derived from a model of the system under test (SUT). The resulting test cases are applied to the system under test (Fig.1).

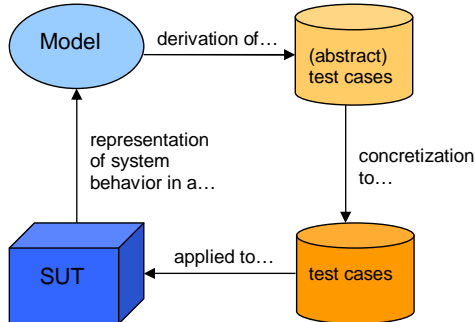


Figure 1: Model-based testing

The model can be created manually (as part of or additionally to the software development process) or can be built automatically. The model has to be *formal*, i.e. the system behavior must be depicted in an unambiguous way, ideally as some kind of finite state machine defining the possible system behavior. Because manual modeling of complex software is expensive and time-consuming, we are extracting the model from the source code.

## A. AUTOMATED MODEL EXTRACTION

The *C-source code* is examined by static analysis to create the *syntax tree*. For further testing analysis also the *control flow graph* is generated. By executing the basic statements of the syntax tree the resulting *automaton model* describing the system states is build. The description of the automaton model is formulated in an automata language (e.g., SAL or SMV) [3]. See also Fig.2.

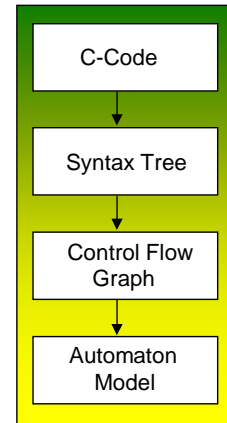


Figure 2: Model Extraction

## II. TEST CASE GENERATION

Our aim is to find appropriate test cases matching the system requirements. Consequently we are interested in certain execution traces of the program. These traces can be identified by means of model checking techniques [4]. Beside its original purpose for formal verification of systems, model checking has become an applicable tool for test case generation [5]. In general, model checking is used to verify a logic formula on a system model. A way to use model checking for test case generation is producing *counterexamples* [6]: For finding a test case corresponding to a specific system requirement  $f$ , we state that  $f$  is *not feasible* within the system model.

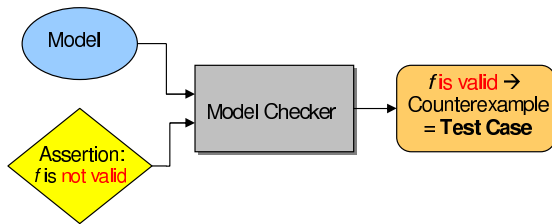


Figure 3: Test Case Generation

So we provide the negated formula  $\neg f$  to the model checker. The model checker searches the state space of the model to prove if this formula is valid or not. In the case of a violation of the formula  $\neg f$  the model checker dispenses a path on which  $f$  is *true* (a counterexample). This path is one instance of an execution trace of the program, where the property  $f$  holds and can thus be used as a test case to test the requirement  $f$  (see Fig.3).

In addition we are forcing the model checker to find test cases by providing further properties. These properties are derivatives and variants of the original requirements from the specification.

### III. RELATED WORK

Currently the elaborate techniques for test case generation introduced above have only been applied to a few case studies (see for example [7]). The systems under test are either very simple applications (especially hardware with boolean data types) or mainly state-based systems, resp. applications of very high safety criticality, for instance flight guidance systems in avionics, or nuclear reactor safety systems. Both the modeling of the system and the automated generation of test cases are extensive. The testing effort for applications in the automotive domain is only reasonable, if it is possible to automate most of the necessary steps.

### IV. PRELIMINARY RESULTS

At the moment we can successfully extract the model and generate test cases in an automated way. The conditions for testing applications in the automotive domain differ from the above case studies in several ways: In general, the modeling for building the system is done with environments like Matlab Simulink, the resulting models are not formal. Only a small part of the application is state-based, the main functionality of the control system under test is influenced by multitude variables of scalar type. The main challenge of the introduced test case generation method is the state space explosion for systems with many variables of non-boolean type. There are attempts to solve this issue by applying abstraction mechanisms (e.g. [8]), but actually these mechanism are rarely automated.

### V. FUTURE WORK

Our task is to apply automated abstraction mechanism to reduce the state space, like data type abstraction, decomposition of the system and counterexample refinement. There is a lot of ongoing research to incorporate such abstraction techniques mechanically to apply them without human interaction [9]. Recently we are engaged with reducing the complexity of the system model by abstraction to enhance the performance of the test case generation methods.

### VI. ACKNOWLEDGMENTS

This work has been supported by the FIT-IT research project “Systematic test case generation for safety-critical distributed embedded real time systems with different SIL levels (TeDES)”; the project is carried out in cooperation with TU-Graz, Magna Steyr, and TTTech.

### REFERENCES

- [1] IEC. IEC 61508 Functional safety of electrical/electronic/programmable electronic safety-related systems. Technical report, IEC, 1998.
- [2] M. Broy, B. Jonsson, J.-P. Katoen, M. Leucker, and A. Pretschner, editors. *Model-Based Testing of Reactive Systems*. Springer, 2005.
- [3] I. Wenzel, B. Rieder, R. Kirner, and P. Puschner. Automatic timing model generation by CFG partitioning and model checking. In *DATE '05: Proceedings of the conference on Design, Automation and Test in Europe*, pages 606–611. IEEE, 2005.
- [4] E.M. Clarke, O. Grumberg, and D.A. Peled. *Model Checking*. The MIT Press, 2000.
- [5] Paul Ammann, Paul E. Black, and William Majurski. Using model checking to generate tests from specifications. In *ICFEM*, page 46, 1998.
- [6] D. Beyer, A.J. Chlipala, T. Henzinger, R. Jhala, and R. Majumdar. Generating tests from counterexamples. In *ICSE '04: Proceedings of the 26th International Conference on Software Engineering*, pages 326–335, 2004.
- [7] Paul Ammann and Paul E. Black. Model checkers in software testing. Online: <http://citeseer.ist.psu.edu/ammann02model.html>.
- [8] John Rushby. Ubiquitous abstraction: A new approach for mechanized formal verification. In *Second International Conference on Formal Engineering Methods (ICFEM '98)*. IEEE, 1998.
- [9] E. Clarke, O. Grumberg, S. Jha, Y. Lu, and H. Veith. Counterexample-guided abstraction refinement for symbolic model checking. *J. ACM*, 50(5):752–794, 2003.

# The Smart Car - a distributed controlled autonomous robot

Gernot Klingler, Alexander Kößler and Wilfried Elmenreich (Faculty Mentor)

Institut für Technische Informatik

Technische Universität

Vienna, AUSTRIA

Email: e0125519@student.tuwien.ac.at

**Abstract** — This work concerns the design and implementation of the distributed controlled system of a four wheeled robot called "Smart Car". The Smart Car's task is to navigate through a static obstacle course by perceiving its immediate environment with the help of a combination of infrared and ultrasonic distance sensors.

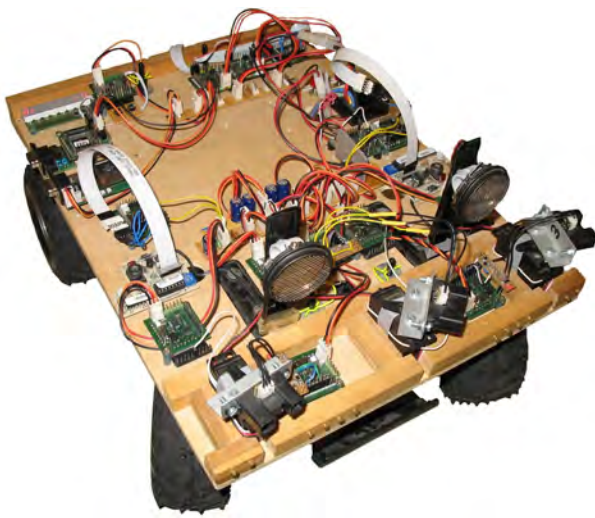


Figure 1: The Smart Car

## I. INTRODUCTION

The initial motivation for the design of the Smart Car, shown in Figure 1, was the need of a "real-live-demonstration object" for the TTP/A communication protocol. TTP/A is a Time Triggered Protocol for SAE Class A applications (TTP/A). This protocol is the latest member of the family of protocols for the *Time Triggered Architecture* (TTA) developed at the *Institut für Technische Informatik* at the Technische Universität in Vienna, Austria. TTP/A has a *Smart Transducer* interface standardized by the *Object Management Group* (OMG) [1] with the purpose of interconnecting transducer (sensor and actuator) nodes, providing hard real-time guarantees for communication. TTP/A uses the *Interface File System* (IFS) [1] which provides a unique addressing scheme for all relevant data in the *Smart Transducer* network, i.e. transducer data, configuration data, self-describing information, and internal state reports of a *Smart Transducer*. Standardized in this fashion, TTP/A represents an inter-

esting option for various sensor network applications like mobile robots. Existing projects on mobile robots typically use point to point wiring or event-triggered communication systems like CAN [2] or Ethernet [3]. The Smart Car also shows the utilization of *Sensor Fusion* [4] which is the combination of sensor data of a number of unreliable sensor measurements to a more reliable measure value. Furthermore robots always have and always will fascinate people. Especially for students this represents an extremely attractive and challenging research field.

## II. SYSTEM ARCHITECTURE OF THE ROBOT

The Smart Car's operation can be categorized into four main fields as shown in Figure 3 – software, electrical hardware, electro-mechanical hardware and mechanical hardware. The software layer consists of the application software and the TTP/A-protocol software. The application software exchanges data with the protocol software running on the same node and performs the tasks which are required for communicating in the distributed fieldbus network according to the rules specified in the protocol definition. The electrical hardware layer consists of a fieldbus network, complete with TTP/A nodes and the car's TTP/A communication bus. The smart car consists of 12 ATMega 128 nodes like the one shown in Figure 2. The *five sensor nodes* (three infrared-nodes and



Figure 2: ATMega128 Node

two ultrasonic nodes) collect the raw data from sensors, transform the data to a standardized digital representation, check and calibrate the signal, and transmit this digital signal via the TTP/A Protocol communication protocol. The *four servo nodes* control the servos on which the infrared sensors are mounted and the servo which is responsible for the steering direction. The *display node* shows debugging information. The *engine node* controls the speed of the vehicle. The *navigation node* receives

the sensor data (already calibrated by the sensor-nodes) and performs a navigation algorithm to find the best way through the obstacles and sends the calculated steering direction and speed values to the corresponding nodes.

All the nodes are arranged as a cluster, and exchange information on a serial bus with the TTP/A protocol.

The *electrical/electromechanical hardware layer* refers to the sensors, power supplies, servos, LED indicators and other components such as additional power supply busses. The *mechanical layer* consists of the main chassis of the Smart Car, which is an off-the-shelf four wheeled model car fitted with a wooden mounting board.

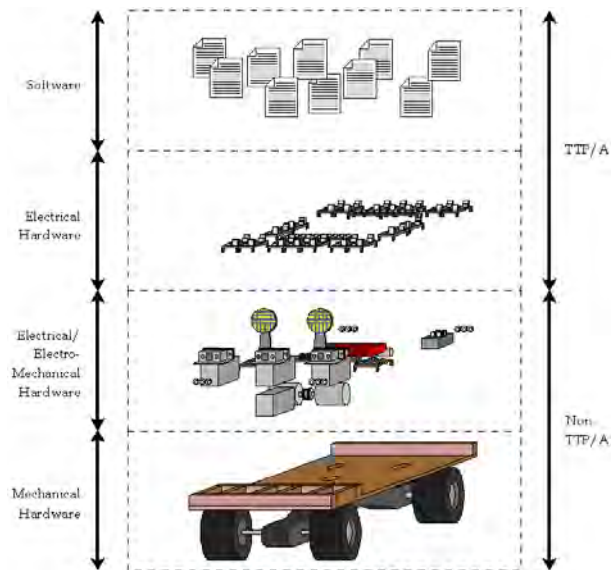


Figure 3: Hardware layers of the car

### III. SHORT DESCRIPTION OF THE NAVIGATION ALGORITHM

Before the navigation algorithm can start, the navigation-node collects the data from the sensor nodes and generates a grid with the *"robust certainty grid algorithm"* - a fault tolerant sensor fusion algorithm that was developed by Elmenreich, Schneider and Kirner [5]. The grid is seen by the car as a 17x10 array which represents a 170x100cm region around the car. The algorithm works with at least three sensors and can tolerate repeated sensor failures, with the ability to reintegrate recovered sensors. The algorithm merges the sensor data of the sensors and calculates "obstacle-likelihoods" for every element in the grid-array. When the grid-generation is completed, the grid serves as an input for the navigation algorithm. The navigation algorithm calculates - according to the grid - the direction with the least risk and sends its result to the node controlling the steering-direction and the speed of the car. If the algorithm cannot find a way, the vehicle stops.

In a future version of the navigation algorithm we plan to implement backtracking, which means that if the car

cannot find a further way, it navigates the same way back and tries to take another way through the obstacles.

### IV. RESULTS OF THE WORK WITH THE SMART CAR

The work on the Smart Car has been performed within the scope of a Bachelor's Thesis. While the mechanical hardware was available from previous projects, the work included a redesign of the transducer network, the implementation of the Smart Transducers and the setup of the *Sensor Fusion* and navigation subsystem.

The Smart Car acts as a model system for the research on designing, configuring and debugging of TTP/A networks. The car is also used for sensor data generation for the research on sensor fusion. The limited hardware resources in embedded systems sometimes led to massive problems, especially the complex dependable navigation algorithm is a very resource-hungry application. While coping with problems and pitfalls of programming embedded systems, we also learned that debugging a distributed embedded system is a challenging job.

As such, the Smart Car acts as a *Drosophila Melanogaster* for intelligent distributed embedded systems.

### ACKNOWLEDGEMENTS

The authors want to thank Angela Schögendorfer for her constructive comments on this paper. This project was supported by the Austrian FWF project TTCAR under contract No. P1806-N04.

### REFERENCES

- [1] Object Management Group OMG. Smart transducers interface v1.0. 2003. Available at <http://doc.omg.org/formal/2003-01-01>.
- [2] G. Novak and M. Seyr. Simple path planning algorithm for two-wheeled differentially driven (2WDD) soccer robots. In *Proceedings of the Second Workshop on Intelligent Solutions for Embedded Systems (WISES'04)*, pages 91–102, Graz, Austria, June 2004.
- [3] Y.-J. Cho, J.-M. Park, J. Park, S.-R. Oh, and C. W. Lee. A control architecture to achieve manipulation task goals for a humanoid robot. In *Proceedings of the IEEE International Conference on Robotics and Automation (ICRA-98)*, pages 206–212, Piscataway, USA, May 1998.
- [4] W. Elmenreich. *Sensor Fusion in Time-Triggered Systems*. PhD thesis, Technische Universität Wien, Institut für Technische Informatik, Vienna, Austria, 2002.
- [5] W. Elmenreich, L. Schneider, and R. Kirner. A robust certainty grid algorithm for robotic vision. In *Proceedings of the 6th IEEE International Conference on Intelligent Engineering Systems (INES)*, May 2001. Available at <http://www.vmars.tuwien.ac.at>.

# Automated solution evaluation during a practical examination

Alexander Köbler, Wilfried Elmenreich (Faculty Mentor)  
Institut für Technische Informatik  
Technische Universität  
Vienna, AUSTRIA  
Email: {koe,wil}@vmars.tuwien.ac.at

**Abstract** — *Checking the programming skills of students in form of an exam is a common used practice at many schools and universities. Testing such embedded programs is a tough job due to limited debugging and test interfaces and typically program functionality in the value and time domain. Moreover, in our application task we also have a stringent requirement for a fast testing phase, since there is a limited number of target systems which are reused for subsequent examinations during one day. In this paper we present an approach for an automated evaluation of a student's solution in such an embedded system.*

## I. INTRODUCTION

The exam regarded for this work consists of an exam with a preparation phase on paper, a live programming phase on a computer and an evaluation and testing phase on embedded hardware. As a result we only regard if the student succeeded to program the embedded hardware successfully, thus this is binary decision between either "correct" or "incorrect". If the exam is done on computer and real hardware, like ours, the possibility to evaluate the coded program is very important.

One of the biggest problems in this kind of examinations comes by getting close to the end of the working time, when every student wants to be sure her/his program works correctly and meets all specifications. Usually a supervisor has to evaluate the students program. In case of embedded systems programming this is not always easy, because it is very difficult to check a specification due to limited I/O and debugging features (e.g. the result of a program may only be a flashing LED) and the temporal aspect (e.g. it is difficult to exactly tell, if the blinking frequency of the LED meets the specification). There are just two possible solutions for this problem.

Reviewing the solutions manually after the examination day is not economically, since reviewing involves downloading the program to the embedded hardware and checking the program behavior - a sumptuous and complicated task in embedded systems that would take days. Moreover, the students like to have feedback on the correctness of their programs during examination in order to decide when they can move on to next exam task.

Therefore, we aim at an automated evaluation during the exam time which instantly gives the student feedback about the correctness of her/his work. This would improve our exam situation in two ways. First, we do not need stuff to give the students information if their programs are working correctly, because every student can evaluate her/his program at any time using the automated test system. This means that the supervision personnel can look after the real problems (hardware faults, spec-

ification problems ...). Second, there is no time needed after the exam to review all work. This means at the end of the examination every student knows if the solutions she/he produced were correct or not.

Currently, there does not exist much published work on automated evaluations for embedded programming exams. A notable exception is the work presented in [1], which focuses on the automatic evaluation of embedded systems homework and exams.

## II. EXAM SETUP

It would be important to find an environment setup for the exam which meets some security rules. Therefore it is useful to turn off/restrict access to the internet and provide no possibilities for students to get data in and out using digital media.

"Figure 1" shows the principle of this system consisting of four parts:

*Task specification*; In contrast to evaluation by hand an automated evaluation system needs a much more detailed specification to be accepted right by the evaluator. In most cases the students' solution will manipulate some kind of information got as input and hand it to the evaluator, which decides if the manipulation was done right. This means the output format has to be exactly defined in the task specification. If the evaluator is not programmed to be tolerant the difference between a good and bad program may be found in the missing '\r' in the new line statement '\r\n'. When evaluating solutions with analogue variables, it is required to define tolerances, espe-



Figure 1: The principle of the automated evaluation

cially if the analogue variable is digitalized.

Second, the *sample solution*. It's task is to exclude hardware faults and demonstrates the students how the right solution should behave. Therefore, it is very important that the sample code is correct and very well tested, otherwise the students could be confused and they will not trust the automated assessment even if the evaluation itself works correctly. Another sample solutions' requirement is, that it must be possible for the evaluator to distinguish between a sample solution and a student's solution, while for the student there should be no difference between the task specification and the sample solution. For example if the challenge is to generate a counter, increasing its value from 0x00 to 0x7F it might be an good idea to reserve the MSB for indicating the sample solution, if set. Nice side effect in this case is that the evaluator doesn't need to check for overflow of the counter, because it will then be determined as sample solution and not accepted as a correct student's solution.

The *evaluator* is the third – and main part – our system consists of. It does the evaluation if the student's program meets the specifications (or not), or if the running program is the sample program, and gives feedback about this information to the PC. The communication between the Gateway Node and the PC is realized with a small Client-Server-protocol "Figure 2". The client (PC) sends a request to the Gateway Node containing an unique id (the Matrikelnummer has been approved working very well). If the Gateway Node receives the request it might start the evaluation process (if the students program is waiting for explicit input) or just get the evaluation result from the evaluator. Next step is to digitally sign the id previously transmitted. We do this as a security trait, so we can ensure that the response is really from our Gateway Node and not forged by some student. The complexity of this signature is determining for the security of the whole system. If this algorithm can be found out by students it would be possible to fake a response of the Gateway and get points for a task which wasn't solved correct. If  $c_{hack}$  specifies the costs to find out the algorithm of the signature and  $c_{solve}$  are the costs to solve the exercise legally the following connection should exist

$$c_{solve} \ll c_{hack} \quad (1)$$

This could be reached by reducing the given time and complexity of the problem the students should solve or by increasing the complexity of the digital signature. Since the microcontrollers are very powerful today also strong cryptography algorithms could be chosen. Due to the limited time every student has available on the machine, the limited possibility to compare different signed ids, and the missing chance to get the signed ids out of the lab without memorizing it, also weaker signature methods reach an adequate level of security.

The fourth, last, but therefore not least important, part of the automated evaluation system is the *client application* which is located at the students PC. When a student wants to check if the solution she/he programmed during the exam fits the specification she/he starts the client program, which does the previous described communication with the Gateway Node. The application can differentiate 4 states. If the protocol aborts because

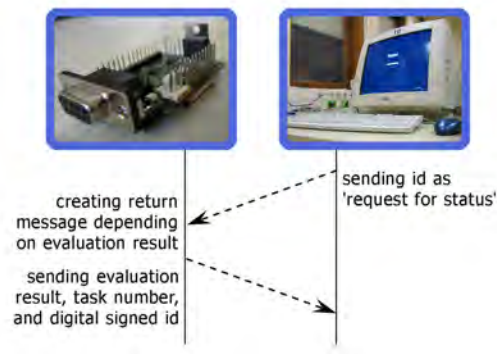


Figure 2: Client Server protocol between PC and Gateway Node

of some reason (hardware failure, connection failure, ...) the application will report a 'communication error' otherwise the application will report if the evaluated program works correctly, incorrectly, or is the sample program. If the student's solution is correct it will save the returned signed key in a specified hidden file in the user's home directory. The results have to be stored locally, because in the exam environment the network is turned off for security reasons. If a successful evaluation happened once, the exercise will be marked as solved, even if a later evaluation would report a wrong solved exercise. This means, that it is very important to minimize the possibility that the evaluator reports wrong solutions as correct. One option to ensure that no incorrect solution is accepted is to use a significant number of test cases to decide if a program works well.

### III. CONCLUSION

We have designed an automatic evaluation system for embedded systems programming exams that allow a fast on-site evaluation of the students' solutions. In the design we have regarded aspects of test tolerance and evaluation faults as well as security aspects. The system has been used in the course "Embedded Systems Programming" for the evaluation of two programming tasks, which have been given to 70 students. The results promise a dependable and fair possibility to evaluate student's work with reduced effort for tutors and the teaching personnel.

### ACKNOWLEDGMENTS

This project was supported by the Austrian FWF project TTCAR under contract No. P1806-N04.

### REFERENCES

- [1] Ch. Tröhdhandl V. Legourski and B. Weiss. A system for automatic testing of embedded software in undergraduate study exercises. In *Proceedings of the Workshop on Embedded Systems Education (WESE'05)*, pages 44–51, September 2005.

# A Fourier Transform 3D-Model for Wave Propagation in layered orthotropic Media

Felix Kramer and Holger Waubke (Faculty Mentor)

Acoustic Research Institute

Austrian Academy of Science

Vienna, Austria

Email: fkramer@kfs.oeaw.ac.at

**Abstract** — *In order to assess and prevent noise emission in the environment of traffic routes, prognosis models for wave propagation are of interest for many applications. This contribution introduces a new model for wave propagation and simulation in layered orthotropic media. The model uses a component-wise Fourier transform to obtain the general solution within one layer. After that, balances at layer boundaries are used to obtain a grid of stress and displacement vectors. The accuracy of the model is tested, and results are presented.*

## INTRODUCTION

The simulation of vibrations induced by machinery and traffic has become of increasing concern within the last decades, due to frequent construction of high speed trains and mass rapid transport systems. The soil is assumed to consist of  $n$  orthotropic layers. For each layer, the following parameters are needed: the shear modulus  $G$ , the Young's modulus  $E$ , the Poisson ratios  $\nu$ , the density  $\rho$  and width  $d$ . Additionally, homogenous behavior in the horizontal directions is assumed:  $E_y = E_x$ ,  $G_{yz} = G_{zx}$ , and  $\nu_{yz} = \nu_{zx}$  hold. As can be found in [1], the wave equation takes the special form

$$B\sigma + \rho\omega^2\hat{u} = \hat{B}E\hat{D}\hat{u} + \rho\omega^2\hat{u} =: \hat{A}\hat{u} = \hat{b}. \quad (1)$$

for a differential operator  $B$ , where  $b$  is some external force. We denote the Fourier transform  $\hat{f}$  of a function  $f(\alpha)$  by  $\mathcal{F}_{\alpha,k_\alpha}(f)(k_\alpha)$ . The displacement vector  $u := u(x, y, z, t)$  is Fourier transformed in all directions, yielding  $\hat{u}(k_x, k_y, k_z, \omega)$ . Thus, the differential operator  $D$  is substituted by the polynomial operator  $\hat{D}$ . The transformed wave equation then takes the form

$$\hat{B}E\hat{D}\hat{u} + \rho\omega^2\hat{u} =: \hat{A}\hat{u} = \hat{b}, \quad (2)$$

where  $\hat{A}$  and  $H := E\hat{D}$  are symmetric. In order to cope with the boundary conditions, it is useful to implement a grid in  $(k_x, k_y, \omega)$ .

## DERIVING THE EQUATIONS

### THE GENERAL FORM OF A SOLUTION

The condition  $\det(\hat{A}) = 0$  is necessary for solutions of  $\hat{A}\hat{u} = 0$ ,  $\hat{u} \neq 0$  to exist. The roots of the polynomial  $\det(\hat{A}(k_z))$  are denoted by  $\kappa$ , and the vectors

of the corresponding kernel be denoted as  $\Psi$ . As the model assumes the media to be layered with respect to the  $z$ -direction, therefore  $\hat{u}$  is transformed back over the  $z$  direction, yielding  $\tilde{u}(k_x, k_y, z, \omega)$ . By variation of constants, the general form of the solution can be expressed as

$$\tilde{u} = \sum_{i=1}^6 (c_{h,i} + c_{p,i}(z)) \Psi_i \exp(j\kappa_i z), \quad (3)$$

$$\tilde{\sigma} = \sum_{i=1}^6 (c_{h,i} + c_{p,i}(z)) H_i \Psi_i \exp(j\kappa_i z) \quad (4)$$

for  $z$ -dependent coefficients  $c_{p,i}(z)$  from a particular solution.

### CALCULATION OF STRESS AND DISPLACEMENT VECTOR AT LAYER BOUNDARIES

In order to derive the equations for the particular solution, a discrete impact at depth  $d$  inside a layer is assumed. This yields

$$\hat{p}(k_x, k_y, k_z, \omega) = \exp(j(x_0 k_x + y_0 k_y + z_0 k_z + t_0 \omega)) f. \quad (5)$$

As the model is invariant to translation, the origin of the coordinates  $(x, y, z, \omega)$  is set to the point of impact, so that  $\hat{p} = f$ . Note that if the origin is assumed in the middle of the layer, a transformation factor  $\exp(z_p)$  is yielded. A Fourier backward transform gives  $\hat{p}$  as right hand side of Eq. (2). It is to be taken into account that the balance of stresses only holds for the components that act at the interface of the layer boundary. A layer with width  $d$  is considered, loaded with an impact vector  $\hat{p}$  in depth  $d_p$ . The layer is split at the depth of the impact  $d_p$ , and two layers with identical material parameters are derived. For the upper virtual layer let  $\tilde{u}_u$  and  $\tilde{u}_m$  be the transformed displacement at the upper and lower boundary, respectively. For the lower virtual layer, let  $\tilde{u}_n$  and  $\tilde{u}_d$  be the displacement vector at the upper boundary and  $\tilde{u}_d$  the one at the lower boundary. Obviously,  $\tilde{u}_m = \tilde{u}_n$  holds. The equations for displacements and stress at the point of impact can be established now. The stress vectors  $\tilde{\sigma}_{r,m}$  and  $\tilde{\sigma}_{r,n}$  at the virtual layer boundary differ by  $\hat{p}$ . The coefficient vector  $a$  (for the solution in the upper layer) and  $b$  (for the lower layer) consist of homogenous and particular part,  $a = a_h + a_p$ ,  $b = b_h + b_p$ . where  $a_h = b_h$ .

The particular part  $b_p = 0$  as the lower virtual layer is treated as an unloaded layer. The particular part  $a_p$  has to satisfy

$$\tilde{u}_{p,m} = \sum_{i=1}^6 a_{p,i} \Psi_i = 0, \quad \tilde{\sigma}_{p,m} = \sum_{i=1}^6 a_{p,i} H_{r,i} \Psi_i = \hat{p}. \quad (6)$$

The coefficient of the displacements and stresses of the unified layers are denoted by  $c = c_h + c_p$ . The particular component of the solution is given by  $c_p = a_p = M^{-1} \hat{p}_0$ . Correction factors  $\exp(\pm \frac{1}{2} j \kappa_i d)$  arise componentwise for the layer boundaries due to the position of the origin,  $\exp(j \kappa_i z_p)$  for the particular solution. The matrices  $\Theta$  and  $\Xi$ , as well as the vector  $\tilde{p}$ , allow to rewrite

$$\tilde{u} =: \Theta c_h + \begin{pmatrix} \Theta_u \tilde{p} \\ 0 \end{pmatrix} = \tilde{u}_h + \tilde{u}_p, \quad (7)$$

$$\tilde{\sigma}_r =: \Xi_r c_h + \begin{pmatrix} \Xi_{r,u} \tilde{p} \\ 0 \end{pmatrix} = \tilde{\sigma}_{r,h} + \tilde{\sigma}_{r,p}. \quad (8)$$

where  $\Theta_u, \Xi_{r,u}$  consist of the upper three rows of  $\Theta$  resp  $\Xi_r$ . Substituting  $c_h = \Theta^{-1}(\tilde{u} - \tilde{u}_p)$  into the stress equations, and defining  $K := \Xi_r \Theta^{-1}$ , it holds that

$$\tilde{\sigma}_r = \Xi_r \Theta^{-1}(\tilde{u} - \tilde{u}_p) + \tilde{\sigma}_{r,p} = K \tilde{u} - K \tilde{u}_p + \tilde{\sigma}_{r,p}, \quad (9)$$

for a loaded layer. The case for an unloaded layer can easily be deduced from the general case by setting the partial component to zero.

#### BALANCE AT LAYER BOUNDARIES

Now, a system of  $n$  layers is considered. The layers are numbered in the canonical way, such that  $\tilde{u}_i$  is the displacement at the upper boundary of the  $i$ -th layer. For unloaded layers, the balance of stresses yields

$$K_{i,d} \begin{pmatrix} \tilde{u}_i \\ \tilde{u}_{i+1} \end{pmatrix} = K_{i+1,u} \begin{pmatrix} \tilde{u}_{i+1} \\ \tilde{u}_{i+2} \end{pmatrix} \quad (10)$$

#### BOUNDARIES OF LOADED LAYERS

The layer  $k$  is assumed to be loaded. Let the indices  $h$  and  $p$  denote the homogeneous and the particular part of the solution. With  $\tilde{\sigma}_{k,u} = \tilde{\sigma}_{k-1,d}$  it holds that  $\tilde{\sigma}_{k-1,d} = \tilde{\sigma}_{k,u} = \tilde{\sigma}_{h,k,u} + \tilde{\sigma}_{p,k,u}$ , and as the stress vector at the upper boundary takes the form  $\tilde{\sigma}_{k,u} = \Xi_{k,u}(c_k + \tilde{p}_k)$  (see Eq. (7)), the balance of stresses at the layer boundaries can be established. For the displacement  $\tilde{u}_1$ , which occurs at the boundary between air and soil, the boundary conditions are assumed to be of von Neumann type. For the bottom halfspace, boundary conditions are derived by Sommerfeld conditions.

#### SYNTHESIS

Again, a system of  $n$  layers is considered, including the  $k$ -th one, which is assumed to be loaded. Putting together the results, the equation to be solved is established defining the supervector  $U := (\tilde{u}_1, \dots, \tilde{u}_n)^T$ . So, it delivers a linear equation  $LU = V$ , where  $L$  is an  $n \times n$  block band matrix with  $3 \times 3$  blocks.

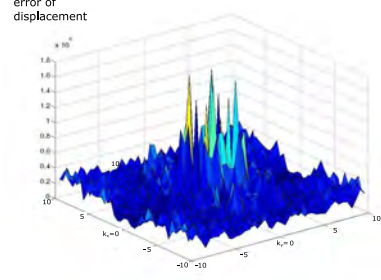


Figure 1: The relative error of  $U$  for a four layer system;

#### OBTAINING THE GRIDS

With the solution  $U$  it is possible to compute the stress vector as well as the displacement vector at arbitrary points. By implementing a grid in the  $z$ -direction, the four dimensional grid in  $(k_x, k_y, z, \omega)$  can easily be derived by evaluating in  $z$ . A Fourier back transform in  $k_x$  and  $k_y$  finally yields a grid in the coordinates  $(x, y, z, \omega)$ , which was the intended result.

#### TESTING THE MODEL

Results were computed for  $(k_x, k_y) \in [-10, 10]^2$ ,  $\omega = 10$  kHz.

**Numerical Accuracy:** The numerical stability is checked by running a symbolic computation software (MAPLE 9.5) with the data, and comparing the results to the ones of the C++ program. accuracy up to the fifth decimal position is detected. The relative error is smaller than  $1.6 \times 10^{-13}$ .

**Physical consistency:** The second test is checking physical consistency. For a system of layers, the solution is computed. By introducing a virtual layer boundary at a random depth, one layer is split in two with identical material parameters. The results must coincide at the layer boundaries(9). The relative error is smaller than  $10^{-5}$ .

#### ACKNOWLEDGEMENTS

This work is financed by the Austrian Federal Ministry for Transport, Innovation and Technology.

#### REFERENCES

- [1] W.M. Ewing, W.S. Jardetzky and F. Press, *Elastic Waves in Layered Media*, (McGraw-Hill, New York, 1957).
- [2] F. Ziegler and P. Borejko, "Seismic Waves in Layered Soil: The Generalized Ray Theory", in *Structural Dynamics-Recent Advances*, edited by G. I. Schueller, (Springer, Berlin, 1991).
- [3] H. Waubke, "Waves in a Layered Orthotropic Medium with and without Random Properties", in *10th International Congress on Sound and Vibration*, (Stockholm, 2003).

# Power Equivalent Gaussian Beam for Terrestrial Optical Wireless Link Power Budget

Petr Krivak, Otakar Wilfert  
Institute of Radio Electronics  
Brno University of Technology  
Brno, Czech Republic

Email: xkriva10@stud.feec.vutbr.cz, wilfert@feec.vutbr.cz

**Abstract** — This contribution deals with definition of power equivalent Gaussian beam (PEGB) that is needed for both standard power budget process of optical wireless link (OWL) and laser beam modeling. Measurement of geometrical and power characteristics of the laser beam is presented.

The PEGB calculation becomes from the analogy between relative intensity distributions and the normal distribution. The intensity distribution is based on the measurement of the elliptical symmetry beam spot according to the Gaussian curvature. The derivation of PEGB is based on two preconditions: the PEGB transmits the same power with the same on-axis intensity.

## I. INTRODUCTION

Using the circular symmetry optical beam makes the modeling of OWL function easy. In practical, however, a laser diode with elliptical spot as a transmitter is used (see Figure 1) and simultaneously circular optical elements (lenses, photodiodes, etc.) are applied. This is reason for definition PEGB supported by measurement of the total transmitted power elliptical symmetry, beam radiuses  $w_x(z)$  and  $w_y(z)$  of the wavefronts of a Gaussian beam.

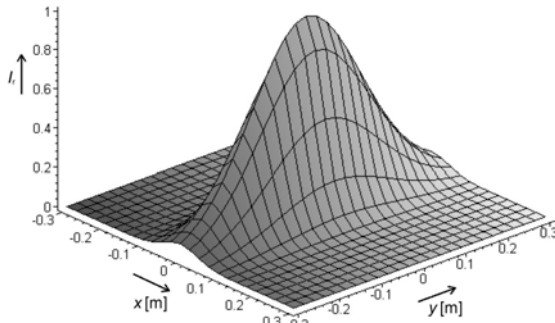


Figure 1: Normalized beam intensity  $I_r$  distribution at elliptical symmetry beam's spot

The beam radiuses  $w_x(z)$  and  $w_y(z)$  are defined in [1] as a radial distance from beam axis, where is the relative intensity decrease to  $e^{-2}$  (circa 13.5%). These

values should be either taken from the measurement, using the Gaussian curve approximation (Figure 2).

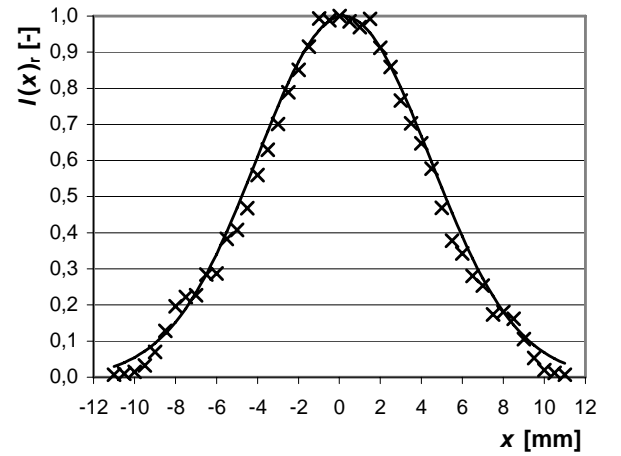


Figure 2: Normalized beam intensity  $I_r$  distribution, get by measured values approximation.

The approximation is given by

$$I_r(x, z) = e^{-\frac{(x-\mu_x)^2}{2\sigma_x^2}}, \quad (1)$$

where the mean  $\mu_x = 0$  and the variance  $\sigma_x$  is given by

$$\sigma_x^2 = \left(\frac{w_x(z)}{2}\right)^2. \quad (2)$$

According to this, the whole relative beam intensity is given as a multiply of a single axis relative beam intensities

$$I_r(x, y, z) = e^{-2\left(\frac{x^2}{w_x^2(z)} + \frac{y^2}{w_y^2(z)}\right)}. \quad (3)$$

For the circular symmetry beam is it

$$I_r(x, y, z) = e^{-2\left(\frac{x^2+y^2}{w^2(z)}\right)}. \quad (4)$$

The definition of PEGB results from mathematical comparison both the total power in real elliptical symmetry beam and total power calculated in circular symmetry PEGB. The total power in circular symmetry Gaussian beam is the double integral of the optical intensity over a transverse plane  $S(x, y)$ , say at a distance  $z$  [2],

$$P = I_0(0, z) \iint_S e^{-2\left(\frac{x^2+y^2}{w^2(z)}\right)} dS, \quad (5)$$

where  $I_0$  is the optical intensity on the beam axis at a distance  $z$ . Total power of the elliptical symmetry beam is given analogically by

$$P = I_0(0, z) \iint_S e^{-2\left(\frac{x^2}{w_x^2(z)} + \frac{y^2}{w_y^2(z)}\right)} dS. \quad (6)$$

We introduce the  $w_x$  to  $w_y$  ratio  $k$  as a ratio of main to auxiliary elliptical radiuses, so

$$w_x(z) = kw_y(z), \quad (7)$$

and

$$P = I_0(z) \iint_S e^{-2\left(\frac{x^2+k^2y^2}{w_x^2(z)}\right)} dS. \quad (8)$$

The easier way to calculate these integrals over the whole  $x, y$  plane is based on using the axis transformations. The total powers are

$$P = I_0(z) \frac{\pi w^2(z)}{2}, \quad (9)$$

$$P = I_0(z) \frac{\pi \sqrt{k} w_x^2(z)}{2} \quad (10)$$

or

$$P = I_0(z) \frac{\pi w_y^2(z)}{2\sqrt{k}}. \quad (11)$$

PEGB is defined as a circular symmetry Gaussian beam with the same total power and the same optical intensity on the axis as a real elliptical symmetry beam. Following this definition we can calculate the radius  $w_{\text{PEGB}}$  of PEGB by comparison of (9) and (10) or (11). The result is

$$w_{\text{PEGB}}(z) = \sqrt{k} w_y(z) = \sqrt{\frac{1}{k}} w_x(z), \quad (12)$$

$$w_{\text{PEGB}}(z) = \sqrt{w_x(z) w_y(z)}. \quad (13)$$

## II. CONCLUSIONS

The given result shows the advantage - the calculation of PEGB parameters is easy and allows us to work with elliptical beams, in spite of calculating with circular ones.

Even that, in some cases, where the circular laser beam spots are necessary, we are able to collimate the laser beam using the combination of two cylindrical lenses or using the prism pair. This solution is surely better, but increases the overall costs.

## ACKNOWLEDGMENTS

This research has been supported by the Grant Agency of Czech republic under contracts No. 102/03/H105 and No. 102/05/0571.

## REFERENCES

- [1] L. C. Andrews, R. L. Phillips and C. Y. Hopen. Laser Beam Scintillation with Applications. Spie Press, Washington, 2001.
- [2] B. E. A. Saleh and M. C. Teich. Fundamentals of Photonics. Wiley, New York, 1991.

# A Portable Real-Time Communication System for Embedded Systems with Heterogeneous Hardware

Stefan Krywult and Wilfried Elmenreich (Faculty Mentor)

CLARA\*Robot Laboratory  
Vienna University of Technology  
Vienna, Austria

Email: {stefan.krywult,wilfried.elmenreich}@clara.tuwien.ac.at

**Abstract** — *In the automotive and avionics industry the application of real-time communication has become self-evident over the last years. However, most real-time protocols are not adequate for heterogeneous, deeply embedded distributed systems as they require a lot of resources and their implementation is hardly portable. In addition, only a few features of these complex protocols are used in such applications.*

*After the analysis of various real-time protocols we have created and tested a portable version of the TTP/A protocol on the hardware of the Tinyphoon, an autonomous research robot developed within CLARA.*

## I. BACKGROUND

The growing complexity of embedded systems leads to modular and distributed systems, which allow considering each subsystem on its own and increase the flexibility and the reusability of the system. Temporal requirements do not only concern each single subsystem but also the communication system providing the interconnection.

This work compares various standard and real-time protocols and discusses their applicability in deeply embedded systems considering the Tinyphoon<sup>1</sup> soccer robot[1] as a case study. The Tinyphoon is a small autonomous and mobile robot in the shape of a cube with a side length of 7cm. It is designed in a modular way and consists of three subsystems: one for vision (Vision Unit), one for decision making (Decision Making Unit) and one for locomotion (Motion Unit). The architecture of the Tinyphoon robot is shown in figure 1.

**Vision Unit** Two cameras mounted on a rotatable head take pictures simultaneously. Each of them is processed on a separate core of a dual-core Blackfin DSP<sup>2</sup>. Another DSP calculates a 3D image and performs object recognition. An ARM7-TDMI processor is used for communication.

**Decision Making Unit** An embedded 32-bit processor running either Linux or Windows CE merges data received from the sensors, the vision unit and other robots

\*Consortium and Laboratory on Advanced Robotics Architectures, a working group of the Center of Excellence for Autonomous Systems of the Vienna University of Technology

<sup>1</sup>www.tinyphoon.com

<sup>2</sup>Digital Signal Processor

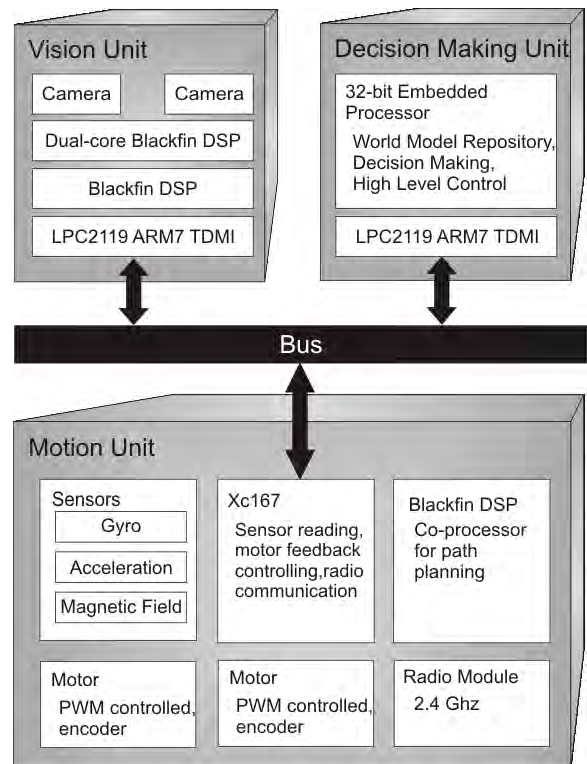


Figure 1: The Architecture of the Tinyphoon Robot

to create a world model and makes decisions based upon that model. This unit also uses an ARM7-TDMI processor for communication.

**Motion Unit** The main task of this unit is the feedback control of the motors. A Blackfin DSP acts as a coprocessor for path planning that needs a lot of computing power. A gyro, a magnetic field and two two-axis acceleration sensors are also integrated on the Motion Unit.

## II. PROBLEM STATEMENT

Currently the communication is implemented in an event-triggered way using the CAN protocol. The timeliness of the communication cannot be guaranteed because it depends on the cooperation of every subsystem. The behavior of the modules is only defined in the functional

domain but it remains undefined in the temporal domain. Therefore, the system lacks temporal composability[2]. Hence, a real-time communication system is required that allows a global scheduling of the communication and fits the special needs of mobile, small and deeply embedded, distributed systems that operate in a rapidly changing environment. Additionally, a strategy is needed for making software implementations of real-time systems highly portable.

Normally, in real-time systems safety and fault tolerance are the most important criteria whereas size, cost and power consumption are rather negligible. By contrast in deeply embedded systems such as the Tinyphoon robot space and energy are of primary concern while fault tolerance is not considered. Thus, a fast but resource saving real-time communication system is required that delivers information to the subsystems in time and with a minimal jitter.

### III. CREATING THE ON-BOARD TIME-TRIGGERED COMMUNICATION SYSTEM

We have analyzed CAN[3], LIN[4], TTP/A[5], TTP/C[6] and the Flexray[7] protocol, considering size (in the RAM/ROM or on a printed circuit board), maximum communication speed, availability (hardware, software, intellectual property), real-time features, the application programmer's interface and licensing issues. CAN is integrated on many microcontrollers in hardware, LIN and TTP/A are available in software and TTP/C and Flexray implementations are available in the form of external communication controllers. Real-time communication with CAN can only be realized using an additional TDMA<sup>3</sup> scheduling on top of the core protocol or using time-consuming polling. LIN uses polling innately that allows real-time communication but lacks efficiency.

Therefore, we have decided to adopt the TTP/A protocol, because of its excellent efficiency and the availability of an open source C implementation for Atmel's 8-bit RISC AVR platform. TTP/A is completely implemented in software and, besides an interrupt-enabled UART<sup>4</sup> and an interrupt-enabled timer unit, that are integrated on most off-the-shelf microprocessors, no additional hardware is needed.

Various 16-bit (Infineon XC167) and 32-bit (Philips LPC2119) processor and DSP (Blackfin family) architectures are used on the Tinyphoon. Therefore, software implementations of real-time protocols have to be highly portable to avoid the need of maintaining multiple versions. Currently all important C compilers conform to the ISO C 90 standard[8]. Language constructs defined in later standards (e. g. inline functions) have to be avoided, because not all compilers are able to understand them. Anyway, the keyword *inline* is only a hint and may be ignored by the compiler even if it is understood. Hence, macros have turned out to be the only re-

liable means that are available on all C compilers and that are suitable to encapsulate time critical functionality that is hardware-specific. So a hardware abstraction layer based on macros has been introduced, which minimizes and isolates platform-specific parts of the source code. To prove the concept, TTP/A is currently ported from the 8-bit AVR architecture to a 32-bit ARM processor.

### IV. CONCLUSION

Within the context of this work a portable version of the TTP/A protocol has been created. It allows adapting TTP/A to new hardware architectures very rapidly and provides an efficient real-time protocol for the use in embedded systems. The effort of maintaining the core protocol source code has been confined because the hardware-independent parts of the protocol code remain unchanged during the process of porting. Current evaluations on an ARM7 TDMI core and an Atmel AVR have demonstrated the portability. In the future we plan to adopt the TTP/A protocol to support high speed applications that deal with large chunks of data as it is necessary for sharing image recognition data and complex world models among distributed components on the Tinyphoon.

### ACKNOWLEDGMENT

This work was supported by the Austrian FWF project under contract No. P18060-N04.

### REFERENCES

- [1] Novak and Mahlknecht. Tinyphoon - a tiny autonomous mobile robot. Technical report, Institute for Computer Technology, Vienna University of Technology, Vienna, Austria, 2005.
- [2] Kopetz. *Real-time systems: design principles for distributed embedded applications*. Kluwer Academic Publishers, 1997.
- [3] Robert Bosch GmbH. CAN specification, version 2.0, 1991.
- [4] LIN Consortium. LIN Specification Package, Revision 2.0, 09 2003.
- [5] Kopetz et al. Specification of the TTP/A protocol. Research Report 61/2001, Technische Universität Wien, Institut für Technische Informatik, 1040 Vienna, Austria, 2001.
- [6] TTAGroup. Time-triggered protocol TTP/C high-level specification document, Protocol Version 1.1, edition 1.4.3, 2003.
- [7] FlexRay Consortium. Flexray communication system, protocol specification, version 2.0, 2005.
- [8] International Organization for Standardization. ISO/IEC 9899:1990 information technology - programming language C, 1990.

<sup>3</sup>Time Division Multiple Access

<sup>4</sup>Universal Asynchronous Receiver Transmitter

# Procedures of Detection and Removal of Blotches on Scanned Optical Sound Tracks using MatLab

Andy Kuiper and Milan Sigmund (Faculty Mentor)  
Institute of Radio Electronics  
Brno University of Technology  
Brno, Czech Republic  
Email: xkuipe00@stud.feec.vutbr.cz

**Abstract** — *This paper briefly describes procedures which make it possible to detect and remove blotches from optical sound tracks. Hereby the restoration is carried out in image domain with the special aim to retain the authenticity of the scanned optical sound track. This means that the original sound quality of the movie during its original showing should be retrieved. The methods developed were realized using MatLab which provides a vast set of tools with its image processing toolbox.*

## I. INTRODUCTION

Film-recordings from the beginning of the 20th century are subject to deterioration. This is caused by the changing chemical characteristics of the original material. Therefore almost 90% of all silent movies and half of all sound movies produced before 1950 are irreparably destroyed [1].

Film-restoration and film-preservation have been done for decades, whereby both were done manually and not in digital form.

Due to the progressive development of technical equipment and steadily declining prices it is nowadays possible for institutions, such as universities, to carry out research on digital restoration [2].

MatLab provides a vast set of tools, especially in cooperation with the "Image Processing Toolbox", for the development of restoration-methods.

## II. SPECIFICATION OF OPTICAL SOUND

The procedure of optical sound recording gives the possibility of storing the audio track on the film. The principle of this procedure is the same for an audio track as it is for the picture. For displaying the picture or playing the audio the material is scanned using light dependent sensors. The collected light is converted into electrical signals which are amplified[3]. The principle is shown in Figure 1 which also gives an idea of how minute an optical sound track is in comparison to the film-picture.

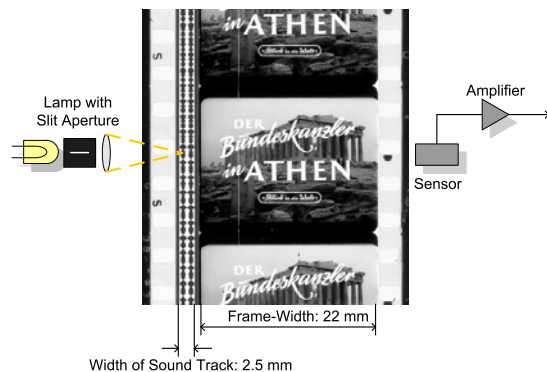


Figure 1: Principle: Optical Sound

## III. EXPERIMENTS

### A. BLOTCH DETECTION

The procedure of blotch detection is shown in Figure 2. First the input image is binarised and then the edges are detected using a canny edge operator. The remaining objects are morphologically closed and thinned. The the blotch skeleton is filled using a scan line algorithm.

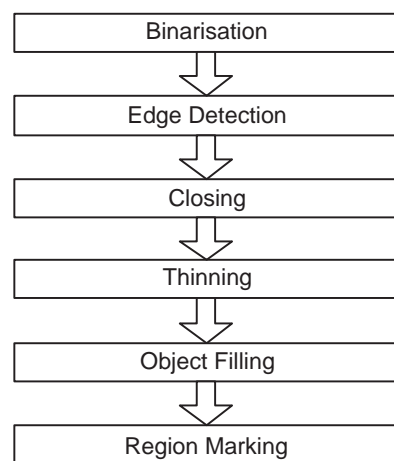


Figure 2: Scheme: Blotch Detection

## B. BLOTCH RESTORATION

The procedure of blotch restoration is shown in Figure 3. The blotch is cut out in a rectangular area where the track is then rotated in x direction in extent of y as shown in Figure 4. During the rotation the "sum of all differences" between the rotating and steady part is calculated simultaneously. The best fit will be copied to the missing region.

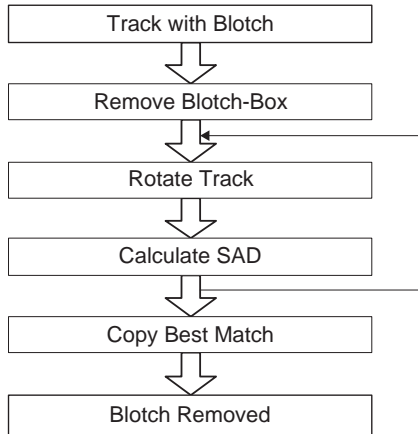


Figure 3: Scheme: Blotch-Restoration

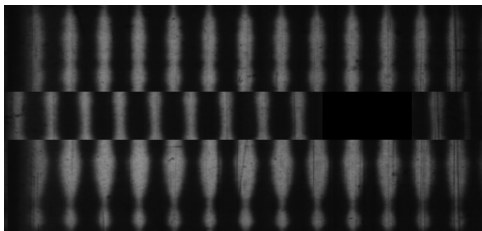


Figure 4: Rotation: Finding "Best Match"

## IV. RESULTS

A faulty area of the scanned optical sound track with blotch is shown in Figure 5. This type of blotch is very common and appears when there is dirt on the film positive during the copying process. It can also be seen that the other traces are symmetrical and carry no noticeable greater faults.

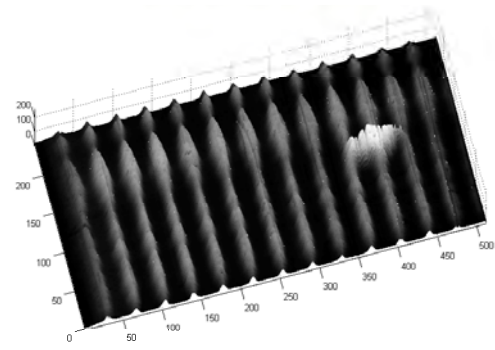


Figure 5: Sound Track with Blotch

After applying the methods for detection and removal of blotches the previously faulty area of the sound track appears as shown in Figure 6.

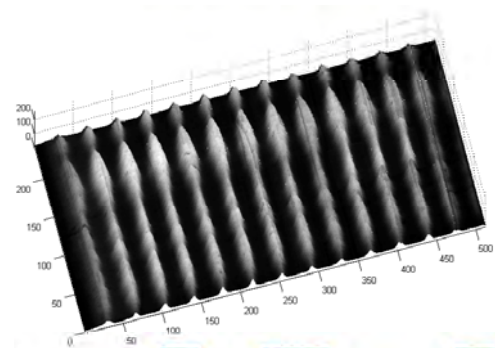


Figure 6: Restored Sound Track

## ACKNOWLEDGMENTS

Supported by the Grant Agency of Czech Republic - Project-No. 102/03/H109.

## REFERENCES

- [1] D Richter, D Poetsch, A Kuiper. Localization of faults in multiple double sided variable area code sound tracks on motion picture films using digital image processing. In *Proceedings of Radioelektronika 2003*, Brno, Czech Republic, 2003. ISBN 80-214-2383-8.
- [2] A Kokaram. *Motion Picture Restoration - Digital Algorithms for Artefact Suppression in Degraded Motion Picture Film and Video*. Springer Verlag, 1998. ISBN 3-540-76040-7.
- [3] A Kuiper. Detection of dirt blotches on optical sound tracks using digital image processing. In *Proceedings of Radioelektronika 2003*, Brno, Czech Republic, 2005. ISBN 80-214-2904-6.

# Forward Error Correction Coding Schemes in Ultra Wideband Communications

Vishwas Lakkundi and Roman Marsalek  
Institute of Radio Electronics  
Brno University of Technology  
Brno, Czech Republic  
Email: {vishwas,marsaler}@feec.vutbr.cz

**Abstract** — *In this paper, we consider the forward error correction schemes suitable for ultra wideband communications and present the preliminary error performance results obtained using convolutional encoding and Viterbi decoding schemes in an additive white Gaussian noise channel environment. The results indicate a coding gain of over 5 dB at an error floor of  $10^{-6}$ . In addition, super orthogonal codes and serially concatenated convolutional codes have the potential to offer an enhanced error performance.*

## I. INTRODUCTION

Forward error correction (FEC) coding is an integral part of system design in new generation wireless communication applications. It is a commonly used means of achieving data transmission with low error rates. Ultra wideband (UWB) is an emerging wireless technology in the personal area network (PAN) domain, wherein very high data rates and GHz frequency bands are common phenomena. Hence, their system design requirements are demanding and quite different than conventional wireless technologies.

Convolutional encoding and Viterbi decoding are recommended in UWB specifications. A few new techniques such as super orthogonal convolutional codes have been proposed lately. There is enough scope to experiment with new, novel FEC schemes, such as parallel and serially concatenated convolutional codes, in order to enhance the performance further, and support future applications.

A short description of UWB technology is provided in the next section. The subsequent section deals with FEC schemes used in UWB and their salient features. The final section depicts some of the experimental results we've obtained so far.

## II. ULTRA WIDEBAND TECHNOLOGY

UWB is a new emerging radio design standard and is based on transmitting very short-duration pulses, often of duration of only nanoseconds or less, whereby the occupied bandwidth is very high. This allows it to deliver data rates in excess of 100 Mbps,

while using small amounts of power and operating in the same bands as existing communications, without producing significant interference. UWB is fundamentally different from all other radio frequency communications, in that it achieves wireless communications without using a sine-wave RF carrier. Instead, it uses modulated high-frequency low-energy pulses of less than one nanosecond in duration.

UWB is still under development. However first UWB chip sets are already available. This is valid for IEEE802.15.3 and for IEEE802.15.3a standards, although the latter is yet to be completed. UWB has the potential to replace WLAN or Bluetooth for short range applications. Advantages include higher transmission speeds (at least for point-to-point connections), resistance against multipath fading and the intended price level [3].

## III. FEC SCHEMES

Interference issues pose restrictions on the maximum data rate that can be supported. One way to overcome the destructive effects of interference and simultaneously maintaining a certain performance level is to apply error correction coding.

Code Type	Constraint Length & Generator Polynomials	Rate	Implementation Requirements
Convolutional	Constraint length $L=6$ , Generating polynomial (65, 57)	$\frac{1}{2}$ or $\frac{3}{4}$	Mandatory for Tx: Rate $\frac{1}{2}$ & $\frac{3}{4}$ Mandatory for Rx: Rate $\frac{1}{2}$ Optional for Rx: Rate $\frac{3}{4}$
Convolutional	Constraint length $L=4$ , Generating polynomial (15,17)	$\frac{1}{2}$ or $\frac{3}{4}$	Mandatory for Tx: Rate $\frac{1}{2}$ & $\frac{3}{4}$ Optional for Rx: Rate $\frac{1}{2}$ & $\frac{3}{4}$

Table 1: Summary of FEC schemes for UWB [4]

UWB specifications recommend the use of convolutional encoding and Viterbi decoding for FEC [4]. Table 1 provides the salient features of these schemes.

An error correction coding scheme dedicated for UWB-IR communications should: be of low complexity, be scalable, provide reasonable bit error rate (BER) performance, and introduce very small delays. Super orthogonal and turbo super orthogonal codes are some of the potential candidates.

#### A. SERIALY CONCATENATED CODES

As shown in Figure 1, serially concatenated convolutional codes consist of a series made of an outer encoder, an interleaver and an inner encoder. The scheme can be generalized to  $n$  cascaded encoders with  $n-1$  interleavers in between.

These codes could be tried in place of their parallel concatenated counterparts, namely turbo codes. Since *a-posteriori* probability algorithms are more complex for block codes than for convolutional codes, and as the interleaver gain is normally higher for properly designed convolutional constituent codes, serially concatenated convolutional codes are more suitable for practical applications.

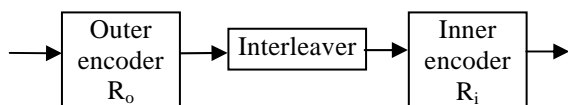


Figure 1: Rate- $k/n$  serially concatenated convolutional code ( $n, k, N$ )

## IV. EXPERIMENTS AND RESULTS

Error performance of a rate-1/2 convolutional code with constraint length  $L=6$  and generator polynomial (65, 57) is depicted in Figure 2. Decoding is performed by the soft-decision Viterbi algorithm. An AWGN channel is considered. It is evident that the convolutional scheme yields a coding gain of about 4.5 dB at an error floor of  $10^{-5}$  and furthermore, a coding gain of over 5 dB seems achievable at an error floor of  $10^{-6}$ .

Our future work will focus on relevant tasks in the direction of enhancing the error performance of UWB further. More complex scenarios of the FEC scheme used above and, in addition, the use of other coding schemes mentioned above would be considered.

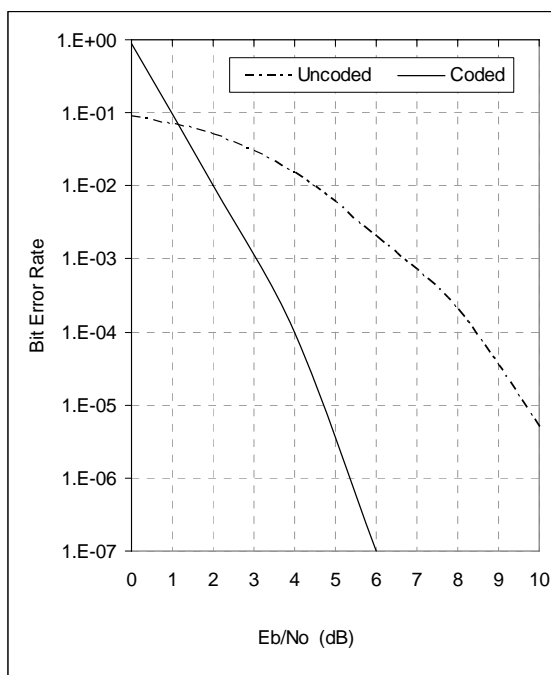


Figure 2: UWB error performance over an AWGN channel

## ACKNOWLEDGMENTS

This work has been supported the Czech Grant Agency under grants No. 102/03/H109 ('Methods, Structures and Components of Electronic Wireless Communication'), and No. 102/04/0557 ('Development of Digital Wireless Communication Resources') and by the research program No. MSM0021630513 ('Electronic Communication Systems and Technologies in the New Generation').

## REFERENCES

- [1] M. Ghavami et al. Ultra Wideband Signals and Systems in Communication Engineering. John Wiley & Sons, 2004.
- [2] D. Porcino and W. Hirt. UWB Radio Technology: Potential and Challenges Ahead. IEEE Communications Magazine, July 2003.
- [3] UWB Forum, [www.uwbforum.org](http://www.uwbforum.org)
- [4] DS-UWB Physical Layer Submission to 802.15 Task Group 3a, IEEE P802.15 Working Group for Wireless Personal Area Networks, July 2004, <http://www.ieee802.org/15/pub/04/15-04-0137-03-003a-merger2-proposal-ds-uwb-update.doc>

# Construction of a Fault-Tolerant Wireless Communication Topology Using Distributed Agreement

Heinrich Moser and Ulrich Schmid (Faculty Mentor)  
 Embedded Computing Systems Group  
 Institute of Computer Engineering  
 Vienna University of Technology, Austria  
 Email: {moser, s}@ecs.tuwien.ac.at

**Abstract** — *This paper presents a proven correct implementation of a distributed topology construction algorithm based upon agreement on minimal-weight clusters for creating a  $\Delta$ -regular,  $\Delta$ -node connected fault-tolerant communication network. It adapts to crashing nodes, moving nodes and changing communication cost. We analyze the requirements imposed upon the system model by this class of agreement-based algorithms and show that our implementation works in asynchronous distributed systems augmented with unreliable failure detectors.*

## I. INTRODUCTION

During recent years, wireless networks without fixed infrastructure (“ad hoc networks”) have become of increasing importance. A particularly critical component with respect to energy-efficiency and fault-tolerance is topology control [1], i.e., constructing a suitable topology for connecting the wireless nodes. Formally, we want to map a communication graph containing all possible links between nodes onto an overlay graph whose connections are a suitable subset of those links. In ad hoc networks, this needs to be done in a decentralized way. Our topology construction method is based upon a clustering scheme which recursively forms groups consisting of  $\Delta$  fully-connected nodes agreeing on a certain joint minimality condition. These groups are treated like single nodes subsequently. Based on this scheme, which so far has been introduced in a centralized approach only [2], this paper introduces a fully distributed algorithm constructing and continuously maintaining a  $\Delta$ -regular and  $\Delta$ -connected overlay graph, providing fault-tolerant multi-hop communication by ensuring that  $\Delta$  node-disjoint paths exist between each two nodes. Furthermore, the  $\Delta$ -regularity provides power efficiency in large-scale wireless networks by ensuring that every node has exactly  $\Delta$  connections.

## II. TOPOLOGY CONSTRUCTION METHOD

We will use the example in Figure 1 to illustrate the general idea of the construction method [2,3]: The algorithm starts with a communication graph  $G$ , where arbitrary edge weights represent communication costs. Figure 1(a) shows the communication graph  $G$  with communication

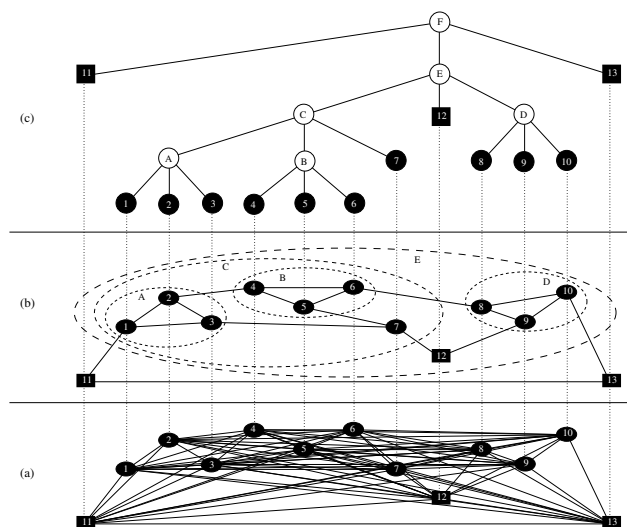


Figure 1: Communication Graph (a), Overlay Graph (b), Topology (c)

costs represented by distance. From this graph, the algorithm constructs an overlay graph  $G'$  for a given  $\Delta$ . Figure 1(b) depicts such a graph for  $\Delta = 3$ , and Figure 1(c) provides the tree representation corresponding to the constructed topology.

The basic grouping principle of the algorithm can be seen in Figure 1(b): Each of the  $\Delta$  members of a group is connected to all of the  $\Delta - 1$  other members (internal connections) and has exactly one connection left (external connection). Since there are  $\Delta$  members in a group, a group has  $\Delta$  external connections left, which are available in higher level groups. From the point of view of higher-level groups, groups hence look like nodes.

For example, in Figure 1(b), the regular nodes (1, 2, 3), (4, 5, 6) and (8, 9, 10) are combined into groups with id  $A$ ,  $B$  and  $D$ , respectively. Such a group is formed if all members agree upon the fact that the sum of the weights (i.e. the communication cost) of their internal connections (e.g.  $4 - 5$ ,  $4 - 6$ ,  $5 - 6$ ) is minimal over all alternative group constructions. It has been shown that this overlay graph provides features such as fault-tolerance, power efficiency, link weight flexibility and failure-locality.

### III. THE ALGORITHM

```
1  periodically          /* PROPOSE_GROUP */
2  let the propose module generate a new group proposal
3  broadcast it to the terminal nodes of all proposed members
4  if all participants agree that the new proposal is better
5  all participants join the proposed new group
6
7  periodically          /* CHECK_GROUP */
8  check for group consistency
9  if group is consistent
10 recalculate group weight
11 else
12 all participants leave the group
```

Figure 2: Generic construction algorithm

Based on this scheme we provide as our main contribution a distributed, proven-correct algorithm which builds up and continuously maintains the  $\Delta$ -regular and  $\Delta$ -connected overlay graph, continuously adapting it to the needs of the wireless network (e.g. moving nodes, crashing nodes, newly added or returning nodes). As a by-product, the algorithm produces a hierarchy of clusters represented by a  $\Delta$ -ary tree that reflects the node “density”. This property can be used in higher level services, like data aggregation in sensor networks, routing, naming, as well as geo- and multicasting. Group proposals are provided by a separate component (the propose module), which can be network-specific and allows to trade construction complexity for minimality of the weight sum of the overlay graph (and hence overall energy efficiency, for example).

The algorithm requires

- a potentially fully-connected weighted network.
- our construction algorithm and a propose module (such as the ones developed by Thallner [4]) running on each node.
- a non-blocking weak atomic commitment service [5].
- crash-failure [6] or crash-recovery [7] semantics.
- a stable period, during which there are no changes of the connection weights, no nodes are added or removed, and the non-blocking weak atomic commitment service does not make any mistakes.

The algorithm itself does not contain any explicit synchrony assumptions such as upper bounds on message transmission delays or restrictions regarding processing speeds, i.e., it works in every asynchronous system satisfying the requirements stated above.

Figure 2 contains a very high-level description of the algorithm. Due to size limitations, the annotated, detailed pseudo-code implementation and its correctness proof are omitted from this extended abstract. The interested reader is invited to consult the Master’s Thesis [8] on which this abstract is based. The thesis also contains an analysis of how purely asynchronous systems (based on the FLP model [9]) can be augmented with unreliable failure detectors [6] to guarantee implementability of our algorithm (i.e., availability of a non-blocking weak atomic commitment service).

### REFERENCES

- [1] Rajmohan Rajaraman. Topology control and routing in ad hoc networks: a survey. *ACM SIGACT News*, 33(2):60–73, 2002.
- [2] Bernd Thallner. Fault tolerant communication topologies for wireless ad hoc networks. In *1st Workshop on Dependability Issues in Wireless Ad Hoc Networks and Sensor Networks (DIWANS’04)*, Florence, Italy, June 2004. <http://www.ecs.tuwien.ac.at/W2F/documents/diwans04.pdf>.
- [3] Bernd Thallner and Heinrich Moser. Topology control for fault-tolerant communication in highly dynamic wireless networks. In *Proceedings of the Third Workshop on Intelligent Solutions for Embedded Systems (WISES 2005)*, May 2005.
- [4] Bernd Thallner. *Topology Control for Fault-Tolerant Communication in Wireless Ad Hoc Networks*. PhD thesis, Embedded Computing Systems Group, Vienna University of Technology, April 2005.
- [5] R. Guerraoui. Revisiting the relationship between non blocking atomic commitment and consensus problems. In *Distributed Algorithms (WDAG-9)*. Springer Verlag (LNCS), September 1995.
- [6] Tushar Deepak Chandra and Sam Toueg. Unreliable failure detectors for reliable distributed systems. *Journal of the ACM*, 43(2):225–267, March 1996.
- [7] Marcos Kawazoe Aguilera, Wei Chen, and Sam Toueg. Failure detection and consensus in the crash-recovery model. *Distributed Computing*, 13(2):99–125, April 2000.
- [8] Heinrich Moser. Distributed construction of fault-tolerant overlay networks. Master’s thesis, Embedded Computing Systems Group, Vienna University of Technology, February 2005.
- [9] Michael J. Fischer, Nancy A. Lynch, and M. S. Paterson. Impossibility of distributed consensus with one faulty process. *Journal of the ACM*, 32(2):374–382, April 1985.

# Software Tool CESim for Graphical Design, Simulation and Analysis of C/E Petri Nets

Petr Novosad and Milan Češka (Faculty Mentor)  
Faculty of Information Technology  
Brno University of Technology  
Brno, Czech Republic  
Email: {novosad, ceska}@fit.vutbr.cz

**Abstract** — *This paper presents a new computer tool CESim for editing, simulating and analyzing the C/E Petri nets. These nets are subclass of general Petri nets. The developed program CESim consists of a graphical editor for the C/E Petri net design and automatic and interactive simulator. The tool also provides facilities for analyzing the C/E systems by the case graphs and the occurrence nets. CESim has integrated a genetic algorithm for optimal case graph layout. New term forward reachable cases is introduced.*

## I. INTRODUCTION

Petri nets are mathematical and graphical tool for modeling concurrent, parallel and/or distributed systems. Spreading of the Petri nets to many scientific and technical areas leads to developing aid computer tools. These tools make use of the Petri nets a lot easier and help them to further expand.

## II. C/E PETRI NETS

Condition/Event Petri nets are subclass of general Petri nets. The net places are called conditions because they model boolean conditions. This range restriction of places give the C/E systems a finite state space with maximum of  $2^n$  states, where  $n$  is a number of conditions in the C/E Petri net. The finite state space provides better possibilities for analyzing system features. The well known P/T Petri nets have a possible infinite state space. For definition of further mentioned terms event, step, case, C/E system and a graphical representation of C/E Petri nets see [1, 2].

### A. FORWARD REACHABLE CASES

The C/E systems do not have initial states. The same case class can be constructed from every state of the case class. The case graph is constructed by forward and backward event execution. Only forward event executing can not reach from any case to all other cases. This characteristic is typical only for cyclic systems, where  $\forall c_1, c_2 \in C_\Sigma : c_1 r_\Sigma^* c_2$ . For this reason a new term forward reachable cases was defined.

For C/E system  $\Sigma$ , set of forward reachable cases  $D \subseteq C_\Sigma$  from some starting case  $c_{start} \in C_\Sigma$  is defined as  $D = \{c \mid c \in C_\Sigma \wedge c_{start} r_\Sigma^* c\}$ . The forward reachable cases can be used for further analysis of the C/E systems. One can check what conditions and cases can not arise and what events can not occur depending on the starting case from which the simulation is started. The case graphs of large C/E systems contain large amount of information. Validation using forward reachable cases can reduce this volume of information.

## III. CESIM

The tool CESim in Figure 1 is inspired by existing tools for P/T Petri nets. It is designed for Microsoft Windows operation system. The tool includes three independent views. The first view serves for a net design and a simulation. The second view shows the case graph and the third view shows the occurrence net. This tool is designed for educational purpose. And for this reason it contains output window that shows performed actions and other information about the system. This information also helps to understand the evolution of system during a simulation. CESim provides the same resources for creating all elements of graphical representation of the C/E Petri nets as modern graphical editors. Besides the basic elements of the C/E Petri nets, user has available additional graphical elements for highlighting the meaning of the modeled net.

The tool provides interactive and automatic simulation mode. The simulation works directly with graphical representation of the system. The interactive simulation is entirely controlled by user that can execute enabled events. The automatic simulation is driven by an algorithm with random selection of provided steps. User can control a speed of the simulation, set breakpoints on any case of the system or simulate just one step. The change of a marking during a simulation is done by animated move of tokens between corresponding conditions. Event execution

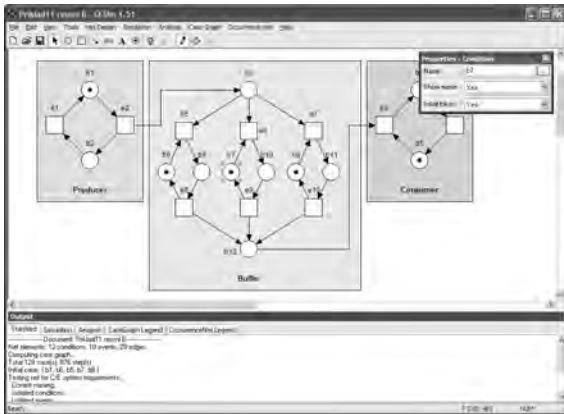


Figure 1: CESim user interface

is written to the output window together with the new system state. These features are also useful in the process of learning the C/E Petri nets. The case class verification option is also available in the simulation mode.

The case graph is one of the most valuable instruments for analyzing the C/E systems. It is a directed graph that shows dependences between cases and steps (see [1]) and it is generated automatically when the simulation mode is entered. The case graph fully cooperates with the simulation and the progress of the simulation can be controlled from it.

Construction of the case graph forms the main part of the C/E system analysis in CESim. This algorithm is computationally demanding for complex C/E systems. Therefore optimization is needed because of the possible state explosion problem. For example, relatively small C/E system consisting of a step with 8 executable events generates case graph with 256 cases and 6305 edges. Optimization techniques were taken from [3].

#### A. AUTOMATIC CASE GRAPH LAYOUT

The majority of C/E systems have a very complex case graphs. CESim has integrated a genetic algorithm for optimal case graph layout. The genetic algorithm is a stochastic algorithm that searches a state space by a population of individuals. The individual in a population is called a chromosome and carries one solution. At the beginning all chromosomes in the population are initialized with randomly spread nodes of the case graph. Then the genetic algorithm works in cycle as follows. The population is evaluated with a fitness function. The fitness function takes into account the number of intersections be-

tween edges or the length of edges between linked nodes or the sum of minimal and maximal distances between nodes in the case graph. Two chromosomes are selected by a tournament selection and crossover and mutation operators are applied onto them. The new chromosomes are placed into a new population and the cycle repeats. It is a generative algorithm with entire population replacement and a simple elitism. For further information about the genetic algorithms see [4].

#### B. IMPLEMENTATION

CESim is implemented in developing tool Microsoft Visual C++ 6.0 using the MFC library. The size of the source code is almost 19 thousands lines. The program is object-oriented. User interface uses single document type document-view architecture.

#### IV. CONCLUSION

The main contribution of my work is the tool CESim. CESim was developed because there was no such tool with graphical interface that provides so specific possibilities of analyzing the C/E Petri nets. The developed tool CESim is fully comparable with similar tools in its category. And exceed other tools in possibilities of analyzing the C/E Petri nets by the case graph and the occurrence net. CESim is supposed to assist students to get familiar with the C/E Petri nets. For this reason a set of demonstration examples were created.

The genetic algorithm satisfied all needs required from it. The advantage of the genetic algorithm is in possibility of exact time control of duration of layout optimization.

#### ACKNOWLEDGMENTS

This work has been supported by the Grant Agency of Czech Republic, grant No. GA102/05/H050 "Integrated approach to education of PhD students in the area of parallel and distributed systems"

#### REFERENCES

- [1] W. Reisig. *Petri Nets - an Introduction*. Springer-Verlag, Berlin, 1985.
- [2] M. Češka. *Petriho sítě*. Akademické nakladatelství CERM, Brno, 1994.
- [3] J. Demel. *Grafy a jejich aplikace*. Academia, Praha, 2002.
- [4] V. Kvasnička. *Evoluční algoritmy*. STU Bratislava, 2000.

# Security Protocols: Analysis and Design

Pavel Ocenasek and Miroslav Sveda (Faculty Mentor)  
Faculty of Information Technology  
Brno University of Technology  
Brno, Czech Republic  
Email: {ocenaspasveda}@fit.vutbr.cz

**Abstract** — *The security protocols are used to establish secure communication over insecure open networks and distributed systems. In the first part of this paper the brief introduction to the analysis and design area is given, followed by the description of the author's presented evolutionary approach, which seems to be useful for automating the security protocol design.*

## I. INTRODUCTION

Security protocols (cryptographic protocols) are intended for secure communication of subjects over an insecure network. The goal is to prevent a spy from reading the contents of messages addressed to others (secrecy). Most security protocols also guarantee an authenticity. This means that if a message appears to be sent by subject A, then A sent exactly this message and it contains the indication of its integrity. To ensure protocol security there are many ways for their analysis [1] [2].

## II. SECURITY PROTOCOLS ANALYSIS

The analysis of security protocols is very important because there is no guarantee that a protocol we use is secure. There are three main approaches used for the security protocol analysis.

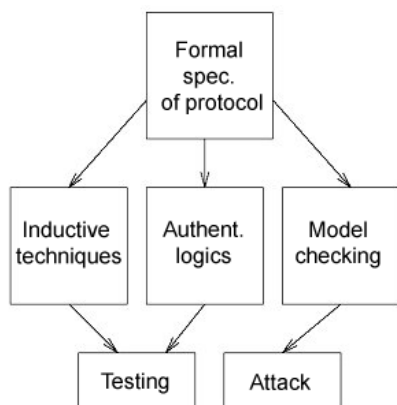


Figure 1: General Approaches in the area of Security Protocol Analysis

## III. SECURITY PROTOCOLS DESIGN

When designing a new secure protocol, we strongly recommend following the robustness principles. Anderson and Needham [6] proposed a number of robustness principles and Abadi and Needham [6] [7] introduce complete analysis of desirable protocol properties and relevant limitations.

Some of them are mentioned below:

- be very clear about the security goals and assumptions,
- be clear about the purpose of an encryption (secrecy, authenticity, etc.): do not assume that its use is synonymous with security,
- be sure to distinguish different protocol runs from each other,
- if timestamps are used as freshness guarantees by reference to absolute time, then the difference between local clocks at various machines must be less than the allowable age of message deemed to be valid; furthermore, the time maintenance mechanism everywhere becomes part of the Trusted Computing Base,
- sign before encrypting; if a signature is affixed to encrypted data, then one cannot assume that the signer has any knowledge of the data; a third party certainly cannot assume that the signature is authentic, so non-repudiation is lost.

As we mentioned above, when designing new security protocol we rely on the use of some specification techniques. Due to limitation of specification languages and logics, there should exist additional cooperation with external verification techniques and/or automation tools. During the design process, the given protocols should be verified at different abstract levels to prevent various security flaws.

## IV. EVOLUTIONARY APPROACH

Current techniques for creating security protocols mostly deal with the human interaction and knowledge. This process could be highly automated with an approach introduced below. The general idea of

evolutionary approach to the protocol design is based on the principles of genetic algorithms. It was outlined by the author in [5] and is still part of his dissertation research.

In general, while the protocol runs, each instruction affects the corresponding sets of knowledge and belief. These modifications are usually described in the corresponding modal logic (e.g. BAN logic [3] [4]).

From the evolutionary-optimization point of view, the sequence of protocol instructions is represented by a chromosome of variable length. There could be generated as many random chromosomes as required for initial population. Each chromosome represents a different protocol and its fitness is computed by simulating its run, according to the changed sets of knowledge and belief.

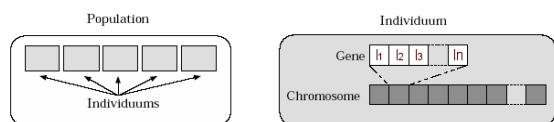


Figure 2: Structure of a Population. Protocol (individual) is encoded as a sequence of instructions.

The following algorithm (based on genetic algorithms) describes the whole flow we use to design security protocols. The principles can be found in [5] and are explained to appreciate the idea of automatic design:

1. Security goals – in this first step we describe what should or shouldn't contain sets of knowledge and belief for each involved subject, which message is secret and cannot be sent unencrypted, which message can never be sent, etc.
2. Initial population – randomly generated protocols (instruction sequences) are encoded into chromosomes. In this step the fitness of all individuals is calculated.
3. Parents for mating – like in standard genetic algorithms, the individuals with the best fitness are chosen to be parents for mating.
4. Crossover – the choice of the right locations in chromosomes for crossover is very important. It may highly affect the chances for a generation of chromosome with better fitness
5. Performing mutation – avoiding jamming in local minima, the mutation is very useful step.
6. Replacing offspring to population - the produced individuals are replaced to the new population and the evolution process starts over again from step 3.

The design is completed when some chromosomes (with best fitness) satisfy the initial presumptions. The result is the chromosome with the best fitness which can be interpreted as a sequence of basic instructions in the cryptographic protocol.

## ACKNOWLEDGMENTS

This paper was created as a part of the research which has been supported by the Grant Agency of the Czech Republic through the following grants: GACR 102/05/0723: A Framework for Formal Specifications and Prototyping of Information System's Network Applications, GACR 102/05/0467: Architectures of Embedded Systems Networks, GACR 102/05/H050: Integrated approach to education of PhD students in the area of parallel and distributed systems, and by the Czech Ministry of Education in frame of MSM 0021630503 Research Intention MIKROSYN: New Trends in Microelectronic Systems and Nanotechnologies.

## REFERENCES

- [1] Ma, L., Tsai, J.: Formal Verification Techniques for Computer Communication Security Protocols. Handbook of Software Engineering and Knowledge Engineering, World Scientific Publishing Company, 2000, p. 23
- [2] Shmatikov, V., Stern, U.: Efficient Finite-State Analysis for Large Security Protocols. CS Department of Stanford University, 1998, p. 10
- [3] Agray, N., van der Hoek, W., de Vink, E.: On BAN Logics for Industrial Security protocols. CCEMAS, 2001, p. 8
- [4] Abadi, M., Tuttle, N.: A Semantic for a Logic of Authentication. Proceedings of the ACM Symposium on Principles of Distributed Computing, 1991, pp. 201-216
- [5] Očenášek, P.: Evolutionary Approach in the Security Protocols Design, In: Proceedings of the First European Conference on Computer Network Defence, University of Glamorgan, GB, Springer, 2005, p. 147-156, ISBN 1-84628-311-6
- [6] Anderson R., Needham R.: Programming Satan's Computer. Computer Science Today: Recent Trends and Developments. Lecture Notes in Computer Science, vol. 1000, Springer-Verlag, 1995, p. 426-440
- [7] Abadi M., Needham R.: Prudent Engineering Practice for Cryptographic Protocols. In: Proceedings of the 1994 IEEE Symposium on Security and Privacy, IEEE Computer Security Press, 1994, p. 122-136

# Meta-Modelling in Tool Support for Time-Triggered Application Development

Christian Paukovits and Wilfried Elmenreich (Faculty Mentor)

Institut für Technische Informatik

Technische Universität Wien

Email: {pauko, wil}@vmars.tuwien.ac.at

**Abstract** — This paper introduces an integrated development environment based on the open-source tool GME (Generic Modeling Environment) for distributed embedded real-time systems using TTP/A as communication subsystem. The tool follows the meta-modelling design approach, and delivers an implementation of the conceptual model of TTP/A applications.

## I. MOTIVATION

Designing and implementing a distributed embedded real-time system is a challenging task due to its inherent complexity. A possible approach to cope with complexity is to employ tools in the design and implementation process that relieve the designer from lower level issues like matching system parameters and determining communication message schedules.

We identified the need for an integrated development tool, which assists the designer from the first draft of the application’s model to the definition of the global communication schedule as well as the local job specification and the compilation and linking of the resulting source code. The intentions are, on the one hand to accelerate the design and implementation phase of an embedded system’s software, on the other hand to reduce the potentials of errors occurring during the whole development process.

The first goal might especially appeal to the academic research, where it is the intention to have shorter development cycles, so that we can implement several diversitive approaches to a problem fast and efficiently, when conducting research among the field of embedded systems. This matter is of interest in the industrial field, too. However, here the second goal is of utmost importance. The less errors we have to remove in source code, the less resources the debugging consumes. Thus, the application of an integrated tool will relieve a project’s budget and other resources.

Existing tools like **Rational Rose**, **LabVIEW** and **Simulink** are well-known, but do not particularly support our time-triggered modelling approach. Therefore, we have adopted the open source tool GME (Generic Modeling Environment) [1] as integrated modelling tool, which supports a meta-level design approach. Although, GME can be modified in order to fit the needs of any target platform and communication technology, this case study deals with TTP/A [2] as the underlying real-time communication system and application design.

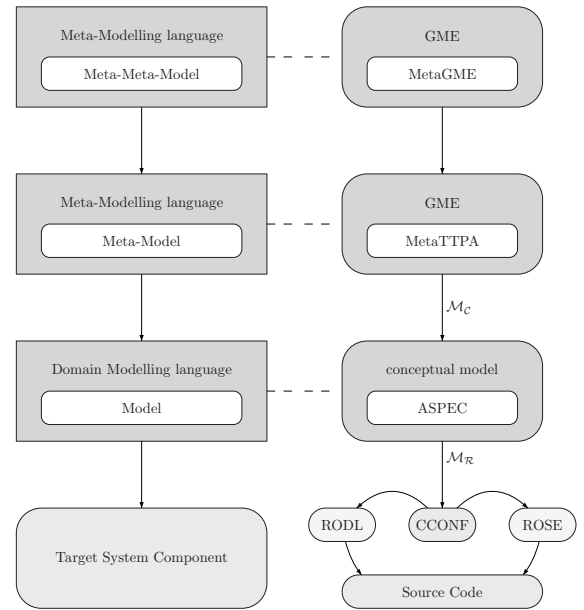


Figure 1: Meta-Modelling with GME

## II. META-MODELLING WITH GME

*Meta-Modelling* combines the strengths of *domain-specific* and *generic notational* approaches. Due to its expressiveness we can describe (meta-)models for our given **domain** of time-triggered distributed embedded real-time systems in a **generic** formalism. Fig. 1 illustrates the functioning of meta-modelling. Firstly, we have one generic model (*meta-meta-model*), which models the *meta-model* of a given domain. Such a meta-model includes the familiar *terminology* as well as *integrity constraints*, which a concrete domain model has to fulfill. Finally, we use that meta-model in order to specify the *model* a concrete target system with a domain-specific point of view.

Furthermore we see from Fig. 1, which role is taken by GME in our case study of TTP/A application development concerning the modelling of the distributed real-time embedded system. The meta-meta-model as well as the meta-model named *MetaTTPA* are expressed by means of GME, which is an UML-related notational style. Then, the *model* of the target system is described using *MetaTTPA*, which defines the *conceptual model* of TTP/A applications.

### III. CONCEPTUAL MODEL

The *conceptual model* is the theoretical basis of TTP/A applications (cf. [3]). It defines a *set of integrity constraints*, a *terminology* and a *design pattern*, how TTP/A applications ought to be designed. MetaTTPA is the implementation in GME of the conceptual model.

The conceptual model defines two major entities of TTP/A applications. The **application specification (ASPEC)** is a formal description of a TTP/A application concerning *functional and temporal requirements*. This includes the *decomposition* among the TTP/A cluster, *dataflow* between jobs, and *deadlines* of dataflow transmissions and job executions. The **cluster configuration (CCONF)** gives information, what each node in the TTP/A cluster does during each TTP/A slot, for instance executing a job, or sending / receiving data on the bus. The functional and temporal requirements from the ASPEC find their manifestation in the cluster configuration.

Each application specification has to fulfill all the integrity constraints defined in the conceptual model in order to be *valid*. Cluster configurations must satisfy the functional and temporal requirements stated in the ASPEC in order to be *feasible*.

### IV. INTEGRATED DEVELOPMENT ENVIRONMENT

In Fig. 2 we find the relation between ASPEC and CCONF. The linking entities are specialized plug-ins of GME, so-called *interpreters*, which support the workflow. A *scheduler* takes a valid ASPEC and applies a scheduling algorithm in order to figure out an appropriate schedule of the application. Then, it creates a cluster configuration. Moreover, a *code generator* produces source code for RODL, ROSE, Interface Files, and job stubs from the CCONF.

The GME tool suite provides a mechanism of *constraint checking* based on OCL constraints. As a result, the integrity constraints imposed by the conceptual model and hence MetaTTPA, which is the implementation of the conceptual model, can be asserted within the GME tool suite. There is no other constraint checking tool involved. In other words, GME is able to ensure validity of application specifications by itself. However, feasibility of cluster configurations can not be checked with that built-in facility, because this is beyond the scope of OCL constraints. So, this task must be done by a scheduler, which calculates cluster configurations.

All the steps beginning from the description of the application specification till the output of source code take place within one meta-modelling tool suite: GME. We have used GME's mechanism of plug-ins to equip the generic tool with TTP/A specific schedulers and code generators. As a result, we elevate such a generic modelling tool to an integrated development environment (IDE) according to our needs for distributed embedded real-time systems using TTP/A as its underlying communication subsystem.

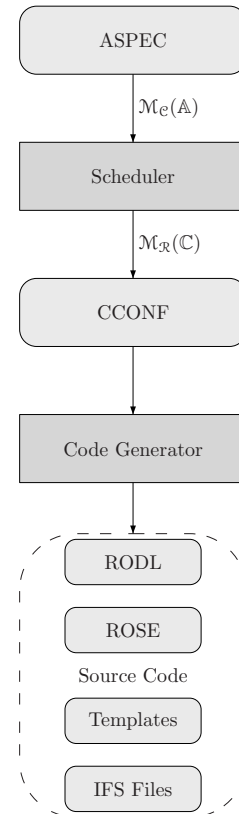


Figure 2: Work-Flow with GME

### V. CONCLUSIONS

We proposed an application of a meta-modelling tool, which assists the designer of distributed embedded real-time systems throughout the whole design work-flow. The tool is especially tailored in order to fit the needs of TTP/A application development. Therefore, it entails an implementation of the conceptual model, and offers an automatic generation of RODLs, Interface Files, and job stubs in application source code files.

### ACKNOWLEDGMENTS

The authors want to thank Susanne Kandl and Christian El Salloum for their constructive comments and ideas on this work. This work was supported by the Austrian FWF project TTCAR under contract No. P18060-N04.

### REFERENCES

- [1] A. Ledeczi, M. Marot, A. Bakay, G. Karsai, J. Garrett, C. Thomason, G. Nordstrom, J. Sprinkle, P. Volgyesi. The Generic Modeling Environment. In *Proceedings of WISP 2001*, Budapest, Hungary, May 2001.
- [2] H. Kopetz et al. Specification of the TTP/A Protocol. Research Report 61/2001, Technische Universität Wien, Institut für Technische Informatik, Treitlstr. 1-3/182-1, 1040 Vienna, Austria, 2001. Version 2.00.
- [3] C. Paukovits. Applying Model-Integrated Design on Time-Triggered Application Development. Master Thesis, Technische Universität Wien, Institut für Technische Informatik, Vienna, Austria, January 2006.

# Validation Framework for Advanced Maintenance Strategies

Harald Paulitsch and Hermann Kopetz (Faculty Mentor)

Institut of Computer Engineering

Vienna University of Technology

Vienna, Austria

Email: {harald,hk}@vmars.tuwien.ac.at

**Abstract** — *Electronics is the predominant cause for car breakdown. This work implements the prototype of an online diagnosis system, which is evaluated by the validation framework. The main purpose of the validation framework is the investigation of the effects of physical faults on a Time-Triggered Protocol (TTP) cluster. The validation framework can expose nodes and the bus to Electromagnetic Interference (EMI) and produce physical bus failures, such as open and short-circuits. Validation campaigns have confirmed the restart rate as a suitable indicator whether a temporary external or an intermittent internal fault has occurred. A main result is also that component internal and borderline failures can be discriminated with high accuracy by the frame status.*

## I. INTRODUCTION

In the automotive industry more and more electronic components are deployed to improve passenger comfort, vehicle safety, and fuel economy. However, the development of diagnostic systems has stayed behind the recent increase in functionality of the embedded systems: the identification of faulty system components in current systems is not always possible. This *fault-not-found phenomena* [1] involves an increasing number of system failures that can not be traced back to a fault. In service stations this leads to the replacement of fully functional components, or, even worse, faulty components remain unchanged. For car manufacturers this implies high warranty costs, negative press coverage and image problems. The main difficulty is the complexity of today's vehicle electronics: electronic components are connected with heterogeneous networks of different physical layers, bandwidth and dependability requirements. Moreover, currently used networks support diagnosis insufficiently.

The Time-Triggered Architecture (TTA) [2] reduces this complexity by an a priori definition of communication schedules, a global time-base, and error containment. These core functionalities also provide the basis for new, more precise diagnostic strategies.

## II. DIAGNOSTIC ARCHITECTURE

In this work the prototype of a diagnostic architecture [3] (depicted in Figure 1) is implemented and evaluated. The prototype implements new diagnostic strategies and consists of the following three parts: error detection at the linking interfaces [4] of the system components, dissemination of the diagnostic information over a dedicated virtual network [5] and the analysis that assesses the state of the system components based on the distributed state of the cluster. Furthermore, a validation

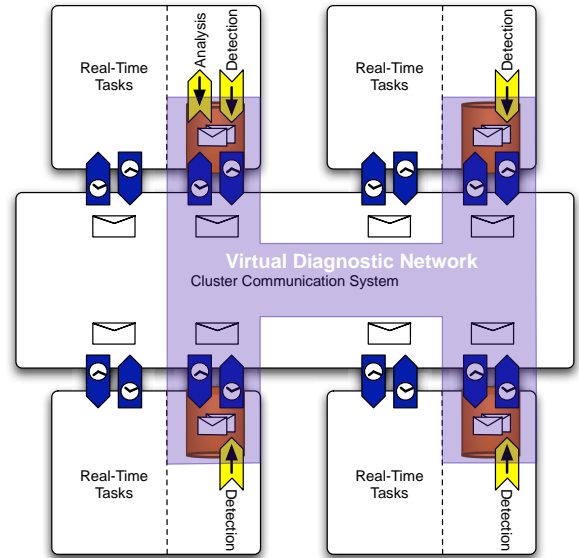


Figure 1: The Diagnostic Subsystem

framework was designed and realized in order to investigate the effects of physical faults on a TTA cluster and to validate the diagnostic architecture.

At the four distributed TTP nodes of the prototype cluster the relevant status area fields of the C2 (AS8202) communication controller are monitored for system diagnosis. These status area fields provide information about the operational state of all nodes and the status of the received frames, as perceived at each particular node. State changes are reported to all other nodes over the virtual network. Since bandwidth is a scarce resource, the virtual network is assigned an adjustable share of the bandwidth and performs fragmentation of diagnostic messages to utilize the allocated bandwidth efficiently. As the occurrences of faults are sporadic events, event semantics in the diagnostic subsystem is appropriate: diagnostic event messages are transferred over the time-triggered communication network. The diagnostic subsystem is encapsulated from the real-time application. Therefore, the diagnosis cannot exert influence on the dependability of the system and has a lower criticality than the real-time application. Loss of diagnostic messages can only lead to a degradation of the diagnosis.

## III. VALIDATION FRAMEWORK

A main part of this work is the design and realization of a validation framework (presented in Figure 2) for conducting validation campaigns in order to examine the

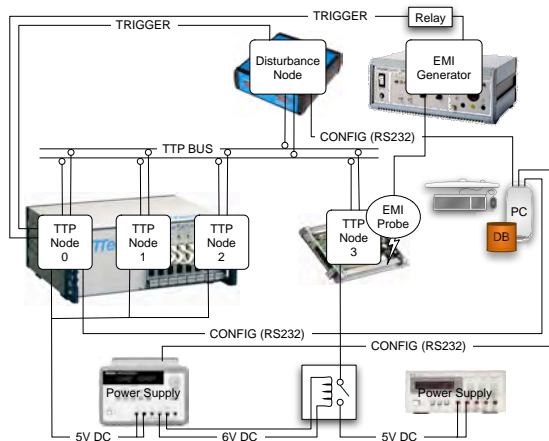


Figure 2: The Validation Framework

diagnostic architecture and to investigate the effects of physical faults on a TTP cluster, interconnected in a bus topology. The validation framework can expose nodes and the bus to Electromagnetic Interference (EMI) and produce physical bus failures, such as open and short-circuits.

An essential aim in the design of the validation framework is the automated execution of experiments in order to repeat experiments at a number sufficient for meaningful statistical analysis. Resetting the cluster before each experiment precludes side effects of one experiment on another. A personal computer forms the central control instance and allows via graphical user interfaces configuration, control, and observation of validation campaigns. Via an embedded triggering application the execution of disturbances is controlled and synchronized with the communication schedule. The outcome of the experiment is logged in an SQL database for offline analysis. The use of the diagnostic architecture for the investigation of effects of physical faults on the distributed state provides scalability: regardless how many nodes are interconnected, the essential information about the detected symptoms at all nodes is disseminated over the dedicated virtual network.

#### IV. VALIDATION CAMPAIGNS

Three validation campaigns are conducted in order to challenge hypotheses regarding the diagnosability of the TTA according to a maintenance-oriented fault model. These campaigns serve to examine the diagnostic architecture and to investigate the effects of physical faults. In the first campaign a spatially separated node is exposed to radiated EMI. In the second campaign EMI is induced on a channel bypassing the protective mechanisms: shielding, twisting, and differential transmission—in order to accelerate the effects of EMI. In the third campaign short- and open-circuits are injected on one channel of the bus. Overall, more than 200,000 experiments have been executed during these validation campaigns.

#### V. CONCLUSION

The prototype of the introduced diagnostic architecture implements reliable diagnostic event message dissemination complying with bandwidth constraints imposed

by the automotive industry. Bandwidth can be adjusted according to the needs of system engineers. Fragmentation of the diagnostic messages facilitates efficient utilization of the bandwidth. Furthermore, the operation on the interface state, abstracting from the internals of the component, enables intellectual property protection. The encapsulation of the diagnostic subsystem precludes probe effects. Moreover, the diagnostic architecture does not restrict implementation choices: both, centralized analysis and distributed analysis are supported. Online diagnosis provides maintenance information in the field, which allows the prolongation of service intervals or even condition-based maintenance.

The validation framework executes experiments synchronously with TTP and collects diagnostic information delivered by the diagnostic architecture for later analysis in an SQL database. It also supports random fault injection. By means of automatic execution experiments can be repeated at a number sufficient for statistical analysis.

The implemented prototype provides the infrastructure for the deployment of diagnostic analysis algorithms. Development of analysis algorithms evolves iteratively with the feedback from validation campaigns. The linking interface state of the controllers is explored for symptoms that indicate failures and their location. By induction, fault effect analysis supplies the basis of the analysis algorithms, which correlate the symptoms detected by the nodes in the time, space, and value domain.

The prime results of the validation campaigns are that the restart rate is confirmed as a suitable indicator whether a temporary external or an intermittent internal fault has occurred. Component internal and borderline failures can be discriminated with high accuracy by the frame status. These results permit a more precise diagnosis and will be applied in an automotive demonstrator.

#### ACKNOWLEDGMENTS

This work has been supported by the A3 Technology Project PEGASUS (project No. 809437/5602), the FP6 Network of Excellence ARTIST2 (Contract No. 004527), and the FP6 Integrated Project DECOS (Contract No. 511764).

#### REFERENCES

- [1] D.A. Thomas, K. Ayers, and M. Pecht. The 'trouble not identified' phenomenon in automotive electronics. *Microelectronics Reliability*, 42:641–651, 2002.
- [2] H. Kopetz and G. Bauer. The time-triggered architecture. *IEEE Special Issue on Modeling and Design of Embedded Software*, January 2003.
- [3] P. Peti, R. Obermaisser, and H. Paulitsch. The diagnostic architecture of the pegasus project car. In V. Turau and C. Weyer, eds., *Proc. of the 3rd Workshop on Intelligent Solutions in Embedded Systems*, pp. 163–174, May 2005.
- [4] H. Kopetz and N. Suri. Compositional design of RT systems: A conceptual basis for specification of linking interfaces. In *Proc. of 6th IEEE Intern. Symposium on Object-Oriented Real-Time Distributed Computing*, pp. 51–60, May 2003.
- [5] R. Obermaisser. *Event-Triggered and Time-Triggered Control Paradigms – An Integrated Architecture*. Real-Time Systems Series. Kluwer Academic Publishers, November 2004.

# Detection of Impulses from the Response of a Scintillation Detector

Ondřej Pirochta and Aleš Prokeš  
 Dept. of Radio Electronics  
 Brno University of Technology  
 Brno, Czech Republic  
 Email: xpiroc00@stud.feec.vutbr.cz

**Abstract** — *This contribution is about the digital signal processing of the signal from a scintillation counter. The digital detection system is implemented in a FPGA device as a part of system for measurement of ionizing radiation.*

## I. INTRODUCTION

The Scintillation detector is used to measure the energy of ionizing radiation. The working principle of the detector is based on interaction between the scintillator and incident radiation, whereat light twinkles are produced. The light twinkles are transformed to a voltage impulse by the photocathode system of the photomultiplier [1]. The height of these impulses is proportional to the energy of the incident ionizing radiation [2]. These impulses are produced randomly and their appearance can be described by a Poisson distribution as shown in (1). Where  $p(k)$  is probability of coming  $k$  impulses during the next period. The parameter  $\lambda$  is proportional to the signal frequency and the time interval.

$$p(k) = \frac{e^{-\lambda}}{k!} \cdot \lambda^k \quad (1)$$

Where  $k$  number of impulses,  $k = 0, 1, 2, \dots$   
 $\lambda = n \cdot T$ ,  
 $n$  signal frequency,  
 $T$  time interval.

The task of the detection system is the creation of a histogram of the heights of incoming impulses. After we obtained this measured histogram we can determine the type of ionising radiation and have conclusions about its activity.

## II. DETECTION

We can use two different methods to measure the height of the impulse. These are either using an analog system or a digital system.

### A. THE ANALOG DETECTION SYSTEM

The analog system consists of a preamplifier, an impulse former and a peak detector. The impulse former is used to shorten the time of an impulse and to remove its d.c. component. The peak detector is used to hold the maximum value of the impulse for a few nanoseconds. The maximum value is converted to digital form and then written to the histogram during this holding time.

### B. THE DIGITAL DETECTION SYSTEM

In case of a digital system values of the measured signal are converted to digital form immediately after being processed by the preamplifier and then filtered and processed by it. The state machine is used for the detection of the height of the impulse. The working principle of the state machine is obvious from figures 1 and 2.

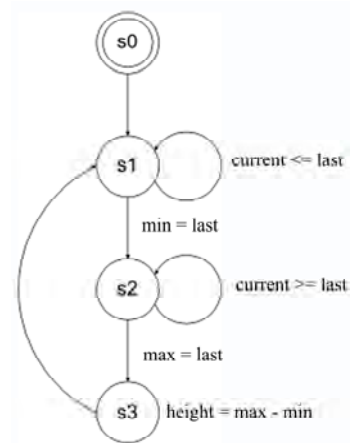


Figure 1: State Diagram

It measures the level of the signal. The state machine detected the minimum of the signal if the current value of the signal is bigger than previous one and if the previous progression was decreasing (state  $s1$  in figure 1). The state machine detected the maximum of the signal if the current value of the signal is smaller than any previous one and if the previous

progression was increasing (state  $s_2$  in figure 1). The height of the impulse is computed by subtraction of the detected minimum value from the detected maximum value. The measured height of the impulse is written into RAM memory if the height of the impulse was bigger than a selected threshold value.

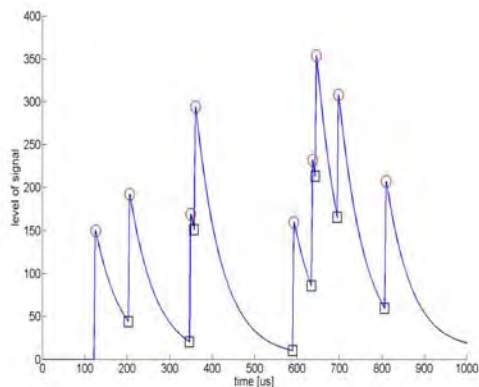


Figure 2: Measured Signal

### III. RESULTS

The described digital detection system including filter, state machine and RAM memory for histogram generation was implemented in an FPGA device. The main advantages of the digital detection in FPGA are that parameters of the detection system can be changed by software and the whole detection system is realized by one chip only. An example of a measured histogram can be seen in figure 3.

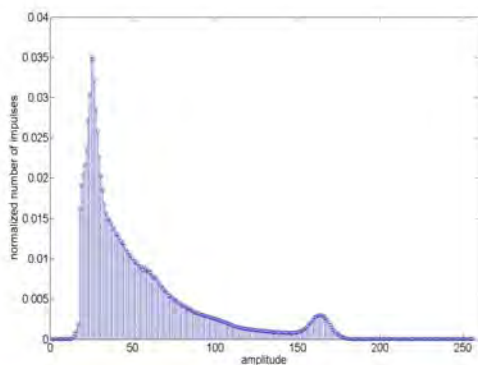


Figure 3: Measured Histogram of Amplitudes

### ACKNOWLEDGMENTS

This work has been supported by the doctoral project of the GACR (Czech Science Foundation) No. 102/03/H109 "Methods, Structures and

Components of Electronic Wireless Communication". and the firm VF, a. s.

### REFERENCES

- [1] O. Pirochta and A. Prokeš. Digitální Zpracování Signálu Odezvy Scintilačního Detektoru. In Sborník semináře o řešení projektu GA ČR 102/03/H109. Metody, struktury a komponenty elektronické bezdrátové komunikace., pages 52 - 53, Brno, Czech Republic, September 2005, ISBN 80-214-3013-3
- [2] O. Pirochta and A. Prokeš. Matematický Model Generátoru Impulsů Scintilačního Detektoru. In Sborník příspěvků konference Vršov 2005. IEEE workshop Vršov 2005., pages 131 – 134, Brno, Czech Republic, September 2005, ISBN 80-214-3008-7

# A versatile networked embedded platform for KNX/EIB

Fritz Praus and Wolfgang Kastner  
Institute of Computer Aided Automation  
Vienna University of Technology  
Vienna, Austria

Email: {fpraus,k}@auto.tuwien.ac.at

**Abstract** — *The deployment of home and building automation systems (BAS) allows to increase comfort, safety and security and to reduce operational cost in the building domain. Today such systems typically follow a hierarchical distributed approach. While control networks interconnect smart sensors and actuators, a backbone network provides the infrastructure for management tasks. Devices interconnecting these networks play a strategic role. Especially in the home domain, the integration of various control and data networks is essential for maximum benefit. The objective of my diploma thesis [1, 2] was to design such an embedded and versatile interconnection platform in hard- and software with a particular focus on the European Installation Bus (KNX/EIB) Twisted Pair (TP).*

## I. INTRODUCTION

KNX/EIB [3] is a popular control network based on an open specification and designed to enhance electrical installations in buildings. It is well-established in central Europe, i.e. Germany, Austria and Switzerland. KNX/EIB is primarily found in large building installations with main application areas being lighting, control of window blinds and HVAC systems. In home area the increase of comfort, safety and security is the major reason for using KNX/EIB.

KNX/EIB features a decentralised design. It is a peer-to-peer network system: Nodes communicate directly with each other using a distributed algorithm for medium access. There are hardly any central control nodes that solely fulfil regulation functions as, for instance, a Programmable Logic Controller (PLC) does. In fact, control and working logic is located at every single node. To put it differently: Every single sensor or actuator implementing the KNX standard is able to handle network communication as well as implementation of the desired logic on its own.

A key feature in KNX/EIB is group communication (process data exchange) based on a form of publisher subscriber model, allowing to address an arbitrary number of receivers by way of a single message. A sender uses a logical group address as its destination address. Receiving stations know their dedicated group (or groups) and can accordingly ignore or process incoming messages. For configuration and management purposes point-to-point messages are used.

KNX/EIB allows various media. The primary used medium is shielded or unshielded Twisted Pair (TP) cabling known as KNX TP1, allowing a free topology with

cable lengths of up to 1000 m per physical segment. Data is transmitted at 9600 b/s. Integration of KNX/EIB into existing installations can be achieved using powerline as communication system. Speed is limited to 1200 b/s respectively 2400 b/s depending on used technology. To further extend KNX/EIB, KNX Radio Frequency (RF) can be used. A subband in the 868 MHz frequency band, reserved for short-range devices, is used. For more details see [4].

The primary goal of my interconnection platform named KNXcalibur (Figure 1) is to be universally applicable as a router, gateway and workstation interface for KNX/EIB. The main purpose is to serve as a basis for further work in the scope of home and building automation (e.g. plug and play facilities, integration into Open Services Gateway initiative (OSGi) environments [5], coupling to other networks, extensions with regard to security issues (EIBsec [6]), setup of set-top boxes, access point for BASys [7]). KNXcalibur is designed as a flexible, extensible, compact and low cost stand-alone device. The used hardware is powerful in the sense that enough processing power and memory are present to implement multiple network services like e.g. for TCP/IP. Both hardware and software design are openly available [<http://eib.praus.at>].

## II. HARDWARE

The leded as well as surface mounted components are fitted on a double sided printed circuit board (PCB) in Eurocard (160 mm x 100 mm) format (Figure 1). A Fujitsu MB90330 microcontroller (MCU) with 24 MHz, 24 KB RAM, and 384 KB Flash ROM forms the central part. It features 4 UARTs, which provide the connection to a PC via two EIA-232 interfaces and connection to KNX/EIB via two TP-UART ICs (standard KNX/EIB interface). Moreover, USB functionality with device (2.0 full speed) and mini host support is integrated into the controller and appropriate connectors are mounted. Via the external bus interface of the MCU a Cirrus Logic CS8900A Ethernet controller is connected, providing 10 MBit/s Ethernet support. To support persistent data storage without writing to the MCU's on-chip flash memory and to extend available memory, a SD/MMC card connection has been integrated.

## III. SOFTWARE

The software of KNXcalibur consists of a low level firmware and various network protocol stacks. The for-



Figure 1: KNXcalibur: Hardware

mer implements the necessary drivers to communicate with the hardware and provides an API to configure, initialise and access the available hardware. It is split into various parts: The UART and TP-UART firmware allow easy asynchronous serial communication with a PC and the TP-UARTs. The SD/MMC firmware provides raw access (byte, block, sector) to an inserted SD/MMC card. In addition, the FAT16 file system is implemented, allowing easy access for advanced application layers. The CS8900A Ethernet controller is accessed via an interrupt driven ISA bus emulation. Access to the USB slave and mini host functions of the MCU is provided by an open implementation by Thesycon Systemsoftware & Consulting GmbH in cooperation with Fujitsu.

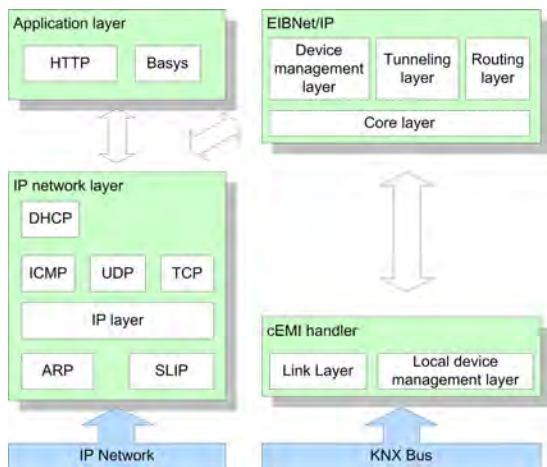


Figure 2: KNXcalibur: Software

On top of the low level firmware various layers are implemented (Figure 2).

The IP network layer forms the basis for many other network protocol stacks. Relevant parts of ARP, SLIP, IP, ICMP, UDP, TCP and DHCP are implemented. Currently only a single TCP connection and no IP fragmentation are supported.

Three HTTP (port 80) applications are possible: The current device status (KNX/EIB connection, SD/MMC card status, ...) is returned in a formatted HTML page.

Second, a simple interface for sending KNX/EIB TP frames is presented, and third, a standard web server facility is implemented: The corresponding file is searched on the SD/MMC card and is then displayed to the user. Besides HTTP, the BASys [7] protocol is implemented.

A KNX/EIB protocol extension called EIBnet/IP describes the transportation of KNX telegrams on top of IP networks. The implemented stack is positioned on top of the IP network layer and on top of the cEMI (frame format of KNX/EIB) handler and acts as a gateway/router between the two networks. It accepts EIBnet/IP frames from UDP/TCP level and cEMI frames from the cEMI handler and processes the received frames according to their message types. Valid packets are passed to the destination service.

#### IV. CONCLUSION

Due to the modular design concept of KNXcalibur, the platform is not limited to the use in a predefined application area. Since both, hardware and software can easily be extended, a basic device for future research has been created. Interfaces to other networked BAS like BACnet or LONWorks as well as to wireless solutions (KNX RF) and security extensions (EIBsec [6]) are currently under investigation.

#### REFERENCES

- [1] Fritz Praus, Wolfgang Kastner, and Oliver Alt. Yet Another All-purpose EIBNet/IP Gateway. In *Konnex Scientific Conference*, 2004.
- [2] Fritz Praus. A versatile networked embedded platform for KNX/EIB. Master's thesis, Vienna University of Technology, Institute of Computer Aided Automation, Automation Systems Group, 2005.
- [3] Konnex Association, Brussels. *KNX Handbook 1.1 and KNX Standard Extensions*, 2004.
- [4] Wolfgang Kastner and Georg Neugschwandtner. EIB: European installation bus. In *The Industrial Communication Technology Handbook*, volume 1, chapter 34. CRC Press, 2005.
- [5] Wolfgang Kastner and Georg Neugschwandtner. Service Interfaces for Field-Level Home and Building Automation. In *5th IEEE International Workshop on Factory Communication Systems (WFCS)*, pages 103–112, September 2004.
- [6] Wolfgang Granzer, Wolfgang Kastner, Georg Neugschwandtner, and Fritz Praus. Security in networked building automation systems. In *6th IEEE International Workshop on Factory Communication Systems (WFCS)*, January 2006.
- [7] Oliver Alt. Entwicklung eines Softwaresystems zur Planung und Inbetriebnahme von Gebäudeautomationssystemen. Master's thesis, Technische Universität Darmstadt, 2003.

# A Graph-Based Approach to Optical Flow Estimation

Christoph Rhemann, Michael Bleyer (Faculty Mentor) and Margrit Gelautz (Faculty Mentor)

Institute for Software Technology and Interactive Systems

Interactive Media Systems Group

Vienna University of Technology

Vienna, Austria

Email: {bleyer, gelautz}@ims.tuwien.ac.at

**Abstract** — *A vector field which describes the apparent motion between two images of a video sequence is commonly known as optical flow. The accurate estimation of these displacement vectors is crucial for several computer vision problems, including video object segmentation and tracking. In this work we propose a new algorithm for computing a dense optical flow field that tackles the inherent problems of optical flow algorithms, namely the estimation of flow vectors in regions of low texture as well as the precise identification of motion boundaries. We try to overcome these problems by taking advantage of color segmentation and robust optimization via graph-cuts. Experimental results show the good performance and robustness of our method.*

## I. INTRODUCTION

The task of a motion algorithm is to automatically compute a dense field of two-dimensional displacement vectors that transform one image into the next in an image sequence. This array of vectors is commonly referred to as optical flow. The accurate estimation of optical flow plays a key-role in several computer vision problems, including motion segmentation, 3D scene reconstruction, robot navigation, video shot detection, mosaicking and video compression.

Major challenges in optical flow estimation are twofold. Firstly, matching often fails in the absence of discriminative image features that can be uniquely matched in the other frame. This is the case in untextured regions as well as in the presence of texture with only a single orientation (aperture problem). Secondly, a pixel's matching point can be occluded in the other frame. Those occlusions often occur at motion discontinuities, which make it specifically challenging to precisely outline object boundaries. Nevertheless, accurate identification of motion discontinuities is often required for applications such as motion segmentation. A large number of optical flow algorithms fail in this respect, since the fact that there are occlusions is simply ignored. In this work, we propose an algorithm that explicitly addresses those problems taking advantage of two recent developments in the computation of dense correspondences, which are robust optimization via graph-cuts [1, 2] and the incorporation of color segmentation [3].

## II. ALGORITHM

The proposed algorithm starts by segmenting the reference image into regions of homogenous color. The color segmentation incorporates the assumption that the motion inside regions of homogeneous color varies smoothly and motion discontinuities coincide with the borders of those regions. The affine motion model is used to describe the motion inside a segment. To initialize the model parameters, we estimate a sparse set of correspondences. Layers are extracted from the initial segments, which represent the dominant motions likely to occur in the scene. Every color segment is then assigned to exactly one layer. This assignment is optimized by minimizing a global cost function with a graph-cut-based technique. The cost function is defined on the pixel level, as well as on the segment level. On the pixel level, a data term measures the pixel similarity based on the current flow field. Furthermore, occluded pixels are detected symmetrically. The segment level is connected to the pixel level in a way that the segmentation information is enforced on the pixel level. Additionally, a smoothness term is defined on the segment level. Moreover we allow our algorithm to use multiple input frames in order to discriminate the motion of different layers when the inter-frame motion is small.

## III. EXPERIMENTAL RESULTS

We demonstrate the performance of the proposed algorithm using the well-known Mobile & Calendar MPEG test sequence that is shown in Figure 1a. In this sequence, the camera pans to the left, while there are moving objects (calendar, train and ball) in the scene. Since no ground truth is available, we have to focus on a qualitative discussion of the results. To present the computed flow values on the segment level, we draw the flow vectors for some pixels in Figure 1b, where we also outline the layer boundaries. We superimpose the layer borders on the reference image in Figure 1c to show their agreement with actual object boundaries. The object outlines seem to be well preserved. Finally, we demonstrate the robustness of our approach by segmenting the complete Mobile & Calendar sequence. The segmentation results for every fifth frame of the Mobile & Calendar sequence

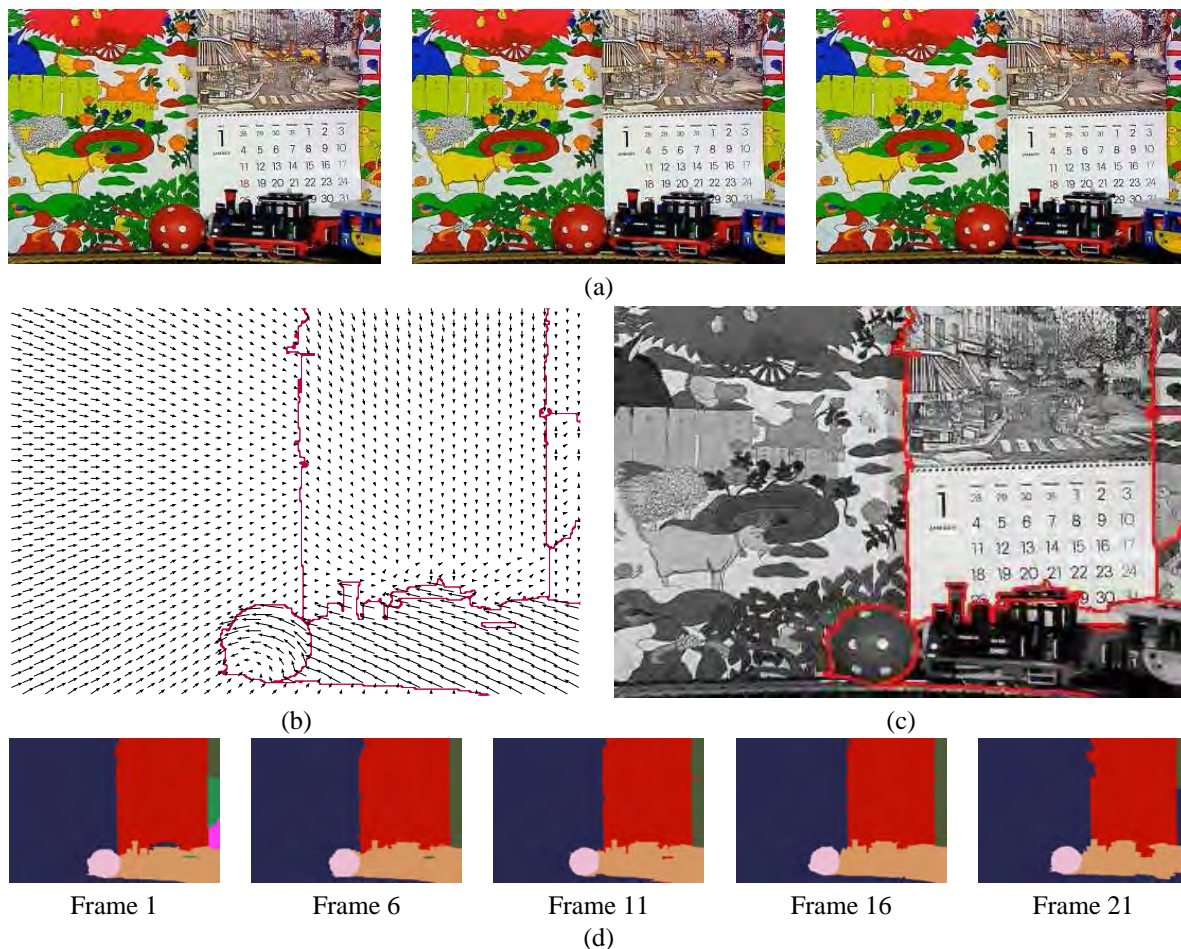


Figure 1: Results for the Mobile & Calendar sequence. (a) Frames 1, 3 and 5 of five input frames. (b) Flow vectors with layer boundaries. (c) Layer boundaries (red) superimposed on input frame 1. (d) Motion segmentation.

are presented in Figure 1d.

#### IV. CONCLUSIONS

In this work, we presented a new algorithm for computing a dense optical flow field between two or more images of a video sequence. The algorithm uses color segmentation to improve the quality of flow estimates in untextured regions and for the accurate detection of motion boundaries. The proposed method uses a layered representation and employs the affine motion model to describe image motion. The tasks of layer extraction and assignment are formulated as energy minimization problems. In order to approximate a minimum of the energy functions, a graph-cut-based optimization scheme is applied. Our method is capable of estimating correct flow information in traditionally challenging regions such as areas of low texture and close to motion discontinuities and can as well be applied to derive a motion segmentation of a complete video sequence. Further research will

concentrate on improving the algorithm by defining criteria for splitting segments that overlap motion discontinuities and by using a more sophisticated motion model.

#### REFERENCES

- [1] V. Kolmogorov and R. Zabih. What energy functions can be minimized via graph cuts? *Transactions on Pattern Analysis and Machine Intelligence*, 26:147–159, 2004.
- [2] J. Xiao and M. Shah. Motion layer extraction in the presence of occlusion using graph cuts. *Transactions on Pattern Analysis and Machine Intelligence*, 27:1644–1659, 2005.
- [3] L. Lucchese and S.K. Mitra. Color image segmentation: A state-of-the-art survey. In *Proceedings of the Indian National Science Academy (INSA-A)*, volume 67, pages 207–221, 2001.

# Design Comprehension of Time-Triggered Real-Time Systems

Bernhard Rumpler and Hermann Kopetz (Faculty Mentor)  
Institute of Computer Engineering, Real-Time Systems Group  
Vienna University of Technology  
Vienna, Austria  
Email: {rumpler,hk}@vmars.tuwien.ac.at

**Abstract** — *The increasing complexity of today's embedded real-time systems requires complexity management to be a first-order goal of any real-time systems architecture. This work on design comprehension is an interdisciplinary research area bridging the gap between computer science on the one side and the cognitive and learning sciences on the other side. It aims at the development of more comprehensible computer architectures.*

## I. INTRODUCTION

The complexity of many of today's embedded real-time systems has reached a threshold of pain where new paradigms for system development are required. For example, unmanaged complexity is one of the most challenging problems in automotive electronics development [1]. The integration process of seemingly simple components often fails due to unexpected complexity at the system level. The need for complexity management in embedded computer system architectures becomes even more important due to the current paradigm shift from federated to integrated architectures in many application domains where multiple application subsystems must be accommodated in a single distributed computer system [2].

## II. DESIGN COMPREHENSION

Massive progress has been made in recent years in the cognitive and learning sciences [3], [4]. Lots of research has been done with regard to what understanding and expertise mean [5]. Moreover, properties of material that is difficult to understand have been identified [6], [7]. The characteristics of human cognition play a fundamental role in understanding complex systems and must be regarded by system designers in order to create comprehensible systems. This is especially important in the area of embedded real-time systems in high dependability domains where failures caused by unmanaged complexity can have fatal consequences.

Although making sense of complex systems is a basic issue in the technical sciences, the recent advances in the cognitive and learning sciences have received surprisingly little attention in computer science. Most concepts and theories that deal with complexity management have been developed without cognitive theories in mind. The

work on *Design Comprehension* aims at bridging the gap between computer science on the one side and the cognitive and learning sciences on the other side with an interdisciplinary approach (see figure 1). The consideration of the characteristics of human comprehension will allow to design more comprehensible systems and can help to improve current complexity management techniques by providing a systematic and scientific basis.

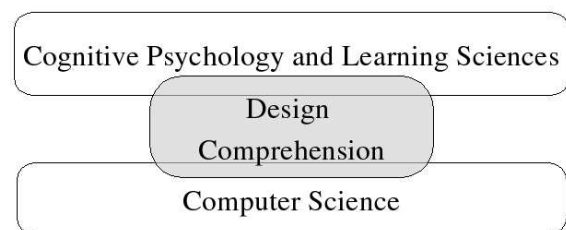


Figure 1: The interdisciplinary approach

## III. SCOPE

The work on *Design Comprehension* involves both architectural aspects as well as system implementation aspects. A *computer architecture* describes the overall design of computer systems that share a set of common characteristics [8]. It provides the basic concepts for the development of a class of computer systems. An architecture reduces the effort of the design process as the most fundamental decisions have already been made. So this is where considerations about complexity must start. A comprehensible computer architecture must be designed with the characteristics of human cognition in mind.

Guidelines for system developers and complexity metrics can only be defined for specific architectures to guide and measure implementational aspects. It is not possible to create guidelines that are applicable to all computer architectures, at least at a level of abstraction that contains more information than just platitudes. Similarly, the creation of metrics for different architectures would just be like comparing apples with oranges as architectures can be quite diverse. To be able to develop guidelines and metrics for a specific architecture, this work focuses on the Time-Triggered Architecture (TTA) [8]. The TTA is

an architecture for highly dependable real-time systems, which is used for automotive and avionics control applications.

#### IV. GOALS

The work on Design Comprehension aims at an optimization of the TTA with regard to human comprehension. This involves architectural aspects, e.g., the structure of component interfaces or the level of abstraction of components. The creation of appropriate abstractions that represent the optimal level of detail for the task at hand is a central aspect. Especially the complex design tools [9], [10] for the TTA can be improved by providing the users a more abstract view of their system, without bombarding them with irrelevant detail.

Regarding system implementation aspects, guidelines and metrics for time-triggered real-time systems shall be developed to keep the overall system complexity low and to be able to identify problematic designs early in the development.

#### V. PRELIMINARY RESULTS

To be able to reduce the complexity of the integration process, the concept of *system-level components* has been developed. System-level components encapsulate all complexity of the application and avoid the propagation of complexity to the system level. Moreover, the components used by the system integrator are all at the same conceptual level which reduces the cognitive load of the integration process.

Traditional approaches for the integration of components in safety-critical real-time systems do not support the concept of system-level components: The integration process is usually characterized by wrapping existing components, creating deep hierarchies of abstractions [11], or the introduction of a central mechanism managing the interaction of the application components [1]. This makes the integration process far more complex as lots of complexity caused by the interactions of the components must be handled by the system integrator.

#### VI. FUTURE WORK

There exist lots of properties that can make embedded real-time systems hard to understand [12]. These properties will serve as a basis for the creation of guidelines for developers of time-triggered systems. Moreover, the development of complexity metrics for the TTA is a future goal.

#### ACKNOWLEDGMENTS

This work has been supported by the FIT-IT program of the Austrian Federal Ministry of Transport, Innovation, and Technology, project number 809442.

#### REFERENCES

- [1] Anthony Phillips, Diana Yanakiev, and Fangjun Jiang. Managing complexity in large-scale control system design. In *Proceedings of the 2004 American Control Conference*, pages 4698–4703, Boston, MA, USA, June 2004. AACC.
- [2] Hermann Kopetz, Roman Obermaisser, Phillip Peti, and Neeraj Suri. From a federated to an integrated architecture for dependable real-time embedded systems. Technical report, Vienna University of Technology, Austria; Darmstadt University of Technology, Germany, August 2004.
- [3] Daniel Reisberg. *Cognition*. W. W. Norton & Company, Inc., New York, second edition, January 2001.
- [4] John Sweller and Paul Chandler. Why some material is difficult to learn. *Cognition and Instruction*, 12(3):185–233, 1994.
- [5] Cindy E. Hmelo-Silver and Merav Green Pfeffer. Comparing expert and novice understanding of a complex system from the perspective of structures, behaviors, and functions. *Cognitive Science*, 28(1), 2004.
- [6] Paul J. Feltovich, Richard L. Coulson, and Rand J. Spiro. Learners’ (mis) understandings of important and difficult concepts: A challenge for smart machines in education. In K. D. Forbus and P. J. Feltovich, editors, *Smart Machines in Education: The Coming Revolution in Educational Technology*, pages 349–375. AAAI Press, 2001.
- [7] Wayne Reeves. *Learner-Centered Design*. Sage Publications, 1999.
- [8] Hermann Kopetz and Günther Bauer. The time-triggered architecture. In *Proc. of the IEEE*, volume 91, pages 112–126, January 2003.
- [9] TTTech Computertechnik AG, Vienna, Austria. *TTP-Build: The Node Design Tool for the Time-Triggered Protocol TTP*, January 2006.
- [10] TTTech Computertechnik AG, Vienna, Austria. *TTP-Plan: The Cluster Design Tool for the Time-Triggered Protocol TTP*, January 2006.
- [11] Delbert L. Swanson. Evolving avionics systems from federated to distributed architectures. In *Proceedings of the 17th Digital Avionics Systems Conference (DASC)*, volume 1, pages D26/1–D26/8. AIAA/IEEE/SAE, 1998.
- [12] Bernhard Rumpler. Cognitive complexity of computer architectures – designing understandable systems. Technical Report 72/2005, Vienna University of Technology, Vienna, Austria, 2005.

# UMTS Network Modelling – Interference Impact to Signal Quality

Zdeněk Růžička and Stanislav Hanus  
 Institute of Radio Electronics  
 Brno University of Technology  
 Brno, Czech Republic  
 Email: xruzic20@stud.feec.vutbr.cz

**Abstract** — This paper describes mathematical model of UMTS network which simulates signal processing and transmission in downlink. Presented model is designed for interference analysis, mainly for multipath propagation influence to channelization codes orthogonality. This model is made by using Matlab.

In the second part of this article the simulation of interference influence to signal quality or bit error ratio is presented as a first task of this model. Finally, the future tasks of this UMTS model are outlined.

## I. INTRODUCTION

Third generation of mobile communications require different approach than previous systems. The main difference is that 3G systems use CDMA technique. This system uses only one frequency for all subscribers connected in the network and individual users are distinguished by channelisation code which spreads user data flow. More about this problematic can be found in [1] and [2]. Mathematical model described in this article is designed for UMTS network interference analysis. All signals with another spreading code are rated like interferences, therefore here are rather different C/I ratios than in 2G systems.

One of the tasks of this model is calculate the signal quality dependence on the interference level.

## II. UMTS MODEL

Described model is programmed in Matlab. Its structure is based on 3GPP specifications [3]. This model simulates DPDCH channel processing in downlink. Basic scheme of the model shows Figure 1.

Data flow is divided into two branches and mapped for modulation purposes. In this case QPSK modulation with pulse shaping by root raised cosine filter is used, therefore binary symbol “1” is mapped as -1 a binary symbol “0” is mapped as 1. Mapped data flow is spread by channelization code to the chip flow. Each branch uses the same code. In UMTS

system Walsh codes are used. The value of spreading factor is between 4 and 256.

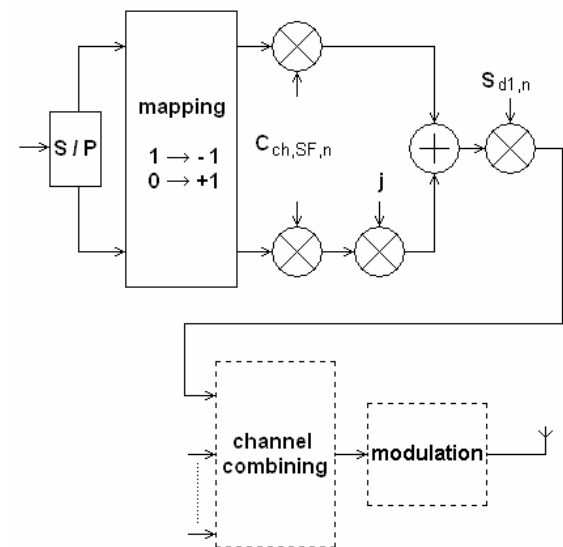


Figure 1: DPDCH channel processing in UMTS

Second branch is multiplied by unit complex number and both branches are then combined into complex chip flow. The chip rate is 3,84Mchip per second. This complex chip flow is multiplied by scrambling code. These codes are complex too and are derived from Gold sequences and serve for Node B recognition.

After this operation channels are combined and modulated to carrier.

Receiving side of the model performs descrambling and selecting required channel by using channelisation code. After this, data flow is restored and required value, in this case bit error ratio of received data flow, evaluated.

The generators of Walsh codes and complex scrambling codes are important parts of this model. Model structure and all used parameters can be modified for the specific situation to obtain required results.

### III. SIMULATION

Presented simulation computes BER of received data flow in dependence on C/I ratio.

This simulation uses UMTS model presented above. The modulation process is omitted by reason of computation time saving, because this simulation is very time consuming process.

The simulation is performed for different spreading factor which is used at the transmitting side. Its value is between 4 and 32. The length of testing data flow is from  $10^5$  to  $10^8$  bits in dependence on spreading factor value and C/I ratio.

Interferences in the radio environment are simulated by white Gaussian noise with appropriate level to obtain required C/I ratio. Simulation result shows Figure 2.

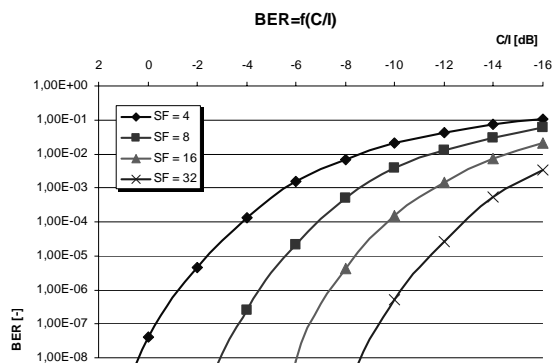


Figure 2: Simulation results

By spreading factor increasing the spreading gain is increased too. This leads to bit error ratio decreasing as can be seen in the simulation results.

### IV. CONCLUSIONS

Presented simulation is only basic feature of described model. UMTS model is designed for interference analysis in UMTS radio environment, especially for problem of orthogonality distortion cause by multipath propagation of the signal between Node B and mobile equipment.

Future task is computing of bit error ratio dependence on orthogonality distortion, corresponding C/I ratio decrease, power level increase and other simulations.

### ACKNOWLEDGMENTS

This work has been supported by the doctoral project of the GACR (Czech Science Foundation) No. 102/03/H109 "Methods, Structures and Components of Electronic Wireless Communication", by the re-

search project No. 102/04/2080, and by the research program No. MSM 0021630513.

### REFERENCES

- [1] J. Korhonen. Introduction to 3G Mobile Communications. Artech House, Norwood, 2001
- [2] J. Lempiäinen, M. Manninen. UMTS Radio Network Planning, Optimization and QoS Management: For Practical Engineering Tasks. Kluwer Academics Publishers, Boston, 2003
- [3] 3GPP Technical Specification Group Radio Access Network - Spreading and modulation (FDD) TS 25.213 V6.3.0. [online], available at <http://www.3gpp.org>, 2005

# Extended Confidence-Weighted Averaging in Sensor Fusion

Angela Schörgendorfer and Wilfried Elmenreich (Faculty Mentor)

Institut für Technische Informatik

Vienna University of Technology

Vienna, Austria

Email: e0125319@student.tuwien.ac.at

**Abstract** — *Systems that deduce information about their environment from sensor data can increase the accuracy and reliability of such information by replicating sensors and combining or "fusing" their measurements. The corruption of single measurements through failures of the sensor or random noise can thus be masked. Research conducted in this field so far, however, has not taken into consideration that the errors committed by sensors are not always uncorrelated. Ignoring such dependencies can lead to a suboptimal fused result.*

*In this work, the approach of confidence weighted averaging is extended to take such dependencies into consideration. The effect of the new approach on fusion results is analyzed using sensor information from a mobile robot.*

## I. MOTIVATION

Due to the possible influence of hardware failures, uncertainties in a system's environment and random noise, measurements obtained from a single sensor are generally unreliable. Systems that depend on information about their environment acquired through sensors can increase the reliability of such information using multiple sensors. By estimating the true value of an observed variable by fusing the information obtained by various sensors, the effects of sensor errors like inaccurate measurements or a complete failure of a sensor on the behavior of the system can be overcome.

While many sensor fusion methods concentrate on the fusion of classifiers or decisions, the field relevant for this work, that of fusing continuous-valued variables, has not been treated as extensively. The task is to combine real-valued measurements of the same variable taken by various sensors at the same point in time to derive an estimate of that variable at that specific point in time. We will therefore not fuse measurements taken in the course of time, as methods like the Kalman filter [1] do.

Existing Methods for such a task, like those suggested by Marzullo [2], Schmid and Schossmaier [3], or Elmenreich [4], do not consider correlations between sensor errors. However, the behavior of sensors can be greatly correlated, for example if they are of the same make and show the same inherent behavior. We will propose a method of calculating a weighted average of measurements, where the weights are determined by the variance

and correlations of measurement errors. The introduction of correlations not only improves the result of a single fusion process but also reduces the risk of propagating imprecise estimates in the case of a more complex architecture.

## II. CONFIDENCE-WEIGHTED AVERAGING

To combine the measurements, a simple mean of all the values does not usually perform well enough. The reason for that is that some sensors may be more reliable than others, so that their measurement can be expected to represent the true value more accurately. It is reasonable to assign more importance and therefore a greater weight to an observation  $x_i$  from a sensor that is more reliable than to one from a less accurate sensor and calculate a weighted average according to (1).

$$x_{FUSED} = \sum_{i=1}^N x_i w_i \quad (1)$$

One way to determine the weights  $w_i$  for such a weighted average is to base them on the variance of the measurement error committed by each sensor as expressed in (2)[4]. The variance of the fused result can be determined through expression (3). For the case that the errors are independent, assigning the weights in this way is optimal in the sense that the expected variance of the fused result is minimized.

$$w_i = \frac{1}{\sigma_i^2 \sum_{j=1}^n \frac{1}{\sigma_j^2}} \quad (2)$$

$$\sigma_{FUSED}^2 = \sum_{i=1}^n w_i^2 \sigma_i^2 \quad (3)$$

The assumption of independency of sensor errors cannot be made in the general case. Ignoring correlations between fusion inputs results in a suboptimal assignment of weights to each observation, and a distorted estimate of the variance of the result. In the case of a system that uses distributed sources of information and fuses data at

various points in the process, the estimated fused variance of a fused value will determine its influence on further fusion processes. Positive correlations, for example, cause the fused variance calculated according to (2) to underestimate the true variance, which in turn leads to a greater weight in the next fusion process than should be assigned.

### III. EXTENDED CONFIDENCE-WEIGHTED AVERAGING

To take advantage of known correlations, the method described above can be extended. The variances and covariances of the sensor errors are expressed in the covariance matrix  $\Sigma = \sigma_{ij}$ . The variance of the result of a weighted average is now

$$\sigma_{FUSED}^2 = \sum_{i=1}^n \sum_{j=1}^n w_i w_j \sigma_{ij}. \quad (4)$$

The vector of weights  $\mathbf{w} = w_i$  that minimizes this fused variance can be calculated as in expressions (5)-(7), where  $\mathbf{c}_1$  represents the first column of  $\Sigma$  without its first element  $\sigma_{11}$ ,  $\sigma_{11}$  is a vector of  $n - 1$  replications of  $\sigma_{11}$  and  $\mathbf{C}^*$  represents  $\Sigma$  without its first column and first row:

$$\mathbf{w}^* = (\sigma_{11} \mathbf{1}^T - \mathbf{c}_1 \mathbf{1}^T - \mathbf{1} \mathbf{c}_1^T + \mathbf{C}^*)^{-1} (\sigma_{11} - \mathbf{c}_1) \quad (5)$$

$$w_1 = 1 - \mathbf{1}^T \mathbf{w}^* \quad (6)$$

$$\mathbf{w} = \begin{bmatrix} w_1 \\ \mathbf{w}^* \end{bmatrix} \quad (7)$$

### IV. MULTI-SENSOR CASE STUDY

In order to obtain sets of real sensor measurements for the evaluation of this method we have used a mobile robot equipped with three infrared sensors and two ultrasonic sensors. The sensors installed on the robot are interfaced by a TTP/A smart transducer network via a gateway node on the robot. Figure 1 shows a schematic representation of the measurement setup. The test obstacles were placed at various distances, while the sensor measurements were logged at a connected PC.

An evaluation of the data has shown that our extended approach to confidence-weighting can reduce the error of fused results, but shows its greatest advantage in an improved estimation of the variance of the result. The estimate is generally much closer to the true variance, so that the reliability relative to other measurements is estimated more accurately.

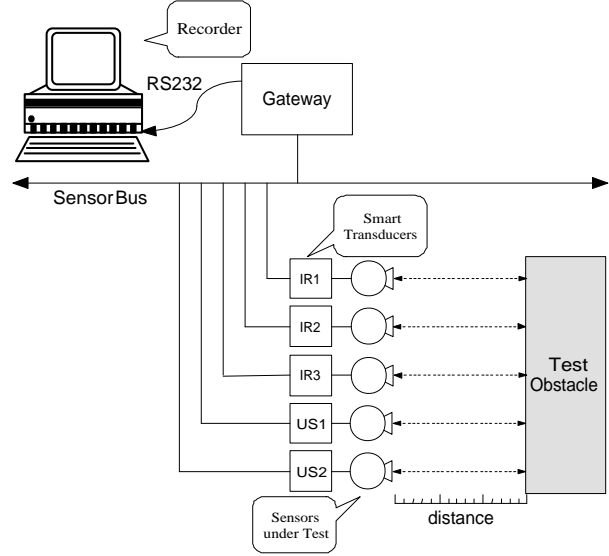


Figure 1: Setup for sensor fusion testing

If fused results are themselves used as inputs into another fusion process, we have found that the correlations between measurements can best be integrated when fusing highly correlated sensors in a first step. When fusing measurements with uncorrelated error first, dependencies between those fused inputs and others that will be added at a later point may be masked and cannot be fully considered in the calculations.

### ACKNOWLEDGEMENTS

This work was supported by the Austrian FWF project TTCAR under contract No. P18060-N04.

### REFERENCES

- [1] R.E. Kalman. A new approach to linear filtering and prediction problems. *ASME Journal of Basic Engineering*, (82):35–45, March 1960.
- [2] K. Marzullo. Tolerating Failures of Continuous-Valued Sensors. *ACM Transactions on Computer Systems*, 8(4):284–304, November 1990.
- [3] U. Schmid and K. Schossmaier. How to reconcile fault-tolerant interval intersection with the Lipschitz condition. *Distributed Computing*, 14(2):101–111, April 2001. Springer-Verlag GmbH.
- [4] W. Elmenreich. *Sensor Fusion in Time-Triggered Systems*. PhD thesis, Vienna University of Technology, Institut für Technische Informatik, Vienna, Austria, October 2002.

# Numerical Simulations of Electrical Characteristics of Piezoceramic Sensor

Petr Sedlak, Jiri Majzner Jan Havranek and Josef Sikula (Faculty Mentor)  
 Department of physics, Faculty of Electrical Engineering and Communications  
 Brno University of Technology  
 Brno, Czech Republic  
 Email: xsedla49@stud.feec.vutbr.cz

**Abstract** — *The paper presents the numerical approach and results for piezoceramic sensor electrical characteristics. A method for the analysis of piezoelectric media based on finite element calculations is presented. Object of study is a disc and the problem is defined as two dimensional axisymmetric task, for simplicity. The own algorithm was developed in MATLAB. The numerical results are compared with experimental results.*

## I. INTRODUCTION

Robust numerical simulations of advanced structures will result in the development of designs that perform better than their passive counterparts while costing less. In order to optimize the design of complicated structures that are subjected to simulation is necessary. Figure 1. presents typical construction of acoustic emission sensor.

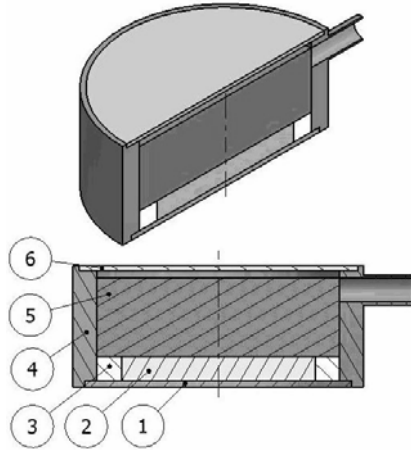


Figure 1: Piezoceramic sensor in detail (1 membrane, 2 piezoceramic segment, 3 insulated ring, 4 case base, 5 damping material, 6 case cover)

The finite-element method is very attractive since it can be applied to any geometry for any set of material properties and loading conditions as long as the appropriate constitutive relationships and

equilibrium conditions are met. Since the method is not restricted by size, one can use the so called zoom feature in finite-element meshing to use different-size elements to describe device. Many researchers have used the finite-element method for modeling piezoelectric sensors and actuators since the 1970s. The first finite element formulation was proposed by Allik and Hughes [1]. A comprehensive paper was written by Lerch [2] on the simulation of piezoelectric devices that included time domain modeling. The numerical approach presented may be used in CAE models for nondestructive testing sensors.

## II. FINITE-ELEMENT MODEL

Piezoelectric materials are anisotropic and the elastic field in such materials is coupled with the electric field. Finite element equations for piezoelectric materials have already been formulated in many papers. A finite-element formulation is presented for modeling the electrical characteristics of piezoelectric ceramic sensors.

Object of study is a disc. For simplicity, the problem is defined as two dimensional case, axisymmetry task. The finite element equations used in the calculation of the resonance frequencies and corresponding eigenvalues are therefore the ones given by [2]

$$\begin{bmatrix} M & 0 \\ 0 & 0 \end{bmatrix} \begin{bmatrix} \ddot{U} \\ \ddot{\Phi} \end{bmatrix} + \begin{bmatrix} D & 0 \\ 0 & 0 \end{bmatrix} \begin{bmatrix} \dot{U} \\ \dot{\Phi} \end{bmatrix} + \begin{bmatrix} K_{uu} & K_{u\phi} \\ K_{u\phi}^T & K_{\phi\phi} \end{bmatrix} \begin{bmatrix} U \\ \Phi \end{bmatrix} = \begin{bmatrix} F \\ Q \end{bmatrix}, \quad (1)$$

where  $U$  is a vector of nodal displacements,  $K_{uu}$  is mechanical stiffness matrix,  $K_{u\phi}$  is piezoelectric coupling matrix,  $K_{\phi\phi}$  is dielectric stiffness matrix,  $M$  is mass matrix,  $F$  is mechanical forces vector and  $Q$  is electrical charges vector. The FE equations are transformed to H-form [3], where the potential in the nodes of the elements are condensed out of the FE equations, and instead the voltage  $V$  is introduced

$$\begin{bmatrix} M & 0 \\ 0 & 0 \end{bmatrix} \begin{bmatrix} \ddot{U} \\ \ddot{V} \end{bmatrix} + \begin{bmatrix} D & 0 \\ 0 & 0 \end{bmatrix} \begin{bmatrix} \dot{U} \\ \dot{V} \end{bmatrix} + \begin{bmatrix} H_{uu} & H_{u\phi} \\ H_{u\phi}^T & H_{\phi\phi} \end{bmatrix} \begin{bmatrix} U \\ V \end{bmatrix} = \begin{bmatrix} F \\ Q \end{bmatrix}. \quad (2)$$

Electrical properties of piezoceramic elements are defined by impedance spectrum. On the base of this spectrum, equivalent capacitances and equivalent inductances are calculated. The frequency dependence of impedance can be computed directly from the FE equations (2) using matrix manipulation. Piezoelectric body is thought as capacitor. Impedance is given by

$$Z(\omega) = 1/Y(\omega), \quad Y(\omega) = i\omega C(\omega), \quad (3)$$

where  $Y(\omega)$  is admittance,  $\omega$  is radial frequency,  $C(\omega)$  is frequency dependent capacity of investigation object. It can be elicited out of equation (2), when harmonic excitation is supposed

$$\begin{aligned} (-\omega^2 M + i\omega D + H_{uu})A &= (F - H_{u\phi} V) \\ V^{-1} H_{u\phi}^T A + H_{\phi\phi} &= Q/V = C(\omega) \end{aligned}, \quad (4)$$

where  $A$  is the displacement of the nodes. The final relation for admittance can be expressed

$$Y(\omega) = -i\omega \left[ H_{u\phi}^T W^{-1} (F/V - H_{u\phi}) + H_{\phi\phi} \right], \quad (5)$$

where  $W = (-\omega^2 M + i\omega D + H_{uu})$  must be computed for each frequency.

### III. RESULTS AND CONCLUSION

On the basis of the presented formulations and considerations the own algorithm was developed in MATLAB. The PCM-51 discs of diameter 10 mm and thickness 3 mm were modelled using 3x10 4-node isoparametric elements. The impedance spectrum was computed and compared with corresponding measurement in frequency range 100 kHz to 2 MHz.

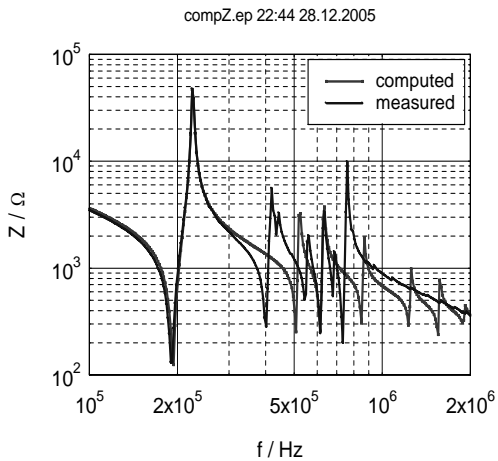


Figure 2: Comparison of measured impedance of a PCM-51 disk with corresponding simulations

In Figure 2. presenting the comparison, differences between simulation and measurement are. This inaccuracy is given by the fact that the computation scheme calculates with constant relative permittivity probably.

The algorithm was also design to solve complex task, not only for piezoceramics disc or ring. This was required to study the influence of other parts in assembly of sensor on impedance spectrum, see Figure 3.

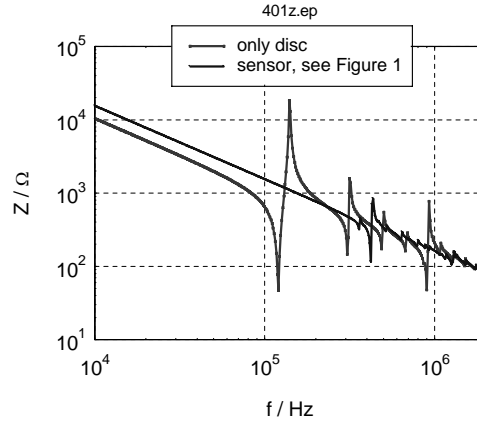


Figure 3: Impedance vs. frequency

### ACKNOWLEDGMENTS

This research has been supported by the Czech Ministry of Education in the frame of MSM 0021630503 Research Intention MIKROSYN New Trends in Microelectronic System and Nanotechnologies and Grant Agency of Czech republic GACR 102/06/0866..

### REFERENCES

- [1] H. Allik, T.J.R. Hughes, Finite element method for piezoelectric vibration, *Int. J. Numer. Methods Eng.* 2 (1970) 151-157.
- [2] Lerch, R.: Simulation of piezoelectric devices by two and three-dimensional finite elements, 1990 *IEEE Transactions on ultrasonic ferroelectrics and frequency control*, MAY 1999, p. 233 – 247.
- [3] Kocbach, J., FE Modeling of Ultrasonic Piezoelectric Transducers, PhD thesis, University of Bergen, 2000. G. Smith and W. Pisecki. The time-triggered sensor paradigm. In *Proceedings of the 10th IEEE International Conference on Intelligent Engineering Systems*, pages 297–300, Honolulu, Hawaii, September 2006.

# Black-Box Modelling of Microwave Amplifiers for Linearization

Daniel Silveira and Gottfried Magerl  
 Institute of Electrical Measurements and Circuit Design  
 Vienna University of Technology  
 Gusshausstrasse 25/354, A-1040, Vienna, Austria  
 Email: daniel.silveira@tuwien.ac.at

**Abstract** — This research is about black-box modelling of a microwave Power Amplifier (PA) and its performance in the almost linear and compression operation modes. An in-band quasi-white noise complex-valued signal is used as input for the identification procedure. A segment of the input-output measurement data is processed to generate an initial model. The model is cross-validated with the entire measurement signal. The first order Volterra kernel is extracted in order to obtain an estimation of the amplifier's memory. A new model is generated and possible performance improvements are studied. The result of this process is a suitable block-structure for the final amplifier model. This resulting model can be used for simulation of linearization systems or even in further identification processes.

## I. INTRODUCTION

With so many emerging transistor technologies and fabrication methods it is very difficult to develop a general behavioral model which can be used with every component. The necessary physical parameters are not available in commercial cases since this constitutes the industry's know-how. However, they are the basis to formulate precise mathematical expressions or parametric models that contain algebraic or differential equations. These facts lead to the use of inductive and data driven amplifier models in many cases.

Among different methodologies used for black-box modelling (as Neural Networks and parametric modelling with differential equations), the modular approach methodology was employed.

The process of achieving the amplifier model consist of two tasks: First, a suitable model structure has to be selected and then the model parameters can be estimated. Finally, the coefficients of the resulting model can be extracted.

The objective of this paper is to present a model identification algorithm as shown in Fig. 1 and presented in details in [1]. At the beginning the estimated first order Volterra kernel from an initial model is evaluated, providing an insight into the amplifier's memory effects. By the use of this parameter a more accurate second model is calculated. Then the gathered information on memory and structure is used for the process improvement and to achieve the final model.

## II. WIENER AMPLIFIER MODEL

The structure chosen was the Wiener Model due to its similarity to the amplifier behavior. This model is com-

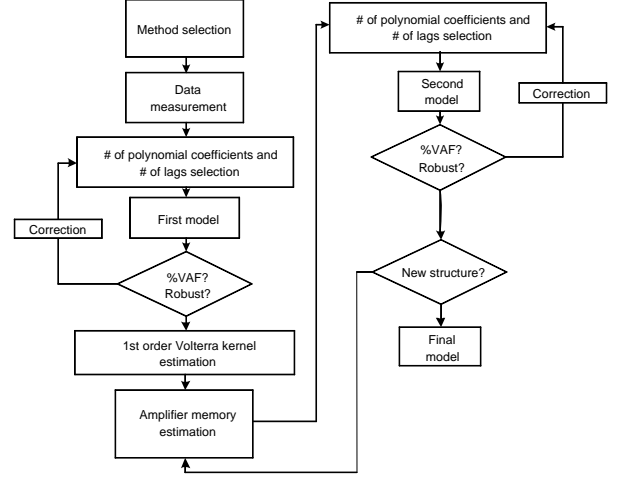


Figure 1: Algorithm used in the identification process

posed of cascaded linear and nonlinear blocks.

The Wiener Amplifier Model (WAM) output can be represented as:

$$y(t) = \sum_{q=0}^Q c^{(q)} \left( \sum_{\tau_1=0}^{T-1} \dots \sum_{\tau_q=0}^{T-1} \mathbf{h}(\tau_1) \dots \mathbf{h}(\tau_q) \cdot u(t - \tau_1) \dots u(t - \tau_q) \right) \quad (1)$$

where  $Q$  denotes the maximum order of the polynomial used,  $c^{(q)}$  are the polynomial coefficients,  $T$  is the memory length,  $t$  and  $\tau_q$  are discrete indexes of the sampling interval and  $h(\tau)$  is the impulse response.

## III. MODEL FITTING TECHNIQUES

This section describes the techniques used in the identification of the WAM linear and nonlinear blocks.

**Linear Block:** The linear block is identified by measured input/output data. Applying the singular value decomposition (SVD), it is possible to find a suitable form for the least mean square estimator of the impulse response function used to estimate the linear block of the WAM. This technique has shown to be computationally efficient and very suitable when the input signal is strong-colored and the SNR is low [2].

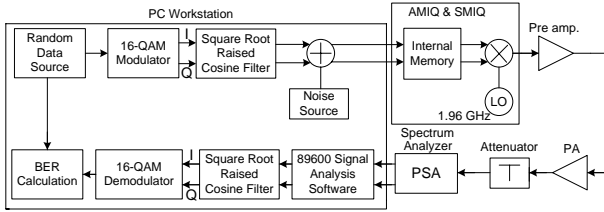


Figure 2: Measurement system used

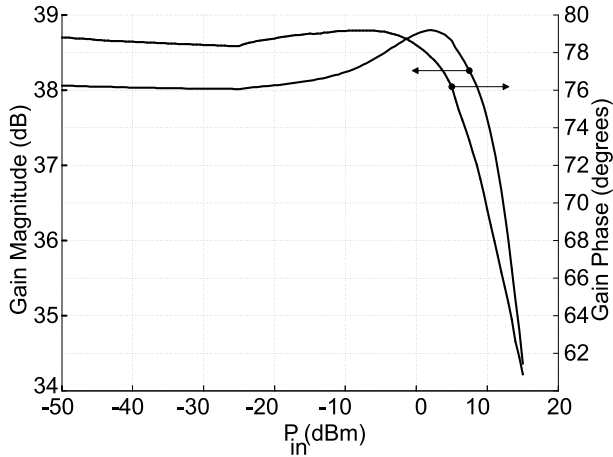


Figure 3: Amplifier gain characteristics curves

**Nonlinear Block:** The input signal for the estimation of the WAM nonlinear block is the convolution between the input measured signal with the already estimated linear block. Then a linear regression in a minimum mean square error sense is applied between this convoluted signal and the measured output signal.

#### IV. MEASUREMENT SETUP

The measurement system is presented in Fig. 2. The class AB main amplifier has the following nominal characteristics: Frequency range of 1.93 . . . 1.96 GHz, maximum output power of +48 dBm and 36 dB Gain. The PA's output signal was measured at a center frequency of 1.96 GHz using an Agilent Performance Spectrum Analyzer (PSA) and processed by the Agilent 89600 Signal Analysis Software.

The measured amplifier gain characteristics curves are shown in Fig. 3. The gain amplitude and phase present significant changes in the area near the 1 dB compression point.

#### V. AMPLIFIER IDENTIFICATION AND INVESTIGATION

The WAMs were calculated using the pseudo-inverse approach with a small segment of the measured input/output signal at different input power levels and cross-validated with the entire data set until a satisfactory %VAF (or NMSE) was achieved (see [3]).

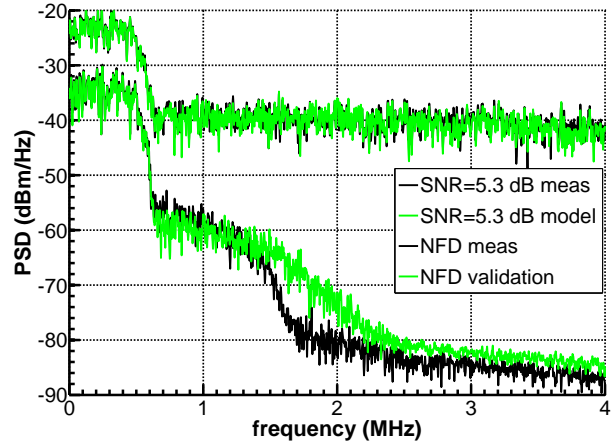


Figure 4: PSD curves for the model estimated with noisy signals (upper curves) at the amplifier compression point and validation using noise free data (lower curves). The curves were normalized and the lower curve was shifted to help the visualization.

The configuration of the measurement setup showed in Fig. 2 provides also the possibility to analyze how the model behaves when the input signal is contaminated with noise, as described in details in [4].

#### VI. CONCLUSION

The research is about the black-box modelling of PA models using the pseudo-inverse approach with complex signals. The pseudo-inverse technique presented reasonable results for PA estimation. The models were analyzed and showed acceptable results when compared with measured data. Another modelling possibilities are being researched.

#### REFERENCES

- [1] D. Silveira, M. Gadringer, H. Arthaber, M. Mayer, and G. Magerl. Modeling, analysis and classification of a PA based on identified volterra kernels. *13th GAAS Symposium*, 1:405–408, 2005.
- [2] M. Lortie and R. E. Kearney. Robust identification of time-varying system dynamics with non-white inputs and outputs noise. *Proceedings of 20<sup>th</sup> Annual International Conference of the IEEE Engineering in Medicine and Biology Society*, 20, no. 6:3036–3037, 1998.
- [3] D. Silveira, M. Gadringer, H. Arthaber, and G. Magerl. RF-power amplifier characteristics determination using parallel cascade wiener models and pseudo-inverse techniques. *APMC Proceedings*, 1:204–207, 2005.
- [4] D. Silveira, M. Gadringer, M. Mayer, and G. Magerl. Analysis of RF-power amplifier modeling performance using a 16-QAM modulation over AWGN channels. *INMMIC*, 1:1–4, 2006.

# Time-Triggered Ethernet

Klaus Steinhammer  
Vienna University of Technology  
Real-Time Systems Group  
Treitlstr. 3/182-1, A-1040 Vienna, Austria  
*klaus@vmars.tuwien.ac.at*

Hermann Kopetz  
Vienna University of Technology  
Real-Time Systems Group  
Treitlstr. 3/182-1, A-1040 Vienna, Austria  
*hk@vmars.tuwien.ac.at*

**Abstract** — *Time-Triggered (TT) Ethernet unifies realtime and non-real-time traffic into a single coherent communication architecture. It is intended to support different types of applications, from simple data acquisition systems, via multimedia systems up to the most demanding safety-critical real-time control systems which require a fault-tolerant communication service that must be certified. TT Ethernet distinguishes between two traffic categories: the standard event-triggered Ethernet traffic and the time-triggered traffic with temporal guarantees. The event-triggered traffic in TT Ethernet is handled in conformance with the existing Ethernet standards of the IEEE. The design of TT Ethernet has been driven by the requirement for certification of safety-critical systems and by an uncompromising stand with respect to the integration of legacy applications and legacy Ethernet hardware.*

## I. TIME-TRIGGERED ETHERNET

The duration of a message transmission over the network depends on the characteristics of the network traffic and the network architecture. We distinguish between two different scenarios: *cooperative senders* and *competing senders*. If senders are competing (as in standard Ethernet [1]) there is always the possibility that two or more messages are sent to a single receiver simultaneously. There are two ways to resolve this conflict: back-pressure flow control to the sender (this is the choice of the bus-based “Vintage Ethernet” [2]) or the storage of the messages within the network (this is the choice of switched Ethernet). Both alternatives involve increased message transmission jitter which is unsatisfactory in real-time systems [3]. Therefore, we conclude that in real-time systems the senders must cooperate to avoid conflicts. This cooperation can be achieved through coordination by reference to a global view of time.

In many industrial domains, e.g. the automotive and aerospace domain, the functional range of distributed applications increases, and therefore the bandwidth requirements are reaching the limits of the currently available communication mediums. This creates a demand for a new communication medium that will support these distributed applications. To drive towards certification, many applications are designed using the time-triggered paradigm, so a new communication medium is needed that supports this architecture. Because Ethernet is well-established in the event-triggered world, there are many

approaches which try to adapt Ethernet in a way, that it can be deployed in applications where temporal guarantees are necessary. All these solutions use the concept of *cooperative senders* in order to guarantee constant transmission delays.

Time-Triggered Ethernet [4] allows competing senders to *coexist* with cooperative senders on the same network while preserving the temporal predictability of the traffic among the cooperative senders. To integrate competing traffic seamlessly in the same network without interfering with the cooperative traffic, Time-Triggered Ethernet introduces two message classes using the standardized Ethernet frame format [1]:

- *Standard Ethernet messages* used for Event-Triggered (ET) traffic by competing transmitters.
- *Time-Triggered (TT) messages*, transferred among cooperative senders.

ET messages are transmitted in those time intervals where the communication medium is not used for transmission of TT messages. To avoid that ET traffic affects the temporal properties of the TT traffic, TT messages preempt all ET messages that are in their transmission path.

Introducing these two message classes guarantees the compatibility to standard Ethernet “commercial off-the-shelf” (COTS) components and existing networking protocols without any modification of the competing transmitters. Further it is possible to realize a scheduled message transfer between all cooperative senders by establishing and maintaining a global time base.

## II. TIME-TRIGGERED ETHERNET CONFIGURATIONS

To provide tailored solutions for different levels of safety requirements a TT Ethernet system can be implemented using the

- standard TT Ethernet configuration, or the
- fault-tolerant TT Ethernet configuration.

### A. STANDARD TT ETHERNET CONFIGURATION

The standard TT Ethernet configuration can be used for real-time applications that require guaranteed message transmission delays, for example multi-media streaming applications.

Any TT Ethernet system consists of a set of computer nodes which are connected to a TT Ethernet switch (Figure 1). A computer node consists of a host computer and a communication controller. For the non-safety-critical configuration of TT Ethernet, two different kinds of communication controllers can be used:

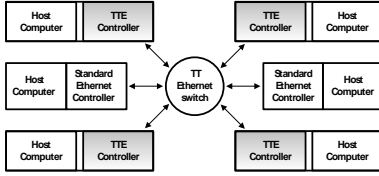


Figure 1: Standard TT Ethernet configuration

- **The COTS Ethernet card** can only be used to receive TT Ethernet traffic. As TT Ethernet conforms to the IEEE 802.3 standard, any COTS Ethernet equipment is able to receive TT messages. The differentiation is done by the Ethernet Type-ID, which is a part of the Ethernet message header [1]. The IEEE standard authority assigned the bit-pattern 0x88D7 exclusively to identify a TT Ethernet message. COTS Ethernet components are *not* allowed to send TT Ethernet messages - they are only allowed to generate ET traffic.
- **The standard TT Ethernet controller** is used in non-safety critical nodes. The communication controller is in charge of executing the TT Ethernet communication protocol, whereas all resources of the host computer are available for the application.

The controllers are connected via a point-to-point connection to the **TT Ethernet switch**. The TT Ethernet switch guarantees predictable transmission delays for TT traffic, even when ET and TT messages are transmitted using the same Ethernet network. Whenever there is a run-time conflict between ET traffic and a TT message the TT Ethernet switch preempts the ET traffic and transmits the TT message with a constant transmission delay. The TT Ethernet switch autonomously retransmits any preempted ET message immediately after the transmission of the TT message has finished. ET messages have therefore no effect on jitter and transmission delay of the time-triggered messages and are handled according to the IEEE 802.3 standard [1]. The TT Ethernet switch is used in non-safety-critical TT Ethernet configurations.

## B. FAULT-TOLERANT TT ETHERNET CONFIGURATION

The fault-tolerant TT Ethernet configuration (Figure 2) is used for safety-critical real-time control applications that require predictable transmission delays and that shall tolerate component failures.

A special kind of TT Ethernet controller is needed for the fault-tolerant TT Ethernet configuration. In order to tolerate communication channel faults, the **safety-critical TT Ethernet controller** transmits and receives

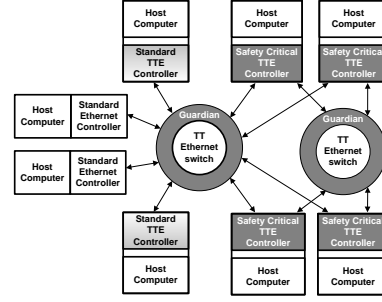


Figure 2: Fault-tolerant TT Ethernet configuration

redundant messages using two communication channels. Furthermore, the safety critical TT Ethernet controller implements services like

- fault isolation,
- fault tolerant time-base, and
- diagnosis.

The TT Ethernet switch in a fault-tolerant TT Ethernet system is similar to the TT Ethernet switch in standard TT Ethernet, but the input and output ports of each switch are monitored and controlled by its **guardian**. The guardian has knowledge about the schedule of the redundantly transmitted TT Ethernet messages and disables the inputs of the switch from controllers that could possibly interfere with the transmission of these messages.

## III. RESULTS AND ONGOING WORK

We implemented a TT Ethernet switch in hardware using an FPGA and implemented a standard TT Ethernet controller in software. Using these components, it is possible to build a non-safety-critical TT Ethernet system.

TT Ethernet defines message periods from 2 seconds down to  $63 \mu s$ . With the software implementation of the TT Ethernet controller it is possible to use message periods down to 4 ms while reaching a precision of the global time in the magnitude of  $120 \mu s$ .

Currently we are working on an FPGA implementation of the standard TT Ethernet controller. Implementing the TT Ethernet protocol in hardware will give us the possibility to use all the defined message periods while reaching a precision of the global time of about  $1 \mu s$ .

## REFERENCES

- [1] IEEE Standard 802.3, 2000 Edition. Carrier Sense Multiple Access with Collision Detect on (CSMA/CD) Access Method and Physical Layer Specifications.
- [2] Bernard Jouga. How Ethernet becomes industrial. *Workshop: The use of Ethernet as a fieldbus*, September 2001.
- [3] H. Kopetz. *Real-Time Systems: Design Principles for Distributed Embedded Applications*. Kluwer Academic Publishers, 1997. ISBN 0-7923-9894-7.
- [4] Hermann Kopetz, Astrit Ademaj, Petr Grillinger, and Klaus Steinhammer. The Time-Triggered Ethernet (TTE) Design. In *8th IEEE International Symposium on Object-oriented Real-time distributed Computing (ISORC)*, Seattle, Washington, May 2005.

# Efficient Position-based Communication in Wireless Ad-hoc Networks

Hannes Stratil\* and Ulrich Schmid (Faculty Mentor)  
Institute of Computer Engineering  
Vienna University of Technology  
Vienna, Austria  
Email: {hannes,s}@ecs.tuwien.ac.at

**Abstract** — A wireless ad-hoc network needs a suitable multi-hop routing protocol to facilitate the communication between arbitrary nodes. This paper presents SDT/VAR, an efficient protocol for communication in wireless ad-hoc networks. Our approach is based on the duality of Delaunay triangulation and Voronoi diagram, and guarantees the scalability of the wireless ad-hoc network, because the SDT/VAR protocol is completely independent of the total number of nodes in the network.

## I. INTRODUCTION

Wireless ad-hoc networks are a hot topic in wireless computing that attract a lot of attention to military, government and commercial customers. Wireless ad-hoc networks are made up of nodes that communicate with each other over a wireless medium in the absence of a fixed infrastructure and any centralized control. Direct communication between two arbitrary nodes is generally not possible and hence a *multi-hop routing* protocol is required. Routing in wireless ad-hoc networks is nontrivial since mobility, erroneous nodes and changes in node activity status cause frequent and unpredictable topology changes. Routing is usually addressed at the network layer of the OSI 7-layer hierarchy. The overall network layer responsibilities are divided between the topology control sublayer and the routing sublayer. *Topology control* and routing are two of the common problems in the context of wireless ad-hoc networks. The aim of the topology control sublayer is to construct an appropriate topology to improve the efficiency and performance of the overlying algorithms. The routing sublayer manages the message exchange between non-neighbor nodes in a wireless ad-hoc network. Algorithms proposed until today generally separate topology control and routing, but a common development upon one efficient data structure lead to considerably increased performance.

## II. THE SDT/VAR COMMUNICATION PROTOCOL

The primary idea of our work is the combination of two different topics of computer science — i.e., wireless ad

hoc networks and computational geometry. The *Short delaunay triangulation* (SDT) [1] is a powerful topology based on the construction rules of the *Delaunay triangulation* and the *Voronoi-aided routing* (VAR) [2] protocol is an efficient implementation of the well known *greedy/perimeter routing* approach [3]. The computation of the Short delaunay triangulation yields automatically to local *Voronoi diagrams* for the efficient implementation of Voronoi-aided routing. The duality of Delaunay triangulation and Voronoi diagram can be seen in Figure 1.

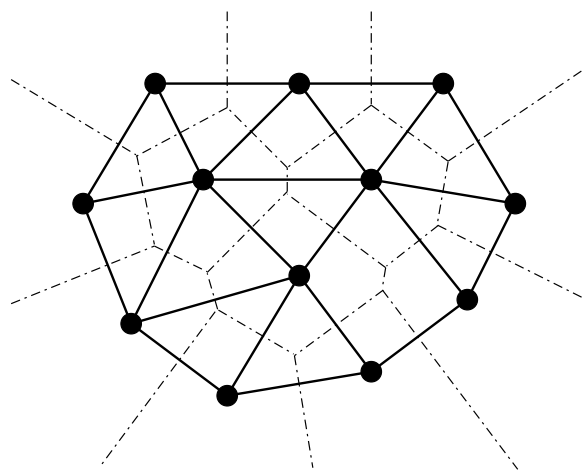


Figure 1: *Delaunay triangulation* (dashed lines) and *Voronoi diagram* (solid lines)

The greedy forwarding approach is a totally localized approach: The routing decision at a node is only based on its own position, the position of its single hop neighbor nodes and the position of the destination node. When an intermediate node receives a message for a specific destination node, it forwards a message to that neighbor node who is closest to the destination node, i.e., the neighbor node with the shortest euclidean distance to the destination node. Greedy routing can be used until the message reaches the destination or a node where no neighbor is closer to the destination than the node itself. At such a local minimum, greedy routing is no longer possible and a recovery strategy is required. A well-known recovery

\*This research is supported by the Austrian Science Fund (FWF) under grant no. P18264-N04 (SPAWN-Project).

strategy is perimeter routing. The perimeter routing approach uses the Right hand rule to forward a message along the perimeter of the faces of a planar topology. Each node that receives a message forwards the message on the next edge counterclockwise with respect to itself from the ingress edge. The Right hand rule traverses the interior of a closed polygonal face in clockwise edge order or in counterclockwise edge order if it is the exterior face. If a node is reached, with position is closer to the destination node than the node where the greedy strategy previously failed, the greedy routing algorithm takes over control again. The planarity of the topology is an indispensable property to guarantee the functionality of perimeter routing.

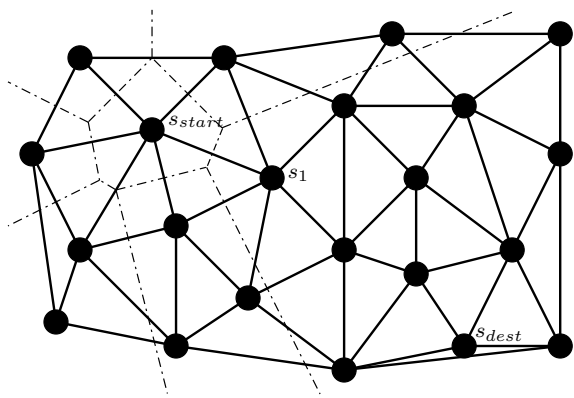


Figure 2: **Greedy Routing:** Node  $s_{start}$  wants to send a message to node  $s_{dest}$ . Node  $s_{start}$  use its local Voronoi diagram and a point-location algorithm to find the neighbor node which is closest to the destination — this is  $s_1$  — and forwards the message to this node. Each node to the same until the message reach the destination.

The Short delaunay triangulation (SDT) algorithm computes the underlying topology for greedy/perimeter routing. The topology fulfills the required planarity and is the densest possible planar topology. The density of a topology is important to guarantee the existence of efficient paths between the nodes and an equal distribution of network load. The Voronoi-aided routing (VAR) algorithm uses the same data structure than the topology for efficient forwarding of a message to a destination. Both algorithms are totally localized. They use only information of the single hop neighbor nodes for the computation of the topology resp. to forward a message. Local computation guarantees the scalability of the network, because a localized algorithm is completely independent of the total number of nodes in the network.

### III. CONCLUSION

A common implementation of topology control and routing like the SDT/VAR approach is the most efficient im-

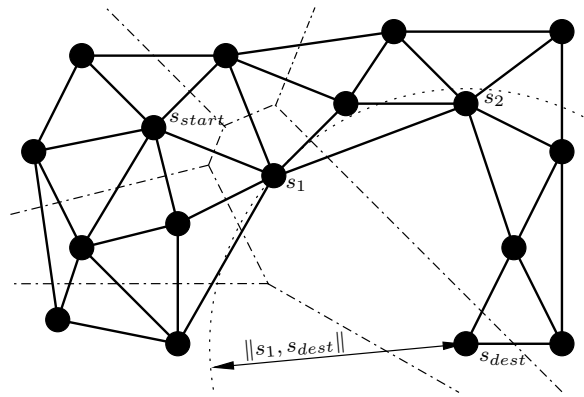


Figure 3: **Greedy/Perimeter Routing:** Node  $s_{start}$  wants to send a message to  $s_{dest}$  and forwards the message in greedy mode to  $s_1$ . Node  $s_1$  is closer  $s_{dest}$  than its neighbor nodes. Hence,  $s_1$  initiates the perimeter mode and forwards the message to node  $s_2$ . Node  $s_2$  is closer to  $s_{dest}$  than  $s_1$  and so the message will be forwarded in greedy mode again.

plementation of greedy/perimeter routing. The computation of the topology has time complexity  $O(n \log n)$ , where  $n$  only is the number of single hop neighbor nodes. This matches the lower bound on the construction of a planar topology. The routing algorithm uses the same data structure and only requires  $O(\log n')$  time complexity to find the next node in the communication path, where  $n' \leq n$  is the number of single hop neighbor nodes in the topology. This number can be significantly lower than the number of single hop neighbor nodes in the communication graph. The number of single hop neighbor nodes is on average 6 in the Delaunay triangulation.

### REFERENCES

- [1] Hannes Stratil. Distributed construction of an underlay in wireless networks. In *Proceedings of the Second European Workshop on Wireless Sensor Networks*, pages 176–187, Istanbul, Turkey, January 2005.
- [2] Hannes Stratil. An efficient implementation of the greedy forwarding strategy. In *Proceedings of the Workshop on Sensor Networks*, pages 365 – 369, Ulm, Germany, September 2004.
- [3] Brad Karp and H. T. Kung. GPSR: Greedy perimeter stateless routing for wireless networks. In *Proceedings of the Sixth annual ACM/IEEE International Conference on Mobile Computing and Networking (MobiCom 2000)*, pages 243–254, August 2000.

# Time-Multiplexed Multiple Constant Multiplication

Peter Tummeltshammer and Andreas Steininger  
 Institut für Technische Informatik  
 Technische Universität Wien  
 {petertu, steininger}@ecs.tuwien.ac.at

**Abstract** — An important primitive in the hardware implementations of linear DSP transforms is a circuit that can multiply an input value by one of several different constants. We propose a novel implementation of this circuit based on combining the addition chains of the constituent constants. We compare the area-efficiency of this addition chain based approach against a straightforward approach based on a constant table and a full multiplier.

## I. INTRODUCTION

This paper is concerned with the arithmetic circuit for *sequential multiple constant multiplication*. The input  $x$  is a fixed-point value of a specified bitwidth. The output of the circuit is  $c_i x$  where  $c_i$  is one of  $N$  fixed-point constants  $\{c_1, c_2, \dots, c_N\}$  selected according to a  $\lceil \log_2 N \rceil$ -bit control input  $i$ .

## II. MULTIPLICATION BY ONE CONSTANT

Area-efficient arithmetic circuits to multiply a fixed-point input by a single fixed-point constant have been studied extensively. In literature, the best approach in terms of minimum number of additions (and subtractions), is reported by Gustafsson, et al. in [1] and solved for constants up to 19 bits.

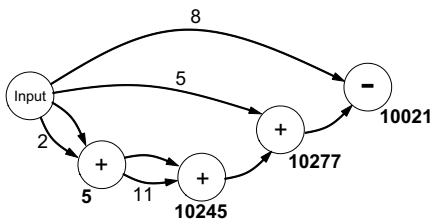


Figure 1: The DAG corresponding to multiplying by 10011100100101.

A single constant multiplication can be best represented as a directed acyclic graph (DAG) as shown in Fig. 1. The nodes of the graph represent additions resp. subtractions and the edges represent the dataflow between them. Each edge is labelled by a positive integer  $k$ , which represents the shift, or scaling by  $2^k$ , applied to the operand at this edge. In the trivial case  $k = 0$ , we omit the label. Each node can be labelled by the intermediate constant  $f$  at this node. We call these numbers the *fundamentals* of the DAG following [2]. In other words,

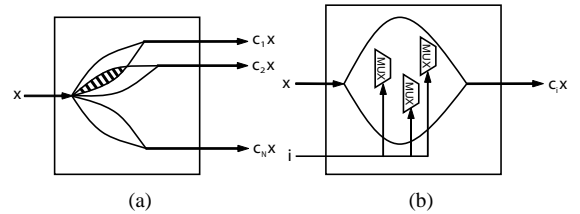


Figure 2: DAG based multiplierblock for (a) parallel and (b) sequential multiplication by  $N$  given constants.

if  $x$  is the DAG input and  $f$  is the fundamental of a node, then the output of this node is  $fx$ .

## III. MULTIPLYING BY MULTIPLE CONSTANTS

In this section, we consider the problem of multiplying an input  $x$  by a given set  $\{c_1, \dots, c_N\}$  of  $N$  constants again using only additions and shifts. There are two fundamentally different scenarios: (1) *Parallel multiplication* is performed by a multiplier block that simultaneously outputs the  $N$  values  $c_1 x, \dots, c_N x$ . (2) *Sequential multiplication* is performed by a logic block that outputs  $c_i x$  as controlled by an input that specifies  $i$ .

**Parallel multiplication.** Most of the known parallel multiplication methods [3] also use a DAG-based approach. The basic idea is to achieve savings by generating the given constants DAGs that “overlap” in terms of fundamentals. The resulting multiplier block is shown as a schematic in Fig. 2(a). The leaf-shaped structures are the single constant DAGs for  $c_1, \dots, c_N$ . An overlapping region is highlighted. Overlapping, or sharing of properly chosen fundamentals yields savings.

**Sequential multiplication.** In this paper, we are interested in sequential multiple constant multiplication. The most straightforward implementation of this logic block would be to use a full multiplier and store the preset constants in a lookup table. Again the question arises whether it is possible to exploit redundancy or inherent structure of the problem using a DAG based approach.

In parallel multiplication each unique fundamental is instantiated as one adder. In sequential multiplication however, since only one product is visible through the output at any moment, the results of some adders are unused. This opens the opportunity for the fundamentals from different DAGs, equal or not, to share the same

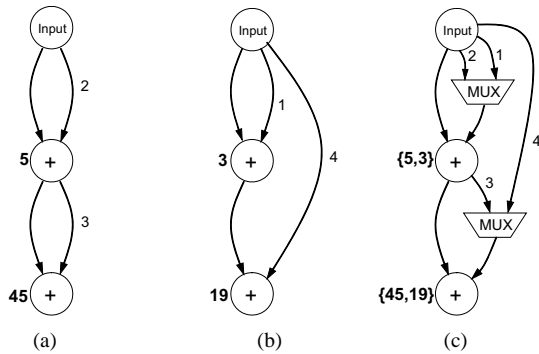


Figure 3: Optimal DAGs for 45 (a) and 19 (b) and the fused DAG (c) produced by our algorithm.

adders by time-multiplexing, thus exploiting the topological similarities between the DAGs to a much larger degree. This is the basic idea behind our solution (see Fig. 2(b)), which inserts multiplexers into the DAG for adder sharing and thus reduced area requirements. Fig. 3 shows a small example of how our algorithm works. It “fuses” the DAGs’ adders and tries to minimize the number of introduced multiplexers.

#### IV. EXPERIMENTAL RESULTS

The proposed algorithm has been implemented in a tool<sup>1</sup> that takes as input the  $N$  constants and generates the Verilog netlist of an area-optimized fused multiplication circuit for these constants. We present a comparison of circuits generated by our DAG fusion algorithm against the baseline sequential multiple constant multiplication scheme comprising a full multiplier and a constant table. They were synthesized for a commercial  $0.18\mu\text{m}$  standard cell technology ASIC library.

Fig. 4 and 5 present a representative example, for an input bitwidth of 16 and a maximum constant bitwidth of 16. The x-axis shows the number of constants fused, and the y-axis shows the circuits’ area in microns in Fig. 4, and the circuits’ critical path delay in ns in Fig. 5. For each point the comparison is based on the average performance over 10 sets of randomly selected constants, of a maximum bitwidth of 16.

For small values of  $N$ , our solution yields considerably smaller synthesized circuit area. However, for sufficiently large values of  $N$ , the fused multiplier circuits grow to be too expensive with respect to the baseline approach where only the constant table expands with  $N$ .

The critical paths for fused-DAG multipliers are approximately two times greater than the corresponding baseline designs in all cases. From a performance standpoint, one should always utilize the standard multiplier design especially when optimized multiplier macros are available.

<sup>1</sup><http://www.ecs.tuwien.ac.at/mitarbeiter/petertu/mcmgen/>

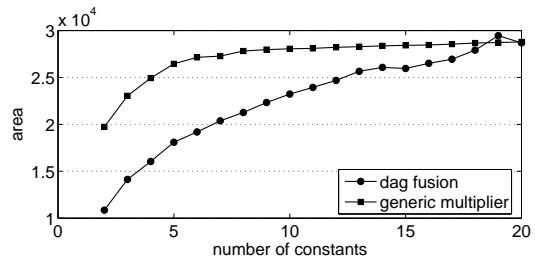


Figure 4: Average synthesized area of fused DAGs and a generic multiplier solution

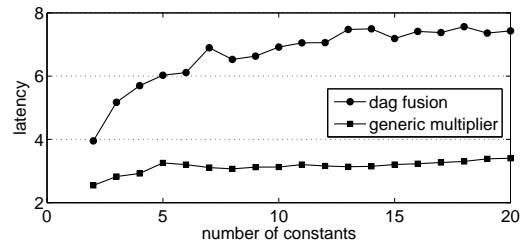


Figure 5: Average synthesized critical path delay of fused DAGs and a generic multiplier solution

#### V. CONCLUSIONS

We proposed a new architecture to support multiplication by one of several constants according to a control input. For an interesting and relevant space of problems, our approach can offer considerable saving in circuit area albeit for the penalty of increased latency.

#### ACKNOWLEDGEMENTS

This work was supported by a fellowship of the Vienna University of Technology for short-term scientific research at the Carnegie Mellon University in the SPIRAL project [4]. The author wants to thank James C. Hoe and Markus Püschel for their support throughout his research internship.

#### REFERENCES

- [1] O. Gustafsson, A.G. Dempster, and L. Wanhammar. Extended results for minimum-adder constant integer multipliers. In *IEEE International Symposium on Circuits and Systems*, volume 1, pages I–73–I–76. IEEE, May 2002.
- [2] A. G. Dempster and M. D. MacLeod. Constant integer multiplication using minimum adders. *IEE Proceedings G*, 141(5):407–413, 1994.
- [3] Y. Voronenko and M. Püschel. Multiplierless multiple constant multiplication. *Journal of Algorithms*, 2005.
- [4] M. Püschel et al. SPIRAL: Code generation for DSP transforms. *Proceedings of the IEEE, special issue on "Program Generation, Optimization, and Adaptation"*, 93(2):232–275, 2005.

# Sandbox Geography

Florian A. Twaroch and Andrew U. Frank  
Institute for Geoinformation and Cartography  
Vienna University of Technology  
Vienna, Austria

Email: {twaroch, frank}@geoinfo.tuwien.ac.at

**Abstract** — *The present work investigates formal models of spatial conceptualizations. Algebraic specifications are derived from recent findings in developmental psychology. The proposed models consider adaptation as a crucial element and are of specific interest for raising the usability of geographic information systems. Interoperability of geographic information often fails due to different conceptualizations. The work aims to overcome these differences by finding transition mechanisms between spatial conceptualizations.*

## I. INTRODUCTION

“Hard sciences” like physics and geometry define how to build models of spatial reality into a geographical information system. This results in systems lacking user friendliness and suffering from low acceptance because humans conceptualize spatial reality differently. There is a need for conceptualizations of the world that are not based on physical or geometrical principles but on common sense respectively naïve conceptualizations [1].

In order to model these conceptualizations, studies of the human mind should be considered. The psychologists Andrew Meltzoff and Alison Gopnik introduce the theory theory, a theory about how children build conceptualizations (theories) of reality [2]. Conceptualizations in their sense are very small and underlie frequent change when counterevidence is observed. Children build theories of the world that are based on testing hypothesis in a way scientists do. In the present work formal models of these theories are proposed.

Theories are often considered to be something big like Einstein’s theory of relativity or Darwin’s theory of evolution. In the context of the paper theories are assumed to be small units. Philosophers like Roberto Casati and H.N. Castañeda would rather refer to *theoritas* – small theories – to distinguish them from fully fledged theories [3].

We expect that formal models about people’s commonsense understanding of space help to address interoperability problems under a new paradigm, make robots more “intelligent”, and human-machine interfaces more usable.

## II. HYPOTHESIS

We hypothesize that human spatial conceptualizations can be built using algebras. Here algebras in their simplest definition are assumed, as being a set of sorts, operations, and axioms. A change in a spatial description can be reflected in those algebras by an adaptation of axioms.

## III. THE SANDBOX

For testing the hypothesis space related experiments of developmental psychology are simulated with an agent based approach. Here we do not carry out empirical studies on our own. We rely on a plethora of available studies [2, 4, 5]. The interpretations of these studies are used to build the conceptual model of a spatial cognizing agent.

An agent can be seen as anything that perceives its environment through sensors and acts on its environment through effectors [6]. The knowledge base of the agent is structured in algebras. A two tiered reality beliefs model allows to model errors in an agent’s perception by separating facts from beliefs. This distinction is vital for modeling situations where agents are puzzled. This always happens when beliefs about the “real world” do not fit together with the actual facts.

Current results show that the spatial cognizing agent has to rely on external sources of information through perception and on self-reflection mechanisms in order to gain more advanced conceptualizations. The agent can hold more than one spatial conceptualization of a certain fact in the environment and makes use of all of them. In the following section an example is discussed to show the methodology of the present thesis.

## IV. AN ALGEBRA BASED AGENT

When looking for lost objects, like keys, we follow a number of rules. Empirical experiments showed that these rules develop in childhood and that the same rules seem to appear in infants as old as some months when watching an object disappear [4, 5].

First we look at the place the keys have last been visible, if we have no success in finding them we continue to search in the place they usually are. In the case of no success we go back the path we moved along recently. If all these rules fail an irrational search strategy in random places could be applied, before we give up searching the object. These rules form the basis for the development of the following algebras.

Two algebras in a pseudo code notation are presented. The operation *isAt* returns TRUE when the agent has knowledge about the current object's position and FALSE when he has no clue where to look for the lost object. The function *loc o* stands for the current perception of the agent about the object location. The functions *last o*, *usual o*, and *path o* stand for the prediction of the object location for an *object o* at the last-visible-seen, usual-seen, and along-trajectory-moving-seen object location. The *placeholder a* is instantiated with an agent's state of mind at a certain time point. An initial theory for a lost object seems to consider just the last-visible-seen-location. The initial algebra is shown in equation (1).

*Algebra Lost a where*

*Operations*

$$isAt: a \rightarrow o \rightarrow Bool \quad (1)$$

*Axioms*

$$isAt = loc\ o == lastseen\ o$$

This kind of theory will not work as contradictions between observations and predictions will occur. The object can not always be retrieved in the last seen position. Further perception will lead to new evidence that objects can be retrieved also in positions like the usual-seen location. A new theory will be formed and will predict that the lost object could be at the last-visible-seen-location OR a usual-seen location.

In order to reflect this insight in the previous algebra the *isAt* axiom has to be adapted. As objects also move in space, new contradiction will arise. Another exchange of the *isAt* axiom will be necessary. Disappeared objects can also reappear along the path they moved. The more advanced algebra that is achieved after two transitions is shown in equation (2).

*Algebra Lost o where*

*Operations*

$$isAt: a \rightarrow o \rightarrow Bool$$

*Axioms*

$$isAt = (loc\ o == lastseen\ o) \parallel (loc\ o == usualseen\ o) \parallel (loc\ o == path\ o) \quad (2)$$

The conceptualization of the location of a lost object changed from the initial to an advanced algebra, because contradictions were observed. The change in the algebra for lost objects is reflected in an adaptation of the axiom. This proves the hypothesis, that human spatial representations can be modelled using algebra, for the selected example.

## V. FUTURE RESEARCH

We assume that spatial theories are very small in the number of axioms. More spatial theories have to be formalized to confirm this assumption. Especially models for agents that move in their environment are needed.

Future research will also address multiple agent systems, where commonsense concepts about space can be exchanged among agents. Agents that are exposed to the same perceptions in an environment should end up in the same spatial conceptualizations of the environment. Still some agents may hold different conceptualizations as they are exposed to a different set of perceptions. In order to link different spatial conceptualizations structural similarities in the models will be exploited to build new algebraic specifications.

The investigation of formal models about humans' commonsense understanding of space will enable geographic information systems to interoperate better with other systems and also with the human user. Information and not just data!

## REFERENCES

- [1] M. J. Egenhofer and D. M. Mark, "Naive Geography," presented at COSIT - Spatial Information Theory: A Theoretical Basis for GIS, Semmering, Austria, 1995.
- [2] A. Meltzoff and A. Gopnik, *The scientist in the crib*: Perinneeal, 2001.
- [3] R. Casati, "The Structure of Shadows," in *Time and Motion of Socio-Economic Units*, A. U. Frank, J. Raper, and J. P. Cheylan, Eds. London: Taylor and Francis, 2000, pp. 99-109.
- [4] T. G. R. Bower, *Learning in Infancy*. San Francisco: W.H. Freeman and Company, 1974.
- [5] T. G. R. Bower, *The Rational Infant - Learning in infancy*. New York: W.H. Freeman and Company, 1989.
- [6] S. Russel and P. Norvig, *Artificial Intelligence - A modern approach*: Prentice-Hall Internation, Inc., 1995.

# Implementing an Active Noise Reduction Solution on a FPGA

Christian VARGA, Faculty Mentor Andreas STEININGER  
Vienna University of Technology  
Embedded Computing Systems Group E182-2  
Treitlstrasse 3, A-1040 Vienna

Email: e0025334@stud3.tuwien.ac.at, steininger@ecs.tuwien.ac.at

**Abstract** — *The aim of this project is to develop a digital noise reduction system by using a hybrid approach, combining passive and active solutions. The core digital sound processing implementation is realised on a FPGA by using VHDL as programming language. Regular approaches use specialised hardware - digital signal processors - for this task. Therefore a main goal of this project is to show that FPGA hardware is able to compete with DSP circuitry. Previous research on this topic conducted by the ECS group [1], to show the feasibility to implement such circuitry on current hardware.*

## I. INTRODUCTION

Two ways exist to reduce unwanted noise - *passive* and *active* approaches:

The *passive* method relies on the physical effect of sound passing through materials. If a sound wave hits a material, parts of the wave are *reflected*, *absorbed* and an amount of sound - depending on the properties of the material - passes through the medium. The amount of sound that passes through defines the quality of the material in terms of noise reduction. While high frequencies are damped very effectively, lower frequencies are more likely to penetrate the material. In order to counter this behaviour the *passive* solutions tend to become very unhandy.

*Active* solutions on the other hand use electrical components to create so called *anti-noise* – a noise signal which is phase-shifted by 180 degrees. By interference the two signals cancel each other out. The focus for this project lies on the digital filter implementations. The advantage is the high level of customisation which can be obtained by using programmable logic. The major drawback of *active* solutions is the growth of complexity regarding high frequency noise signals, because higher order filters are needed.

The aim of this project is to develop active noise cancellation circuitry by using a FPGA as signal processor. Combination with passive elements improves the overall performance. This can be obtained by using *active* filters for lower frequencies and *passive* elements for the higher bands creating a *hybrid* solution as shown in Figure 1.

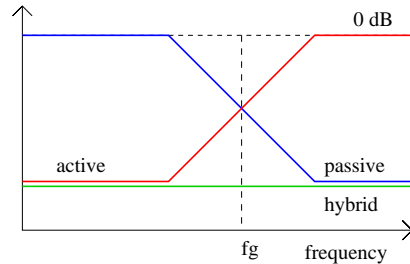


Figure 1: Frequency responses for active and passive filters

## II. ADAPTIVE FILTERS

The filter functionality will be implemented using a modified version of the *Least-Mean-Squares* [2] algorithm. The advantage of the LMS algorithm is the low computational complexity while providing excellent results. Numeric issues are of importance here, since the arithmetic used in this implementation will be *fixed-point*[3]. Simulations have shown, that using a modest word length of 16 bits has no significant impact on the filter quality compared to 32 bits *floating-point* simulations. The 16 bit were divided into 4 bits for integer and signum and 12 bits for the fractional part. See Section IV for actual results of the simulations.

The core will implement the *Filtered-X LMS* algorithm, which is an improved variation of the basic LMS. In [4] an implementation is presented for a DSP using Filtered-X LMS. It provides faster convergence times and is more stable by incorporating path estimates of the components used. This is especially important for real-world applications because the transfer function can not be estimated in advance and depends on factors such as the D/A converter, headphone and microphone transfer functions and the person itself.

## III. DESIGN

The design, depicted in Figure 2, involves two major entities: the headphone and the filter logic.

The headphone itself is modified to enable feedback to the digital algorithm. Inside the earcups there are error detection microphones which sample the noise passing through the earcups. On top of the head there is a

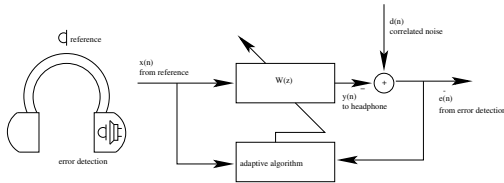


Figure 2: Device setup

reference microphone which samples the environmental noise. The anti-noise is emitted through the built-in speakers. Other approaches do not use the error microphone [5].

The sound processing logic consists of an FPGA as sound processing core and external *analog/digital, digital/analog* converters to connect to the analog circuitry - i.e. (pre-)amplifiers, microphones and speaker. The filter is an adaptive type, this means the coefficients are updated based on a given optimality criterium. The *error microphone* is crucial at this stage, since it provides essential feedback information to the adaptive algorithm. The microphone has therefore to be of higher quality and (nearly) linear frequency response.

#### IV. PRELIMINARY RESULTS

The VHDL implementation was evaluated by using a waveform containing a sinusoidal wave and a speech signal, which was distorted with a broadband white noise. Figure 3 shows plots of the resulting waveform. On the left the whole waveform is shown, on the right a zoom of the first 25000 samples. The image shows the characteristic adaption curve of the LMS algorithm.

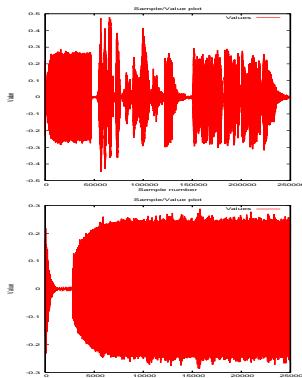


Figure 3: LMS filtering

Audible noise is heard during the first 2000 samples at a sampling frequency of 44.1 kHz. The actual sampling frequency used will be lower at about 8 kHz. The plots are produced by using the LMS simulation data obtained from the VHDL behavioural model using a word length of 16 bits. The converter chips which provide the

interface to the core offer a word size of 12 bits. The conversion result is internally spread over the 16 bits.

#### V. CHALLENGES

One of the challenges is to implement fixed-point arithmetic on the FPGA. The *Stratix II* hardware used in the project provides some DSP capabilities to the user like adder, multiplier and MAC (multiply-accumulate) entities operating on unsigned bit values. By using the correct bit format, they can be incorporated into the design to speed up processing. To prevent overflows the internal range of the signals will be scaled to the interval (-1;1).

Additionally an external converter board has to be built to support the number of needed converters - two ADCs and a DAC. The board presently used features only one converter. The selection of the converters is crucial here, since they will provide additional distortion into the calculation.

The timing of the entities is crucial to this project, since many modules have to work hand in hand to achieve the filtering and they have to perform in real-time. Therefore a suitable sampling frequency providing good noise compensation at feasible calculation time is of main concern.

#### VI. CLOSING WORDS

The project is still work-in-progress. Nonetheless preliminary results gathered from simulations look very promising. The mixture of actual filter technologies has the ability to provide high-quality noise reduction with a minimum of hardware cost and complexity that might outperform commercially available devices.

#### REFERENCES

- [1] Peter Tummeltshammer Gottfried Fuchs. Machbarkeitsstudie für digitale Schallunterdrückung. Vienna University of Technology.
- [2] Paulo S. R. Diniz. *Adaptive Filtering - Algorithms and Practical Implementation*. Kluwer Academic Publishers, Boston / Dordrecht / London, 1997.
- [3] Erick L. Oberstar. Fixed Point Representation And Fractional Math. <http://www.superkits.net/whitepapers.htm>, 2004-2005.
- [4] S. Weiss R.W. Stewart, R. Duncan. Multi-channel active noise cancellation using the DSP56001. *Acoustics, Speech, and Signal Processing, IEEE International Conference on*, 1:185-188, 1993.
- [5] C. Averty Say-Wei Foo, T.N. Senthilkumar. Active noise cancellation headset. *Circuits and Systems, 2005. ISCAS 2005. IEEE International Symposium on*, 1:268-271, 2005.

# Simulating Distributed Real-Time Systems

Daniel Albeseder\* and Josef Widder (Faculty Mentor)

Technische Universität Wien  
Embedded Computing Systems  
{da,widder}@ecs.tuwien.ac.at

**Abstract** — *We study the temporal behavior of synchronous distributed real-time systems. To properly investigate such timing behavior, proper modeling of link as well as task schedulers is required. The results of this modeling that allows to simulate message-driven algorithms are presented in this paper.*

## I. INTRODUCTION

**Problem domain** These days distributed systems become increasingly important particularly in the real-time domain. Distributed algorithms and hard real-time problems are well studied separately but there are many open issues concerning the combination of message-driven distributed algorithms (algorithms which only react on message arrivals) and real-time scheduling which need further research. For time-driven algorithms the combination with real-time scheduling was already studied in quite detail [2, 5]. Unfortunately, the problem domain of message-driven distributed algorithms cannot be isolated from the real-time scheduling problems, since the results of the scheduling decisions influence the timing of the distributed algorithm resulting in varying message patterns. Since we consider message-driven distributed algorithms, these messages influence the real-time scheduling on other nodes which in turn results in further varying message patterns, and thus a circular pattern evolves. So these problems need to be addressed in union which results in recursively dependent job release times.

**Contribution** There already exist a few distributed algorithm simulators (and many tools for simulating and calculating real-time scheduling problems), but there is a lack of software that analyzes distributed algorithms for real-time systems. Therefore, we developed a task model which captures the combined problem whilst remaining simple to handle. Furthermore, a simulation environment was built based on this new task model.

## II. TASK MODEL

A distributed algorithm is executed by a set of distributed tasks. Every task consists of one or more jobs. Every job is triggered/released by an incoming message. We distinguish between interrupt and user-level jobs. Interrupt jobs are triggered by incoming messages or inter-

\*Supported by the FWF-project *Theta* (project no. 17757-N04).

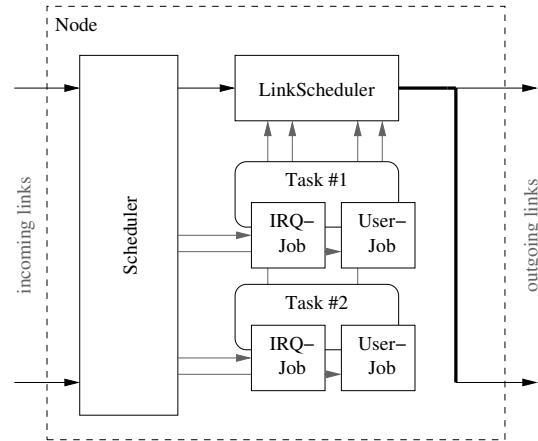


Figure 1: simulation model of a single node

nal timers — via a virtual timer message — whereas user-level jobs are invoked by an interrupt job via a virtual message (simulating buffering in shared memory for instance) or by another user-level job also via a virtual message. Messages can be sent by any job.

Every job naturally has a non-negative execution time just as every message has a non-negative transmission delay. The end-to-end delay is defined as the delay from the instant a job decides to send a message until the time this message is perceived at the target job. Evidently the end-to-end delay is a composition of transmission delay, the job's execution time and the waiting times due to blockage from other jobs. The scheduling discipline is therefore very closely coupled to the magnitude of the end-to-end delays.

## III. SIMULATION MODEL

The simulation model (as drafted in Figure 1) of a node consists of a *Scheduler* responsible for scheduling *jobs* as well as dynamically spawning new *jobs* of existing tasks due to incoming messages. The *Task* object holds task-specific shared data which every job of the corresponding *Task* can access. The *LinkScheduler* is responsible for sending messages on the correct links of the node. In order to be able to support sparsely connected networks, the *Scheduler* redirects messages not targeted to the node's address to the *LinkScheduler* and, thus, en-

ables routing.

Two nodes are connected via *Channel* modules which are able to simulate various link behaviors (e.g. FIFO stubborn channels, etc.). To be able to simulate booting behavior of systems an *AppSpawn* module spawns tasks at designated times. Additionally there exists one *DataCollector* module for monitoring all data from the designated task.

#### IV. SIMULATION ENVIRONMENT

The simulation environment is built on the public-source simulation environment OMNet++ [1] which is well extensible while having a sophisticated graphical environment for experimentation. Custom modules can easily be developed in C++ by deriving them from existing modules. Thus, new scheduling disciplines, other link characteristics or special routing facilities can be implemented very quickly.

#### V. TARGETED RESEARCH AREA

One special area of current research on distributed algorithms are algorithms working in the  $\Theta$ -Model [6, 7, 8]. This model is not based on assumptions on concrete values of the maximum and minimum end-to-end delay but only on a bound on their ratio. This could increase the assumption coverage of distributed designs, e.g. in situations of overload. The simulation environment is being used to study this model in more detail in order to get a better understanding of timing in distributed systems.

It is expected that overloads of distributed algorithms spread over the network, resulting in a higher coverage of the  $\Theta$ -Model compared to other partially synchronous systems. How overloads spread is relevant for the efficiency of algorithms and therefore one central issue in our research. Since this is closely coupled to the scheduling disciplines in use, it should be researched which disciplines cooperate best with the  $\Theta$ -Model so that several algorithms can run concurrently without violating the assumptions.

First experimental evaluations using Linux workstations where already conducted in [3] and [4]. The results from these experiments showed that some correlation between the minimum and maximum end-to-end delay exists at least in some settings and hence pushed the confidence in the practical applicability of the  $\Theta$ -Model for real-world systems. The simulation environment should increase the flexibility of the system specification and therefore be able to search for possible advantageous hardware/software structures (especially scheduling and queuing disciplines) more easily.

In the simulation environment our first study considered a distributed system of five nodes, each running five instances of a clock-synchronization algorithm. All delays were assumed to be deterministic and non-

changing. This setting also revealed some correlation between the minimum and maximum end-to-end delay due to scheduling effects. It also showed the importance of the booting times of the algorithms to the system especially if we consider scheduling delays to be greater than zero.

In parallel with the simulation, further evaluations are planned using embedded hardware boards. These will run a real-time operating system for executing the algorithms.

#### VI. CONCLUSION

Since the task and simulation model are open and flexible, they can be used for simulating algorithms with various timing assumptions. This can range from strictly synchronous lock-step behavior to the fully asynchronous case. This makes it a very powerful tool also suitable for the research of the  $\Theta$ -Model.

#### REFERENCES

- [1] OMNet++. <http://www.omnetpp.org>, last tested in February 2006.
- [2] Tarek F. Abdelzaher and Kang G. Shin. Combined task and message scheduling in distributed real-time systems. *IEEE Trans. Parallel Distrib. Syst.*, 10(11):1179–1191, 1999.
- [3] Daniel Albeseder. Experimentelle Verifikation von Synchronitätsannahmen für Computernetzwerke. Diplomarbeit, May 2004. (in German).
- [4] Daniel Albeseder. Evaluation of message delay correlation in distributed systems. In *Proceedings of the Third Workshop on Intelligent Solutions for Embedded Systems*, Hamburg, Germany, May 2005.
- [5] Riccardo Bettati and Jane W.-S. Liu. End-to-end scheduling to meet deadlines in distributed systems. In *International Conference on Distributed Computing Systems*, pages 452–459, 1992.
- [6] Jean-François Hermant and Josef Widder. Implementing reliable distributed real-time systems with the  $\Theta$ -model. In *Proceedings of the 9th International Conference on Principles of Distributed Systems (OPODIS 2005)*, LNCS, Pisa, Italy, December 2005. Springer Verlag. (to appear).
- [7] Gérard Le Lann and Ulrich Schmid. How to implement a timer-free perfect failure detector in partially synchronous systems. Technical Report 183/1-127, January 2003.
- [8] Gérard Le Lann and Ulrich Schmid. How to maximize computing systems coverage. Technical Report 183/1-128, April 2003.

# Analysis of the Influence of Background Traffic on FTP Traffic in WAN Network

Anna Shklyeva and Vit Novotny (Faculty mentor)  
Faculty of Electrical Engineering and Communication,  
Brno University of Technology,  
Purkynova 118, 612 00 Brno, Czech Republic

Email: xshkly00@stud.feec.vutbr.cz, novotnyv@feec.vutbr.cz

**Abstract** — In this paper an analysis of the influence of background traffic on the FTP traffic by means of the OPNET software is carried out. Characteristics of network components are described and the network operation is modeled. Parameters of network utilization and FTP server download response time are collected and analyzed.

## I. INTRODUCTION

Many subscribers use phone lines for data transmission, including the FTP traffic transmission. We have analyzed the influence of background traffic on the FTP traffic in a WAN network. The term background traffic represents the data transfer excepting the FTP traffic. The OPNET program has been used for this purpose. This program provides a comprehensive development environment supporting the modeling of communication networks and distributed systems. The OPNET environment incorporates tools for all phases of simulation, data collection, and data analysis. [1]

## II. CONFIGURATION OF NETWORK

A network which connects the central office of a company with its affiliates has been simulated in the OPNET environment. Connection lines with a capacity of 64 kbps have been used (Figure 1).

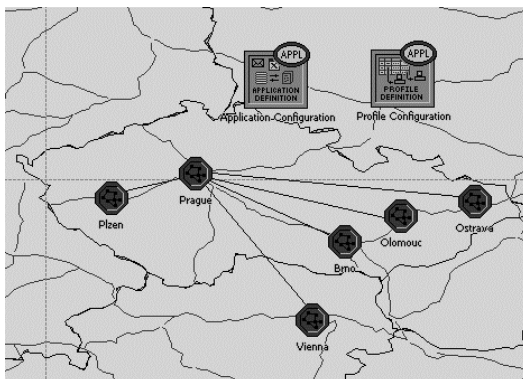


Figure 1: Organization of the network

The affiliates of the company are located in the cities of Plzen, Brno, Vienna, Olomouc, Ostrava. The central office is located in Prague, where the FTP server of the network is situated (Figure 2).

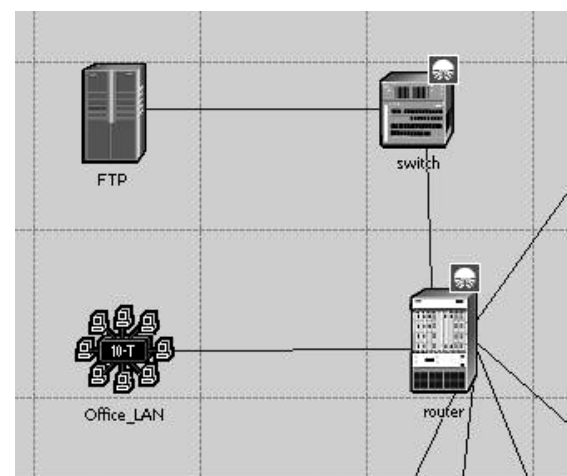


Figure 2: The local network in Prague

The FTP-server model represents a server node with server applications running over TCP/IP and UDP/IP. This node supports one underlying Ethernet connection at 10 Mbps, 100 Mbps, or 1 Gbps. In this network the connection at 10 Mbps and Ethernet protocol have been used.

A local area network according to the standard 10base-T has been constructed at each office. The switching speed has been established at 500000 pkts/sec and the number of workstations in the given local network is 10.

First the simulated network was analyzed only with the FTP traffic. Then the background traffic was added into the given network.

In Figure 3 we can see that the background load on this link will be 55 000 bps for the first 800 seconds of the simulation. For the next 500 seconds, the background load on the link will be 0 bps, and for the last part of the simulation, the load will be 25 600 bps (which is 40 percent of the total capacity of the link).

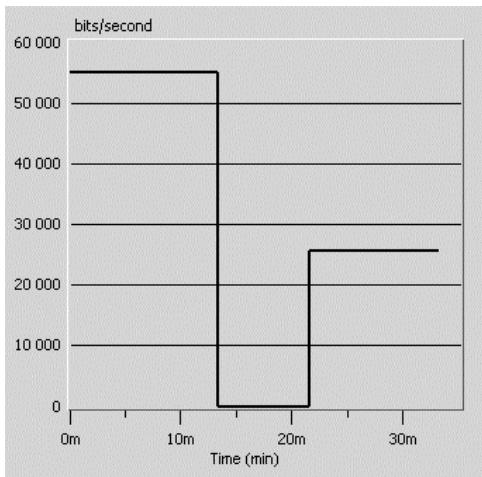


Figure 3: Background traffic intensity

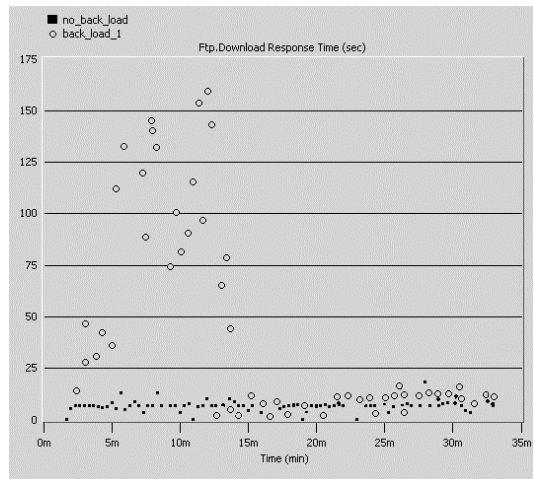


Figure 5: Download response time for FTP

### III. COLLECTION AND ANALYSIS OF DATA

After modeling the throughput with and without background traffic, the utilization statistics for the links and for the global FTP download time in the network have been calculated.

An example of the utilization statistics for the link between the central office and the affiliates is shown in Figure 4. A download response time in the given network with and without the influence of the background traffic is depicted in Figure 5.

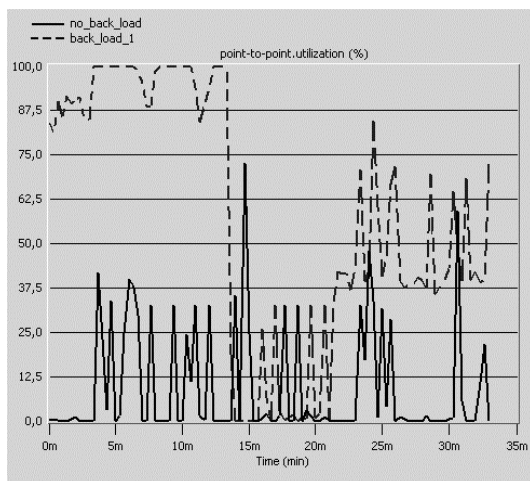


Figure 4: Utilization of Brno – Prague link

### IV. CONCLUSION

The sufficient download response time from FTP server should not exceed 20 sec in common networks. As can be seen in the graphs, the download response time reaches about 150 sec at a background traffic of 55 kbps and the utilization of the network is 100 %. Such parameters are unsuitable for subscribers. When the background traffic does not exceed 40 % of the throughput of a 64 kbps channel, the download response time does not exceed 20 sec. Therefore, to provide an effective functionality of the network, it is necessary that the background traffic does not exceed 40 % of the network throughput.

### ACKNOWLEDGMENTS

This work was supported by the Czech Republic Grant Agency project No. 102/06/1569 and the Ministry of Education project No. 3300/2006/F1a.

### REFERENCES

- [1] OPNET Modeler – environment for network modeling and simulation. Instruction manual.
- [2] Cisco Systems: Multimedia Traffic Engineering for HFC Networks. A White Paper on Data, Voice, and Video over IP. Cisco Systems, San Jose, 1999.
- [3] Internet site of the OPNET Technologies, Inc.: <http://www.opnet.com/>.

# Area-Efficient Dual-Port Memory Architecture for Multi-Core Processors

Hassan Bajwa and Xinghao Chen (Faculty Advisor)  
City College and Graduate Center of the City University of New York  
Convent Ave. and 140th St., New York, NY, USA

Email: [bajw@ees1s0.engr.ccny.cuny.edu](mailto:bajw@ees1s0.engr.ccny.cuny.edu); [xchen@ccny.cuny.edu](mailto:xchen@ccny.cuny.edu)

**Abstract** With multi-core processor technologies moving into the mainstream applications, making cache memory highly accessible by multiple processors becomes a necessity, with many technical challenges. Multi-port cache memory would provide the needed accessibility to multiple CPUs. Historically, multi-port memory designs have been implemented with dedicated word and bit lines for each port. Since the silicon areas used by word and bit lines dominate the entire memory area, duplicating the word and bit lines results in multiplying the silicon area of a single-port memory. In this paper, we propose a dynamic memory partitioning technology with the use of isolation nodes, to facilitate dual-port accesses without duplicating the word and bit lines for the second port, thus maximizing the utilization of silicon space.

## I. INTRODUCTION

Advances in integrated circuit technology have led to much faster and high-performance microprocessors. However, latency in memory access time has emerged as a serious limitation in overall system performance [1]. Design shops and manufacturers responded with fast memory systems by using efficient readout and layout algorithms [2, 3], hierarchical cache memory [4], high-speed memory clock [5], and multiple ports to access memory partitions in parallel [3, 5].

Figure 1 shows the schematic of a conventional dual-port SRAM cell. Adding additional word and bit lines and access transistors  $T7$  and  $T8$  to the single-port SRAM cell allows simultaneous access and dual-port capabilities. It also doubles the silicon area. This hardwired dual-port memory architecture (as well as multi-port memory configured similarly) has been extensively used in multi-core processors in recent years. While most of the research efforts to improve memory speed focused on the structure of elementary cells and multi-level cache and memory hierarch, little attention has been given to the efficient utilization of silicon area of memory systems. In dual-core or systems-on-chip (SOC) applications, memory often takes more than 50% of the chip area.

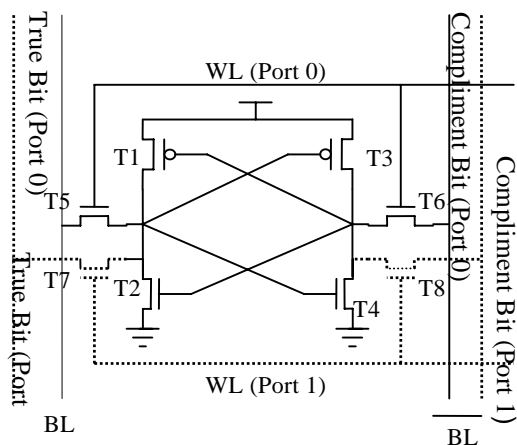


Figure 1. Single & Dual-Port SRAM Cell

We developed a new dual-port memory architecture (which can be extended to multi-port), which employs a technique that dynamically partitions a memory into two virtually independent sections. The technique allows dual-port accesses without duplicating the word and bit lines for the second port, hence, maximizing silicon area utilization.

Traditionally, driving long bit lines in large memories increases latency and power dissipation. The proposed dynamic memory partition technique would reduce the length of bit lines, resulting in reduced bit line latency and power dissipation.

## II. DYNAMICALLY PARTITIONED MEMORY

Our investigation shows that a hardwired dual-port memory can be implemented without duplicating the word and bit lines for the second port by using dynamic partitioning. Figure 2 shows the structural configuration (in the case of SRAM). It places an isolation control line (ICL) between two neighbouring word lines. The isolation nodes controlled by the isolation control lines are interconnect switches, which are placed on the bit lines between the access transistors on neighbouring word lines. When one isolation line turns OFF its isolation nodes (switches), the

memory is literally separated into two virtually-disjoint sections, with the upper port accessing the upper section and lower port accessing the lower section. When all isolation nodes are ON, both the upper and lower ports share the bit lines from each end to access the same memory cells.

With this new dual-port configuration, identification and setting of the isolation control line for dynamic partitioning (DP) must be carried out before accessing selected memory cells by dual-port memory operations. The DP overhead is of minimal, because it takes place in association with setting the memory-access addresses and bit line pre-charge. Overall, the impact of DP delay is minimal and insignificant, if not zero. The use of isolation nodes would appear to increase the silicon area. In reality, this increase is insignificant, since silicon area used by memory is dominated by word and bit lines. Figure 3 shows a block diagram of the new dual-port memory architecture with dynamic partitioning.

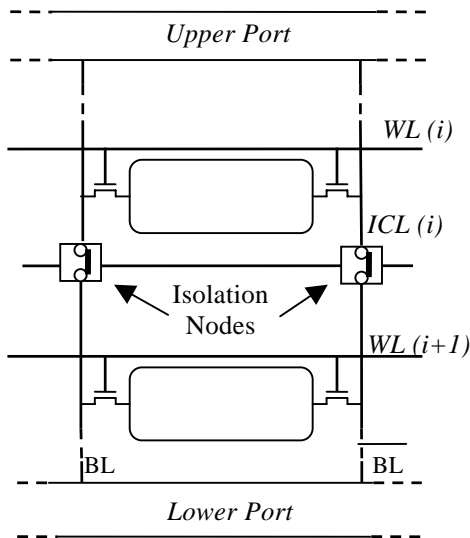


Figure 2. Placement of Isolation Nodes and Control Lines

### III. CONCLUSION

We proposed an area-efficient hardwired dual-port memory architecture by employing a dynamic partitioning technique which uses isolation nodes and control lines. Compared with the classic hardwired dual-port memory architecture, our preliminary analysis has shown that the new area-efficient hardwired dual-port memory architecture provides a compact design with no significant

impact to the timing of memory access largely due to the elimination of word and bit lines for the second port.

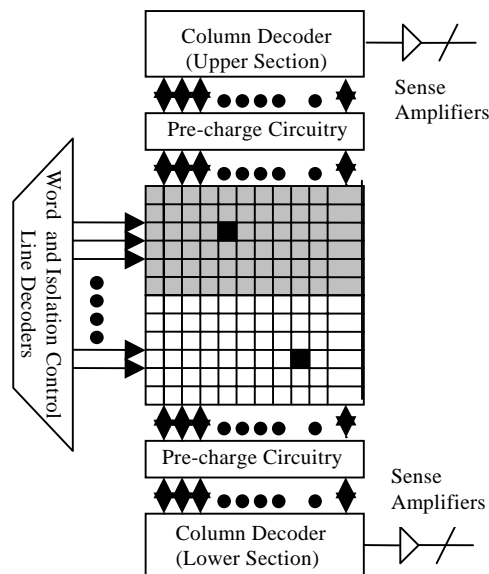


Figure 3 Block Diagram of Dual-Port Memory with Dynamic Partitioning

### REFERENCES

- [1] A. Cristal, O.J. Santana, F. Cazorla, M. Galluzzi, T. Ramirez, M. Pericas, and M. Valero, "Kilo-instruction Processors: Overcoming the Memory Wall." IEEE Micro, Vol. 25, No. 3, pp. 48-57, May-June 2005.
- [2] Y. Choi and T. Kim, "Memory Layout Techniques for Variables Utilizing Efficient DRAM Access Modes in Embedded System Design." In the Proceedings of Design Automation Conference, pp. 881-886, June 2003.
- [3] R.D. Adams, "High Performance Memory Testing: Design Principles, Fault Modeling and Self-Test." Kluwer Academic Publishers, Boston, 2003.
- [4] N. Shibata, M. Watanabe, and Y. Tanabe, "A Current Sensed High Speed and Low Power First-In First-Out Memory Using a Word/Bit Line Swapped Dual-Port SRAM Cell." IEEE Journal of Solid-State Circuits, Vol. 37, No. 6, pp. 735-750, June 2002.
- [5] W. Fang, J. Lijiu, "Design of High Speed 2-Write/6-Read Eight-Port Register File ASIC." In the Proceedings of the 5th International Conference on ASIC, Vol. 1, pp. 498-501, October 2003.

# Multilayer Adhesive Bonding Under Hot Air Stream

Daniela Andrijasevic, Werner Brenner and Johann Nikolics (Faculty Mentor)  
Institute of Sensor- and Actuator Systems  
Vienna University of Technology  
Vienna, Austria  
Email: Daniela.Andrijasevic@TUWien.ac.at

**Abstract** — *Micro Electro Mechanical Systems (MEMS) are complex 3-D systems consisted of several micro components, made of different materials in different processes with different individual functions integrated into one optimised structure. In last few years packaging and bonding of MEMS have become important issues, due to the fact that they generate 70 % of total costs in the production cycle [1]. Moreover, the commonly used bonding techniques, e.g. anodic bonding or fusion bonding are difficult due to additional process requirements, like high voltage, high process temperature, process time, etc. Multi layer adhesive bonding reported here seems to be alternative and promising solution allowing obtaining high bond strength at low process temperature and accurate positioning while using a standard micro manipulator.*

## I. INTRODUCTION

Using adhesives in micro-system techniques was not very popular due to its chemical instability and remarkable changes of mechanical properties during the life cycle. Nevertheless, with improvement of adhesives properties in general sense, they are becoming more important in the field of microbonding. Some of the most favoured adhesives characteristics are:

- improved stress distribution over the entire bonding area,
- fatigue resistance of adhesively bonds to cyclic loading,
- high resistance to mechanical shock and vibration,
- ability to bond dissimilar as well as similar materials including metals, plastics, glass, ceramics,
- significant weight and significant cost savings without decrease of relevant bonding strength parameters [2].

A new concept for adhesive bonding of components with dimensions less than 300  $\mu\text{m}$  in complex 3D structures is presented in this paper. The adhesive is deposited on the substrate and then the micro-component is carried and placed at the requested position. Afterwards, the stream of hot air is applied in order to soften the glue and to emboss the mi-

cro-part. After cooling down at room temperature, the glue hardens and final bond is achieved.

## II. EXPERIMENTAL WORK

In order to prove the working principle of proposed technique including its advantages and to perform different experiments, a special setup was developed, and more details about it can be found in [3].

## III. BONDING PROCESS

The biggest advantages of using glues with low softening point in micro assembly and packaging are fast and short bonding procedure.

Up to date, two different types of adhesives – Polyurethane foil and hot melt glue on the Polyethylene base were investigated. Excellent moisture resistance, no requirements for surface pre-treatment, low outgassing, resistance to harsh environment (corrosive environment) are some of the most important benefits of used glues. Their main properties are shown in Table 1.

Type of adhesive	State	Softening point ( $^{\circ}\text{C}$ )	Thickness ( $\mu\text{m}$ )	Deposition method
Hot melt glue	solid	65	~ 12	spinning
Adhesive film	solid	72	50	lamination

Table 1: Adhesive properties

The adhesive foil has been laminated to basic substrate using rubber rolls. The hot melt glue was dissolved in PGMA ((1-Methoxy-2-Propyl)-Acetat) in mass-proportion of 55% of PGMA and 45% of glue, and applied by spinning (800 rpm, 40 s) on the basic substrate. Subsequently, the substrate was baked at 70  $^{\circ}\text{C}$  for 5 minutes in order to evaporate the solvent from the applied film, leaving the pure glue on the substrate. The average thickness of the adhesive layer after spinning was 12  $\mu\text{m}$ .

#### IV. MECHANICAL STRENGTH OF BONDS

Mechanical strength of bonds made with examined adhesives was measured by pull test. The measurements were performed as following. The glass stamps (1 cm × 1 cm) were glued on the substrate with investigated adhesives and afterwards they were connected with Force Gage. By increasing the curing temperature, the strength of bond made with adhesive foil increased significantly, while the strength of join made with hot melt glue dropped rapidly because of adhesive evaporation (the layer of adhesive was not thick enough to realize rigid join). In both cases, obtained mechanical strength was comparable with strengths achieved by other conventional techniques.

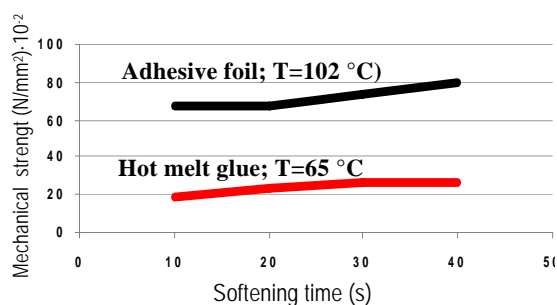


Figure 1: Maximal mechanical strength of bonds obtained with hot melt glue and PU foil versus exposure time.

#### V. STRUCTURE REALISATION

In the first phase of experiments, the investigated technique was used for bonding single mode optical fibers (core diameter 9 μm; cladding diameter 125 μm) to the basic substrate and for bonding glass to glass. Those both enabled effective assessment of the bonding-technique quality.

For positioning and joining optical fibre in V-groove, few different approaches were employed: The hot melt glue which hardens after baking was softened at low temperature of around 65 °C and the fiber was embossed onto it. Bonding with foil can be performed in two ways. First, the foil is laminated to the substrate, softened at the 90 °C and the fiber is embossed in the soft material. Second, the fiber is positioned onto the V-grooves and covered with foil. After the foil softens, the fiber adheres to the substrate. The quality of final, cured bonds was analyzed by optical inspection.

A bond realized by a foil applied onto the fiber is shown in Figure 2. The substrate-nozzle distance was 3 mm and temperature at the nozzle outlet was 120 °C. The preform softened continuously, adhered on the substrate and fixed fiber in the requested position.

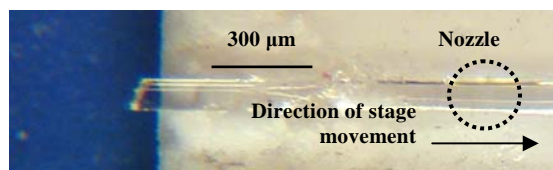


Figure 2: Top view of optical fibers (125-μm diameter) joined in V-groove with adhesive foil.

In the second test, glass stamps with dimensions 1 cm × 1 cm are bonded to the glass substrate using the hot melt glue. The bond is made only over the stamp edge. The adhesive in the middle is not heat affected, and there are no any changes in the material or structure. This opens new possibility for forming cavities or membranes using adhesives adequately. The appearance of bubbles was minimized by exposing the adhesive to the hot air stream for a longer period.

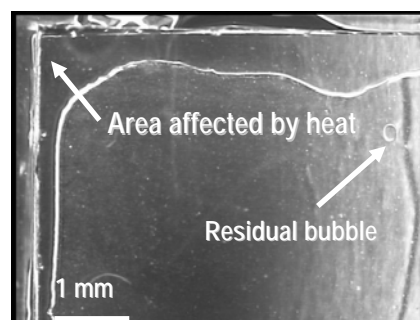


Figure 3: Top view glass stamp bonded to the glass substrate.

#### ACKNOWLEDGMENTS

This work was financially supported by FP6 Marie Curie Research Training Network “Advanced Methods and Tools for Handling and Assembly in Microtechnology - ASSEMIC”, funded by the European Commission, Contract no. MRTN-CT-2003-504826.

#### REFERENCES

- [1] Grace H.R., „Barriers to Commercialisation: A report card”, in MEMS Manufacturing, November 2005
- [2] W. Brenner. “Epoxyes Pace Growth of High-Performance Bonding Technology“, <http://www.masterbond.com>
- [3] D. Andrijasevic, I. Giouroudi, W. Smetana, S. Boehm, W. Brenner. “Hot Gas Stream Application in Micro-bonding Technique“, Photonics West 2006, MOEMS-MEMS, San Jose, USA, 2006.

# Quantum-Mechanical designed Terahertz Laser

A. Benz, G. Fasching, K. Unterrainer (Faculty Mentor)  
Institut für Photonik und Zentrum für Mikro- und Nanostrukturen  
Technische Universität Wien  
Vienna, Austria

R. Zobl, A.M. Andrews, T. Roch, W. Schrenk, G. Strasser  
Institut für Festkörperelektronik und Zentrum für Mikro- und Nanostrukturen  
Technische Universität Wien  
Vienna, Austria

Email: alexander.benz@tuwien.ac.at

**Abstract** — We present the development of a THz quantum cascade laser showing multimode emission from 2.8 THz up to 3.3 THz. The threshold current density is  $500 \text{ A/cm}^2$  at 5 K, it lases up to a heat-sink temperature of 145 K in pulsed mode operation. Due to a refined bandstructure design and a double-metal waveguide with a confinement near 100 %, the structure is also capable of continuous wave mode operation. The depopulation of the lower laser state is based on LO-phonon emission with a scattering time of 1 ps, thereby a stable population inversion is guaranteed.

## I. INTRODUCTION

The Terahertz-frequency region ( $1 \text{ THz} = 10^{12} \text{ Hz}$ ) lies between the microwaves and the infrared spectral region. Due to the large demand of coherent sources in this spectral range for applications like medical imaging, chemical sensing and security applications large effort is put into the development of the THz-technology to close the THz-gap.

The RF-electronics is able to generate frequencies up to around 0.1 THz, limited by the RC-time-constant of the system. The photonics on the other hand generates frequencies down to around 100 THz, defined by the bandgap of the used semiconducting material. Changing the wavelength requires the selection of a new material or of a new material composition. A new concept for coherent light sources is the quantum cascade laser (QCL), which was developed for the mid-infrared spectral region. The major advantage of the QCL-structure is the possibility to design the emission wavelength nearly independent of the used semiconductor by band structure engineering. The wavelength is defined by the energy difference of quantized states in the conduction band. That means QCLs are unipolar devices. Therefore the surface recombination, which severely reduces the performance of classical semiconductor lasers, can be neglected. The first working QCL in the THz frequency region was reported in 2002 [1].

## II. MEASUREMENT RESULTS

Here, we present a QCL working in the THz spectral region at 3 THz, corresponding to an energy difference of the involved states of 12 meV. The design is based on intersubband transitions in an gallium-arsenide / aluminium-gallium-arsenide heterostructure. Starting from a design published by B.S. Williams [2], we have optimized the wavefunctions further to achieve the largest possible dipole matrix element for the desired transitions. The lower laser state is depopulated via LO-phonon emission. The large energy separation of 36 meV between the lower laser state and the ground state enables a high maximum working temperature as thermal back-filling is prevented. The scattering time of the lower laser state is around 1 ps, thereby a stable population inversion is established.

The used microcavities are Fabry-Perot resonators. Also other microcavities like microrings or microdiscs have already been successfully used for THz lasers [3]. The resonators have been etched by reactive ion etching (RIE), thus ensuring smooth facets and sidewalls. The facets act as mirrors with a reflectivity of 90 % due to the impedance mismatch between the double-metal waveguide and the surrounding air. The thickness of the optically active region is  $15 \mu\text{m}$ , the emission wavelength inside the material is around  $27 \mu\text{m}$  therefore the mode is heavily quenched. The double-metal waveguide has been chosen as it has a confinement of the optical mode within the active region of nearly 100 % and low waveguide losses.

The presented QCL has a threshold current density of  $500 \text{ A/cm}^2$  (Figure 1). Lasing ceases at a current density of  $1 \text{ kA/cm}^2$  as for this high current the structure is misaligned and the electron transport through the structure is not efficient any more. The maximum working temperature is 145 K in pulsed mode operation. At this temperature the thermal energy is equal to the energy of

the optical transition. The structure is also capable of lasing in continuous-wave mode operation up to heat-sink temperature of 25 K. The spectrum shows multi-mode emission from 2.8 THz up to 3.3 THz (Figure 2).

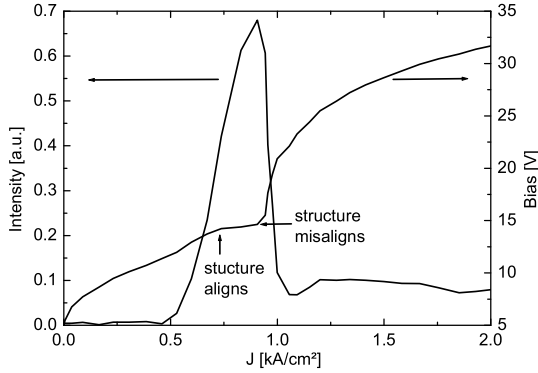


Figure 1: Emission versus Current of a double-metal ridge ( $200 \times 120 \mu\text{m}$ ). The threshold current density is  $0.5 \text{ kA/cm}^2$ , lasing ceases at  $1 \text{ kA/cm}^2$ .

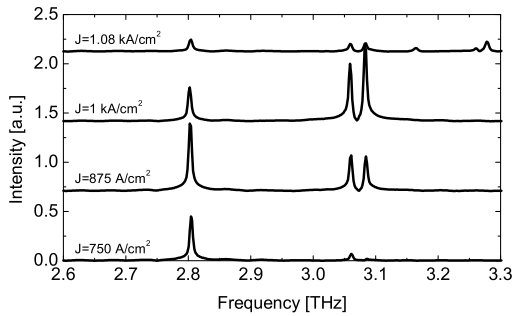


Figure 2: Spectrum of a double-metal ridge ( $200 \times 120 \mu\text{m}$ ) at different currents. Fabry-Perot modes are observable from 2.8 THz up to 3.3 THz.

### III. CONCLUSION

We presented a THz QCL emitting around 3 THz with a threshold current density of  $500 \text{ A/cm}^2$  and a maximum working temperature of 145 K. A double-metal waveguide with a confinement near unity was used. The Fabry-Perot resonators were RIE-etched to ensure

smooth sidewalls and facets. Thereby the waveguide losses were strongly reduced. The improvements in the bandstructure and the waveguide led to a device capable of continuous-wave mode operation.

### ACKNOWLEDGMENTS

This work was partly supported by the Austrian Scientific Fund FWF (SFB-ADLIS) and the EC (TERANOVA, POISE).

### REFERENCES

- [1] R. Köhler, A. Tredicucci, F. Beltram, H.E. Beere, E.H. Linfield, A. Giles Davies, D.A. Ritchie, R.C. Iotti, and F. Rossi. *Nature*, 417:156, 2002.
- [2] B.S. Williams, H. Callebaut, S. Kumar, Q. Hu, and J.L. Reno. *Appl. Phys. Lett.*, 82:1015, 2003.
- [3] G. Fasching, A. Benz, K. Unterrainer, R. Zobl, M. Andrews, T. Roch, W. Schrenk, and G. Strasser. *Appl. Phys. Lett.*, 87:211112, 2005.
- [4] V. Tamosiunas, R. Zobl, J. Ulrich, K. Unterrainer, R. Colombelli, C. Gmachl, K. West, L. Pfeiffer, and F. Capasso. *Appl. Phys. Lett.*, 83:3873, 2003.

# High-level Modeling, Analysis and Verification on Programmable Hardware Design

Aleš Smrčka

Department of Intelligent Systems  
Faculty of Information Technology,  
Brno University of Technology,  
Brno, Czech republic  
Email: smrcka@fit.vutbr.cz

## I. ABSTRACT.

Implementation of network components in hardware is a trend in advanced high-speed network technologies. Incoming packets can be analysed in fast programmable cards using FPGA. Designing such a system is not easy and requires a detailed analysis. Author's research is concentrated on analysis and verification of a non-trivial hardware system—e.g., the network monitor and analyser Scampi [4] that has been developed within the Librouter project. The Scampi analyser is implemented in FPGA on a special add-on card. It analyses packets incoming with the speed of several Gbps. This work presents an abstract model of the design and verification of several safety properties. The main task was to check if there is a risk of buffer overflow and how to set the length of buffers to prevent this. First, there has been made a timed analysis by hand and then these automated tools have been used—model-checkers Uppaal [5] and TReX [1]. This work shows how to model such a complex system and particular results of analysis and verification. It also proposes a framework for modeling and analysis of systems where the throughput of requests, their speed, and the length of buffers are important. The proposed models can be reused when verifying and analysing of systems of the given kind.

In Scampi and related projects [4], we apply formal verification on two different levels: (1) on the level of the source code, i.e. VHDL code, and (2) on the level of suitable abstract models. Its advantage is the precise coverage of the real system. The disadvantage is that the system is too complex to be checked in this way completely—we are only able to verify some selected components. To check the key features of the entire system, we work with abstract models. The source code verification of Scampi is also described [2].

## II. RESEARCH RESULTS.

There will be presented author's experience from high-level modeling, analysis, and verification of Scampi. Here, a special focus is put on checking the throughput of the system – the optimal length of buffers, timing, and

reliability—response time, an appropriate behavior under extreme conditions such as a DoS attack.

The work on Scampi project deals with the methodology how to analyse, model and verify large or complex hardware system—w.r.t. timing such as delays or throughput. Current results include patterns of high-level abstract models such as buffers, patterns of executive simple components, and the methodology how to create the model of a complex component. More detailed results of some patterns is presented in [3].

At the present, author's research is oriented on creation of abstract models from VHDL source code. Special focus is given to parameters of hardware architecture, e.g., in a buffer, the parameter could be the number of items. The goal is to use automatically created models to verify the system for all values of considered parameter.

## REFERENCES

- [1] A. Bouajjani, A. Collomb-Annichini, and M. Sighireanu. TReX: A tool for Reachability Analysis of Complex Systems. In *Proc. of CAV'01, LNCS 2102*, 2001. Springer-Verlag.
- [2] Jan Holeček, Tomáš Kratochvíla, Vojtěch Rehák, David Šafránek, and Pavel Simeček. How to Formalize FPGA Hardware Design. Technical Report 4/2004, CESNET, October 2004.
- [3] Petr Matoušek, Aleš Smrčka, and Tomáš Vojnar. High-Level Modeling, Analysis, and Verification of Scampi2. Technical Report 8/2005, CESNET, November 2005.
- [4] Jiří Novotný, Otto Fučík, and David Antoš. Project of IPv6 Router with FPGA Hardware Accelerator. In *Proc. of Field-Programmable Logic and Applications, 13th International Conference FPL 2003*, 2003. Springer-Verlag.
- [5] P. Pettersson and K.G. Larsen. UPPAAL2k. *Bulletin of the European Association for Theoretical Computer Science*, 70:40–44, February 2000.



# Signal Detection with Needle and Segmental Ionization Detector

Cernoch Pavel and Jirak Josef

Department of Electrotechnology, Faculty of Electrical Engineering and Communication  
Brno University of Technology

602 00 Brno, Czech Republic

Email: xcerno07@stud.feec.vutbr.cz, jirak@feec.vutbr.cz

**Abstract** — *This article deals with signal detection by a needle ionization detector and by a halved segmental ionization detector in the environmental scanning electron microscope. The signal detection dependency on the shape and size of an ionization detector electrode and its position towards a specimen is studied. Electron trajectories in an electrostatic field in a vacuum simulated via program Simion 3D 7.0 are considered during the experiment.*

## I. INTRODUCTION

The gaseous ionization detector [1] is often utilized for signal detection at a higher pressure in the specimen chamber of the environmental scanning electron microscope. In the experiment, it was examined the influence of the detector electrodes shape, size and position towards the specimen on the signal detection. These parameters lead to different types of the contrasts in a specimen image, the material, topographic, shadow and diffusion contrasts. For the explanation of observed contrasts acquired by the ionization detectors, the electron trajectories in the detectors electrostatic fields were simulated via program Simion 3D 7.0 during the experiment.

## II. EXPERIMENT

Two types of the ionization detector differing in the shape, size and position of the electrode were examined. In the first case, the ionization detector consisting of two electrodes of sharpened needles positioned at the left and right side above the specimen was used. As shown in Figure 1a, the needle ionization detector with the tips diameter of 3  $\mu\text{m}$  was made by modification of a segmental ionization detector, described below. The needle electrodes were orientated towards the specimen, as illustrated in Figure 2. The signal was detected by the left or right needle electrode at a voltage of 450 V, as shown in Figure 4a, Figure 4b and Figure 5a. As the second type, the halved segmental ionization detector consisting of four concentric plate electrodes divided into

left and right halves was used, as seen in Figure 1b. The signal was detected by the left and right smallest electrodes ( $A_L + A_R$ ) at a voltage of 450 V while all other electrodes were grounded, as shown in Figure 3 and Figure 5b.

## III. SIMULATION

Since the program Simion 3D 7.0 simulates the ions trajectories in the vacuum, it cannot give a true picture of the process of the signal electrons amplification by the impact ionization in gas environment in the space between the specimen and the detector electrodes. However, the program is able to explore the influence of the detector electrostatic fields on the signal electrons. The electron trajectories were simulated for electron energies from 5 eV (most probable energy of secondary electrons) to 15 keV (most probable energy of back-scattered electrons when the primary electron energy is 20 keV). The simulations of the secondary electron trajectories with energy of 5 eV emitted from the specimen are illustrated in Figure 6 for needle ionization detector.

## IV. RESULTS AND CONCLUSION

Fig. 4a and Fig. 4b show no change of the angle of view at the specimen, a change of shadow and diffusion contrasts, respectively, at the signal detection by the left or right needle electrode of the needle ionization detector, although it was expected before this experiment. The explanation of this behavior is visible from the electron trajectories simulations in Figure 6. At the detection by one of the needle electrodes, all low-energy electrons are attracted to this electrode. According to the simulations, the change of shadow and diffusion contrasts should be observed when both of detector electrodes are attached to the same voltage and the signal is detected only by one of these electrodes. This connection is designed for a future experiment. As obvious from the simulations, high-energy back-scattered electrons are influenced by the ionization detectors electrostatic fields insignificantly. The comparison be-

tween the signal detection by the needle and the halved segmental ionization detector is shown in Figure 5a and Figure 5b. Obviously, both ionization detectors provide the same topographic and material contrasts, the same ratio of secondary and back-scattered electrons, respectively. However, a significantly smaller detection electrode area at detection by the needle ionization detector requires a significantly higher probe current, which results in lower topographic contrast.

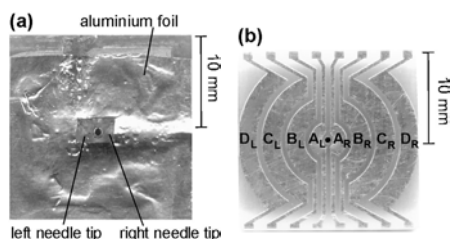


Figure 1a, b: (a) Needle ionization detector, aluminium foil grounded; (b) halved segmental ionization detector

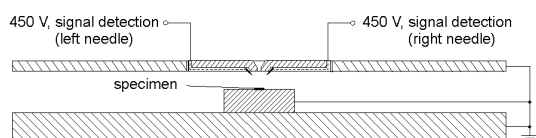


Figure 2: Signal detection with needle ionization detector by left or right needle electrode at voltage of 450 V; distance between electrodes and specimen 2 mm; specimen grounded

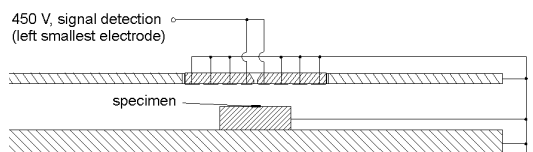


Figure 3: Signal detection with halved segmental ionization detector by electrodes  $A_L+A_R$  at voltage of 450 V; all other electrodes and specimen grounded; distance between electrodes and specimen 3 mm

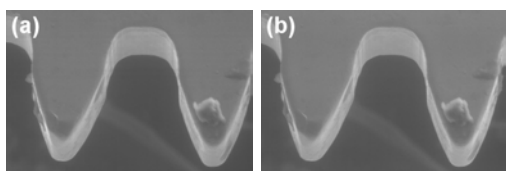


Figure 4a, b: Observation of brass toothed wheel by needle ionization detector by left (a) and right (b) electrode at voltage of 450 V; water vapors environment 700 Pa, mag. 500x

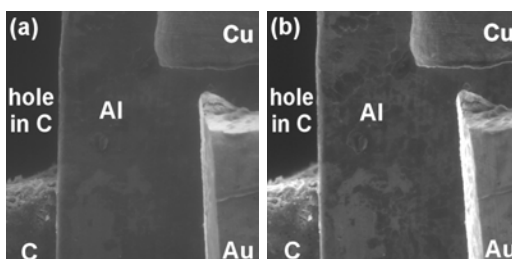


Figure 5a, b: Material and topographic contrasts; specimen consisting of hole in carbon, carbon, aluminium foil, cuprum foil, gold foil; water vapors environment 700 Pa, mag. 700x; (a) needle ionization detector, detection by left electrode at voltage of 450 V; (b) halved segmental ionization detector, detection by electrodes  $A_L+A_R$  at voltage of 450 V; all other electrodes grounded; 10 times higher probe current in case of (a) then in case of (b)

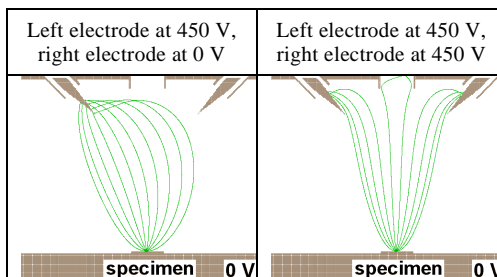


Figure 6: Electron trajectories simulation for needle ionization detector in vacuum; voltage of 450 V on left needle electrode, voltage of 0 V or 450 V on right needle electrode; specimen grounded; projection angle of electrons 0 to 180 degrees for 10 electrons

## ACKNOWLEDGMENTS

This research is supported by project GACR No. 102/05/0886 and project MSM 0021630516.

## REFERENCES

- [1] G. D. Danilatos. Theory of Gaseous Detector Device in the Environmental Scanning Electron Microscope. Academic Press, Sydney, 1990, ISBN 0-12-014678-9.

# Automation of Microassembly Process in SEM Chamber with a Novel Protective Covering Plate

Aleksandra Cvetanovic, Werner Brenner and Helmut Detter (Faculty Mentor)  
Institute of Sensor and Actuator Systems  
Vienna University of Technology  
Vienna, Austria

Email: [Aleksandra.Cvetanovic@TUWien.ac.at](mailto:Aleksandra.Cvetanovic@TUWien.ac.at)  
[Werner.Brenner@TUWien.ac.at](mailto:Werner.Brenner@TUWien.ac.at)

**Abstract** — *This paper presents a novel approach for assembly of micro particles in a SEM chamber. A new set up, called Protective Cover for Micro-components, which allows the positioning of the micro parts on the platform inside the chamber without gluing them on the platform and the quick positioning of microcomponents in a given system is proposed.*

*Besides, for the automated assembly process it is very important that the particles stay on the exactly defined location and position. It makes a necessary basis for modular assembly system.*

*The need for standardisation in micro world becomes more and more essential. The uniformity of parts, operations and tools is a strong support to an automation assembly system.*

## I. INTRODUCTION

The assembly in the SEM chamber has its application in cases where a great resolution, depth of field as well as large working distance is needed, since SEM has more advantages in comparison to the light microscope.

The restrictions concerning manipulation of micro parts, its positioning and orientation in the given system exist, too: an evacuation process decelerates the work and complicates it, samples prepare (drying, sputtering) takes the time and many processes are not allowed: gluing (except special low outgasing adhesive), cell manipulation, magnetically processes or processes with evaporation.

Further difficulties by assembly of the microparts, as in SEM so under the light microscope, point out the absence of the adequate standard tools for manipulation and the phenomena occurring in the range  $\mu\text{m}$  and  $\text{nm}$  in general. [1]

During evacuation of the SEM chamber and, particularly in the beginning of the process, it is possible that the microparts under manipulation are sucked into the pump, due to the produced air stream.

This possibility increases as the size of the microparts decreases. Yet if the aspect ratio of the particle is bigger and the particle lies on its wider side the mentioned possibility decreases. Furthermore, the occurring van der Waal's force is stronger in the case of more polished particles due to adhesion.

This means that manipulations with the gripper are more complicated. Therefore this phenomenon has to be prevented since it is highly undesirable.

## II. SYSTEM OVERVIEW

The system is presented in Figure 1. It consists of a novel protective covering plate, a SEM compatible platform and a holder.



Figure 1: The protective covering plate with platform and holder

It operates in a following way:

First, the particles are placed on the disks that will be covered with the covered plate. The cover plate is screwed in the middle together with a platform. After the vacuum in the SEM chamber is formed, the cover is opened by rotation of the platform below it. Then, the particles which were covered, are exposed to the electron beam, and can be picked up. All assembly tasks on any other disk are then performed accordingly to the procedure described in algorithm of assembly.

The system “cover plate-platform” has predefined tolerances thus preventing rapid pressure changes which could suck off the particles or disturb the stability of the electron beam.

It should be noted that the pressure which could suck the particle is considerably lower when the particle is in the chamber, without the protective cover, particularly in the beginning, which causes more chances for suction of the particles. Towards equations (1) and (2) based on analogy between fluid mechanics and electric circuits, the Figure 2 shows pressure change in the SEM chamber with and without protect.

$$p_{without}(t) = p_{atm}(t=0) e^{-\frac{t}{R_1 C_1}} \quad (1)$$

$$p_{with}(t) = p_{atm} \left( \frac{T_1}{T_1 - T_2} e^{-\frac{t}{T_1}} - \frac{T_2}{T_1 - T_2} e^{-\frac{t}{T_2}} \right) \quad (2)$$

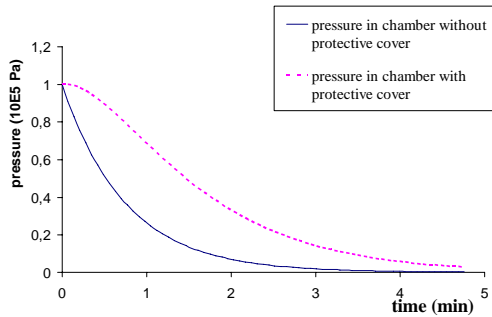


Figure 2: Comparison between case without and the case with protective cover

### III. EXPERIMENTAL RESULTS

Figure 3 shows samples, a ferric powder 40-60  $\mu\text{m}$  and a wire  $\Phi = 15 \mu$  on the disk before and after the two “pump-vent” cycles. There is no difference in the position of the objects.

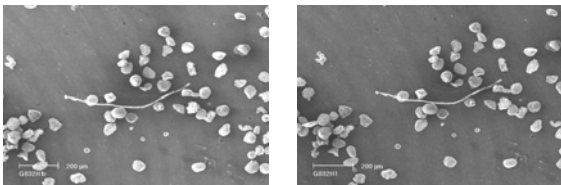


Figure 3: Before and after exposing

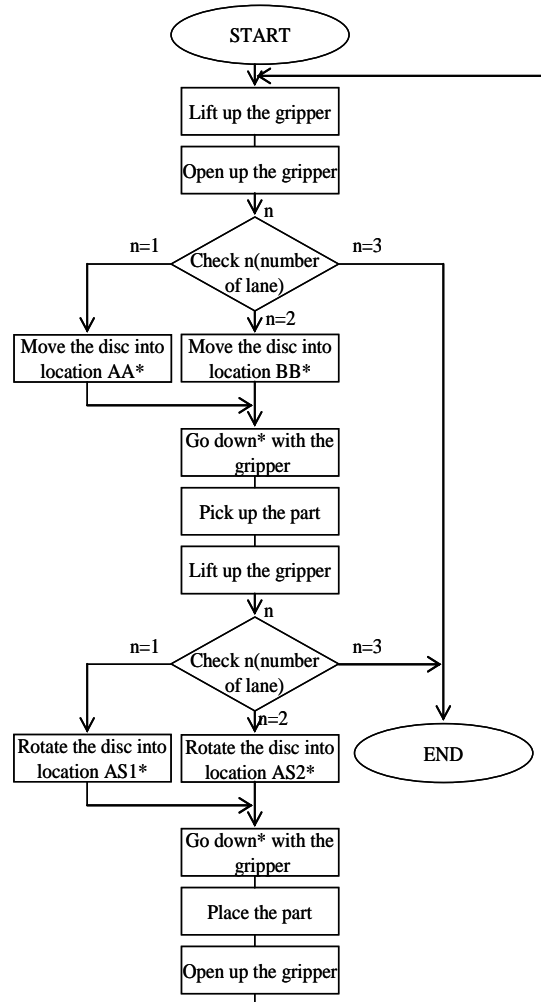
### IV. ALGORITHM OF ASSEMBLY

Three actuators for the automation of process are used:

1. microgripper control, open/ close position
2. microgripper control, up/ down position

### 3. disk control, rotation

The following algorithm describes the working principle for one sequence (one microassembly process) with two parts:



AA\*-preadjusted position of micropart 1 on the disk

BB\*-preadjusted position of micropart 2 on the disk

AS1\*-defined position for assembly micropart 1

AS2\*-defined position for assembly micropart 2

down\*- collision between microgripper and disk have to be prevented.

### REFERENCES

- [1] S. Fatikow, J. Seyfried, St. Fahlbusch, A. Bürkle und F. Schmoeckel, A Flexible Microrobot-Based Microassembly Station, Journal of Intelligent and Robotic Systems: 135-169, 2000

**Symposium 2**

**Material Sciences**



# Rubber ferrite composites containing strontium hexaferrite

Bellušová D., Kyselá G., Ťrögiová E., Hudec I.,  
Institute of Polymer Materials, Department of Plastics and Rubber,  
Slovak University of Technology, Faculty of Chemical and Food Technology,  
Radlinského 9, 812 37 Bratislava, Slovakia

**Abstract** – *The aim of the paper was the study of the influence of composition of rubber ferrite composites filled with carbon black and strontium hexaferrite. Rubber ferrite composites tested in this work have interesting mechanical, chemical and magnetic properties. These properties were studied using five level two factors experimental design method. The study indicates that mechanical properties are affected by the weight ratio of ferrite fillers to carbon blacks. The total content of both fillers has practically no effect on the vulcanization characteristics and most of the mechanical properties (without modulus M300) of prepared rubber ferrite composites, too. The magnetic properties of rubber ferrite composites are depended on weight ratio of magnetic fillers to carbon blacks and total fillers content.*

## I. INTRODUCTION

Ferrites remain one of the best magnetic materials ever discovered and cannot be easily replaced by any other magnetic materials because they are inexpensive, stable and have a wide range of technological applications. Magnetic hard ferrites represents chemical compounds of metal oxides with strong magnetic properties, where are ideal for permanent magnets [1]. It is well known that the incorporation of magnetic polycrystalline ceramic ferrites in various elastomeric matrixes produces flexible magnets or elastomeric magnets, known as rubber ferrite composites [2]. The incorporation of magnetic fillers in the rubber matrix imparts magnetic properties of the rubber matrix considerably. The mechanical properties of rubber ferrite composites depend strongly on properties of rubber matrix, magnetic fillers and interfacial condition between the components.

## II. EXPERIMENTAL

Composite materials were filled with carbon black and strontium hexaferrite. Hard magnetic filler strontium hexaferrite powders SrFe<sub>12</sub>O<sub>19</sub>, type FD 8/24 with coercive force 210 kA/m and average particles size ranges from 1 to 30 microns (µm) were mixed by various loading with elastomeric matrix to form rubber ferrite

composites. The content of strontium hexaferrite was changed from 5.8 to 27.7 wt% and the content of carbon black was changed from 8.6 to 29.1 wt%. The composites were prepared in laboratory mixer FARREL BR 1600 and after homogenization they were cured and molded into 2 mm sheets in thickness at temperature 150 °C.

## III. RESULTS

The influence of the weight ratio of magnetic fillers to carbon blacks ( $x_1$ ) and the total content of fillers ( $x_2$ ) on the vulcanizations, mechanical and magnetic properties of rubber ferrite composites were studied using five level two factors experimental design method (DOE).

$$x_1 = F/C \quad (1)$$

$$x_2 = F+C \quad (2)$$

where: F – magnetic fillers weight  
C – carbon blacks weight

For description of response surfaces of evaluated properties the regression equations “in (3)” were used.

$$Y = b_0 + b_1x_1 + b_2x_2 + b_{12}x_1x_2 + b_{11}x_1^2 + b_{22}x_2^2 \quad (3)$$

where: Y is evaluated parameter,  
 $b_0, b_1, b_2, b_{12}, b_{11}, b_{22}$  are regression coefficients,  
 $x_i$ , are the factors on the coded levels [3].

Conditions for experimental design are shown in “Table 1”, where coded levels are recalculated to real values for both factors.

Factor/ coded level	$x_1 = F/C$	$x_2 = F+C$
- 1.414	0.2	50
- 1	0.610051	54.23231
0	1.6	64.45
1	2.589949	74.66769
1.414	3	78.9
Step	0.989949	10.21769

Table 1: Conditions for experimental design

“Table 2 and 3” show calculated regression coefficients for evaluated properties, where statistically significant coefficients are typed in the bold.

Coefficient	$\Delta M$ [Nm]	$t_{90}$ [min]	Br [ exp-2 T]
b0	<b>2.244</b>	<b>16.499</b>	<b>19.862</b>
bk0	0.269	1.467	3.447
b1	<b>-0.258</b>	0.364	<b>8.567</b>
b2	0.147	-0.879	<b>3.148</b>
bki	0.213	1.159	2.725
b11	0.111	0.063	-2.231
b22	-0.029	0.188	<b>3.398</b>
bkii	0.228	1.244	2.923
b12	0.098	-1.375	<b>4.008</b>
bkij	0.301	1.640	3.853
SE+/-	0.217	1.181	2.776
SLF+/-	0.267	1.021	5.805

Table 2: Regression coefficients of vulcanizations characteristics and remanent magnetization of composites

From “Table 2” is evident, that value  $\Delta M$  decreases with the increasing of the weight ratio of ferrite fillers to carbon blacks and the total content of fillers (ferrite and carbon black) has practically no effect on the studied vulcanization characteristics. Remanent magnetization increases with the increasing of both investigated factors.

Coefficient	M300 [MPa]	Tensile strength at break [MPa]	Elongation at break [%]	Shore [ShA]
b0	<b>5,058</b>	<b>13,552</b>	<b>593,599</b>	<b>39,480</b>
bk0	0,595	2,158	31,724	1,033
b1	<b>-1,552</b>	<b>-2,314</b>	21,008	<b>-2,650</b>
b2	<b>0,554</b>	0,692	-11,597	0,686
bki	0,471	1,706	25,082	0,817
b11	<b>0,940</b>	0,899	-21,873	0,598
b22	<b>-0,125</b>	-0,469	8,361	-0,152
bkii	0,505	1,830	26,901	0,876
b12	<b>-0,670</b>	-0,843	3,400	-0,800
bkij	0,666	2,412	35,468	1,155
SE+/-	0,479	1,738	25,549	0,832
SLF+/-	0,733	0,906	39,274	1,639

Table 3: Regression coefficients of mechanical properties of composites

The total content of fillers has practically no effect on the most of the mechanical properties without M300, which is affected by both investigated

factors. Tensile strength at break and Shore A decrease with the increasing of the weight ratio of ferrite fillers to carbon blacks as seen in “Table 3”. “Figure 1” shows the example of 3D-diagram of tensile strength at break.

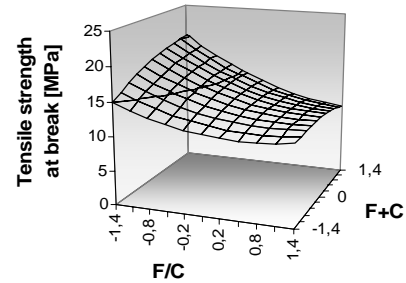


Figure 1: The influences of evaluated factors on the tensile strength at break.

#### IV. CONCLUSION

The influences of hard magnetic fillers on vulcanisation characteristics, mechanical and magnetic properties of filled elastomeric compounds were studied. Results showed that the total content of fillers (ferrite and carbon black) has practically no effect on the studied vulcanization characteristics and most of the mechanical properties (without M300) of prepared elastomeric composites, too. Modulus M300 and remanent magnetization are affected by both investigated parameters. Tensile strength at break, Shore A and  $\Delta M$  are decreasing with the increasing of the weight ratio of ferrite fillers to carbon blacks. Optimal vulcanization time and elongation at break are influenced by no studied parameters.

#### REFERENCES

- [1] M.R. Anantharaman, at all. Dielectric properties of rubber ferrite composites containing mixed ferrites. *Journal of Physics D: Applied Physics*, 32(15): 1801-1810, August 1999.
- [2] J. Slama, at all. Magnetic powder filled polymers. *IEEE Transactions on Magnetics*, 30(2):1101-1103, March 1994.
- [3] Montgomery D.C. *Design and analysis of experiments*, John Wiley & Sons, 3 rd edition, 1991.

# Ofloxacin-releasing biodegradable chitosan microspheres

Silvia Bubeníková,<sup>1\*</sup> Lucia Vodná,<sup>1</sup> Dušan Bakoš,<sup>1</sup> Igor Lacík<sup>2</sup>

<sup>1</sup>Institute of Polymer Materials, Faculty of Chemical and Food Technology,  
Slovak University of Technology,  
Radlinského 9, Bratislava, Slovakia

<sup>2</sup>Polymer Institute, Slovak Academy of Science,  
Dúbravská cesta 9, Bratislava, Slovakia

\*Email: [silvia.hanzelova@stuba.sk](mailto:silvia.hanzelova@stuba.sk)

**Abstract** — *The goal of this study was to investigate the effects of preparation conditions and capsule composition of chitosan microspheres on drug release behaviour. Ofloxacin, the fluoroquinolone antibiotic was used as a model drug. The microspheres were prepared by polyelectrolyte complexation of chitosan with chondroitine sulphate and tripolyphosphate. The amount of released ofloxacin was determined using UV-VIS spectrophotometer.*

## I. INTRODUCTION

The concept of local antibiotic delivery via biodegradable polymer skin defect fillers with multifunctional properties for the treatment of skin infections is highly appealing. Biopolymers in form of microspheres can be used to obliterate surgical dead space and to provide targeted local bactericidal concentrations in tissue for extended periods [1]. Eventually, the specific drug release from microspheres could guide the healing of the wounds. The present experimental study was carried out to test chitosan/tripolyphosphate/chondroitin sulphate microspheres on the *in vitro* release of ofloxacin, which is a commonly used antibiotic for wound healing.

## II. MATERIALS AND METHODS

### A. MATERIALS

Highly viscous chitosan (CHIT) in form of powder was obtained from Fluka, catalog number 48165, chondroitin-4-sulphate (CHS) was obtained from Merck, Germany, catalog number 23068, tripolyphosphate (TPP) was obtained from Acros, Belgium, catalog number 218675000, and ofloxacin (OF) was purchased from SIGMA, catalog number 08757-1G. All other chemicals were of analytical grade.

### B. CAPSULE PREPARATION

1 g of chitosan and 0.9 g of NaCl were dissolved in 60 ml of 0.5 wt% acetic acid solution (pH 2.2) under stirring at 40°C. After dissolution, the pH of the chitosan solution was modified to 5 with 1 wt% NaOH aqueous solution and filled to 100 ml with distilled water so that the final concentration of chitosan solution was 1 wt%. 0.2 g of ofloxacin was dissolved in 10 g of chitosan solution. Two types of aqueous polyanion solutions in 0.9 wt% NaCl were prepared, namely 0.5 wt% TPP and 0.5 wt% CHS. The pH of polyanion solutions was adjusted to 7.

The CHIT/OF solution was dropped through a concentric nozzle producing droplets of size around 1 mm by air-stripping into the TPP solution continuously flowing in the multi-loop reactor where the polyelectrolyte complexation takes place and CHIT/TPP microspheres are formed [2]. The reaction time was set to 40 s. After the reaction, microspheres were separated, washed and collected in 0.9 wt% NaCl solution at pH 7. About 1 ml of CHIT/TPP microspheres was coated in 0.5 wt% CHS solution for 1 min and another 1 ml of for 10 min. After the reaction, microspheres were washed and stored in 0.9 wt% NaCl solution at pH 7. This procedure led to preparation of three types of microspheres, with and without the CHS layer, which were further tested in OF release studies.

### C. RELEASE STUDY

0.5 ml of capsules was stored in 10 ml of 0.9 wt% NaCl at 37°C. The drug release was determined using Cecil CE 7250 UV/VIS spectrophotometer at 293 nm, which is the specific wavelength for ofloxacin. The kinetics was followed during 28 days.

## III. RESULTS AND DISCUSSION

The chitosan-based microspheres were of core-shell architecture, typically with the average diameter of 800 µm and membrane thickness of 10s of µm. Fig-

Figure 1 shows an example of CHIT/TPP microsphere with CHIT/TPP-based membrane and CHIT gel core.

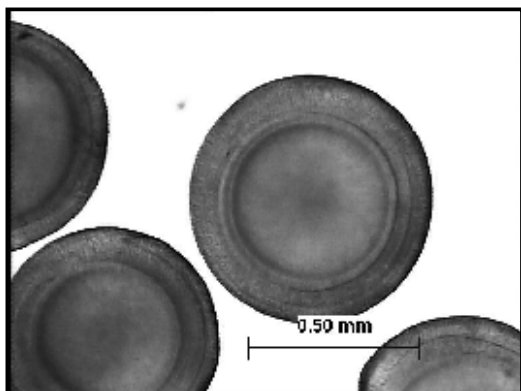


Figure 1: CHIT/TPP microsphere

The different types of chitosan microspheres in terms of composition and preparation conditions were compared with respect to the release of ofloxacin. We observed that the amount of released drug was dependent on the capsule composition. The total amount of released OF was higher in case of CHIT/TPP compared to CHIT/TPP/CHS microspheres. Faster release of the drug was characteristic for microspheres prepared without CHS layer, which should be the favorable feature in case of strong and acute infection. However, when the long term treatment is needed, then a delayed drug release is preferred. This can be easily achieved by using microspheres with CHS coating layer, where the kinetics of drug release can be controlled by reaction time. The rate of ofloxacin release is inversely proportional to the time of exposure of CHIT/TPP microspheres to CHS solution.

#### IV. CONCLUSION

The amount and the kinetics of released ofloxacin from chitosan-based microspheres can be controlled by using different conditions of preparation and chemistry of type of microspheres. There is a high potential that the ofloxacin-containing chitosan microcapsules could be effectively used in controlled drug delivery for various purposes.

#### ACKNOWLEDGEMENTS

This work was supported by Science and Technology Assistance Agency under the contract No. APVV-51-016002, Centre of Excellence of SAS CEDEBIPO, and EU project SustainPack.

#### REFERENCES

- [1] Gimeno, C., J. Borja, D. Navarro, L. Valdes, J. Garcia-Barbal, and J. Garciade-Lomas.: *Chemotherapy*, 44:94–98, 1998.
- [2] I. Lacík, A. V. Anilkumar and T. G. Wang: *J. Microencapsulation*, 18:479A, 2001.

# Formation of Crosslinked Inorganic-Organic Polymers as Matrices for the *In Situ* Preparation of Lanthanide Oxide Nanoparticles

Claudia Feldgitscher and Guido Kickelbick  
 Vienna University of Technology, Institute of Materials Chemistry  
 Getreidemarkt 9, A 1060 Vienna, Austria  
 Email: Claudia.Feldgitscher@tuwien.ac.at

**Abstract** — A new method for the preparation of hybrid materials containing lanthanide oxide particles is presented, in which the particles are formed in a crosslinked inorganic-organic polymer matrix consisting of hydrophobic polysiloxane chains and hydrophilic poly(ethylene oxides) (PEOs). NMR, FT-IR and thermal analysis (TGA) showed the success of the crosslinking hydrosilation reactions. Swelling experiments gave further insights in the hydrophilic/hydrophobic nature of the network and in its ability to take up water. As a proof of principle the polymers were infiltrated with  $FeCl_3$  salts that were hydrolyzed to obtain iron oxide containing crosslinked networks.

## I. INTRODUCTION

Lanthanides and their oxides are in the focus of recent scientific investigations due to their electronic structure and the resulting optical and magnetic properties leading to various applications such as luminescent biomedical stains, optical fibres and lightning devices [1]. Lanthanide oxide nanoparticles are usually prepared in emulsions or by precipitation from solution [2-4]. In this project a new method is introduced in which crosslinked polymer structures are used as the reaction environment. Thus composite materials can be prepared combining the properties of a stable crosslinked polymer with the magnetic and optical qualities of the lanthanide oxide.

Polysiloxanes are widely used because of their low  $T_g$ , high flexibility and their high thermal stability [5, 6], whereas PEOs serve in ion conducting molecules as macromolecules that coordinate the ions. The combination of these characteristics promises systems for confined space nanoparticle precipitation. The polymers can be swollen in aqueous metal salt solution leading to incorporation and arrangement of the ions next to the hydrophilic component of the polymer. Treatment with bases causes the hydrolysis of the metal ions whereas the matrix is not harmed.

## II. RESULTS AND DISCUSSION

### A. PREPARATION OF CROSSLINKED POLYMERS

PEOs (Aldrich) of molecular weights ranging from 200 to 600 g/mol were end group functionalized following a known procedure [7]. The resulting allyl end-capped PEOs were used as crosslinking molecules in Pt-catalyzed hydrosilation reactions with Si-H functionalized polysiloxanes (Figure 1). Two different commercially available polysiloxanes were investigated more closely: PMHS (polymethylhydrosiloxane) and PDMS-*b*-PMHS (polydimethylsiloxane-*b*-methylhydrosiloxane).

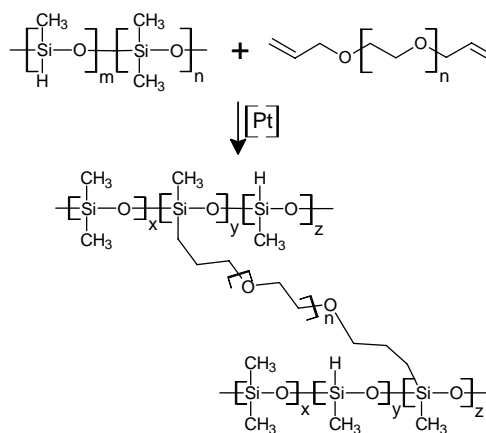


Figure 1: Crosslinking of a PDMS-*b*-PMHS polymer by allyl end-capped PEO

The reaction progress was monitored with IR-spectroscopy, following the diminution and final disappearance of the prominent and characteristic Si-H vibration at around  $2160\text{ cm}^{-1}$ . Mono functionalized di- or triethylene glycole monomethylethers were introduced subsequently by hydrosilation to achieve a higher grade of hydrophilicity and to saturate all reactive Si-H bonds.

It was found that complete conversion of all Si-H groups in the polysiloxane was difficult to achieve

most likely because of sterical reasons. If the catalyst concentration was increased too much it led to an undesirable coloration of the polymer due to formed colloidal platinum and once crosslinked, a purification of the matrix is difficult.

The hydrosilation is affected by solvent interactions. Gelation points were reached faster when performing the addition in THF than in toluene, but this did not result in an observable change in the IR-spectra or TGA-curves.

## B. SWELLING BEHAVIOR

The swelling experiments were carried out in water or toluene saturated atmospheres. The amount of swelling was determined gravimetrically and the swelling degree was calculated as the difference of the mass of the swollen sample and the mass of the dry sample divided by the mass of the dry sample. Both the water and the toluene uptake showed exponential behavior to time in all samples (Figure 2).

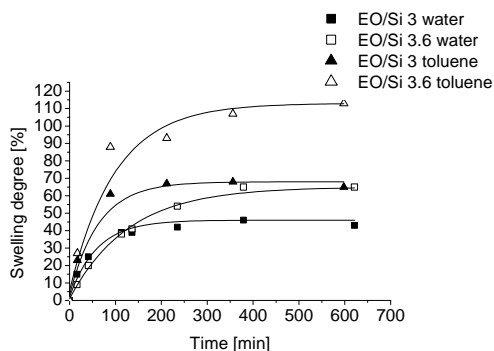


Figure 2: Dependency of degree of swelling to time

The water uptake was linear to the amount of ethylene oxide units (EO) present in the crosslinked polymer as expected (Figure 3). The crosslinked PMHS samples still induced a hydrophobic character, because of the still high number of Si-CH<sub>3</sub> units in the polymer. In all samples the swelling degree was higher for toluene, although linearity was not clearly shown.

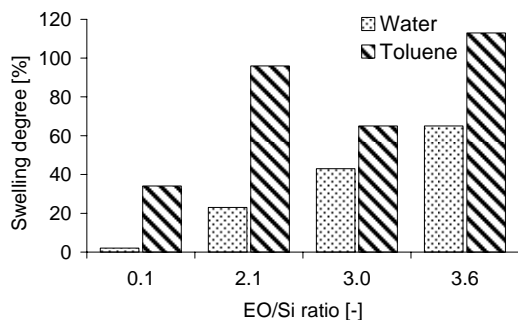


Figure 3: Correlation of swelling and hydrophilicity

## C. INFILTRATION WITH FE-IONS

Infiltration experiments showed that it is possible to produce oxidic iron compounds in the polymer matrix, by the infiltration of the crosslinked systems with aqueous FeCl<sub>3</sub> solutions and subsequent precipitation with NH<sub>4</sub>OH. However the introduction of the lanthanide ions like Nd<sup>3+</sup> and Yb<sup>3+</sup> was shown to be more difficult. Due to the bigger ion radii of the lanthanides and their preferable coordination of water, further matrix modifications are necessary. The introduction of functionalities capable of coordinating lanthanides is the method of choice to extend the preparation route used for iron doped polymers to lanthanide systems.

## ACKNOWLEDGMENTS

The financial support by the Austrian *Fonds zur Förderung der wissenschaftlichen Forschung* for this project (FWF Project No. P17731) is gratefully acknowledged.

## REFERENCES

- [1] J.-C. G Buezli and C. Piguet. Taking Advantage of Luminescent Lanthanide Ions. *Chem. Soc. Rev.*, 34(12):1048-1077, 2005.
- [2] R. Bazzi, M. A. Flores-Gonzalez, C. Louis, K. Lebbou, C. Dujardin, A. Brenier, W. Zhang, O. Tillement, E. Bernstein and P. Perriat. Synthesis and luminescent properties of sub-5-nm lanthanide oxides nanoparticles. *J. Lumin.*, 102-103:445-450, 2003.
- [3] C. Rill and G. Kickelbick. Lanthanide Oxide Particles Prepared by a Microemulsion Approach. In preparation.
- [4] G. Wakefield, H. A. Keron, P. J. Dobson and J. L. Hutchison. Synthesis and Properties of Sub-50-nm Europium Oxide Nanoparticles. *J. Coll. Int. Sci.*, 215(1):179-183, 1999.
- [5] R. Bischoff and S.E. Cray. Polysiloxanes in macromolecular architecture. *Prog. Polym. Sci.*, 24: 185-219, 1999.
- [6] D. Graiver and G. Fearon. *Silicon-Containing Polymers*. Kluwer Academic Publishers: Dordrecht, 2000, 233-243.
- [7] J. Bauer, N. Hüsing and G. Kickelbick. Tunable block copolymers based on a polysiloxane backbone by anionic ring-opening polymerization. *J. Polym. Sci. Part A*, 42(16):3975-3985, 2004.

# APPLICATION OF ELECTROCHEMICAL METHOD IN THE STUDY OF CORROSION PROPERTIES OF SYSTEM Fe POWDER / METAL COATING

Zuzana Feckova and Ladislav Lux  
Department of Chemistry  
Technical University of the Kosice  
Kosice, Slovakia

Email: zuzana.feckova@tuke.sk

**Abstract** – In this paper the corrosion potential changes has been studied in the system of a paraffin-impregnated graphite electrode (PIGE)/Fe powder immobilized on PIGE/Ni coating of different thickness. In order to investigate the corrosion behaviour a suitable solution of aggressive components was used. The value of the corrosion potential was determined by Tafel analysis. For deposition of one-component Ni coatings on Fe powder particles the galvanostatic method was used.

## INTRODUCTION

Powder materials are important inputs for technological processes. The metal coatings can be applied to improve the mechanical properties, surface morphology, wear and corrosion resistance of basic materials in powder metallurgy. Electrochemical deposition of metal plating on Fe powder particles is one of the process that give equable coherent metal film which offers anti-corrosive protection [1, 2].

Our experiments demonstrate, that voltammetry of immobilized microparticles is suitable for the determination of the corrosion potential of metals, especially advantageous in the case of powdered metals.

## EXPERIMENTAL

A paraffin-impregnated graphite rod (PIGE) with or without Fe powder was used as the working electrode. This working electrode, together with a suitable reference electrode (Ag/AgCl/3 M KCl) and an auxiliary Ni electrode formed a three-electrode system. Iron powder fraction 63 - 100  $\mu\text{m}$  was used for experiments.

The electrolyte, containing 1.2 M  $\text{NiSO}_4$ , 0.3 M NaCl and 0.3 M  $\text{H}_3\text{BO}_3$ , was used as a nickel-plating bath. The electrolytic coating process was carried

out for time 10, 20, 30, 40, 50, 100 and 200 min. The deposition constant current -1mA was applied.

Voltammetric measurements were recorded on ECA STAT 110 PS (ISTRAN, Bratislava, Slovakia). The experiments were performed in electrolyte 1.2 M  $\text{Na}_2\text{SO}_4$ , 0.3 M  $\text{H}_3\text{BO}_3$  and 0.3 M NaCl. This solution was previously deaerated with pure nitrogen. The experiments were carried out in a three-electrode electrochemical cell with a platinum plate as counter-electrode, Ag/AgCl/3 M KCl as reference and PIGE as the working electrode.

Cyclic voltammograms with 10 cycles were recorded at a scan rate of 1 mV/s.

All experiments were carried out at room temperature.

## RESULTS AND DISCUSSION

The nickel deposition is usually made in the electrolyte where relatively high concentrations of nickel are required. In the galvanostatic electrolysis is the most suitable value of pH around 2 from the point of view of the deposit quality [3]. However, in this work the deposition was performed at pH 4 in order to suppress hydrogen evolution.

The value of the corrosion potential, i.e. the zero-current potential, can be determined by extrapolating the linear parts of the Tafel plot up to their intersection (Figure 1).

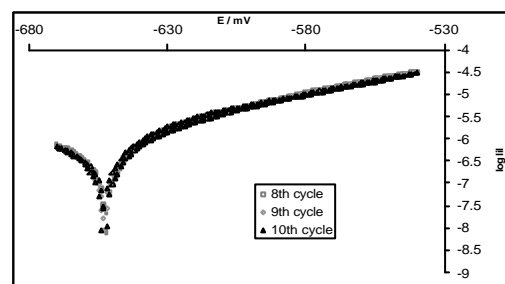


Figure 1: Polarization curves of pure Fe particles

This value can be determined graphically or by means of a regression analysis of each section. The precision of this determination is  $\pm 0.5\%$  (mean rel. dev.) [4, 5].

The corrosion potential of the system Fe particles/Ni coating of different thickness was determined in the way described above and Figure 2 represents 3 cycles of polarization curve of this system.

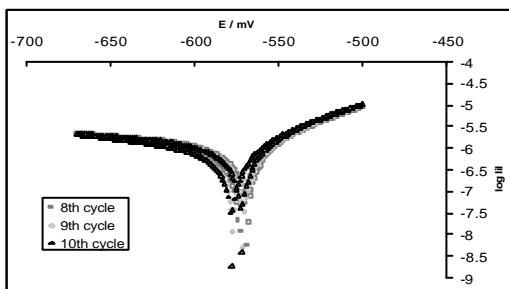


Figure 2: Polarization curves of Fe/Ni coating, deposition time of Ni was 100 min

In the course of this study it was observed that the corrosion potential slightly shifts negatively from one cyclic polarization to the other until the values finally remain constant after seven cycles (Figure 3). This effect can be explained as the result of a progressive decrease of the original thickness of Ni coating on Fe particles surface.

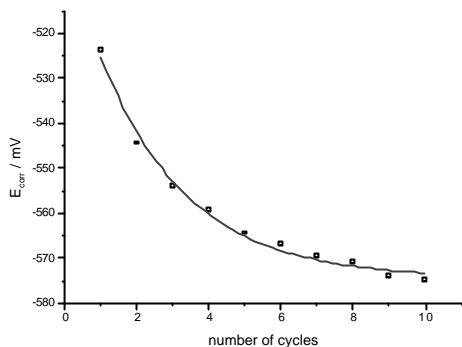


Figure 3: Dependence of the corrosion potential on the number of polarization cycles

Figure 4 shows the influence of Ni coating deposition time on the corrosion potential of the system Fe particles/Ni coating. The values of the corrosion potential shift to that of pure Ni coating on the PIGE.

The electrolytic plating of the powder particles by the metallic coating is used for upgrading the

basic material properties. Electrochemical deposition of the metal film on the powder is one of the processes giving the best homogeneity of the product. Ni coatings have favourable mechanical and protective characteristics.

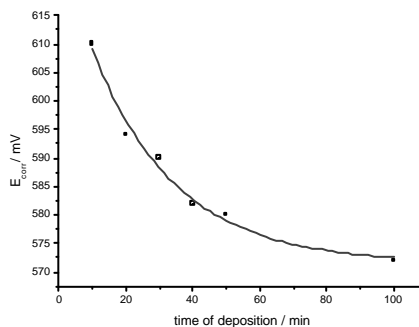


Figure 4: Influence of deposition time on corrosion potential of Fe/Ni coating

#### ACKNOWLEDGEMENTS

This work was supported partially by the Grant Agency of the Slovak Republic under projects No. 1/1108/04 and by the APVT agency under project No.20-009404.

#### REFERENCES

- [1] A.Turonova and M. Kabatova. Surface treatment of the powder material by metal coatings. In *Vrstvy a povlaky*, pages 146-150, Trencin, Slovakia, May 2003.
- [2] R. Orinakova et al. Corrosion behaviour of coated cellular material *Surface and Interface Analysis*, 36(8): 784-787, August 2004.
- [3] F. A. Lowenheim. *Electroplating*. Fairfield Graphics, USA, 2nd edition, 1978.
- [4] I. Zezula and M. Galova. Application of abrasive stripping voltammetry in corrosion science. *J. Solid State Electrochem.*, 3(4): 231-233, May 1999.
- [5] L.Pikna and M. Galova and L. Lux. Investigation of corrosion properties of iron powder. *Acta Mechanica Slovaca*, 6 (2): 27-32, February 2002.

# A new optical Set-up of a Refractive Holographic Confocal Microscope

Zdeněk Foret,

Institute of Physical Engineering, Faculty of Mechanical Engineering,  
Brno University of Technology,  
Brno, Czech Republic

Email: [zdenek.foret@post.cz](mailto:zdenek.foret@post.cz)

**Abstract** — *In this paper is presented a new set up of the holographic microscope working in reflection mode. We report on the construction details of the mechanical components which lead to an improved measurement accuracy and make adjustment easier. The holographic microscopy is an effective tool for recording and reconstructing the complete optical information. The process is based on real-time incoherent holography principle.*

## I. INTRODUCTION

This method uses an incoherent holography principle in real-time process [1]. Both the image phase and the image amplitude are reconstructed from the interference signal in the out – put plane. The interference image is recorded with a CCD camera and consecutively is processed by the PC.

It is possible to make optical sectioning through the specimen without its destruction [2]. This is very useful in biology. The quality of recorded information depends on an accuracy of alignment of the microscope. The aim is to realize the easy operated construction with revolving turret for objective lenses. The holographic microscope has no scanning system because all object points of the whole viewed field are imaged simultaneously. Therefore the speed of imaging process is limited only by the image detection and used hardware.

## II. EXPERIMENTAL SET UP

In this configuration (Fig. 1) we remove some of the imperfections (e.g. difficult alignment and lengthy changing of the objectives) of the holographic microscope prototype, which was made in our institute.

Source of light is splitted by the diffraction grating into two beams. One is passing to the object branch and the other to the reference branch.

If these two branches are of the same length, the image hologram is formed in the output plane.

The holographic microscope imaging properties are strongly dependent on the type of illumination source. The broadband (halogen lamp) and narrowband (halogen lamp with interference filter or laser diode). To achieve the confocal imaging, it is necessary to use spatially incoherent light. The most effective way to convert spatially coherent light of the laser diode into the spatially incoherent light is using of a two diffuser system. A rotating diffuser associated with a motionless difusser is inserted to the laser beam.

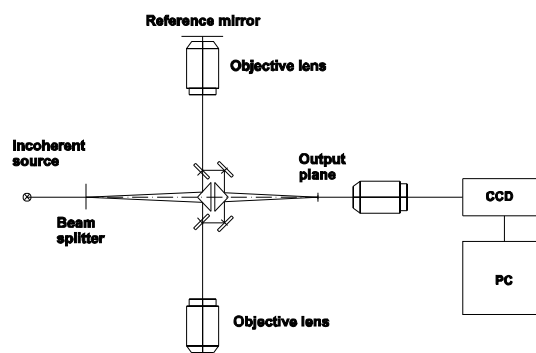


Figure 1: Experimental set up of holographic microscope.

## III. CONCLUSION

The result of this project is engineering design of the new laboratory version of the holographic microscope. We verified the mechanical parts in the experimental set up. Mechanical parts are able to reproduce positioning with required accuracy.

A suitable applications arise especially in materials science for noncontact surface inspection and profiling of reflective materials. The nanometer-scale measurement of surface profiles is possible due to the image-phase processing.

The holographic microscope is suitable for imaging of living tissues owing to nondestructive optical sectioning capability.

#### ACKNOWLEDGMENTS

The author is grateful to his colleagues Luděk Lovicar and Radim Chmelík for the text preparation. The work is supported by the grant 202/04/1410 of the Grant Agency of the Czech Republic and by the grant A 1065203 of the Grant Agency of the Academy of Science of the Czech

Republic and Ministry of Education of CR grant MSM0021630508.

#### REFERENCES

- [1] Sun P. C., Leith E. N.: Broad-source image plane holography as a confocal imaging process, *Applied Optics* **33** (1994), 597-602.
- [2] Chmelík R., Harna Z.: Parallel-mode confocal microscope, *Optical engineering*, **38** (1999), 1635-1639.

# Influence of Electrical and Thermal Ageing on the Course of Complex Permittivity of Thermikanit

Martin Frk<sup>1</sup> and Rostislav Stráník<sup>2</sup>

<sup>1</sup>Department of Electrical and Electronic Technology, <sup>2</sup>Department of Physics  
Brno University of Technology  
Brno, Czech Republic

Email: [frkmar@feec.vutbr.cz](mailto:frkmar@feec.vutbr.cz)

**Abstract** — *The article deals with observation and evaluation structural modifications of high-up temperature mica-based insulation material Thermikanit 26.000 in course of thermal ageing. by the dielectric relaxation spectroscopy, infra-red spectroscopy method. The objective of the research was to determine or at least to identify the degree of thermal and electrical degradation after a defined stress and to obtain some findings regarding the ageing processes. Another objective would be to find an evidence for the relation between an occurrence of the breakdown and some features in the dielectric and infrared spectra. Experimental results are analyzed and their potential implications for material diagnostics are discussed.*

## I. INTRODUCTION

Some applications make use of electrical machines and apparatuses working permanently at temperatures close to 300 °C. The occurrence, even if only hypothetical, of these temperatures necessitates to use advanced insulation materials able to withstand these temperatures for the entire working life of the equipment in question. During this time, the insulation will be exposed to both high temperature and electrical stress. Both these factors are likely to bring about degradation. The objective of the research was to determine or at least to identify the degree of degradation after a defined stress and to obtain some findings regarding the ageing processes.

## II. SAMPLES AND AGEING

The material under study was Thermikanit 26.000. It is a composite material system containing, according to specifications, 91 % of non-calcinated mica paper a 9 % of silicon binder [1]. After the delivery from the manufacturer, it was stabilized at the temperature of 320 °C for 500 hours. From the sheets of Thermikanit were prepared square shaped testing specimens with the sizes approximately 60 x 60 mm and nominal thickness 0,31 mm. Samples were provided with silver electrodes evaporated onto their surface and

conditioned at the room temperature in the 0 % moisture environment (in the presence of silica gel).

All sample were exposed to electrical ageing at the voltage level of 3 and 4 kV for 600 hours or were exposed to thermal ageing at the temperature 320 °C, 420 °C and 520°C for 1000 hours. In the course of thermal and electrical ageing were measured both parts of complex permittivity by the dielectric relaxation spectroscopy method, the chemical structure were detected by the infra-red spectroscopy method.

## III. MEASUREMENT

### A. DIELECTRIC RELAXATION SPECTROSCOPY METHOD

The object of this method were investigation of temperature and frequency dependences of complex permittivity. Measurements were done with the purpose-built measuring capacitor that was designed for temperatures up to 350 °C. The sample was inserted into the electrode system that was situated in the temperature unit. In this way a capacitor was formed. Investigation of both parts of complex permittivity was carried out in the frequency range 100 Hz – 1 MHz. It was used precision LRC meter HP 4284A, made by Hewlett Packard. The function of this instrument is based on bridge techniques with auto-calibration. It was measured capacity  $C_p$  and  $\text{tg } \delta$  at the temperatures 20, 100, 200 and 300 °C. From this values were evaluated parts of complex permittivity  $\epsilon^*$ . Dependencies of loss number  $\epsilon''$  of Thermikanit as a function of temperature and frequency (3D-chart) with the ageing time as parameter are presented in fig.1.

### B. INFRA-RED SPECTROSCOPY METHOD

Infra-red spectroscopy is an experimental tool for obtaining information about chemical structure of materials. The interpretation of infrared spectra involves the correlation of absorption bands in the spectrum of an unknown material with the known absorption frequencies for types of bonds [2].

Obtained infra-red spectra of Thermikanit in course of thermal ageing at temperatures 420 °C and 520 °C are presented in fig. 2.

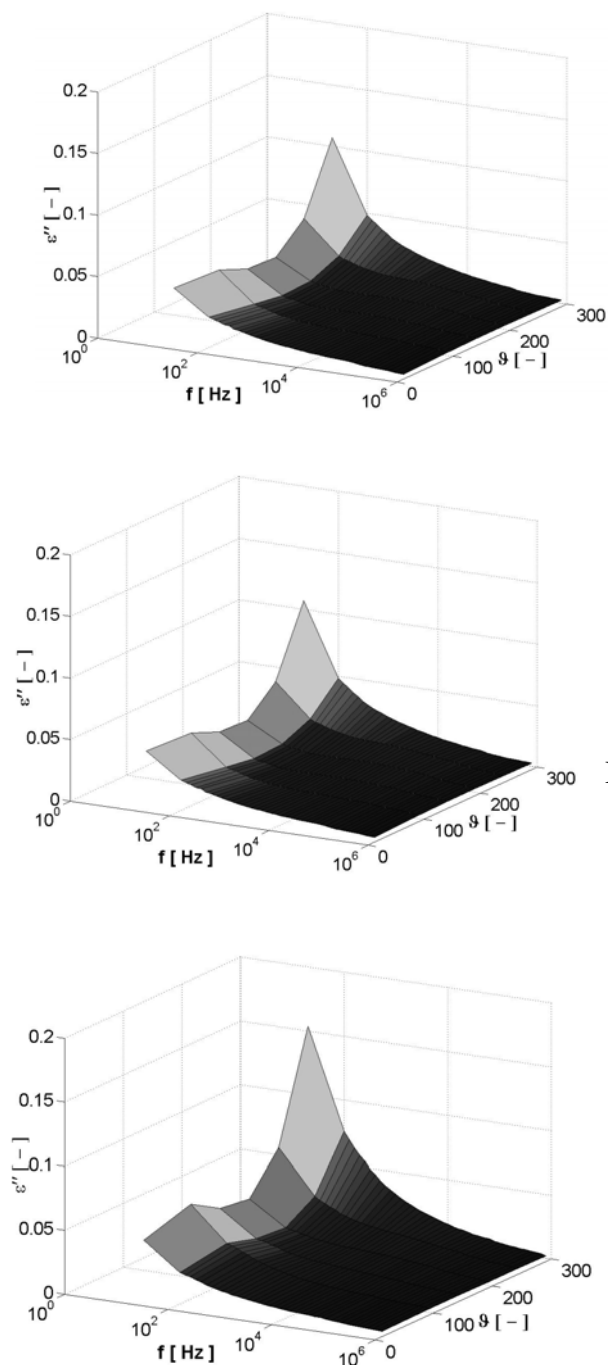


Figure 1: Temperatures and frequencies dependencies of loss number of the Thermikanit; a) 0 h / 4kV, b) 80 h / 4kV, c) 200 h / 4kV

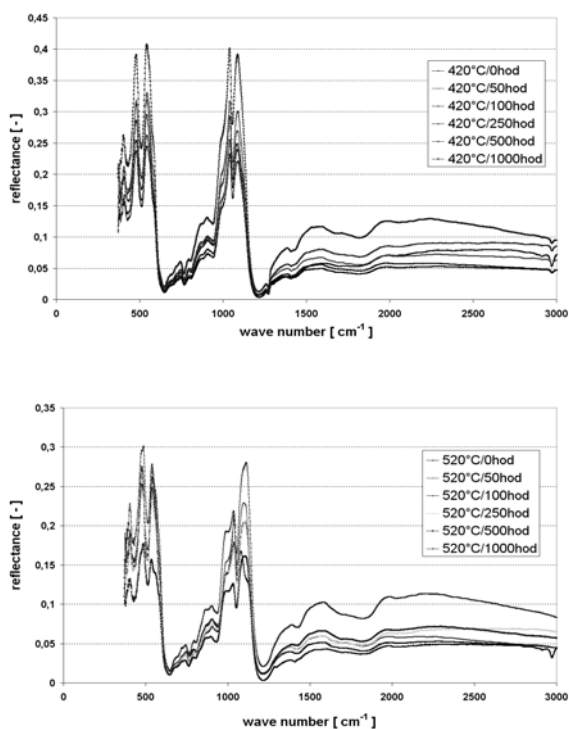


Figure 1: Infra-red spectra of Thermikanit in course of thermal ageing

#### IV. CONCLUSION

The thermal and electrical ageing process brings about an increase of both parts of the complex permittivity, at all frequencies. The temperature behaviour follows at both ageing levels the same pattern. Both components of the complex permittivity decrease with increasing temperature to about 150 °C and then start to increase again; the effect is more pronounced at higher ageing level.

The values of reflectance increased with the time of thermal ageing and the absorption peak of the CH in Si-CH<sub>3</sub> (wave number 2920-2960 cm<sup>-1</sup>) gradually disappeared which means decrease the number of Si-CH<sub>3</sub> bonds. At the ageing temperature 520 °C is this process very fast (after 50 hours is not yet observable the peak of Si-CH<sub>3</sub> bond) and at the temperature 320 °C are not observed chemical changes of Thermikanit.

#### REFERENCES

- [1] [www.elektroisola.cz](http://www.elektroisola.cz)
- [2] Smith, B. C. Infrared spectral interpretation: a systematic approach CRC 1999 Press LLC p. 200. ISBN 0-8493-2463-7.

# Magnetic and superconducting properties of HoNi<sub>2</sub>B<sub>2</sub>C single crystal

René Fuger and Harald W. Weber (Faculty Mentor)  
Atomic Institute of the Austrian Universities  
Vienna University of Technology  
1020 Vienna, Austria  
Email: rfuger@ati.ac.at

**Abstract** — We report on magnetic measurements on a HoNi<sub>2</sub>B<sub>2</sub>C single crystal at low temperatures. The magnetic and the superconducting phase diagram were determined for different crystal directions and the superconductive properties evaluated as a function of temperature and applied field. The critical current density was calculated from magnetization loop measurements.

## I. INTRODUCTION

The interplay between the two collective phenomena, magnetism and superconductivity, has been of great scientific interest for many years. In the rare earth transition metal borocarbides (with the rare earth elements Ho, Er, Tm and Dy showing a magnetic moment) superconductivity and magnetism appear in the same temperature range. In the case of HoNi<sub>2</sub>B<sub>2</sub>C the superconducting transition temperature and the temperature for the magnetic transition are at 8.5 K.[1] HoNi<sub>2</sub>B<sub>2</sub>C shows a transition to an antiferromagnetically ordered state at  $T_N=5.2$  K, whereas for temperatures above  $T_m \approx 6$  K paramagnetic behavior prevails. Additionally, in the temperature range  $T_N < T < T_m$ , two incommensurate antiferromagnetic structures exist at zero field. Details about the magnetism in HoNi<sub>2</sub>B<sub>2</sub>C were mainly revealed by neutron diffraction experiments (Ref. [2]-[7]). The superconducting transition is very sensitive to magnetic fields and shows a reentrant behavior in external fields.

## II. EXPERIMENTAL

Measurements of the magnetic moments were performed on a HoNi<sub>2</sub>B<sub>2</sub>C single crystal. The magnetic and the superconducting phase diagram were determined in three different crystal directions and the superconductive properties evaluated as a function of temperature and applied field. The critical current density was calculated from magnetization loops using the Bean model. In addition, the angular dependence of the magnetic moment was measured at various magnetic fields and temperatures.[9]

## III. RESULTS

The phase diagrams for fields along the [100] (a-axis), the [110] (diagonal in the ab-plane) and the [001] (c-axis)

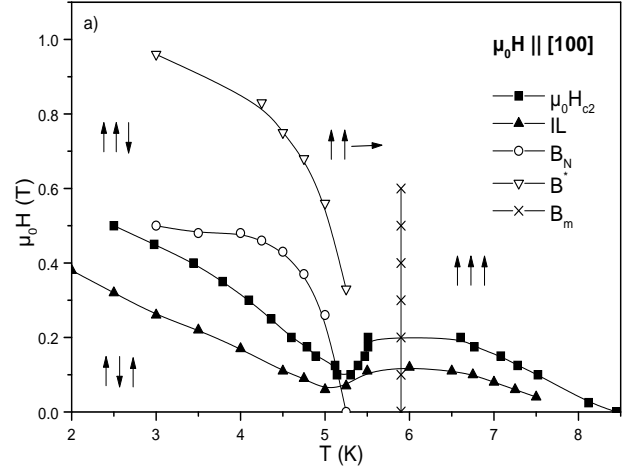


Figure 1: Phase diagram for magnetic fields along the [100] direction of the HoNi<sub>2</sub>B<sub>2</sub>C single crystal showing the  $H_{c2}$  curve, the irreversibility line and the magnetic transition lines. The different magnetic phases and their order states are indicated by arrows.

direction of the single crystal were established. Figure 1 shows an example for  $H \parallel [100]$ . The upper critical field ( $\mu_0 H_{c2}$ ), the irreversibility line (IL) and the magnetic phase transitions are plotted there. The upper critical fields  $\mu_0 H_{c2}$  were determined from ac SQUID (superconducting quantum interference device) measurements with an ac field amplitude of 30  $\mu$ T. A tangent criterion fitting the linear slope of the in-phase signal of the susceptibility  $m'(T)$  was used for the evaluation. The irreversibility points were taken from  $m(T)$  (first deviation of the zero field cooled from the field cooled curve) as well as from  $m(\mu_0 H)$ -loops (merging of the  $m^+$  and  $m^-$  branches) measured in a SQUID and a VSM (vector vibrating-sample magnetometer). The magnetic transitions can also be seen in these experiments.

The irreversible magnetic moment of the magnetization loops (see e.g. Figure 2) was used to determine the critical current density  $J_c$  from the Bean model. [8] This can be done safely, because the loop measurements show symmetric irreversible magnetization curves and

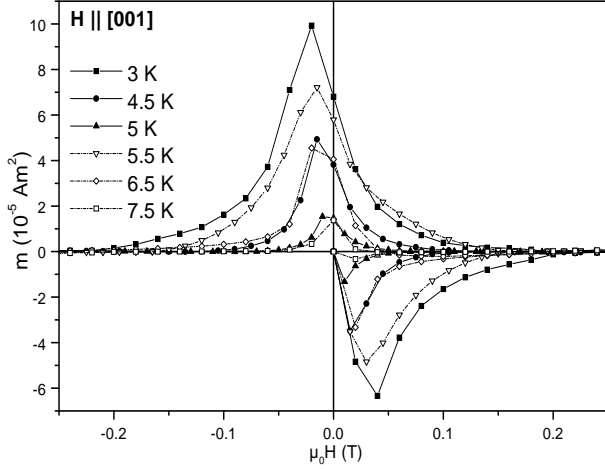


Figure 2: Magnetization loops for fields along [001] at different temperatures.

large remanent fields as demonstrated by the data for  $H \parallel [001]$  in Figure 2 as an example for all our results. Figure 3 shows the critical current densities for fields parallel to [100], the inset presents its temperature dependence at various fields.

#### IV. CONCLUSIONS

We have presented a thorough characterization of a  $\text{HoNi}_2\text{B}_2\text{C}$  single crystal in the superconducting and the magnetically ordered state. The critical current densities were evaluated, they are of the order of  $10^8 \text{ Am}^{-2}$  at 3 K.

#### REFERENCES

- [1] K. H. Müller, G. Fuchs, S. L. Drechsler, and V. N. Narozhnyi, Handbook of Magnetic Materials, edited by K. H. Buschow (Elsevier Science, Amsterdam, 2002), Vol. 14, Chap. 3
- [2] A. I. Goldman, C. Stassis, P. C. Canfield, J. Zarestky, P. Dervenagas, B. K. Cho, D. C. Johnston, and B. Sternlieb, Phys. Rev. B **50**, R9668 (1994)
- [3] T. E. Grigereit, J. W. Lynn, R. J. Cava, J. J. Krajewski, and W. F. Peck Jr., Physica C **248**, 382 (1995)
- [4] J. W. Lynn, S. Skanthakumar, Q. Huang, S. K. Sinha, Z. Hossain, L. C. Gupta, R. Nagarajan, and C. Godart, Phys. Rev. B **55**, 6584 (1997)
- [5] P. C. Canfield, S. L. Budko, B. K. Cho, A. Lacerda, D. Farrell, E. Johnston-Halperin, V. A. Kalatsky, and V. L. Pokrovsky, Phys. Rev. B **55**, 970 (1997)
- [6] C. Detlefs, F. Bourdarot, P. Burlet, P. Dervenagas, S. L. Budko, and P. C. Canfield, Phys. Rev. B **61**, R14916 (2000)
- [7] K. D. D. Rathnayaka, D. G. Naugle, B. K. Cho, and P. C. Canfield, Phys. Rev. B **53**, 5688 (1996)
- [8] C. P. Bean, Phys. Rev. Lett. **8**, 250 (1962)

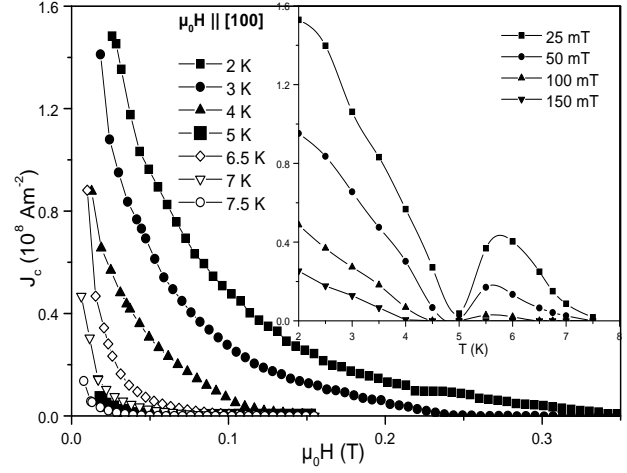


Figure 3: Critical current densities for fields along [100] at different temperatures. The inset shows the temperature dependence of  $J_c$  at four selected fields.

- [9] C. Krutzler, R. Fuger, M. Eisterer, G. Fuchs, G. Behr and H. W. Weber Phys. Rev. B **72**, 144508 (2005)

# Binuclear Copper(II) Complexes as Building Blocks for the Synthesis of Inorganic-Organic Nanocomposites

Fatmir Hamza and Guido KICKELBICK  
Institute of Materials Chemistry  
Vienna University of Technology  
Getreidemarkt 9, 1060 Vienna, Austria  
fhamza@mail.zserv.tuwien.ac.at

**Abstract** — *The formation and characterization of binuclear copper(II) complexes with polymerizable groups and their self-assembly characteristics was studied. The compounds  $\text{Cu}_2(\text{L}_1)_4 \cdot 2\text{CH}_3\text{OH}$  **1**,  $\text{Cu}_2(\text{L}_2)_4 \cdot \text{H}_2\text{O}$  **2**,  $\text{Cu}_2(\text{L}_3)_4 \cdot 2\text{DMF}$  **3**,  $\text{Cu}_2(\text{L}_1)_4 \cdot \text{C}_4\text{N}_2\text{H}_4$  **4** with  $\text{L}_1$  = methacrylate,  $\text{L}_2$  = vinyl acetate and  $\text{L}_3$  = adamantane carboxylate were synthesized and their molecular structure was characterized. Single crystal X-ray analysis reveals that all of these compounds are binuclear complexes in the typical paddle-wheel structure containing four bridging carboxylates and two axial ligands occupying the residual free coordination sites. These two positions allow exchange reactions with different molecules and can be used for the formation of inorganic-organic hybrid materials via coordinative interactions.*

## I. INTRODUCTION

Inorganic-organic nanocomposites are promising systems for a variety of applications because of their extraordinary properties arising from the synergistic combination of the inorganic and the organic building blocks [1]. The combination of polymers with metal complexes can lead to novel nanocomposites which show structures that are determined by the metal complexes, their organization, and the polymeric backbone. Such polymers can be obtained either using metal complexes with polymerizable groups [2, 3] that are (co)polymerized with other monomers or by polymers that include functional groups attached to their chain which allow reaction with metal complexes. Copper(II) carboxylates were chosen in this study as building blocks for preparation of inorganic-organic nanocomposites because of their rigid structure, potential additional coordination sites, the possibility of ligand exchange reactions for further functionalization, and - dependent on the metal-metal interaction - interesting additional properties (electronic, magnetic, etc.) (Fig. 1). Copper (II) carboxylates of the type  $\text{Cu}_2(\text{L}_1)_4 \cdot 2\text{CH}_3\text{OH}$  **1**,  $\text{Cu}_2(\text{L}_2)_4 \cdot \text{H}_2\text{O}$  **2**,  $\text{Cu}_2(\text{L}_3)_4 \cdot 2\text{DMF}$  **3**, and  $\text{Cu}_2(\text{L}_1)_4 \cdot \text{C}_4\text{N}_2\text{H}_4$  **4** were synthesized and

used in some preliminary investigations of their ability to form nanocomposites.

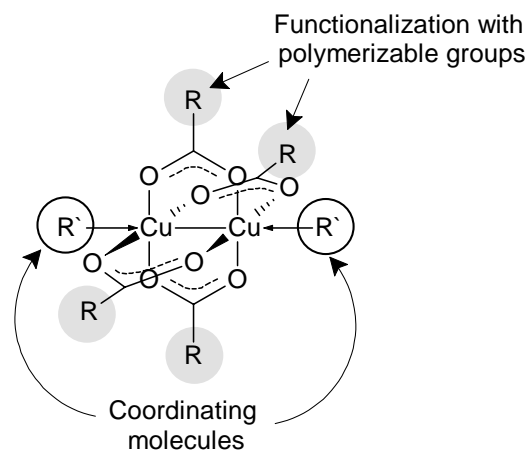


Figure 1. Schematic drawing of a binuclear Cu(II)carboxylate with its potential interaction sites.

## II. RESULTS AND DISCUSSION

Compound **1** and **2** were prepared through reaction of  $(\text{HL}_1)$ ,  $(\text{HL}_2)$  with basic Cu(II) carbonate. Compound **3** was prepared through reaction of  $(\text{NaL}_3)$  solution with Cu(II) nitrate trihydrate following crystallization from DMF. Slow diffusion of ethanol solutions of **1** and pyrazine into each other led to formation of **4** which is a coordination polymer [4] consisting of binuclear Cu-complexes bridged by pyrazine as axial ligand.

### A. CRYSTAL STRUCTURE

The crystal structure of **1** (Fig. 2) contains two binuclear cage complexes, each with inversion symmetry. In each dimer, two Cu ions are bridged by four methacrylate groups, forming a cage structure, and the methanol ligands are bonded through their O atoms to the Cu atoms in the axial positions. Compound **2** has a binuclear typical paddle-wheel structure as **1** with four vinyl acetate bridging ligands and two water molecules as axial ligands

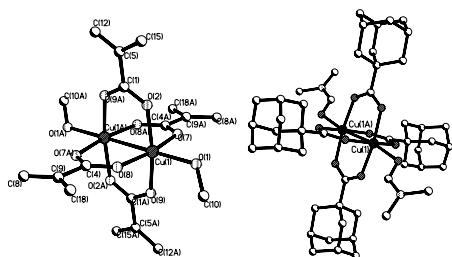


Figure 2: Molecular structure of **1** and **3**.

The crystal structure of **3** contains two binuclear cage complexes, each with inversion symmetry and two uncoordinated DMF molecules. The Cu atoms in compound **3** are bridged by four adamantane groups, forming a cage structure, and the DMF ligands are bonded through the amide oxygen to the Cu atoms in the axial positions. The separation between  $\nu_{as}(\text{COO}^-)$  and  $\nu_{s}(\text{COO}^-)$  for all complexes is less than  $200\text{ cm}^{-1}$ , indicating a bidentate coordination mode for coordinated carboxylate groups. The IR spectra are in good agreement with the presented crystal structures.

## B. NANOCOMPOSITES

In order to construct novel coordination polymers with polymerizable groups, we combined pyrazine with  $\text{Cu}_2(\text{L}_1)_4 \cdot 2\text{CH}_3\text{OH}$  leading to compound **4**. The structure **4** consists of linear chains of binuclear copper methacrylate units linked by pyrazine ligands (Fig. 3). All reported compounds were used as building blocks to prepare nanocomposites.

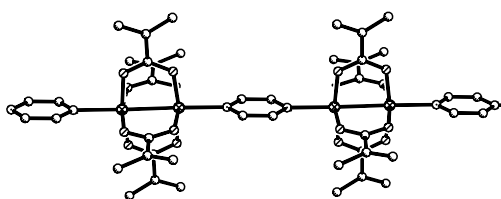
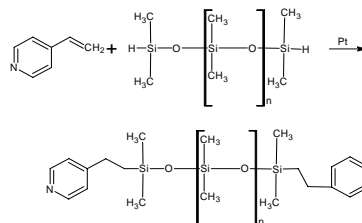


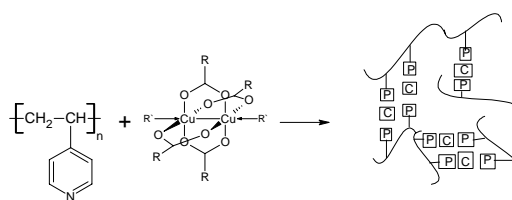
Figure 3: Molecular structure of **4**.

Polymers containing these molecular building blocks were prepared using end-group functionalized polysiloxanes as linkers that allow a bonding to the axial coordination positions forming coordinating polymers. End-group functionalized polysiloxanes were prepared by a hydrosilylation reaction of Si-H terminated siloxanes with vinylpyridine. The thus formed oligomers were used as a second component together with the metal complex to

produce nanocomposites. In other approach poly(vinyl pyridine) chains were crosslinked by the metal complexes and thus nanocomposite was formed (Scheme 2).



Scheme 1: Synthesis of end-group functionalized polysiloxanes



Scheme 2: Synthesis of metal containing nanocomposites.

## ACKNOWLEDGMENTS

We thank the Fonds zur Förderung der wissenschaftlichen Forschung Austria (FWF Project nr.: P17424) for the Financial support of this work.

## REFERENCES

- [1] C. Sanchez, G. J. de A. A. Soler-Illia, F. Ribot, T. Lalot, C. R. Mayer, and V. Cabuil, Designed Hybrid Organic-Inorganic Nanocomposites from Functional Nanobuilding Blocks. *Chemistry of Materials*, pages 3061 – 3083, 13, 2001.
- [2] B. J. Edmondson and A. B. P. Lever Copper(II) Complexes of Unsaturated Acids. *Inorganic Chemistry*, pages 1608-1612, 4, 1965.
- [3] N. Ryoji, M. Wasuke, T. Satoshi, M. Masahiro, H. Makoto, N. Hiromitsu, Microporous Structure of a Chain Compound of Copper(II) Benzoate Bridged by Pyrazine *Chemistry Letters*, pages 367-368, 5, 1999.
- [4] Bell, S. J.; Jennings, K. L.; Danielson, E. D.; Solomon, E.I.; Musselman, R. L, Single crystal morphology of the copper acetate dimmers  $\text{Cu}_2(\text{CH}_3\text{COO})_4 \cdot 2\text{H}_2\text{O}$  and  $\text{Cu}_2(\text{CH}_3\text{COO})_4\text{pz}$  *Journal of Crystal Growth*, pages 108-111, 154, 1995.

# The Structure and Mechanical Properties of ADI in Dependence on Heat Treatment Conditions

Klára Hanzlíková<sup>1</sup> – Stanislav Věchet<sup>1</sup> – Jan Kohout<sup>2</sup>

<sup>1</sup>Department of Material Science and Engineering  
Faculty of Mechanical Engineering, Technical University  
Brno, Czech Republic

Email: [klara.hanzlikova@centrum.cz](mailto:klara.hanzlikova@centrum.cz)  
[vechet@fme.vutbr.cz](mailto:vechet@fme.vutbr.cz)

<sup>2</sup>Department of Physics,  
University of Defence  
Brno, Czech Republic

Email: [jan.kohout@unob.cz](mailto:jan.kohout@unob.cz)

**Abstract** — *Thanks to extraordinarily favourable both mechanical and technological properties, austempered ductile iron is ranked with very prospective structural materials. Its structure and consequently also mechanical properties can be substantially influenced by conditions of isothermal transformation. The dependence between matrix composition and mechanical (static as well as fatigue) properties of unalloyed nodular cast iron, which was isothermally heat treated at transformation temperature of 380 °C, is studied in the present contribution.*

## I. INTRODUCTION

Presented work deals with high strength variant of nodular cast iron, so-called ADI (Austempered Ductile Iron). This material is obtained by isothermal treatment of nodular cast iron. It consists of austenitization, isothermal transformation in the bainitic belt and final cooling, usually in water.

Owing to its excellent mechanical as well as technological properties, austempered ductile iron belongs among very prospective structural materials [1, 2]. The structure of ADI matrix is usually created by bainitic ferrite with high strength and by stabilized austenite with high deformability. Their portion and partially also their properties are determined by transformation conditions, i.e. the isothermal transformation temperature and the dwell [3-5]. The austenitization conditions play only a marginal role. The dependence between matrix composition and mechanical (static as well as fatigue) properties of two unalloyed nodular cast irons, which were isothermally heat treated at

transformation temperature of 380 °C, is studied in the present contribution.

## II. EXPERIMENT

Chemical composition of experimental materials is given in the table 1.

Element	H 380 a	H 380 b
C	3,49	3,56
Si	2,46	2,24
Mn	0,25	0,25
P	0,02	0,02
S	0,007	0,004
Mg	0,042	0,054

Table 1: Chemical composition [wt. %]

Cylindrical testing bars for static tensile test (M11x1,  $D_0 = 6\text{mm}$ ,  $L_0 = 30\text{mm}$ ) and for fatigue tests (M16x1,  $D_0 = 7\text{mm}$ ,  $L_0 = 10\text{mm}$ ) were made of these materials.

Isothermal refining was performed in order to get bainitic structure. Austenitization took one hour at temperature 900 °C in NaCl salt bath. Isothermal transformation was realized at temperature 380°C in AS 140 salt bath. The dwell at transformation temperature varied in the range from 2 minutes to 9 hours. Heat treatment was finished by cooling in water bath.

For structure evaluation metallographic cuts were made on screw heads' front faces. Structure was observed etched and not etched by light microscope OLYMPUS GX 71. The content of

stabilized austenite was determined using quantitative X-ray phase analysis.

Static tensile test was performed at room temperature (20°C) on tug-machine PC - TIRAtest 2300 with force range 10 kN. Loading speed was  $v = 2$  mm/min. Fatigue test was performed at normal temperature (20°C) on high-frequency-resonance pulsator AMSLER 10 FHP 1478 at test frequency  $f = 201$  Hz. Wöhler curves were determined by symmetrical cycle tensile – press. The regress analysis was used for Wöhler curves defining. For regression by least square method the three-parameter non-linear Stromeyer function was used (1), where as  $\sigma$  stress amplitude or maximum stress of loading cycle is considered,  $a$ ,  $b$ ,  $K$  are parameters of regression curve, and  $N$  is the number of cycles to failure or to test stoppage.

$$\sigma = aN^b + K \quad (1)$$

### III. RESULTS

The composition of structural mixture in the matrix of both ADI transformed at 380°C is very substantially influenced by the length of isothermal transformation dwell. Maximum content of stabilised austenite, 35% approximately, was obtained for the transformation dwell of 60 minutes (Fig. 1).

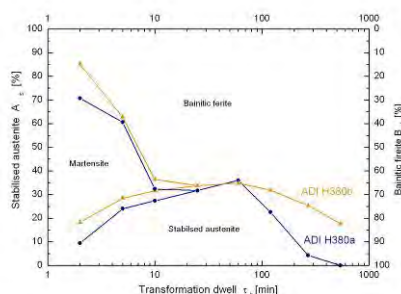


Figure 1: The structure composition of ADIs in dependence on the transformation dwell.

Mechanical properties of both studied materials are substantially influenced by the length of isothermal transformation dwell, because of microstructural changes proceeding during transformation (Fig. 2). The UTS and yield strength values increase with the transformation dwell prolonging. Maximum average values of  $R_m = 1100$  MPa and  $R_{p0,2} = 860$  MPa were reached for the longest transformation dwell, when bainitic ferrite was the prevalent structural component in the matrix. Values of elongation to the fracture and fatigue limit correspond to the

amount of stabilised austenite. The Maximum of the elongation to the fracture, on the average 7 %, and fatigue limit, on the average 260 MPa, was measured for transformation dwell of 60 minutes. It coincide with the maximum content of stabilised austenite in the ADI matrix.

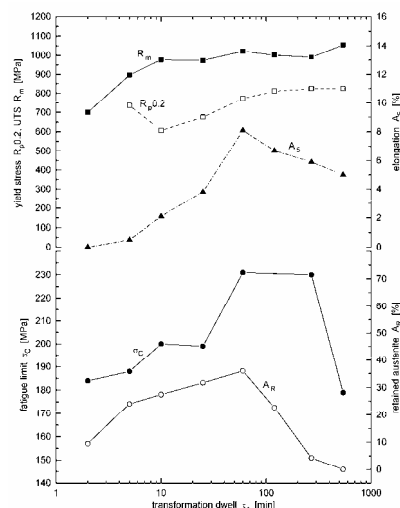


Figure 2: Mechanical properties of ADI H380a in dependence on the transformation dwell.

Pursuant to results it is possible to say, that in dependence on the transformation dwell the ADI with high variety of mechanical properties can be produced. However, the optimal combination of mechanical properties of ADI obtained by isothermal transformation at the temperature of 380°C is reached for transformation dwell of 60 minutes.

### ACKNOWLEDGMENTS

Presented studies were partially supported by grant project BD 135 3021 of Technical university of Brno, Faculty of Mechanical Engineering.

### REFERENCES

- [1] I.C.H. Hughes.: Nodular Cast Iron. Brit. Foundryman Vol. 74 (1981), p. 229.
- [2] J.R. Keough : Foundry Management and Technology Vol. 123 (1995), Nr. 11, p. 27.
- [3] E. Dorazil: High Strength Austempered Ductile Cast Iron (Horwood, Chichester 1991).
- [4] K. Hornung : Heat Treatment of Metals (1986), Nr. 4, p. 87.
- [5] T. Podrábský, E. Dorazil: Giesserei-Praxis (1991), Nr. 8.

# Investigation of an atmospheric-pressure radio-frequency capacitive plasma jet

Stefan Haslinger, Johannes Hell, Johann Laimer  
 Institut für Allgemeine Physik  
 Vienna University of Technology  
 Vienna, Austria  
 Email: haslinger@iap.tuwien.ac.at

**Abstract** — We have constructed a large area atmospheric pressure plasma jet (LAAPPJ). The LAAPPJ was operated with helium and argon at a gasflowrate of 1.5 mmol/s. The electrical properties of the discharge were studied by measuring the voltage and the discharge current simultaneously. Pictures of the discharge were taken with a digital camera and spectroscopic data was recorded from 200 nm to 1100 nm.

## I. INTRODUCTION

The generated atmospheric pressure glow discharge operates at a gas-kinetic temperature near room temperature. However, large area glow discharges at atmospheric pressure were considered to be rather unstable. We sustained two stable discharge modes, namely the  $\alpha$  - and the  $\gamma$  - mode [1-6]. Both modes are considered to be interesting, targeting diagnostics and technical applications, especially sterilisation, etching, deposition, surface modification and decontamination. The properties of this plasma make this atmospheric pressure plasma source an attractive alternative to vacuum plasmas that have been used in material processing applications.

## II. EXPERIMENTAL SETUP

The LAAPPJ consists basically of two planar, parallel oriented, water cooled copper electrodes with a variable gap spacing from 0.5 mm to 2.5 mm.

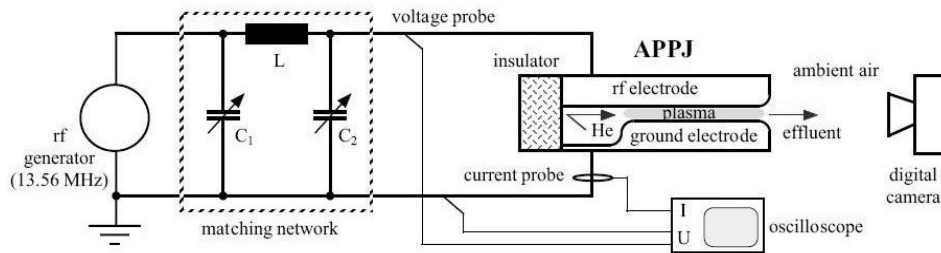


Figure 1: Experimental Setup

The discharge is maintained by a radio-frequency generator at 13.56 MHz as shown in Figure 1. A manually adjusted impedance matching network was used. Helium or Argon flows through the gap spacing and is exhausted into the ambient air.

## III. THEORY

The plasma properties can be described using a hybrid-model by measuring  $U_0$ ,  $I_0$ ,  $\phi$ . The equivalent circuit shown in Figure 2 describes electrical properties and the ion matrix sheath model [7] correlates optical measurements to sheath parameters. The insulators between the electrodes are considered by adding a parasitic capacitance  $C_{\text{parasitic}}$  in Figure 2.

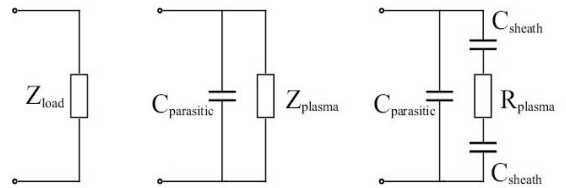


Figure 2: Equivalent Circuit

Calculation of the current density given in (1) can be done, if the plasma covered surface  $A_p$  is measured. To calculate the electric fields as in (2) and the electron densities in the bulk as in (3), it is necessary to measure the sheath thickness  $d_{\text{sheath}}$  at a gap spacing  $d$ . Whereas  $e$  is a unit of charge (C) and  $\mu_e$  is the electron mobility ( $\text{Vm}^{-1}\text{s}^{-1}$ ).

$$j_{sheath} = \frac{U_0}{A_{plasma} \sqrt{R_{plasma}^2 + \left(\frac{2}{\omega C_{sheath}}\right)^2}} \quad (1)$$

$$E_{bulk} = \frac{U_0 R_{plasma}}{(d - 2d_{sheath}) \sqrt{R_{plasma}^2 + \left(\frac{2}{\omega C_{sheath}}\right)^2}} \quad (2)$$

$$n_{bulk} = \frac{(d - 2d_{sheath})}{e\mu_e A_{plasma} R_{plasma}} \quad (3)$$

#### IV. RESULTS AND DISCUSSION

Our optical measurements of the sheath thickness and the calculations from the equivalent circuit show that there has to be paid more attention on the correct determination of the sheath thickness in order to calculate electric fields as in (2) and electron densities as in (3) in the  $\alpha$ -mode. Therefore we obtain an electron density up to  $10^{12} \text{ cm}^{-3}$  in the bulk.

The sheath breakdown at a critical electron density ends up in the  $\gamma$ -mode and a higher electric field in the sheath [7]. Therefore the averaged field in the sheath is much higher than in the bulk.

Optical emission spectroscopy shows that the sheath breakdown results in higher electron energies. Electronic states up to 22.7 eV in Helium and up to 13.5 eV in Argon are excited.

##### A. HELIUM DISCHARGE IN $\alpha$ - MODE

The spectrum in the  $\alpha$ -mode as in Figure 3 is dominated by NO-bands and  $\text{N}_2$ -bands in the lower spectral range. A strong O I line appears at 777 nm.

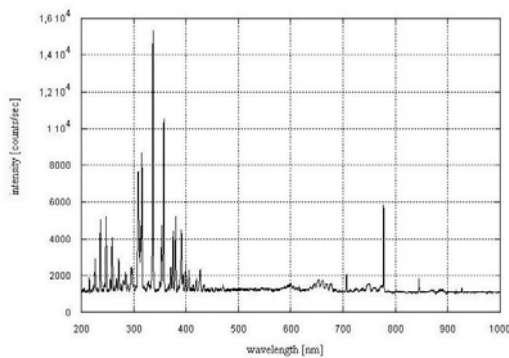


Figure 3: Spectrum of a He  $\alpha$ -discharge

##### B. HELIUM DISCHARGE IN $\gamma$ - MODE

In comparison to the  $\alpha$ -mode, the higher electron energies in the  $\gamma$ -mode excite He I states up to  $1s3s$  at 22.7 eV. In the spectral range from 300 nm to 500 nm there are still some  $\text{N}_2^+$ -bands as shown in Figure 4. Various He I lines occur more intensively.

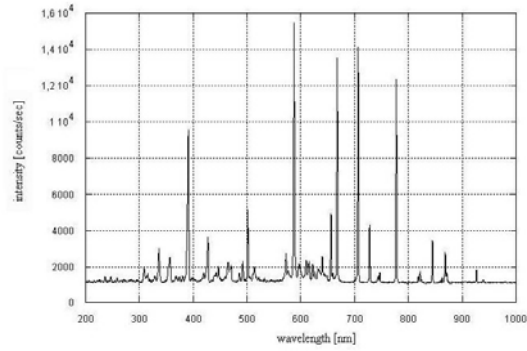


Figure 4: Spectrum of a He  $\gamma$ -discharge

#### V. CONCLUSION

The LAAPPJ operated with Helium and Argon shows two operation modes, the  $\alpha$ -, and the  $\gamma$ -mode. The equivalent circuit model can be used for the description of the electrical properties and the calculations of the plasma bulk properties even if the model should be improved in respect to sheath dynamics. We assume that both, the  $\alpha$ - and the  $\gamma$ -mode can produce high densities of oxygen radicals that can be used for various applications in material science.

#### REFERENCES

- [1] Schuetze A, Jeong JY, Babayan SE, Park J, Selwyn GS, Hicks RF. IEEE Trans Plasma Sci 1998;26:1685–94.
- [2] Park J, Henins I, Herrmann HW, Selwyn GS, Jeong JY, Hicks RF, Shim D, Chang CS. Appl Phys Lett 2000;76:288–90.
- [3] Park J, Henins I, Herrmann HW, Selwyn GS. J Appl Phys 2001;89:15–9.
- [4] Park J, Henins I, Herrmann HW, Selwyn GS. J Appl Phys 2001;89:20–8.
- [5] Selwyn GS, Herrmann HW, Park J, Henins I. Contrib Plasma Phys 2001;6:610–9.
- [6] Wang S, Schultz von der Gathen V, Dobelev HF. Appl Phys Lett 2003;83:3272–4.
- [7] Raizer YP, Shneider MN, Yatsenko NA. Radio-Frequency Capacitive discharge. Boca Raton: CRC; 1995.

# 1/f noise in submicron MOSFETs

Jan Havranek and Petr Sedlak  
Department of Physics  
Brno University of Technology  
Brno, Czech Republic

Email: xhavra03@stud.feec.vutbr.cz

**Abstract** — *The objectives of this paper are experimental investigations of the nature of the 1/f noise, if the source is mobile carrier number fluctuations or a fluctuation in the mobility. Experiments were performed in low frequency range, where the 1/f noise for submicron structures as MOSFETs and HEMTs is dominant. There are a low number of carriers in the active volume of those nanoscale devices; therefore it is supposed that 1/f noise will be dominant. Thus new valuable experimental results of noise spectral density and its relation like charge carriers mean free path, mobility, dependence on temperature and electric field intensity will be obtained.*

## I. INTRODUCTION

Electrons and holes in semiconductor constitute thermo dynamical system, which fluctuates around equilibrium state. Fluctuations of macroscopic parameters are exhibit of statistical behaviors of micro processes, which proceeding in semiconductors. These processes can be partly independent on spherical coordinates like generation or recombination processes but also dependent on spherical arrangement e.g. transport carriers.

At first are fluctuations caused by quantum transitions of carriers, on the other hand are caused by carriers energy change after absorption or emission of photon. If current with current density  $\vec{J} = en\vec{v}$  leads through the sample, than the fluctuation of current density is

$$\vec{J} = en\Delta\vec{v} + ev\Delta\vec{n} \quad (1)$$

Here  $en\Delta\vec{v}$  are current fluctuation originate due to mobility carriers fluctuation which cause thermal noise and on the other hand, term  $ev\Delta\vec{n}$  in (1) represent current fluctuation due to number of carriers variation. This two mechanisms impose the most important sources of noise e.g. thermal noise, burst or RTS noise, generation-recombination (GR) noise, 1/f noise and 1/f<sup>a</sup> noise.

## II. NOISE TERM DEFINITION

In order to keeps things simple, we consider white noise of a resistor. This frequency and bias-independent noise is described in terms of a voltage by the well-known formula.

$$U_R^2 = 4 \cdot k \cdot T \cdot \Delta f \cdot R \quad (2)$$

Where  $U_R^2$  is effective noise voltage in V<sup>2</sup>, R is resistance value and member  $4 \cdot k \cdot T \cdot \Delta f$  represents power with dimension A\*V.

Since the term  $4 \cdot k \cdot T \cdot \Delta f$  represents a power, and if we normalize this power to  $\Delta f$ , we end up with a power density. Usually, this normalization is done for  $\Delta f = 1\text{Hz}$ .

$$\frac{U_R^2}{\Delta f} = S_U = 4 \cdot k \cdot T \cdot R \quad (3)$$

The term  $U_R^2 / \Delta f$  is called power noise spectral density but more appropriate term therefore is volt-

age noise spectral density. Its symbol is usually  $S_U$  and its dimension is V<sup>2</sup>/Hz. This result can be plotted against frequency. In case of our resistor, it is a constant value. For semiconductors, such a plot can also exhibit frequency dependencies, e.g. 1/f noise. In any case, such a plot shows a spectrum.

## III. 1/ NOISE

A pretty often measurable phenomenon is noise with a spectrum proportional to 1/f. This leads to the name 1/f noise. Another name is flicker noise. Present theories of 1/f noise assume that there are two sources of 1/f noise, fundamental quantum 1/f noise and excess 1/fa noise. We suggest, that flicker noise is caused by electromagnetic interactions among the fluctuators or that chemical defects and mobile impurities make source of this kind of noise.

An empirical description after Hooge is a spectrum with

$$S_U = \frac{\alpha_H \cdot U^2}{N \cdot f}, \quad (4)$$

where  $N$  means total number of moving charges in the device,  $f$  is measuring frequency and the Hooge-Parameter  $\alpha$  is a material characteristic.

Random Telegraph Signals (RTS) are fluctuations in current or voltage between discrete levels. Researchers believe that  $1/f$  noise and RTS noise originate from similar physical sources.  $1/f$  or flicker noise is a superposition of all the electrically active RTS's. In sub-micron MOS devices, the two level fluctuations are generally attributed to the capture and emission of single electron by traps in the gate oxide. The RTS, characterized by small discrete changes of drain current can provide much insight regarding the microscopic origins of the individual defects near the Si/SiO<sub>2</sub> interface. RTS can also be caused by fast interface states. These are harder to detect, however, due to much shorter time constants involved. Often the RTS signals due to the fast interface states are superimposed on the slow RTS states, and could be easily mistaken as high frequency generation-recombination noise if the time-domain analysis is not performed in a sufficiently fast oscilloscope.

#### IV. NOISE MEASUREMENT TECHNIQUE

The block diagram of the basic apparatus is shown in fig.1. Measuring set-up consists of noise voltage source, low impedance low noise preamplifier, optional passive LP or HP filter and also with computer which is served for processing of measured data and in our case also for controlling preamplifier through RS 232C interface.

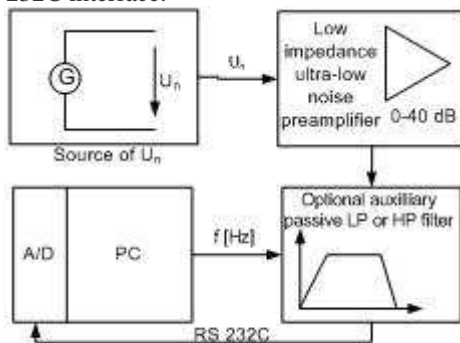


**Fig. 1:** *Measuring set-up*

Noise signal, which is random physical process, is fetched to low noise amplifier where is the extremely low signal amplified to level, which is acceptable for further processing with A/D card in computer. Due to low level of noise signal mentioned above we require unique properties of amplifier, the emphases is laid

especially on amplification (typically 100 dB and more) and also on intrinsic noise of amplifier (exemplary 10-18 V<sup>2</sup>/Hz), which must be much more lower than level of measured noise. Amplifier is also equipped with selective filters (slope at least 40 dB/dec) to obtain amplified signal in appropriate narrow band and communication interface (RS232, IEEE 488) for controlling its functions with computer.

For correct interpretation of measured data is necessary to keep certain conditions during measurement. The main effects which may influence measured data are:

- Modification of temperature, magnetic or electric field during measurement
- Disturbance of 50 Hz signal
- Drop of power supply voltage
- Process must be stationary and ergodic

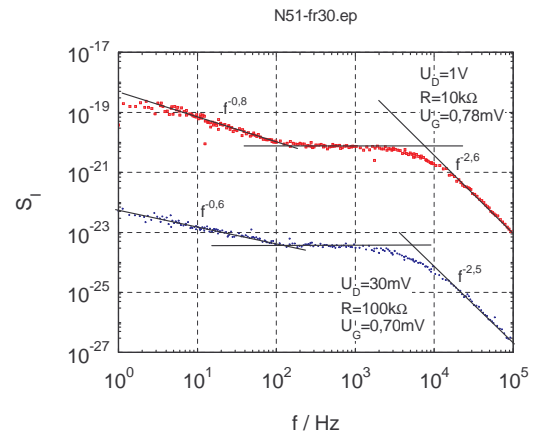


**Fig. 2:** *The current noise spectral density vs. frequency for sample N51*

#### V. CONCLUSION

Description of  $1/f$  noise sources in submicron MOSFETs transistors has been carried out. Measuring set-up block diagram and resulting current noise spectral density was shown. Noise spectroscopy is one of the promising methods for non-destructive testing of electronic components and knowledge of noise sources in MOSFETs is also very important in transistor downscaling.

#### VI. REFERENCES

- [1] J. Havranek and M. Blaha. Stochastic processes in MOSFET transistors, In Proceedings of the 10th Student Conference on electrical engineering and informatics, pages 7–11, Pilsen, Czech Rep. September 2006.

# Nonlinear Spectroscopy of Metallic and Rock Samples

Stepan Hefner, Josef Sikula (Faculty Mentor) and Martin Blaha

Department of Physics  
FEEC, Brno University of Technology  
Brno, Czech Republic

Email: {xhefne00,xblaha10}@stud.feec.vutbr.cz, sikula@feec.vutbr.cz

**Abstract** — Present ultrasonic non-destructive testing (NDT) methods of material are mainly based on analysis of elastic wave reflection, absorption and interference. This paper describes analysis, principles and apparatus for nonlinear ultrasonic spectroscopy of rock and metallic samples and also discusses their limitations. The nonlinear ultrasonic spectroscopy is used to investigate cracks and defects in samples and also is used to detect rate of samples damage.

## I. INTRODUCTION

Nonlinearity of cracks and defects are sources of nonlinear signal distortion and then amplitude of higher harmonics is used as a measure of sample quality and homogeneity. We are used non-linear effects of wave propagation and creation of higher harmonic signals in the vicinity of defects. In the considered case the interaction of the waves amplifies the non-linear effects, which give information on material characterization by non-destructive testing.

These effects were observed by two basic groups:

- A) measurements using a single-frequency harmonic ultrasonic signal. Defects are sources of anharmonic atom potential energy and due to this anharmonicity, second and third harmonic signal is produced.
- B) measurements using two harmonic ultrasonic signals (intermodulation products are detected).

## II. MEASURING SETUP

Measurement of nonlinear ultrasonic spectroscopy frequency dependence requires wave generators, power amplifiers, ultrasonic exciters and sensor, amplifier with filter of competent quality and also quality digitising signal device. The control software is important, not only for measuring, but also for further processing of measured data.

Our apparatus for automatic measurement of nonlinear ultrasonic spectroscopy consists of (exciting partition) two wave generators Agilent 33220A, two

high-frequency power amplifiers WPD100 with maximal output power 100 W, two high-power piezoceramics exciter (HTP02, HTP03). Receiving part consist of filter, amplifier AMP 22 with frequency band filter. The amplified signal is led to digital oscilloscope with sampling rate 200 Msa/s. The digitised signal is stored in computer and noise spectral density frequency dependence evaluated using discrete FFT. The control software was written in Borland C++ Builder and this version is based on Windows operating system.

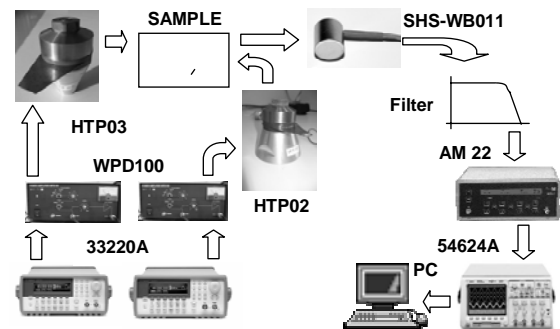


Figure 1: Measurement set-up

Measuring was performed for granite, steel and magnesian samples. Steel samples were cyclic loaded while the magnesian and granite samples were submitted to the temperature stress. Magnesian samples were also submitted under stress by plunge in liquid nitrogen.

## III. RESULTS AND DISCUSSION

Materials with undamaged structure are essentially linear in their response, while the same material, when damaged, becomes highly nonlinear. In spectrograms it's represented by harmonics and sideband generation.

### A. MEASUREMENT WITH ONE HARMONIC ULTRASONIC SIGNAL

In the first case the non-linearity gives rise to another harmonic signal of frequency  $f_v$  plus further additional frequency signals, according to Fourier series expansion.

$$f_v = n f_1 \quad / n = 0, 1, 2, \dots \infty \quad (1)$$

Samples (with and without damage) were tested by method with one harmonic exciting ultrasonic signal, where amplitude of higher harmonics signal were used for the measurement of the sample destruction (see Fig. 2). Exactly second, third and fifth harmonic signal components of response were investigated (see Fig. 3). After cyclic loaded process amplitude of third and fifth harmonic components was higher considering base harmonic signal.

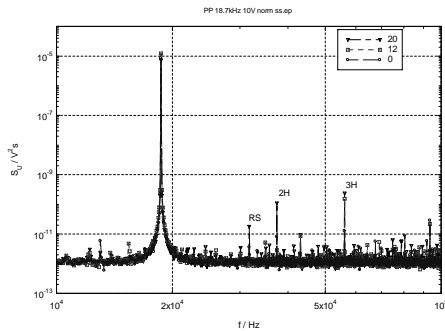


Figure 2: Frequency spectrum of three steel cyclic loaded samples (0, 12 000 and 20 000 cycles). Frequency of first harmonic is 18.7 kHz.

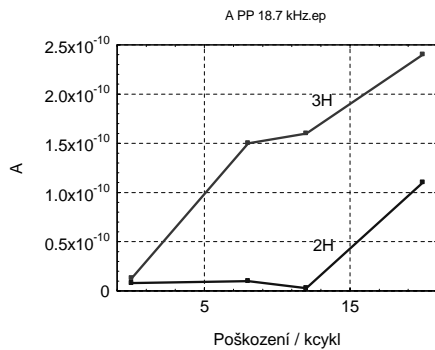


Figure 3: Second and third harmonic versus cyclic loading (frequency of first harmonic is 18.7 kHz).

#### B. MEASUREMENT WITH TWO HARMONIC ULTRASONIC SIGNALS

In the second case, where two exciting frequencies  $f_1$  and  $f_2$  were used, other subharmonic signals with basic frequency  $f_v$  arise, according to the following equation.

$$F_v = / \pm m f_1 \pm n f_2 / \quad / m, n = 0, 1, 2, \dots \infty (2)$$

Ultrasonic signal of heated rock and magnesian sample was analyzed at room temperature before and after warming-up. On the Fig. 4 are shown two granite samples (with and without damage), excited by one constant frequency (15 kHz) and by one variable frequency (16 to 18 kHz). For our measurements were as an optimal investigation of distances compo-

ponents. After warming-up process were amplitudes of distance harmonic components higher than amplitudes of distance components before warming-up.

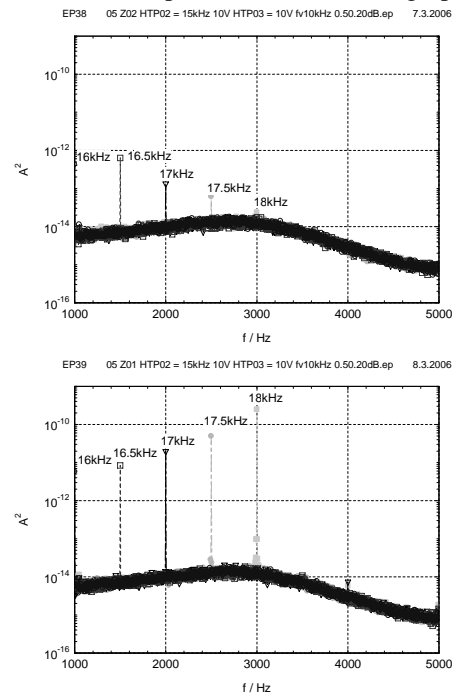


Figure 4: Frequency spectrum of granite sample without damage (upper) and with damage (lower).

#### IV. CONCLUSION

1. Ultrasonic signals and their frequency responses are changed during high temperature and mechanical ageing.
2. Relative value of third and fifth harmonics increases after thermal or mechanical treatment.
3. We suppose that this effect is related to crack creation in the sample due to high temperature gradient.

Following production areas are typical for profitable application: continuous production tests for faults – car parts, bearings, machine parts, material for production process. First-line maintenance (replacement or repair is only carried out when really necessary, not earlier) – aerospace, nuclear power plants, structure (bridge) and building supporting elements.

#### REFERENCES

- [1] K. Hájek. Experimental methods for nonlinear ultrasonic spectroscopy (analysis and application), Defektoskopie 2003, Ostrava, ISBN 2003
- [2] K.R. McCall. Theoretical study of nonlinear elastic wave propagation. J. Geophys., 1994.

# Local probe magnetisation measurements of high temperature superconductors

F. Hengstberger and H. W. Weber (Faculty Mentor)

Atomic Institute of the Austrian Universities

Vienna University of Technology

1020 Vienna, Austria

Email: hengstb@ati.ac.at, weber@ati.ac.at

**Abstract** — A magnetic scanning technique (magnetoscan) is presented, which was developed to detect local inhomogeneities in high temperature bulk superconductors. The system consists of a permanent magnet, which is moved together with a scanning Hall probe over the sample surface. The magnetic field  $B_z(x, y)$  perpendicular to the top sample surface, generated by shielding currents in the superconductor, is spatially assessed. Local variations of the critical current density  $J_c(x, y)$  and defects, such as cracks, can be resolved in this way.

## I. INTRODUCTION

High temperature superconductors for technical applications show hysteretic behaviour when exposed to magnetic fields. This is due to (artificial) defects on the nanometer scale, which act as pinning centers for the flux lines. After a magnetisation loop, remnant currents—equivalent to a gradient in the flux density—remain in the sample.

This property is exploited in bulk superconductors, i.e. cylindrical monoliths with a diameter of a few centimeters and a height of about one centimeter [1]. In this geometry the flux density gradient results in a cone like field distribution. The maximum flux density trapped inside the sample is the key property for applications and reveals the average critical current density ( $J_c$ ) the specimen is able to carry. Hall mapping measurements, where the flux density perpendicular to the top sample surface  $B_z$  is spatially recorded, are among the standard techniques to obtain the trapped field distribution.

One disadvantage of this method is that the supercurrents of the entire sample volume contribute to the total signal. Information on the local properties, such as the local critical current density  $J_c(\vec{r})$ , inhomogeneities and cracks induced during the growth of the sample, is not obtainable. The volume in which the supercurrents flow can be reduced by replacing the homogenous field by a small permanent magnet, which is placed above the scanning Hall probe. Thus shielding currents flow in an area of approximately the diameter of the permanent magnet and spatial variations of material properties can be detected. The penetration depth of the permanent magnet's field is usually less than 1 mm. This implies that a thin layer at the top sample surface is analysed.

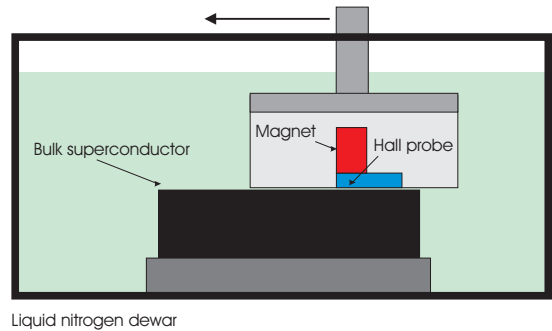


Figure 1: Setup of the measurement

## II. EXPERIMENTAL

A sketch of the measurement setup is shown in figure 1. The superconducting bulk, the Hall probe and the magnet are immersed in liquid nitrogen.

Permanent magnets with a diameter and a height ranging from 2-6 mm and 2-10 mm, respectively, reaching an induction of about 100 mT on the top of the sample are used in these experiments. A stepping motor system with a spatial resolution of  $10 \mu\text{m}$  carries out the  $x, y$ -positioning.

The active surface of the Hall probe, which is the signal averaging area of the sensor, is  $50 \times 50 \mu\text{m}^2$ . More details can be found in [2].

## III. RESULTS

Figure 2 shows the contour lines of the sample's magnetic response measured with this technique. The scan clearly reveals a number of cracks in the specimen (white arrows). Additionally, islands of high critical current density are obtained (white circles), which result from the growth kinetics of the bulk. The data were collected on a mesh of  $0.25 \times 0.25 \text{ mm}^2$  within one hour, equivalent to 0.25 seconds per datapoint.

Tests performed on tapes with a sheet thickness of only a few  $\mu\text{m}$  of superconducting material proved the sensitivity of this experiment also for small superconducting volumes. This and the ability to collect data over large sample dimensions within a short time, motivated us to

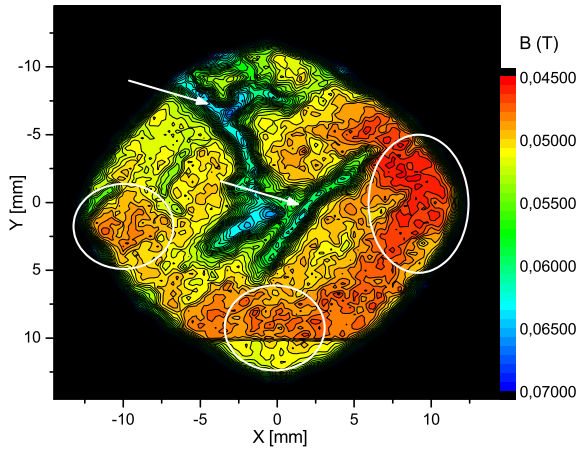


Figure 2: Cracking of a bulk superconductor

adapt this scanning technique for superconducting tapes with lengths of up to 20 cm. This method is particularly suitable whenever a fast determination of the sample homogeneity is desired prior to magnetic or transport current measurements.

#### REFERENCES

- [1] D. A. Cardwell. Processing and properties of large grain (RE)BCO. *Mat. Sci. Eng. B* 53:1–10, 1998.
- [2] M. Eisterer and S. Haindl and T. Wojcik and H. W. Weber. 'Magnetoscan': a modified Hall probe scanning technique for the detection of inhomogeneities in bulk high temperature superconductors. *Supercond. Sci. Technol.* 16:1282–1285, 2003.

# Edge isolation of the silicon solar cells - an etching paste approach

Jiri Hladik, Radim Barinka and Ivan Szendiuch  
Department of Microelectronics  
Brno University of Technology  
Brno, Czech Republic  
Email: xhladi06@stud.feec.vutbr.cz

**Abstract** — *This paper deals with investigation of a process of the edge isolation provided by the etching paste. The local etching is one of many methods suitable for opening a p-n junction and it could substitute mechanical grinding. The main aim of this work was verify the suitability of paste dispensing parameters and paste activation temperature found before. The samples were prepared and their characteristics compared with standard mechanical grinded solar cells.*

## I. MOTIVATION

After most emitter diffusion techniques, especially the  $\text{POCl}_3$  diffusion, the front contact is connected with the back contact through the emitter around the edge of the solar cell [1]. As a common technique in a company Solartec Ltd. is used mechanical grinding. This approach has some disadvantages e.g.: limitation of wafer size, high breakability by use of thin wafers and crystal damage. These undesirable features could be solved by using an etching paste.

## II. EXPERIMENT

We used an etching paste produced by a company Merck. A viscous, strong caustic etchant was applied locally with a dispenser. The etchant was extruded with compressed air through a hollow needle, working as a dispense nozzle. A precise placement was conducted with device that is capable finding an edge of the wafer (variable wafer size) The following parameter were used for dispensing (see Table 1)

Dispensing pressure	240 [kPa]
Dispensing velocity	50 [mms <sup>-1</sup> ]
Nozzle diameter	500 [ $\mu\text{m}$ ]

Table 1: The dispensing parameters

With these parameters is possible to obtain a smooth none breaking lines of dispensed paste and paste weight about 30 mg.

We conducted the tests on 100 Si single crystal wafers and this quantity we divided to 4 batches with ID 1798, 1799, 1811 and 1813. The first step was etching the saw damage and surface texturisation. Followed both side  $\text{POCl}_3$  diffusion. After diffusion were 50 wafers (batch no. 1798,1811) processed with paste etching.

The etching process consists of these steps:

1. extruding the paste on rear side of silicon wafer,
2. thermal activation of the paste on a hotplate with temperature 170 °C,
3. removing residues from the wafer by rinse with demineralised water.

Figure 1 shows etched trench after rinsing. Next technological steps were HF cleaning of phosphorus glass and deposition of  $\text{SiN}_x$ . Then the wafers were printed using silver paste for the front side and aluminium paste for the back side, fired and galvanised. Further were none edge isolated wafers mechanically grinded.

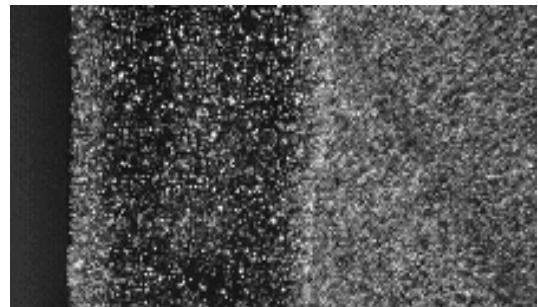


Figure 1: Detail of the etched trench-left side

After finishing technological operations the electrical characteristics were measured on a sun simulator and to localize the shunts were used Light Beam Induced Current (LBIC).

## III. RESULTS

On the pictures (Figure. 2, 3) you can see results of two batches etched cells. Samples were measured in a Solartec's sun simulator, where maximum value of  $R_{\text{shunt}}$  or  $R_{\text{sh}}$  is 11. Therefore we can measure only to this upper limit. Mechanical grinded cells have  $R_{\text{sh}}=11,0 \Omega\text{cm}^2$ .

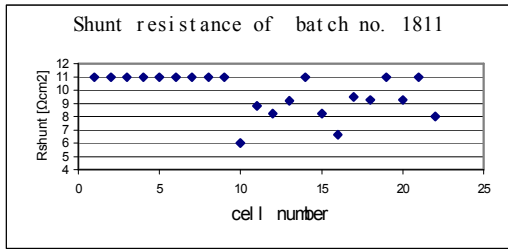


Figure 2:  $R_{sh}$  in a batch with some inhomogeneous prints.

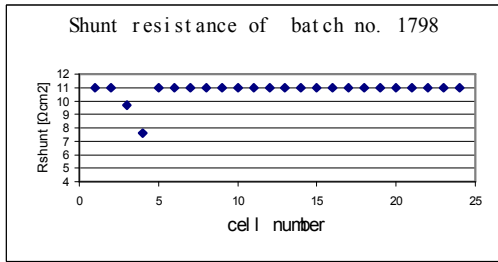


Figure 3:  $R_{sh}$  in a batch with homogenous prints.

Next electrical characteristics show Figures 4-6. The low efficiency values were probably reached due to low quality material.

The values of etched wafers show slightly better scores in comparison with none etched wafers (see Figures 4,5). This is more evident in Figure 5, short circuit current parameter. In contrast with increasing  $I_{sc}$  we can see certain correlation with decreasing fill factor (Figure 6).

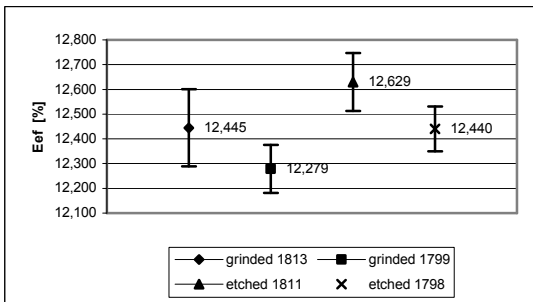


Figure 4: Efficiency- means values and deviations.

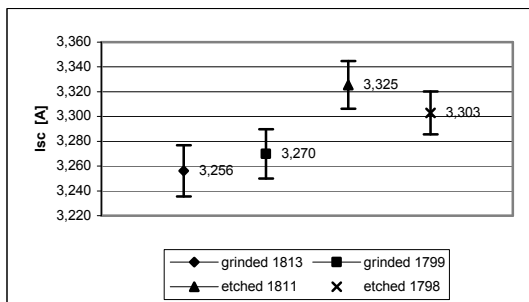


Figure 5: Short circuit current-means values and deviations.

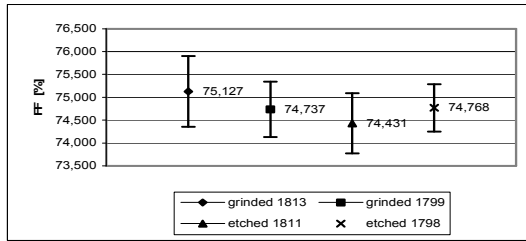


Figure 6: Fill factor-means values and deviations.

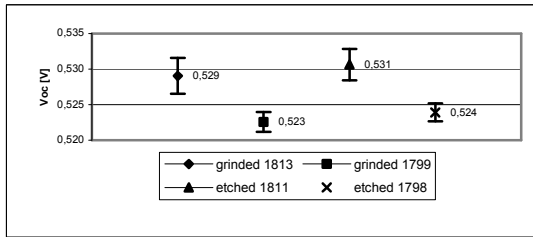


Figure 7: Open circuit voltage-means values and deviations.

Cells were further analyzed by LBIC Figure 8. It shows evident shunts although the right picture was taken from cell with  $R_{sh}=11,0 \Omega\text{cm}^2$ . Even good quality prints lead to none complete p-n junction opening. This problem can probably be solved with bigger amount of dispensed paste. Therefore cost of this operation will increase.

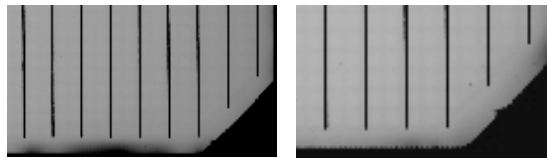


Figure 8: Left picture shows the shunts near the edge with  $R_{sh}=9,2 \Omega\text{cm}^2$  and right with  $R_{sh}=11,0 \Omega\text{cm}^2$ .

#### IV. CONCLUSION

We conducted tests with 100 single crystal silicon solar cells. A half of this quantity we isolated with an etching paste and other half with common mechanical grinding.

Results indicate that this approach is comparable to mechanical grinding. However, some shunts still remain and therefore a room for further power improvement of solar cells still exists.

#### REFERENCES

- [1] A. Hauser, G. Hahn, M. Spiegel. Comparison of different techniques for edge isolation, Proceedings of the 17th Photovoltaic Solar Energy Conference, pages 1739-1742, Munich, 2001.

# Fabrication of Cellular Ceramic Structures by Gelcasting and Rapid Prototyping

Johannes Homa and Jürgen Stampfl (Faculty Mentor)  
Institute of Material Science and Technology  
Vienna University of Technology  
Vienna, Austria  
Email: jhoma@mail.tuwien.ac.at

**Abstract** — *The fabrication of cellular ceramic structures by conventional ceramic forming techniques is either impossible or very expensive.*

*In this work an approach for the fabrication of highly complex ceramic structures by rapid prototyping is presented. By using Solidscape's T612 Benchtop a sacrificial mould is produced for casting. A ceramic slurry is poured into the mould and polymerised in situ by forming a gel. Only by the combination of gelcasting and rapid prototyping highly complex structures such as certain diesel particulate filters can be produced.*

## I. INTRODUCTION

Most of the ceramic forming techniques do not support the usage of sacrificial moulds, but this is crucial for the fabrication of very complex cellular ceramic structures. There are some rapid prototyping (RP) techniques, which are able to produce cellular ceramic structures, but they are often limited to one material and the surface quality is not sufficient. In this work an approach is introduced where a thermoplastic sacrificial mould is built by an RP process and then filled with a ceramic slurry. A ceramic forming process which is generic and can be used with a sacrificial mould is gelcasting. Only the combination of rapid prototyping techniques for the production of the mould and gelcasting can be used to produce highly complex cellular ceramic structures with a good surface quality [1,2].

Gelcasting moulds are in contrast to slip casting non-porous moulds and they can be fabricated by a wide range of materials. Moulds are usually made of metal, plastic, glass or wax whereas the mould complexity is often limited by the fabrication process. Rapid prototyping is as well an appropriate technique to produce complex moulds. In this work the Solidscape's T612 Benchtop is used to produce high complex moulds [3].

## II. GELCASTING

Gelcasting is a novel forming process for making complex-shaped ceramic and metallic parts. The technique was originally developed by Janney et al. at the Oak Ridge National Laboratory, USA, in the late 1980ies to overcome the disadvantages of ceramic injection moulding. A low viscosity slurry, consisting of ceramic or metallic powder, an aqueous or non aqueous solvent, dispersant and two organic monomers, is poured into a mold and polymerised in situ. The green body, which has a high strength, is then dried, debinded and sintered [4,5].

## III. RP-MOULDS

Gelcasting moulds need to have different properties than moulds for other ceramic processes. In contrast to slip casting the mould has to be made of a non-porous material, because the slurry solidifies by polymerisation and not by removing the liquid from the slurry. Although a wide range of materials can be used to fabricate the moulds, some materials especially silicone based materials inhibit the gelation reaction. It should be possible to remove the mould from the part and not the part from the mould, because gelcast parts have a lower strength than injection moulded parts. Effective mould release agents should be used to make the demoulding easier, but it has to be taken into consideration that some release agents might inhibit the gelation [3].

Using Solidscape's T612 Benchtop all requirements listed above are fulfilled. The thermoplastic material is non porous and does not inhibit the gelation. The demoulding of the part is done by melting the thermoplastic material at a temperature of approximately 100°C and therefore no release agent has to be used. Furthermore every desired shape, which is castable can be realised and produced within a very short period of time.

#### IV. APPLICATION

The combination of rapid prototyping techniques and gelcasting can be used to fabricate specially designed ceramic diesel particulate filter (DPF), which cannot be produced by other forming techniques. In Figure 1 a CAD model of a DPF is shown.

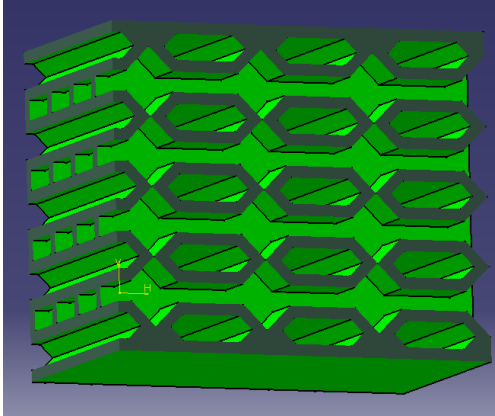


Figure 1: CAD model of a DPF

The constant wall thickness of the hexagonal channels require a sacrificial mould for casting. The mould was build with Solidscape's T612 Benchtop and cast with  $\text{Al}_2\text{O}_3$ .

In Figure 2 an already debinded and sintered DPF made of  $\text{Al}_2\text{O}_3$  is shown.

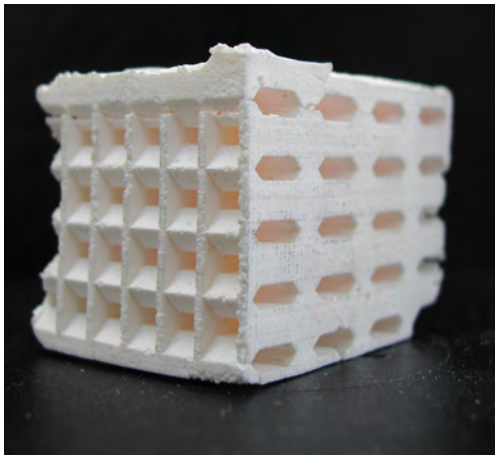


Figure 2: DPF made of  $\text{Al}_2\text{O}_3$

#### REFERENCES

- [1] J. Stampfl et al., Rapid Prototyping of Ceramic and Polymeric Cellular Materials, IFMBE Proceedings, EMBEC '02, pp 172-173, 2002.
- [2] J. Stampfl et al., Rapid prototyping and manufacturing by gelcasting of metallic and ceramic slurries, Materials Science and Engineering, pp187-192, 2002.
- [3] R. Gilissen et al, Gelcasting, A near net shape technique, Materials and Design, 21, pp251-257, 2000
- [4] M. Janney et al., Development of Low-Toxicity Gelcasting Systems, Journal of American Society, 81, pp 581-591, 1998.
- [5] M. Janney et al., Method for Molding Ceramic Powders Using water-based Gel Casting, US Patent 5028362, 1991.

#### ACKNOWLEDGMENTS

Financial support by the Austrian Research Promotion Agency (FFG) under the project "Rapid Prototyping zellulärer Keramiken" (Project-number: 810064) is kindly acknowledged.

# Structuring methods capable of building 3D parts with feature resolutions from 50 $\mu\text{m}$ to 100 nm

Robert Inführ,<sup>1,2</sup> Christina Fritscher,<sup>2</sup> Volker Schmidt,<sup>3</sup>

Ladislav Kuna,<sup>3</sup> Robert Liska,<sup>1</sup> Helga Lichtenegger,<sup>2</sup> Jürgen Stampfl<sup>2</sup>

<sup>1</sup>Institute of Applied Synthetic Chemistry, Vienna University of Technology,  
Getreidemarkt 9/163 MC; 1060 Vienna, Austria;

<sup>2</sup>Institute of Materials Science and Technology, Vienna University of Technology,  
Favoritenstrasse 9-11 A-1040, Vienna, Austria

<sup>3</sup>Institute of Nanostructured Materials and Photonics, Joanneum Research, Weiz, Austria  
Email: robert.infuehr@tuwien.ac.at, rliska@otech7.tuwien.ac.at,  
jstampfl@pop.tuwien.ac.at

**Abstract** — Three methods for building 3D parts by photopolymerisation at feature resolutions from 50  $\mu\text{m}$  to below 1  $\mu\text{m}$  are introduced.

For a Digital Light Processing based RP process organosoluble polymers, stable in an aqueous environment, were developed. Organosoluble molds made by RP proved to be suitable for the shaping of materials derived from water-based sol-gel processing.

UV Laser Micro-stereolithography photopolymers are developed and optimized to tap the full potential of the devices resolution..

Photoinitiators for Two Photon Polymerisation (2PP) are tested and developed.

## I. INTRODUCTION

Rapid Prototyping (RP) is a suitable manufacturing method for fabricating structures with high geometric complexity and heavily undercut features, which cannot easily be fabricated by traditional manufacturing methods. [1]

Nowadays RP is increasingly employed to produce tools or even to manufacture production quality parts in small numbers. RP parts can also be used as molds to expand the range of final part materials.

## II. STRUCTURING METHODS

For fabrication of 3D parts by **Digital Light Processing (DLP)**, a CAD model is sliced into thin layers and every slice is projected into the bottom layer of a resin tank by a micro-mirror array. The light sensitive resin is cured within a few seconds, and after moving up the build platform, the next layer is exposed. The feature resolution is 50  $\mu\text{m}$  in the xy-plane and 30  $\mu\text{m}$  in z-direction.

Commercial light-sensitive resins for Rapid Prototyping of cellular materials are often unsuitable for different molding techniques since removal of the mold uses thermal decomposition at temperatures of up to 600°C.

For molding thermo-sensitive sol-gel materials, photocurable resins were developed, which give organosoluble polymers, that are stable in an aqueous environment. Such organosoluble molds (Figure 1) made by RP proved to be suitable for the shaping of materials derived from water-based sol-gel processing.

In this way, hierarchically structured organic-inorganic hybrid materials were shaped [2,3]. Figure 2 shows the wet nanostructured silica gel after the mold was removed.

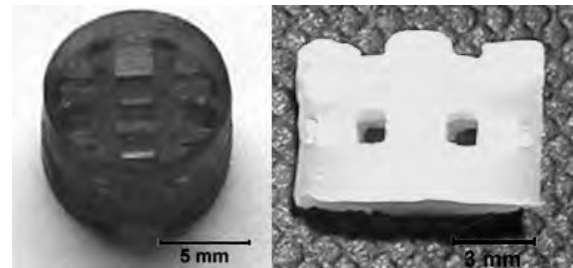


Figure 1:  
Organosoluble mold

Figure 2: Molded nano-  
structured wet silica gel

With a recently acquired **UV Laser Micro-stereolithography** unit higher resolutions can be achieved. The process involves the photocuring of polymer parts in layers by tracing a laser beam on the surface of a liquid photopolymer. Once one layer is completely traced, it is lowered a small distance into the liquid and a subsequent layer is traced, adhering to the previous layer.

Figure 3 shows a cellular 3D structure that was built by UV Laser Micro-stereolithography. Currently photopolymers are developed and

optimized to tap the full potential of the devices resolution ( $xy \sim 5 \mu\text{m}$ ,  $z \sim 10 \mu\text{m}$ ).

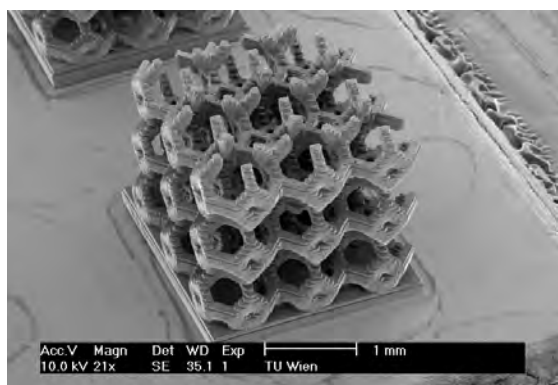


Figure 3: Cellular structure made by UV-Laser Microstereolithography

The **Two Photon Polymerisation (2PP)** process employs femtosecond laser pulses of 800 nm which are focused into the volume of a photopolymer, being transparent at the laser wavelength. Solidification is performed in a highly localised volume due to the quadratic dependence of the two-photon absorption rate on the laser intensity. When two photons of 800 nm are absorbed simultaneously by a suitable photoinitiator they act as one 400 nm photon to start polymerisation. By 2PP feature resolutions below the diffraction limit of the used light are possible. Smallest lateral resolution that can be obtained is around 100 nm [4].

By now we found a new highly cross-conjugated photoinitiator for 2PP which makes it possible to build parts at a photoinitiator concentration below 0,005 wt% (Figures 4,5).

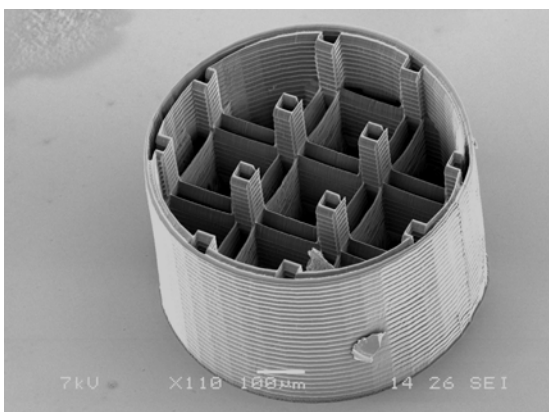


Figure 4: Part built by Two Photon Polymerisation (2PP)

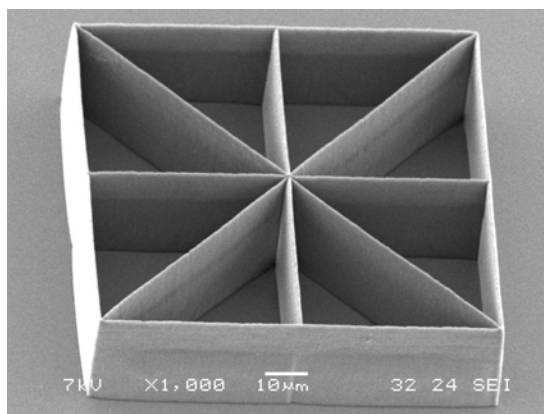


Figure 5: Part built by Two Photon Polymerisation (2PP)

#### ACKNOWLEDGMENTS

Financial support by the “Austrian Nano Initiative” under contract no. N-703 and TU innovative project “3D-Microfab” is kindly acknowledged.

#### REFERENCES

- [1] Stampfl, J.; Wöß, A.; Fratzl, P.; Seidler, S.; „Rapid Prototyping of Ceramic and Polymeric Cellular Materials“; IFMBE Proceedings, editors: H.Hutten, P. Krösl, EMBEC’02, Vienna; 172-173
- [2] Fritscher, C.; dissertation (not yet completed); Institute of Materials Science and Testing, Vienna University of Technology ;
- [3] Brandhuber, D., Hüsing, N.; Raab, C.K.; Torma, V.; Peterlik, H.; „Cellular mesoscopically organized silica monoliths with tailored surface chemistry by one-step drying/extraction/surface modification processes.“; J. Mater. Chem.; 15; (Advance Article); (2005)
- [4] Kenji Takada; Hong-Bo Sun; Satoshi Kawata; „Improved spatial resolution and surface roughness in photopolymerization based laser nanowriting“; Applied Physics Letters; 86, 071122; (2005)

# Hybrid Inorganic-Organic Materials by Coordinative Linkage between Polymers and Metal Alkoxides

Sorin Ivanovici and Guido Kickelbick  
Institute of Materials Chemistry, Vienna University of Technology,  
Getreidemarkt 9, A1060 Vienna, Austria  
Email: sorin.ivanovici@tuwien.ac.at

**Abstract** — The aim of this study is the synthesis of various hybrid inorganic-organic polymers using monomers carrying  $\beta$ -keto ester sites coordinated to metal alkoxides and the modification of different polysiloxanes by metal alkoxides. Various  $\beta$ -keto esters were synthesized and their coordination behavior with Ti- and Zr-alkoxides was investigated. The thus obtained complexes were used as (co)monomers in controlled radical polymerizations and applied in sol-gel reactions to form nanocomposites. Polysiloxane block copolymers modified with Ti-alkoxides were also synthesized. The metal-alkoxides functionalities were hydrolyzed to form the respective metal oxides. The study showed that depending on the solvent employed in the process hybrid nanoparticles or gels could be obtained.

butyl acetoacetate – HAAEMA, HAAPMA, HAABMA) were carried out in stoichiometric ratios 1:1 and 1:2 in different solvents to investigate the coordination of the  $\beta$ -keto esters ligands. EAA which does not carry an additional unsaturated group was used as a model compound. Scheme 1 presents the general pathway for the synthesis and coordination of  $\beta$ -keto esters ligands to metal alkoxides. The products were investigated by means of  $^1\text{H}$  NMR, 2D NMR, FT-IR, and single crystal X-ray diffraction experiments. The full characterization of these compounds revealed that the  $\beta$ -keto esters acted as chelating ligands in all cases. Ti-coordination compounds presented a dynamic behavior in solution due to ligand exchange reactions.

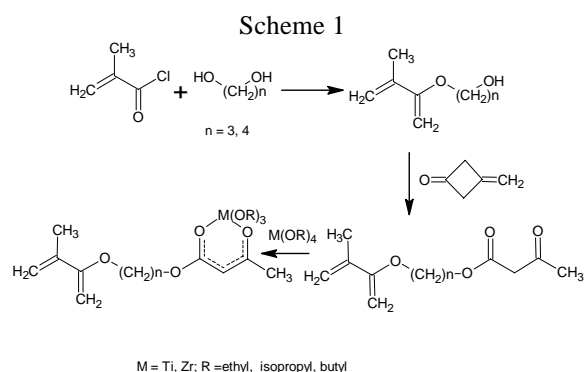
## I. INTRODUCTION

Structured inorganic-organic nanocomposites are promising systems for a variety of applications. It is desirable to use well-defined molecular building blocks in their preparation due to a better prediction of structure-property relationships.[1, 2]  $\beta$ -Keto esters are regularly used for the modification of transitional metal alkoxides to obtain a better control of their reactivity in the sol-gel process.[3] When the ligand carries in addition an unsaturated functionality the metal complexes can be transferred into nanocomposite materials by further reactions such as polymerizations.[4] Polysiloxanes as inorganic polymers show other properties than typical organic polymers such as polymethacrylates and are therefore an interesting polymer class.[5]

## II. RESULTS AND DISCUSSION

### A. HYBRID POLYMERS CONTAINING METAL ALKOXIDES

The reactions between  $\text{M}(\text{OR})_4$  ( $\text{M} = \text{Ti}, \text{Zr}$ ;  $\text{R} = \text{Et}, ^i\text{Pr}, \text{Bu}$ ) and different  $\beta$ -keto esters (ethyl acetoacetate-EAA, methacryloyloxy ethyl, propyl and



When  $\text{Zr}(\text{O}^i\text{Bu})_4$  was coordinated a decomposition of the  $\beta$ -keto esters was observed.

From all the coordination compounds investigated  $\text{Ti}(\text{OEt})_3\text{AAEMA}$  and  $\text{Ti}(\text{O}^i\text{Pr})_3\text{AAEMA}$  were further used in homo- and copolymerizations with MMA because of their well-defined structure. Polymers without metal coordination were investigated with size exclusion chromatography (SEC) for reasons of comparison (Figure 1). The analyses showed the incorporation of both monomers in the polymer chains and a quite low polydispersity index (1.41) which is in agreement with the different reactivity of the two monomers (HAAEMA and MMA).

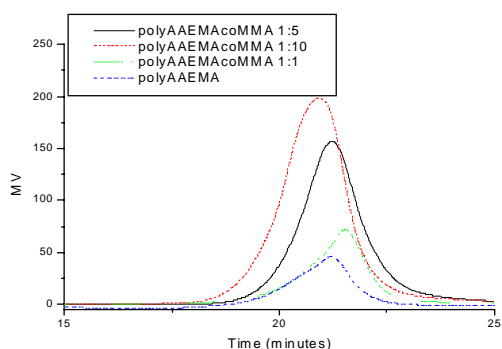
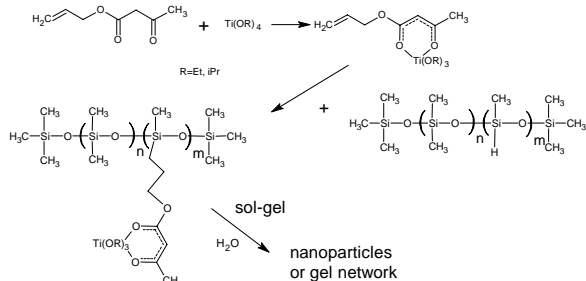


Figure 1. SEC plot of PolyAAEMA-MMA copolymers in 1:1, 1:5 and 1:10 ratio between the monomers

NMR and FT-IR data of the metal containing polymers showed the successful incorporation of the metal alkoxides in the polymers. Thermogravimetric analyses revealed a slight increase of the decomposition temperature by metal alkoxide incorporation which is further improved after applying the sol-gel process to produce metal oxide containing polymers.

#### B. POLYSILOXANES MODIFIED WITH TITANIUM OXIDES: NANOPARTICLES AND GELS

In a different approach nanocomposites based on polysiloxanes and metal oxides were prepared.  $\beta$ -Keto esters with double bonds active for hydrosilylation were coordinated to metal alkoxides ( $M(OR)_4$ ;  $M = Ti, Zr$ ;  $R = \text{ethyl, butyl, isopropyl}$ ). Coordination was proved by NMR and FT-IR spectroscopy. Hydrosilylation reactions between a series of  $\beta$ -keto esters coordinated to metal alkoxides and different dimethylsiloxane-*block*-hydrosiloxane polymers resulted in a series of metal containing polysiloxanes. The structure of these copolymers was investigated by spectroscopic methods which showed a complete functionalization of the polysiloxane chains. In a second step the metal alkoxide functionalities were hydrolyzed to form the respective metal oxides (Scheme 2).



Scheme 2. The synthesis of hybrid materials based on Ti oxide and polysiloxanes

Depending on the solvent used in the subsequent sol-gel process nanoparticles or bulk gels were obtained. Applying the sol-gel process in alcohols resulted in nanoparticles most likely due to the coiling of the polysiloxane chains in the alcohol based on the low solubility. The resulting structures are fixed by condensation reactions of the hydrolyzed metal alkoxides. The nanoparticles were investigated by TEM, NMR, FT-IR, and dynamic light scattering (DLS). Figure 2 shows the TEM and DLS analyses for one characteristic sample. The size was dependent on the modified polysiloxane concentration. When toluene was employed as a solvent a bulk gel network was formed due to the unfolding of the polysiloxane chains based on the high solubility of the poly(dimethylsiloxane) chains in this solvent, which led to the rapid growth of the nucleation centers into a gel network.

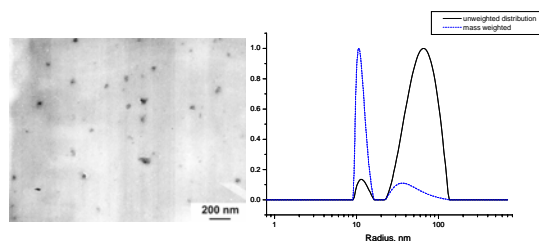


Figure 2. TEM picture (left) and DLS distribution function (right) of Ti oxide nanoparticles modified with polysiloxanes

#### ACKNOWLEDGMENTS

Financial support of this work by the Austrian Fonds zur Förderung der wissenschaftlichen Forschung (FWF, Project nr.: P17424) is gratefully acknowledged. We thank Dr. Michael Puchberger for the help with 2D NMR analyses, Helmut Fric for crystal structure analyses, and Christoph Rill for the help with TEM analyses.

#### REFERENCES

- [1] G. Kickelbick, *Prog. Polym. Sci.*, **2003**, 28, 83-114.
- [2] C. Sanchez, G. J. de A. A. Soler-Illia, F. Ribot, T. Lalot, C. R. Mayer, V. Cabuil, *Chem. Mater.* **2001**, 13, 3061-3083.
- [3] U. Schubert, *J. Mater. Chem.*, **2005**, 15, 3701-3715.
- [4] M. In, C. Gerardin, C. Sanchez, *J. Sol-Gel Sci. Technol.*, **1995**, 5, 101-114.
- [5] Abe, T. Gunji, *Prog. Polym. Sci.* **2004**, 29, 149-182.

# Copper matrix composites with multi-wall carbon nanotubes

Thomas Janhsen and Christian Edtmaier (Faculty Mentor)

Institute for Chemical Technologies and Analytics  
Vienna University of Technology  
Vienna, Austria

Email: tjanhsen@mail.tuwien.ac.at

**Abstract** — Carbon nanotubes were highly dispersed and within a copper matrix for the production of metal matrix composites. The matrix metal copper was built up by wet-chemical precipitation and conventional powder metallurgical methods respectively. Intermediate layers of copper or nickel were also tested.

The most interesting properties comprise the thermal conductivity and the coefficient of thermal expansion. The weight fraction of the carbon nanotubes is varied between 0.5 and 3 w/w. The investigated composites showed thermal conductivities in the range of  $300 \text{ W}\cdot\text{m}^{-1}\cdot\text{K}^{-1}$  with equal or lower coefficients of thermal expansion than copper.

## I. INTRODUCTION

The focus of this project lies within the development of materials with high thermal conductivity, which are exposed to extreme environments. The research is focused on the preparation of copper multi-wall carbon nanotube (or short MWCNT) composites with regard to a high overall thermal conductivity and a low coefficient of thermal expansion (CTE) together with a good machinability. Main applications of these new materials are heat sinks.

## II. MATERIAL SYSTEMS

Copper was chosen as matrix metal because of its high thermal conductivity ( $401 \text{ W}\cdot\text{m}^{-1}\cdot\text{K}^{-1}$ ) and its good machinability.

As MWCNTs exhibit superior thermal properties, given in [1] (thermal conductivity approx.  $3000 \text{ W}\cdot\text{m}^{-1}\cdot\text{K}^{-1}$ , radial and axial CTE, given in [2] and [3], between  $0.5\text{--}3.5 \cdot 10^{-6}\cdot\text{K}^{-1}$ ) they are in best compliance with the requirements for these composites.

## III. PRODUCTION OF THE COMPOSITES

The low wettability between the matrix metal and the reinforcement (surface tension [4] for copper:  $1270 \text{ mN}\cdot\text{m}^{-1}$  and for MWCNTs:  $100\text{--}200 \text{ mN}\cdot\text{m}^{-1}$  respectively) is one of the main problems in the pro-

duction of these composites, as well as the high degree of entanglement of the Nanotubes.

### A. POWDER PROCESSING

Wet-chemical electroless precipitation reactions were employed for the creation of a sufficient interface [5] and the build-up of the matrix. These methods allow homogeneous dispersions [6] of the MWCNTs with different dispersing agents in aqueous solutions of copper-precursor salts ("molecular level mixing"). For better deagglomeration of the MWCNT-carpets ultrasound was applied. When the MWCNTs are evenly distributed in the solution, the precursor salts are reduced to give the corresponding metals.

An alternative way for the optimisation of the interface is first to cover the MWCNTs with intermediate layer of appropriate metals and subsequently building up the matrix. In this two-way approach also combinations of different metals for coating of the MWCNTs and the matrix metal were investigated, e.g. nickel/copper (Ni/Cu).

### B. COMPACTION OF POWDERS

The dried powders gained by these methods were further reduced under hydrogen atmosphere. Cuboids with dimensions of  $36 \times 10 \times \text{approx. } 7 \text{ mm}$  were formed by cold-pressing and subsequently sintered and hot-pressed to achieve high densities. With these samples the thermal conductivity and the CTE were determined.

## IV. RESULTS

### A. INTERFACE OPTIMISATION

Coating of the MWCNTs by wet-chemical methods yielded homogeneous and dense layer of metal (copper, nickel, titanium, molybdenum etc.) on the MWCNTs (see Figure 1, picture taken with a FEI Tecnai F20-FEGTEM).

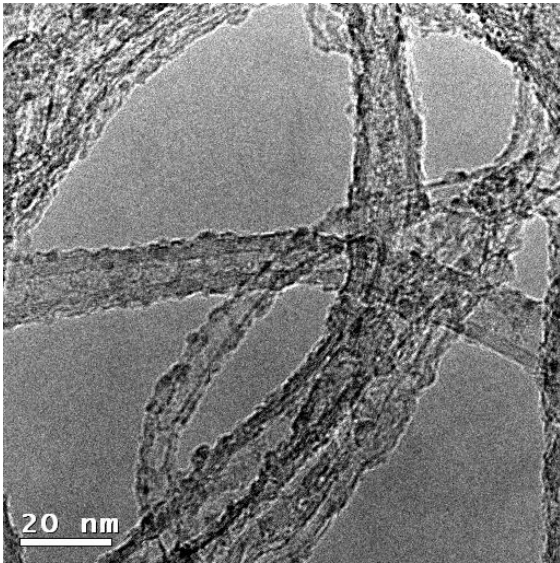


Figure 1: Copper-coated MWCNTs

#### B. PROPERTIES

1. By optimising the production process of the samples densities could be enhanced up to values between 95 and 99 % of the theoretical (i.e. calculated) densities.
2. Diffusivity and thermal conductivity were measured by flash method (ANTER Flashline 3000) and gave values up to  $280 \text{ W}\cdot\text{m}^{-1}\cdot\text{K}^{-1}$  (see Figure 2).
3. For samples with 0.5 and 1 w/w of MWCNTs respectively, coated with 0.25 w/w nickel, values of CTE equal to copper (see Figure 3) were determined (horizontal dilatometer, NETZSCH DIL 402-C).

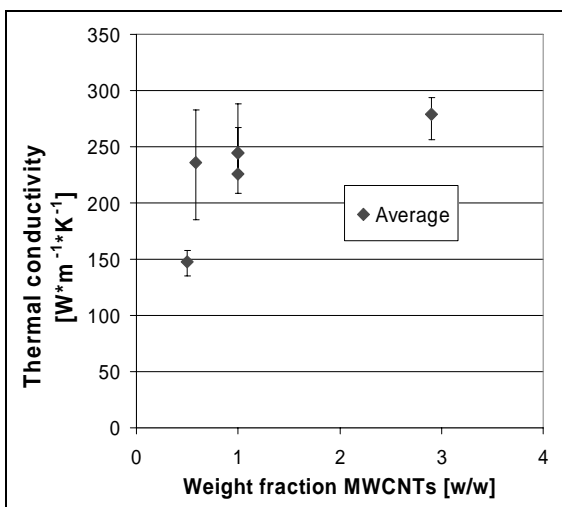


Figure 2: Thermal conductivity and weight fraction of MWCNTs

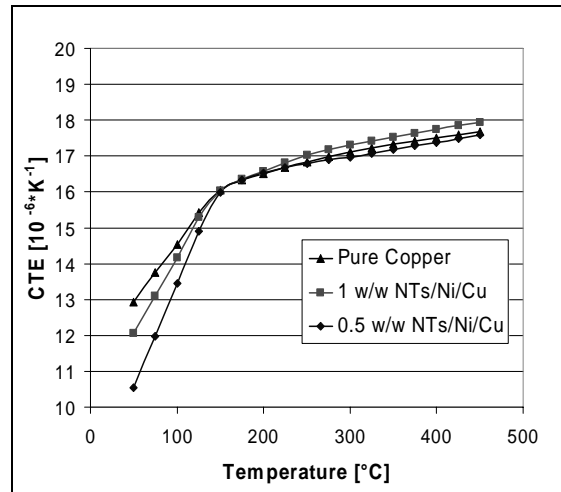


Figure 3: CTE as function of temperature

#### ACKNOWLEDGEMENTS

This work has been performed within the framework of the Integrated European Project „Ex-treMat“ (contract NMP-CT-2004-500253) with financial support by the European Community. It only reflects the view of the authors and the European Community is not liable for any use of the information contained therein.

#### REFERENCES

- [1] P. Kim et.al. Thermal transport measurements of individual multiwalled nanotubes. *Phys. Rev. Lett.*, 87(2):215502-1 – 215502-4, 2001.
- [2] R.B. Pipes and P. Hubert. Helical carbon nanotube arrays: thermal expansion. *Composites Science and Technology*, 63(11):1571-1579, 2003.
- [3] R.S. Ruoff and D.C. Lorents. Mechanical and thermal properties of carbon nanotubes. *Carbon*,33(7):925 – 930, 1995
- [4] F.Z. Kong. Continuous Ni-Layer on multi-wall CNTs by an electroless plating method. *Surface and coatings*, 155(1):33 – 36, 2002
- [5] Li-Ming Ang. Decoration of activated carbon nanotubes with copper and nickel. *Carbon*, 38(2000): 363 – 372, 2000
- [6] J. Ning et.al. Surfactants assisted processing of carbon nanotubes-reinforced  $\text{SiO}_2$  matrix composites. *Ceramics International*, 30:63 – 67, 2004

# Influence of filler particle size on structure and properties of polypropylene/clay composites

Daniela Klimová, Viera Khunová, Pavol Lukáč  
Slovak University of Technology, Faculty of Chemical and Food Technology,  
Institute of Polymer Materials, Department of Plastics and Rubber,  
Radlinského 9, 812 37 Bratislava,  
E-mail: danka.klimova@stuba.sk

**Abstract** — *In the work the role of the type of organic modifiers (silane and alkylammonium) on the filler particle size and structure of melt prepared PP/clay composites was investigated. It was found that silane modification led to formation of conventional micro-structured composites with high adhesion on PP/MMT interphase. Modification of MMT by alkylammonium led to formation of exfoliated nanocomposites with improved mechanical, thermal and gas barrier properties.*

## I. INTRODUCTION

Polypropylene (PP) is a semi-crystalline engineering thermoplastic and it is known for its balance of strength, modulus and chemical resistance. It has many potential applications in automobiles, appliances and other commercial products in which creep resistance, stiffness and some toughness are demanded in addition to weight and cost savings[1]. The most used clay for nanocomposites preparation is montmorillonite (MMT). The key factor in property improvement plays filler particle size and shape. For composites with high mechanical properties, however, the silicate nanolayers must be separated (exfoliated) and uniformly dispersed in the polymer matrix [2]. To achieve exfoliated structure of composites, MMT has to be modified.

This work investigated the role of filler particle size on structure and properties of PP/MMT composites. The main attention was given to examination of influence of silane and alkylammonium organic modifiers on the characterization of mechanical, thermal and gas barrier properties of PP-organoclay composites.

## II. EXPERIMENTAL

Homo polypropylene was supplied by Slovnaft, montmorillonite was supplied by Envigeo. The composites were prepared by melt compounding polypropylene and montmorillonite clay in a twin screw extruder (6.7kg/hour, rotor speed 214min<sup>-1</sup>, barrel

temperature profiles from 180°C to 200°C). All composites contained 5% w/w of clay which is considered to be an appropriate level for polymer nanocomposites.

Micro-structure of the prepared composites was investigated by using electron scanning microscopy. The thermal behaviour of the PP/clay composites was measured by thermogravimetric analysis on Perkin-Elmer TGA 7 analyser. Mechanical testing was realised under ASTM D 638M Type M-III tensile dumbbell test. Pieces were cut from the compression moulded sheets and tensile strength was measured at ambient temperature using a crosshead speed of 50 mm.min<sup>-1</sup>.

The determination of barrier properties of prepared composites to air was measured by the constant volume method at room (CSN 64 0115) at room temperature and pressure 8 bar. The permeability was calculated from the linear pressure increase and free volume of the equipment.

## III. RESULTS

The study of structure of composites modified by different intercalants revealed that modification by silane did not lead to formation nor intercalated neither exfoliated structure montmorillonite (Fig.1a,b). The structure of composites is typical of those of conventional microcomposites (Fig.1a). From the detailed view it is evident, that silane modification increased filler/matrix adhesion.

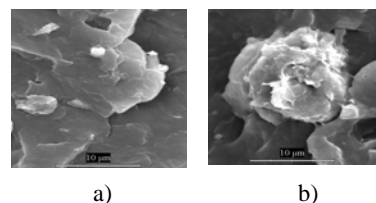


Fig.1: Structure of MMT modified by silanes:  
a) overall view, b) detail

Unlike silane treatment, modification of MMT by octadecylamine led to formation of exfoliated

nanocomposite structure (Fig.2a) with the high degree of filler particle dispersion and homogeneity (Fig.2b).

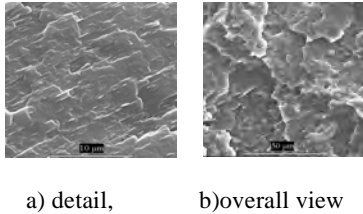


Fig.2: Structure of MMT modified by octadecylamine: a)detail, b) overall view.

Thermo gravimetric analysis has been carried out to estimate the thermal stability of polypropylene and its composites (Fig.3). The analysis has confirmed positive influence of filler on thermal stability in untreated as well as in both, silane and alkylammonium modified MMT/PP composites.

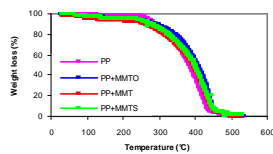
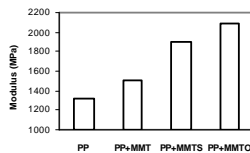


Fig. 3: Influence of clay on thermal properties of PP/clay composites

Positive influence of studied organic modifiers was observed also in investigation of mechanical properties. The values of modulus are shown in Fig.4.

Fig.4: Influence of clay modification on mechanical properties of PP/clay composites

The strongest impact of the clay modification was observed in barrier properties study. In composites



prepared with MMT and MMTS, due to poor dispersion and agglomeration of filler particles, permeability dropped from the level  $10^{-18}$  up to  $10^{-15}$   $m^2.Pa^{-1}.s^{-1}$ . On the other hand, polypropylene nanocomposites containing MMTO showed increases of gas barrier properties up to 40 %.

#### IV. CONCLUSION

In the work it was shown that the silane modification of MMT led to improvement of filler/polymer interphase, but has no effect on the interphase spacing of clay. Modification of MMT by alkylammonium led to formation of exfoliated nanocomposites with improved application properties.

#### ACKNOWLEDGMENTS

The work was supported by Scientific Grant Agency of the Ministry of Education of Slovak Republic VEGA 1/2110/05

#### REFERENCES

- [1] Y. Zhou et al., J. Mat.Sci and Eng. A 402, (2005), 109-117
- [2] M. Modesti, Polymer 46 (2005), 10238

# New Approach to Electrochemical Sensor Electrodes Construction

Klosová, Hrdý and Hubálek (Faculty Mentor)  
Faculty of Electrical Engineering and Communication  
Department of Microelectronics  
Brno University of Technology  
Brno, Czech Republic

Email: {Klosová}k\_kacka@yahoo.com  
{Hrdý}hrdyr@email.cz  
{Hubalek}hubalek@feec.vutbr.cz

**Abstract** — *A new method of fabricating sensing elements of microsensors is described. The method consists in producing nanostructures on active areas of the microsensors. Firstly, nanoporous alumina which serves as a template is created on the active areas. Then the nanopores in the template are filled with a metal by electrodeposition. After dissolving the template, highly ordered nanostructures are obtained.*

## I. INTRODUCTION

In today's world, the main aims in the field of sensor technology are to miniaturize all electronic devices including electrochemical microsensors and their sensing elements. In order to keep their qualitative properties it is essential to create more indented surface on a small area. Therefore on the active areas of the sensing elements arrayed nanostructures are fabricated.

First step in fabrication of microsensors is creating microstructures (interdigitated microelectrodes) on a Si wafer which is covered by silicon nitride. The microstructures are created by electron beam lithography and lift-off method (which serves the purpose of Au coating). The second step consists in creating of an aluminium layer and its anodization. The process of anodization results in a formation of nanopores. Anodized nanoporous alumina is then used as a template for metal electrodeposition.

## II. EXPERIMENTS AND RESULTS

### A. CREATION OF NANOPOROUS TEMPLATE

Anodized porous ceramic is an interest of many scientists for a long time. It can be applied in various electronics, magnetic and optical devices [1]. A lot of methods can be employed for fabrication of arrayed porous nanostructures like lithography, metal deposition through template and deposition of material into a selfordered template. Lithography provides the best control over the formation, proportions and order of

nanoparticles. However it is the most expensive method of the creation of templates.

For the creation of hexagonal pore array can be used anodized alumina, as a basic material, deposited on N-type Si substrate. The thickness of deposited layer is 2  $\mu\text{m}$  [2]. The fabrication of a nanoporous ceramic is a simple procedure during which the pore array is formed. The diameters of the pores are ranging from 10nm to 100 nm. The deposition itself involves problems such as formation of crystalline domains and insufficient adhesion [3]. As a deposition method magnetron sputtering is used in combination with vapor deposition (VD). The aluminium layer is annealed in vacuum before the anodization process. For the anodization itself two solutions are used, namely  $(\text{COOH})_2$  and  $\text{H}_2\text{SO}_4$  which have to be intensively stirred [4]. Anodization process consists of two steps. First, only a part of the layer is anodized and then dissolved. It results in the creation of arrayed pits for the second step, in which the rest of the aluminium layer is anodized. After that, the ceramics is etched by  $\text{H}_3\text{PO}_4$  in order to open and widen the pores [5]. The result of this process is 1-2  $\mu\text{m}$  thick nanoporous ceramic structure with good dielectric properties which can be used as a template for electrodeposition of metals.

### B. FORMATION OF NANOWIRES OR NANOTUBES

The second step in fabrication of sensing element of the sensor, which follows after anodization, is creation of nanostructures. The nanoporous anodized alumina, which was fabricated on the electrode, is used as a template which the nanostructures are formed through. After dissolving the template, the required nanostructures are obtained. All technology process steps and result are shown in (fig. 1).

The width and the density of created nanostructures are given by the template. The length of nanostructures depends on amount of deposited metal, thus according to the Faraday's law (with certain limitation determined by linear and spherical diffusion) the required length of nanostructures can be achieved if the current density and the time of electrodeposition

are adequate [6]. Either nanotubes or nanowires (nanorods) can be produced by the template-based electrodeposition method. The most relevant parameters which can determine the type of nanostructure are ultrasound waves and the width of the pores. In the case of using ultrasound waves during the electrodeposition process the created nanostructures tend to be nanotubes. The diameter of the pores has a significant impact on the type of structure. The smaller is the diameter of the nanopores in the template the higher is the probability that only nanowires will be created. The dependence of the type of nanostructure on the electrolyte concentration was not proved but it is probable that pH of the electrolyte can also modify the type of structure.

It is also possible to create different sorts of nanotubes by altering the parameters which can modify the type of the nanostructure. For instance, the nanotubes can differ in wall thickness. The physical and mechanical properties of electrodeposited metals can be influenced mainly by the conditions during the electrodeposition. The most important parameters which can affect the properties are the composition of used bath, the temperature of the bath, the pH, impurities, the current density, and the concentration of the solution [7].

#### ACKNOWLEDGMENTS

This research has been supported by Grant Agency of the Academy of Sciences of the Czech Republic under the contract GAAV 1QS201710508 Impedimetric chemical microsensors with nanostructured electrode surface, and by the Czech Ministry of Education within the framework of Research Plan MSM 0021630503 MIKROSYN New Trends in Microelectronic Systems and Nanotechnologies.

#### REFERENCES

- [1] N.M. Yakovleva, A.N. Yakovlev, and E.A. Chupakhina. Structure of Al<sub>2</sub>O<sub>3</sub> Films Prepared by Two-Step Anodization, *Inorganic Materials*, Vol. 34, No. 7, 1998, pp. 711-713.
- [2] O. Jessensky, F. Müller, and U. Gösele. Self-organized Formation of Hexagonal Pore Structure in Anodic Alumina. *J. Electrochem. Soc.* Vol. 145, No.11 (1998) 3735-3740.
- [3] R.Hrdý, J.Hubálek. Selfordered pore structure of anodized alumina thin film on Si substrate. *Technical digest of EDS 05, Brno, Czech Rep.* 2005, pp. 300-304.
- [4] Y. Kanamori, K. Hane, H. Sai and H. Yugami. 100nm period silicon antireflection structures fabricated using a porous alumina membrane mask. vol. 78, No 2, 2001.
- [5] A.N. Govyadinov and S.A. Zakhvitcevich. Field Emitter Arrays Based on Natural Selforganized Porous Anodic Alumina. *Technical Digest of IVMC'97, Kyongju, Korea, 1997*, pp.735-738.
- [6] K. Klosová and J. Hubálek. Nanowires and Nanotubes Formation using Anodisc Alumina Films as Templates, In conference proceedings NENAMAT - NANO'05, Brno, Czech rep. 2005, pp. 318-321.
- [7] C. Oropeza. A new approach to evaluate fracture strength of UV-Liga fabricated nickel specimen, Louisiana State University, 2002.

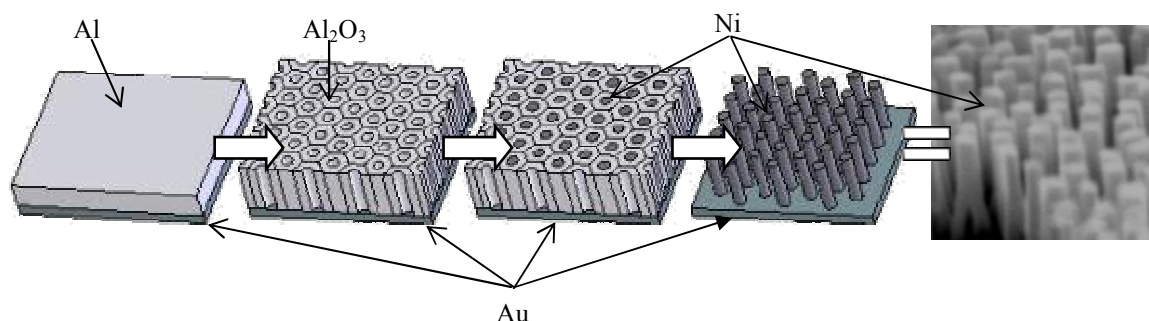


Fig. 1: Process of nanostructure creation

# The Supercapacitors of Double Layer Type

Martin Kocian and Jiri Vondrak  
Faculty of electrical engineering and communication  
Brno University of Technology  
Brno, Czech Republic  
Email: [xkocia03@stud.feec.vutbr.cz](mailto:xkocia03@stud.feec.vutbr.cz)

**Abstract** — *The article will deal with construction of supercapacitors of double layer type – selected materials, method of construction of supercapacitors. The supercapacitors have big capacity – tens up to thousands farads. These properties make supercapacitors of considerable interest for accumulating of electric energy. That we can use in car industry, telecommunications, backup system of energy, etc.*

*The charge time of a supercapacitor is about 10 seconds. The ability to absorb energy is, to a large extent, limited by the size of the charger. In normal use, a supercapacitor deteriorates to about 80 percent after 10 years. There is no danger of overcharge or 'memory'.*

## I. THE PRINCIPLE

The double layer supercapacitor can be described as a metal electrode immersed in the electrolyte. When we apply on chemically inert electrode higher positive potential with respect to the electrolyte, it will accumulate negative ions and repel positive ions. So a space charge will be created several tens nanometre thick, which is in theoretical electrochemistry called the electric double layer. The capacity of the spatial charge is high due to higher concentration of charge carriers. We are talking about tens or hundreds farads on cubic centimetre. Their creation or disappearance is physical process, which is not bound with any reconstruction of chemical structures or compounds and is perfectly reversible. The lifetime of supercapacitors is very long therefore. When we use inert carbon with big specific surface area as electrode material (till 2000 square metres on gramme) and joined by suitable binding agent and pressed on current collector, we obtain such supercapacitors with mentioned attributes.

The main disadvantage of supercapacitor is low potential range. In water solution, we are limited with potential, of water decomposition on hydrogen and oxygen. The critical potential is 1,224 volts theoretically. Exceeding this limit causes the formation of gaseous hydrogen and oxygen in the capacitor. We can solve this problem using organic

solvents, like those used in lithium batteries. Propylene carbonate, ethylene carbonate, acetonitrile and so on are suitable. Voltage range of these capacitors therefore increases up to 2,3 – 4,0 volts [1,2,3].

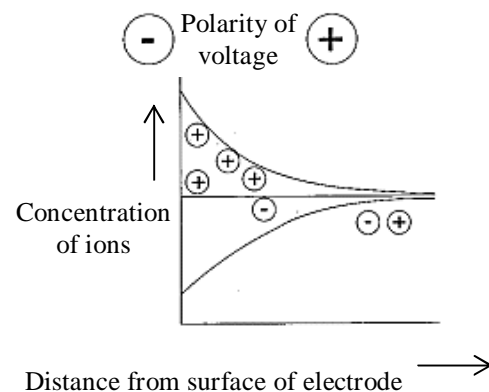


Figure 1: The formation of spatial charge by metal inert electrode

## II. EXPERIMENTAL PART

### A. THE PREPARATION BY THE OLD METHOD

The electrodes are prepared from metal screen, carbon (expanded graphite), binding agent (Sokrat) and conditioner ( $\text{NH}_4\text{HCO}_3$ ). The ingredients are mixed and put on metal screen. The electrodes are dried in oven on 130 °C at 20-30 minutes.

### B. THE PREPARATION BY THE NEW METHOD

The electrodes are prepared from metal screen, carbon (expanded graphite), binding agent (teflon) and conditioner ( $\text{NH}_4\text{HCO}_3$ ). The carbon is boiled in water about one hour then teflon is added in minimum quantity. The mix is filtrated and dried in oven and then is added conditioner. The mix is put on metal screen and pressed in the hand press and then the electrodes are dried in oven on 130 °C at 20-30 minutes.

C. THE MEASUREMENT GLASS VESSEL

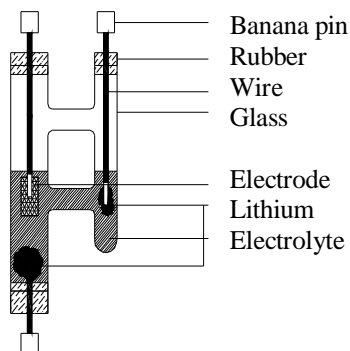


Figure 2: The glass vessel

D. THE MEASUREMENT OF THE ELECTRODES

The supercapacitors are measured on device Autolab in programme GPES (cyclic voltametry).

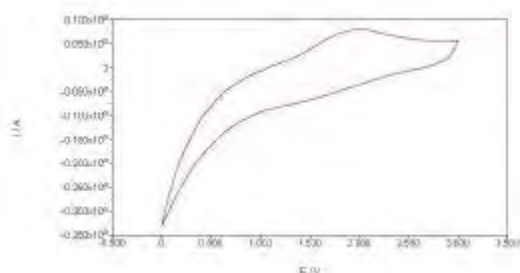


Figure 3: The graph of cyclic voltametry

The difference of currents is obtained from the graph of cyclic voltametry and then capacity is calculated from this formula:

$$C = \frac{1}{2} \frac{\Delta I}{n} [F] \quad (1)$$

where C [F] is capacity,  $\Delta I$  [A] is difference of currents and  $v$  [V/s] is rate of change potential in volts per second ( $v$  is 0.01 V/s).

The electrodes are measured in the liquid electrolytes (0,5 mol.l<sup>-1</sup> electrolyte  $\rightarrow$  1.064 g LiClO<sub>4</sub> + 20 ml propylencarbonate).

E. THE RESULTS

	C[F/g]
old method	7,6
new method	30,5

Table 1: The table of results

III. CONCLUSION

The capacity of the electrochemical supercapacitors depends on many objects – carbon, binding agent, substrate, chemical additive, molar concentration of electrolyte, clarity of chemicals, clarity of working environment, procedure of preparation, etc. – all of objects increase or decrease the capacity of the supercapacitors.

This article shows the procedure of preparation can increase the capacity several times. The difference of the old and new method is in uniformity of the binding agent.

ACKNOWLEDGMENTS

This work was supported by the Grant FRVS (2958/G1) and by the Ministry of Education (project MSM 0021630516).

REFERENCES

- [1] J. Vondrak, M. Sedlarikova and collective. The electrochemical supercapacitors in use. Sdelovaci technika, 2002.
- [2] J. Vondrak, M. Sedlarikova and collective. The electrochromism, supercapacitors, lithium-ionts batteries. Sdelovaci technika, 3/2001.
- [3] B. E. Conway. Electrochemical supercapacitors. Scientific fundamentals and technological applications, Kluwer Academic / Plenum Publisher, New York, 1999

# Materials from renewable resources used in rubber mixtures

Zuzana Kramárová<sup>1</sup>, Peter Bugaj<sup>1</sup>, Jozef Feranc<sup>1</sup>, Miroslav Ďuračka<sup>2</sup>, Eugen Špirk<sup>1</sup>, Peter Šuri<sup>3</sup>,  
Anton Karvaš<sup>3</sup>, Ivan Chodák<sup>4</sup>, Pavol Alexy<sup>1</sup>(Faculty Mentor)

<sup>1</sup> *Slovak University of Technology, Faculty of Chemical and Food Technology, Dept. of Plastics and Rubber, Radlinskeho 9, 812 37 Bratislava, Slovak Republic,*

<sup>2</sup> *VUCHT a.s. Nobelova 34, 83603 Bratislava, Slovak Republic*

<sup>3</sup> *Matador a.s., Rubber Research Institute, T. Vansovej, Puchov, Slovak Republic*

<sup>4</sup> *Slovak Academy of Sciences, Polymer Institute, Dubravska cesta 9, 842 36 Bratislava, Slovak Republic*

Email: {zuzana.kramarova@stuba.sk}

**Abstract** – *Utilization of environmentally friendly materials and materials from renewable resources as a component of rubber blends is a new modern tendency in rubber industry. Some publications and patents discussed about replacement heavy aromatic oil with ecological ones and substitution of traditional rubber fillers as well, mainly in tire industry. New components of rubber blends are applied in order to obtain better mechanical and dynamical properties and better driving properties and it leads to production of so-called “green tires”. Starch is one of these materials which is able to modify dynamical-mechanical properties and by this way it can positive affect the abrasion, rolling resistance and wet traction of tires.*

## I. INTRODUCTION

Dynamical-mechanical analysis of rubber blends is very effective method for prediction of driving properties of tires. Especially dependency of loss factor ( $\tan \delta$ ) on temperature can be used as an indicator for abrasion resistance, low temperature properties, wet traction, rolling resistance and heat built-up [1, 2]. The storage modulus of filled blends increases in dependency on type of filler. Dynamic deformation of elastomers filled with carbon black and silica is accompanied by a decreasing of modulus with increasing of amplitude at low strain values. This behavior is called Payne effect [3]. Payne effect is explaining as a problem of creating own filler structure and its breakdown under dynamical loading [4]. Interactions between filler particles or interactions between filler and elastomer are

responsible for reinforcement of mixtures and better properties of vulcanisates.

Fillers from renewable resources are applied into rubber blends in combination with carbon black and silica in order to obtain improving of driving properties [5]. In dependency on type of used fillers and their concentration it is possible to modify properties in accordance to requirements.

## II. RESULTS AND DISCUSSION

Dynamical-mechanical thermal analysis were used for testing of properties of vulcanisates containing 30 phr of corn starch Meritena 100, collagen hydrolysate Hykol E and amaranth starch covered with protein layer Amarant 1. Dependency of  $\tan \delta$  on temperature is shown on Figure 1 and 2. Natural rubber and styrene-butadiene rubber were used as a polymer matrix. Different chemical character of applied fillers caused changes in shape of  $\tan \delta$  curves. Maximum of  $\tan \delta$  is shifted according to the x-coordinate and value of maximum  $\tan \delta$  is affected by type of filler as well.

REM was used for observation of vulcanisates morphology (Figure 3). Corn starch is incorporated into rubber in solid particles form. No changes in shape and size of particle were observed. Amaranth starch creates agglomerates. Size of these agglomerates is comparable to corn starch particles. Collagen hydrolysate forms own domains. Compatibility of collagen hydrolysate with polymer matrix is very good. However the cohesive strength is weak.

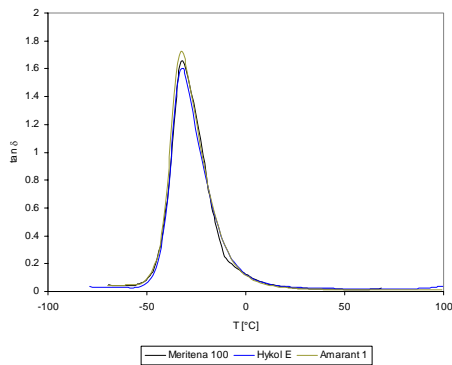


Figure 1 Dependency of  $\tan \delta$  of natural rubber vulcanisates filled with various type of fillers from renewable resources on temperature

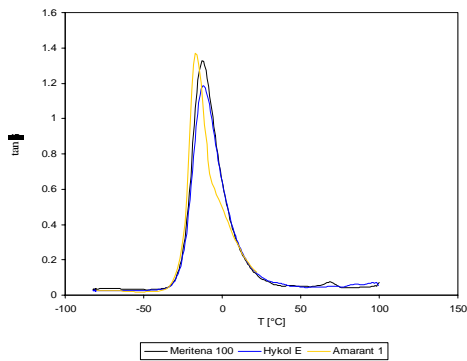


Figure 2 Dependency of  $\tan \delta$  of styrene-butadiene rubber vulcanisates filled with various type of fillers from renewable resources on temperature

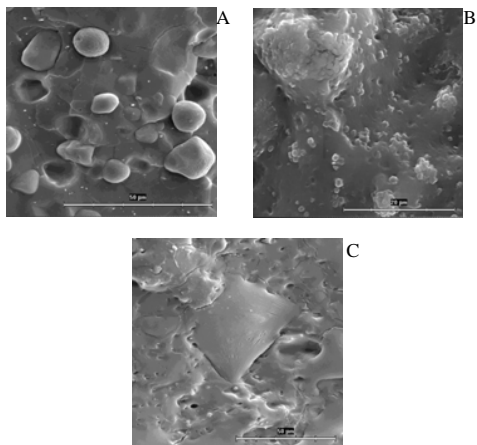


Figure 3 REM of natural rubber vulcanisates filled with 30 phr of corn starch (A), amaranth starch (B) and collagen hydrolysate (C)

### III. CONCLUSIONS

Materials from renewable resources are potentially utilizable as components for rubber blends. They are able to modify properties of vulcanisates, especially dynamical properties as well as driving properties of tires. In combination with carbon black and silica they cause improving of tensile strength and modules.

### III. REFERENCES

- [1] Nordsiek, K.H., Kautsch. Gummi Kunstst., 38, p. 178, 1985
- [2] Wang, M.J., Rubber Chem. Technol., 71, p. 520, 1997
- [3] Payne, A.R., Reinforcement of elastomers, 3, p. 69-123, 1965
- [4] Maier, P.G., Molecular Interpretation of the Payne effect, Kautsch. Gummi Kunstst., 49, p. 18-21, 1996
- [5] Read, K., Tire Technology International, 6, p. 14-17, 2003

# Hybrid Electrochromic Cells Employing Sol-Gel and Polymeric I<sub>3</sub><sup>-</sup>/I<sup>-</sup> Redox Electrolytes

Ondřej Krejza and Jiří Vondrák  
Faculty of Electrical Engineering and Communication  
Brno University of Technology  
Czech Republic  
Email: [ondrej.krejza@phd.feec.vutbr.cz](mailto:ondrej.krejza@phd.feec.vutbr.cz)

**Abstract** — *The aim of this study is the comparison of the hybrid electrochromic (HEC) cells incorporating sol-gel and polymeric I<sub>3</sub><sup>-</sup>/I<sup>-</sup> redox electrolyte.*

## I. INTRODUCTION

An electrochromic material is able to change its optical properties when a voltage is applied across it. The optical properties should be reversible; it means that the original state should be recoverable if the polarity of the voltage is changed [1].

### A. HYBRID ELECTROCHROMIC DEVICES

The advantage of HEC (Figure 1) cells compared to the usual battery-type EC cells is that the counter-electrode with intercalation properties can be replaced with a thin Pt layer on SnO<sub>2</sub>:F glass. The redox pair was introduced in electrolytes with the dissolution of I<sub>2</sub> and one of the iodide salts like LiI, KI or NaI, their dissolution being dependent on the properties of the electrolyte matrix. Transformation of iodide and triiodide species according to reaction  $I_3^- + 2e^- \leftrightarrow 3I^-$  may occur on Pt and WO<sub>3</sub> electrodes, while the optical modulation of HEC cells remains to be determined by active electrochromic WO<sub>3</sub> film and intercalation/deintercalation of certain cations (H<sup>+</sup>, Li<sup>+</sup>, K<sup>+</sup>, Na<sup>+</sup>).

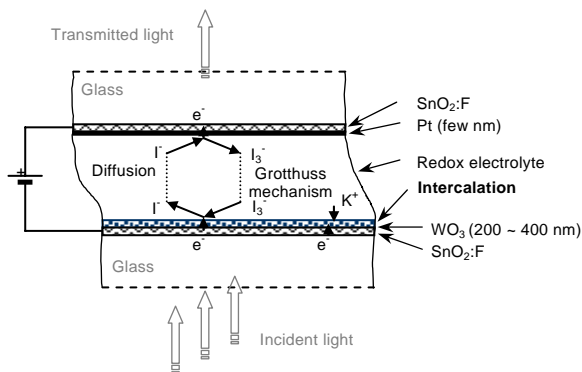


Figure 1: Schematic representation of an HEC cell.

## II. EXPERIMENTAL

Optically active WO<sub>3</sub> films covering SnO<sub>2</sub>:F glass substrates were nanocrystalline with the grain size 30 nm and were prepared by using peroxy-synthesis route and thermally treated at 450 °C for 30 minutes. A drop of the redox electrolyte was placed on WO<sub>3</sub> film and immediately covered and pressed with platinised SnO<sub>2</sub>:F glass substrate serves as counter electrode. To compare the electrochemical properties of active layer with different pre-treatment I have prepared two samples of HEC cell with WO<sub>3</sub> pre-heated. The electrochemically active layer WO<sub>3</sub> film in which HEC with ICS-PPG 4000 sol-gel electrolyte contained LiI and KI salts was thermally treated at 450 °C for 30 minutes and then re-heated at 300 °C for 10 minutes before assembling. The HEC cells contained PMMA electrolyte were stored in a desiccator for one day in order to avoid creating of air bubbles. Appearing of these bubbles is probably connected with shrinking of polymer electrolyte due to the polymerisation.

### B. ICS-PPG-BASED POLYMER ELECTROLYTE

The sol-gel electrolyte was prepared from unhydrolyzed organic-inorganic precursor ICS-PPG that was synthesized from 3-isocyanatopropyltriethoxy silane (ICS) and poly(propyleneglycol)-bis-(2-aminopropyl)ether (PPG) with molar weight 4000 [2]. After the dissolution of Li+I<sub>2</sub> or KI+I<sub>2</sub> acetic acid was added as catalyst for the gelation of ICS-PPG precursor. Co-solvent sulpholane was chosen because of its high boiling point in order to prevent its evaporation from the HEC cell.

### C. PMMA-BASED POLYMER ELECTROLYTE

The polymeric PMMA electrolyte was prepared as a mixture of methyl methacrylate (MMA) monomer, polymeric PMMA resin containing 1 % of dibenzoylperoxide served as polymerisation initiator (Superacryl<sup>®</sup>, Spofa-Dental, Czech Republic) and optional component [3]. Optional component was presented by LiI and I<sub>2</sub> dissolved in propylene carbonate.

#### D. MEASUREMENT

In-situ UV-visible spectroelectrochemical measurements of the HEC cells were made using the HP 8453 (Hewlett Packard, USA) diode array spectrophotometer in combination with an Eco Autolab (Eco Chemie, The Netherlands). Potentiostat module PGSTAT 12 was used to perform cyclic voltammetry and chronocoulometry measurements. The cyclic voltammetric (CV) curves were obtained by the scan rate of  $20 \text{ mV}\cdot\text{s}^{-1}$  and were scanned from 0 V to -2 V, reversed to 2 V and then finished at 0 V (Figure 2). The kinetics of the coloration and bleaching was obtained by applying a chronocoulometric (CC) technique by performing the intercalation of  $\text{K}^+$  ions at -1,5 V for 100 s and deintercalation at 2 V (100 s). Reported potentials correspond to the potential applied to the  $\text{WO}_3$  film (working electrode) with respect to the platinumised  $\text{SnO}_2:\text{F}$  glass substrate (counter electrode).

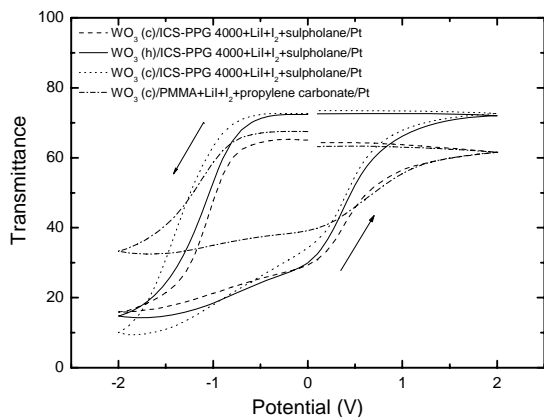


Figure 2: Transmittance changes of various HEC cells during in-situ UV - visible measurements. Cyclic voltammetry was performed between -2 V and 2 V with the scan rate of 20 mV/s; h –  $\text{WO}_3$  prepared at 450 °C then re-heated prior the cell preparation; c –  $\text{WO}_3$  prepared at 450 °C and not re-heated prior the cell preparation.

### III. RESULTS AND DISCUSSION

The in-situ UV-visible measurements of HEC cells revealed the largest optical modulation ( $>50\%T$ ) for redox electrolytes with the composition ICS-PPG 4000+LiI(KI)+ $\text{I}_2$ +sulpholane (Figure 2). The electrochromically active  $\text{WO}_3$  films that were used in these cells were prepared by peroxo synthesis route and thermally treated at 450 °C for 30 minutes. However, the effect of their additional heat-treatment directly prior the preparation of the cells was tested and will be addressed in view of its influence on surface hydroxyls. For HEC cells consisting of thermally re-

treated  $\text{WO}_3$  the bleaching was faster than the coloration.

#### ACKNOWLEDGMENTS

This work was supported by the Grant Agency of the Academy of Sciences of the Czech Republic (KJB208130604) and Ministry of Education (FRVS No. 2943/2005).

#### REFERENCES

- [1] C. G. Granquist. Electrochromism and Electrochromic Devices chapter of The CRC Handbook of Solid State Electrochemistry, CRC Press, 1997.
- [2] B. Orel, A. Šurca Vuk, P. Lianos. Solid State Ionics 165, 235-246, 2003.
- [3] J. Vondrák, J. Reiter, J. Velická, M. Sedlaříková. Solid State Ionics 170, 79-82, 2004.

# Conservation of Historical Papers with Chitosan

Katarína Kunovská and Ľudmila Černáková (Faculty Mentor)  
Institute of Polymer Materials, Faculty of Chemical and Food Technology  
Slovak University of Technology  
Bratislava, Slovak Republic

Email: katarina.stechova@stuba.sk, ludmila.cernakova@stuba.sk

**Abstract** — *The aim of our study was to prolong the lifetime of acidic papers by application with cellulose like polymer - chitosan. This natural polysaccharide is prepared by deacetylation of renewable source chitin. Shells of crustaceans (marine animals) consist of chitin. Solution of chitosan was prepared and spread on papers. The mechanical properties of modified papers and morphology of the surface were investigated. A change of properties was studied also after thermal accelerated ageing. Improvement of modified papers properties was observed.*

## I. INTRODUCTION

Most of historically important writings and visual images have been recorded on paper. Particularly papers manufactured in second half of 19<sup>th</sup> century have a limited storage life due primarily to acidity induced as part of paper manufacturing processes. Alum rosin was used as a sizing agent [1]. Sulphuric acid has been released with time. Exposure to acidic air pollutants and oxygen also contributes to paper degradation [2]. Oxygen improves oxidation of cellulose and carbonyl and carboxyl groups are formed with the result of acidity increase. Paper has changed properties during the time of storage.

Degradation of paper is mainly a result of acid hydrolysis of the cellulose chains. Acids break cellulose bonds randomly and drastically reduce degree of polymerization of cellulose that result in a worsening mechanical and optical paper properties. Paper turns yellow and becomes fragile and brittle. To save weak papers, methods for deacidification and strengthening have been developed.

Derivatives of cellulose are usually used for the strengthening of deteriorated papers in conservation practice [3]. Chitosan is chemically similar to cellulose but in its structure has pendant amino groups. Chitosan is known for being biocompatible and non-toxic. It has antimicrobial activity and improves water resistance [4]. Chitosan could be new environmental friendly alternative that improves paper protection.

## II. EXPERIMENTAL

Solutions of different chitosan concentrations were prepared and spread on paper. Total increase of weight was 3,5 g chitosan / 100 g paper. Mechanical properties such as tensile strength and folding endurance of modified papers were measured. All tested papers were stored at climatic conditions (temperature  $23 \pm 1$  °C, relative humidity  $49 \pm 1$  %) before mechanical properties were measured.

Stability of treatment was studied by thermal accelerated ageing. Untreated and treated papers were aged at temperature 105 °C for 12 days.

Morphology of films created on the surface was investigated. Microstructure of untreated paper is displayed on Figure 1a. Paper is formed of fibres and fine fibres. Figure 1b shows microstructure of paper after spreading with chitosan. Chitosan covers fibre structure of paper and forms colourless layer on the surface.

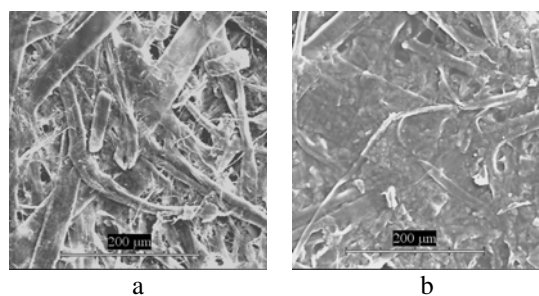


Figure 1: Microstructure of paper, a-untreated paper, b- paper covered with chitosan

## III. CONCLUSIONS

Effect of natural polymer - chitosan on properties of paper sheets was studied. Chitosan improves mechanical properties of paper. It forms a colourless layer on the surface. Changes of pH values were measured after chitosan solution application. Acidity of samples was changed to almost neutral values.

## ACKNOWLEDGMENTS

This work was supported by Slovak Ministry of Education (Project No. 661/2003).

## REFERENCES

- [1] I. Brückle. The role of alum in historical papermaking. *Abbey Newsletter* 17, 4, 1993.
- [2] H. J. Porck and R. Teygeler. Preservation science survey. An overview of recent developments in research on the conservation of selected analog library and archival materials. Council on library and information resources, Washington DC, European commission on preservation and access, Amsterdam 2001.
- [3] A. Makova, I. Kuka, Z. Kyskova. The use of native modified starches and cellulose derivatives in restoration-conservation practice comparison of their adhesive qualities. In *Proceeding of the International Conference on Chemical Technology of Wood Pulp and Paper*, pages 424 –427, Bratislava, September 2003.
- [4] M. Mucha and D. Miskiewicz. Application of modified chitosan for improving water resistance of paper. In *Proceedings of 40th IUPAC International Symposium on Macromolecules*, World polymer congress, Macro 2004, Paris, July 2004.

# FIB EDX Tomography – 3D Characterization of Al-Si eutectics

Fernando Adrián Lasagni and Hans Peter Degischer (Faculty Mentor)

Institute of Materials Science and Technology

Vienna University of Technology

Vienna, Austria

Email: {lasagni, hpdegi}@pop.tuwien.ac.at

**Abstract** — A detailed study of the 3D morphology of different eutectic architectures of unmodified and Sr-modified AlSi7-12 alloys is represented by means of a new Focused Ion Beam – Energy Dispersive Spectroscopy (FIB-EDX) method. These 3D structures can be reconstructed from sequential 2D sectioning and subsequent computer imaging. Both aluminum and silicon phases are identified with a voxel resolution of  $\sim 60 \times 75 \text{ nm}^2$  in the image plane and  $\sim 60\text{-}300 \text{ nm}$  between each slice. EDX imaging is applied in case of very low contrast between the constituent phases by Scanning Electron Microscopy (SEM) in Secondary Electron (SE) or Back Scattering Electron (BSE) modes. The eutectic structure and the interconnectivity between lamellar Si are investigated, as well as the morphological changes induced by the addition of Sr.

## I. INTRODUCTION

The excellent castability and mechanical properties of AlSi-alloys make them popular foundry alloys. These alloys can be modified and/or heat-treated to improve their ductility [1,2].

The morphology of these alloys depends strongly on the Si content as well as the casting process. As cast alloys contain dendritic  $\alpha$ -grains with an eutectic structure in-between formed by lamellar Si separated by the  $\alpha$ -phase. The Si forms initially a percolating network [3] of a few  $\mu\text{m}$  width between the dendritic arms of primary  $\alpha$ -Al consisting of several thin ( $\sim 1\text{-}2 \mu\text{m}$ ) lamellae. The addition of Sr or Na (0.1-0.3wt.%) modifies the eutectic morphology into a fibrous network [3] improving both ductility and tensile strength of the alloy [2].

In order to determine the 3D architecture of different phases in a heterogeneous metal, X-ray tomography is a very attractive technique which enables a microstructural characterization with a spatial resolution close to that of an optical microscope [4], if synchrotron radiation is applied. This technique has been mainly used for porosity determination and fracture crack evolution [5,6,7], since voids produce very high contrast with all materials. The resolution of phase contrast images

is somewhat less and has been applied to observe thixotropic Al-Si structures [8].

In this work, a tomographic Focused Ion Beam – Energy Dispersive Spectroscopy (FIB-EDX) method was performed in order to determine the architecture of the eutectic Si in unmodified and Sr-modified AlSi-alloys. In comparison with conventional X-ray tomography, this new technique achieves a resolution 100-times higher, where details of some nanometres can be measured. Furthermore, EDX mapping can be performed in order to investigate components with very low contrast during SEM observation in SE or BSE modes.

## II. RESULTS & DISCUSSION

Figure 1-a depicts a reconstructed three-dimensional image obtained from 2D sectioning in AlSi7Sr. The fibrous morphology of the modified eutectic is clearly observed, showing Si fibers and branches of about  $0.2\text{-}0.4 \mu\text{m}$  in diameter and some micrometers in length ( $\sim 3\text{-}5 \mu\text{m}$ ) oriented in many different directions. These fibers are mostly interconnected by nodes of some nanometers in cross section ( $\sim 0.05\text{-}0.1 \mu\text{m}^2$ ). The intersection of 3 different grains is observed in Figure 1-b, separated by Si-free grain boundary zones of about  $1 \mu\text{m}$  width. Grain A (See Figure 1-b) shows a long thick Si fiber along the grain boundary with interconnected Si branches growing parallel to the y-axis. Complete interconnection and similar orientation of fibrous Si is observed in the grain B, while Si fibers in grain C oriented are perpendicular to those of grain A and B. In this grain (C), Si fibers seem to be mostly interconnected but some distance from the grain boundary isolated short fibers are also observed.

The architecture of the reconstructed eutectic Si in AlSi7 (Figure 1-c) is completely different from that of the Sr-modified version, presenting Si plates of about  $1\text{-}3 \mu\text{m}$  thickness. These plates are separated into two different regions (each with clearly preferential Si orientation), which are interconnected by nodes. The connectivity between the Si plates corroborates the formation of a Si-network studied in a previous work [4]. These

connecting nodes are much thicker ( $\sim 1\text{-}4\mu\text{m}^2$ ) than those of the AlSi7Sr-alloy. Since the 3D reconstruction was performed in a sample with only

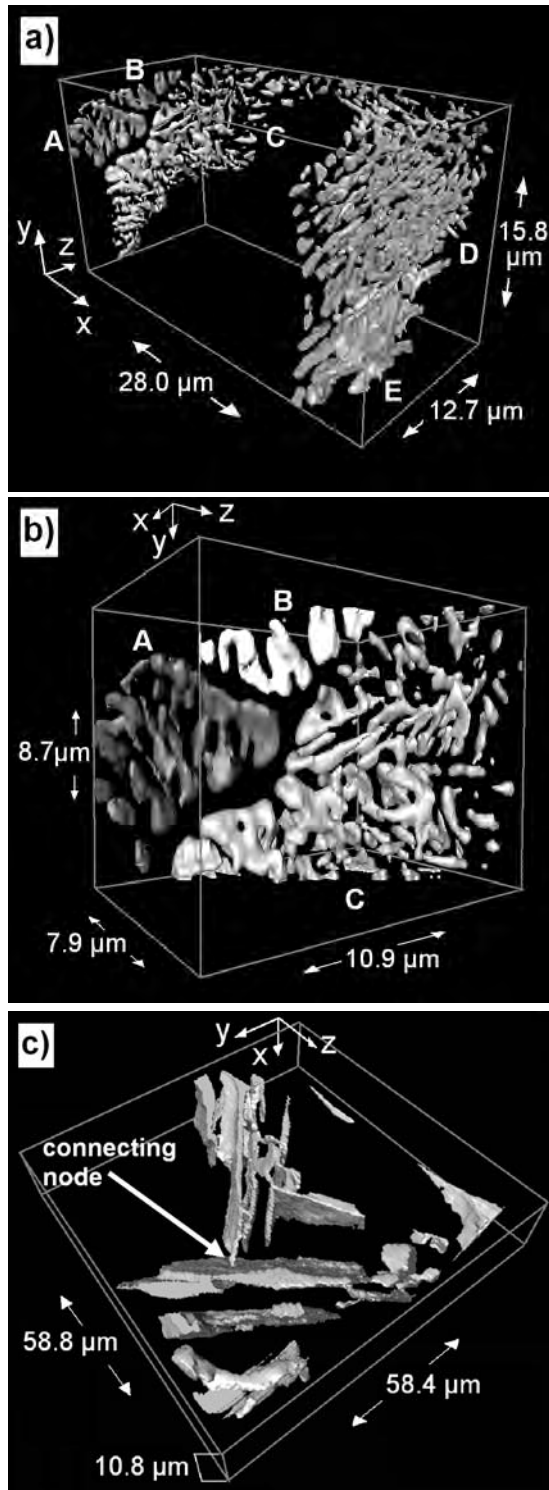


Figure 1: 3D reconstruction of the eutectic Si in AlSi7Sr: a) whole studied region, b) union of three different grains; and c) AlSi7 alloy

about  $10\mu\text{m}$  in the milling direction (x-axis), the real size of the Si plates is not observed. A previous investigation [3] of chemically extracted Si revealed plates between  $40\text{-}80\mu\text{m}$  long and wide.

### III. CONCLUSIONS

High resolution 3D-observation of eutectic-Si phases can be performed by means of a new 3D-FIB technique, which so far could not be resolved by synchrotron computer tomography. The 3D-representation of the studied unmodified AlSi7 alloy presents a lamellar Si morphology with interconnecting nodes and regions with almost perpendicular orientation of Si plates. The addition of 170ppm Sr produced full modification of the eutectic Si-structure into a fibrous morphology. The observed Si fibers seem to be mostly interconnected near the grain boundaries. The thickness of Si fibers and branches also increases towards the Si-free grain boundaries.

### ACKNOWLEDGMENTS

F. Lasagni would like to thank F. Mücklich and A. Lasagni of the Saarland University for SEM investigation.

### REFERENCES

- [1] S.A. Kori, B.S. Murty, M. Chakraborty, *Materials Science and Engineering*, A283: 94-104, May 2000.
- [2] M.M. Haque, *Journal of Materials Processing Technology*, 55, 193-198, 1995.
- [3] F. Lasagni, H.P. Degischer, M. Papakyriacou, *Journal of Practical Metallography*, accepted for publication, February 2006.
- [4] H. Yasuda, I. Ohnaka, Y. Mizutani, T. Morikawa, S. Takeshima, A. Sugiyama, Y. Waku, A. Tsuchiyama, T. Nakano, K. Uesugi, *Journal of European Ceramic Society*, 25, 1397-1403, February 2005.
- [5] J-Y Buffière, S. Savelli, P.H. Jouneau, E. Maire, R. Fougères, *Materials Science and Engineering*, A316, 115-126, February 2001.
- [6] J-Y Buffière, H. Proudhon, E. Ferrie, W. Ludwig, E. Maire, P. Cloetens, *Nuclear Instruments and Methods in Physics Research B*, 238, 75-82, August 2005.
- [7] L. Dupuy, J.-J. Blandin, *Acta Materialia*, 50, 3251-3264, April 2002.
- [8] S. Verrier, M. Braccini, C. Josserend, L. Salvo, M. Suery, P. Cloetens, W. Ludwig, in *Proceedings of the 6th Int.Conf.Semi-Solid Proc.of Alloys & Comp.*, Ed. G.L. Chiarmetta and M. Rosso, 771-776, September 2000.

# Laser Interference Metallurgy

## New Surface properties through advanced microstructure design

Andrés Lasagni and Frank Mücklich (Faculty Mentor)  
Institute of Functional Materials  
Saarland University  
Saarbrücken, Germany  
Email: a.lasagni@mx.uni-saarland.de

**Abstract** — *The Laser Interference Metallurgy method allows the creation of periodic pattern of features with a well defined long-range order on surfaces in the scale of typical microstructures. By means of interfering laser beams of a high-power pulsed laser, a direct, periodical, and local heating through photo-thermal interaction between light and metal can be achieved. This work intends to give an overview of the different structures types that can be obtained in thin metallic films depending on the configuration of the samples as well the energy per unit area of the laser beams. The structuring regimes are explained in terms of thermal properties of the layers*

### I. INTRODUCTION

Laser Interference Metallurgy [1, 2] is a recently developed method to produce periodic surfaces on metals with a well defined long range order from the sub-micrometer level up to micrometers. This method makes use of the interference patterns which are obtained when coherent laser beams are overlapped. The additional advantage of irradiating the surface of the sample with a high-power pulsed laser leads to a direct, periodical, and local heating of the metal based on photo-thermal nature mechanisms. Consequently, different metallurgical effects can be explored.

The interference theory permits to calculate the interference patterns of multiple-coherent laser beams. Thus, the geometrical arrangement of the laser beams prior the laser interference experiments can be calculated. Moreover, the two-dimensional fast Fourier transformation of a desired periodical pattern permits to calculate the laser-beam configuration to obtain the pattern (inverse problem) [3].

In this work, it will be demonstrated that the interference patterns employed for the laser experiments can be successfully calculated prior experiment. The structuring regimes which are obtained depending on the configuration of the samples (layer with the lower melting point on the top or bottom) will be presented.

### II. EXPERIMENTAL

Metallic thin films were produced by physical vapour deposition with an Ar-ion-gun sputtering facility (Roth & Rau, UniLab) on a glass substrate under a vacuum of 10 Pa. The thickness of the films was monitored in-situ by a microbalance (Tectra, MTM-10). A high power pulsed Nd:YAG laser with a wavelength of 266 nm, a frequency of 10 Hz and a pulse duration of 10 ns was employed for the laser experiments. The primary laser beam was split into two or three beams to interfere with each other on the sample surface. One pulse was chosen in all experiments. All the structures shown in this paper were produced in air at room temperature. The samples were imaged with a high-resolution scanning electron microscope (SEM) at 5 kV acceleration voltage.

### III. RESULTS AND DISCUSSION

#### A. INTERFERENCE THEORY

Under the assumption of plane waves, the total electric field ( $E$ ) of the interference pattern can be obtained by the superposition of each individual “i” beam:

$$E = \sum_{i=1}^n E_i = \sum_{i=1}^n E_{i0} e^{-ik \sin \alpha_i (x \cos \beta_i - y \sin \beta_i)}, \quad (1)$$

where  $E_{i0}$  is the amplitude of the electric field of the i-beam;  $\alpha_i$  is the angle between the beam direction and the vertical direction perpendicular to the interference plane;  $\beta_i$  is the angle between the projection of the beam on to the interference plane and the x-direction; and  $k$  is the wave-number:

$$k = 2\pi / \lambda \quad (2)$$

where  $\lambda$  denotes the wave length of the beam.

The intensity of the overlapped beams is given by:

$$I = \frac{c\epsilon_0}{2} |E|^2, \quad (3)$$

where  $c$  is the speed of light and  $\epsilon_0$  the permittivity of free space.

Two-beam interference ( $n=2$ , Fig 1d) produces a linear pattern (see Fig. 1c). Three-beam interference ( $n=3$ , Fig 1e) produces different 2-D arrays depending on the magnitude of the electric-field of each individual. For the symmetric configuration ( $E_{01}=E_{02}=E_{03}$ ;  $\alpha_1=\alpha_2=\alpha_3$ ;  $\beta_1=0$ ,  $\beta_2=2/3\pi$ ,  $\beta_3=-2/3\pi$ ) a hexagonal dot-type pattern is obtained (Fig. 1b). However if the intensity of each laser beam is not the same ( $E_{01}=E_{02}=1/3E_{03}$ ), a combination of the line type with the dot-type pattern is obtained (Fig. 1a).

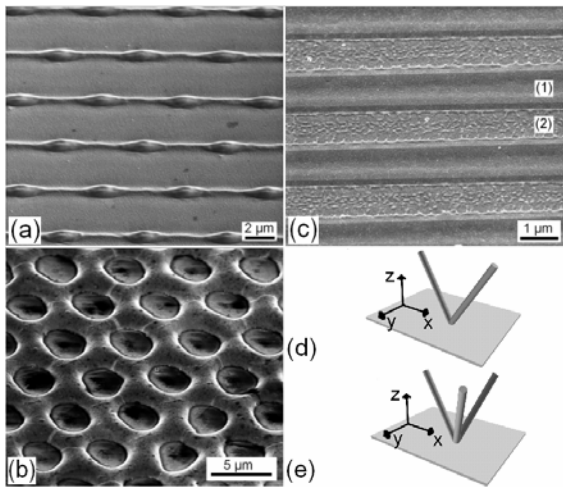


**Figure 1.** (a) Surface topography obtained using 3 laser-beams arranged in symmetrical configuration and an intensity ratio of 100:33:33 (sample Fe(top)/Al(bottom)). (b) Hexagonal lattice structure with defined removal of material at the interference maxima (sample Cu(top)/Al(bottom)). (c) Al-Fe micro pattern obtained by local periodic removal of the upper layer (Al) at the interference maxima positions (sample Al(top)/Fe(bottom)). (d) three and (e) two beams configuration.

## B. STRUCTURING OF THIN-METALLIC FILMS

In the case of thin metallic films [4, 5], according to the laser fluence (energy per unit area) and depending on the configuration of the samples, different topography regimes can be obtained. Each topographic regime is characterized by a different structuring mechanism. If the metal with the higher melting point is placed at the top of the samples, two topography types can be obtained. At lower laser fluences, only the lower layer is molten and the structuring is produced by liquid flow of the molten material of the lower layer towards the maxima of energy without removal of material (Fig. 1.a). The flow of molten material is produced by a pressure gradient

during resolidification. If the laser fluence is increased, both layers are molten at the interference peaks. Next, the molten metal is removed obtaining a large structure height (Fig. 2.b).

In the second case, if the metal with the lower melting point is placed at the top of the sample, three different topography regimes are presented depending on the laser fluence [6, 7]. The first topography type occurs without removal of material at the interference maxima and is caused by local thermal dilatation of the metallic layer during the laser heating. If the laser fluence is high enough so that the upper layer reaches its melting point, the upper layer is removed at the interference maxima but the second layer remains in the solid state (Fig. 2.c). At higher laser fluences, both layers are molten resulting in a 3rd topographic type. It means that not only the shape of the periodical structures depends on the laser but also on the layer configuration. Moreover, the formation of long ordered intermetallic phases can be explored obtaining a composite material [6, 8].

The presented method opens the door to a big number of possible applications in the field of surface engineering. For example, the production of biocompatible surfaces for implants [9], improvement of the absorption of solar cells [10], and the modulation of friction and wear resistance of surfaces [11].

## REFERENCES

- [1] F. Mücklich, A. Lasagni, C. Daniel, *Intermetallics*, 13 (2005) 437-442
- [2] A. Lasagni, M. Seyler, C. Holzapfel, W. Maier, F. Mücklich, *Adv. Mater.*, 17 (2005) 2228-2232
- [3] A. Lasagni, C. Holzapfel, F. Mücklich, *Proc. Mat. Res. Soc. Symp.* 890-Y04, 02.1-6
- [4] A. Lasagni, F. Mücklich, *Appl. Surf. Sci.*, 247 (2005) 32-37
- [5] A. Lasagni, F. Mücklich, *Appl. Surface Sci.* 240 (2005) 214-221
- [6] A. Lasagni, C. Holzapfel, F. Mücklich, *Adv. Eng. Mater.*, 7 (2005) 6, 487-492
- [7] A. Lasagni, F. Mücklich, *Practical Metallography*, 43 (2006) 1, 16-29.
- [8] C. Daniel, A. Lasagni, F. Mücklich, *Surface and Coatings Technology*, 180–181 (2004) 478–482
- [9] F. Yu, F. Mücklich, P. Li, H. Shen, S. Mathur, C.-M. Lehr, U. Bakowsky, *Biomacromolecules*, 6 (2005) 1160-1167
- [10] A. Lasagni, M.R. Nejati, R. Clasen, F. Mücklich, *Adv. Eng. Mater.* (accepted)
- [11] C. Daniel, F. Mücklich, *Wear*, 257 (2004) 266-270

# Silica-Based Capillary Monoliths. New Stationary Phases for Liquid Chromatography

Stefan Laschober and Erwin Rosenberg (Faculty Mentor)

Institute of Chemical Technology and Analytics

Vienna University of Technology

Vienna, Austria

Email: e9727027@stud3.tuwien.ac.at

**Abstract** — *Aim of the presented work was to develop a synthetic protocol to obtain MTMS based monolithic capillary columns. Synthetic protocols based on basic and on acidic catalysed sol-gel reaction have been developed so far. Several influential parameters as temperature, reactionary mixture composition, catalyst concentration and ageing procedures have been examined. Morphological characteristics were studied by scanning electron microscopy and nitrogen adsorption. Results for the acidic hydrolysis protocols have shown that the obtained morphological features are strongly influenced by the mentioned synthetic parameters.*

## I. INTRODUCTION

The development of new analytical methods is driven by both, new achievements in instrumentation, analytical methodology and the development of new materials. One of the areas of research where this has become most evident is the general trend of miniaturisation which has also had great impact on analytical separation techniques and lead to an increased importance of micro-high performance-liquid chromatography ( $\mu$ -HPLC), micro-capillary electrophoresis ( $\mu$ -CE) and capillary electrochromatography (CEC). Reduced sample amount and solvent use are the main advantages of miniaturised separation techniques as well as being ideally compatible with electrospray-mass spectrometric detection [1-3].

One of the most interesting new materials for (miniaturised) capillary chromatography are monolithic stationary phases. These are characterised by a high macroporosity which leads to excellent flow properties (low column back pressure even at flow rates up to ten times higher than typically used in packed column chromatography) while offering excellent or even superior separation performance when compared to packed columns of equivalent particle diameter as a consequence of their meso- and microporous structure.

These hierarchically structured materials provide, in a combination of the two pore regimes, the high

surface area as well as short diffusion pathlengths for the analyte molecules for optimum chromatographic separation. In this way, high chromatographic efficiency can be obtained even at high flow rates, inaccessible to packed columns. Further to these theoretical advantages, monolithic columns have the practical advantage of being self-supporting. They do thus not require end frits to keep the stationary phase within a confined volume which may deteriorate column efficiency and lead to bubble formation, as is particularly a problem in capillary electrophoresis (CE) and CEC.

## II. SYNTHESIS OF SILICA-BASED CAPILLARY MONOLITHS

There are several synthetic routes to obtain monolithic stationary phases [4]. Producing the silica based monoliths directly inside a capillary (of 0.53 mm I.D. or less) is convenient in that the monolith does not have to be clad in a subsequent (and very sophisticated) process, but it adds to the constraints for the synthesis of the monolith. In particular, shrinking of the monolithic material during and after synthesis has to be avoided by chemical bonding to the capillary wall.

The presented work makes use of sol-gel synthesis, since it can be performed at room temperature and under very mild (even physiological) conditions. This synthetic route furthermore offers great flexibility in the choice of reaction parameters, and thus the ability to tailor the properties of the resulting product to a certain extent [3]. The chosen protocol [5] uses methyltrimethoxysilane (MTMS) as precursor, which ultimately leads to a methylsilsesquioxane (Me-SiO<sub>1.5</sub>) bulk material.

The main advantage of this approach is that a bulk material is obtained that already possesses a hydrophobic surface. No further chemical modification of the bulk material (typically done by reaction with C8- or C18 silanes) is necessary to provide a surface suitable for reversed phase separation. Further assets of this approach are the

potentially higher durability of this column under extreme conditions (low or high pH and elevated temperature) and improved inertness of the column towards basic compounds (particularly important in pharmaceutical analysis) due to a reduced number of surface silanols.

In brief, the reaction mixture is filled into a 0.53 mm I.D. fused silica capillary of several cm length. The capillary is then sealed and put into an oven for gelation over night. Several parameters such as catalyst concentration, reaction solution composition and gelation temperature have been varied in order to study the dependence of the resulting xerogel morphology on them.

### III. MORPHOLOGICAL CHARACTERISATION

The morphology of the column materials was characterised by scanning electron microscopy (SEM) in the back-scattered electron mode on a JEOL 6400 instrument. This allows for a lateral resolution of approximately 200 nm. In addition to the morphological characterisation, nitrogen adsorption measurements [5] and liquid chromatographic measurements [7] have also been demonstrated to provide valuable information on the structure and physico-chemical properties of the materials

### IV. RESULTS

It is currently accepted that the mechanism for the formation of the xerogel structure is phase separation occurring during the gelation process. The structure of the two co-continuous phases will be frozen at the onset of gelation. Parameters influencing the phase system and influencing the gelation time will therefore determine the resulting xerogel structure.

Results show that most of the monolithic xerogels produced according to the present procedure possess a skeletal structure with a continuous open pore network. Pore- and skeletal diameters can be tailored by changing the parameters for synthesis accordingly. Pore diameters can be varied from 0.8 to 15  $\mu\text{m}$ , diameters of the xerogel network can be varied from 0.4 to 12  $\mu\text{m}$ , respectively. Specific surface areas have been observed up to 340  $\text{m}^2/\text{g}$ , although many materials completely lack a considerable amount of inner surface area. The strong dependency of the monolith structure and porosity on the parameters of synthesis requires rigid control for reproducible results. Under these conditions, however, monolithic silica-based columns can be synthesised that have great potential for use in all liquid phase capillary separation techniques.

### ACKNOWLEDGMENTS

I want to thank Dr. Elisabeth Eitenberger for conducting the measurements on the JEOL 6400 instrument and Dr. Doris Brandhuber for providing nitrogen adsorption measurements.

### REFERENCES

- [1] Tanaka N., Kobayashi H., *Anal. Bioanal. Chem.*, 376, 298 (2003)
- [2] Tanaka N., Kobayashi H., Nakanishi K., Minakuchi H., Ishizuka N., *Anal. Chem.* 73, (2001) 420A
- [3] Unger K.K., du Fresne von Hohenesche C., Ditz R., in: Schüth F., Sing K.S.W., Weitkamp J. (eds.): *Handbook of Porous Solids*, Wiley-VCH, Weinheim (2002)
- [4] Li W., Fries D., Malik A., *J. Chromatogr. A*, 1044, 23 (2004)
- [5] Sulyok M., Vienna University of Technology, PhD Thesis (2004)
- [6] Kimata K., Iwaguchi K., Onishi S., Jinno K., Eksteen R., Hosoya K., Araki M., Tanaka N., *J. Chrom. Sci.*, 27, 721 (1989)
- [7] Popp M., Diploma Thesis, Vienna University of Technology (2004)

# Preparation And Properties Of Electrochromic Device

Michal Macalik and Marie Sedlarikova (Faculty Mentor)  
Faculty of Electrical Engineering And Communication  
Brno University of Technology  
Brno, Czech Republic  
Email: xmacal01@stud.feec.vutbr.cz

**Abstract** — The tin oxide thin films doped with the fluorine and the antimony were prepared by a spray pyrolysis method from  $\text{SnCl}_2$  precursor. The fluorine (FTO) and antimony (ATO) dopant ratio were varied and the lowest resistivity was founded for the both type of dopants. The films have moderate an optical transmission. The vanadium oxide films were dip-coated on the FTO (0,7 wt. %) layers. The coating solution was prepared by dissolving a  $\text{V}_2\text{O}_5$  powder in a  $\text{H}_2\text{O}_2$  solution. The 0,5M  $\text{LiClO}_4/\text{PC}$  gel electrolyte was used as a ion conductor layer. The vanadium oxide films showed a reversible multichromism (yellow  $\leftrightarrow$  green  $\leftrightarrow$  blue) upon  $\text{Li}^+$  ion insertion/extraction.

## I. INTRODUCTION

The electrochromic devices can be applied in practice in special devices such as information displays, mirrors with regulated light reflectance and surfaces with regulated radiation “Smart windows“. The electrochromic materials can change their optical properties upon charge insertion/extraction. This effect is created by insertion of ions from the electrolyte (ion conductor) into the structure of the host material (electrochromic film) in the present of electric voltage. Electrochromic layers have composition of special thin films coated on glass substrates. The following “figure 1“ shows the composition of electrochromic device.

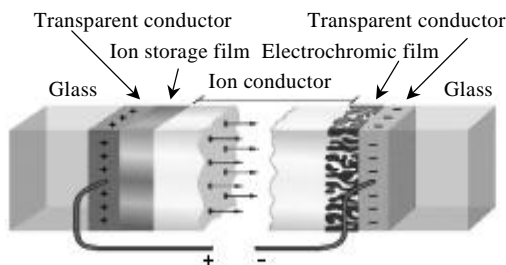


Figure 1: Basic design of an electrochromic device, indicating transport of positive ions under the action of an electric field [1]

## II. EXPERIMENTAL

Microscopic glass slides were used as substrates. The size of the glass support was 20 x 20 mm.

Preparation of tin layers: 10 g  $\text{SnCl}_2 \cdot 2\text{H}_2\text{O}$  was dissolved in 4 ml of 15%  $\text{H}_2\text{O}_2$  under agitation. This solution was heated at 80°C and 50 ml ethanol was added. The  $[\text{NH}_4\text{F}/\text{SnCl}_2]$  ratio by weight percentage in the spray liquid is kept at values of 0, 4, 7, 10 and 13, the  $[\text{SbCl}_3/\text{SnCl}_2]$  ratio at 0, 0,1, 0,25, 0,4, 0,7 and 1. Higher  $\text{SbCl}_3$  concentration has negative influence on film structure and the optical transmission is lowered [2]. The respective deposition temperature was 420 °C.

Preparation of vanadium layers: 0,5 g  $\text{V}_2\text{O}_5$  was dissolved in 30 ml of 15%  $\text{H}_2\text{O}_2$ . This red-brownish solution was very unstable and it had to be placed into a water-bath at 80 °C for 0,5 h [3]. It was obtained very viscous solution. This solution was diluted with distilled water in the ratio 2:1, 1:1, 1:2, 1:3 and one part was kept neat. The glass substrates with FTO (7% wt.) were dipped into these solutions and covered with different thickness of vanadium layers. These samples were heat-treated in an oven at 150 °C for 1 h and homogenous greenish films were obtained.

The 0,5M  $\text{LiClO}_4/\text{PC}$  polymer gel electrolyte was applied like the ion conductor and ion storage layer is represented by FTO film.

## III. RESULTS AND DISCUSSION

It seems probable that the droplets of the solution evaporate immediately when they touch the substrate. The surface of the layer consists of small particles formed probably by rapid evaporation of the droplets.

In the fluorine doped tin oxide films, the F anion substitutes for an  $\text{O}^{2-}$  anion in the lattice, creates more free electrons and decreases the value of  $R_{\text{sh}}$  [4]. The minimum value is obtained at  $\text{NH}_4\text{F}/\text{SnCl}_2 = 7$  wt.%. Increasing the value of  $R_{\text{sh}}$  after a specific level of F content probably represents a solubility limit of F in the tin oxide lattice.

When Sb is added to  $\text{SnO}_2$ , Sb is incorporated into the  $\text{Sn}^{4+}$  sites of the  $\text{SnO}_2$  lattice substitutionally. In

ATO samples, Sb is in two different oxidation states namely,  $\text{Sb}^{5+}$  and  $\text{Sb}^{3+}$ . During the initial addition of Sb in tin oxide film, the  $\text{Sb}^{5+}$  substituted on the  $\text{Sn}^{4+}$  site act as donors and create excess electrons. At  $\text{SbCl}_3/\text{SnCl}_2 = 0,25$  wt.%, the film reaches the minimum value of sheet resistance. Further addition of Sb introduces the  $\text{Sb}^{3+}$  sites, which act as acceptors. The Sb species would compensate the donor levels, which were created by the Sb species, leading to an increase in the  $R_{sh}$  [4].

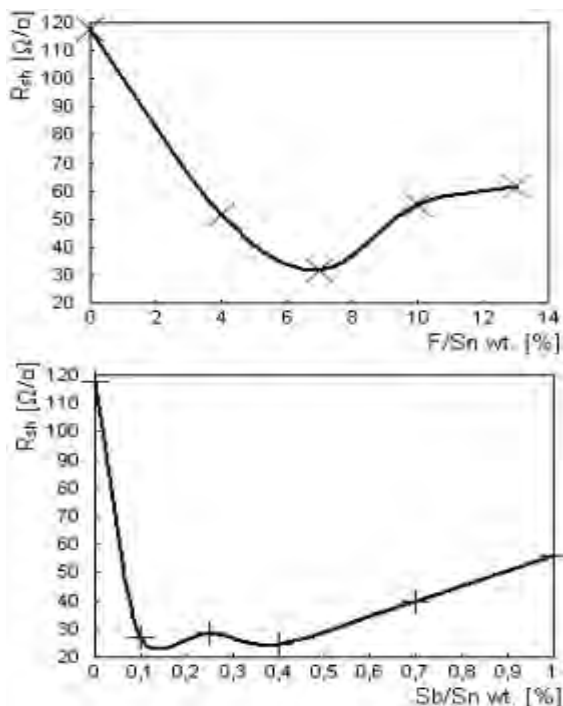


Figure 2: Variation of sheet resistance with dopant ratio for  $\text{SnO}_2$  films

The optical transmission of the electrochromic device samples was measured between 300 and 900 nm for all. The results for sample diluted in the ratio 1:2 and for neat solution are shown in “figure 3 and 4”.

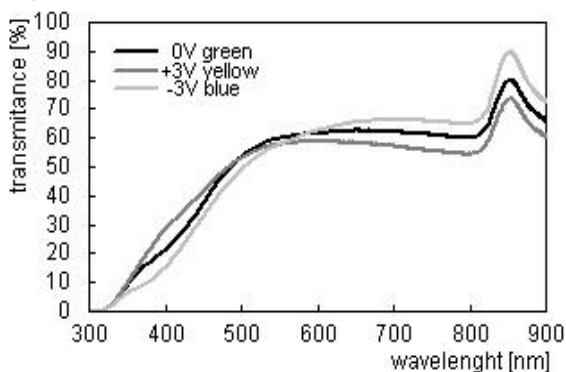


Figure 3: Electrochromic device with diluted  $\text{V}_2\text{O}_5$  layer in the ratio 1:2

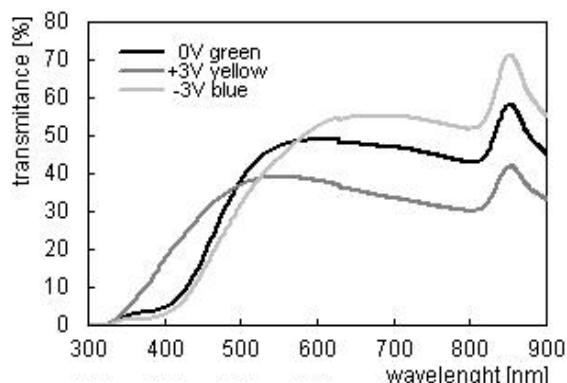


Figure 4: Electrochromic device with neat  $\text{V}_2\text{O}_5$  layer

Us we can see from the figures 3 and 4, the thicker layer lowers the optical transmission, but the difference between color change is stronger.

## CONCLUSION

The fluorine and antimony dopant ratio were varied and the lowest resistivity were founded. For FTO is the best value  $30 \Omega/\square$  ( $\text{F}/\text{Sn} = 0,7$  wt.%) and  $20 \Omega/\square$  ( $\text{Sb}/\text{Sn} = 0,25$  wt.%) for ATO. The films have moderate optical transmission. Vanadium oxide films were dip-coated on FTO (0,7 wt. %) layers. Coating solution was prepared by dissolving  $\text{V}_2\text{O}_5$  powder in  $\text{H}_2\text{O}_2$  solution. The vanadium oxide films showed a reversible multichromism (yellow  $\leftrightarrow$  green  $\leftrightarrow$  blue) upon  $\text{Li}^+$  ion insertion/extraction. The transmittance modulation range can be varied by adjusting the film thickness.

## ACKNOWLEDGMENTS

This work was supported by the Grant Agency of the Academy of Sciences (grant No. B208130604).

## REFERENCES

- [1] C. G. Granqvist. Electrochromic devices. Journal of the European Ceramic Society, 25:2907–2912, 2005.
- [2] M. Macalik. Thin Layers of  $\text{SnO}_2$  Deposited by Spray Method. In Proceedings of the 11th Student EEICT 2005, pages 279 – 283, Brno University of Technology, FECC, 2005.
- [3] Z. Wang, J. Chen, X. Hu. Electrochromic properties of aqueous sol-gel derived vanadium oxide films with different thickness. Thin Solid Films, 375:238-241, 2000.
- [4] B. Thangaraju. Structural and electrical studies on highly conducting spray deposited fluorine and antimony doped  $\text{SnO}_2$  thin films from  $\text{SnCl}_2$  precursor. Thin Solid Films, 402:71-78, 2002.

# Rheological, morphological and mechanical properties of poly( $\epsilon$ -caprolactone) - thermoplastic starch blends

Anna Nahálková, Peter Bugaj, Veronika Fuleová, Pavol Alexy (Faculty Mentor)  
Institute of Polymer Materials  
Slovak University of Technology, Faculty of Chemical and Food Technology  
Bratislava, Slovak Republic  
Email: {anna.nahalkova@stuba.sk, peter.bugaj@stuba.sk, pavol.alexey@stuba.sk}

**Abstract** - Three types of starch were used for the preparation of thermoplastic starch. Natural corn starch, modified corn starch and pre-gelatinized corn starch. Plasticization was made at two temperatures - 20°C and 80°C at the constant concentration of plasticizer - 30%wt. Thermoplastic starches were prepared in a twin screw extruder and afterwards polycaprolactone (PCL) with thermoplastic starch blends were prepared as well. The blends were characterized by mechanical properties and scanning electron microscopy. In further experiments, the pre-gelatinized corn starch was plasticized in concentration range of plasticizer 25 - 40 %wt. and blended with PCL.

## I. INTRODUCTION

Polycaprolactone (PCL) is linear polyester produced by ring-opening polymerization of  $\epsilon$ -caprolactone. It is a semicrystalline polymer which exhibits low glass transition temperature and melting point about 60-70°C. The PCL is a flexible polymer with high elongation at break and low Young modulus. Its physical properties and commercial availability make it very attractive, but due to its low melting point (~65°C), PCL is difficult to be processed by conventional techniques for thermoplastic materials. However, this difficulty can be partially overcome by blending of the PCL with other components, such as native or thermoplastic starch. Moreover, replacement of the expensive synthetic PCL matrix with starch reduces the cost of the produced material and it also positively modifies its biodegradability.

Thermoplastic starch (TPS) is obtained from native starch by simultaneous destruction of starch particles and plasticization with plasticizer under high shear forces and elevated tempera-

tures. Natural starch cannot be processed by conventional plastics technology plasticizing process because degradation of starch starts at a temperature lower than its melting point.

## II. EXPERIMENTAL

### A. MATERIALS

The polycaprolactone, having a molar mass of ~80 000 g/mol, was supplied by SOLVAY, Warrington, Great Britain under the trade name CAPA 6800. The native cornstarch MERITENA 100 was provided by T&L, Slovakia, WAXY maize starch and pre-gelatinized GEL- INSTANT starch were provided by CERESTAR, Benelux.

### B. EXTRUSION

Thermoplastically processable starches (TPS) and PCL/TPS blends were prepared in a laboratory-scale LABTECH co-rotating twin screw extruder ( $\Phi=16$ ,  $L/d=40$ ). The extrusion conditions, established by experiment, were: for TPS: temperature profile: 100/140/150/2x160/140/140/3x130; screw speed: 200 rpm, for PCL/TPS blends: temperature profile: 110/120/130/140/3x150/140/120/110; screw speed: 110 rpm. The venting zone under the vacuum pump was used for removing of volatile substances (preferably water) from the melt at the end of the extruder. Glycerol was used as plasticizer and it was thoroughly pre-mixed with the corn-starch powder before twin-screw processing.

### C. MECHANICAL PROPERTIES

Tensile strength, Young modulus, elongation at break were measured on a Metrotest. The crosshead speed was 50 mm/min

#### D. SCANNING ELECTRON MICROSCOPY (SEM)

The specimens were fractured, after freezing in liquid nitrogen and the morphology of the fracture surfaces was evaluated using a scanning electron microscope (Tesla BS-300).

### III. RESULT AND DISCUSSION

#### A. BLEND MORPHOLOGY

In polymer blends, it is essential to study the morphology of the final product since most of its properties, especially its mechanical properties, depend on it. In Figure 1, the SEM images of PCL/TPS blends are presented. For starches, that were plasticized at 20°C, the best melting properties as well as fine phase dispersion was achieved in the case of PCL/pre-gelatinized corn starch blend. This effect is probably due to the previous reduction of the crystallinity of the starch. A similar morphological structure was observed also in the case of PCL blend containing modified corn starch, which was plasticized at a higher temperature, but blend based on PCL/pre-gelatinized corn starch exhibits higher values of elongation at break and tensile strength.

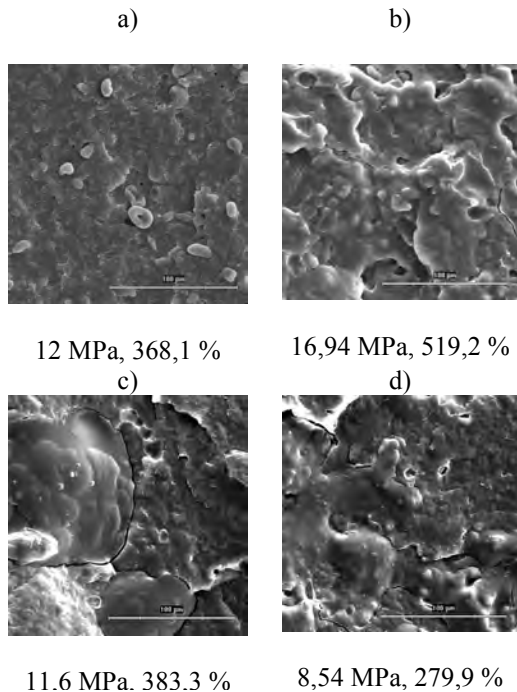


Figure 1: SEMs and mechanical properties (tensile strength, elongation at break) of PCL/TPS blends with (a) natural corn starch, (b) modified corn starch, (c) pre-gelatinized corn starch plasticized at 20°C; (d) modified corn starch plasticized at 80°C

#### B. MECHANICAL PROPERTIES

The changes in mechanical properties of PCL/TPS in dependence on the plasticizer concentration at the constant content of pre-gelatinized corn starch plasticized at 20°C - 30%wt. are presented in Table 1.

Glycerol content (wt.%)	Tensile strength (MPa)	Elongation at break (%)
25	7.4	232.8
30	5.9	149.4
35	9.0	376.9
40	16.6	618.4

Table 1: The mechanical properties of PCL/TPS with various content of plasticizer

All evaluated properties of the final blends were improved following the rising concentration of plasticizer in starch.

#### IV. CONCLUSIONS

The morphological and mechanical properties of PCL blends containing three types of starch plasticized at two temperatures were investigated. The best melting properties as well as fine phase dispersion was achieved in the case of PCL/pre-gelatinized corn starch blend.

The mechanical properties of the PCL/pre-gelatinized corn starch plasticized in concentration range of plasticizer 25 – 40 %wt were investigated. All evaluated properties of the final blends were improved following the concentration of plasticizer in starch.

# Excessive Grinding and Its Effect on Ageing of Calciumsulphate $\alpha$ -Hemihydrate

Ivo Ostradecký, Marcela Fridrichová  
Institute of Technology of Building Materials and Components  
Faculty of Civil Engineering  
University of Technology in Brno  
Brno, Czech Republic  
Email: ostradecky.i; fridrichova.m@fce.vutbr.cz

**Abstract** – *The influence of excessive grinding on selected properties of a new alpha hemihydrate and properties after ageing was studied. Grinding can cause lattice distortion of crystal structure of hemihydrate and this has influence on particle size, particle size distribution, specific surface and water adsorption ability thereby reactivity, water gypsum ratio, setting time, strengths. One alpha hemihydrate was used and grinded in a vibrating and ball mill for 5 and 15 minutes. The ageing of hemihydrate was carried out by 65 and 98% relative humidity.*

## Introduction

Alpha hemihydrate ( $\alpha$ -CaSO<sub>4</sub>·0,5H<sub>2</sub>O) is produced under higher temperature and pressure in saturated vapour in autoclaves either as a pressed blocks or suspension or only in higher temperature in a salt or acid lotion. By these conditions crystallize the good shaped crystals of alpha hemihydrate in orthorhombic system without any lattice or surface defects. The hemihydrate is than grinded in a mill to reach required fineness. Intensive grinding can cause surface and lattice defects and these influence behaviour of the final product. It is expected that on broken surfaces and surfaces that were exposed to intensive friction is higher surface energy. Particles with surface charge may attract more air moisture than usually grinded particles which can cause change of binder phase composition, reactivity and other important properties.

The ageing process of calciumsulphate hemihydrate was already studied by many authors, but the effect of deterioration originating from grinding process and its influence on ageing of hemihydrate was not studied so far.

## Material and methods

An industrially produced alpha hemihydrate was used to carry out our research. It was dried first by 40°C 24 h to replace free moisture before all measurements were carried out. The binder was grinded in two different laboratory mills. The vibrating mill (SCW) and ball mill (SKM) were used to additional grinding for 5 and 15 minutes. The grinding balls affect the material mostly by gravimetrically effect and with slight friction whereas by grinding in a vibrating mill the leading grinding effect is caused by intensive friction between grinding balls and material.

Original and grinded binder specimens were than aged by 65 and 98% relative humidity for 90 days. Specimens of binds were spread on plastic scales in layer max. 8mm. During ageing was measured moisture adsorption gravimetrically. After ageing for 1, 3, 14 and 90 days were determined changes in phase composition by means of wet chemical phase analyse, XRD analyse, specific surface BET, REM microscopy, hydration by mean of differential scanning calorimetry DSC and solubility of a new specimens.

## Results and discussion

The effect of grinding in various mills and grinding times showed higher efficiency of a ball mill on particle size. That confirms also results obtained from DSC. The in ball mill grinded specimens showed earlier reached hydration maximum and faster hydration. But the whole hydration warm is by all specimens the same. By ageing by 65% relative humidity were reached equilibrium moisture of specimens after 21 days and stayed constant. There was no effect on phase composition. The specific surface has become smaller because

of so-called healing effects. By the hydration showed specimens no significant changes in comparison to specimens before ageing. The specimens aged by 98% relative humidity did not reached equilibrium moisture within 90 days and the grinded specimens adsorbed much more moisture than originally alpha hemihydrate. Also phase composition has changed remarkable as secondary dihydrate appeared in a large scale in all specimens. The higher fineness of specimen more newly hydrated dihydrate after ageing on particle surfaces. This caused drop of specific surface thereby reactivity. Secondary dihydrate act as a setting accelerator, but because of high amount of hemihydrate particles covered with dihydrate longer hydration time is needed as hydration is controlled by diffusion into the particles via surface layer of dihydrate with lower solubility than hemihydrate.

Material Properties	Phase	$\alpha$ -HH		Vibrating mill				Ball mill			
	Age			SCW 5		SCW 15		SKM 5		SKM 15	
Phase composition [%]	r.h. [%]	65	98	65	98	65	98	65	98	65	98
	GV [%]	6,5	8,4	6,1	6,7	6,1	6,7	6,8	11,7	6,8	11,9
	FF [%]	0,9	1,1	0,2	0,8	0,1	0,9	0,9	0,8	0,9	0,8
	HH [%]	93,7	83,3	93,1	93,1	94,4	93,7	93,9	61,3	92,8	57,8
	AIII [%]	0,0	0,0	0,0	0,0	0,0	0,0	0,0	0,0	0,0	0,0
	AIIIs [%]	0,8	0,7	1,6	1,1	0,8	0,7	0,9	0,9	1,2	0,8
	DH [%]	0,0	10,2	0,8	0,7	0,4	0,4	0,5	33,5	0,7	36,1
Weight change during ageing 90 days [%]		0,9	7,7	1,0	10,0	1,0	10,4	0,9	11,6	0,9	12,7
Specific surface area BET [m <sup>2</sup> /g]	New	0,72		0,67		0,89		0,95		1,22	
	14 days	0,70	0,48	0,63	0,60	0,48	0,66	0,75	0,71	0,96	0,97
	90 days	0,59	0,57	0,62	0,62	0,75	0,51	0,66	0,41	0,99	0,57

Table 1: Phase composition, specific surface and adsorption of  $\alpha$ - hemihydrates after 90 days of ageing

## Acknowledgement

This research was carried out in laboratories of the F.A.Finger-Institut für Baustoffkunde, Bauhaus-Universität Weimar. The paper was written with the kind help of Dipl.-Ing. Saskia Nowak.

## Literature

- [1] Fischer H.-B.; Krivenko P.V.; Sanitsky M.: Zum ‘Altern‘ von Gipsbindemitteln. *15. ibausil Weimar 2003., Tagungsband 2*, S. 1127-1138
- [2] Fischer H.-B., Nowak S., Ostradecky I.: Změny vlastností alfa a beta sádry při uložení ve vlhkém prostředí. *Sádra 2005*, Vysoké učení technické v Brně, FAST, s.12-19, ISBN 80-214-3041-9
- [3] Hummel H.-U.; Abdussaljamov B.; Fischer H.-B.; Stark J.: Untersuchungen zur hygro-mechanischen Stabilität von kristallinem Calciumsulfat-Halbhydrat, Teil 1, *ZKG Internat.*, 54 (2001) 5, S. 272-279
- [4] Hummel H.-U.; Abdussaljamov B.; Fischer H.-B.; Stark J.: Untersuchungen zur hygro-mechanischen Stabilität von kristallinem Calciumsulfat-Halbhydrat, Teil 2, *ZKG internat.*, 54 (2001) 8, S. 458 – 465
- [5] Lehmann H.; Mehta S.K.: Einfluß der Kristallitgröße auf die physikalisch-chemischen Eigenschaften verschiedener Calciumsulfat-Hydrate, *TIZ* 91(1973) 8, S. 217-222
- [6] Nowak S.; Fischer H.-B.: To the aging behaviour of Calcium Sulphate Binders, *Cheminè Technologija Nr. 3 (33)*, Kaunas Technologija 2004, S. 58-65, ISSN 1392-1231
- [7] Sanitsky M.A., Fischer H.-B., Soltysik R.A. :Fine-ground gypsum binders with mechanical-chemical activation. In *14.ibausil, (2000), Band 1*, s. 0259 – 268

# Three Dimensional Micromechanics Finite Element Model for Shape Memory Alloys Based on Return Mapping

Andrej Pukšič and Franc Kosel  
Faculty of Mechanical Engineering  
University of Ljubljana  
Ljubljana, Slovenia

Email: {andrej.puksic, franc.kosel}@fs.uni-lj.si

**Abstract** — A numerical algorithm for solving 3-D constitutive equations for shape memory alloys is presented in this paper. The crystal plasticity idea is applied and the integration of the corresponding constitutive equations is achieved by means of the return mapping algorithm. To model the polycrystal structure of real materials, the finite element method is used. 24 habit planes variants are considered in each crystal grain and a selection algorithm is applied to achieve consistency of transformation conditions. Preliminary calculations show our model's accordance with experimental observations on a qualitative level.

## I. INTRODUCTION

Shape memory alloys (SMA) have a unique capability of recovering the original shape after sustaining relatively large deformations. This is called shape memory effect when referred to the capability of shape recovery after deforming at low temperature, unloading and subsequent heating. However, if deformed at higher temperatures shape can be recovered by unloading only at constant temperature and this is called superelasticity. Both effects are attributed to a diffusionless phase transformation called the martensitic transformation (MT) during which the material transforms from the austenite phase to the martensite phase.

Originally, only the behaviour of SMA under uniaxial loading has been studied. Due to the complexity of mechanisms behind the MT further interesting behaviour was observed under multi-axial loading. Therefore, present interest is directed towards developing multi-axial material model. Here a model based on the crystal plasticity idea is presented. This idea takes advantage of the similarity of the crystal plasticity and MT which both involve shear-like mechanisms. First, the corresponding constitutive equations for a single crystal as proposed in [1] are briefly presented. Then it is shown how the equations can be solved for a polycrystal numerically by applying the return mapping algorithm and incorporating it into the finite element method. Finally, some results are presented.

## II. CONSTITUTIVE EQUATIONS

Martensite can be formed from austenite in several ways, which means that various variants of martensite exist. The variants are identified by the habit plane normal and the shear direction. 24 habit planes have been observed experimentally in SMAs, so 24 variants are considered here. The resolved shear stress on the  $r$ -th variant may be calculated as

$$\tau^r = \alpha_{ij}^r : \sigma_{ij}, \quad r = 1, \dots, 24 \quad (1)$$

where  $\alpha_{ij}^r$  stands for the Schmid factor, and  $\sigma_{ij}$  for the stress tensor of the crystal grain.

Stress-induced martensite transformation starts at the  $r$ -th variant when the resolved shear stress at that variant reaches its critical value  $\tau_{cr}^r$ , which is a material property and is assumed to depend on temperature and hardening [1]:

$$\tau_{cr}^r(T, \gamma^r) = \tau_{cr}^r(T_{ref}) + \beta(T - T_{ref}) + \sum_{i=1}^{24} h_{ri} \gamma^r, \quad (2)$$

where  $\gamma^r$  is the shear transformation strain of the  $r$ -th variant,  $h_{ri}$  the hardening coefficients tensor,  $\beta$  is the temperature coefficient and  $T_{ref}$  the reference temperature, for example, the room temperature.

If we express the transformation condition as

$$F^r = \tau^r - \tau_{cr}^r, \quad (3)$$

it is obvious that  $F^r \leq 0$  and  $F^r = 0$  only when transformation is in progress at the  $r$ -th variant. State where  $F^r > 0$  is physically inconsistent.

The transformation strain component of the total strain of the crystal grain is calculated from

$$\varepsilon_{ij}^{tr} = \sum_{r=1}^{24} \alpha_{ij}^r \gamma^r \quad (4)$$

and the total strain is expressed as

$$\varepsilon_{ij} = \varepsilon_{ij}^{el} + \varepsilon_{ij}^{tr} + \varepsilon_{ij}^{th}. \quad (5)$$

We obtain the elastic part  $\varepsilon_{ij}^{el}$  from the Hooke's law

and the thermal part  $\varepsilon_{ij}^{th}$  from the thermal strain law.

### III. NUMERICAL ALGORITHM

#### A. RETURN MAPPING ALGORITHM (RM)

The presented constitutive equations can be solved numerically step-by-step. That is, a set of variables  $\{\varepsilon_{ij}^{n+1}, \gamma^{r,n+1}, T^{n+1}\}$  at step  $n+1$  is calculated from a known state  $\{\varepsilon_{ij}^n, \gamma^{r,n}, T^n\}$  in the previous step. For simplicity sake we assume the temperature constant. First, we increase strain by a chosen increment  $\Delta\varepsilon_{ij}^{n+1}$ , so  $\varepsilon_{ij}^{n+1} = \varepsilon_{ij}^n + \Delta\varepsilon_{ij}^{n+1}$  and then we apply the RM which consists of the following steps:

1. Calculate a trial state by applying the constitutive equations, but assuming only elastical state, that is, setting  $\gamma^{r,n+1,trial} = \gamma^{r,n}$ .
2. Create a set  $\Gamma = \{r / F_r^{n+1,trial} \geq 0, r = 1, \dots, 24\}$  of active variants. If no such variants exist go on to the next step  $n+2$ .
3. Calculate the increase of transformation strain  $\Delta\gamma^{r,n+1}$  from the condition  $F_r^{r,n+1} = 0$  for all active variants. At this point the so called Kuhn-Tucker complementarity conditions should be checked. However, to ensure the convergence of the finite element method this must be done later on.
4. Update other variables inserting the calculated transformation strain in the constitutive equations.

#### B. FINITE ELEMENT METHOD (FEM)

To describe the polycrystal structure of material, every element in the FEM mesh represents a crystal grain. Its crystal lattice orientation is determined by randomly assigning Eulerian angles relative to the global coordinate system, as in [2].

When the RM is incorporated into the FEM we get a nonlinear system of equations which is solved by the Newton method. Jacobian requires the calculation of  $\partial\sigma_{ij}^{n+1} / \partial\varepsilon_{ij}^{n+1}$  which can be derived analitically.

Only after solving the FEM equations must we check the Kuhn-Tucker conditions. If these are not fulfilled the set of active variants  $\Gamma$  must be corrected and calculation repeated, similar as in [3].

### IV. RESULTS

Some preliminary calculations were made using material properties for a Cu-based SMA provided in [2]. A standalone computer program was written and the stress-strain response was simulated on a cube under uniaxial tension/compression load (Figure 1).

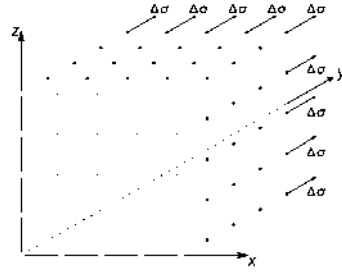


Figure 1: Finite elements mesh and loads

Figure 2 shows the model's ability to capture the tension-compression asymmetry, which is in accordance with experimental observations, at least qualitatively. Our model also describes the basic temperature dependence and predicts the closed loop at cyclic loading.

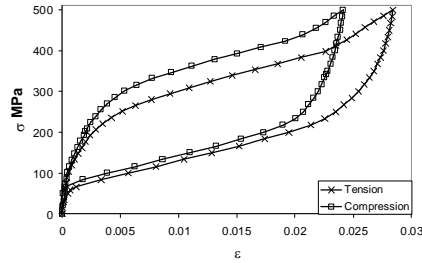


Figure 2: Tension-compression asymmetry

### V. CONCLUSIONS

The results show that our model is capable of capturing some of the basic and more advanced phenomena that occur in SMA. However, the model still needs to be upgraded to take account of more effects. Furthermore, experiments should be conducted to compare the numerical and experimental results and to determine the material properties required by the model.

### REFERENCES

- [1] M. Tokuda, M. Ye, M. Takakura, P. Sittner. Thermomechanical behavior of shape memory alloy under complex loading conditions, *International Journal of Plasticity*. 15(2):223-239, 1999
- [2] Y. Kitajima, N. Sato, K. Tanaka, S. Nagaki. Crystal-based simulations in transformation thermomechanics of shape memory alloys, *International journal of plasticity*, 18(11):1527-1559, 2002
- [3] A.S.J. Suiker and S. Turteltaub. Computational modelling of plasticity induced by martensitic phase transformations. *International Journal for Numerical methods in Engineering*, 63(12):1655-1693, 2005

# Preparation of Lanthanide Oxide Nanoparticles from Microemulsions and by Controlled Precipitation

Christoph Rill and Guido Kickelbick

Vienna University of Technology, Institute of Materials Chemistry

Getreidemarkt 9, A1060 Vienna, Austria

Email: christoph.rill@tuwien.ac.at

**Abstract** — Nanoparticles based on the three selected lanthanides neodymium, ytterbium, and europium were prepared by a microemulsion approach and by controlled precipitation in the presence of coordinating ligands such as phosphonic acids and their derivatives. The effects of preparation parameters including the surfactant type, counter ion, pH, and temperature on the particle size were investigated by dynamic light scattering (DLS) and transmission electron microscopy (TEM). The microemulsions were found to lead to often uncontrollable particle agglomeration making this system difficult to optimize, especially at increased temperature. The use of phosphonates as growth-limiting ligands generally yields small and redispersible nanoparticles.

## I. INTRODUCTION

Nanoparticles have conquered a wide range of research fields such as surface-coatings [1] or catalysis [2] because of their unique properties induced by their electronic structure and large surface area. Paired with the specific electronic structure of lanthanides, nanoparticles based on these rare earth metals or their oxides have great potential in fields of optical or magnetic materials and applications, e. g. as luminescent markers in immunoassays [3]. A surface functionalization is usually necessary if the nanoparticles should be used in technological devices, and it is known that – because of their high stability and good compatibility to both organic materials and inorganic metal oxides – phosphonic acids and their esters represent ideal coupling molecules for the preparation of organic-inorganic materials [4].

We applied two different synthetic methods in the preparation of nanoparticles, the first one using the confined space of reversed micellar systems formed by water and one of the surfactants polyethyleneoxide(10)-octylphenylether (TX-100), sodium dodecylsulfate (SDS), or cetyl-trimethylammonium bromide (CTAB) in cyclohexane. The second method involves the precipitation of the nanoparticles from a solution of the respective metal salt in the presence of different coordinating ligands acting as capping agents

limiting the particle growth and as surface-functionalizing groups, e. g.  $\beta$ -diketones, sulfonates, or phosphonates. Our study focused on different phosphonic acid derivatives including dialkyl allylphosphonate and dialkyl undecenylphosphonate, both containing polymerizable groups, which were prepared by a Michaelis-Arbuzov reaction [5].

## II. RESULTS AND DISCUSSION

### A. WATER-IN-OIL MICROEMULSIONS

DLS measurements of the prepared nanoparticle dispersions reveal that the type of lanthanide, counter ion, and surfactant can have a large influence on the particle size (Figure 1). The two representative TEM micrographs displayed in Figure 2 show that this is to a large degree attributable to particle agglomeration during both the preparation and the extensive purification procedures. This agglomeration tendency inevitably led to problems with the reproducibility of the sample particle size. However, it was possible to determine the following trends for increasing particle size in the order of:

lanthanide ion:  $\text{Eu}^{3+} < \text{Yb}^{3+} < \text{Nd}^{3+}$

counter ion: acetate < nitrate < chloride

surfactant: TX-100 < CTAB < SDS

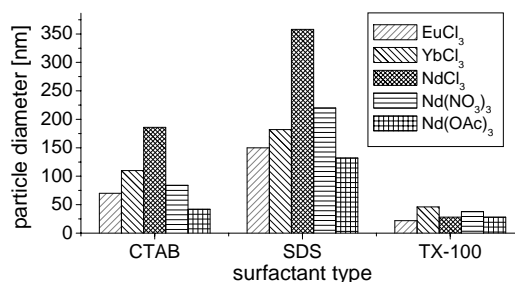


Figure 1: Dependence of particle size on lanthanide, counter ion, and surfactant type

The preparation temperature was raised to 60°C in order to achieve higher crystallinity of the samples but it was not possible to obtain similar results at this increased preparation temperature, because here the

reproducibility problems were more pronounced. This can be explained by both the thermal destabilization of the microemulsions (the non-ionic TX-100 emulsion phase-separated at this temperature) and kinetic effects which influence the droplet exchange processes governing the particle growth. X-ray diffraction (XRD) showed that while the particles are generally amorphous when prepared at room temperature, a higher degree of crystallinity can be achieved at a higher temperature.

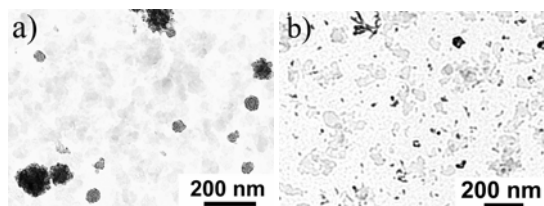


Figure 2: TEM micrographs of particles obtained from  $\text{NdCl}_3$  using **a)** SDS and **b)** Triton X-100

Increasing the pH of the microemulsion containing the precipitating agent ammonium hydroxide, thus offering an excess of precipitating agent, leads to a strong increase in particle size. Acidifying the lanthanide solution, on the other hand, was found to have almost no effect on the particle size.

#### B. CONTROLLED PRECIPITATION

These samples were prepared according to a procedure by Wakefield et al. [6], however, using phosphonates as coordinating ligands which limit the particle growth during their precipitation. The TEM images displayed in Figure 3 show that small and well dispersible nanoparticles with a narrow size distribution can be obtained by this method.

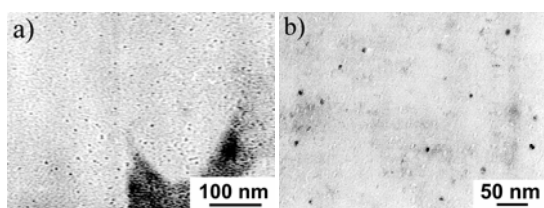


Figure 3: TEM micrographs of nanoparticles prepared using **a)** trioctylphosphine oxide and **b)** phenylphosphonic acid as ligand

While the type of alkyl chain of the phosphonic acid did not have a major influence on the size of the obtained particles, it does affect their redispersibility in various solvents. The particle size was found to be sensitive to the concentration of the components in the preparation mixture.

We observed that the use of a phosphonic acid as ligand generally leads to the premature formation of a

precipitate, presumably a phosphonate salt of the respective lanthanide. Thus, the dialkyl esters, rather than the acids, were employed. The fact that these esters successfully stabilize the nanoparticles suggests that during the precipitation they are hydrolyzed at the particle surface. Infrared spectroscopic measurements of surface modified materials revealed that the phosphonates are bound to the surface in a tridentate fashion with a delocalization of the  $\pi$ -electrons.

This preparation method provides quite a simple way for the in-situ surface modification of nanoparticles with the possibility to introduce various functionalities such as polymerizable groups via the phosphonate. It is feasible to use these functionalities for the incorporation of the modified nanoparticles in organic matrices, thus yielding inorganic-organic nanocomposites.

#### ACKNOWLEDGMENTS

Financial support of this work by the Austrian *Fonds zur Förderung der wissenschaftlichen Forschung* (FWF Project No. P17731) is gratefully acknowledged. We thank the University Service Center for Transmission Electron Microscopy of the Vienna University of Technology for providing the opportunity to carry out electron microscopic measurements.

#### REFERENCES

- [1] N. Burniston, C. Bygott, and J. Stratton. Nano technology meets titanium dioxide. *Surf. Coat. Int., Part A*, 87(A4):179-84, 2004.
- [2] S. Eriksson, U. Nylen, S. Rojas, and M. Boutonnet. Preparation of catalysts from microemulsions and their applications in heterogeneous catalysis. *Appl. Catal., A*, 265(2):207-19, 2004.
- [3] W. O. Gordon, J. A. Carter, and B. M. Tissue. Long-lifetime luminescence of lanthanide-doped gadolinium oxide nanoparticles for immunoassays. *J. Lumin.*, 108(1-4):339-42, 2004.
- [4] P. H. Mutin, G. Guerrero, and A. Vioux. Hybrid materials from organophosphorus coupling molecules. *J. Mater. Chem.*, 15(35-36):3761-68, 2005.
- [5] B. A. Arbuzov. Michaelis-Arbuzov and Perkov reactions. *Pure Appl. Chem.*, 9(2):307-35, 1964.
- [6] G. Wakefield, H. A. Keron, P. J. Dobson, and J. L. Hutchison. Synthesis and Properties of Sub-50-nm Europium Oxide Nanoparticles. *J. Coll. Int. Sci.*, 215(1):179-82, 1999.

# Ordered arrays of metallic nanoparticles for nanoelectronics

Jana Röschlová, Martin Weis, Marek Vančo, Drahoslav Barančok, Ján Vajda and Július Cirák  
Dept. of Physics, Faculty of Electrical Engineering and Information Technology,  
Slovak University of Technology, Ilkovičova 3, 81219 Bratislava, Slovak Republic.  
Email: Jana.Roschlova@stuba.sk

**Abstract** — *The dependence of the physical properties of the bulk magnetic materials is a well-known phenomenon. The interest in this field is focused on low-dimensional ordered systems of materials with nanometer-size particles, which exhibit novel electronic, optical, magnetic, chemical and bio-medical properties. In this paper we report on the preparation of well ordered Langmuir-Blodgett films of  $\gamma$ -Fe<sub>2</sub>O<sub>3</sub> nanoparticles with a mean size of 10nm. Arrangement and homogeneity were confirmed by scanning electron microscopy as well as atomic force microscopy. Magnetic properties were measured by the magneto-optical Kerr effect*

## I. INTRODUCTION

The construction of novel nanostructured materials attracts much attention in materials research due to potential applications in electronics, optics and magnetism. Physical properties of materials are in this case determined only by three parameters: the size of particles, their composition and topology of the system. The choice of technology used for organization of the system is thus important from the point of view of macroscopic properties. Preparation and processing of fine magnetic nanoparticles (NPs) is motivated for the last several decades by their variety of applications, such as ferrofluids [1], data storage [2], and medicine [3]. A major basic scientific interest in small magnetic particles has focused on studies of the magnetic properties of single-domain magnetic particle assemblies [4].

We present the formation of ordered arrays of ferrite NPs by means of the Langmuir-Blodgett technology whose superior property wells in the capability of depositing a defined number of monolayers (layer-by-layer) at ambient temperature.

## II. LB FILM PREPARATION

The Langmuir-Blodgett (LB) technique has been used to produce two-dimensional arrays of organically functionalized NPs of  $\gamma$ -ferrite (maghemite) approx. 10 nm in diameter encapsulated in oleic acid envelope [5]. The NPs dissolved in chloroform were added onto the water surface. After evaporation of

the volatile solvent the particles spontaneously formed a Langmuir monolayer at the air/water interface. The  $\pi$ -A isotherm proved suitable stability of the monolayer as far as 30 mN/m which corresponds to a solid 2-dimensional state. The limiting area per a nanoparticle was about 100 nm<sup>2</sup>, which is in good agreement with a SEM figure.

For preparation of defect-free NP layers it was necessary to hydrophobize the substrate (silicon wafer) surface. The formation of self-assembled 1-hexadecane thiol monomolecular film on an evaporated gold layer was carried out for this purpose (Fig. 1). Alternatively, a silanized silicon wafer was used as a substrate for magneto-optical measurements. The transfer of the monolayer onto a solid substrate was performed in a LB trough by vertical dipping at surface pressure of 10 mN/m. Two types of monolayer were used: pure NPs and NPs—stearic acid mixture.

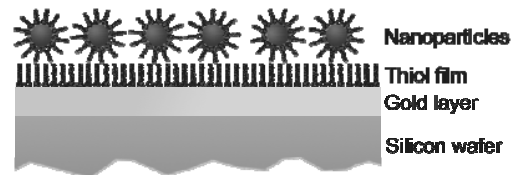


Figure 1: Sketch of the NP layer structure

## III. EXPERIMENTS

For measurement of physical and structural properties of planar array of magnetic NPs were used various surface analysis techniques.

### A. MAGNETO-OPTICAL KERR EFFECT

The respective in-plane magnetization component causes a rotation of the polarization plane combined with a change in the ellipticity which can easily be detected by the polarizing microscope (analyzer). Due to variation of the magnetic field strength it is possible to measure the magnetization reversal during a hysteresis cycle.

As revealed by the magnetization curves measured by following longitudinal MO Kerr effect the films deposited on silanized silicon behave as

superparamagnetic at room temperature: they do not exhibit a significant hysteresis.

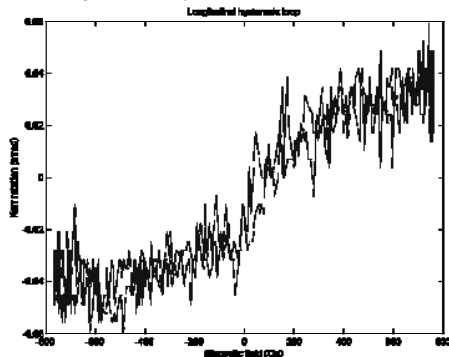


Figure 2: Hysteresis measured by MOKE.

### B. SCANNING ELECTRON MICROSCOPY

Scanning electron microscopy (SEM) provides ideal opportunity to order observation of conductive NPs in planar isolating matrix. The SEM measurement confirms homogeneity of the particle coating of all samples. All specimens exhibit low density of defects of the monolayer, local defect is induced by the surface roughness (see Fig. 3). Particle mean-size is estimated  $10 \pm 2 \text{ nm}$ .

At the specimen with silanized surface the islands of deposited particles have short range order as shown in Fig. 3 in the insert (2-dimensional fast Fourier transform (FFT) calculation).

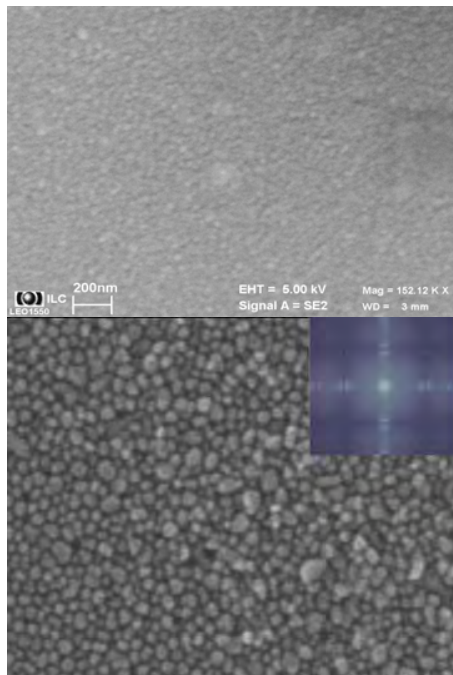


Figure 3: Scanning electron microscope images. High homogeneity and short range order is observable (2D FFT is shown in the insert).

### C. ATOMIC FORCE MICROSCOPY

Atomic force microscopy (AFM) provides additional information about arrangement of particles onto the surface. AFM measurement (see Fig. 4) exhibit minimal surface roughness and defect distribution. The height of surface undulations is quantized (one step is approx. 4 nm) and is caused by scanning across different number of deposited layers onto the substrate.

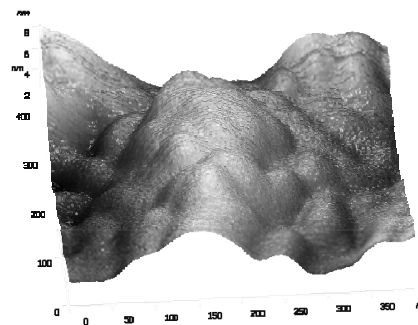


Figure 4: AFM image of specimen surface.

## IV. SUMMARY

Two-dimensional systems of  $\gamma$ -ferrite NPs were prepared by the LB technique. The magneto-optical Kerr effect measurements confirm a superparamagnetic behaviour at room temperature. SEM as well as AFM confirmed homogeneity of the distribution for various deposition conditions and observed the short-range order in the NPs arrays.

## REFERENCES

- [1] R.W. Rand, H.D. Snow, W.J. Brown, *J. Surg. Res.* **33**, (1982) 177..
- [2] M.H. Kryder, *MRS Bull*, **21**(9), (1996) 17.
- [3] M. Bruchez Jr., M. Moronne, P. Gin, S. Weiss, A. P. Alivisatos, *Science*, **281**, (1998) 2013.
- [4] W.T. Coffey, D.S.F. Crothers, Yu.P. Kalmykov, J.T. Waldron, *Phys. Rev. B*, **51**, 22, (1995) 15947.
- [5] A. B. Bourlinos, A. Simopoulos, D. Petridis, *Chemistry of Materials* **14**, (2002) 899.

# Synthesis and properties of copolyamides from $\epsilon$ -caprolactam and nylon salts

Jozef Ryba, Michal Krištofič, Iveta Vassová, Mária Dulíková  
Slovak University of Technology, Faculty of Chemical and Food Technology,  
Institute of Polymer Materials, Department of Fibres and Textile Chemistry,  
Radlinského 9, 812 37 Bratislava, jozef.ryba@stuba.sk

**Abstract** — The objective of this contribution was to synthesize and evaluate properties of the ternary copolyamides based on  $\epsilon$ -caprolactam, CL, with suitable comonomers containing nitrogen in their molecules. As comonomers  $\epsilon$ -caprolactam and the nylon salt from adipic acid and diethylenetriamine, ADETA, and the nylon salt from adipic acid and hexamethylenediamine, AH were used.

For this purpose a serie of different ternary copolyamides was synthesized according to five-level three-factor experimental design. Amount of low molecular compounds, LMC, and relative viscosities,  $\eta_r$ , of these copolyamides were determined and evaluated as a dependance of the copolyamide composition.

## I. INTRODUCTION

Copolyamides based on  $\epsilon$ -caprolactam, CL, (as additives for poly- $\epsilon$ -caprolactam) have a great advantage: good compatibility with homopolymer PA 6 what assures good processability of blends and properties of blend fibres as well [1].

Using comonomers with certain polar atom or group like oxygen, nitrogen etc. copolyamides with these atoms or groups in their macromolecules can be prepared and they are able to form bonds with other polar molecules such as water, dyestuffs and to improve their sorption and fixation so the sorption of water vapour and dyestuffs as well could be better [2]. Higher water sorption and formation of conductive system avoid to charge a copolymer to a great extent. Nylon salts as comonomers can function as polymerization accelerator so the poly (addition-condensation) reaction time  $t_r$  can be strongly lower than this for preparation of homopolymer poly- $\epsilon$ -caprolactam [3].

Lower („damaged“) spatial regularity in copolyamide in comparison with homopolymer brings lower crystallinity and higher sorption in amorphous regions.

## II. EXPERIMENTAL

Samples were prepared by poly(addition-condensation) reaction proceeding in melt in the  $N_2$  atmosphere. The mixture of powdered CL, AH and ADETA was heated in the glass apparatus immersed in the thermostated oil bath. The temperature was raised gradually and all three components melted and homogenized together. A short time later the polyreaction started (evaporation and condensation of reaction water) and the viscosity of the melt was gradually increased to the temperature of 270 °C at the end of reaction time. Compositions of copolyamides prepared are in table 1.

Sample	Amount of comonomers [wt. %]		
	AH	ADETA	CL
1	9,40	6,66	83,94
2	14,21	1,85	83,94
3	27,09	19,19	53,73
4	40,95	5,32	53,73
5	3,45	31,03	65,52
6	39,65	4,41	55,94
7	4,10	0,90	95,00
8	41,00	9,00	50,00
9	28,27	6,21	65,52
10	28,27	6,21	65,52
11	28,27	6,21	65,52
12	28,27	6,21	65,52
13	28,27	6,21	65,52

Table 1. Composition of copolyamides according to experimental design

The melt of copolyamide was poured onto the metal plate, cut into granules and extracted 2 h in boiling water. This extraction was used for determination of LMC amount. The relative viscosity value,  $\eta_r = \eta/\eta_0$ , (0.5 g of extracted copolymer solution) in 96 % sulfuric acid was determined viscosimetrically.

### III. RESULTS

Sample	Content of low molecular compounds [wt.%]					
	½	1	2	3	4	5
1	18,04	13,15	10,59	10,04	9,12	8,30
2	15,01	12,02	9,28	8,61	8,19	7,97
3	25,40	24,60	20,52	19,32	18,57	17,63
4	11,44	8,77	7,60	6,52	6,05	5,27
5	40,58	34,29	33,34	31,62	31,50	30,71
6	12,77	3,65	2,75	1,32	1,03	0,61
7	50,02	35,22	28,95	20,82	18,74	15,59
8	16,79	10,62	9,00	7,90	7,49	7,08
9	16,58	9,40	4,68	3,87	3,71	2,67
10	16,34	9,49	5,12	4,27	3,32	2,90
11	27,63	11,35	7,69	6,58	6,13	3,66
12	25,88	10,83	7,37	6,26	5,65	3,63
13	20,18	11,44	7,40	6,44	5,49	3,17

Table 2. Content of low molecular compounds

Sample	Relative viscosity $\eta_r$					
	½	1	2	3	4	5
1	1,22	1,32	1,54	1,54	1,50	1,47
2	1,29	1,44	1,58	1,67	1,58	1,46
3	1,21	1,26	1,30	1,53	1,45	1,30
4	1,24	1,35	1,45	1,56	1,55	1,42
5	1,21	1,24	1,27	1,43	1,43	1,24
6	1,32	1,47	1,54	1,57	1,50	1,43
7	1,18	1,34	1,48	1,66	1,57	1,55
8	1,26	1,31	1,38	1,58	1,53	1,31
9	1,26	1,39	1,44	1,64	1,53	1,44
10	1,29	1,40	1,42	1,60	1,54	1,46
11	1,26	1,43	1,44	1,53	1,54	1,49
12	1,30	1,44	1,44	1,55	1,51	1,51
13	1,31	1,42	1,43	1,60	1,54	1,47

Table 3. Relative viscosity of polymer solutions

### IV. CONCLUSION

1. Influence of polyreaction time,  $t_r$  is unambiguous from the point of LMC content and relative viscosity as well.

Content of LMC drops with the polyreaction time permanently for all samples with the polyreaction time, most rapidly when the weight ratio of AH salt to ADETA salt is approximately 9:1.

2. Influence of functional comonomers i.e. AH and ADETA nylon salts is clear. The higher is an amount of AH and lower of ADETA the higher is the relative viscosity and the lower is the amount of LMC.

3. Relative viscosity exhibits a dependence with a maximum at the polyreaction time  $t_r = 3$  h (4 h). Higher polyreaction time does not favour a formation of copolyamide with higher molecular weight.

### ACKNOWLEDGMENTS

Support of the National Grant Agency of Slovakia APVV – Grant No. 20-011404 and VEGA 1/2475/05

### REFERENCES

- [1] M. Krištofič et al. Chemical Papers **54**, 2000, 53-58
- [2] M. Krištofič et al. Proceedings 5 th World Textile Conference AUTEX, Portorose, Slovenia, 2005, 590-594
- [3] M. Krištofič et al. Fibres and Textile, vol. 12, 2005, 104-110

# Photonic Crystal Cavities for Quantum Cascade Lasers

S. Schartner, S. Golka, M. Austerer, C. Pflügl, W. Schrenk, and G. Strasser  
Zentrum für Mikro- und Nanostrukturen  
TU Wien  
Vienna, Austria  
Email: stephan.schartner@tuwien.ac.at

**Abstract** — *We present our progress towards the development of photonic crystals as a resonator for GaAs-based quantum cascade lasers. The scope of the presentation concerns the development of a dry etching process used to define the structure. As a first result, reflectivity measurements are presented reproducing the photonic band structure.*

## I. INTRODUCTION

Quantum cascade lasers (QCLs) are semiconductor lasers operating in the mid infrared (MIR) region. Their dynamic development over the last decade gave rise to a variety of powerful coherent emitters [1]. This made QCLs interesting for real world applications, such as free space communications or chemical sensing [2]. Especially the latter application is calling for surface emitting multi-wavelength laser arrays which could be realized by 2D Photonic crystals (PhCs). In contrast to conventional resonator designs like 2<sup>nd</sup> order distributed feedback gratings, the cavity dimensions are clearly scaled down and, additionally, PhCs provide advantages concerning threshold minimization, lowering beam divergence, and waveguide design freedom. Recently the first MIR PhC was proven to work in the InP material system [3].

Similar to the crystal structure of a solid a synthetic periodic structure with a lattice constant of the order of the optical wavelength produces an altered dispersion and intriguing propagation effects appear in the vicinity of flat band regions. The low group velocity increases the photon lifetime in the resonator and the high photon density of states directly enhances the lasing transition probability. Both is improving the performance of a laser. Flat band regions matching the 2<sup>nd</sup> order Bragg condition additionally allow to vertically diffract the light out of the surface. This is especially important for the naturally TM-polarized laser light generated in the intersubband transition based QCL.

## II. FABRICATION

PhCs are usually realized in quasi-2D slab structures by etching holes into the active material, which creates a periodic perturbation of the refractive index. To realize a structure as described above, highly anisotropic etching is required to reach grating depths as deep as the vertical waveguide. In device processing [4] there is a necessity for the development of an adequate etching process using a reactive ion etching (RIE) facility. Common attempts in chlorine based GaAs RIE use a Cl<sub>2</sub>/Ar mixture. As it was hardly possible to find a regime which was free of under-etch, we switched to use a SiCl<sub>4</sub>/N<sub>2</sub> ambience [5].

Analysis of EDX spectra showed that under certain process conditions plasma chemistry leads to a Si containing sidewall deposition which is inert to chlorine chemistry and therefore allows etching of deep vertical structures (Figure 1). The physical removal of the SiN<sub>x</sub> hardmask in the etching process is sufficiently low to obtain an etchant-to-mask selectivity up to 50:1. Due to the effect of a heavy RIE lag - the deterioration of etching rates in small structures - the depth is so far contained to approximately 5 μm.

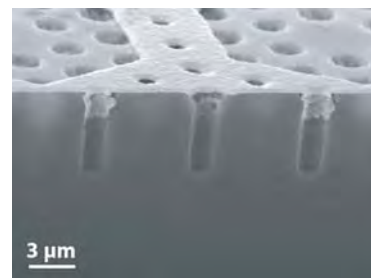


Figure 1: SEM picture of a finished and cleaved device.

## III. CHARACTERIZATION

As a first characterization, reflectance measurements were carried out and compared to calculations by C.

Adreani at the University Pavia, Italy (Figure 2). The disruptions in reflectivity which can be addressed to the coupling to PhC modes coincide with those obtained from calculations proving that the expected properties were reached.

Due to the mismatch of the reached etch depth to the depth required by the vertical waveguide used lasing was not achieved so far. Simulations show that the optical mode is pushed away from the active region into the highly absorptive lower cladding layer. The work is therefore now concentrated on further improving the etching process as well as on the application of a thinner vertical waveguide such as a surface-plasmon guide.

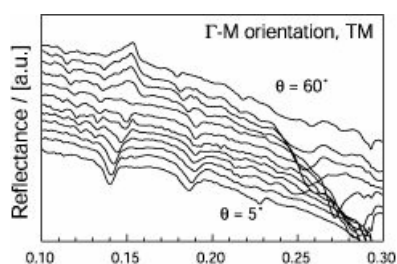


Figure 2: The spectrum received from a reflectance measurement appears as a background signal interrupted by resonant features.

#### ACKNOWLEDGMENTS

This work was partly supported by the European NMP project ANSWER, the Austrian FWF (ADLIS) found, the MNA network and the GMe agency.

#### REFERENCES

- [1] M. Beck, D. Hofstetter, T. Aellen, J. Faist, U. Oesterle, M. Ilegems, E. Gini, H. Melchior. Continuous wave operation of a mid-infrared semiconductor laser at room temperature. *Science* 295:301, 2002.
- [2] K. Namjou, S. Cai, E. Whittaker, J. Faist, C. Gmachl, F. Capasso, D. Sivco, A. Cho. Sensitive absorption spectroscopy with a room-temperature distributed-feedback quantum-cascade laser. *Opt. Lett.* 23:219, 1998
- [3] R. Colombelli, K. Srinivasan, M. Troccoli, O. Painter, C. Gmachl, D. M. Tennant, A. Sergent, D. L. Sivco, A. Y. Cho, F. Capasso. Quantum cascade surface-emitting photonic crystal laser. *Science* 302:1374, 2003
- [4] S. Schartner, S. Golka, C. Pflügl, W. Schrenk, G. Strasser. Deeply etched waveguide structures for quantum cascade lasers. *Microelectron. Eng.* in print, 2006

- [5] S. Golka, C. Pflügl, W. Schrenk, G. Strasser. Quantum cascade lasers with lateral double-sided distributed feedback grating. *Appl. Phys. Lett.* 86:111103, 2005

# Nano-patterning and growth of self-assembled nano-structures

M. Schramboeck, A.M. Andrews, T. Roch, W. Schrenk, A. Lugstein, G. Strasser  
Zentrum für Mikro- und Nanostrukturen  
TU Wien  
Vienna, Austria  
Email: matthias.schramboeck@tuwien.ac.at

**Abstract** — *GaAs substrates were patterned using various patterning techniques including holographic lithography and e-beam lithography. The patterns were transferred into the substrate using wet chemical and dry etching. Subsequently, InAs quantum dots (QDs) were grown on the patterned substrates with and without a layer of strained InGaAs underneath. Alignment of the QDs according to the underlying pattern is demonstrated. The dot density, the lateral and the size distribution was measured using atomic force microscopy.*

## I. INTRODUCTION

In recent years, quantum dots (QDs) have attracted an increasing attention due to their appealing electronic and optical properties. As they offer the ultimate limit in carrier confinement with discrete atomic like energy states they gave rise to novel optoelectronic device applications mainly situated in the near- and far-infrared region. QDs can be grown in a self-assembled growth mode using material systems with a different lattice constant such as Si/Ge or In(Ga)As/GaAs. However, QDs grown using this Stranski-Krastanow growth mode usually show an undesired fluctuation in size and density. Especially for device applications it would be desirable to have more control over the size and the density of the QDs and to have control over the lateral position of the QDs on the substrate. The growth of QDs on patterned substrates has already shown promising results [1, 2, 3, 4]. Among the lithographic techniques for pattern preparation, the most common is electron beam lithography followed by either plasma enhanced or wet chemical etching [5, 6]. In the following, we investigate three methods for pattern preparation. Holographic lithography, focused ion beam (FIB) assisted substrate preparation and e-beam lithography. Holographic lithography was studied because it provides an easy and efficient way to create nanosized patterns over large areas. Also the setup is very flexible and the pattern spacing can be varied over a large range. FIB pattern preparation has the advantage that no lithography is needed and thus contamination of the substrate coming from the resist

and other chemicals used in processing can be avoided.

## II. PATTERN PREPARATION

### A. LASER HOLOGRAPHY

For laser holography a He-Cd laser at a wavelength of 325 nm was used as an ultraviolet (UV) light source. After coating the GaAs substrate with photoresist it was then exposed in a holographic apparatus twice, with the sample rotated 90° after the first exposure. The nano-scale grid patterns were then transferred onto the GaAs using wet chemical etching or dry etching. Patterns with a pitch as small as 180nm could be realised. The pattern depths range from 20 nm to 30 nm.

### B. FOCUSED ION BEAM

Maskless patterning of GaAs substrates with ion beams focused to nanometer diameters for subsequent MBE overgrowth has been investigated. Using a focused ion beam offers the advantage that the patterns can be written directly onto the substrate and no lithographic processing is needed. The focused ion beam experiments were performed with a Micrion 2500 FIB system using 50 keV Ga<sup>+</sup> ions. The depth and diameter of the holes are determined by the dwell time, that is how long the to be sputtered holes are exposed to the ion beam. With this technique patterns with different periods can be realised very easily. Patterns with a pitch as small as 200nm and a depth of the sputtered holes of 30nm are demonstrated.

### C. E-BEAM LITHOGRAPHY

GaAs substrates were also patterned using e-beam lithography. As a resist the ZEP7000-22 was used with a thickness of 100 nm. Dot arrays with various diameters and pitches were created, whereas the smallest has a pitch of 100 nm and a hole diameter of 40nm. Afterwards, the substrates were dry etched

with a RIE Plasmalab 100 using Argon plasma. The etch depths were between 30 and 50 nm.

### III. OVERGROWTH

Before overgrowth the patterned substrates were cleaned thoroughly using solvents. Any residual resist was removed in an oxygen plasma. Afterwards an HCl dip was performed followed by a rinse under DI water. The patterned substrates were then inserted into the molecular beam epitaxy (MBE) chamber and oxide was thermally removed under an  $\text{As}_4$  overpressure. In situ reflection high energy electron diffraction (RHEED) was used to monitor the substrate surface. For the atomic force microscopy (AFM) measurements performed on the sample, a Digital Instruments Dimension 3100 atomic force microscope operated in tapping mode has been used. The result can be seen in Figure 1. Although, the original depth of the pattern has been reduced during overgrowth the alignment of the QDs to the underlying pattern is clearly visible. Furthermore, it is noticeable that the QDs are located not in the holes but at the local maxima of the pattern, which is explained in the following. In a coherent compressively strained film, the three-dimensional pattern creates a region of tensile stress at the local maxima and compressive stress at the local minima. Thickness and composition of this layer are crucial for avoiding film relaxation while still transferring the strain from the InGaAs layer to the GaAs buffer layer above, because the GaAs buffer is locally under tensile strain (larger lattice parameter) and thus it is energetically favorable for the InAs QDs to form there. This strain gradient creates a lower barrier to InAs QD nucleation closely matching the pattern.

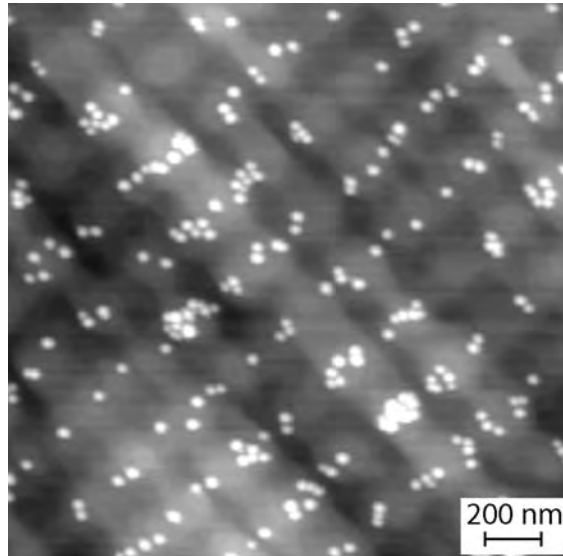


Figure 1:  $3\mu\text{m}\times 3\mu\text{m}$  AFM micrograph of a patterned substrate overgrown with 20nm InGaAs, 10nm GaAs and 0.495 nm InAs. The pattern with a period of 230 nm was created using holographic lithography.

### ACKNOWLEDGMENTS

This work was partly supported by the European projects ANSWER, SANDiE, and IR-ON, the Austrian agencies GMe and FWF, and the MNA Network.

### REFERENCES

- [1] M. Schramboeck, W. Schrenk, T. Roch, A. M. Andrews, M. Austerer and G. Strasser, *Microelectron. Eng.* accepted (2006).
- [2] G. S. Kar, S. Kiravittaya, M. Stoffel, and O.G. Schmidt, *PRL* **93**, 246103 (2004).
- [3] Z. Zong, and G. Bauer, *Appl. Phys. Lett.* **84**, 1922 (2004).
- [4] K. Meneou, K. Y. Cheng, a Z. H. Zhang, C. L. Tsai, C. F. Xu, and K. C. Hsieh, *Appl. Phys. Lett.* **86**, 153114 (2005).
- [5] Watanabe, El Pelucchi, B. Dwir, Mn H. Baier, K. Leifer, and E. Kapon, *Appl. Phys. Lett.* **84**, 2907 (2004).
- [6] H. Heidemeyer, U. Denker, C. Müller, and O. G. Schmidt, *PRL* **91**, 196103 (2003).

# Biophotopolymers for Rapid Prototyping of Cellular Bone Replacement Materials

Monika Schuster, Claudia Turecek,<sup>§</sup> Bertrand Kaiser,<sup>#</sup> Franz Varga,<sup>§</sup> Jürgen Stampfl,<sup>#</sup> Robert Liska  
Institute of Applied Synthetic Chemistry – Division of Macromolecular Chemistry, Vienna University  
of Technology, Getreidemarkt 9/163/MC A-1060 Vienna, Austria

<sup>§</sup>Ludwig Boltzmann Institute of Osteology, Hanusch-Krankenhaus, Heinrich Collin-Straße 30 A-1140  
Vienna, Austria

<sup>#</sup>Institute of Materials Science and Testing, Vienna University of Technology, Favoritenstr. 9-11 A-  
1040 Vienna, Austria

E-mail: [monika.schuster@ias.tuwien.ac.at](mailto:monika.schuster@ias.tuwien.ac.at) [rliska@otech7.tuwien.ac.at](mailto:rliska@otech7.tuwien.ac.at)

**Abstract** — *The disadvantages of materials, which are currently used in orthopedic surgery have led to the development of new synthetic biocompatible and biodegradable materials. For the fabrication of a cellular implant Rapid Prototyping is the method of choice, because of its possibility to produce 3D cellular structures of nearly arbitrary shape. In these investigations a monomer formulation has been developed that achieves the requirements from both, the medical and the fabrication point of view.*

## I. INTRODUCTION

Autografts and allografts, tissue obtained from the same or another subject of the same species, are the standard material for tissue repair and substitution. Both have some serious disadvantages, such as limited availability and the possibility of donor site morbidity in the case of autografts and complications such as viral transmission and immunogenicity in the case of allografts. To overcome these drawbacks new synthetic biocompatible and biodegradable materials have been developed.

Rapid Prototyping is a computerized fabrication technique that offers the possibility to produce highly complex three-dimensional objects out of photocurable liquids by radical polymeri-

zation. In our present project we aim at the development of such acrylate-based formulations for cellular implants. Figure 1 describes the planned overall pathway towards cellular biocompatible bone replacement materials.

## II. RESULTS AND DISCUSSION

Degradable polymers that are already in clinical use are usually based on polyesters such as poly( $\epsilon$ -caprolactone) or poly( $\alpha$ -hydroxy acids) (e.g. copolymers of lactic and glycolic acid). These polyesters cannot be used in the case of larger defects, e.g. after removal of a bone tumor, because of their hydrolytic degradation, which causes quite fast loss in mechanical strength. Moreover, the locally high concentration of free acids can result in tissue necrosis.

To overcome the problem of uncontrolled hydrolytic cleavage of ester containing monomers, biodegradability is introduced by acrylamide-based crosslinkers that can be cleaved enzymatically in vivo. Compared to the polyesters, which can only be processed by solvent or melt techniques, only acrylate or acrylamide-based formulations are suitable for fast and UV-controlled curing using Rapid Prototyping.

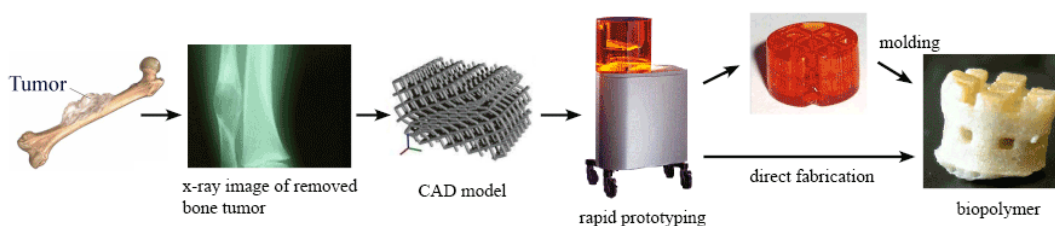


Figure 1: pathway towards bone replacement material

To tune the material properties regarding processability, biocompatibility as well as mechanical and degradation properties several components such as a basic crosslinker, reactive diluents, fillers and initiators have been considered.

A methacrylamide modified gelatin hydrolysate with additional moieties for improved organosolubility can be used as *basic crosslinker*, which should also support the attachment and proliferation of bone building cells.

Processing properties of the formulation and the network density of the polymer can be tuned by *reactive diluents*. A variety of commercially available photocurable monomers were tested concerning biocompatibility (cell seeding experiments with MG63 osteoblast-like cells), reactivity (Photo Differential Scanning Calorimetry) and mechanical properties (Dynamical Mechanical Analysis and Bending Strength Test). Diisobutylacrylamide, trimethylolpropanetriacrylate and urethanedimethacrylate seem to be quite promising candidates due to their good results in all criteria.

The *photoinitiating system* consisting of camphorquinone and N,N-dimethylamino-benzoic acid ethyl ester was selected for the preparation of test specimens for the biocompatibility tests of the monomers because of its known biocompatibility [1]. To tune the absorption characteristics, bisacylphosphine oxides and hydroxyalkylphenones as well as the new 1,5-diphenyl-1,4-diyne-3-one [2] were also found to be excellently suitable.

*Soluble filler materials* like poly(vinyl alcohol) or cellulose acetate butyrate showed appropriate biocompatibility and can be applied to tune the viscosity for an optimum resolution of the stereolithographic shaping process. *Inorganic fillers* such as hydroxyapatite and  $\beta$ -tricalciumphosphate have already been described to be osteoconductive [3] and can be used to improve the mechanical properties of the polymer.

Three-dimensional structures were prepared by molding techniques using organo-soluble molds [4] and by direct printing using Direct Light Projection, Microstereolithography or Two Photon Absorption (Figure 2).

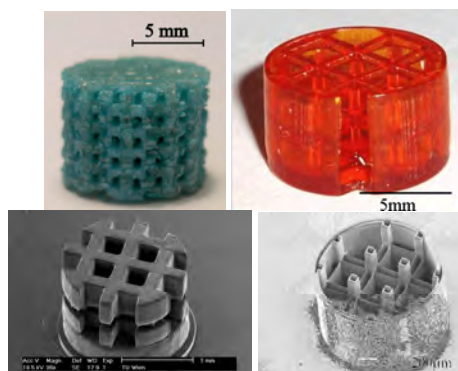


Figure 2: biocompatible structures prepared (a) from an organosoluble mold; (b) by Direct Light Projection; (c) by Microstereolithography and (d) by Two Photon Absorption

#### ACKNOWLEDGMENTS

Urethanedimethacrylate provided by IVOCLAR VIVADENT AG, photoinitiators from Ciba SC, and financial support by the “Austrian Nano Initiative” under contract no. N-703 is kindly acknowledged.

#### REFERENCES

- [1] K.A. Davis, J.A. Burdick, K.S. Anseth. Photoinitiated crosslinked degradable copolymer networks for tissue engineering applications. *Biomaterials*, 24:2485-2495, 2003.
- [2] R. Liska, B. Seidl. 1,5-Diphenyl-1,4-diyne-3-one: A Highly Efficient Photoinitiator. *Journal of Polymer Science Part A: Polymer Chemistry*, 43:101 – 111, 2005.
- [3] J.S. Temenoff, A.G. Mikos. Injectable biodegradable materials for orthopaedic tissue engineering. *Biomaterials*, 21:2405-2412, 2000.
- [4] M. Schuster, R. Inführ, C. Turecek, J. Stampfl, F. Varga, R. Liska. Photopolymers for Rapid Prototyping of Soluble Mold Materials and Molding of Cellular Materials. *Chemical Monthly* 2006, accepted.

# Improvement of Grout for Prestressed Tendons

Marijana Serdar, Irina Stipanovic, Dubravka Bjegovic  
 Faculty of Civil Engineering  
 University of Zagreb  
 Zagreb, Croatia  
 Email mserdar@grad.hr

**Abstract** — *Good corrosion protection of prestressed structures is essential for structural integrity and long-term durability. Grout is the last but most important corrosion protection layer in prestressed structures. With correct materials, good design and high-quality installation of grout it is possible to minimize the risk of corrosion. Within this paper the influence of different admixtures on physical and mechanical grout properties and in the end on corrosion protection effectiveness of selected grouts, for the application in post-tensioned structures are researched.*

## I. INTRODUCTION

The main aim of construction engineers today is not only to make structures functional and aesthetic but to make them reliable for a long period of time. Prestressed concrete is one of the most widely used structural materials because it offers good durability properties, a range of engineering solutions and a variety of aesthetic opportunities. In past few decades inspections have shown that corrosion is one of the main reasons for deterioration of prestressed structures. Corrosion protection of post-tensioning systems can be provided by six possible levels according to the system details [1], as shown in Figure 1.

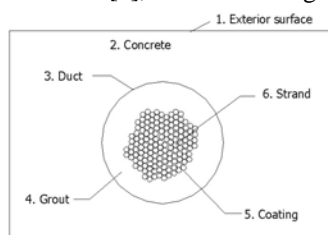


Figure 1: Levels of corrosion protection

Grout is the last but most important corrosion protection layer in prestressed structures. With correct materials, good design and high-quality installation of grout it is possible to minimize the risk of corrosion. The main role of grout is to fill the holes between protective duct and prestressing strand and to suppress the flow of water and chloride ions.

Within this paper the influence of different admixtures on physical and mechanical grout properties and in the end on corrosion protection effectiveness of selected grouts, for the application in post-tensioned structures are researched. The main goal of the project was to evaluate the influence of different admixtures on behaviour of grouts for prestressed tendons and to design an optimum grout, grout that combines desirable fresh properties along with good corrosion protection. [2]

## II. EXPERIMENTAL PROGRAM

### A. MATERIALS

Grout for bonded post-tensioning is a combination of Portland cement and water, along with different admixtures needed to obtain required properties. Two types of cement have been used:

1. PC 30z 45S – Portland Cement 30% slag, Class 45, slow hydration
2. PC 45B – Portland Cement Class 45, without slag, fast hydration.

Water/cement ratio was varied from 0.35 to 0.44. Admixtures used in grouts preparation are listed in Table 1.

Admixtures	Producer	Name
Superplasticizer	Degussa	Glenium 50
	Sika	Viscocrete-20 HE
Expansive	Degussa	Stabilmac
	Sika	Intraplast- A
	KGK	Tricosal
	TKK	Injektin
Anti-bleeding	Sika	Intracrete
Inhibitor	Sika	Ferrogard 901
	Cortec	MCI 2007

Table 1: Admixture used in grout mixtures

### B. TESTING

Different grout mix designs for prestressed tendons with various admixtures were tested

according to European standards EN 445, 446, 447 for grouting, to define their behaviour in fresh and hardened state. Properties tested, methods and acceptance criteria are given in Table 2.

Property	Test method EN 445: 1996	Criteria EN 447: 1996
Flowability	Flow cone test	< 25 s
Bleeding	100 mL cylinder	< 2%
Volume change	Can method	>-1% <+5%
Compressive strength	Prism 4×4×16 cm	>30 MPa

Table 2: Grout performance specification

On the basis of these results best grout designs were selected for accelerated corrosion testing, as listed in Table 3.

No	w/c	Admixtures
1	0.44	-
2	0.40	1% Intraplast-A, 2% Intracrete
3	0.35	0,35% Viscocrete
4	0.40	0,18% MCI 2007, 1% Intraplast-A
5	0.40	0,2% Glenium 51, 1% Stabilmac

Table 3: Selected grouts for corrosion testing

Accelerated corrosion testing was performed on grout specimens with embedded prestressing rebar. Setup for accelerated corrosion is shown in Figure 2.

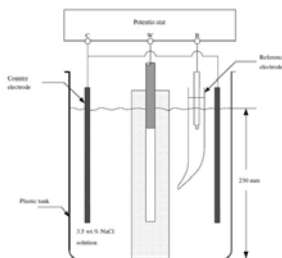


Figure 2: Setup for accelerated corrosion test

Corrosion of prestressing steel in grout specimens was evaluated by impressing 10 V anodic potential for acceleration of corrosion. The effectiveness of the inhibitors and admixtures added to grout was evaluated by measuring corrosion potentials, current vs. time and time-to-cracking of the grout specimens [3].

### C. RESULTS

Compressive strength was satisfied by all grout mixtures, but on the other hand very few grout

mixtures met all three requirements according EN 447 for fresh property. Grout mixtures listed in Table 3 met all requirements and are considered to be designs for optimum grouts.

Corrosion testing have shown that specimens 2, 3, 4 have best corrosion protection properties. Typical curve of corrosion current vs. time is shown in Figure 3.

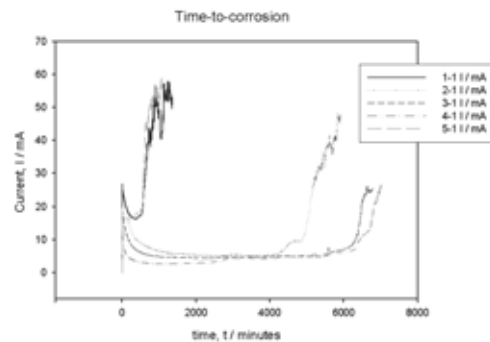


Figure 3: Curve of corrosion current vs. time

### D. CONCLUSIONS

On the basis of performed testing following conclusions can be given:

- superplastizicer is necessary for lower w/c, but they increase bleeding;
- silica fume reduced bleeding, but decrease fluidity;
- volume change requirement is fulfilled only with addition of expansive admixture;
- for corrosion protection effective grout the use of admixtures and inhibitors is inevitable.

Testing of the high-performance grout is necessary to determine suitability as well as for quality assurance/quality control in the field.

### REFERENCES

- [1] J. Corvel, A. Moreton. Post tensioning tendon installation and grouting manual, FHWA, 2004.
- [2] A. J Schokker, B. D. Koester, J. E. Breen, M. E. Kreger. *Development of High Performance Grouts for Bonded Post-Tensioned Structures*, Center for Transportation Research, University of Texas at Austin, October 1999.
- [3] L. Bertolini, B. Elsener, P. Pedferri, R. Polder. *Corrosion of steel in concrete*, Wiley-VCH, Weinheim, 2004.

# Electronic and Magnetic Structure of Spintronics Materials from ab-initio Bandstructure Calculations

Martin Sieberer and Peter Mohn (Faculty Mentor)

Institute for General Physics

Vienna University of Technology

Vienna, Austria

Email: {ms , phm}@cms.tuwien.ac.at

**Abstract** — *On the basis of ab-initio calculations employing density functional theory (DFT) we investigate half-metallic ferromagnetism in zinc-blende and wurtzite compounds composed of group I/II metals as cations and group V elements as anions as well as the effect of transition metal substitution in cuprous oxide  $\text{Cu}_2\text{O}$ . For the first class of compounds we find that the formation of ferromagnetic order requires large cell volumes, high ionicity and a slight hybridization of anion p and cation d states around the Fermi energy. For the second class of compounds we find magnetic order at the transition metals in these otherwise strongly correlated electron compounds.*

The application of magnetically doped semiconductors in opto-electronic and spin-electronic devices as well as in quantum computing will have a tremendous scientific and technological importance for the future years. The aim of our project is thus to understand and to predict new materials and novel phenomena for nanomagnetism and spinelectronics. Our approach relies on calculations of the electronic and magnetic structure based on the density functional formalism, various codes like the ASW, FP-LMTO, LMTO-CPA, and VASP are used. Our investigation concentrates on the so called "new" materials like the most recently discovered magnetic phases of Ca with a group-V element like CaAs [1] as well as Mn, Fe, Co, and Ni doped  $\text{Cu}_2\text{O}$  [2].

We first investigated the stability of CaAs, the prototype [3] of the so-called half-metallic-ferromagnets (HMF) of this type, considering several structures, e.g. zinc-blende (ZB), wurtzite (WZ), sodium chloride (NaCl) and the experimentally found structure NaO ( $\text{P}\bar{6}2\text{m}$ ). For this purpose the FLAIR code has been used [4]. Our calculated lattice constant for the true ground state (NaO) with  $a=15.03$  bohr and  $a/c=1.326$  (fixed) is in good agreement with the experimental values of  $a=14.84(2)$  and  $c=11.19$ . Furthermore we found out that the ground state of CaAs determined experimentally is energetically rather far away from the structures which are expected to exhibit HMF ( $\approx 1.4$  eV/f.u.). However, since e.g. CrAs and CrSb have already been prepared successfully in the ZB structure even though it is not their equilibrium crystal structure, also for CaAs (or other iso-electronic compounds) a preparation as a thin film on a substrate may be possible.

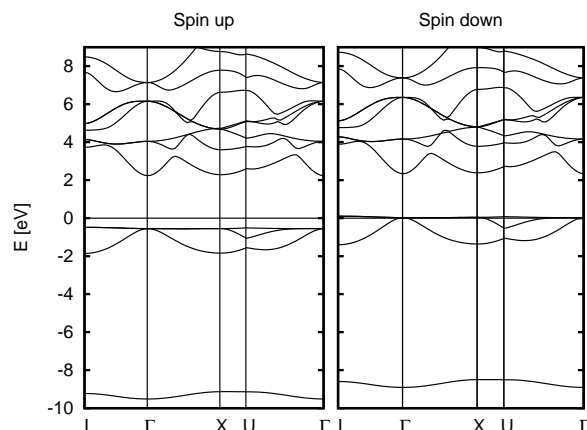


Figure 1: Band structure of ZB-CaAs for both spin channels. A half filled, extremely flat band is present at the Fermi energy.

All ZB compounds composed of group I/II elements as cations and group V elements as anions investigated combine two key features, namely a relatively wide band-gap of approximately 2 eV present in both spin channels, and a ferromagnetic ground state with an integer magnetic moment obeying a simple  $|8 - n|$  rule,  $n$  being the total number of valence electrons. The large difference in electronegativity between the constituent elements leads to a charge transfer causing a gap between occupied bands having predominantly p character and empty bands with s and/or d character. The band structure for CaAs as one representative is plotted in Fig. 2, most interesting is the uppermost occupied band being almost dispersionless. This flatness is caused - amongst others - by the relatively large lattice constant of these compounds (between 9.15 bohr for MgN and 15.37 bohr for BaSb). For the representatives having cations with empty d-bands in the energetic proximity of the Fermi energy (e.g. Ca, Sr, Ba), additionally a curious anion-p - cation-d hybridization occurs, which further reduces the dispersion of the so-called flat band. All compounds investigated exhibit a well localized magnetic moment proportional to the number of holes in the almost atomiclike

anion p-band. A systematic study of these compounds showed that the origin of this p-electron magnetism can be understood in terms of the Stoner-criterion, which predicts instabilities towards magnetism due to the high density of states at the Fermi energy in the hypothetical non-magnetic state caused by the flat band. Comparisons of the total energy between a ferromagnetic (FM) and an antiferromagnetic (AFM) ground state - including augmented spherical wave (ASW) calculations that allow for the set up of so-called spin-spirals - in all cases showed relatively large energy gains (between 50 meV and 220 meV) for the system to adopt the FM ground state. In a mean field approximation also the paramagnetic Curie temperature has been estimated, resulting in a value of 680 K for CaAs, which would be well suited for technological application.

Another highly interesting group of materials are the oxide-based diluted magnetic semiconductors, which are attracting increasing attention due to recent reports on room temperature ferromagnetism in anatase  $\text{TiO}_2$  and wurtzite  $\text{ZnO}$  doped with several transition metal ions. We have explored a new suitable host, namely cuprous oxide ( $\text{Cu}_2\text{O}$ ), which has already been prepared with a small concentration of Mn [5, 6, 7] and Co [8] on the copper sites. For this purpose we have used the LSDA+U technique in combination with PAW potentials as implemented in VASP [9]. Cuprous oxide ( $\text{Cu}_2\text{O}$ ) is a p-type semiconducting oxide with a direct band-gap of approximately 2.1 eV that crystallizes in a cubic structure ( $\text{Pn}\bar{3}\text{m}$ , No. 224) built up from Cu atoms located on a conventional fcc lattice and oxygens at the positions  $(\frac{1}{4}, \frac{1}{4}, \frac{1}{4})$  and  $(\frac{3}{4}, \frac{3}{4}, \frac{3}{4})$ . The calculated gap is too small (0.48 eV), but otherwise - due to the formally fully occupied 3d shell - one expects band theory to give good results. We have investigated the effect of different transition metals ( $TM$ ) on the copper site, assuming a doping rate of 3.22 %. We have taken into account relaxations as well as correlations on the impurity site via LDA+U, employing the LDA+U parameters  $U=5$  eV and  $J=0.95$  eV, respectively. It turned out that the supercells  $TM_1\text{Cu}_{31}\text{O}_{16}$  exhibit a great variety of magnetic ground states. Ni and Co substitution introduces stable, integer magnetic moments per cell, and thus results in either insulating (Co, Ni  $U=5$  eV) or half metallic (Ni  $U=0$ ) ground states. While Fe doped  $\text{Cu}_2\text{O}$  can still be considered as a half metal, the situation is not that clear for the Mn doped system, which exhibits strong deviations from an integer magnetic moment when the Hubbard parameter  $U$  is increased. For semi-metallic  $\text{Mn}_2\text{Cu}_{30}\text{O}_{16}$  and insulating  $\text{Co}_2\text{Cu}_{30}\text{O}_{16}$  the exchange interactions between magnetic substituents up to the fifth nearest fcc neighbor-shell have been investigated. While in the Mn doped compound exchange independently of  $U$  favors an antiferromagnetic spin arrangement for all

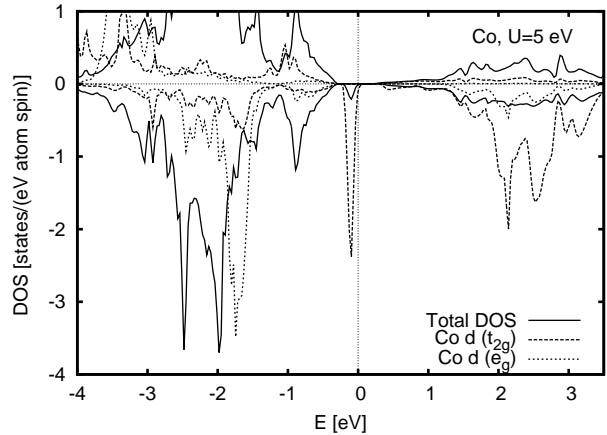


Figure 2: Density of states (DOS) for  $\text{Co}_1\text{Cu}_{31}\text{O}_{16}$  assuming a Hubbard  $U$  of 5.0 eV, the values are normalized to the number of atoms. The insulating ground state is also present when  $U$  is switched off.

pairs of Mn ions studied, the insulating compound exhibits a stronger tendency towards ferromagnetism, especially when  $U$  is set to zero. Unfortunately, moderate clustering can be expected in  $\text{Co}_2\text{Cu}_{30}\text{O}_{16}$ , with nearest neighbor Co atoms that destroy the insulating ground state in favor of a half metallic one. Furthermore, the magnetic interactions between Co substituents are short-ranged, contrary to the system  $\text{Mn}_2\text{Cu}_{30}\text{O}_{16}$  with rather long-ranged interactions.

## REFERENCES

- [1] M. Sieberer, J. Redinger, S. Khmelevskiy, and P. Mohn. *Phys. Rev. B*, 73:024404, 2006.
- [2] M. Sieberer, J. Redinger, S. Khmelevskiy, and P. Mohn. to be published.
- [3] K. Kusakabe, M. Geshi, H. Tsukamoto, and N. Suzuki. *J. Phys.: Condens. Matter*, 16:5639, 2004. see also cond-mat/0402641 v1.
- [4] <http://www.uwm.edu/weinert/flair.html>, 2005.
- [5] M. Wei, N. Braddon, D. Zhi, P. A. Midgley, S. K. Chen, M. G. Blamire, and J. L. MacManus-Driscoll. *Appl. Phys. Lett.*, 86:072514, 2005.
- [6] L. Pan, H. Zhu, C. Fan, W. Wang, Y. Zhang, and J. Q. Xiao. *J. Appl. Phys.*, 97:10D318, 2005.
- [7] M. Ivill, M. E. Overberg, C. R. Abernathy, D. P. Norton, A. F. Hebard, N. Theodoropoulou, and J. D. Budai. *Solid-State Electronics*, 47:2215, 2003.
- [8] S. N. Kale, S. B. Ogale, S. R. Shinde, M. Sahasrabudde, V. N. Kulkarni, R. L. Greene, and T. Venkatesan. *Appl. Phys. Lett.*, 82:2100, 2003.
- [9] G. Kresse and J. Furthmüller. *Phys. Rev. B*, 54:11169, 1999.

# Polyamide fibers filled by inorganic nanoparticles Boehmite: mechanical and thermal properties

Škrovanová L.\* , Borsig E.\* , Erler J.\*\* , Muelhaupt R.\*\*

\*STU FCHPT, Department of Fibres and Textile, Radlinskeho 9, 812 37 Bratislava, Slovakia

\*\* AL Universität Freiburg, Stefan-Meier str. 31, D-791 04 Freiburg, Germany

e - mail: lubica.fleischmannova@stuba.sk

**Abstract** — *The aim of this work was to investigate the effect of nanofiller Boehmite on the mechanical and thermo mechanical properties of nanocomposite fibres, namely on dependency of tensile strength of fibres on nanofiller content, Boehmite as well as on drawing ratio. Production of electrostatic charge on surface of the fibres was also investigated. The nanocomposite fibres were characterized using thermo - mechanical analysis (TMA) and Differential Scanning Calorimetry (DSC).*

## I. INTRODUCTION

Compounding polymeric matrix with inorganic materials has the interesting topic of scientific research and industrial application. The inorganic particles in the polymeric matrix can provide mechanical, thermal or barrier properties of the polymer. Most studied polymer – inorganic involve layered systems like clays or plate-shaped systems like montmorillonite, mica, kaolin and aluminium hydroxides. In this paper was used inorganic material Boehmite. [1]

Boehmite particles are colloidal rod-like species with a high anisotropy. It is white to dark reddish-brown orthorhombic mineral,  $\text{AlO}(\text{OH})$ , present in bauxite [2]. DISPERAL is the trade names for the high purity, highly dispersible, colloidal Boehmite alumina powders manufactured by Sasol “Figure 1”[3].

## II. EXPERIMENTAL PART

### A. MATERIALS

The materials used for preparation of the samples were Boehmite nanofiller, trade mark: Disperal OS1, Sasol (well-defined rod-shaped Boehmite,  $\gamma\text{-Al}_2\text{O}_3$  and polyamide 6 (PA6) ( $\eta = 2,59$ ) from Nylstar Humenne.

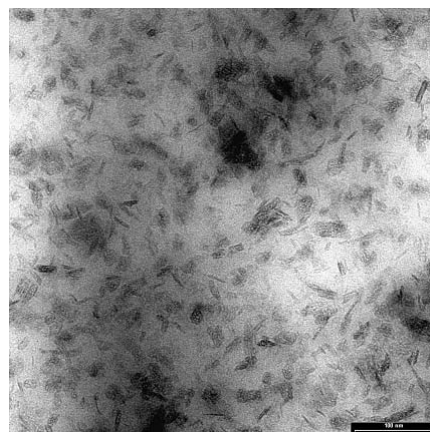


Figure 1: DISPERAL OS-1 – organically modified Boehmite dispersed in polymer (mineral filled PA 6 polymer composite) [4]

### B. SAMPLE PREPARATION (PA6-DISPERAL OS1 NANOCOMPOSITES FIBRES)

The samples of nanocomposite PA6 / Disperal OS1 with various contents of nanofiller (0,5; 1,0; 2,0; 3,0 and 5,0 wt.% ) were prepared in Freiburg University by melt-compounding it in a parallel feed twin-screw extruder of Collin.

The nanocomposite fibres were prepared by spinning process in laboratory spinning machine at 250°C. Then the prepared fibres were drawn to various drawing ratios ( $\lambda$ ).

### C. DIFFERENTIAL SCANNING CALORIMETRY (DSC)

The measurements were performed on Perkin Elmer DSC7 calorimeter. Samples of fibres were heated from 40°C to 250°C at a rate of 10°C/min. They were cooled back to 40°C at a rate of 10°C/min, which was followed by second heating run with the same parameters as the first heating.

### D. TMA – THERMAL CONTRACTION OF FIBERS

Thermal Contractions were measured by TMA 50 (Shimadzu). The samples were heated from 25°C to 130°C and then cooled back.

E. MECHANICAL AND ELECTROSTATIC PROPERTIES OF NANOCOMPOSITE FIBERS

Mechanical properties of fibres were measured on INSTRON machine. From received curves dependencies, tensile and elongation of fibres were calculated.

Electrostatic properties of nanocomposite fibres were measured on FD 28 STAFCHARGE machine.

III. RESULT AND DISCUSSION

DSC results shows that the presence of Disperal OS1 causes the decreasing of crystallinity ( $\beta$ ) of PA6 in nanocomposite fibers "Table 1".

Content of Disperal OS1 (wt.%)	$\lambda = 3$		$\lambda = 4$		$\lambda = 5$	
	$\beta$ (%)	$\Delta H_M$ (J/g)	$\beta$ (%)	$\Delta H_M$ (J/g)	$\beta$ (%)	$\Delta H_M$ (J/g)
0.0	32,7	62,1	33,4	63,4	35,5	67,4
0.5	32,6	61,9	32,2	61,1	35,5	67,4
1.0	32,7	62,2	32,6	73,4	35,2	66,8
2.0	31,4	59,7	31,7	60,2	30,4	57,8
3.0	31,4	59,6	32,4	61,5	30,4	57,7
5.0	28,5	54,1	35,5	67,5	29,8	56,7

Table 1: Crystallinity ( $\beta$ ) and melt enthalpy after first heating of PA6 – Disperal OS1 fibers with various content of nanofiller

With rising contents of nanofiller an improvement of dimensional stability of unstabilized nanocomposite fibers was observed using TMA. The contractibility of PA6 nanocomposite fibers decreased with increasing content of nanofiller.

The nanofiller Disperal OS1 till ~1wt.% has a relatively low influence on tensile strength of PA6 nanocomposite fibres. At higher content of nanofiller the tensile strength was lower at all observed drawing ratios i.e.  $\lambda = 3, 4$  and  $5$  "Figure 2" and the elongations of nanocomposite fibres PA6, with higher content of nanofiller, over then 1wt. %, grow up "Figure 3".

The effect of nanofiller Disperal OS1 on electrostatic properties, the increasing content of nanofiller in fibers causes decreasing charging but the unchanging of the fibers is very fast.

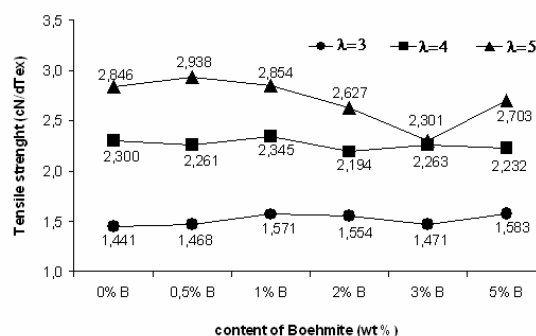


Figure 2: Dependence of tensile strength of fibres on content of Boehmite (Disperal OS1) in fibres.

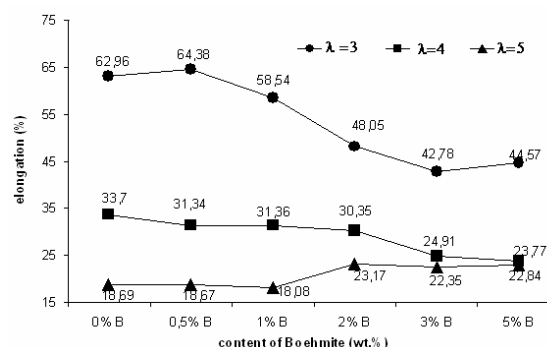


Figure 3: Dependence of elongation ( $\epsilon$ ) of fibers on content of Boehmite (Disperal OS1) in fibres

ACKNOWLEDGMENTS

Support of the National Grant Agency of Slovakia APVV – Grant No. 20-011404 and VEGA 1/2475/05

REFERENCES

- [1] C. Ozdilek, K. Kazimierczak, D. van der Beek, S. J. Picken, Polymer 45, 5207–5214, 2004.
- [2] P.A. Buining, A.P. Philipse, H.N.W. Lekkerkerker, Langmuir, 10 : 2106; 1994.
- [3] <http://www.chemicals-technology.com/contractors/catalysts/alumina/>.
- [4] <http://www.chemicals-technology.com/contractors/catalysts/alumina/alumina4.html>

# Influence of ferromagnetic fillers on properties of rubber blends

Eva Ürögiová, Ivan Hudec, Denisa Bellušová  
Slovak University of Technology, Faculty of Chemical and Food Technology,  
Institute of Polymer Materials, Department of Plastics and Rubber,  
Radlinského 9, 812 37 Bratislava, eva.simigova@stuba.sk

**Abstract** — *The present work focus on the investigation of the influence of hard magnetic ferrite fillers on the properties of rubber blends. In composite magnetic materials, the magnetic powder as well as the polymer effects the processability and physical properties of the final product. Magnetic hard fillers represent chemical compounds of metal oxides with strong magnetic properties, which are ideal for permanent magnets.*

*Rubber ferrite composites containing different types of strontium ferrites in a rubber matrix have been prepared and their vulcanization, physical, mechanical and magnetic properties have been evaluated. The influence of particle size distribution and magnetic fillers content on properties of filled vulcanizates has been studied.*

## I. INTRODUCTION

Rubber ferrite composites are composite materials with ferromagnetic fillers as one of the constituents and rubber blend as polymer matrix [1]. Ferrites are a very well established family of magnetic materials. In terms of technological applications one may distinguish between two main types of ferrites, soft and hard ferrites. Soft magnets are materials which domain walls easily moved by applied magnetic fields. Those with less mobile domain walls are termed hard magnets [2]. The formula composition of magnetic hard ferrites can be generally represented as  $(\text{MeO})\cdot(\text{Fe}_2\text{O}_3)_6$ , where Me is divalent metal (eg. Sr, Ba, Pb of mixture of them) [3,4].

The present work reports the structural characteristics of four different types of strontium ferrites and the influence of particle size distribution and magnetic fillers content on properties of filled vulcanizates.

## II. EXPERIMENTAL

Four different types of strontium ferrites were used for preparing of ferromagnetic rubber composites. Strontium hexagonal ferrites  $\text{SrFe}_{12}\text{O}_{19}$ – Sr ferrite with coercitive force 112 kA/m; type FD 8/24 with coercitive force 105 kA/m; type FD 30/26 with coercitive force 131 kA/m and type D380 with

coercitive force 137 kA/m were used as a hard magnetic filler. To investigation the particle size, porosity and surface area of ferrite fillers the method of mercury porosimetry was used. The standard rubber blend based on natural rubber SIR 20 and butadiene rubber SKD was used as a polymer matrix. A standard sulphur-based vulcanization system was used.

The composite materials in concentration scale 30-50 weight % of ferromagnetic filler were prepared by mixing in a laboratory mixer at 80°C and 40 rpm rotor speed. Prepared mixtures were vulcanised at the temperature 150°C (optimum cure time  $t_{c90}$ ) in a hydraulic press. The specimen thickness was 2 mm.

## III. RESULTS

The characterization of ferromagnetic fillers incorporates determining of structural, physical and magnetic parameters of used fillers. In order to clarifying of structural characteristics of several ferromagnetic fillers surface area and porosity of fillers by method of mercury porosimetry were investigated. The structural characteristics of different types of strontium ferrites are shown in table 1.

	Sr	D 380	FD 30/26	FD 8/24
Volume of pores >10 $\mu\text{m}$ [ $\text{cm}^3/\text{g}$ ]	5,01	0,05	0,03	0,14
Total specific surface [ $\text{m}^2/\text{g}$ ]	2,11	0,80	6,14	3,39
Total porosity [%]	72,09	59,96	59,97	67,94
Total volume of pores [ $\text{g}/\text{cm}^3$ ]	0,24	0,25	0,30	0,42

Table 1: Structural characteristics of ferromagnetic fillers

Particle size distribution of different types of Sr ferrites are illustrate in Fig. 1.

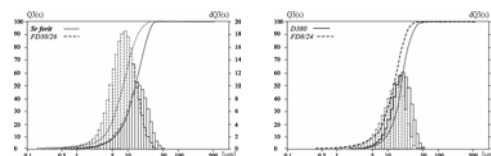


Fig. 1: Particle size distribution of Sr ferrites

The vulcanization characteristics were measured at 150°C using a Rheometer Monsanto S100. Obtained results of the optimum cure time  $t_{c90}$  are shown in Fig. 2. Presence of ferromagnetic filler in rubber compound effected decreasing of optimum cure time  $t_{c90}$ . With the increasing of amount of ferrite filler in the compounds  $t_{c90}$  decreased.

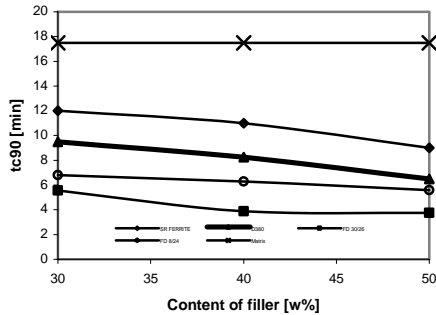


Fig. 2: Vulcanization characteristics of rubber blends with Sr ferrites filler

All mechanical properties of the compounds were tested after vulcanization at  $t_{c90}$  with the TiraTest machine according to ISO37. The values of measured properties are shown in table 2.

Type of filler	Content of filler [w%]	Elongation at break [%]	Tensile strength [MPa]	Modulus 200% [MPa]
Matrix	0	649,40	9,80	2,08
Sr ferrite	30	341,30	12,80	7,26
	40	338,30	13,44	7,02
	50	206,10	7,87	7,87
D 380	30	465,90	15,07	4,90
	40	408,80	12,35	5,21
	50	302,40	7,72	4,82
FD 30/26	30	403,30	12,67	5,06
	40	209,10	6,09	5,49
	50	136,30	5,49	0
FD 8/24	30	361,70	12,55	5,63
	40	239,20	7,76	6,12
	50	231,30	9,05	7,65

Table2: Mechanical properties of rubber blends with Sr ferrites filler

From table 2 is evident, that all mechanical properties besides elongation at break increase compared with rubber blend without ferromagnetic filler. Elongation at break and tensile strength decreased with increasing amount of ferrite filler in composite material.

The values of remanent magnetisation Br for ferromagnetic rubber composites are shown in Fig. 3.

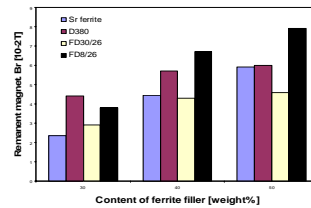


Fig. 3: The variation of remanent magnetisation Br with content of ferrite filler in rubber blends

From obtained results is evident, that remanent magnetisation Br increase with increasing of magnetic filler content in rubber blend. The higher value of remanent magnetisation Br  $7,9 \cdot 10^{-2} T$  accounts strontium ferrite type FD8/24 by 50% ferrite content in the sample was obtained. Composites with strontium ferrite of FD8/24 type showed the best magnetical and mechanical parameters and its incorporating into matrix was not difficult.

#### IV. CONCLUSION

Four different types of strontium hexagonal ferrites powders  $SrFe_{12}O_{19}$  with the particle size in a range 5-50  $\mu m$  were incorporated into a rubber matrix with loading levels 30-50 weight %. Results showed that the cure time decreased with the increasing of amount of ferrite filler in the compound. All studied mechanical properties besides elongation at break increase with filler content in comparison with rubber blend without ferromagnetic filler. The remanent magnetization linearly depends on the weight fraction of the magnetic filler in rubber blends. The changes of monitored properties of ferromagnetic rubber composites in comparison with standard rubber blends are acceptable for their practical application.

#### REFERENCES

- [1] K.A. Malini, J. Am. Ceram. Soc.82, (1999), 269-279
- [2] [http://www.elidis.cz/cz/ferit\\_jadra.php](http://www.elidis.cz/cz/ferit_jadra.php)
- [3] M.R. Anantharaman, J. Phys., D, Appl. Phys. 32 (1999) 1801
- [4] B. Schroter, Macromol. Chem., Rapid Comm. 3 (1982), 623

# Structure of Lyocell Fibres and its Influence on the Fibre Properties

Ksenija Varga<sup>1</sup>, Mohammad Abu Rous<sup>1</sup>, Elisabeth Ingolic<sup>2</sup> and K. Christian Schuster<sup>3</sup>

<sup>1</sup>Christian-Doppler-Laboratory “Textile and Fibre Chemistry in Cellulosics”, Leopold-Franzens University of Innsbruck, Institute for Textile Chemistry and Textile Physics, Höchsterstrasse 73 A–6850 Dornbirn

<sup>2</sup>Research Institute for Electron Microscopy (FELMI), Technical University Graz

<sup>3</sup>Lenzing AG, Textile Innovations, A–4860 Lenzing

Email: k.varga@lenzing.com

**Abstract** — *The structure of Lyocell fibres was investigated using a fluorescence and transmission electron microscopy. Fluorescent dye diffusion measurements showed that the Lyocell fibres consist of three major zones: outer semi-permeable skin and middle porous zone where the dye diffusion occurs quickly and inner compact core where the dye diffusion occurs slowly. Highly resolved TEM micrographs showed homogenous pore distribution where even fibre skin with 150 nm thickness becomes visible.*

## I. INTRODUCTION

Lyocell fibres are regenerated cellulose fibres produced by solvent (N-Methylmorpholine-N-Oxide) spinning process. Due to its excellent moisture management, Lyocell fibres possess excellent physiological properties like high wear comfort, temperature control as well as smooth and cool touch. Background for these properties is the fibre nano-structure, which is a result of a spinning process [1]. Since the fibre properties highly depend on an inner structure, it is necessary to investigate and understand the structure, also develop the methods for its characterisation. Basis structural researches would supply a better understanding of the structure formation and changes during the spinning processes and further treatments. Classical analysis methods, such as water retention measurements and inverse size exclusion chromatography [2] could deliver quantitative information about the pore structure and even the pore size distribution, but no information on their spatial distribution. Investigation results of the large cellulose blocks regenerated from blocks of N-Methylmorpholine-N-Oxide solution showed a possible skin-core structure of the Lyocell fibres [3]. The mayor topic of this ongoing work is to visualise the pore distribution in relationship with the fibres physical and chemical properties.

## II. EXPERIMENTAL SETUP

For the fluorescent microscopy, the Lyocell fibers (1,3 dtex, 38 mm) were dyed with optical brightener Calcoflour (Uvitex BHT, Ciba, CH) for various dyeing times. The cross-sections were prepared on the Richter microtome after being embedded in the 2-hydroxyethylmethacrylate resin. The dye diffusion was measured with microscope software [4].

For the transmission electron microscopy, the isoprene was polymerized into swollen fibres and the samples were stained with OsO<sub>4</sub> to achieve a required contrast. The treated fibres were embedded in the Epon resin and ultra-thin cross-sections were prepared on the Leica microtome using a diamante knife [5].

## III. RESULTS AND DISCUSSION

The substantive fluorescent dye Calcoflour was used as a molecular probe to explore the internal pore structure of Lyocell fibres. Its intrusion depends on the time and on the structure of the pores. Fluorescence microscopy could deliver qualitative and semi-quantitative information about the dye diffusion into different fibres.

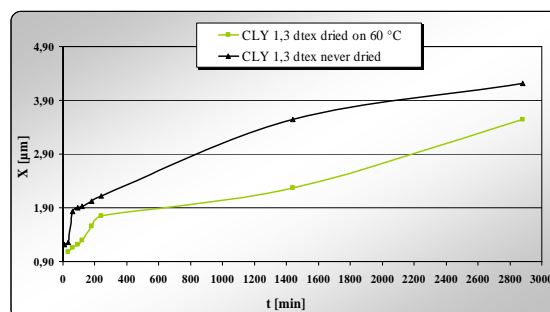


Figure 1: Fluorescent dye diffusion into dried and never-dried Lyocell fibres

The experiments had shown that the never-dried Lyocell fibres are much more accessible to the dye than dried fibres (Fig.1). The intrusion of the dye could even reach the centre of the cross-section in some cases revealing a fairly open porous system, which collapses after first drying.

The fluorescence microscopy observation gave a dye distribution profile which fits with the assumed skin-core model [3, 4].

The diffusion depth measurements confirm the three different zones in the Lyocell fibres: semi-permeable skin, through which the dye diffusion occurs rapidly, middle open porous zone, where the dye diffusion also occurs quickly and the inner compact core, where the dye diffusion occurs very slowly.

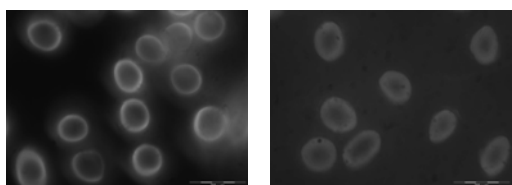


Figure 2: Fluorescence microscopy micrographs – left dyeing time 90 min; right – dyeing time 2880 min

Highly resolved TEM micrograph (Fig. 3) showed that the Lyocell fibres have homogenous pore distribution. In high magnification images, even a highly porous fibre skin with 150 nm thickness becomes visible, giving the first time an image of the Lyocell fibres structure in the wet state [5].

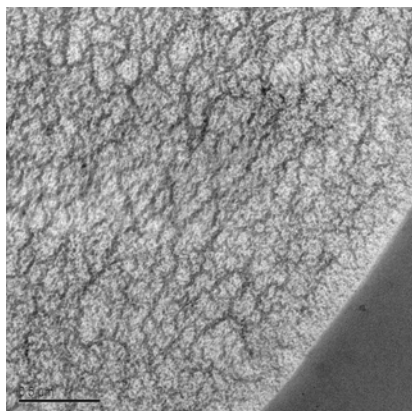


Figure 3: TEM micrograph of the Lyocell fibre – an  $\text{OsO}_4$  post stained cross-section [4]

#### IV. CONCLUSIONS

The approach to investigate the Lyocell fibres structure with fluorescence and transmission electron microscopy has been demonstrated. The researches confirm that there are different zones in the fibre cross-section: more open outer part where dye diffusion occurs quickly and inner,

more compact part, where dye diffusion occurs slowly. With fluorescent dye diffusion measurements through various dyeing times, the different Lyocell fibre types also could be determined [4]. TEM can serve as a method to visualise the pore structure and as a reference method to evaluate and explain the results of the less sophisticated methods, like dyeing techniques, applied in a routine fibre production structure analysis [5].

#### IV. OUTLOOK

The approach of our group is to understand the structure of man-made cellulose fibres, influencing their physical and mechanical properties.

Further efforts will be focused on the detailed analysis of the various Lyocell fibre types produced under different process parameters by fluorescent dye diffusion measurements as well as electron microscopy.

The obtained results will be assimilated with the researches based on the thermoanalytical methods in order to explain the physiological behaviour of the Lyocell fibres and the textiles made herein.

#### ACKNOWLEDGEMENTS

The authors gratefully acknowledge the Christian-Doppler Society Vienna for financial support and Mr. Karl Reiter, Lenzing AG, for the microscope sample preparation.

#### REFERENCES

- [1] K.C. Schuster et al.: Environmental Friendly Lyocell Fibres, in *Natural Fibres, Plastics and Composites*, ed. F.T. Wallenberger and N.E. Weston, 123–146, Kluwer Academic Publishers, Boston/Dordrecht/New York/London, 2003.
- [2] K. Brederek, A. Blüher: Porenstrukturbestimmung von Cellulosefasern durch Ausschlusschromatographie, *Melliand Textilberichte* 8, pages 652–662, 1992.
- [3] O. Biganska: Etude physico-chimique des solutions de cellulose dans la N-méthylmorpholine-N-Oxyde, Thesis, Ecole Nationale des Mines de Paris, December 2002.
- [4] M. Abu Rous et al.: Fluorescent molecular probes for the characterisation of the fibres structure and distribution of textile resin finishing on Lyocell, *Lenzinger Berichte* 83, pages 92–98, 2004.
- [5] M. Abu Rous et al.: Visualisation of the fibrillar and pore morphology of cellulose substrates applying transmission electron microscopy, *Cellulose*, in Print.

# Collagen/Hyaluronic Acid Membranes For Tissue Engineering

Lucia Vodná, Silvia Bubeníková, Dušan Bakoš  
Institute of polymer materials, Faculty of Chemical and Food Technology  
Slovak Technical University  
Bratislava, Slovak Republic  
Email: [lucia.vodna@stuba.sk](mailto:lucia.vodna@stuba.sk)

**Abstract** — *New biodegradable materials used to treat local wounds and infections have been studied. The main advantage of these materials is their excellent biocompatibility, non-toxicity and controlled biodegradation without causing side-effects [1]. On the other hand, these biopolymer systems can be also used as donors of cells or local antibiotics for tissue engineering applications. The 3D biodegradable membrane, Coladerm, based on the polyelectrolyte complex, as well as the release of local antibiotics has been studied.*

## I. INTRODUCTION

The 3D biodegradable membrane, Coladerm, is based on the polyelectrolyte complex consisting of hyaluronic acid and enzymatically treated a high-crystallinity collagen [2], which is crosslinked by starch dialdehyde derivatives [3]. The application of the Coladerm membrane in a topic implantation as a synthetic skin substitute is combined with the risk of bacterial infection. Therefore to anticipate infections, it is convenient to anchor antibiotics into the membrane. In our case the fluoroquinolone antibiotic ofloxacin was used, which is appropriate for treating anaerobic bacteria [4]. The Coladerm membrane acts as an excellent donor of this antibiotic.

## II. MATERIALS AND METHODS

### A. MATERIALS

The following polymers were used for membrane preparation: collagen (HYPRO, clear 99,9% crystalline), hyaluronic acid (CPN, microbiologically prepared (*Streptococcus zooepidermicus*), MW  $1,5 \cdot 10^6$ ). The following antibiotic was used: Ofloxacin (SIGMA). All other chemicals were of analytical grade.

### B. COLADERM PREPARATION AND RELEASE STUDYING

0.4g of ofloxacin was dissolved in 20ml of 0.5M  $\text{CH}_3\text{COOH}$  and mixed with 3g of collagen dispersed in 100ml of water. 0.24g of dissolved hyaluronic acid in 20ml of water was added. The complex was modified by 4.6ml of 1.3% starch dialdehyde solution.

In the other experiment, 3g of collagen in 100ml of water was mixed with 20ml of 0.5M  $\text{CH}_3\text{COOH}$ . 0.24g of hyaluronic acid dissolved in 20ml of water containing 0.4g of ofloxacin was added. The complex was modified by 4.6ml of 1.3% starch dialdehyde solution.

Membranes were prepared by casting the viscous reaction mixture into Teflon form and dried at 37°C.

Peaces of the membrane were dipped into 0.9% NaCl at 37°C and the antibiotic release was measured using Cecil CE 7250 UV/VIS spectrophotometer.

## III. RESULTS AND DISCUSSION

The release of ofloxacin was studied using UV/VIS spectrophotometric determination at 293 nm. The 0.9% NaCl solution at the temperature 37 °C was used as solvent. The kinetics was followed during 28 days, corresponding with the time of Coladerm degradation in the body. The detailed results of the kinetics of the antibiotic release will be presented in the poster.

## IV. CONCLUSION

The release of ofloxacin is more regular if it is bounded with hyaluronic acid before the polyelectrolyte complexation comparing to primary bounded ofloxacin to collagen. It means, ofloxacin release can be faster or slower choosing the way of complex preparation. Both modifications of the Coladerm membrane can be applied in local severe or long lasting treatments.

## REFERENCES

- [1] Williams, D.F., Biofunctionality and biocompatibility, In *Materials Science and Technology, Medical and Dental Materials* (Volume Editor D.F. Williams), VCH Publishers, Inc., Cambridge, 1989
- [2] Reháková, M. et al, *J Biomed Mat Res*, 30 (1996) 3, p. 369-372
- [3] Sw. Pat., 01, 93, 058, 1982
- [4] Christian, J. S., *Prim Care UpdateOb Gyns*, 3 (1996) 3, p. 87-92

# Order in low-dimensional systems: the Langmuir film study

Martin Weis, Marek Vančo, Jana Röschlová, Július Cirák, Drahoslav Barančok and Jan Vajda  
 Dept. of Physics, Faculty of Electrical Engineering and Information Technology,  
 Slovak University of Technology, Ilkovičova 3, 81219 Bratislava, Slovak Republic  
 Email: martin.weis@stuba.sk

**Abstract** — Maxwell's displacement current flowing through metal electrode/air gap/Langmuir monolayer was detected. Presented MDC experimental results obtained during a lateral compression of the monolayer are analysed by a model based on the analogy with a non-ideal gas of polar molecules, assuming the Boltzmann statistics of orientational distribution. The theoretical model is presented for a monolayer of thin rodlike molecules (stearic acid) Experimental results from the mode of step-compression are confronted with the theoretical model based on the analogy with a non-ideal gas of polar molecules which was derived from Lagrange's motion equation.

through, NIMA Technology, UK), results in the change of the surface concentration of the molecules as well as in the orientational change of direction of the molecular electric dipoles. The change of the orientational polarization vector can be expressed as Maxwell's displacement current flowing through the monolayer. For our experiment we used stearic acid (Aldrich-Fluka).

## I. INTRODUCTION

The Langmuir-Blodgett (LB) technique can be used to prepare a well-ordered monomolecular layer and multilayer films of amphiphilic organic materials. In this technique an insoluble monolayer is formed at the air/water interface by the movable barrier to a specified surface pressure-area state and subsequently transferred to solid substrate. Recently with increasing interest in the low-dimensional systems, applications were used in the field of physics, chemistry and biology [1,2]. For all these applications, it is essential to have a uniform film with well-defined parameters prepared by reproducible technique. Hence, the investigation of irreversible phenomena in the Langmuir film is prior necessity.

## II. EXPERIMENTAL SETUP

During the last 15 years the Maxwell displacement current (MDC) measuring technique, for the dynamic study of monolayer, was developed [3,4]. In experiment, MDC flows through the metal electrode/air gap/Langmuir monolayer/water surface structure (see Figure 1, top). The core of the experiment is based on a short-circuited capacitor being formed by two parallel plates between which a monolayer of organic molecules is situated at the air/water interface (Langmuir monolayer). MDC is here generated by the change in dielectric polarization provided mechanically. Compression of the monolayer by means of a movable barrier (computer-controlled Langmuir

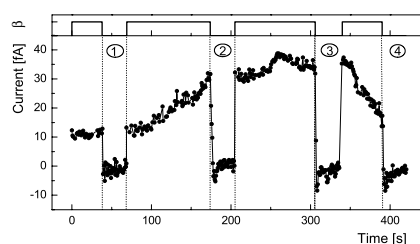
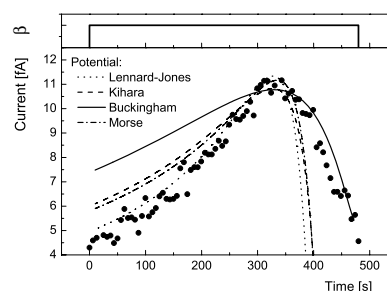
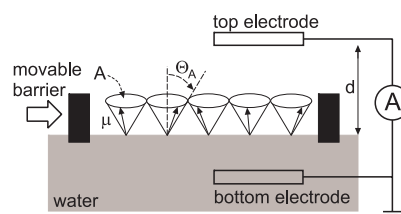


Figure 1: (top) Sketch of the experimental setup for MDC measurement. Rod-like polar molecules execute precessional motion at the water surface with maximal tilt angle  $\Theta_A$ . (middle) The experimental results MDC of continuous compression (represented by the compression rate  $\beta$ ) is compared with our calculations using various standard potentials. (bottom) Time records of the MDC in the mode of a step-compression.

### III. THEORETICAL APPROACH

#### A. CONTINUAL COMPRESSION

As we showed in our previous studies [5] the current flowing in the outer circuit can be expressed as a time change of the induced charge

$$I = \frac{\partial Q_i}{\partial t} = \mu N G \frac{\partial \langle \cos \Theta \rangle}{\partial t} + \mu \langle \cos \Theta \rangle G \frac{\partial N}{\partial t} \quad (1)$$

where  $\mu$  is the dipole moment of one molecule,  $N$  is the number of molecules under the top electrode and  $G$  is the geometrical factor depending only on the distance between the top electrode and the top plane of the monolayer, and on the radius of the circular electrode.  $\langle \cos \Theta \rangle$  stands for the statistical mean value  $\cos \Theta$ , where  $\Theta$  is the angle between the vector of dipole moment and the vertical  $z$ -axis and is defined by a relationship

$$\langle \cos \Theta \rangle = \frac{1}{Z} \int \cos \Theta \exp\left(-\frac{\bar{U}}{kT}\right) d\Omega \quad (2)$$

where  $d\Omega$  is the solid angle in which the molecule is situated,  $Z$  is partition function and  $\bar{U}$  is the mean value of the interaction energy consisted of dipole-dipole potential and standard potential. Calculation for various potentials is shown in Figure 1 (middle).

#### B. STEP-COMPRESSION MODE

We also suggest a simple molecular model [6] to analyze mechanically induced MDC behaviour of a Langmuir film using the Lagrange motion equation for molecular tilt  $\Theta$ , which characterize the dipole moment of the molecule. Experimental data were successfully explained using intermolecular potential with the Buckingham form and the spatial averaged dipole-dipole interaction. The barrier effect (monolayer – movable barrier interaction) was also taken into consideration in the analysis.

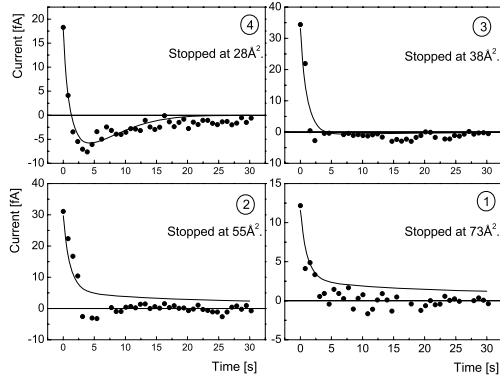


Figure 1: Detailed analysis of the relaxation process following a stop of the barrier (Fig. 1 – bottom). Solid lines represents our calculations.

The molecules have a tilt  $\Theta \in \langle 0, \Theta_A \rangle$  from vertical axis, where the maximal possible tilt angle  $\Theta_A$  is a function of the area per molecule and is defined by the relation  $\cos \Theta_A = \sqrt{1 - A/A_C}$  ( $A_C$  is the critical area for the molecule lying on the water surface) [3]. The system has a spontaneous trend to expand, therefore we assume that the molecules have tilt  $\Theta = \Theta_A$ . In the spherical coordinates, where one molecule is at the centre of the system, for a generalized variable the Lagrange motion equation of a cluster of  $n$  molecules has form

$$\frac{\partial}{\partial t} \left( \frac{\partial L}{\partial \dot{\Theta}} \right) - \frac{\partial L}{\partial \Theta} = 0 \quad (3)$$

The kinetic energy consists of rotation, precession and translation energy. The latter one consists of mean value  $\frac{1}{2} kT$ , where  $i$  is degree of freedom (constant value for given temperature  $T$ ; disappear by time derivation) and its change  $\frac{1}{2} m \dot{r}^2$ .

After energy terms substitution, application of friction term  $-\xi' \dot{\Theta}$  to the motion equation is possible Eq.(3) rewritten as

$$\ddot{\Theta} = -\frac{\pi}{(n-1)m} \left( \frac{\partial U}{\partial A} \tan \Theta + \xi' \frac{\dot{\Theta}}{\cos^2 \Theta} \right) \quad (4)$$

where  $\xi' = \xi/2A_C$ . The theoretical calculations satisfactorily fit the experimental data (Figure 2).

### IV. CONCLUSION

Analysis of the molecular motion by the Lagrange equation explains the observed two-dimensional orientation-translation relaxation process in the monolayer after stopping its compression. The proposed model fits differences of various molecular concentrations of the monolayer and we obtain very good match of the measured relaxation process with the theoretical calculations.

### REFERENCES

- [1] E. Sackmann, *Science*, 271 (1996), 43.
- [2] R. Lipowsky, *Nature*, 349 (1991), 475.
- [3] M. Iwamoto, Y. Majima, *Thin Solid Films* 178 (1989) 87.
- [4] D. Barančok, J. Cirák, P. Tomčik, J. Vajda, *Phys. Stat. Solidi* 169(2) (1998), 267.
- [5] J. Vajda, M. Weis, D. Barančok, J. Cirák, P. Tomčik, *App. Surf. Sci.* 229/1-4 (2004), 183.
- [6] J. Vajda, M. Weis, D. Barančok, J. Cirák, P. Tomčik, *Centr. Euro. J. Physics* 3(1) (2005), 139.

# Simulation of Interstitials Redistribution and Phase Profiles in Dissimilar Welds of Creep-Resistant Steels

Bronislav Zlámal and Rudolf Foret  
Institute of Materials Science and Engineering  
University of Technology  
Brno, Czech Republic  
Email: zlbr@email.cz, foret@fme.vutbr.cz

**Abstract** — *The simulation of carbon and nitrogen redistribution was performed and subsequent structural changes in laboratory weld joints of the 6CrMoV 8-3-2 and X12CrMoVNb 10-1 heat-resistant steels were studied. For the calculation the Thermo-Calc and DICTRA software were used. The aim of the work was to compare the simulation of chemical composition profiles and phase profiles of the weld at the temperature range 600-900°C with experimental results. The results showed that simulation was in a good agreement with experiment.*

## I. INTRODUCTION

The efficiency of conventional fossil power plants strongly depends on steam temperature and pressure. Research and development of creep-resistant steels for high-efficient power plants are being now promoted worldwide in order to reduce emissions of environmentally damaging gases such as CO<sub>2</sub>. The development of stronger high temperature materials call for not only creep strength improvement but also resistance to fireside and steamside corrosion and weldability. Great advancement has been achieved in the analysis of microstructure instability causing a loss of creep strength and the theoretical modelling of precipitation sequences taking place in dissimilar creep-resistant steels welds. Using the CALPHAD approach [1] with appropriate databases local and global phase equilibrium problems concerning the base material and weld joints can be solved. The DICTRA software package [1, 2], which contains Thermo-Calc as a subroutine, is used as a conductive tool for simulation of processes in dissimilar welds.

## II. EXPERIMENTAL PROCEDURES

The dissimilar laboratory welds of bainitic 6CrMoV 8-3-2 (T25) steel, currently being developed, and modified martensitic X12CrMoVNb 10-1 (P91) steel (Table 1) have been subject of study. The cylindrical samples (diameter

12 mm, height 4 mm) from both base materials were welded by means of an electric current pulse within a protective Ar atmosphere. The former set of dissimilar welds consisted of base steels in as-received states. In the latter set both base materials were ion-nitrided and homogenized at 1050°C/24h before welding to increase nitrogen content. A subsequent analysis of the nitrided samples (materials T25+N and P91+N) informed us that the homogenization was successful in the case of material T25+N but not for P91+N. The nitrogen content in the P91+N material remained higher on the surface after homogenization and the exponential function  $N^{**}=0.8e^{(-1.83x)}$  fits best the experimental over-all nitrogen content in P91+N ( $x$  in mm gives the distance from the surface for the P91+N material).

All joints were annealed at 600°C/240h and 900°C/18h. Subsequently they were cut perpendicularly to the weld interface. Microstructural analyses were made on these surfaces. The redistribution of carbon and nitrogen was measured using the wavelength dispersive X-ray method (Electron Probe X-ray Microanalyzer Jeol JXA-8600). Carbon extraction replicas from surfaces close to the weld (carburized and decarburized zones) and from unaffected sides of the weld (basic materials) were used in order to characterize the microstructure. The chemical composition of precipitates was derived from the energy dispersive X-ray analysis used on Philips CM12 TEM/STEM microscope equipped with EDAX Phoenix analyser. TEM diffraction was used to confirm the analyzed phases. The redistribution of interstitial elements (C, N) and phase profiles in the weld joints were simulated using DICTRA software for annealing conditions above. For the simulations the STEEL thermodynamic database [3] and DIF kinetic database [4] were used. The results from the simulation were compared with experimental observations.

Steel	C	Mn	Si	Cr	Mo	V	Nb	N*	N**
T25	0.06	0.42	0.34	1.91	0.31	0.22	0.058	0.024	0.11
P91	0.12	0.38	0.44	9.96	0.89	0.22	0.070	0.069	$0.8.e^{(-1.83x)}$

Table 1: Chemical composition of creep-resistant steels [wt. %] (N\* gives the nitrogen content in initial steels, N\*\* represents the nitrogen content in the nitrided material)

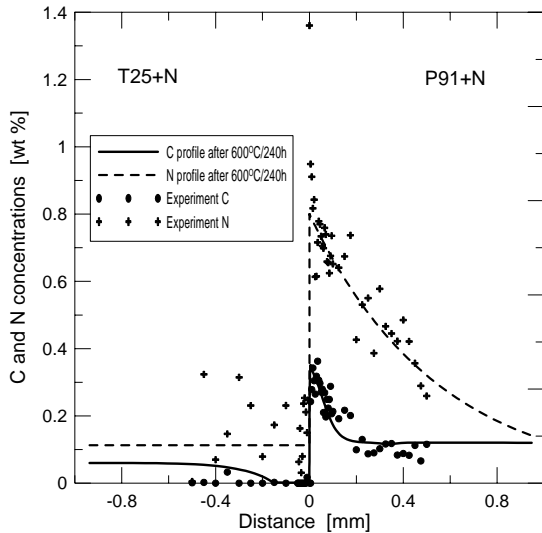


Fig. 1: Redistribution of C and N at 600°C/240h

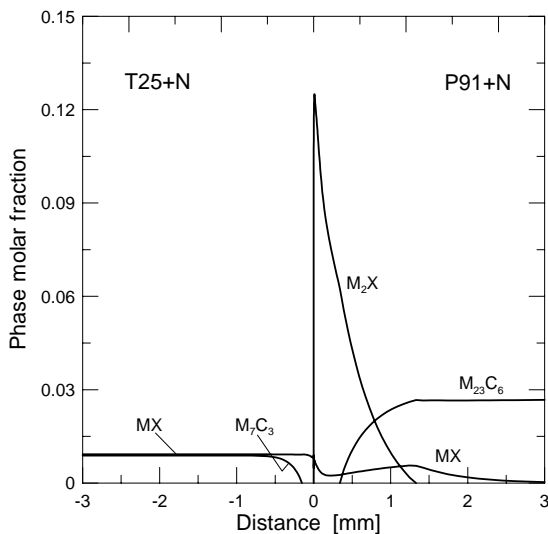


Fig. 2: Simulated phase profile in the weld joint annealed at 600°C/240h

### III. RESULTS

The up-hill diffusion of carbon was observed in the weld joints annealed at 600°C/240h. The carbon diffused from the T25 (T25+N) material to the P91 (P91+N) material in accordance with the carbon activity difference calculated. The carbon depleted

zone (CDZ) inside the T25 steel and the carbon enriched zone (CEZ) inside the P91 steel were formed in the vicinity of the T25|P91 and T25+N|P91+N weld joint interface (Fig. 1). In the joint T25+N|P91+N the initial nitrogen profile remained stable because of very low nitrogen activity difference between the steels under study in the temperature interval 600-900°C. The height of peaks of the calculated carbon and nitrogen profiles corresponded to measured values as well as the depth of carbon enriched zone and nitrided zone. The phase profiles, with peak of  $M_{23}C_6$  carbides in CEZ of P91 steel in the first set and with peak of  $M_2X$  carbonitrides in second set (Fig. 2), were calculated for both sets of samples and confirmed by experimental measurements.

In the weld joints annealed at 900°C/18h the carbon diffusion was very slow because of small activity gradient between the joined steels. Phase profiles with MX and  $M_2X$  carbonitrides were calculated to be stable and also confirmed by experimental observations.

The simulation and experimental results led to conclusion that the weld joints T25|P91 and T25+N|P91+N exposed to elevated temperature around 600°C represents much risk in practical service as a consequence of C and N redistribution.

### ACKNOWLEDGMENTS

Support of the Grant Agency of the Czech Republic (No. 106/03/0636) is gratefully acknowledged for funding.

### REFERENCES

- [1] Saunders, N. and Miodownik, A. P. CALPHAD (Calculation of Phase Diagrams) – A Comprehensive Guide. Elsevier Science Ltd, Amsterdam, 1998, 479 p. ISBN 0-08-0421296.
- [2] Borgenstam, A. et al. Journal of Phase Equilibria, 21/3 (2000), p. 269-280.
- [3] Unucka, P. Equilibria in multicomponent systems C-Cr-Fe-Mo-X. PhD thesis, Brno: BUT FME, 2004, p. 93.
- [4] Sopoušek, J. et al. Science and Technology of Welding and Joining, 9/1, (2004), p. 59-63.

# Metal-Semiconductor Contact Modeling and Transport Characteristics Detectors of Radiation Based on the CdTe

Alexey Andreev, Jiri Zajacek (Supervised by: Doc. Ing. Lubomír Grmela, CSc.)

Department of Physics, Faculty of Electrical Engineering and Communication  
Brno University of Technology  
Technicka 8, 616 00, Brno, Czech Republic  
Email: xandre00@stud.feec.vutbr.cz

## Abstract

*Contact metal - semiconductor is an obligatory element of all semiconductor devices. Contact energy diagrams of CdTe detectors have been modeled on the basis of the semiconductor parameters - work functions of the metal; affinity, work function, gap zone width and acceptor energy activation of the semiconductor. Series VA characteristic measurements in the dark were carried out at dependence on temperature and we have found current's function depending from temperature. We have found differences in transport characteristics after temperature degradation process.*

## I. INTRODUCTION

Experimental studies of transport and noise characteristics of CdTe sensors have been carried out. There are three different 1/f noise sources; bulk and surface 1/f which is proportional to square of current and contact 1/f noise with current noise spectral density proportional to higher than second power of current. Experimental results are used to characterize contact technology preparation. Contact prepare by deposition of gold from aqueous solution of AuCl<sub>3</sub>. Low and high ohmic samples reveal contact resistance. This one is dominant noise sources for low ohmic samples, while high ohmic samples are sources 1/f with dominant mobility fluctuation.

Blocking contacts metal - semiconductor or Schottky barriers have received the most application in semiconductor devices. We shall consider a condition of occurrence of Schottky barrier.

$$J_T = AT^2 \exp\left(-\frac{\Phi}{kT}\right) \quad (1)$$

The current of thermionic emission from a surface of any solid state material is defined by Richardson's equation "(1)".

Thermodynamic work function from the semiconductor  $\Phi_S$  for Au - CdTe p-type contact is more than thermodynamic work function from metal  $\Phi_{Au}$ . In this case according to the equation thermionic emission current from a surface of semiconductor  $J_S$  will be less, than a thermionic emission current  $J_{Au}$  from a surface of metal:

$$\Phi_S > \Phi_{Au} \quad J_S < J_{Au}$$

At contact of such materials during the initial moment of time the current from metal in the semiconductor will exceed a return current from the semiconductor in metal and in surface areas of the semiconductor and metal volumetric charges - positive in metal and negative in the semiconductor will collect. There will be an electric field in the contact area therefore there will be a bend of power zones. Thermodynamic work function will decrease on surfaces of the semiconductor owing to field effect. This process will pass until in the field of contact will not equalize thermionic emission currents and accordingly thermodynamic work functions values on a surface.

There are energy diagrams of various stages of metal - the semiconductor contact formation shown in "Figure 1" and "Figure 2".

## II. VA CHARACTERISTICS

We have measured sample's VA characteristics twice. Results of the first measurements for sample are following: VA characteristic is non-linear. There can be observed forward and reverse direction. Sample resistance increases with decreasing temperature.

Results of the second VA measurements for sample are following: we have observed resistance increasing with decrease temperature, but its VA characteristics has changed. Sample's resistance at first and second measurement before temperature  $t = 60^\circ\text{C}$  the same as sample's resistance at second

measurement. When temperature  $t > 60^{\circ}\text{C}$  resistance of first measuring sample decreases rapidly than resistance of second measuring sample.

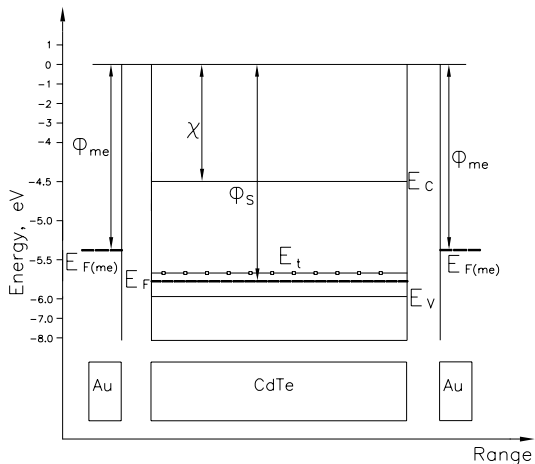


**Figure 1:** The metal and the semiconductor band energy diagram before occurrence of Contact

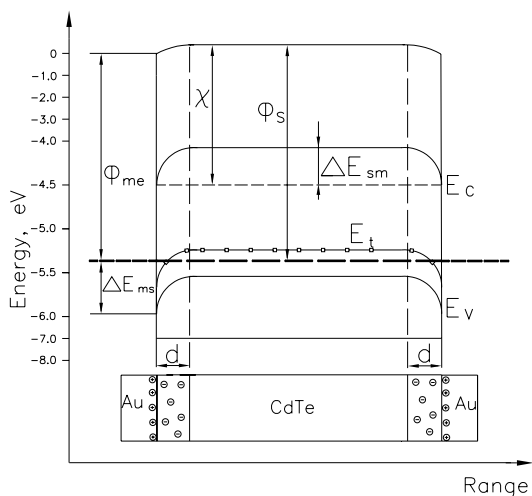


**Figure 2:** The band energy diagram of metal – semiconductor contact

Based on the known values of work functions Au  $\Phi_{Au}$ , and affinity  $\chi$  CdTe, gap zone width  $E_g$  and acceptors concentrations were calculated by MATLAB following values with both a case of absence of an external voltage, and a case of enclosed external voltage  $V_E$ :

$\Delta E_{ms} = 0.6$  eV – potential barrier from metal in the semiconductor;  $\Delta E_{sm} = 0.42$  eV – potential barrier from the semiconductor in metal;  $E_{F(s)} = -5.79$  eV - fermi level position;  $d = 57.8$  microns - depleted zone width

The Cadmium Telluride single crystals were prepared by Physical Institute of Charles University in Prague. The VA characteristics and noise spectral density was measured at room temperature under dark and illumination. VA characteristics are nonlinear.

#### ACKNOWLEDGMENTS

This research has been supported by GACR No.102/05/2095 and by the Czech Ministry of Education in the frame of MSM 0021630503 Research Intention MIKROSYN “New Trends in Microelectronic System and Nanotechnologies”.

#### REFERENCES

- [1] Schauer, P., Sikula, J., Moravec, P.: Transport and Noise Properties of CdTe(Cl) Crystals, Microelectronics Reliability 2001, p431, 41.
- [2] Gurtov, V., A.: Solid state electronics, Petrozavodsk 2004, 37-39
- [3] Sze, S., M.: Physics of Semiconductor Devices, J.Wiley & Sons New York 1981
- [4] Asad, I. at all.: Physical model of Current Noise Spectral Density versus dark current in CdTe detectors, ICNF 2001. Gainesville 2001, p339

# Zinc Oxide Crystal Growth by Molten fluxes

Chun-Min Feng, Glen Kowach  
The City College of New York and the Graduate Center  
The City University of New York  
New York, USA

Email: ChunMin@sci.ccny.cuny.edu, Kowach@sci.ccny.cuny.edu

**Abstract** — Zinc oxide (ZnO) is an important material for many industrial applications including transparent electronic conductors, piezoelectric resonators, and ultraviolet light emitting diodes. Recently, manganese-substituted ZnO (Mn-substituted ZnO) is of interest as a possible spintronic material with an electronic carrier-mediated ferromagnetic Curie temperature above room temperature. Several reports indicate a ferromagnetic transition in Mn-substituted p-type ZnO above room temperature. However, due to the difficulty of producing high quality bulk crystals, this observation remains controversial. We are studying methods to grow single crystals from molten fluxes, such as boron oxide, vanadium oxide, potassium hydroxide and sodium hydroxide. The reaction conditions, phase diagrams, and quantity of Mn substitution in the ZnO crystals is determined by X-ray diffraction and scanning electron microscopy (SEM) with energy-dispersive spectroscopy (EDS).

## I. INTRODUCTION

In this work we will present ZnO crystal growth by different fluxes. There are many reports studying of ZnO crystal growth using different fluxes available in literature.<sup>[1-3]</sup> However, a systemic study on crystal growth from fluxes is still lacking. Hence, the present investigation is focused on systematic crystal growth using important phase diagram information, such as, eutectic temperature, composition, and phase change.

Zinc oxide (ZnO) possesses the wurtzite structure and is a wide band gap semiconductor (3.3 eV). Due to the large band gap, it is used in UV optical devices. There are many applications of this novel material; however recently ferromagnetic properties in Dilute Magnetic Semiconductors (DMS) are very attractive. Mn-substituted ZnO is one of the proposed DMS material, but it difficult to increase high Mn concentration. Since Dietl et al<sup>[4]</sup> predict that ZnO may have high temperature ferrmagnetism by substituting with a transition metal.

In this paper we describe high quality ZnO crystal growth by different molten fluxes. Different fluxes,

such as boron oxide ( $B_2O_3$ ) vanadium oxide ( $V_2O_5$ ), and hydroxide (NaOH, KOH, or both), to grow ZnO crystals.

## II. EXPERIMENT

All chemicals are ordered from Alfa Aesar. In the ZnO- $B_2O_3$  system, we use  $B_2O_3$  43.19 g (99.98%) and ZnO 230.20 g (99.0%). A furnace with  $MoSi_2$  heating elements is used. After packing in a platinum crucible, the sample is heated to 1300 °C and hold for 2 hr. Then it is cooled to 1165 °C at a rate of 3.2°C/hr. When the temperature reached 1165 °C the flux was poured off to reveal the crystals.

In the ZnO-NaOH system, we put ZnO 1.01 g and NaOH (98%) 4.88 g. We pack mixture in an aluminum crucible the sample heated to 500 °C and hold for 48 hr. Then it is cooled to room temperature at a rate of 1.1°C/hr. In this case we remove the flux by washing crystal with deionized water.

## III. RESULTS AND DISCUSSION

Various experiments using fluxes, like,  $V_2O_5$ ,  $B_2O_3$ , and NaOH, show growth of high quality ZnO crystals. The obtained in different fluxes are explained below.

Green ZnO crystals (Fig. 1) are obtained in ZnO- $B_2O_3$  system crystal growth. After poured off the  $Zn_2B_2O_3$  molten mass, the plate-like ZnO crystals stay in Pt-crucible and some flux adhered on crystal. By comparing the observed powder x-ray diffraction (XRD) patten with the reported JCPDS data (JCPDS 36-1451), the flux is identified as  $Zn_3B_2O_6$  (JCPDS 37-1486).

For the ZnO-NaOH system, ZnO have the same color as in ZnO- $B_2O_3$  system. The SEM image of ZnO crystal is shown in Fig 2. A clear hexagonal habit of ZnO can be seen from it. In addition some white powders are found to stick to the crystals.

#### IV. FIGURES



Fig 1 As grown ZnO crystals sitting in Pt-crucible.  $Zn_2B_2O_6$  flux is still sticking on the crystal surfaces. (CMF 8)

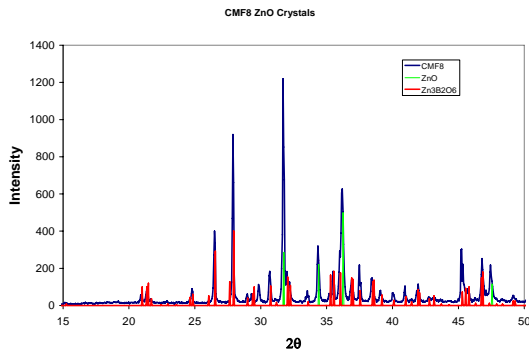


Fig. 2 The ZnO XRD pattern demonstrates ZnO (JCPDS 36-1451) crystal and zinc borate ( $Zn_3B_2O_6$  JCPDS 37-1486). (CMF 8)

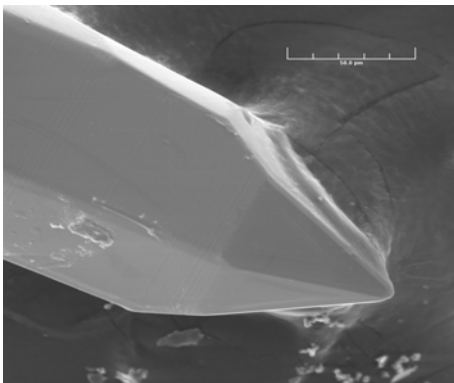


Fig. 3 SEM image of ZnO shows the hexagonal structure (CMF 26 C)

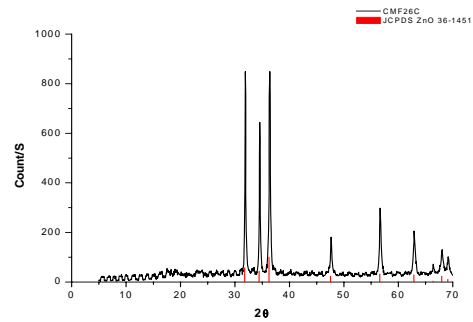


Fig.4 Powder x-ray diffraction pattern of ZnO crystal confirm with JCPDS (CMF 26C)



Fig. 5 EDS pattern of ZnO crystal shows Zn is predominated in crystals with aluminium traces (CMF 26 C).

#### V. CONCLUSION

The ZnO crystals obtained from different fluxes are studied by SEM, EDS, and XRD are obtained from different fluxes.

This study provides an optimised method to grow high quality ZnO crystals which can be exploited for growing high Curie temperature ZnO-based spincs materials.

#### ACKNOWLEDGMENTS

We acknowledge The City College of New York financial support.

The authors thank for S.N. Achary Ph.D. for XRD analysis.

#### REFERENCES

- [1] Ikumaro Kubo *Japanese journal of applied physics* **4** (1965) 225
- [2] D.E. Harrison *Journal of Crystal Growth* **3**, **4** 674 1968
- [3] B. M. Wanklyn *Journal of Crystal Growth* **7**, 107 1970
- [4] T. Dietl, H. Ohno, F. Matsukura, J. Cibert, D. Ferrand *Science* **287** 1019 (2000)

# Ultrasonic Characterization of Microstructure for High Purity Metals

Fei Zeng and Feng-Bao Lin  
The City College of New York  
New York, The United States  
Email: zengfei@ce.ccny.cuny.edu

**Abstract** — *In this study, a range of microstructures of high purity niobium was obtained by annealing in ultrahigh vacuum at different temperatures (600-800°C) after routine cold-rolling and recrystallization heat treatments. The ultrasonic velocity and attenuation data of these samples with different microstructures were measured. Ultrasonic velocity data indicate that velocity is insensitive to the variation of microstructure during annealing. Ultrasonic attenuation measurements show that attenuation is approximately proportional to the average grain size, which provides a potential application to determine the mean grain size nondestructively and rapidly.*

## I. INTRODUCTION

It is well known that the grain size of a polycrystalline material is a very important engineering parameter which influences its mechanical properties such as yield strength by Hall-Petch equation [1, 2]. Usually, grain size is measured by optical metallography, however it is more convenient to use a non-destructive method for the measurement of average grain size of a material. In recent years, quantitative assessment of the microstructures and mechanical properties of materials has been carried out through the measurement of ultrasonic parameters such as attenuation and velocity [3].

In the present study, the possible use of ultrasonic velocity and attenuation measurements to estimate average grain size in high purity niobium is explored. Niobium is the primary material for superconducting radio frequency (SRF) accelerator cavities) because niobium has the highest critical superconducting temperature of all pure metals [4]. The current study was undertaken to investigate the changes in ultrasonic velocity and attenuation with annealing.

## II. EXPERIMENTAL PROCEDURE

Two different lots of high purity niobium samples (denoted K and P) were obtained from Teledyne Wah Chang. The specimens were heat-treated at

different temperatures in order to obtain the specimens with varied grain sizes. Each series include an as-received sample (cold-rolled and recrystallized) and samples annealed for 6 hrs at 800, 750, & 700°C and for 10 hrs at 600°C. All the samples have parallel opposing surfaces necessary for the ultrasonic velocity and attenuation measurement. The wave propagation direction is along the sheet normal direction in each case.

Each of the samples was sectioned for examination transverse to the rolling direction in order to observe any banding or elongation of the microstructure due to processing. Coarse polishing was performed using diamond slurry, followed by intermediate polishing. The final polishing was performed using a procedure of repeated polishing and etching with alumina and an etchant.

Ultrasonic velocity and attenuation measurements were carried out using both longitudinal and shear broadband piezoelectric transducer from Panametrics. The pulser/receiver is in conjunction with an oscilloscope and a transducer. The gated backwall echoes from the oscilloscope were transferred to a personal computer for further processing.

## III. RESULT AND DISCUSSION

Figure 1 shows a typical microstructure of the as-received and annealed samples observed in this study. The as-received samples demonstrate a relatively uniform microstructure and the annealed samples show heterogeneous microstructure where a coarse grain size bands and a fine grain size bands are visible in the micrograph.

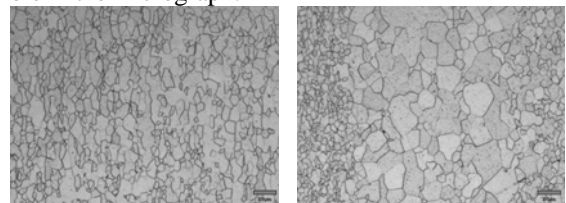


Figure 1: Micrograph from as-received (left) and annealed (right) niobium samples

Figure 2 graphically illustrates the linear intercept grain size as a function of annealing temperature for each of the sample lots (K, P) by optical microscopy. It can be seen from the plot that grain size increases with increasing temperature.

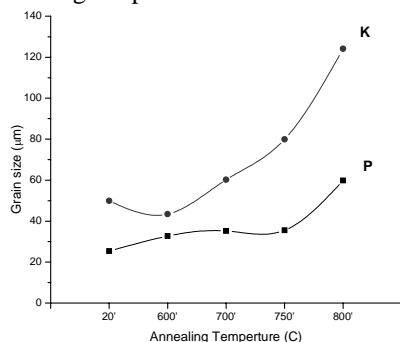


Figure 2: Lineal intercept grain size as a function of annealing temperature for P & K samples set.

Figure 3 gives the relationship between the longitudinal velocity and annealing temperature. It can be observed that the longitudinal velocities for each batch of samples (K&P) are shown to be very close to each other, which suggests that the longitudinal velocities are insensitive to annealing. In the case of the shear wave speeds (see Figure 4), the velocity of the shear wave polarized in the rolling direction (RD) remains essentially constant, while the wave polarized in the transverse direction (TD) trends upwards.

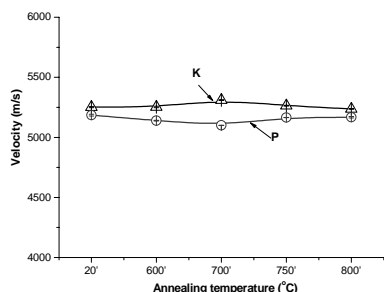


Figure 3: Ultrasonic longitudinal velocity data for K and P sample lots

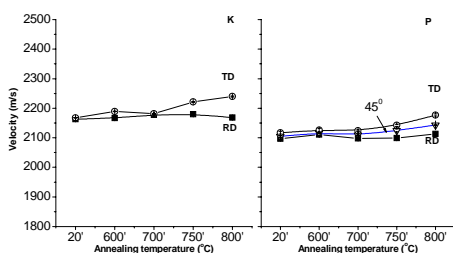


Figure 4: Ultrasonic shear velocity data in K and P samples lots

Figure 5 shows the relationship between measured attenuation and the grain size of the samples. It can be seen from the plot that attenuation increases with increasing grain size and a straight line fit is obtained using these data points.

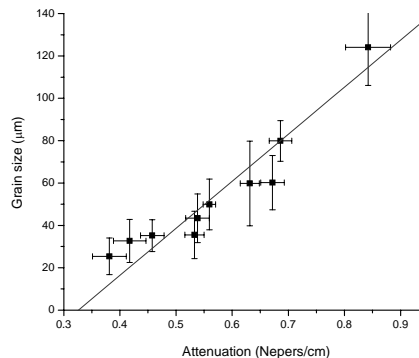


Figure 5: Ultrasonic attenuation data as a function of average grain size of the samples

#### IV. CONCLUSION

Ultrasonic velocity and attenuation measurements have been made on high purity polycrystalline niobium to characterize the microstructural change of the samples during annealing. The variation in longitudinal and shear wave velocity with annealing is very subtle, which indicates that ultrasonic velocity is insensitive to the variation of microstructure during annealing. Ultrasonic attenuation data is found to be approximately proportional to the average grain size and it is concluded that the ultrasonic attenuation measurement is particularly useful to characterize the microstructural changes during heat treatments.

#### ACKNOWLEDGMENTS

The author is grateful to Dr. S. R. Agnew in the University of Virginia for constant encouragement and support.

#### REFERENCES

- [1] Hall, E.O. (1951), Proc. Phys. Soc., Ser. B, Vol. 64, pp. 747-753.
- [2] P. Petch, N.J. (1953), J. Iron and Steel Institute, pp. 25-28, May.
- [3] Papadakis, E.P. (1984) "Physical acoustics and microstructure alloys", Intl Metl Rev 1, pp 1-24.
- [4] Grber, J. (1993), Superconducting RF Cavities: A Primer, Ph.D. Dissertation, Cornell University.

# Two-dimensional Micro- and Nanoparticle Monolayer Films

Carlos A. Silvera Batista and Ilona Kretzschmar (Faculty Mentor)  
Chemical Engineering Department  
The City College of New York  
New York, USA  
csilver00@ccny.cuny.edu  
kretzschmar@ccny.cuny.edu

**Abstract** — *Close-packed particle monolayer films are interesting precursors for many applications such as sensors, catalyst carrying templates for membranes, and can even be employed as shadow masks.*

*This project aims to determine the optimum volume-fraction required for the formation of large-area, self-assembled micro- and nanoparticle monolayers in a cylindrical crystallization cell under constant humidity. The results show that large-area particle monolayers can be obtained for particle volume fractions of 0.0020, but that the cylindrical cell setup is limited with respect to the range of applicable volume fractions and control over the speed of the receding meniscus.*

## I. INTRODUCTION

The inherent challenge in the formation of particle monolayers is to find conditions under which the formation of multilayer domains, voids, and point defects is suppressed. Among the techniques available, convective self-assembly is of special interest because of its simplicity and reported ability to fabricate large areas of close-packed monolayers [1]. As indicated by Deegan et al. [2], the driving force for the self-assembly of particles is the convective fluid flow resulting from the evaporation of the solvent from the particle solution. Dushkin et al. [3] report that the most influential factors required to get large areas of particle monolayers without defects are the solvent evaporation rate, the concentration of particles in the solution (volume fraction), the particle size distribution, and the contour of the contact line.

In this paper we report our experimental findings on the convective assembly of 2.4  $\mu\text{m}$  diameter particle monolayers in a cylindrical crystallization cell and the influence of the particle volume fraction on the monolayer quality.

## II. MATERIALS AND METHODS

Solutions of 2.4  $\mu\text{m}$  sulfonated polystyrene particles (PS) from IDC (USA) are used for the experiments. The working solutions are prepared

based on the number of particles needed to cover 100, 75, 50, and 25% of the available substrate surface in the hypothetical case of complete monolayer formation with hexagonal close packing. The cell load is the amount of solvent placed in the cell (20, 25, and 30  $\mu\text{l}$ ). A total of ten solutions with volume fractions from 0.0038 to 0.0008 are studied (Table 1). The substrate is a single-crystal silicon wafer with a natural oxide layer. Prior to an experiment, the substrate is submerged in a sulfuric acid-Nocromix mix (components purchased from Fisher) for one hour and thoroughly rinsed with di-ionized water.

Cell Load	Theoretical Substrate Area Covered by Particles			
	100%	75%	50%	25%
30 $\mu\text{l}$	0.0034	<b>0.0025</b>	<b>0.0017</b>	0.0008
25 $\mu\text{l}$	0.0041	<b>0.0031</b>	<b>0.0020</b>	0.0010
20 $\mu\text{l}$	0.0051	0.0038		

Table 1: Volume fractions of solutions.

The crystallization cell consists of a Teflon ring, a glass slide that protects the substrate, and two clamps that press the ring onto the substrate to prevent leaking. The Teflon ring with an inner diameter of 1 cm is used to create a concave meniscus profile during the assembly process. The cell is placed in a chamber with a constant nitrogen flow providing a relative humidity of  $(14 \pm 1)\%$ . The nitrogen flow rate is low enough to prevent the disturbance of the gas-liquid interface during the assembly. The cell is loaded with the respective amounts of solution (Table 1) and left in the  $\text{N}_2$  chamber until all solvent has evaporated.

## III. RESULTS AND DISCUSSION

Optical inspection of the ten samples prepared from the solutions listed in Table 1 reveals that the films prepared from the 100% solutions (column 1, Table 1) show multilayer domains while the 25% solutions (column 4) show loosely packed structures. The 20 $\mu\text{l}$ /75% solution forms large multi-

layer domains. Solutions with volume fractions between 0.0017 – 0.0031 show large-area monolayers. Scanning electron microscope (SEM) images reveal further details about the films obtained with the 50%/25 $\mu$ l, 75%/25 $\mu$ l, 50%/30 $\mu$ l, and 75%/30 $\mu$ l solutions (Figure 1).

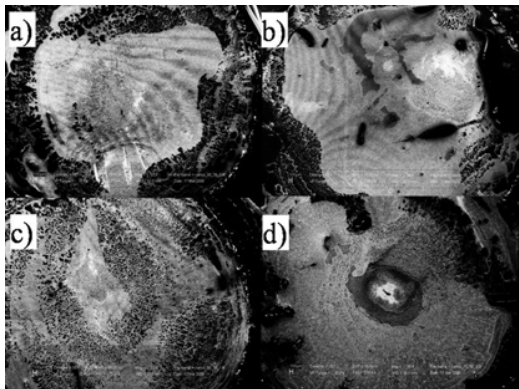


Figure 1: Scanning Electron Images at 34 $\times$  of assembled crystals: a) 50%/25 $\mu$ l, b) 75%/25 $\mu$ l, c) 50%/30 $\mu$ l, and d) 75%/30 $\mu$ l.

Birefringence patterns are observed for the films obtained with the 50%/25 $\mu$ l and 75%/25 $\mu$ l solutions (stripped patterns in Figures 1a and b). Observation of birefringence is indicative of thin domains of hexagonal-packed particles. The pattern extends over areas as large as 45 mm<sup>2</sup>. On the other hand, no birefringence is observed for the films formed with the 50%/30 $\mu$ l and 75%/30 $\mu$ l solutions pointing to less dense packing. High magnification SEM images of films from the 50%/25 $\mu$ l and 75%/25 $\mu$ l solutions show that the 50%/25 $\mu$ l crystal is indeed a compact monolayer, while the 75%/25 $\mu$ l film has small areas of bilayers (Figure 2). However, note the 50%/25 $\mu$ l monolayer still has voids and grain boundaries.

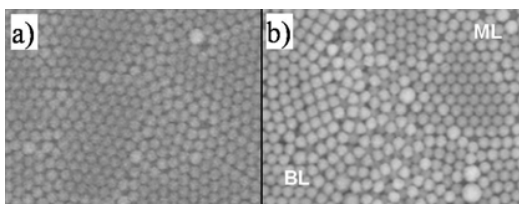


Figure 2: High magnification SEM images in variable pressure mode: a) 50%/25 $\mu$ l and b) 75%/25 $\mu$ l. ML = monolayer, BL = bilayer.

In results presented by Velev [4], close-packed monolayers were obtained using a set-up that al-

lows pulling a volume of the working solution at a specific speed, which is equivalent to the speed with which the meniscus recedes in our crystallization cell. They find that for each volume fraction there are specific pulling speeds at which the particles assemble into monolayers, bilayers, multilayers, or submonolayers. As a result, they developed an operational phase diagram for their set up. Using their phase diagram, we can assess the limitations of our set up: (i) limited control of the speed of the receding meniscus and (ii) narrow range of volume fractions that can be explored. The fact that some samples present monolayers and multilayers simultaneously is a consequence of the quite low volume fractions used in our experiments. However, our crystallization cell is much simpler than the set-up used in [4], and further exploration of the assembly of nanoparticles (i.e., small volumes) is warranted.

#### IV. CONCLUSION

Large domains of particle monolayers are obtained with the cylindrical crystallization cell. The 0.0020 volume fraction solution results in the largest domains of close-packed monolayers. Although the particle monolayers are usable for further experiments, it is still desirable to reduce the number of grain boundaries and voids even more.

#### ACKNOWLEDGMENTS

We are grateful for the continuous support received from the NYC-LSAMP program, the generous CCNY start up funds, and CCNY travel support.

#### REFERENCES

- [1] X. M. Lin, H. M. Jaeger, C. M. Sorensen, K. J. Klabunde. Formation of Long-Range-Ordered Nanocrystal Superlattices on Silicon Nitride Substrates. *J. Phys. Chem. B* 105: 3353-3357, 2001.
- [2] R. D. Deegan, O. Bakajin, T. F. Dupont, G. Huber, S. R. Nagel, T. A. Witten. Capillary Flow as the cause of ring stains from dried liquid drops. *Nature* 389: 827-829, 1997.
- [3] C. D. Dushkin, G. S. Lazarov, S. N. Kotsev, H. Yoshimura and K. Nagayama. Effect of growth conditions on the structure of two-dimensional latex crystals: experiment. *Colloid Polym. Sci.*, 277: 914 – 930, 1999.
- [4] B. G. Prevo and O. D. Velev. Controlled, rapid deposition of structure coatings from micro- and nanoparticle suspension. *Langmuir* 20: 2099-2107, 2004.

# Bubble and Droplet Motion in a Yield-Stress Fluid

John Paul Bir Singh and Morton M. Denn  
Benjamin Levich Institute for Physico-Chemical Hydrodynamics  
The City College of New York  
New York, USA

Email: jsingh@che.ccny.cuny.edu, denn@che.ccny.cuny.edu

**Abstract** — *The goal of this research is to study the motion and interaction of bubbles and drops in yield-stress materials. We have developed a finite element based code and implemented level set methods to track the drop interface. We have obtained converged solutions for the slow gravitational settling of a Newtonian fluid droplet through a Bingham material in a closed container. The code employs a regularization method for the stress constitutive equation. The shape of the yield surface has been calculated as a function of the regularization parameter.*

## I. INTRODUCTION

Many liquid-like materials exhibit a *yield stress*. These materials flow above a critical stress, but they deform as linearly elastic bodies below this stress. Yield-stress materials, which are often colloidal suspensions, are commonly experienced in consumer products applications, foodstuffs, etc. The waste sludge tanks at the Department of Energy's Hanford site contain radioactive colloidal suspensions that exhibit a yield stress; the motion of flammable bubbles in these materials is a matter of particular concern. An excellent review by Bird *et. al.* [1] lists about forty fluids which show yield stress.

The solution of complex flow problems for yield-stress materials is particularly challenging because of the possible existence of "yielded" regions in which flow can occur and "unyielded" regions in which only elastic deformation is possible. The interface between these regions is not known *a priori*.

Beris and coworkers [2] studied the problem of flow past a solid sphere. Using a finite element based computations they were able to calculate the shape of yielded region around the sphere for range of parameters. Their work was followed by Liu *et. al.* [3] with a computational study of interacting spheres in yield stress fluids.

## II. PROBLEM FORMULATION

We have constructed an in-house finite-element code that utilizes the method of level sets to track the deformable phase interface [4], [5]. The complete

problem formulation is in 2-dimensions. The fluid rheology is characterized by the Bingham fluid model, in which the stress in excess of the yield stress is a linear function of the deformation rate [6], [7]. The code employs a regularization method for the stress constitutive equation [2] in order to formulate the problem in terms of continuous variables over the entire space. Mathematically,

$$\tau = (\eta_p + \frac{\tau_o}{\sqrt{\pi^2 \dot{\gamma}^2 + \epsilon^2}}) \dot{\gamma} \quad (1)$$

Where  $\tau$  is the stress,  $\tau_o$  is the yield stress,  $\eta_p$

is the plastic viscosity,  $\dot{\gamma}$  is the shear rate  $\pi_2$  is the second invariant of strain rate, and  $\epsilon$  is the regularization parameter. In the limit as  $\epsilon \rightarrow 0$  the equation reduces to the Bingham model.

The drop is kept in the centre of a closed box and it falls under the force of gravity. The radius of the drop is of the order of 0.05 times the length of the computational box.

## III. RESULTS

We have obtained converged solutions for the slow gravitational settling of a Newtonian fluid droplet through a Bingham material. There can be no motion when yield stress exceeds the buoyant stress, and flow is markedly affected by the yield stress at smaller values, approaching Newtonian fluid behaviour as the yield stress vanishes.

The Figure 1 shows stress contours for the case with yield stress of 0.01. The density ratio is 2, and viscosity ratio is 1. Capillary number is infinite and  $\epsilon$  is  $4.54 \times 10^{-4}$ . The lower bound on the regularization parameter is provided by increase in numerical error at smaller values. Drop viscosity and interfacial tension have little effect on the shape of yield surface.

The continuing work is addressing the problem of extending the results to bubble motion and interacting drops as well.

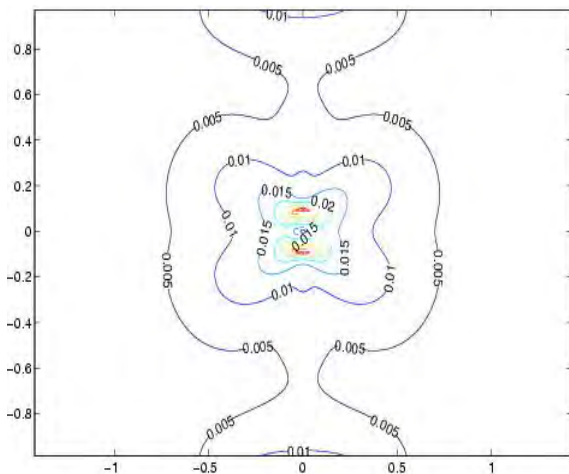


Figure 1. Stress contours; Yield stress= 0.01.

#### ACKNOWLEDGMENTS

The work has been supported by the NSF-CREST, City College of New York.

#### REFERENCES

- [1] R.B. Bird, G.C. Dai, B.Y. Yarusso, Rev. Chem. Eng. 1, 1982.
- [2] A.N. Beris, J.A. Tsamopoulos, R.C. Armstrong, R.A. Brown, Creeping motion of a sphere through a Bingham Plastic, J. Fluid Mech. 158, 1985.
- [3] B.T. Liu, S.J. Mueller, M.M. Denn. Interactions of two rigid spheres translating collinearly in creeping flow in a Bingham material, Journal of Non-Newtonian Fluid Mech. 81, 2003.
- [4] S. Osher and J. A. Sethian, Fronts propagating with curvature dependant speed: Algorithms based on Hamilton-Jacobi formulations. J. Comput. Phys. 83, 1988.
- [5] M. Sussman, P. Smereka and S. Osher, A level set approach for computing solutions to incompressible two-phase flow. J. Comput. Phys. 114, 1994.
- [6] J. Oldroyd, A rational formulation of the equations of the plastic flow for a Bingham solid *Proc. Camb. Philos. Soc.* 43, 1947.
- [7] W. Prager, Introduction to Continuum Mechanics, Ginn, Boston, 1961.

# Orientation Transitions in Dispersed Liquid Crystalline Droplets

Rajesh K. Goyal and Morton M. Denn  
Benjamin Levich Institute for Physico-Chemical Hydrodynamics  
The City College of the City University of New York  
New York, NY 10031 USA  
Email: {rkgoyal, denn}@che.cuny.edu

**Abstract** — *The orientation distribution in a nematic liquid crystalline droplet is calculated using a simulated annealing technique. A first-order transition between axial and radial conformations at a critical value of a parameter that represents the effect of droplet size and surface and bulk potentials is observed in spherical droplets. A similar transition occurs in a deformed droplet at a critical extension.*

## I. INTRODUCTION

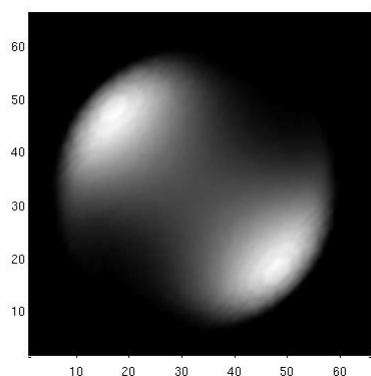
Multiphase systems containing liquid crystalline dispersed phases are of interest for a variety of technological applications. Low molar mass liquid crystals are essential components in display technology [1]. Dispersed polymeric liquid crystals are employed in barrier films and self-reinforced composites [2], and they are effective in very small concentrations as processing aids for flexible thermoplastics [3-5]. Blends in which the dispersed phase is a polymer with side-chain liquid crystallinity are of interest for electrorheological applications [6,7]. The material properties, which are affected by the liquid crystalline orientation distribution in the droplet, appear to depend sensitively on the nature of the interface between the liquid crystalline dispersed phase and the isotropic matrix material. The orientation distribution satisfies a minimum free energy condition in a quiescent droplet.

We have implemented a simulated annealing technique utilizing the Metropolis algorithm over a spatial discretization of the droplet to calculate the minimum free energy configuration for the director orientation of a nematic liquid crystal subject to variable surface anchoring. This approach allows free choice of the elastic constants (splay,  $K_{11}$ ; twist,  $K_{22}$ ; bend,  $K_{33}$ ; and saddle-splay,  $K_{24}$ ) in the Frank free energy expression [8], as well as the surface anchoring strength  $W$  in the Rapini/Papoular surface anchoring energy. To conserve the nematic symmetry in the calculations, an algebraically equivalent tensorial expression for the Frank elastic

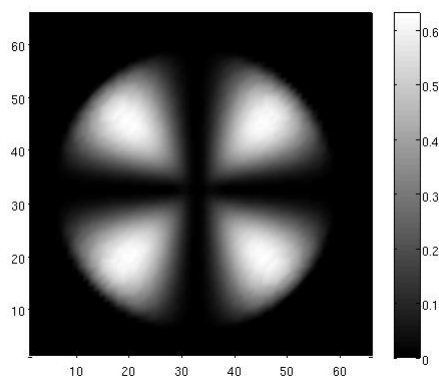
energy originally derived by Gruhn and Hess [9] has been modified to incorporate the surface constant  $K_{24}$ .

## II. RESULTS

There is clearly convergence of the algorithm with respect to the number of computational cells. A first-order transition from an axial conformation (Figure 1(a)) induced by the bulk nematic potential over most of the droplet to a radial conformation (Figure 1(b)) induced by the strong surface anchoring is observed in a spherical droplet of radius  $R$  for equal bulk constants ( $K_{11}=K_{22}=K_{33}$ ) when the dimensionless anchoring strength parameter  $WR/(2K_{11}-K_{24})$  exceeds a value of 5.9. A scaling argument based on a transition between perfectly parallel and radial alignments predicts a transition at a value of  $WR/(2K_{11}-K_{24})$  of order 3, which is acceptably close to the computed transition. A similar transition occurs at a critical elongation of a deforming droplet (Figure 2(a) and 2(b)). Indeed, affine deformation of a sphere will lead to alignment that is nearly orthogonal to the surface of the spheroid throughout much of the bulk for a sufficiently large aspect ratio. This is borne out by the degree of parallel ordering exhibited at large deformations for large values of dimensionless anchoring strength parameter, where substantial deviation from parallel ordering transverse to the axis of elongation is restricted to tip regions. There is a finite geometric range over which the orientation distribution can be trapped in a strong secondary minimum in the energy surface; multiple orientations can exist in this range, depending on the initial state.

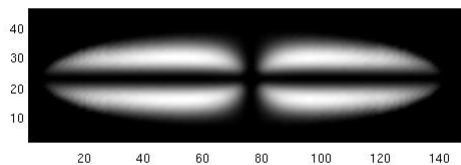


1(a)

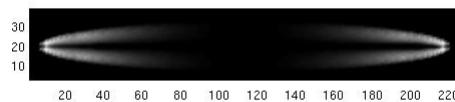


1(b)

Figure 1: Simulated optical microscopic textures of axial (a) and radial (b) conformations inside spherical droplets.



2(a)



2(b)

Figure 2: Simulated optical microscopic textures of radial (a) and axial (b) conformations inside spheroidal droplets of different extensions.

#### ACKNOWLEDGMENTS

This research was supported in part by the National Science Foundation under Grant CTS-0112358. Dr. Xianfeng Li provided important assistance during the initial stages of the work.

#### REFERENCES

- [1] Drzaic, P. S., *Liquid Crystal Dispersions*, World Scientific, Singapore, 1995.
- [2] Qin, Y., *Polym. Adv. Technol.* **7**, 151 – 159 (1996).
- [3] Brody, H., European Patent 0 041 327 (1981).
- [4] Brody, H., European Patent 0 154 425 (1985).
- [5] Cogswell, F. N., US Patent 4386174 (1983).
- [6] Orihara, H., Y. Hosoi, K. Tajiri, Y. Ishibashi, M. Doi, and A. Inoue, *J. Rheol.* **43**, 125 – 136 (1999).
- [7] Tajiri, K, H. Orihara, Y. Ishibashi, M. Doi, and A. Inoue, *J. Rheol.* **43**, 137 – 146 (1999).
- [8] de Gennes, P. G., and J. Prost, *The Physics of Liquid Crystals*, 2<sup>nd</sup> Ed., Oxford U. Press, New York, 1993.
- [9] Gruhn, T. and S. Hess, *Z. Naturforsch* **51a**, 1-9 (1996).

# Raman Imaging and Spectroscopy of Individual Carbon Nanotubes

Li Zhang and Zhonghua Yu (Faculty Mentor)  
City College of New York and the Graduate Center  
The City University of New York  
New York, U.S.A  
Email: lzhang@sci.cuny.cuny.edu

**Abstract** — Raman imaging and spectroscopy with 633 nm excitation wavelength was performed on individual single-wall carbon nanotubes (SWNTs) grown on silicon substrate. The Raman spectra reveal both metallic and semiconducting type carbon nanotubes, with a broad distribution in diameter centered at 1.6 nm. Primary results show that interaction with Si substrate and other nanotubes has a significant effect on the Raman spectroscopy of a carbon nanotube.

measured at various positions along a single nanotube. Fig. 2 displays typical Raman spectra (G-mode) from two different types of nanotubes. Our Raman spectroscopy results show that these ultralong nanotubes consist of both semiconducting and metallic types. Characterization of nanotube diameters shows a broad distribution, with an average diameter of about 1.6 nm.

## I. INTRODUCTION

Single-walled carbon nanotubes (SWNTs) exhibit completely different electronic and optical properties depending on their physical structure [1]. A particularly interesting and important property is that nanotubes with similar diameter may be either metallic or semiconducting, while the variation of the tube diameter causes the semiconducting SWNT's bandgap to shift dramatically. Recent advances in the chemical vapor deposition (CVD) synthesis of SWNTs have enabled growth of high-quality, ultralong (a few mm) individual nanotubes [2,3], which could find potentially important applications in the field of nanotechnology.

## II. DISCUSSION

We use resonance Raman spectroscopy to investigate the electronic and vibrational properties of individual ultralong carbon nanotubes grown on the silicon substrate by chemical vapor deposition (CVD) [3]. The nanotube diameter and its electrical conductivity type (semiconducting or metallic) can be determined from the Raman frequency and lineshape. Raman imaging and spectroscopy with 633 nm excitation was performed with a home-built scanning confocal Raman microscope. Despite strong background from the Si substrate, our Raman microscopy is capable of imaging individual nanotubes. A typical Raman image of a  $40\mu\text{m} \times 40\mu\text{m}$  area is shown in Fig.1. Raman spectra were

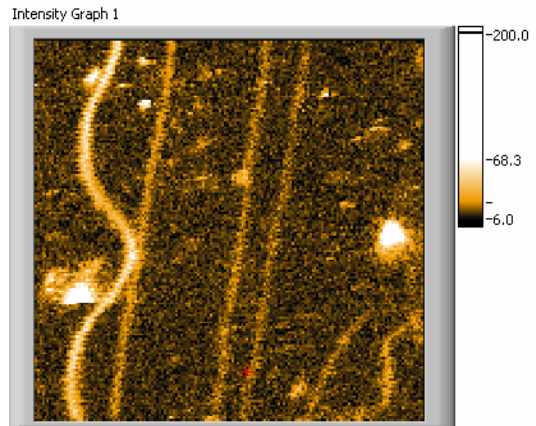


Figure 1: Raman imaging of nanotubes on Si substrate ( $40\mu\text{m} \times 40\mu\text{m}$ )

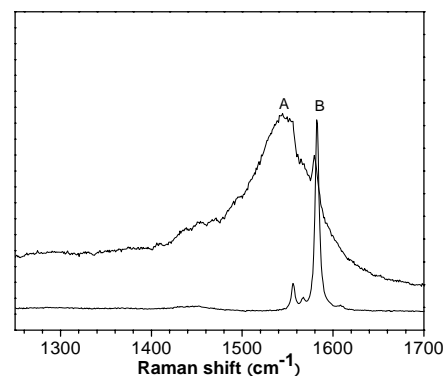


Figure 2: Raman spectra of two different types of Nanotubes. (A) G-band of a metallic tube; (B) G-band of a semiconducting tube

The effect of Si substrate and intertube interaction on Raman spectroscopy of SWNTs is investigated by growing nanotubes suspended across a slit on the Si substrate [2, 3]. The Raman spectra of the suspended nanotube are compared to those of the same nanotube sitting on the substrate. It is expected that the deformation of a nanotube due to the substrate contact will affect both the electronic and vibrational structures of SWNTs, thus changing the Raman frequency and intensity. Intertube interaction was also found to affect the Raman spectra of a nanotube.

#### ACKNOWLEDGMENTS

We thank Limin Huang and Stephen O'Brien at Columbia University for providing nanotube samples, and PSC-CUNY for financial support.

#### REFERENCES

- [1] M. S. Dresselhaus, G. Dresselhaus, R. Saito, A. Jorio. Raman spectroscopy of carbon nanotubes. *Physics reports*, 409:47-99, 2005.
- [2] L. Huang, X. Cui, B. White, and S. P. O'Brien. Long and oriented single-walled carbon nanotubes grown by ethanol CVD. *J. Phys. Chem. B*, 108(42):16451-16456, 2004.
- [3] L. Huang, S. J. Wind, and S. P. O'Brien. Controlled growth of single-walled carbon nanotubes from an ordered mesoporous silica template. *Nanoletters*, 3(3): 299-303, 2003.

# Numerical Modeling of the Performance of a Silicon-on-Insulator Based High-Temperature-Resistance Pressure Sensor

Xiaojun Wang and Feng-Bao Lin  
The City College of New York  
The City University of New York  
New York, NY, USA

Email: xjwang@ce.ccny.cuny.edu, flin@ce.ccny.cuny.edu

**Abstract** —A pressure sensor made from bonding an SOI based MEMS chip on a cantilever beam was analyzed numerically in this study. The selection of the bonding material is an important factor during the packaging design process. It is found that the packaging structure with relatively soft bonding materials shows uniform deformation in the piezo-resistive areas and achieves the stress and strain distributions in the packaging structure for best performance in operation. Transient thermo-mechanical modeling was also conducted in this study to demonstrate the capability of sheltering the thermal shock on the sensor.

whole structure. An SOI chip is attached to the beam by adhesive materials. The material properties used for the simulation are shown in Table 1.

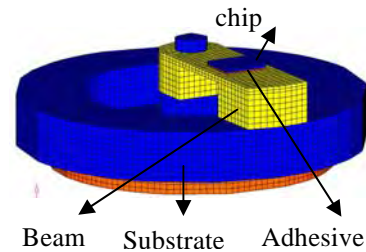


Figure 1: Finite element model of the pressure sensor which consists of four components

## I. INTRODUCTION

Silicon on insulator (SOI) is becoming a favourable technology to make membrane as compared to traditional poly-silicon due to its high temperature capability. In this study, a high temperature pressure sensor is designed based on a SOI based Micro Electro Mechanical System (MEMS) chip bonded on a cantilever beam which is also designed to shelter the thermal shock (Figure 1). The selection of the bonding materials is a very important factor during the packaging process, and the performance, such as the linearity, range and life-time, for the packaging structure of the pressure sensor is also limited by factors such as the CTE (coefficient of temperature expansion), Young's modulus, and thermal conductivity of bonding materials. The specific structure model of this pressure sensor is presented and the numerical results are also provided to give a guide for on the bonding material selection. In addition, the transient thermo-mechanical behaviour of the sensor is also characterized in the modelling.

## II. FE MODEL AND MATERIALS PROPERTIES

The finite element model of the pressure sensor for the numerical simulation is shown in Figure 1. A beam is included as a portion of the sensor for the

	Substrate	Beam	Chip
Density (g/cm <sup>3</sup> )	7.8	7.8	2.3
Modulus(Gpa)	196	196	96
Possion	0.27	0.27	0.22
SpecificHeat (J/kg°C)	490	490	700
Conductivity (W/m°C)	30	30	100

Table 1: Materials properties which were used in the simulation

## III. MODELING AND RESULTS

Four types of bonding material properties shown in Table 1 were selected to simulate the performance of the pressure sensor. Case 4 in Figure 2 shows better uniform chip stress distribution on the place where the piezo-resistances are located. Therefore, the best linearity of the pressure sensor can be obtained with this adhesive material. Also, best sensitivity, which is proportional to the stress in the chip, can be obtained using a smaller thickness of this bonding material as indicated in Figure 3.

	Adhesive			
	1	2	3	4
Density (g/cm <sup>3</sup> )	14.5	7.42	2.23	1.2
Modulus(Gpa)	67.8	54.2	62.7	4.1
Possion	0.42	0.34	0.2	0.42
SpecificHeat (J/kg° C)	128	230	430	230
Conductivity (W/m° C)	57	68	20	30

Table 2: Properties of the bonding materials used for selection

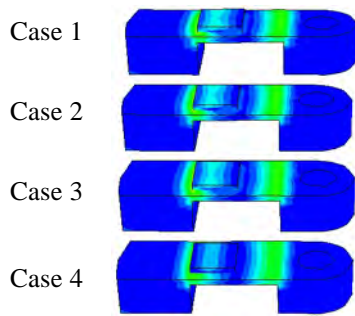


Figure 2: Chip stress distributions comparison with different adhesive material properties.

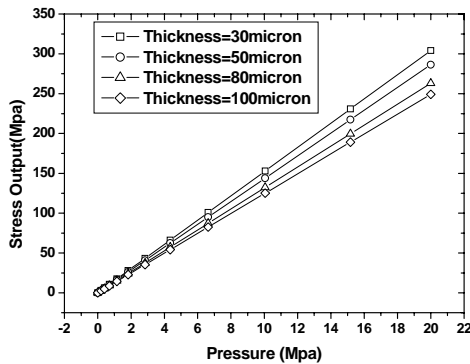


Figure 3: Chip stress output varies with the applied pressure for different thicknesses of the bonding material

A thermal shock with the maximum temperature of 2000°C is applied to the exposed areas of the pressure sensor. The maximum temperature is maintained steady for 1500ms during the thermal shock. The result shows that the chip is within the safe temperature of 120°C for about 500ms.

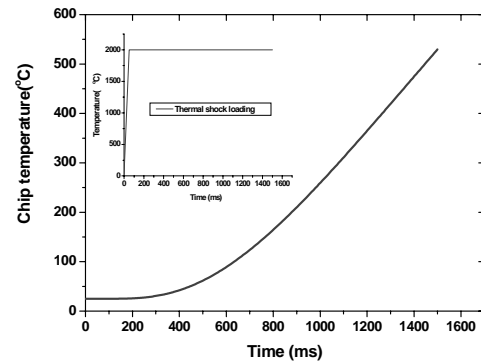


Figure 4: Chip temperature varies with time when thermal shock is applied on the exposure area of the sensor

#### IV. CONCLUSION

A packaging structure of SOI based pressure sensor with a soft bonding material shows a relative uniform deformation in the piezo-resistive areas, and its stress distribution also helps achieve an optimization condition in operating the designed sensor. In addition, the thermo-mechanical interaction modeling demonstrates the preferable thermal resistance of this pressure sensor.

#### ACKNOWLEDGMENTS

The authors would like to acknowledge the support provided by Professor Sheng Liu.

#### REFERENCES

- [1] K. Petersen, J. Brown, T.Vermeulen, et al. Ultra-stable, high-temperature pressure sensors using silicon fusion bonding, Sensors and Actuators, A21-23, pp,96-101,1990.
- [2] B. Diem. P. Rey, et al. SOI' SIMOX' from bulk to surface micromaching, A new age for silicon sensors and actuators, Sensors and Actuators, A46-47,pp,8-16,1995.
- [3] H. Terabe, H. Arashima, N. Ura, et al. A silicon pressure sensor with stainless diaphragm for high temperature and chemical application, 1997 International Conference on Solid-State Sensors and Actuators, Transducers, pp,1481-1484,1997
- [4] X.Song, S. Liu. A performance prediction model for a piezoresistive transducer pressure sensor, ICEPT, shanghai, China, 3,pp,350-354, 200.

# Non-Linear Oscillatory Crystallization in the Formation of Rhythmic Bands in the Palisades Sill, New Jersey

Karin A. Block<sup>1</sup> and Jeffrey C. Steiner<sup>2</sup>, (Faculty Mentor)

<sup>1</sup>Department of Earth and Environmental Sciences, The Graduate Center

<sup>2</sup>Department of Earth and Atmospheric Sciences, The City College of New York  
City University of New York

New York, NY, United States of America

Email: kblock@sci.ccnycuny.edu

**Abstract** — *The composition of rhythmic layers in Palisades Sill dolerites correspond to a range of liquidus temperatures that indicate each set of bands is cooled and isolated, until an abrupt rise in temperature causes the crystallization of a new cycle. Turbulent convection causes perturbations in the cooling regime, which may be manifested by non-linear oscillation in the advective transport of cations as suggested by Wang and Merino [1]. In this model, a positive feedback system encourages plagioclase crystallization, but is curtailed when a limiting species, such as  $Al^{3+}$ , is depleted, causing the competing phase, pyroxene, to take over. The process repeats until the thermal regime changes due to convective cooling or interruption by a later pulse of fresh magma.*

## I. INTRODUCTION

Rhythmic banding is an integral and widely-debated feature of the world's famous large igneous intrusions. A large variety of mechanisms have been proposed for the production of rhythmic bands including Ostwald ripening, crystal settling, thermal oscillations, and oscillations in nucleation kinetics (see [1] for a review).

The Palisades Sill of New York and New Jersey is a large dolerite intrusion that extends 150 km along strike and with an average thickness of 300 m. The intrusion has been the subject of study for over 100 years, in part because it is exposed in a large number of outcrops, but also because its geochemical and mineralogical features are analogs of much larger, less accessible intrusions.

The sill contains a number of layered features that continue to challenge modern petrologic models including:

1. An Mg-olivine layer approximately 10 m above the basal contact
2. A series of rhythmically banded sections that have been recently documented in Fort Lee and Alpine, New Jersey

3. Highly fractionated granophyres near the upper contact of the intrusion where the upper and lower crystallization fronts meet at the Sandwich Horizon.

## II. RHYTHMIC BANDING

### A. MINERALOGY

Rhythmic bands have recently been mapped in the Palisades intrusive sheet of New York and New Jersey at 80-150 m above the basal contact. In contrast to the very pronounced banding of the Muskox, Bushveld, and other layered intrusions, the Palisades bands are diffuse, cm-scale layers where the dominant phase alternates between pyroxene and plagioclase. The rhythm of crystallization is characterized by a distinct chain of fine-grained plagioclase crystals of approximate length 0.6 mm, followed by assemblages of plagioclase and augite of sub equal size, which, at 2 mm in size, are much larger than crystals in the initial plagioclase band. Percent plagioclase gradationally decreases up-section until the onset of the next fine-grained band.

### B. X-RAY SPECTROMETRY AND MICROANALYSIS

Qualitative chemical analysis by energy dispersive x-ray spectrometry and quantitative verification by electron probe microanalyses reveal a small range of compositions corresponding to a narrow range of liquidus temperatures (Figure 1). Bulk compositions of the rhythmic bands were processed with thermodynamic software MELTS [2]. Temperatures oscillate between approximately 1150 and 1200 degrees C. However, zonation in plagioclase and pyroxene crystals indicates that crystals cooled and were isolated at lower temperatures, followed by abrupt rise in temperature, which caused the nucleation of a new plagioclase-rich band.

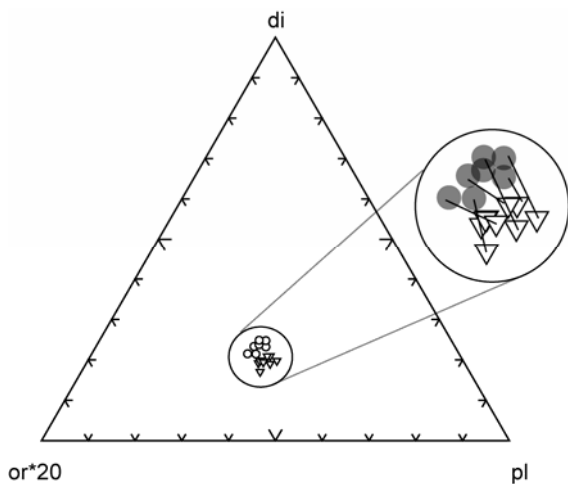


Figure 1: Diopside-Plagioclase-Orthoclase composition of rhythmic bands. Circles correspond to dark bands while triangles correspond to light bands. Pairs of bands are linked by tie lines indicating cotectic or near-cotectic crystallization.

### III. DISCUSSION

The present interpretation parallels models advanced for the Stillwater Complex, where the perturbations are caused by turbulent thermal convection [3], and are geochemically manifested by a non-linear oscillation in the advective transport of cations carried by silica polymers [1]. The two competing phases are augite and plagioclase, which compete for  $Ca^{2+}$

In the case of the Palisades, the liquidus phase is plagioclase, which crystallizes at the thermal boundary layer at a rate dictated by the diffusivity of the limiting species,  $Al^{3+}$ . The rate of plagioclase crystallization decreases as  $Al^{3+}$  is depleted, thus accumulating competing cations,  $Mg^{2+}$  and  $Fe^{2+}$ , at the crystal-liquid interface, which cause pyroxene to nucleate (Figure 2).

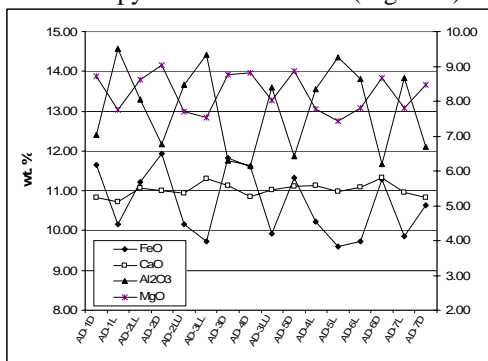


Figure 2: Oscillation in cation concentration follows pattern of rhythmic banding.

### IV. CONCLUSION

The extensive nature of rhythmic bands in the Palisades and the relatively large thickness of the horizon can be easily reconciled by a combination of thermal fluctuations coupled with oscillatory advective transport of cations to the thermal boundary layer.

Whole rock chemistry reveals that a small range of high temperatures prevailed during the rhythmic banding event and oscillation in the cation species show that nucleation was dictated by the rate of diffusion of the species.

We propose that the mechanisms that produce rhythmic layering the Palisades are common in this setting and that the interruption or convolution of layers may be indicators of disturbances such as tectonic shifts or further magmatic input.

### ACKNOWLEDGMENTS

The authors thank The City College of New York Division of Science and the Office of the Dean for their support.

### REFERENCES

- [1] Y. Wang and E. Merino. Oscillatory Magma Crystallization by Feedback between the Concentrations of the Reactant Species and Mineral Growth Rates. *Journal of Petrology* 34(2): 369-382, 1993
- [2] Ghiorso, M. S. and R. O. Sack Chemical mass transfer in magmatic processes IV. A revised and internally consistent thermodynamic model for the interpolation and extrapolation of liquid-solid equilibria in magmatic systems at elevated temperatures and pressures. *Contributions to Mineralogy and Petrology* 119: 197-212, 1995
- [3] Jackson, E. D. The cyclic unit in layered intrusions -- a comparison of repetitive stratigraphy in the ultramafic parts of the Stillwater, Muskox, Great Dyke, and Bushveld Complexes. *Geol. Soc. of S. Afr. Spec. Publ. 1: 391-424, 1970*

# Viscoelastic Behaviour of Plasticized Poly(3-hydroxy butyrate)

A. Hähndel, H.-J. Radusch

Institut für Werkstoffwissenschaft / Kunststofftechnik  
Martin-Luther-Universität Halle-Wittenberg  
Halle (Saale), Germany

E-Mail: andreas.haehndel@iw.uni-halle.de

**Abstract** - *Poly(hydroxy alkanates) PHA and especially Poly(3-hydroxy butyrate) PHB as naturally occurring biodegradable polyesters received increasing attention during the last decade [1]. According to structure and properties, PHB is often compared with standard polypropylene. In this work PHB was modified by external plasticization to improve the poor mechanical properties of e.g. brittleness. Furthermore an unconventional experimental processing method under laboratory conditions, rotational molding of casted solution, was performed for the cautious treatment of the thermosensitive PHB to obtain film specimens for viscoelastic and thermal characterization.*

## I. INTRODUCTION

Poly(3-hydroxy butyrate) PHB is a natural occurring biodegradable and biocompatible polyester. The production of the material is possible by bacterial fermentation from renewable resources [2]. Biological degradability in combination with advanced mechanical properties is the basis for a variety of interesting applications, including packaging industry and medicine [3]. PHB is often compared with standard polypropylene. PHB is a crystallizable material with transition temperatures of about 0°C (glass transition) and 177°C (crystalline melting point). Tensile strength of the pure material, dependent on the molar mass, is in the range of 3.5 up to 4 GPa [4]. The major disadvantage of PHB for processing is the poor thermal stability. Conventional melt processing causes a rapid molecular weight reduction and loss of mechanical properties [5]. Several modifications for improving the properties of PHB were investigated in terms of change crystallinity and rheological behaviour of the melt [6-8]. In this work low molecular, oligomer or polymer plasticized PHB was characterized to understand the molecular mechanisms running during plasticization and application of plasticized PHB in a large temperature range.

## II. MATERIALS AND EXPERIMENTAL

A poly(3-hydroxy butyrate) with molecular weight of 171.000 g/mol,  $T_m$  of 173°C and  $T_g$  of 10°C was used, naturally generated with isotactic structure by *Methylobacterium* MB 126 from BSL Olefinverbund GmbH Schkopau. The crystallinity of the pure material was approximately 60% measured by DSC. As plasticizers  $\epsilon$ -caprolacton [ $\epsilon$ -CL], poly(ethylen glycol) 400 [PEG400], glycerol [GLY], castor oil [CTO] and triacetyl glycerol [TAG] were used. All these plasticizers are partially miscible in different ratio with PHB. The plasticizers were dissolved in a PHB-chloroform solution. These solutions were casted into a rotational mold glass cavity and a film of PHB-plasticizer mixture has been deposited during evaporation of the solvent onto the wall. The mechanical investigations were made using a MARK III DMTA system (Rheometric Scientific). The measurements were carried out in tensile mode at a frequency of 1 Hz in a temperature range of -100°C to 150°C. Storage and loss modulus as well as loss factor  $\tan \delta$  were measured in dependence on temperature. The samples were loaded only in reversible linear elastic deformation of 0,05%. The thermal characterization was made using the DSC 820 from Mettler Toledo (heat flow). Starting at room temperature the samples were cooled down to -100°C, heated up to 180°C, cooled down again to -100°C, and heated up to 200°C. The temperature was changed with a rate of 10 K/min.

## III. RESULTS AND DISCUSSION

Plasticization via solution casting leads to a shift and broadening of the glass transition region, e.g. over 60 K in case of PEG. These effects can be interpreted in the first range as a weakening of intermolecular bonds between the PHB molecules. The broadening of the glass transition region gives rise to assume that the amorphous PHB phase infiltrated by the low molecular plasticizer

molecules is more relaxed over a broad temperature range.

Glass Transition from DSC and DMTA of PHB+diff. Plasticizer

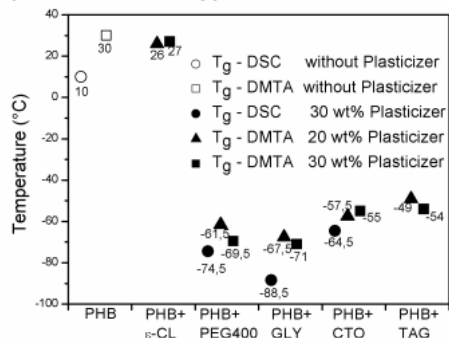


Figure 1:  $T_g$  from DSC and DMTA

In the case of castor oil it was detected that plasticization caused a smooth nearly linear decrease of the storage modulus in the temperature range of  $-60^{\circ}\text{C}$  up to  $70^{\circ}\text{C}$ . The loss factor in this region shows only a minor change. This could be caused by a continuously interrelated weakening of the intermolecular bonds in PHB by the different constituents of castor oil. Above  $60^{\circ}\text{C}$  the loss factor of all samples increases suddenly associated with a stronger or weaker increase or change of the storage modulus. This can be assumed as the point where PHB begins to sweat out his physical bonded plasticizers.

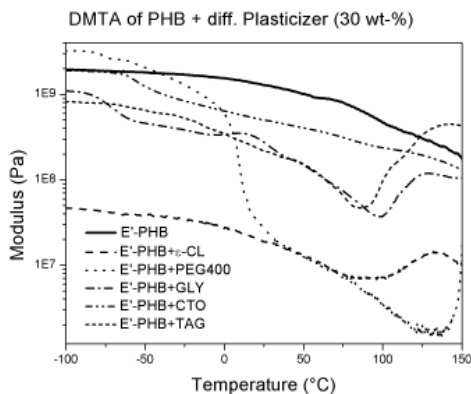


Figure 2: Storage Modulus  $E'$  of PHB and plasticized specimens

Together with the structure weakening effect of the amorphous phase an effective reduction of the degree of crystallinity can be observed from the results of the DSC measurements. The reduced degree of crystallinity of softened PHB is assumed to be caused by the presence of the plasticizer molecules and their intensive interaction with the polar groups of PHB. The modulus of elasticity of solution casted neat PHB at  $20^{\circ}\text{C}$  (storage

modulus, DMTA) was 1.34 GPa and of the modified, e.g. PHB+GLY, 0.97 GPa.

#### IV. CONCLUSION

PEG and GLY have turned out to be the most effective low molecular plasticizers for PHB in this study evaluated by the  $T_g$  shift. All plasticizers show a good plasticizing effect indicated by the reduction of the modulus of elasticity. An improved ductile behaviour because of the significant decrease in elastic modulus at room temperature can be assumed. That has to be investigated e.g. by tensile test in the future. Plasticization and solution casting of PHB are favourable methods for the generation of modified PHB with enhanced ductility and better possibility for the use of this material in biomedical and biodegradable applications.

#### REFERENCES

- [1] P.J. Hocking, R.H. Marchessault. Biopolyesters, Chemistry and Technology of Biodegradable Polymers, chapter 4, pp. 48-96, London 1994
- [2] P.A. Holmes. Application of PHB - a Microbially Produced Biodegradable Thermoplastic, Phys. Technol. 6, 32, 1985
- [3] P.A. Holmes. Biologically produced (R)-3-Hydroxyalkanoate Polymers and Copolymers. Development in crystalline polymers-2, London 1988
- [4] S. Mecking. Biologisch abbaubare Werkstoffe - Natur oder Petrochemie, Angewandte Chemie Vol. 116, 9, 1096-1104, 2004
- [5] Th. Lüpke, H.-J. Radusch, K. Metzner. Solid state processing of PHB-powders. Macromolecular Symposia, 127, 227-240, 1998
- [6] G. Ceccorulli, M. Pizzoli, M. Scandola. Effect of a Low Molecular Weight Plasticizer on the Thermal and Viscoelastic Properties of Miscible Blends of Bacterial Poly(3-hydroxybutyrate) with Cellulose Acetate Butyrate. Journal of Macromolecules, 26,6722-6726, 1993
- [7] A. M. el-Hadi Abdel Ghaffar. Development of biodegradable materials based on Poly(3-hydroxybutyrate). Diss. Martin-Luther-Universität Halle-Wittenberg, 2002
- [8] H.J. Choi, J. Kim, M. S. Jhon. Viscoelastic characterization of biodegradable poly(3 hydroxybutyrate-co-hydroxyvalerate). Polymer 40, 4135-4138, 1999

# MBE-grown $\text{Zn}_x\text{Cd}_{(1-x)}\text{Se}/\text{Zn}_x\text{Cd}_y\text{Mg}_{(1-x-y)}\text{Se}$ multi-quantum wells for intersubband devices

Hong Lu and Maria C. Tamargo (Faculty Mentor)  
The City College of New York and the Graduate Center  
City University of New York  
New York, USA

Email: hlu@ccny.cuny.edu, tamar@sci.ccny.cuny.edu

**Abstract** — *In this paper we investigate the use of the wide bandgap II-VI materials  $\text{Zn}_x\text{Cd}_{(1-x)}\text{Se}/\text{Zn}_x\text{Cd}_y\text{Mg}_{(1-x-y)}\text{Se}$  to fabricate intersubband devices such as quantum well infrared photodetectors and quantum cascade lasers operating in the mid-infrared wavelength range. The materials were grown by molecular beam epitaxy or MBE, and the desired structures were designed using theoretical calculations. All the samples were characterized by X-ray Diffraction (XRD), Photoluminescence (PL) and Fourier Transform Infrared Spectroscopy (FTIR), etc. Excellent growth control and material quality were demonstrated. Intersubband absorption spectra were observed by FTIR in the wavelength range of 3-5  $\mu\text{m}$ , as desired, which fit well with the theoretical prediction based on the envelope function approximation.*

## I. INTRODUCTION

Molecular beam epitaxy (MBE) is an extremely versatile thin film growth technique that can produce single crystal layers with atomic dimensional control and thus has the potential for the preparation of novel structures and devices.

Intersubband (ISB) devices are semiconductor devices that rely on transitions between quantized energy levels within a band (the conduction band or the valence band), as opposed to the more typical band-to-band transitions used in most photonic devices. As a result of this, ISB devices offer some interesting advantages such as ultra-high speed and high (>100%) quantum efficiency.

Multi-quantum well (MQW) structures (a typical structure is shown in Figure 1) made from II-VI semiconductors have important applications in ISB devices such as quantum well infrared photodetectors (QWIPs) [1] and quantum cascade lasers (QCLs) [2] due to their widely adjustable bandgaps. In particular,  $\text{Zn}_x\text{Cd}_{(1-x)}\text{Se}/\text{Zn}_x\text{Cd}_y\text{Mg}_{(1-x-y)}\text{Se}$  is a II-VI semiconductor system recently investigated in our lab whose interband emission can cover the whole visible wavelength range by simply changing the QW width.

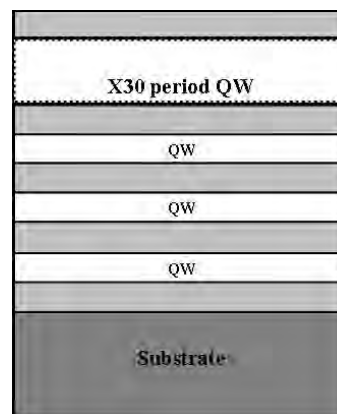


Figure 1: A typical MQW structure

Recently, contactless electroreflectance (CER) was used to determine the conduction band offset (CBO) of the  $\text{Zn}_x\text{Cd}_{(1-x)}\text{Se}/\text{Zn}_x\text{Cd}_y\text{Mg}_{(1-x-y)}\text{Se}$  system. For a  $\text{Zn}_{0.5}\text{Cd}_{0.5}\text{Se}/\text{Zn}_{0.29}\text{Cd}_{0.24}\text{Mg}_{0.47}\text{Se}$  single QW the CBO was estimated to be 590 meV [3] and for the limit composition of this lattice-matched system,  $\text{Zn}_{0.5}\text{Cd}_{0.5}\text{Se}/\text{Zn}_{0.13}\text{Mg}_{0.87}\text{Se}$ , the CBO was estimated to be as large as 1.12 eV [4].

## II. EXPERIMENT

In this work, a series of high quality  $\text{ZnCdSe}/\text{ZnCdMgSe}$  MQWs with different QW thicknesses have been grown on InP (001) substrates by MBE, using the optimized conditions achieved before [5]. The MQWs were characterized by a series of techniques, including X-ray diffraction (XRD), photoluminescence (PL), time-resolved PL, scanning electron microscopy (SEM), CER, and FTIR measurements. Doping of the QW layers by n-type dopants to  $10^{+18}/\text{cm}^3$  levels, which is needed to obtain IR absorption, has also been accomplished. All the experimental data show that the grown  $\text{ZnCdSe}/\text{ZnCdMgSe}$  MQWs have excellent material quality as required for device applications. The observation of ISB absorption in the expected wavelength range dem-

onstrates that this II-VI material is very promising for ISB devices.

### III. RESULTS AND DISCUSSION

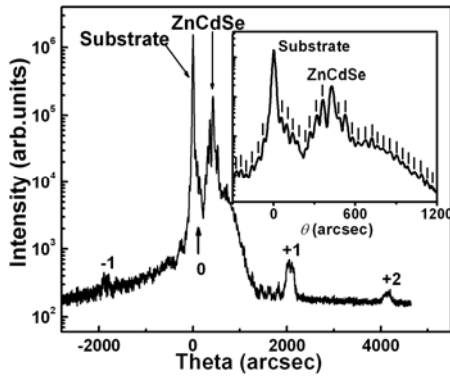


Figure 2: Double crystal XRD rocking curve of a MQW sample.

Figure 2 shows a double crystal XRD rocking curve of a MQW sample. Three satellite peaks due to the superlattice structure were observed as well as clear thickness fringes, more clearly evident in the inset, indicating excellent crystalline quality.

The 77 K PL spectra of two samples with different QW widths are shown in Figure 3. Sharp and bright emission from the MQW can be seen for both samples at 525 nm (2.36 eV) and 545 nm (2.27 eV). A signal at 568 nm (2.18 eV) is the emission from ZnCdSe bottom and cap layers. The full width at half maximum (FWHM) of the PL emission lines of the two samples are 41 meV and 36 meV, evidence of good material quality and QW alignment.

Intersubband absorption has been observed by FTIR measurements (as shown in Figure 4). The absorption peak occurred at 3.99  $\mu\text{m}$  and 5.35  $\mu\text{m}$ , respectively, corresponding to the transition from the ground state to the first excited state within the QW. The results agree well with the theoretical prediction (see the inset of Figure 4).

#### ACKNOWLEDGMENTS

This work was supported by NSF Grant # ECS0217646, NASA Grant # NCC-1-03009, and the Institute for Ultrafast Spectroscopy and Lasers, and New York State Center for Advanced Technology for Ultrafast Photonic Materials and Applications.

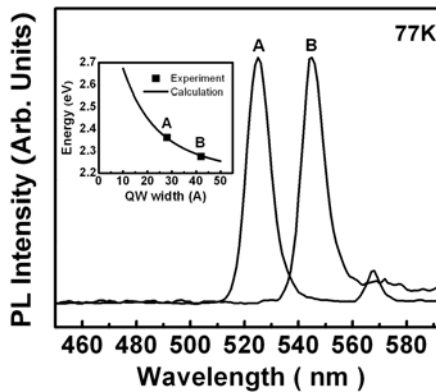


Figure 3: PL spectrum of two MQW samples with different QW width at 77K.

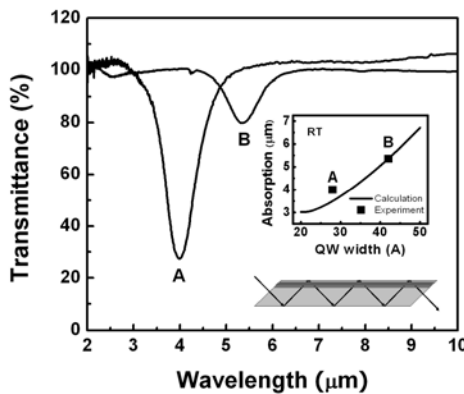


Figure 4: RT FTIR spectrum of two MQW samples with different QW widths.

Special thanks to Dr. A. Shen, Dr. S. K. Zhang and Dr. R. R. Alfano from the City College of New York, to Dr. C. Y. Song and Dr. H. C. Liu from the National Research Council of Canada.

#### REFERENCES

- [1] B. F. Levine, *J. Appl. Phys.* 74, R1, 1993.
- [2] J. Faist, F. Capasso, D. L. Sivco, C. Sirtori, A. L. Hutchinson, and A. Y. Cho, *Science* 264, 553, 1994.
- [3] M. Muñoz, H. Lu, X. Zhou, and M. C. Tamargo, *Appl. Phys. Lett.* 83, 1995, 2003.
- [4] M. Sohel, X. Zhou, H. Lu, N. Perez-Paz, M. Muñoz, M. C. Tamargo, *J. Vac. Sci. Technol. B* 23, 1209, 2005.
- [5] L. Zeng, S. P. Guo, Y. Y. Luo, W. Lin, M. C. Tamargo, H. Xing, and G. S. Cargill III, *J. Vac. Sci. Technol. B* 17, 1255, 1999.

**Symposium 3**

**Environmental Sciences**



# Delignification of Atmospheric Aerosol Samples

Rui Andrade, Alexandre Caseiro, Casimiro Pio, Anne Kasper-Giebl, Heidi Bauer, Hans Puxbaum

Institute for Chemical Technologies and Analytics  
Vienna University of Technology  
Vienna, Austria

Departamento de Ambiente e Ordenamento

Aveiro University  
Aveiro, Portugal

Email: rui@myspeleo.com

## I. INTRODUCTION

The exceedance episodes of PM<sub>10</sub> concentrations limit values in Austria still remain a major environmental problem. Source apportionment is therefore an important and appropriate tool in order to provide decision makers with a basis to produce measures towards the protection of public health.

Organic matter accounts for an important fraction of the atmospheric aerosol and its characterisation and quantification are a major issue for source apportionment. Cellulose has successfully been identified as a tracer for vegetative detritus [1]. Plants contain about 20 to 30% of lignin, up to 20% of hemicellulose and 50% of cellulose, a portion of which is encapsulated by lignin [2]. (Buttler and Bailey, 1973)

## II. EXPERIMENTAL

On the method described by Puxbaum and Kunit, cellulose is saccharified to glucose which is then photometrically determined. Cellulose associated with lignine and hemicellulose is previously made available by an alkaline peroxide pretreatment step. However, on routinely used quartz fiber filters this pretreatment step fails, thus allowing only the measurement of „free cellulose“.

This work aims to develop and optimize a variant delignification step that could be used prior to cellulose saccharification on quartz fiber filters, making it possible to determine „total cellulose“, as well as investigating alternative delignification procedures and comparing them on a labor intensiveness accuracy point of view.

## III. RESULTS

So far, some improvements on the alkaline peroxide delignification step described by Puxbaum and Kunit showed a potential for delignification on quartz fiber filters. Namely, a polypropylene filter working as physical support for the quartz fiber filter prevents the latter to crumble in the hydrogen peroxide solution. Furthermore, this allows the recovery of eventual losses that could occur during the digestion or the subsequent filtration.

Also, an efficient vacuum filtration provides an adequate dryness of the filter, thus avoiding the high temperature drying in an oven, where the quartz fiber filter would stick to the glass Petri dish supporting it.

Other delignification procedures will be tested in a near future.

## REFERENCES

- [1] M. Kunit and H. Puxbaum. Enzymatic Determination of the Cellulose Content of Atmospheric Aerosols. *Atmospheric Environment*, Vol. 30, No. 8, 1233-1236, 1996.
- [2] G. W. Buttler and R. W. Bailey. *Chemistry and Biochemistry of Herbage*, Vol. I, Academic Press, New York 1973.



# Sustainable Energy Production in Microbial Fuel Cells

S. Beisteiner, S. Hein, A. Wolfsberger and P. Holubar (Faculty Mentor)  
University of Natural Resources and Applied Life Sciences Vienna  
Department of Biotechnology, Institute of Applied Microbiology  
Muthgasse 18, A-1190 Vienna, AUSTRIA  
Email: peter.holubar@boku.ac.at

**Abstract** — Traditionally sewage sludge and solid wastes are stabilised by anaerobic digestion with biogas as a useful product. A recently found alternative is the direct electricity production from organic waste in microbial fuel cells (MFC). Microorganisms cleave organic substrates under anaerobic conditions and use an electrode as final electron acceptor instead of oxygen, iron or nitrate.

High efficiency can be achieved and most of the substrate's energy is converted to power. Some experiments were made to investigate how different microorganisms produce electricity under changing conditions (different substrates and different constructions of fuel cells).

## I INTRODUCTION

The most common way to stabilise sewage sludge and solid wastes is the anaerobic digestion process with biogas as a product. This gas can then be used in a further process step to produce electric and thermal energy. A main disadvantage of the process is its low electric efficiency.

A recently found alternative is the direct energy conversion from organic waste into electricity in microbial fuel cells (MFC).

In a microbial fuel cell energy of an organic compound and an oxidant is converted to electric energy. Electrons are set free by microorganisms cleaving an organic substrate under anaerobic conditions. These electrons are not transferred to oxygen or some other electron acceptor, but are carried forward to a presented electrode (the anode). In this energy conversion process, mediators occupy the important function of transferring electrons from the microorganisms on to the electrode. MFCs working with different types of low molecular weight redox species as assisting electron carriers are known. In some MFCs, artificial mediators are added, such as neutral red [1]. Considering the final disposal of sewage sludge or the reuse of waste water, toxic or dangerous substances, such as most of the known artificial me-

diators, should be avoided due to expensive post processing and conditioning.

Special types of microorganisms (metal reducing bacteria) can be used to operate mediator-free MFCs since they possess cytochromes in their outer membrane. These enable the microorganisms to directly transfer electrons to an electrode by growing on its surface.

The electrons released at the anode pass through an outer circuit to a second electrode (the cathode) where they are exposed to oxygen. Protons, which are also produced during the substrate oxidation in the anaerobic part of the fuel cell, are guided to the aerobic compartment through a proton exchange membrane to complete the electric circuit. At the cathode water is formed by electrons, oxygen and protons. In this process, nothing but water and carbon dioxide are produced. A schematic overview of energy production in an MFC is given in Figure 1.

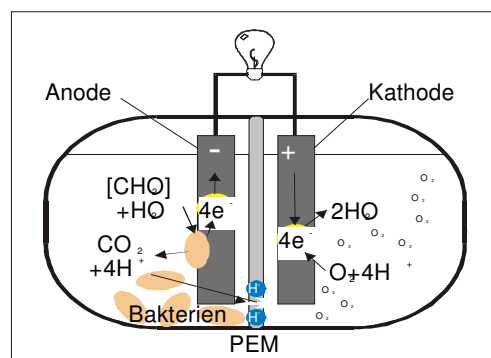


Figure 1: Process of power production in an MFC

## II MATERIALS AND METHODS

Experiments were carried out at 35 °C, because the optimal temperature for the growth of microorganisms lies between 20 and 40 °C.

Both sewage sludge and specially enriched bacteria solutions [2] were used for our tests.

Two different constructions of MFCs were tested. The first type was carried out as a two chamber fuel cell where the anaerobic and aerobic compartments were separated by a proton exchange membrane made of Nafion® [3]. The anode compartment contained bacteria or sewage sludge, while the aerobic part was filled with a  $K_3Fe(CN)_6$  solution which facilitated the electron transfer from the cathode to the final electron acceptor oxygen. The electrodes were made of graphite rods. Oxygen was bubbled into the solution continuously to guarantee oxygen saturation.

The second construct was done as a single chamber microbial fuel cell [4]. The anode compartment was designed in the same way as for the other setup, while instead of a second compartment, an air cathode was used in this case.

To get information about the condition of the fuel cells, they were monitored both online (current, voltage and redoxpotential) and offline (pH, COD, volatile suspended solids (VSS), volatile fatty acids (VFA), optical density (OD) and gas composition). Glucose, acetate, lactic acid, propionic acid and a synthetic feed representing maize silage were taken as examples for substrates with high energy content.

## III RESULTS AND DISCUSSION

Main objectives of the project were to test different constructions for Fuel Cells and to demonstrate the possibility to generate electricity using sewage sludge and to work out a stable characterisation of working conditions to provide a stable performance of the MFCs.

Different conclusions could be drawn from the performed experiments: electricity generation from sewage sludge without special inoculation or enrichment of bacteria is possible. Electricity generation is dependent on the pH of the solution and the concentration of volatile fatty acids.

For proper operation of the fuel cell it is necessary to keep the pH of the solution in the anode compartment to a value between 6,5 and 7,5. The highest cell voltage was reached at a neutral pH. The formation of a functional biofilm on the anode seems to be a requirement for current generation. Power densities up to 160 mW m<sup>-2</sup>, with a cell voltage of max. 0,4 V could be reached. Moreover,

different substrate compositions and concentrations and general conditions for a stable performance in order to increase the power-output were tested. Artificial maize silage, glucose, acetate, and lactate as well as propionic acid are suitable as substrate. When propionic acid was used as a substrate, power generation occurred rather slowly.

Although power output of MFCs is still quite low, new constructions will lead to a far better performance, so there could be lots of future applications for MFCs as alternative energy sources in many different regions.

## IV CONCLUSION

Two different types of microbial fuel cells were tested for generating power out of sewage sludge or enriched bacteria solutions. Electricity generation directly from sewage sludge was possible, power densities up to 160 mW m<sup>-2</sup>, with a cell voltage of max. 0,4 V were reached. Many different substrates are appropriate to the fuel cells.

## ACKNOWLEDGEMENT

The project CROPGEN is funded by the European Commission on the project number: SDES6-CT-2004-502824.

## REFERENCES

- [1] D.H. Park and J.G. Zeikus. Electricity Generation in Microbial Fuel Cells Using Neutral Red as an Electronophore. *Applied and Environmental Microbiology*, pages 1292-1297, Lansing, Michigan, April 2000.
- [2] B.H. Kim and H.S. Park. Enrichment of microbial community generating electricity using a fuel-cell-type electrochemical cell. *Applied Microbiology and Biotechnology* (2004), Issue 63, pages 672-681, Seoul, Korea, August 2003.
- [3] U. Schröder, J. Nießen and F. Scholz. A Generation of Microbial Fuel Cells with Current Outputs Boosted by More Than One Order of Magnitude. *Angew. Chem.*, Issue 115, pages 2986-2989, Greifswald, Germany, 2003.
- [4] H. Liu, R. Ramnaraana and B.E. Logan. Production of Electricity during Wastewater Treatment Using a Single Chamber Microbial Fuel Cell. *Environ. Sci. Technol.*, Issue 38, pages 2281-2285, Pennsylvania, February 2004.

# Odour and Corrosion Problems in Pressure Sewers

Fátima Bertrán de Lis, Ernis Saracevic and Norbert Matsché  
Institute for Water Quality, Resources and Waste Management  
Vienna University of Technology  
Vienna, Austria

Email: {fbertran, erni, nmatsche}@iwag.tuwien.ac.at

**Abstract** — Sulphide generation in sewers and waste water facilities is a world wide problem and much research has been done concerning this issue to determine its causes, effects, prevention and control. Due to the lack of experience in Austria the Federal Ministry of Agriculture Forestry Environment and Water Management initiated the project „KUGPIA“ (Korrosions- und Geruchsprobleme in Abwasserdruckleitungen: Odour and Corrosion problems in pressure sewers). Within this project investigations were carried out in several pressure mains from different waste water treatment plants (WWTP) in order to assess the efficiency of the available technologies to control sulphide generation.

## I. INTRODUCTION

Sewers are necessary to collect and dispose waste water to the WWTPs. Long residence times of waste water in these facilities allow bacteria to use up oxygen and nitrate leading to anaerobic conditions. As a result of anaerobic processes organic acids and sulphide are produced. Attached bacteria growth at the pipe wall as biofilm is mainly responsible for these processes. Waste water composition, temperature, pH and pipe dimensions are also considered to be decisive factors for sulphide generation.

Dissolved sulphide is not only a possible cause for bulking sludge in WWTPs, but due to the pressure decrease may as well leak from the waste water into the atmosphere at the discharge point of the pipe.

Apart from its annoying odour (odour threshold between 0,002 and 0,15 ppm), H<sub>2</sub>S at higher concentrations can be as toxic as HCN and has already caused many fatal accidents in sewer systems. Sulphide production is also a main cause of corrosion problems, due to its biochemical oxidation to sulphuric acid under aerobic conditions. Corrosion processes related to hydrogen sulphide can lead to considerable damage, especially in concrete sewers [1].

Because of these reasons, sulphide was chosen as an indicator for anaerobic conditions in the sewer. A prototype monitoring station for observation of hydrogen sulphide production related processes was

installed at a discharge point of a pressurized sewer pipe [2]. The concept of the monitoring station aimed at low cost of the applied sensors, easy installation and low maintenance demand. Different probe systems were applied, such as a multi-electrode in-situ probe for ion sensitive electrodes (S<sup>2-</sup> and NO<sub>3</sub><sup>-</sup>) and electrodes for pH and redox. Reference sulphide measurements were carried out using the methylen-blue method (DIN 38405-D26).

Several technologies have been proposed to control hydrogen sulphide in sewers. Most of these try to prevent or control sulphide generation. Within this project some of the most applied technologies like pipe “pigging” or mechanical cleaning to remove the biofilm from the pipe wall, pneumatic waste water transport to minimise retention times, air or oxygen supply or addition of nitrate salts to avoid anaerobic conditions were tested. Finally the addition of iron salts proposed to eliminate accumulated sulphide by precipitation was also evaluated.

## II. RESULTS

It was observed, that there are many effective methods to control sulphide generation. However, depending on the characteristics of the pressure sewer, some methods may be more suitable and efficient than others.

In existing pressure sewers, chemical addition of nitrate and iron salts was successfully tested (Figure 1 and Figure 2) and can be recommended due to its easy adaptability.

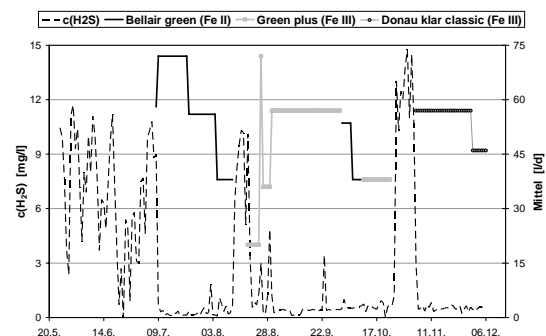


Figure 1: Fe (II) and Fe (III) dosage

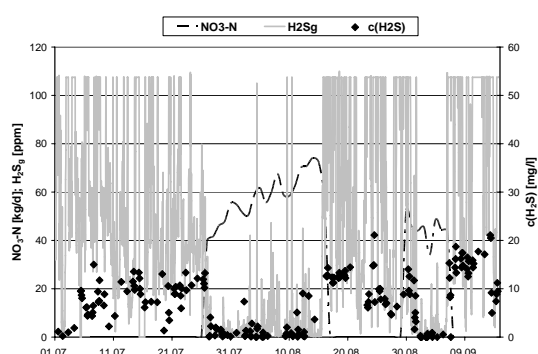


Figure 2: Nitrate dosage

For the selection of the intended chemical, local conditions for a pre-evaluation of the sulphide potential [3], possible chemical wastage and costs must be taken into account.

A comparison of the different treatment methods with addition of chemicals for the control of sulphide generation is shown in Figure 3.

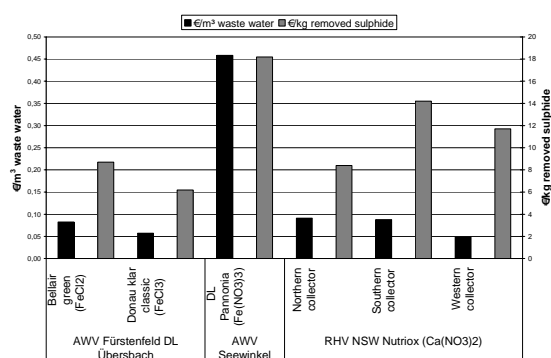


Figure 3: Costs of chemical addition

These costs depend on the costs of the chemicals and their relevant concentration of active component. In this project the following data apply:

- $\text{FeCl}_2$ : 2,51 kmol  $\text{Fe}^{2+}$ /t and 345 €/t
- $\text{FeCl}_3$ : 2,47 kmol  $\text{Fe}^{3+}$ /t and 245 €/t
- $\text{Fe}(\text{NO}_3)_3$ : 1,32 kmol  $\text{Fe}^{3+}$ /t, 3,97 kmol  $\text{NO}_3^-$ /t and 790 €/t
- $\text{Ca}(\text{NO}_3)_2$ : 5,46 kmol  $\text{NO}_3^-$ /t and 240 €/t

As can be seen from the graph the costs for chemical dosage vary between 4,9 and 45,8 cent/ $\text{m}^3$ . Since sulphide generation depends on the characteristics of the pressure sewer, the specific cost per  $\text{m}^3$  waste water can vary accordingly as can be seen from the three different costs for the three different sewers of the RHV NSW, where the same chemical ( $\text{Ca}(\text{NO}_3)_2$ ) was applied (Figure 3).

For the alternative treatment methods, in which no chemicals were used, operating costs were based on either material used and labour costs

(pigging) or consumption of electricity (air supply systems).

The traditional “pigging” was shown to have a very short lasting effect in comparison with its high price and therefore application is limited to few cases. On the contrary, a “pigging” with Leca® (Light expanded clay aggregate) combined with the chemical addition, was observed to reduce the consumption of chemicals for approximately one week.

The use of adsorptive chemicals like zeolite to remove sulphide from the water was not effective. This was probably because of a saturation of its adsorption capacity by other waste water compounds.

Pipe cleaning with pure water could be a low cost alternative for short and thin pipes, only limited by the availability of nearby water sources and the capacity of the WWTP to cope with the resulting dilution.

Before designing new pressure sewers, the cost efficiency of systems for sulphide control such as pneumatic waste water transport or air/oxygen supply should be evaluated. Air supply can especially be recommended in cases of high sulphide generation potential like small diameter pipes collecting high concentrated waste waters. While this alternative can also be adopted in existing pipes, a pneumatic waste water transport system cannot be retrofitted.

The selection of the pressure sewers within this project covered a wide spectrum of pipe dimensions (pipe diameters from 80 until 440 mm) and different installations (simple pipes until pipes connected in series with intermediate pumping stations). The costs of the applied methods varied between 0,03 and 0,30 €/m<sup>3</sup> waste water and between 8 and 20 €/kg treated sulphide. For average residence times in the range of 3 and 6 hours and pipe lengths between 3 and 5 km additional costs of about 0,05 €/m<sup>3</sup> waste water are to be expected.

## REFERENCES

- [1] Lens P.N.L. and Hulschoff Pol L. (2000). Environmental Technologies to treat sulfur pollution. Principles and engineering. IBSN 1900222094 IWA London.
- [2] Saracevic E., Winkler S., Brooks L., Bertrán de Lis F. and Matsché N. (2005): A prototype system for monitoring of hydrogen sulphide production related processes in sewer networks. Proceedings of the 2<sup>nd</sup> IWA Conference on Instrumentation, Control and Automation. Busan, Korea. May 29 - June 2, 2005.
- [3] Boon, A. G. and Lister, A. R., (1975). Formation of sulphide in a rising main sewer and its prevention by injection of oxygen. Progress in Water Technology.7, pp. 289-300.

# Development of a Simulation Method to predict Ultraviolet Disinfection Reactor Performance and Comparison to Biodosimetric Measurements

Christoph Buchner<sup>1</sup>, Christoph Reichl<sup>2</sup> (Company mentor) and Norbert Vana<sup>3</sup> (Faculty mentor)

<sup>1,3</sup>Atomic Institute of the Austrian Universities  
Technical University of Vienna

Vienna, Austria

<sup>2</sup>arsenal research – Austrian Research Centers  
Vienna, Austria

Email: Christoph.Buchner@arsenal.ac.at,  
Christoph.Reichl@arsenal.ac.at, vana@ati.ac.at

**Abstract** — *Nowadays, water disinfection with ultraviolet radiation becomes increasingly important. This work presents a simulation method to predict the disinfection efficacy of an UV disinfection reactor and compares the results to biodosimetric measurements to assess the achieved accuracy.*

*Multiple CFD simulations have been performed, particle tracks were generated and the radiation field inside the reactor has been modelled. The reduction equivalent fluence (REF), an important quantity in biodosimetry, has been calculated.*

*The simulated pressure loss of the reactor agreed very well with the experiments. Despite a lack of experimental data for certain parts of the disinfection process, good predictions of the REF were obtained. Average error values varied between 7 and 25%, depending on the chosen radiation model.*

## I. INTRODUCTION

Disinfection of potable and wastewater using additives like chlorine or ozone has a long tradition. Nowadays, water treatment with ultraviolet (UV) radiation becomes increasingly important. Disinfection facilities exist in various sizes, ranging from conventional single-lamp reactors to multi-lamp arrays with up to 8000 lamps for waste water treatment. Commonly, quasi-monochromatic (low pressure) as well as polychromatic (medium pressure) ultraviolet lamps are employed whose radiation permeates the water flow. Pathogenic micro-organisms, which are present in the fluid, are deactivated by the incident photon rays and lose their danger of infection for humans.

Currently, reactor disinfection efficacy is judged by means of biodosimetric measurements: Water flowing through the reactor is spiked with micro-organisms of known concentration. When determin-

ing the concentration of viable micro-organisms after passing through the reactor, a reduction value is obtained, which can be used to calculate the Reduction Equivalent Fluence (REF). The exact procedure of certifying UV disinfection reactors, which is specified in the ÖNORM M 5873-1 [1], is complex and costly.

There has been extensive research going on concerning the different aspects of UV disinfection modelling. It would exceed the scope of this paper to name even most of the relevant publications which were examined, therefore only a small number of publications is cited [2-5].

The aim of this work is to combine the different aspects of Ultraviolet Disinfection (UVD) into an overall simulation of a small UVD reactor. This simulation includes Computational Fluid Dynamics (CFD) simulation of the water flow, particle tracking of micro-organisms in the water and radiation modelling of the radiation emitted by the UV lamp. As a result, the calculated disinfection efficacy of the UVD reactor is compared to available data from multiple certification procedures. This comparison will help to judge if the achieved accuracy is sufficient for including the developed procedure into the design process of UV disinfection reactors. Eventually, using simulation techniques, analyses of UV reactors shall provide the basis for reliable geometric optimisation at design time without incurring the cost of prototype certification procedures.

## II. METHODS

The attained REF depends on a combination of multiple effects, namely fluence rate distribution of the UV lamp in the reactor chamber, mass flow and UV transmittance of the water, as well as geometric and hydrodynamic properties of the reactor.

#### A. THE UVD REACTOR

The modelled reactor is a single low-pressure lamp, closed-channel, axial flow reactor designed for flow rates ranging from 0.7 to 6m<sup>3</sup>/h, with a lamp power rating from 60 to 130W. The reactor vessel had an inner diameter of 100mm and a length along the main axis of 1048mm. The quartz sleeve protecting the UV lamp was located along the main axis of the reactor and had an outer diameter of 30mm, running along the entire length of the reactor.

#### B. COMPUTATIONAL FLUID DYNAMICS

From the validation reports, data for 23 different sets of operational parameters (“cases”) were available. For these cases, steady-state calculations have been carried out using the realizable-k-ε turbulence model. It is possible that significant fluctuations occur in the water flow, which influence disinfection results, but cannot be reproduced by steady-state calculations. Unfortunately, at the time being, unsteady calculations were computationally too expensive to perform, especially in light of potential future industry applications of UV disinfection simulation.

#### C. PARTICLES

Particle tracks were calculated by solving the force balance equation for the particle in question. Approximately 26000 particle tracks were calculated for every case using a discrete random walk approach to allow statistically reliable calculations.

#### D. RADIATION MODELLING

Several radiation models have been implemented, which exhibit different degrees of physical realism.

There exists, however, one major limitation of the radiation modelling: The UV conversion efficiency judges the lamp’s performance in converting electrical power to radiation. Because this value is difficult to determine experimentally, the efficiency had to be calculated indirectly. This was achieved by comparing available UV sensor readings with results from radiation models, thus “calibrating” the efficiency to a certain radiation model. Therefore, the calculated REF depends on the calculated efficiency value.

### III. RESULTS

To compare the CFD results against the experiments, pressure loss data were available from the validation reports. A quadratic fit ( $R^2=0.9981$ ) has been calculated, and the CFD pressure loss information has been compared to these two data sets. The mean of the absolute values of the error (in %) has been calculated. Compared to the experiment and fit, mean

values of 5.4 and 3.2%, respectively, have been obtained.

When combining particle tracks and radiation data, a fluence value is calculated for every simulated particle. From the whole set of particles, a REF value is obtained. The resultant REF values are compared to experimental data for every case. Mean and standard deviation of the error have been computed. For the different implemented radiation models, mean errors between 7 and 25% have been found. The standard deviations are relatively high, ranging from 8.9 to 15.4%.

### IV. CONCLUSIONS

A simulation method to predict UV reactor disinfection performance has been presented. Calculations have been performed for several radiation models and have been compared to biosimetric measurements. Considering the limited amount of available experimental data for the flow field and fluence rate distribution, good predictions of the REF were obtained. The potential use of this method for designing and improving UVD reactors has been demonstrated.

Future work will encompass unsteady CFD calculations, which will yield unsteady particle tracks. Furthermore, different reactor geometries can be examined. Ray-tracing can additionally be employed to include reflection at the reactor walls.

### REFERENCES

- [1] Österreichisches Normungsinstitut. ÖNORM M 5873-1: Anlagen zur Desinfektion von Wasser mittels Ultraviolett-Strahlen - Anforderungen und Prüfung - Teil 1: Anlagen mit Quecksilberdampf-Niederdruckstrahlern, March 2001.
- [2] Dong Liu. Numerical Simulation of UV disinfection reactors: Impact of fluence rate distribution and turbulence modeling. PhD thesis. North Carolina State University, 2004.
- [3] J. R. Bolton. Calculation of ultraviolet fluence rate distribution in an annular reactor: Significance of refraction and reflection. *Water Research*, 34(13):3315–3324, September 2000.
- [4] A. Cabaj, R. Sommer and D. Schoenen. Biosimetry: Model calculations for UV water disinfection devices with regard to dose distributions. *Water Research*, 30(4):1003–1009, April 1996.
- [5] J. Ducoste, D. Liu, and K. Linden. Alternative Approaches to Modeling Fluence distribution and Microbial Inactivation in Ultraviolet Reactors: Lagrangian versus Eulerian. *Journal of Environmental Engineering*, 131(10):1393–1403, October 2005.

# Contribution of wood burning to PM<sub>10</sub> in Austria

Alexandre Caseiro<sup>1,2</sup>, Casimiro Pio<sup>2</sup>, Anne Kasper-Giebl<sup>1</sup>, Heidi Bauer<sup>1</sup>, Hans Puxbaum<sup>1</sup>

<sup>1</sup>Institute for Chemical Technologies and Analytics  
Vienna University of Technology  
Vienna, Austria

<sup>2</sup>Departamento de Ambiente e Ordenamento (DAO)  
University of Aveiro  
Aveiro, Portugal

Email: [acaseiro@pop.tuwien.ac.at](mailto:acaseiro@pop.tuwien.ac.at)

**Abstract** — *The aim of this work was to assess the contribution of wood burning to PM<sub>10</sub> in Austria, as well as its seasonal and spatial variabilities.*

## INTRODUCTION

The numerous exceedance occurrences of the PM<sub>10</sub> limit values have lead Austrian local authorities to seek after the sources of the ambient particulate matter.

In the scope of source apportionment, it is a major issue to identify and quantify molecular macrotracers specifically related to the variety of sources contributing to PM<sub>10</sub>. Levoglucosan, a pyrolysis degradation product of cellulose (the main constituent of biomass), has been reported as an exclusive tracer for biomass burning [1].

## EXPERIMENTAL

Aerosol samples were collected on quartz fibre filters in three Austrian cities: four sampling sites in Vienna, three in Salzburg as well as in Graz, as part of the local air quality monitoring network operated by local authorities.

In all three cities urban sampling sites were backed with a rural and a suburban one in order to determine the local background aerosol concentration and the urban impact in each city [2]. The data set comprises High Volume aerosol samples collected on a 24 hours basis during the year 2004. In addition to ambient aerosol samples, source profiles of potential contributors to PM<sub>10</sub>, e.g. wood combustion and road dust samples, were analysed.

The use of high pH anion exchange and pulsed amperometry (HPAE-PAD) allowed the separation, identification and quantification of different anhydrosugars, sugars and sugar alcohols, among which levoglucosan.

The contribution of wood burning to PM<sub>10</sub> can be derived from the levoglucosan ambient concentration using the following formula:

$$WB = Levo * 7,35 * 1,7(OM) * 1,1(ip). \quad (1)$$

where *WB* is the wood burning particles concentration, *Levo*, *OM* and *ip* are the levoglucosan, organic matter and inorganic part concentration, respectively.

## RESULTS

The data set allows the determination of the annual trend as well as spatial variations between different kinds of stations and the different cities.

Levoglucosan shows a highly differentiated pattern between the cold and the warm season, peaking during the winter, thus evidencing the high contribution of wood burning to PM<sub>10</sub> during that season.

The analysis of source samples supports that levoglucosan is exclusive to biomass burning

## REFERENCES

- [1] Fine et al. (2001) Chemical Characterization of fine particle emissions from Fireplace combustion of woods grown in the northeast United States. *Environ. Sci. Technol.* 35, 2665-2675
- [2] Puxbaum H., Gomiscek B., Kalina M., Bauer H., Salam A., Stopper S., Preining O. and Hauck H. (2004) A dual site study of PM<sub>2.5</sub> and PM<sub>10</sub> aerosol chemistry in the larger region of Vienna, Austria. *Atmos. Environ.* 38, 3949-3958



# Selective Separation of Carbon Dioxide for Biogas Upgrading

Helmut Feichtner, Alexander Reichhold and Hermann Hofbauer  
Institute of Chemical Engineering  
Vienna University of Technology  
Vienna, Austria  
Email: helmut.feichtner@tuwien.ac.at

**Abstract** — *Biogas, which is obtained by anaerobic fermentation with compositions of about two thirds methane and one third carbon dioxide, has to be purified when fed into public natural gas grids. Therefore experimental and numerical investigations are presented regarding the adsorptive separation of carbon dioxide by means of a weakly basic anion exchange resin. Adsorption isotherms as well as kinetic data for carbon dioxide, methane and water vapour are given. Furthermore numerical calculations have been done for the determination of the temperature profile and breakthrough during thermal regeneration.*

## I. INTRODUCTION

In a number of industrial processes it is advantageous removing existing gaseous carbon dioxide prior further processing. In the present work the main goal lies on purifying biogas up to the requirements of natural gas quality, called the “upgrading” of biogas, with the objective of feeding the obtained gas into the public natural gas grid. Generally, by reduction of gas streams in terms of flow rate, mechanical power can be saved when utilising compressors as well as apparatuses can be designed in smaller dimensions. Hence the potential of saving on both operational and investment costs is given. Furthermore such a process could be applied to the purification of gas streams for catalytic processes like steam reforming or for product gases with specified purity.

## II. ADSORBENT

As the adsorbent material a weakly basic bidispersed anion exchange resin of the type DIAION WA21J supplied by Mitsubishi Chemicals Co. has been used. The same type of adsorbent was investigated by [1], [2], [3], [4] and various other authors with applications like life-support systems or the separation of acidic gases.

The used adsorbent is a highly porous resin consisting of a polymeric matrix made of polystyrene

while the functional groups are formed by tertiary amines as shown in Figure 1.

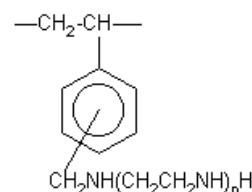


Figure 1: Chemical structure of the adsorbent

Unlike zeolites this anion exchange resin shows no negative influence on the adsorption of carbon dioxide in the presence of water vapour. Quite the contrary, the adsorption capacities were found to increase by various researchers.

## III. THERMOGRAVIMETRIC ANALYSIS

As a first step adsorption experiments were conducted by means of thermogravimetric analysis. According to the adjusted temperature program and variations in the carbon dioxide partial pressure the equilibrium isotherms, as shown in Figure 2, were obtained for carbon dioxide for various temperatures.

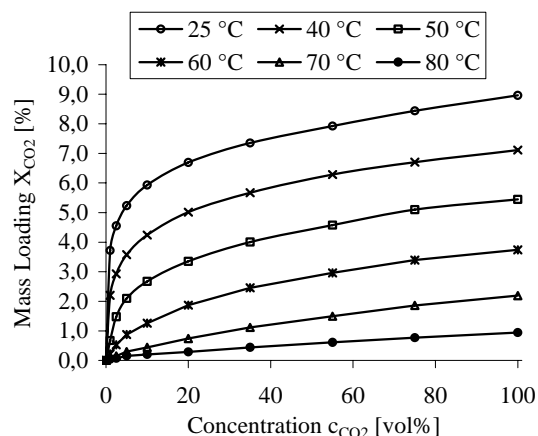


Figure 2: Equilibrium isotherms of CO<sub>2</sub> on WA21J

Analogically, the determination of the equilibrium adsorption isotherm for methane was carried out. Since the adsorbent showed only a small capacity for methane, the measurements were only done for 25 °C (Figure 3).

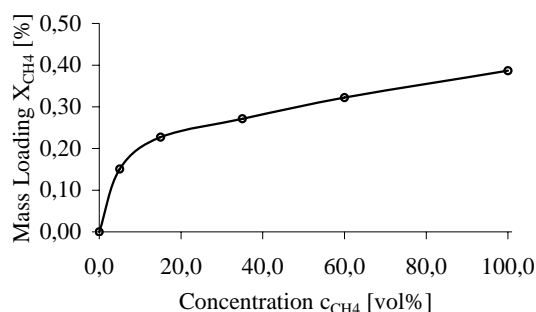


Figure 3: Equilibrium isotherm of CH<sub>4</sub> on WA21J

The differences in the nature of adsorption of water vapour and carbon dioxide was also investigated and can be seen in terms of the kinetics in Figure 4.

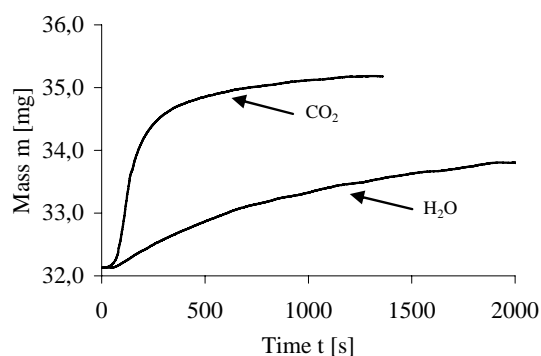


Figure 4: Kinetics of carbon dioxide and water

Summed up, the utilized anion exchange resin exhibits a very high capacity for carbon dioxide and the kinetics for carbon dioxide are very fast. In contrast the adsorbent shows a very low capacity for methane and therefore it can be seen as very selective for the separation of carbon dioxide.

Further high affinities for water vapour but slower kinetics could be observed.

#### IV. NUMERICAL CALCULATIONS FOR TEMPERATURE SWING REGENERATION AND ADSORPTION APPARATUS

For further research in the application of the used adsorbent in upgrading biogas and the design of an adsorption apparatus, numerical calculations have been made regarding the thermal swing regeneration.

A transient, two-phase model, which takes into account the dispersion and the wall heat transfer, was used for these calculations based on the model derived by [6]. The code and calculations were accomplished in the commercial software package MathLab.

A typical chart of the temperature profile for thermal regeneration of the adsorbent in a packed bed process is depicted in Figure 5.

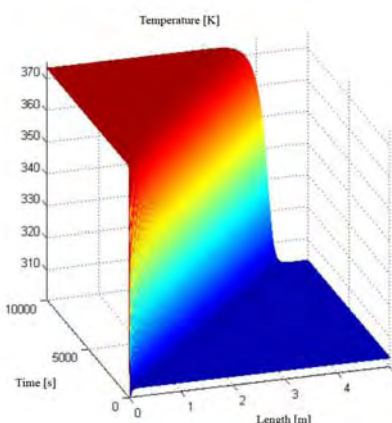


Figure 5: Temperature profile for regeneration

As mentioned above, a laboratory scale adsorption plant has been developed and set up based on the calculations for reasons of verification of the model.

#### REFERENCES

- [1] A. Reichhold. Entwicklung einer intern zirkulierenden Wirbelschicht für kontinuierliche Adsorptions- und Desorptionsprozesse. Diploma Thesis, Vienna University of Technology, 1991
- [2] A. Diaf, R. M. Enick and E. J. Beckmann. Molecular Redesign of Expanded Polystyrene to Allow Use of Carbon Dioxide as a Foaming Agent. I. Reversible Binding of CO<sub>2</sub>. J. Appl. Polym. Sci., Vol. 50: 835-844, 1993
- [3] A. Diaf and E. J. Beckmann. Thermally Reversible Polymeric Sorbents for Acid Gases. III. CO<sub>2</sub>-sorption enhancement in polymer-anchored amines. React. Funct. Polym., 27: 45-51, 1995
- [4] H. Yoshida, S. Oehlenschlaeger, Y. Minami and M. Terashima. Adsorption of CO<sub>2</sub> on Basic Anion Exchange Resins. Ads. Sci. Techn., Proc. Pac. Bas. Conf. Ads. Sci. Techn., 2nd, Brisbane, Australia: 688-692, 2000
- [6] D. Vortmeyer and R. J. Schaefer. Equivalence of One- and Two-Phase Models for Heat Transfer Processes in Packed Beds: One Dimensional Theory. Chem. Eng. Sci., Vol. 29: 485-491, 1974

# Designing tomorrow's energy supply: Polygeneration of transportation fuels, power and heat from biomass

Stefan Fürnsinn and Hermann Hofbauer (Faculty Mentor)  
Institute of Chemical Engineering  
Vienna University of Technology  
Vienna, Austria  
Email: stefan.fuernsinn@tuwien.ac.at

**Abstract** — *As alternative energy resources become increasingly important, innovative energy technologies are needed to meet tomorrow's demands. In this work, a biomass-based large-scale polygeneration plant yielding liquid transportation fuels such as gasoline and diesel, electric power, and district heat is characterized and evaluated by means of stationary computer simulation. The results prove the high energy efficiency of such conversion strategies and highlight the flexibility of combined processes, which lead to economically viable technologies for decentralized energy supply.*

## I. INTRODUCTION

Due to the extensive use of fossil resources such as crude oil, coal and natural gas for power generation, heating and transportation, reserves will reach depletion in the long run. Additionally, atmospheric accumulation of CO<sub>2</sub> as a result of anthropogenic greenhouse gas emissions is becoming increasingly important, as severe effects on climate conditions are likely to be expected [1].

Therefore, alternatives must be found so as to both secure energy supply in the future and allow for sustainable and environmentally friendly energy services.

Biomass is one of the most promising renewable resources, offering a wide variety of applications through thermo-chemical conversion. As a result of biomass gasification, a valuable synthesis gas, consisting primarily of CO and H<sub>2</sub> is obtained, which can subsequently be used for the production of liquid and gaseous transportation fuels, power generation, and the supply of district heat [2].

In polygeneration plants, not the optimization of one of these products individually, but the well-balances cogeneration of all products is focused at, leading to synergetic advantages and increased overall efficiencies.

## II. TECHNOLOGY DESCRIPTION

The production of transportation fuels, power and heat from biomass follows a multi-stage conversion chain, as illustrated in Figure 1.

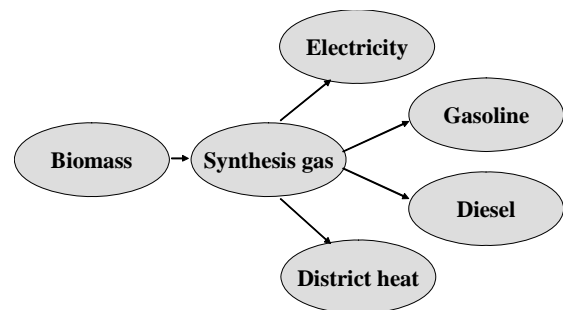


Figure 1: Basic concept of biomass-based polygeneration plants

- Gasification  
Transformation of woody biomass into synthesis gas [3]
- Fuel synthesis  
Catalytic Fischer-Tropsch fuel synthesis (cf. [4])
- Power generation  
Combustion of FT-offgas in gas engine, use of process heat in an ORC [5]
- District heat  
Collection of low-temperature heat and use for local heating

## III. APPROACH

In order to design and evaluate a 30 MW<sub>fuel</sub> power polygeneration plant concept, a stepwise procedure is used (cf. Figure 2).

In an initial step, the different unit operations involved (gasification, Fischer-Tropsch synthesis, gas

engine, heat recovery, etc.) are combined to a feasible plant concept.

Then, models for all conversion steps are established. Especially for gasification and FT-synthesis, chemical reactions are modelled. The plant is then implemented into a stationary simulation software and thus analyzed.

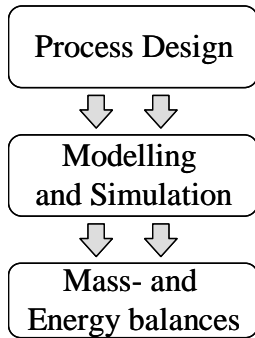


Figure 2: Schematic representation of the scientific approach

From this, mass and energy balances are obtained which serve as a basis for subsequent plant optimization. In the end, profound data for the concept evaluation is thus available.

#### IV. RESULTS AND DISCUSSION

As shown in Table 1, polygeneration plants allow for the combined production of transportation fuels, electric power and district heat in high efficiencies.

Fuel power	kW	30000	%	100
Gross el. production	kW	6358	%	21,2
In-plant consumption	kW	2735	%	9,1
Net el. production	kW	3623	%	12,1
Fuel production	t/a	5297	%	26,9
Thermal power	kW	13437	%	44,8
Total gross efficiency		-	%	92,9
Total net efficiency		-	%	83,8

Table 1: Results for a 30 MW<sub>fuel power</sub> polygeneration plant

Based on a fuel power of 30 MW, more than 3.5 MW of electric power are produced, and more than 13 MW of thermal power are obtained. Furthermore, renewable fuels are synthesized, adding up to nearly 5300 tons per year.

Since fuel economy is one of the most important optimization goals, the high total net efficiency of

nearly 84 % shows the advantages of decentralized energy centres, since the utilization of low temperature heat for heating purposes is possible. In large scale, specialized facilities, where transportation fuels or electric power are maximized exclusively, the use of district heat is generally not possible. Hence, polygeneration plants offer the possibility to supply modern energy carriers efficiently from biomass and actively contribute to a sustainable regional development.

#### REFERENCES

- [1] IPCC. Climate Change 2001: The Scientific Basis. Cambridge University Press, Cambridge, 2001.
- [2] Hofbauer, H., Kaltschmitt, M., Meier, D., Welling, J. Thermochemische Umwandlung. In: Kaltschmitt, M. (Ed.). Energie aus Biomasse. Springer, Berlin, 2001, pages 427-505.
- [3] Knoef, H.A.M. (Ed.). Handbook Biomass Gasification. BTG biomass technology group, Enschede/The Netherlands, 2005.
- [4] Fürnsinn, S., Ripfel, K., Rauch, R., Hofbauer, H. Diesel aus Holz – die Fischer-Tropsch Synthese als zukunftsweisende Technologie zur Gewinnung flüssiger Brennstoffe aus Biomasse. In Proceedings of the Internationale Energiewirtschaftstagung 2005, Vienna, Austria. February 2005.
- [5] Pröll, T. Potenziale der Wirbelschichtdampfvergasung fester Biomasse - Modellierung und Simulation auf Basis der Betriebserfahrungen am Biomassekraftwerk Güssing. PhD-Thesis, Vienna University of Technology, 2004.

# Seasonal Variation of Trace Metals in the PM10 Fraction at Three Sampling Sites in the City of Vienna

Markus Handler, Hannes Zbiral, Hans Puxbaum and Andreas Limbeck (Faculty Mentor)  
Institute of Chemical Technologies and Analytics,  
Vienna University of Technology,  
A-1060 Vienna, Austria  
Email: {m.handler, a.limbeck}@tuwien.ac.at

**Abstract** — *This work is part of a large project, which aim is to identify and quantify sources for PM10-emission in Austrian urban regions. The data of an one-year sampling period at three sampling sites in Vienna will be presented and discussed, focusing on the urban impact, the increase of the immission level in urban areas.*

*As main analytical methods for metal analysis ICP-AES and ETAAS following a microwave supported sample digestion, were used.*

## I. INTRODUCTION

Non-attainment of particulate matter air quality standards is a frequently observed problem encountered in many US and European cities. [1,2] The European Commission has included PM10 limit values for PM monitoring in the new air quality directive. The new EC Directive establishes an annual daily limit of  $40 \mu\text{g PM}_{10} \text{ m}^{-3}$ , and a 24 h limit value of  $50 \mu\text{g PM}_{10} \text{ m}^{-3}$ , which should not be exceeded more than 30 days per year.

For a targeted reduction of PM10 levels, detailed knowledge of sources and there respective contribution to the PM levels is required. Balancing total PM10 mass by chemical species or groups of compounds and multiple approaches including receptor sites outside the regulated area have been proposed to reduce the uncertainties specified above. [3,4,5]

## II. SAMPLING AND ANALYSIS

PM10 samples were collected at three sites in Vienna, throughout the complete annual cycle of 2004. One site was heavily influenced by traffic emissions, the second was placed in a residential area and the third positioned within a remote emission area at the border of the city.

PM10 samples have been analyzed for total, organic and elemental carbon, individual organic compounds, water soluble ions and selected trace metals and mineral components. Si and Al were measured

via XRF, Ca, Mg, Fe, Zn, Cu, Ti, Mn, Pb, As, Sb, Sn, Ba, Sr, Co, Cd, Cr, Ni and V contents of airborne particulate matter samples were determined using ETAAS and ICP-AES.

## III. RESULTS

PM10 aerosol samples were analyzed to determine the seasonal variation of Si, Al and selected trace metals at the investigated sampling locations. At all sites the seasonal variation of the measured elements was very similar showing decreased concentrations in the warm period of the year and increased concentrations in the cold season. Generally the seasonal pattern of an individual aerosol constituent depends on meteorological variations and changes in the source emission and transformation rates of the investigated species.

Due to this multiple site approach – local background and inner city – it was possible to determine an “urban impact” which was calculated from the difference between the observation at urban and local background sites. Annually averaged mineral and trace metal PM10 concentrations at the inner city sites were up to 4 times higher than at the local background site, for some elements only equal amounts were determined, which implicates that the urban impact ranges from not detectable to approximately 300%.

## IV. CONCLUSION

In this presentation, we show that the major part of the urban PM10 metal content is produced inside the city, whereas only a minor fraction results from the transport of aerosols from outside into the urban area.

## ACKNOWLEDGMENTS

This work was financed by the provincial governments of Vienna.

## REFERENCES

- [1] Chow, J.C.; Watson, J.G.; Lowenthal, D.H.; Solomon, P.A.; Magliano, K.L.; Ziman, S.D.; Richards, L. W., 1992. *PM10 source apportionment in California's San Joaquin Valley*. Atmospheric Environment, Part A: General Topics, 26A(18), 3335-54.
- [2] Puxbaum, H., Gomiscek, B., Kalina, M., Bauer, H., Salam, A., Stopper, S., Preinig, O., Hauck, H., 2004. *A dual site study of PM2.5 and PM10 aerosol chemistry in the larger region of Vienna, Austria*, Atmos. Environ. 38, 3949-3958.
- [3] Maenhaut, W.; Schwarz, J.; Cafmeyer, J.; Chi, X., 2002. *Aerosol chemical mass closure during the EUROTRAC-2 AEROSOL Intercomparison 2000*. Nuclear Instruments & Methods in Physics Research, Section B: Beam Interactions with Materials and Atoms 189, 233-237.
- [4] Schauer, J.J.; Cass, G.R., 2000. *Source Apportionment of Wintertime Gas-Phase and Particle-Phase Air Pollutants Using Organic Compounds as Tracers*. Environmental Science and Technology, 34(9), 1821-1832.
- [5] Van Dingenen, R. et al. (26 cowriters), 2004. *A European aerosol phenomenology-1: physical characteristics of particulate matter at kerbside, urban, rural and background sites in Europe*. Atmospheric Environment, 38(16), 2561-2577.

# Hydraulic Design of Single Stones in Biocorridor

Lea Hašková and Jozef Kamenský (Faculty Mentor)

Faculty of Civil Engineering  
Slovak University of Technology  
Bratislava, Slovakia

Email: {haskova , kamensky}@svf.stuba.sk

**Abstract** — *Biocorridors (nature-like fishways) are categorized as fish passes. Fish passes help to pass gradient created by water structure and thus secure migration continuity. Single stones can be a part of biocorridor channel – stones, placed in river bed, producing decreased velocities, bigger depths and natural look. Described computational algorithm for these boulders is based on DVWK standard no. 232/1996 and Darcy-Weisbach formula - takes into account roughness coefficient used in our standards. The depth difference  $\Delta y$  shows that single stones, in same conditions in river bed, increase depths by round 40%.*

## I. BIOCORRIDORS

Biocorridor – a substitute pathway, with the character of natural stream, which forms longer bypass river bed with natural surface imitation. It is formed as a boulder bed with continuous river bottom, spreaded by coarse gravel sand, with sloped banks, slowly flow and cascade water surface.

### A. PARTS OF BIOCORRIDOR RIVER BED

Biocorridors have to have various topography, thus shallow sections are varied with non shallow intersections. This supports species diversity of aquatic habitat. The effect of flowing torrent is reached by placing of following components in biocorridor river bed:

- rocky chutes – boulder system in bottom of river bed, they copy torrent sills, they stabilize bed slope conditions,
- sills in bottom of river bed, riverbed drops – structures from rip-rap, partially interfere in flow profile and thus produce effective roughness,
- single stones – boulders individually placed in river bed on certain length, they don't create a continual body and increase local macroroughness.

### B. BIOCORRIDOR DESIGN PARAMETERS

These parameters result from a compromise between technical solution and requirements of ichthyologists,

which are based on ichthyofauna abundance on natural streams.

- Discharge – basic parameter, regulated by water intake,
- Flow velocity – small velocities near bottom of river bed:  $0,2 - 0,5 \text{ m.s}^{-1}$ ; max. flow velocity in river bed:  $1,6 - 2 \text{ m.s}^{-1}$ ,
- Longitudinal slope of river bed,
- Water depth,
- Max. difference of adjacent water surfaces,

Type of hunting ground	Slope $i_o$	Depth $y$ (cm)	Difference $\Delta y$ (cm)
Trout waters	$\leq 1:15$	30 - 50	20
Nontrout waters	$\leq 1:20$	50 - 80	15

Table 1: Parameters slope, depth and difference depending on type of huntingground

- Diameter of single stones:  $d_s = 0,6 - 1,2 \text{ m}$ ,
- Weight of single stones: 80 – 200 kg,
- Mutual distance of stones in downstream as well as normal direction:  $a_x = a_y = (1,5 - 3).d_s$

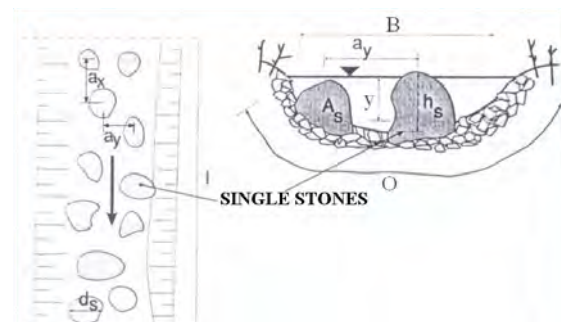


Figure 1: Scheme of stones configuration

## II. COMPUTATIONAL ALGORITHM FOR SINGLE STONE DESIGN

Computational relations are in detail described in DVWK standard no. 232/1996. This simple algorithm enables design of size and numbers of boulders, as well as length, on which these boulders

will be placed, so required parameters of flow are achieved (especially discharge and depth). This calculation includes also transformation of dimensionless Manning coefficient  $n$ , used in Slovakia, to German equivalent sand roughness  $\Delta$  (Table 2):

$$\Delta = 14,84 \cdot R \cdot 10^{\left( \frac{-R^{1/6}}{2 \cdot n \cdot \sqrt{8 \cdot g}} \right)} \quad (1)$$

Material Description	n	$\Delta$ (m)
gravel bed, unworked stone banks and cement mortar, prismatic gravel channel, earth channel with bays without vegetation	0.025	0.0639
concrete bed, riprap banks	0.03	0.1303
gravel bed, riprap banks	0.033	0.1802
vegetation fortification, channels with rough face, irregular profile	0.04	0.3176
Material Description	$\Delta$ (m)	n
river bed from coarse-grained gravel - gravel	0.06	0.025
river bed from heavy stone rockfill	0.2	0.034
banks from green	0.2	0.034
banks from grass and bushes	0.3	0.039
	0.06	0.025
	0.13	0.030
	0.4	0.044

Table 2: Transformation  $n$  to  $\Delta$  and  $\Delta$  to  $n$  ( $b_d = 2,6$  m,  $y = 0,4$  m,  $m = 2$ )

Calculation inputs:

- $Q$  – discharge (given by project requirements),
- $i_o$  – river bed slope (according to situation, condition  $i_o \leq 0,05$ ),
- $m$  – bank slope (1:m) (trapezoidal cross section),
- $y$  – water depth, which we want to achieve,
- $d_s$  – supposed stone diameter ( $d_s = 0,6-1,2$  m)

(this parameter is connected with river bed roughness and consequently combined with roughness of banks covered by vegetation),

- $b_d$  – river bed width ( $b_d = 1,5 - 20$  m),
- $l$  – section length, on which placement of single stones is supposed.

Calculation outputs:

Given discharge	The number of stone rows
Computed discharge	Mean flow velocity $v_m$
Number of boulders	Max. velocity $v_{max}$

Calculation will end, if given and computed discharge become equivalent, whereas this program supposes following simplifications – water flows round the stones and steady uniform flow is being considered.

Water Structure	Žilina	Veľké Kozmálovce	
Inputs	$Q$ ( $m^3 \cdot s^{-1}$ )	1,2	0,6
	$y$ (m) with stones	<b>0,6</b>	<b>0,7</b>
	$b_d$ (m)	5	4
	$m$	2	1,5
	$i_o$	0,002	0,001
Output	$\Delta$ (m) / $n$	0,378 / 0,039	0,377 / 0,038
	$d_s$ (m)	0,8	0,8
	Stone no.	20	13
	$l$ (m)	14,7	6,4
	$v_m$ ( $m \cdot s^{-1}$ )	0,323	0,171
	$v_{max}$ ( $m \cdot s^{-1}$ )	0,527	0,325
Comparison	$n$ (without stones)	0,035	0,035
	$y$ (m) without stones	<b>0.349</b>	<b>0.336</b>
	$\Delta y$ (m)	<b>0.251</b>	<b>0.364</b>

Table 3: Single stone design based on real parameters

## ACKNOWLEDGMENTS

Single stones have positive influence for fish pass regime. They increase depth without increase of discharge (Table 3), after their stabilization scours will be created (refuge possibilities for ichthyofauna), they ruffle water surface and thus water becomes more oxygenated, and also they produce natural look of technical constructions, such as fish passes are. Plumbless advantage of single stones is their simple placement, easy reconstruction and almost prompt effect.

## REFERENCES

- [1] DVWK 232/1996: Fischeaufstiegsanlagen. Wirtschafts und Verlagsgesellschaft Gas und Wasser mbH. Bonn, Germany, 1996.
- [2] E. Mäsiar and J. Kamenský. Hydraulika I. Bratislava, Slovakia, 3<sup>rd</sup> edition, 2000.
- [3] E. Mäsiar and J. Kamenský. Hydraulika II. Bratislava, Slovakia, 3<sup>rd</sup> edition, 2001.
- [4] T. Just and V. Šámal. Revitalizace vodního prostředí. Praha, Czech Republic, 2003.
- [5] <http://hydro.ifh.uni-karlsruhe.de/download/Kap10ps.pdf>

# The possibility of utilization of permeable reactive barriers for remediation of contaminated groundwater

Mária Heželová and Ladislav Lux and Daniela Kladeková\*

Department of Chemistry, Faculty of Metallurgy

Technical University of Košice

\* Faculty of Science, P.J. Šafárik University

Košice, Slovakia

Email: [maria.hezelova@tuke.sk](mailto:maria.hezelova@tuke.sk)

**Abstract** — *Recent research indicates many potential applications of zero-valent iron (Fe) in environmental remediation. Using Fe to remove contaminants from groundwater could be an attractive approach provided it is effective at environmentally relevant pH values. This paper considers the reduction of two types of organic contaminants – nitrobenzene and trinitrophenol by iron powder in laboratory conditions. Owing to the reduction of the contaminants the voltammetric current decreases nearly to zero in the course of two hours.*

## I. INTRODUCTION

Groundwater is the main source of drinking water, but human activities can negatively influence its quality. A permeable reactive barrier (PRB) is considered to be an innovative, green engineering approach used to remediate contaminated groundwater. According to the definition of the Environmental Protection Agency, PRB is:

“an emplacement of reactive media in the subsurface designed to intercept a contaminant plume, provide a flow path through the reactive media and transform the contaminant(s) into environmentally acceptable forms to attain remediation concentration goals down-gradient of the barrier” [1].

There are several advantages associated with the implementation of PRB, such as: ability to treat a wide range of contaminants (organics, inorganics, radionuclides), passive treatment systems, reduction of exposure to contaminants, relatively low maintenance and operational costs. Suitable materials currently employed for use in a PRB as reactive materials are: activated carbon, zero-valent iron, apatite, zeolites, amorphous ferric oxyhydroxide or humic material [2]. The type of reactive media primarily depends on both the nature

of contamination present and the selective remediation approach. The main characteristics used to determine the type of reactive media are reactivity, stability, availability, cost, hydraulic performance and also environmental compatibility [3].

In our laboratory conditions of using two types of contaminants and zero-valent iron as a model of PRB were studied.

## II. EXPERIMENTAL

The concentration of contaminants was determined by voltammetric experiments with the polarographic analyzer PA 4 (Laboratory Apparatus Prague). The three-electrode system consisted of:

- a stationary mercury drop-working electrode,
- a silver chloride electrode with 3 mol dm<sup>-3</sup> aqueous KCl solution–reference electrode,
- a platinum auxiliary electrode.

Cathodic voltammograms were recorded with a 50 mV s<sup>-1</sup> scan rate.

Reaction system was deaerated by purified inert gas (nitrogen, argon) before measurement.

Iron powder, type WV-200 (Kovohuty, Dolný Kubín), was used as a reactive material. The grain size was up to 45 μm.

In the case of nitrobenzene reduction the acetate buffer of original pH value of 4.65 was used as a supporting electrolyte. It was prepared by mixing sodium acetate (0.5 mol dm<sup>-3</sup>) and acetic acid (0.5 mol dm<sup>-3</sup>). All kinetic experiments were performed with constant initial concentration 4.67 × 10<sup>-4</sup> mol dm<sup>-3</sup> nitrobenzene.

Britton-Robinson buffer at pH 1.81 was used as a supporting electrolyte in the case of trinitrophenol reduction. The composition of the buffer was the following: phosphoric acid (0.04 mol dm<sup>-3</sup>), acetic acid (0.04 mol dm<sup>-3</sup>) and boric acid (0.04 mol dm<sup>-3</sup>).

The initial concentration of trinitrophenol was kept constant on value  $2.44 \times 10^{-4} \text{ mol dm}^{-3}$ .

### III. RESULTS AND DISCUSION

For kinetic studies aromatic contaminants such as nitrobenzene and trinitrophenol were used, and iron powder with defined specific surface was used as reactive material. Reaction of aromatic contaminants with Fe powder was treated as kinetics of homogeneous reaction, using a pseudo first-order rate kinetic law. From preliminary experiments relation between kinetic parameters of reduction reaction and surface state as well as size of iron powder were found [4]. Reaction of contaminant with Fe powder always resulted in a decrease of contaminant concentration.

Nitrobenzene, as electroactive species, gives cathodic peak with potential  $-0.61 \text{ V}$  vs. reference electrode in acetate buffer. Based on the formulation of kinetic equation of first-order reaction, the values of rate constant were obtained from dependence  $\ln c_t/c_0$  versus time (where  $c_0$  is an initial concentration and  $c_t$  is an immediate concentration in time  $t$ ). Figure 1 presents above-mentioned dependence for nitrobenzene.

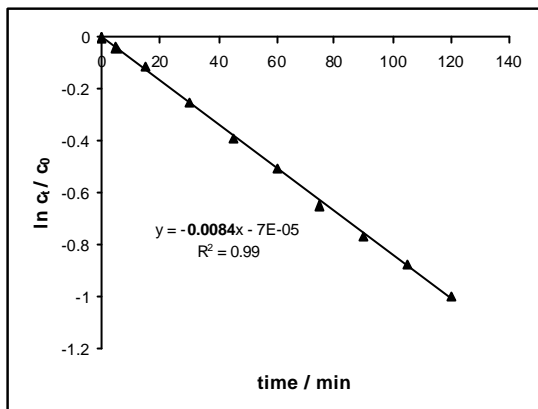


Figure 1: Time dependence of  $\ln c_t/c_0$  for nitrobenzene reduction in acetate buffer. Obtained value of rate constant is  $k = 0.84 \times 10^{-2} \text{ min}^{-1}$ .

Trinitrophenol is voltammetrically reduced in Britton–Robinson buffer. The height of the reduction peak at  $-0.05 \text{ V}$  vs.  $\text{Ag}/\text{AgCl}$  decreases continuously. Figure 2 enables to obtain the value of rate constant for trinitrophenol reduction. From the comparison of rate constant values for two contaminants in study is obvious, that reduction of nitrobenzene is slower than the same process for trinitrophenol.

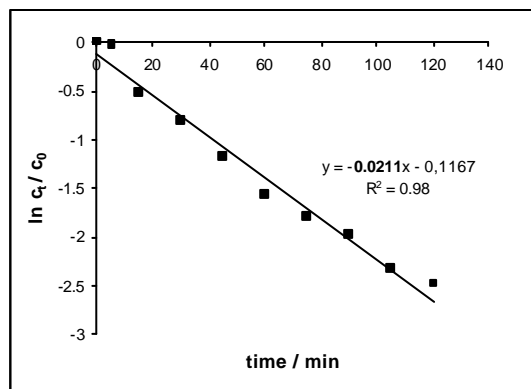


Figure 2: Time dependence of  $\ln c_t/c_0$  for trinitrophenol reduction in Britton - Robinson buffer. Obtained value of rate constant is  $k = 2.11 \times 10^{-2} \text{ min}^{-1}$ .

The precision of measurement of reactions rate by iron powder ranges from 3.15 to 13.73 %. Statistical evaluation of presented results shows that the method seems to be reliable for this purpose. Determined RSD values given for the studied powder materials with different granulometric description within one grain class are acceptable.

### ACKNOWLEDGMENTS

This work was supported partially by the Grant Agency of the Slovak Republic under projects No. 1/1108/04 and 1/2118/05 and by the APVT agency under project No.20-009404.

### REFERENCES

- [1] K. Bronstein. PRB for Inorganic and Radionuclid Contamination, Document for U.S.EPA, august 2005
- [2] M.M. Scherer, S. Richter, R.L. Valentine and P.J.J. Alvarez. Critical Reviews in Environmental Science and Technology, 30 (3), 363, 2000
- [3] Roehl et al. Keller Ground Remediation, U.S.EPA, 1998
- [4] D. Kladeková, M. Heželová, L. Lux and Š. Nižník. The effect of Iron Powder Surface on its Reduction of Nitrobenzene, Transactions of the Universities of Košice, 3-4, 54, 2004

# Using of Genetic Algorithms for Assessment of the Directing Discharge of Water from Reservoir

Lubomír Jaroš and Miloš Starý (Faculty Mentor)  
Institute of Landscape Water Management  
Brno University of Technology, Faculty of Civil Engineering  
Brno, the Czech republic  
Email: {jaros.l, stary.m}@fce.vutbr.cz

**Abstract** — *The contribution deals with assessment of the directing discharge of water from reservoir. For assessment of the directing discharge of water from reservoir was chosen the genetic algorithm method from large set of optimization methods. The solution was computed in MATLAB by Genetic Algorithm and Direct Search Toolbox. The main task of this contribution was verified efficient using of genetic algorithm for determination of the controlling quantity in our fictive reservoir model, which was demonstrated.*

## I. INTRODUCTION

Catastrophic floods in the year 1997 and 2002 invoked the positive change in consideration perception of flood protection in the Czech Republic. That displacement was amplified by large range of financial resources to clearance of claims caused by floods, which had to be expended from public budgets. Thousands of homes, buildings, and various operations have been destroyed or heavily damaged. Hundreds of thousands of people had to be evacuated and, most tragically, 92 people died. The efficient control of water outflow from reservoirs expressively conduces to landscape protection below the reservoir against flood discharges. The protection against floods is never absolute. We can partially decrease the maximum water discharge and highly affect flood hydrograph in the majority of cases. That's why we try to get such like arrangements to be able to decrease negative impacts of floods on the least boundary. These arrangements can classify into two main departments:

1. Structural arrangements - we can classify operations such as: water outflow velocity decreasing from a basin (changes of soil cover type, execution of infiltration belts, main ditches and them polder connections), construction of polders, controlled inundation etc. These arrangements are predominantly very financially sophisticated.
2. Non-structural arrangements - we could nominate warning flood system and effective water outflow operative controlling from reservoirs.

Realizations of these arrangements are considerably less financially sophisticated because we improve already existing systems.

## II. METHOD

The contribution deals with assessment of the directing discharge of water from reservoir. For assessment of the directing discharge of water from reservoir was chosen the genetic algorithm method from large set of optimization methods. The solution was computed in MATLAB by Genetic Algorithm and Direct Search Toolbox.

### A. FITNESS FUNCTION CREATION

To use the Genetic Algorithm and Direct Search Toolbox, you must first write an M-file that computes the function you want to optimize (fitness function). The M-file should accept a vector, whose length is the number of independent variables for the objective function, and return a scalar. In our case, the fitness function was solution of the basic reservoir equation by numerical method Runge-Kutta 4<sup>th</sup> order. The basic reservoir equation was formed

$$V'(t) = \frac{dV(t)}{dt} = Q(t) - O(H(V(t)); u) \quad (1)$$

where  $V(t)$  is state values (quantity),  $Q(t)$  is an input quantity,  $O(H(V(t)))$  is controlled quantity and  $u$  is an action setting (opening of bottom outlets). Reservoir inflow is considered faulty quantity  $z(t) = Q(t)$ , required outflow from the reservoir as a controlling quantity  $w(t)$ , a real controlled outflow as controlled quantity  $y(t) = O(H(V(t)); u)$  as we can see on "Figure 1".

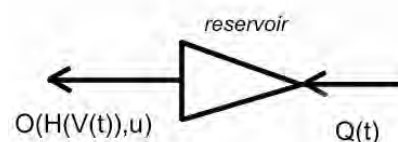


Figure 1: Reservoir scheme

## B. FUZZY REGULATOR TYPE

Used fuzzy regulator is PI (proportionally - integral) type. The describing equation of this regulator is substituted by rules contained in base of rules as follows:

$$\text{if } e = \langle \text{value} \rangle \text{ and } \Delta e = \langle \text{value} \rangle \\ \text{then } \Delta u = \langle \text{value} \rangle, \quad (2)$$

where  $e$  – regulation deviation between controlling and controlled outflow,  $\Delta e$  – change of regulation deviation,  $\Delta u$  – change of action opening (e.g. change of bottom outlets opening). New determined changes of action opening are thus given as sum of action opening in previous time step and  $\Delta u$  change. In regulator Mamdani fuzzy inference system is used. Defuzzification is done with method of area centre. Used membership functions of inputs and output quantities of fuzzy regulator are shown on “Figure 2”.

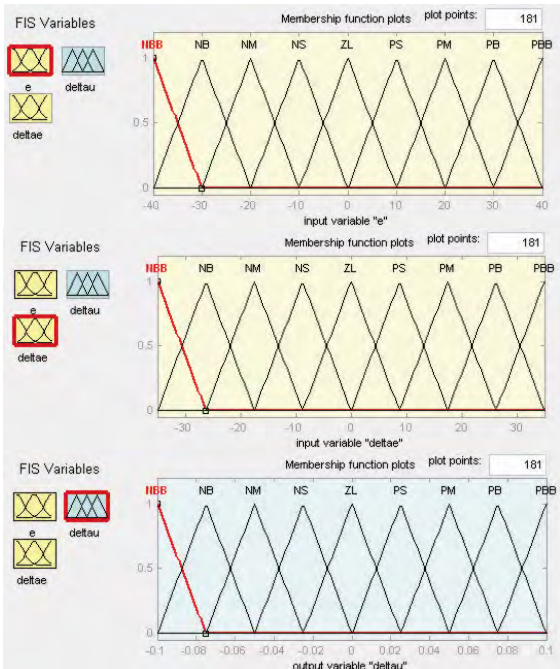


Figure 2: Membership functions of input and output quantities of fuzzy regulator

## III. CONCLUSION

Reached findings showed on “Figure 3”, that in theory the controlling quantity  $w(t)$  would be equal the maximum water discharge from reservoir. The result of controlling quantity  $w(t)$  calculated as  $331,8 \text{ m}^3 \text{ s}^{-1}$  by using the genetic algorithm and the good value of maximum water discharge from reservoir  $y(t)$  corresponded  $336,7 \text{ m}^3 \text{ s}^{-1}$ . In fact, the accuracy of this optimization is directly comparable with computing time length of the solution. The computing time length was equal 4,5 hours on PC AMD 1800+,

RAM 512 MB. This accuracy depends on fuzzy regulator accuracy too.

The main task of this contribution was verified efficient using of the genetic algorithm for determination of the controlling quantity in our fictive reservoir model, which was demonstrated. The disadvantage is only great time demand for optimization depending on accuracy of the solution.

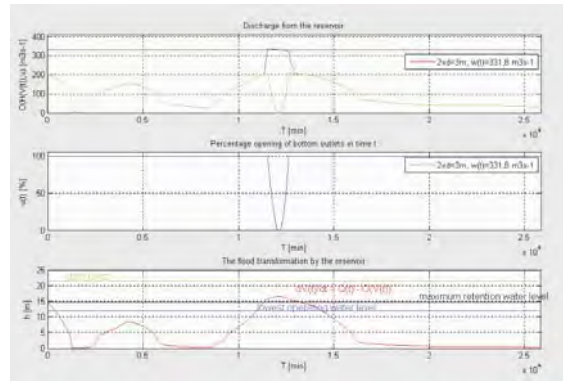


Figure 3: Discharge from reservoir and percentage opening of bottom outlets

## ACKNOWLEDGMENTS

The contribution was written as a part of - the GAČR project: 103/04/0352 Theory of Operative Control of Water Management Systems during the Flood Situations.

The results of research work presented in this paper were achieved partially with subsidization of the Ministry of education of Czech Republic, project 1M6840770001 - CIDEAS.

The contribution was written as a part of – the FRVŠ project: 1921/2006 Using Artificial Intelligence for Control Water Discharge from Reservoir during Flood Passage.

## REFERENCES

- [1] Matlab. *Genetic Algorithm and Direct Search Toolbox*. The Math Works, Natick, 1984-2005.
- [2] J. Dalík. *Numerické metody*. Brno University of Technology, the Academic Publisher CERM, Brno 1997, 145 p., ISBN 80-214-0646-1.
- [3] M. Starý. *Nádrže a vodohospodářské soustavy*. Brno University of Technology, the Academic Publisher CERM, Brno 1990, 165 p., ISBN 80-214-0191-5.
- [4] K. Nacházel and M. Starý and J. Zezulák. *Využití metod umělé inteligence ve vodním hospodářství*. Academia, Prague 2004, 319 p., ISBN 80-200-0229-4.

# New technology for processing of fly ashes

Veronika Kalova and Rostislav Drochytka (Faculty Mentor)  
Institute of Technology of Building Materials nad Components  
Brno University of Technology  
Brno, Czech Republic  
Email: {kalova.v,drochytka.r}@fce.vutbr.cz

**Abstract** — *The usage of industrial waste is economically and ecologically advantageous, it spares raw materials and energy. Annual production of fly ash was 1690 million tons in 2004 in Czech republic. It was used as a secondary raw material only 178 thousand tons. Fluidized fly ash is a product of a relatively new technology of combustion, so-called fluidized combustion. Fluidized fly ash is volume and temperature unstable. On this account it almost can't be used for production of building materials.*

*For the new technology of processing of sintered fly ash aggregate will be used fluidized fly ash. This paper provides details of a first period of the development in which it is searched mixtures suitable for processing of the aggregate.*

## I. INTRODUCTION

All of the high-tech countries make in last decades intensive research of processing capabilities of various kinds of waste as secondary raw materials. The usage of industrial waste is economically and ecologically advantageous, it spares raw materials and energy.

In Czech Republic there is more than 70% of heat energy obtained from coal combustion. It eventuates in relative high production of waste fly ash, which originates from coal combustion as a tough product. Annual production of fly ash was 1690 million tons in 2004. It was used as a secondary raw material only 178 thousand tons.

Properties of fly ashes are indeterminate and affected by quality of burned coal and by technology of combustion. Classical fly ash is a reaction product of a blast furnace combustion and can be used as a secondary raw material for variety of technologies in production of building materials. Fluidized fly ash is a product of a relatively new technology of combustion, so-called fluidized combustion. The problem is that the fluidized fly ash is volume and temperature

unstable. On this account it almost can't be used for production of building materials.

In Czech Republic the fly ash is used for processing concrete, mortar, cement and bricks. The using of fly ash for processing of artificial aggregate was ended a few years ago. Reason of this ending was obsolete and economically ineffective technology of processing. Nevertheless, the produced aggregate were in great range used for production of high quality light-concrete and common concrete too. Number of building companies gave an indication of this produced aggregate.

All these factors helps in generating renewed interest in innovating the technology of production sintered fly ash aggregate in Czech Republic.

## II. RAW MATERIALS

### A. FLUIDIZED FLY ASH

Fluidized fly ashes represent a new category of fly ashes, which are formed by fluidized combustion of powdered coal and lime stone or dolomit by temperature 850°C. This technology was developed for fuel gas desulphurization, it means removal of sulphur dioxide, which originates by burning of sulphur contained in coal. During the dissociative process the released  $SO_2$  is bound to the  $CaO$  by creation of  $CaSO_4$ .

Fluidized fly ashes are characterized by increased content of  $CaO$  (15 – 35%). According to the low temperature of combustion, free  $CaO$  exists in form of so-called soft burnt lime, it means it is reactive.[1]

### B. COAL MULLOCK

Raw materials should contain certain amount of combustible constituent, so that after firing and air inlet they are able to burn with themselves. For fly ash containing low content of combustible constituent it is used coal mullock as an addition.

### C. CLAY

Clay is cheap and appropriate binder to impart cohesive strength to the pelletized nodules.

## III. PRODUCTION METHOD

Sintered fly ash light-weight aggregate can be produced by mixing fly ash with clay and coal mullock (if they are used) and then nodulizing it in pelletizer with proportionate quantity of water. The balls are then dried and sintered under controlled temperature conditions. The hot sintered material is allowed to cool to room temperature and crushed in the jaw crusher. [2]

## IV. DEVELOPMENT OF MIXTURES

In the first period of the development it is searched mixtures suitable for processing of the aggregate. For these mixtures it is used classical and fluidized fly ashes from power stations and heating power stations from whole Czech Republic. It was compounded these mixtures:

- classical fly ash + water, with (10, 20%) or without clay,
- fluidized fly ash + water, with (10, 20%) or without clay,
- classical fly ash (90, 80, 70, 60%) + fluidized fly ash (10, 20, 30, 40%) + water, with or without clay.

It is made samples of dimensions 40x40x160mm from each mixture. After hardening the samples are dried in a drying plant by temperature 130°C and 170°C. Then the compressive strength, tensile strength and absorptivity are monitored. According to the results the suitability of the mixtures for processing the aggregate is evaluated.

## V. CONCLUSION

From measured values of compressive strength of mixtures with various ratio of classical and fluidized fly ash result, that increasing amount of **fluidized** fly ash increases compressive strength too. The highest strength reach mixtures with 100% of fluidized fly ash.

Influence of clay as addition is as follows. Generally we can say, that addition of clay to the

mixture with **fluidized** fly ash implicates decrease of compressive strength. On the contrary, mixtures with **classical** fly ash and clay have higher strength than mixtures without this addition. The strength rises with higher ratio of clay.

Dependence of compressive strength on temperature of drying is the same for mixtures with classical fly ash and fluidized fly ash too. Measured values reflect, that lower temperature of drying causes higher compressive strength.

In the next period of the development it will be examined influence of the indeterminate composition of individual kinds of fly ashes on the properties of mixtures. It also will be review the influence of chemical composition and physical properties of the fly ashes on the quality and the properties of the mixtures.

## ACKNOWLEDGMENTS

The paper was produced within grant GA 103/05/H044 „Stimulation of scientific development of PhD. students at department of building materials engineering” and within project MPO FI-IM2/183 „New technologies of processing and utilizing of sintered fly ash aggregate”.

## REFERENCES

- [1] P. Rovnanikova, P. Rovnanik. Anorganická chemie a chemie anorganických stavebních materiálů. CERM, Brno, Czech Republic, 1 st edition, 2005.
- [2] R. Drochytka. Lehké stavební latky. VUT Brno, Brno, Czech Republic, 1 st edition, 1998.

# Fluid dynamic and reaction modelling of the combustion reactor in a Dual Fluidized Bed biomass-steam gasification system

Priyanka Kaushal and Hermann Hofbauer

Institute of Chemical Engineering

Vienna University of Technology

Vienna, Austria

{pkaushal, hhofba}@mail.zserv.tuwien.ac.at

**Abstract** — *A one-dimensional steady state model of the combustion reactor of a dual fluidized bed biomass steam gasification system has been developed. The combustion reactor is operated as fast fluidized bed (riser) with staged air introduction (bottom, primary and secondary air). Parameter variation at the simulation model shows, that the residual char from the gasifier is only partly converted in the riser. Uncombusted char is circulated back into the gasification reactor and leads to an increase of char hold up in the dual fluidized bed system. The temperature profile predicted by the model is in good agreement with the values measured at 8 MW (fuel power) plant in Güssing/Austria.*

## I. INTRODUCTION

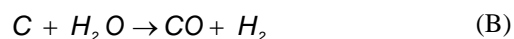
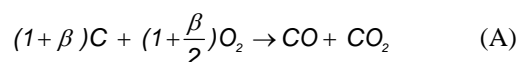
There is a large potential for biomass utilization as a renewable energy source. Efficient conversion of solid biomass (i.e. wood chips) to a medium calorific product gas by means of steam gasification allows the combined production of heat and power (CHP) [1]. Present work focuses on the mathematical modelling of the combustion reactor. The primary aim of this study was to develop a model in order to predict the gas phase concentration and temperature profile along the height of the reactor. Directly measured validation data from the Güssing plant is limited to several temperatures along the height of the riser and the final flue gas composition. Mass and energy balances for the entire plant yield most of the input parameters to the riser simulation: net char combustion rate, bed material circulation rate, estimated char composition, and validated air flow rates.

## II. MODELLING

The modelling task is the description of a fast fluidized bed reactor for combustion of partially volatile fuels. This is a one dimensional steady state model assuming gases as ideal and in plug flow regime. The mass transfer of gaseous species between emulsion and bubble is modelled using a mass transfer coefficient. The combustion reactor is

divided into two zones with different hydrodynamic characteristics: dense zone and transport zone. The transport zone is further divided into two zones – middle and upper zone. The main fuel is biomass char introduced together with the circulating bed material at the bottom of the riser. Char is modelled as a homogeneous matrix of C, H, and O. The combustion reactor also serves as a sink for spent organic solvent (biodiesel/biomass tar) emulsified in water, which is introduced into the middle zone. The solids within a zone are considered to be well mixed. Energy balance is solved in each zone which is assumed to be isothermal. Preheated air/additional fuel are introduced at the lower boundary of each zone. Each zone is further divided into cells. Each cell calculates its local hydrodynamic and thermodynamic state based on the theoretical principles. The cells are solved sequentially from bottom to top with the output of each cell considered as input for the next cell.

The dense zone (bubbling bed) is modelled according to the modified two phase theory[2]. Transport zone is modelled with core-annulus structure[3]. The gas flow rate typically changes with height and hence influences the hydrodynamic state of the system. Primary products of char combustion are CO and CO<sub>2</sub>. The oxygen and solid carbon reaction in a single step can be represented as (A), char gasification reaction (B) is also implemented and gains importance in under stoichiometric condition.  $\beta$  is a stoichiometric coefficient for char combustion describing the ratio of CO to CO<sub>2</sub> and is a function of surface temperature. The ratio of CO, CO<sub>2</sub> and H<sub>2</sub>O release is calculated from the combustion kinetics of carbon and balances of char. The carbon combustion model is based on the combined effects of gas film diffusion and reaction kinetics on a shrinking particle[4]. The hydrogen and oxygen contents of the char are released proportionally to the carbon release. For typical operation condition the gas phase composition along the height of riser is shown in Figure 1.



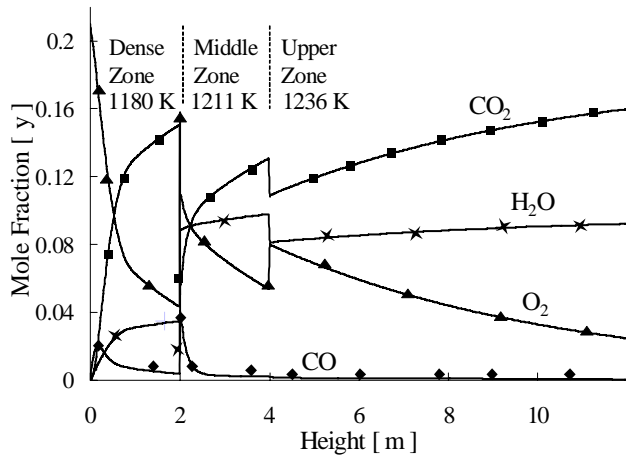


Figure 1: Average gas phase composition in the combustion reactor along the height of reactor

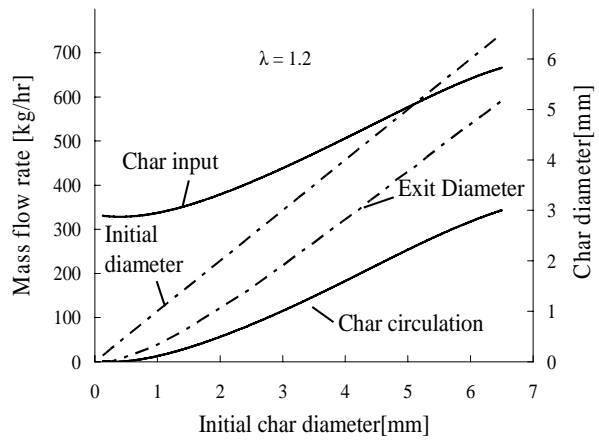


Figure 2: Char circulation as function of char input and initial char diameter (for air ratio of 1.2)

### III. CONCLUSION

A one dimensional steady state model is developed for the combustion reactor of a dual fluidized bed gasification unit. The model is based on the mass and energy balances and covers fluidized bed hydrodynamics and the kinetics of global reactions. Variation in mean particle size and char feed rate are simulated and the char circulation rate is the output of the model. It has been observed that for mean particle size  $> 0.6$  mm, the incoming char is only partly converted in the combustion reactor and is circulated back to the gasification reactor. The back circulation of char in gasification reactor is due to the incomplete combustion of char in combustion reactor while the incomplete combustion of char in combustion reactor is due to the lower residence time of solids in the combustion reactor. The simulation results show that within the operating range CO should always be below 0.1 vol% in the exhaust gas. The potentially higher values observed at the plant could be explained by a significant CO bypass in the riser due to insufficient gas mixing.

### ACKNOWLEDGEMENTS

The authors gratefully acknowledge the financial support from RENET Austria (Knet/Kind public funds program, Austria)

### REFERENCES

- [1] Hofbauer, H., Rauch, R., Bosch, K., Koch, R., Aichernig, C.: Biomass CHP Plant Güssing – A Success Story, Expert Meeting on Pyrolysis and Gasification of Biomass and Waste; Strasbourg, France, October 2002.
- [2] Johnsson, F., Andersson, S., and Leckner, B.: Expansion of a Freely Bubbling Fluidized Bed, Powder Technol., Vol. 68, pp. 117-123, 1991.
- [3] Löffler, G., Kaiser, S., Bosch, K. and Hofbauer, H.: Hydrodynamics of a dual fluidized-bed gasifier—Part I: Simulation of a riser with gas injection and diffuser, Chem. Eng. Sci., Vol. 58(18), pp. 4197-4213, 2003.
- [4] Winter, F., Wartha, C., Hofbauer, H.: Char acterization and emission of single fuel particles under FBC condition, 3rd Int. Conf. on Combustion Technologies for a Clean Environment, July 3-6, Liabon, Portugal, 1995

# Analysis of Humic Like Substances in Airborne Particulate Matter ( $< 10 \mu\text{m}$ ) from Sampling Sites in Austria and Selected Source Samples

Barbara Klatzer, Heidi Bauer und Hans Puxbaum  
Institute of Chemical Technologies and Analytics  
Vienna University of Technology  
Vienna, Austria  
Email: bklatzer@mail.tuwien.ac.at

**Abstract** — *Humic like substances in airborne particulate matter, with an aerodynamic diameter smaller than  $10 \mu\text{m}$ , are determined. The method used, is composed of two isolation steps of humic like substances and a carbon specific detection with a total organic carbon analyser. The samples analysed were taken at measurement sites of the Air Quality Networks of the Austrian local governments. In this work, results from Vienna, Salzburg and Graz are presented. Selected source samples were analysed with the same method aiming at more information about the origin of humic like substances in atmospheric aerosol.*

## I. INTRODUCTION

The climatic conditions on our planet are considerably influenced by atmospheric aerosol. By scattering or absorbing incoming or outgoing radiation the global radiation balance is directly affected. Absorption of radiation by atmospheric aerosol, results directly in a heating effect of the atmosphere whereas scattering is expected to have cooling effects. Indirectly, aerosols have an impact on the radiation balance, by their capability of cloud formation. These two effects are strongly dependent on the composition of the atmospheric aerosol what results in innumerable studies that are concerning the chemical composition of the atmospheric aerosol as well as formation processes. Although up to 50 % of the total mass of ambient aerosol is organic material, only a minor part is identified as specific organic substances [1]. The major contributors to continental organic aerosol are water-soluble macromolecular compounds with chemical characteristics very similar to those of naturally occurring humic acids and therefore called humic like substances or HULIS [2].

A unique method for quantification of humic like substances was developed lately at the Institute of Chemical Technologies and Analytics [3], Vienna University of Technology. This method is now

applied on environmental aerosol samples from urban and rural sampling sites in Wien, Graz and Salzburg and on source samples, which should shed light on the origin of airborne humic like substances.

## II. EXPERIMENTAL

The method is based on a two step isolation procedure of HULIS and the determination of HULIS carbon using a dissolved organic carbon analyser. For both, environmental and source samples, quartz fibre filters were used as a sampling substrate. These filters were extracted first with high-purity and organic free water and then a solution of diluted sodium hydroxide. Figure 1 depicts a schematic flow diagram of the procedure.

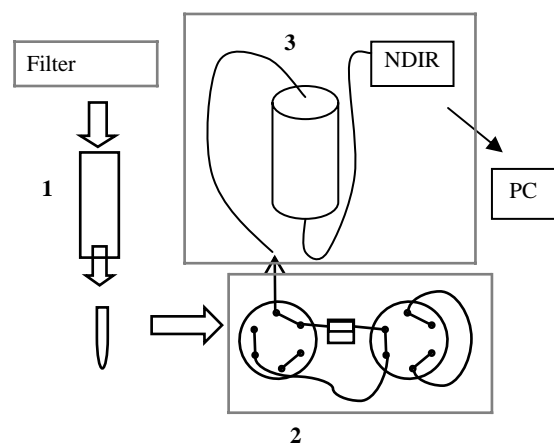


Figure 1: Schematic flow diagram

- One:** C18 polygosil column off-line separation and enrichment step
- Two:** Flow injection system: Ion-exchange column positioned between two six-way-valves
- Three:** Total organic carbon analyser composing of oven and NDIR detector

As a first separation/enrichment step (offline), the extracts were applied on a C18 polygosil solid phase extraction cartridge. The methanolic extracts gained after the first extraction step are then introduced in a flow injection system which is composed of two six-way-valves, a column filled with a strong ion exchanger (SAX), two hplc pumps and a sampling pump. This system is directly connected with the oven of the dissolved organic carbon analyser. The carbon dioxide formed during quantitative combustion at 800°C is then detected with a non-dispersive infrared detector. The online separation step ensures, that only carbon deriving from humic like substances is detected.

### III. RESULTS AND DISCUSSION

The sampling sites are official measurement sites of the Air Quality Networks of the Austrian local governments. Within this work, results of analysis of certain sampling sites from Vienna, Graz and Salzburg are presented. Samples were collected in rural and urban area from January to December 2004. It was found that up to 80% of the organic carbon in the aerosol is formed by HULIS carbon.

To get more clarity about the origin of chemical compounds occurring in atmospheric aerosol, source samples are analysed. Anthropogenic sources for which is assumed that they considerably contribute to the formation of humic like substances [4,5] are wood combustion and cooking. Analyses of aerosol samples deriving from meat broiling experiments gave up to 16 % of HULIS referring to the total mass. Results in the same magnitude were found for the wood smoke experiments. Meat cooking experiments in contrast just gave HULIS contributions to the total mass of around 1%.

### IV. OUTLOOK

Our working group of Environmental Chemistry at the Institute of Chemical Technologies and Analytics is taking part at an joint EU project called POLYSOA which is aiming the application and development of analytical methods to measure high molecular weight compounds in secondary organic aerosols. These SOA polymers will be applied on-line to cell culture systems to test the potentially negative effects SOA polymers may have on the human health. The part of our working group will be the development of an on-line HULIS analyser (based on the method described in this paper) and on-line HULIS measurements at smog-chamber experiments.

### V. REFERENCES

- [1] P.Saxena and L.M.Hildemann. Water-soluble organics in atmospheric particles: a critical review of the literature and application of thermodynamics to identify candidate compounds. *Journal of Atmospheric Chemistry*, 24 (1), 57-109, 1996.
- [2] N. Havers, P. Burba and J .Lambert. Spectroscopic Characterization of Humic-Like Substances in Airborne Particulate Matter. *Journal of Atmospheric Chemistry*, 29, 45-54,1998.
- [3] A. Limbeck, M. Handler, B. Neuberger, B. Klatzer and H. Puxbaum. Carbon-specific Analysis of Humic-like Substances in Atmospheric Aerosol and Precipitation Samples. *Analytical Chemistry*, 77 (22), 7288-7293,2005.
- [4] O.L. Mayol-Bracero, P. Guyon, B.Graham, G.Roberts. Water-soluble organic compounds in biomass burning aerosols over amazonia. *Journal of Geophysical Research*, D20(107), LBA 59-1 – 59-15, 202.
- [5] L. He, M. Hu, X. Huang, Measurement of emissions of fine particulate organic matter from Chinese cooking. *Atmospheric Environment*, 38, 6557-6564,2004.

# Monitoring of n-Alkanes and Polyaromatic Hydrocarbons in the Atmospheric Aerosols

Petra Kotianová<sup>1,2</sup>, Hans Puxbaum<sup>1</sup>, Heidi Bauer<sup>1</sup>, Gabriel Čík<sup>2</sup>

<sup>1</sup>Institute for Chemical Technologies and Analytics, Vienna University of Technology, Getreidemarkt 9/164/AC - Analytical Chemistry, A-1060 Vienna, Austria

<sup>2</sup>Department of Environmental Engineering, FCHFT, Slovak University of Technology, 812 37 Bratislava, Slovak Republic

Email: kotianov@centrum.sk

The topic of PhD thesis is determination of selected organic species in PM<sub>10</sub> fraction of the atmospheric aerosols and emission sources aerosol samples. The research helps to identify and quantify the main contributors to the particulate matter in the atmosphere. In the present paper is summarized one part of obtained results from the atmospheric aerosols analysis.

The aerosol samples were collected at background and inner-city sampling sites in Vienna, Graz, and Salzburg during 2004. Our interest was focused on non-polar and semi-polar organics. Polyaromatic hydrocarbons (benzo[e]pyrene, benzo[ghi]pyrene, coronene) and pattern of n-alkanes (C<sub>20</sub>-C<sub>38</sub>) are markers of vehicle exhaust. Retene can be used for monitoring of wood combustion and benzo(de)anthracene-7-one is typical for natural gas combustion.

Samples were from days, when the concentration of particulate matter in the atmosphere exceeded the EU short term standard for PM<sub>10</sub> (50 µg m<sup>-3</sup> daily mean). The atmospheric aerosol samples were collected on quartz fibre filters. The organic analytes were released by extraction with cyclohexane in ultrasonic bath. After sample treatment, target analytes are determined via gas chromatography-mass spectrometry.

PM<sub>10</sub> concentration is higher in colder months, January-April and November-December. Among the three towns, Graz had the highest PM<sub>10</sub> pollution.

Typically, the individual concentrations of n-alkanes C<sub>20</sub>-C<sub>38</sub> were up to 15 ng/m<sup>3</sup>. The highest concentration was obtained for C<sub>29</sub> in Graz, Don Bosco (55 ng/m<sup>3</sup> in April). The n-alkanes concentrations are lowest in winter season. Carbon preference index values showed a predominant contribution of fossil fuel sources during the colder time of the year. The concentration of n-alkanes increased from spring to autumn because of the additional strong source - vegetative detritus.

Data for polyaromatic hydrocarbons typical for vehicle exhaust correspond with results achieved for n-alkanes from fossil sources. Their concentrations do not varied in wide range over the year, but they are slightly higher in January, February, November, and December. The monthly mean concentrations of vehicle exhaust markers in majority of samples do not exceed 2.5 ng/m<sup>3</sup>. The highest one was measured for benzo(ghi)perylene (4,47 ng/m<sup>3</sup>) at Don Bosco sampling site Graz in November 2004.

The wood combustion tracer retene indicates a relatively small influence of wood burning in Vienna and Salzburg. In Graz higher amounts were observed over the year with a maximum during Easter fires in April (monthly mean concentration 3.68 ng/m<sup>3</sup>).

A higher concentration of benzo(de)anthracene-7-one were expected in winter season, as natural gas combustion is used for cooking all over the year and for heating in winter. Actually, benzo(de)anthracene-7-one showed somewhat higher concentrations in November, December, January, and February. The highest monthly mean concentration of 6.59 ng/m<sup>3</sup> was obtained at Don Bosco sampling site in Graz in February 2004.



# Optimisation of Sampling Design Programmes and Calibration of Water Distribution Models by Genetic Algorithms

Daniel Kozelj and Franci Steinman (Faculty Mentor)  
 Faculty of Civil and Geodetic Engineering  
 University of Ljubljana  
 Ljubljana, Slovenia  
 Email: daniel.kozelj@fgg.uni-lj.si

**Abstract** — *The abstract discusses the development of two optimisation modules for sampling design (SD) and calibration procedures of water distribution systems (WDS) by using genetic algorithms (GA) as the optimisation method. SD is a procedure to determine the optimal number and locations of sampling points for parameter identification of WDS models. GA Optimisation tools are used for solving demanding and comprehensive optimisation problems. GA are one of the optimisation tools based on the simulation of evolution processes and their basic mechanism, i.e. natural selection. The aforementioned modelling approaches were applied to a real WDS system of a part of the Slovenian capital Ljubljana.*

## I. INTRODUCTION

Most water utilities use mathematical models of water distribution systems (hereinafter referred to as “WDS”) for a number of different tasks to assist the development, rehabilitation and operational optimisation of the real WDS. Mathematical modelling of WDS is scientifically well developed discipline successfully finding place among other decision support tools. Until the WDS model is a correct presentation of the hydraulic behaviour of its real system numerous data needs to be collected and used in calibration procedures to correctly identify the unknown model parameters. Since good data is very valuable and costly, it is necessary to collect them due to the specific purpose of the model.

In the area of WDS model calibration, several approaches and methods were developed on the basis of both empirical and theoretical assumptions. One of them are implicit methods of calibration, which are formulated and solved as optimisation problems. For successful calibration of WDS models both quantity and quality of measurements have a great impact on model parameter accuracy, therefore a higher number of measurements provide a higher level of confidence in model prediction and parameter estimations.

To avoid that the WDS model is calibrated on the basis of limited measurements or “poor of information” an optimisation of the sampling design (herein-

after referred to as “SD”) problem needs to be applied. Since both, SD and calibration problem, are large and complex optimisation problems the use of genetic algorithms (hereinafter referred to as “GA”) as a robust and global search optimisation method is appropriate.

## II. CALIBRATION OF WDS MODELS

The calibration process is conducted to provide confidence in the predictions of the model, which will prove the actual operation of the water distribution system and will provide the designer with a reliable decision-making support. Calibration of WDS models is a procedure of determining individual unknown model parameters, which minimizes the differences between the measured system variables on a real WDS and the predicted system variables of the model. To provide both model parameter accuracy and realistic model behaviour great care has to be put into the modelling and measurement collection process.

The developed calibration approach is consisting of the “macro” and “micro” calibration level. The “macro” calibration allows the hydraulic model to become an approximation of the real system, by ensuring that the system variables are in reasonable agreement with collected measurements. At this stage all major possibilities of model discrepancies should be uncovered and resolved. Afterwards the “micro” calibration procedure is applied to identify the unknown model parameter values by using the optimisation method of GA. The objective of the calibration optimisation problem is expressed to allow minimisation of differences between measurements and model predictions:

$$\min E = \sqrt{\frac{\sum_{k=1}^{N_{Load}} \sum_{i=1}^{N_{MH}} (y_{ik}^* - y_{ik})^2}{N_{Load} * N_{MH}}} + \alpha \sqrt{\frac{\sum_{k=1}^{N_{Load}} \sum_{j=1}^{N_{MQ}} (y_{jk}^* - y_{jk})^2}{N_{Load} * N_{MQ}}} - P_e \quad (1)$$

Equation (1) is consisting of three parts, where the first is evaluating pressure differences, the weighted second flow differences and a penalty function.

### III. SAMPLING DESIGN FOR CALIBRATION OF WDS MODELS

The main emphasis of SD optimisation is focused on the determination of optimal measurement locations, where hydraulic quantities are to be observed. The formulation of the SD problem has to be considered with regard to two objectives. The first objective is to obtain representative measurement points for model parameter calibration, and the second objective is to minimise the costs related to the measurement collection process. Since the above-mentioned objectives are mutually contradictory, a solution has to be found which will to the largest extent possible satisfy both objectives.

#### A. CALIBRATION PARAMETER ACCURACY

The first objective function is determined as a function, the purpose of which is to assess the accuracy of hydraulic model parameter values. The aforementioned assessment is done by determining the parameter's confidence region volume. The basis of evaluating SD schemes is the parameter confidence region, which is proportional to the square root of the determinant of the covariance matrix of model parameters. Since the first objective function will be joined with the second objective function, it is appropriate to normalise the evaluated SD scheme with the determinant of the inverse covariance matrix of all potential measurement locations:

$$\max F_1 = \left[ \frac{\det Cov_a^{-1}}{\det Cov_a^{-1}_{full}} \right]^{\frac{1}{2n}} \quad (2)$$

#### B. MEASUREMENT COSTS

In addition to the optimisation of calibration parameter accuracy, the second objective function is taking into account and optimising the costs related to the measurements performed on a system. Its purpose is to minimize the measurement costs and indirectly also the number of measurement locations. The mathematical formulation of the normalized second objective function is the following:

$$\max F_2 = 1 - \frac{N}{N_{full}} \quad (3)$$

The optimisation problem formulation for SD consists of the normalised expressions in (2) and (3) formulated so as to maximise their values are joined into a single expression:

$$\max E = \left( \sum_{i=1}^2 w_i * F_i^p \right)^{1/p} - Pe \quad (4)$$

### IV. APPLICATION AND RESULTS

The optimisation tool of the calibration problem has been applied to the water distribution system of Ljubljana. The aim of the analysis was to calibrate the assembled model to predict system variables as accurately as possible. The calibration optimisation tool has been developed to identify: a) nodal demand at extended period simulation and b) pipe roughness values at steady-state simulations. In both cases GA have been applied as the optimisation method.

Optimising the nodal demands and afterwards the pipe roughness values of the WDS model resulted in a root mean squared error (referred to as "RMS") of pressures of 0.971 (correlation of 1.000) and RMS of flows 2.303 (correlation of 0.999). Results of the calibration process are within of the calibration guidelines and can be thus assessed as successful.

Since the SD scheme of the previous calibration process was carried out according to the "ad hoc" principle, the optimisation of the SD problem was performed to assure quality measurements and therefore a higher level of parameter accuracy for a future calibration.

Out of 95 possible pressure measurement locations the optimisation tool of the SD problem identified 13 locations to be optimal. The selected measurement locations have the highest pressure sensitivities according to model parameter changes and therefore provide most "information" for calibrating model parameters.

### V. CONCLUSION

It can be concluded that the SD and calibration optimisation modules of WDS models were successfully applied to the WDS model of Ljubljana and the optimisation method of GA has proven its robustness in identifying near optimal solutions of the defined optimisation problems.

### REFERENCES

- [1] Ormsbee et al. Calibrating Hydraulic Network Models. Journal AWWA, 89(2):42–50, 1997.
- [2] Kapelan, Z. et al. Multiobjective Sampling Design for Water Distribution Model Calibration. Jour. of Water Resources Planning and Management, 129(6):466–479, November 2003.
- [3] Lansey, K.E. et al. Calibration Assessment and Data Collection for Water Distribution Networks, Jour. of Hydraulic Engineering, 127(4): 270–279, April 2001.
- [4] Goldberg, D.E. Genetic Algorithms in Search, Optimization and Machine Learning, Addison-Wesley Publishing Company, USA, 1989.

# Multi-criteria optimization as a support by the rehabilitation planning of the water mains

Tomas Kucera and Ladislav Tuhovcak (Faculty Mentor)  
Institute of Municipal Water Management, Faculty of Civil Engineering  
Brno University of Technology  
Brno, Czech Republic  
Email: {kucera.t, tuhovcak.l}@fce.vutbr.cz

**Abstract** — *The paper describes the methodology for the making of the annual rehabilitation plans of the water distribution networks. At first, the values of criteria are estimated and calculated for each pipe section in the evaluated network. At first, the pipes are sorted or ranked. At second, the best rehab technology for each pipe section is recommended. Both of the steps of the process are doing by the means of the multi-criteria optimization methods.*

## I. INTRODUCTION

The rehabilitation planning can be seen in three time horizon. At first, it is long term strategy, which is to appoint the rehab objectives and the volume of investments for 15 to 20 years. At second, we can consider the middle term plan, which is usually made for 3 to 5 years. The purpose of the middle term plan is to choose some part of the water-supply for rehab action. At last, it is the short term planning, which is called annual.

## II. ANNUAL REHABILITATION PROCESS

This research work deals with the annual rehabilitation planning of the water mains. The main objective by the rehabilitation planning of any system (for example water mains) is to propose some set of elements as the candidates for rehabilitation. The second objective in this activity is to select right technology for every chose element. The mentioned objectives can be attained by designed process, which is a sequence of several steps:

- definition of the basic elements of the water networks, which are considered in the short-term planning,
- definition of a set of criteria and their acquirement for the evaluation of each element,
- determination of the input data and their obtaining,
- using of the multi-criteria optimisation method for the ranking of evaluated elements,

- proposal of a set of elements for rehabilitation by means of multi-criteria method,
- selection of the right rehab technology for each of the elements recommended for rehabilitation.

### A. BASIC ELEMENTS

In this process, we can consider the hydraulic sections or entities as the basic elements. The hydraulic sections are not favourable for this purpose, because they are often too short. A better approach is to define new elements – these are called entities here. Entity is meant to represent a continuous part of the water network, which is composed of several hydraulic sections with the same parameters.

### B. CRITERIA SET

The very important part of the rehab planning is a choosing of the criteria set, because the selecting and proposal to rehabilitation is dependent on its. By the design of the criteria set, the interest of the operator, the customers and the road users have to be considered, for example: repair cost, water leakage, water quality and hydraulic deficiencies, life time or failure rate.

### C. MULTI-CRITERIA ASSESSMENT

For the select a set of some elements (pipe-sections, entities) for rehabilitation, we can use multi-criteria decision analysis. The selection (for the definition of an annual programme) can be seen as:

- **Sorting procedure:** a score is calculated for each element based on the values of the considered criteria, the elements are sorted into the sort list. The most popular multi-criteria technique is represented by the method of average weighting.
- **Ranking procedure:** elements are compared to each other in pairs according to the values of criteria. Each element is assigned to one of pre-defined categories, which are defined in a hierarchical order. There is no distinction among

elements that are assigned to the same category. The Electre methods have been developed for the ranking procedure. The elements are compared successively to reference profiles for their assignment to a category within Electre Tri.

Thus, by means of a multi-criteria decision analyses, the pipe-sections which are the most cost-efficient for reconstruction can be highlighted and recommended for rehabilitation, and the most suitable rehabilitation technology can be recommended as well.

#### D. CHOOSING OF THE REHAB TECHNOLOGY

The assigning of the right rehab technology to each element is done on basis of the database of the rehabilitation methods, which was designed for this purpose. This database includes the common open-trench and also the trenchless technologies, which are acceptable for the water mains rehabilitation.

The database includes the description of all rehab technologies for water mains in the matrix. The following data will be available for each technology in the mentioned database:

- applicability (what material is applicable for, minimum and maximum diameter),
- costs (unit cost of rehabilitation or repair),
- influence on environment (traffic disruption, dynamic load by rehabilitation, number of holes), on pipe material (corrosion protection, limitation of the incrustation, load-carrying capacity improvement, seal of crack, seal of leakage at sockets), on water quality, on hydraulic properties (roughness changing, diameter changing),
- supplemental information (maximum length of pipe-section, realisation time, armature removing).

The selection of the right rehab method will be made by the interactive elimination according to the values of the calculated criteria.

### III. CONCLUSIONS

The main goal of this research is to design of methodology for annual rehabilitation planning with the using of multi-criteria decision analyses. Necessary steps by this activity are: the design of criteria set for elements selection, the design of the database of the water mains rehabilitation technologies.

### REFERENCES

- [1] Belton, V., Stewart, T. J., 2002: *Multiple Criteria Decision Analysis: An Integrated Approach*. Dordrecht: Kluwer Academic Publishers. ISBN 0-7923-7505-X.
- [2] Le Gauffre, P., Baur, R., Laffréchine, K., 2002: *Multicriteria decision support for annual rehabilitation programmes*. Proceedings of International Conference “Computer Rehabilitation of Water Networks CARE-W”. Dresden: TU Dresden. ISBN 3-86005-335-3.
- [3] Engelhardt, M., O., Skipworth, P., J., Savic, D., A., Saul, A., J., Walters, G., A., 2000: *Rehabilitation strategies for water distribution networks: a literature review with a UK perspective*. Urban Water, vol. 2, no. 2, p. 153-170.
- [4] Tuhovcak, L., Vrbkova, P., Kucera, T., Rucka, J., Viscor, P., 2003: *CARE-W: WP6 - Testing and Evaluation of CARE-W Prototype: Final report from the testing of the CARE-W Prototype and its tools*. Report. Brno.

# Decision Support for the Rehabilitation Planning of the Sewer Network

Stanislav Malanik and Petr Hlavinek (Faculty Mentor)  
Institute of Municipal Water Management  
Brno University of Technology, Faculty of Civil Engineering  
Brno, Czech Republic  
Email: {malanik.s,hlavinek.p}@fce.vutbr.cz

**Abstract** — *The main objective of the owners or operators of sewer networks is to reduce their maintenance cost. For this purpose, having the support tool is advantageous. This tool can be subservient to evaluate the condition of pipes by the chose parameters. The selection of right rehabilitation technology is doing on the basis of that evaluation. The good possibility to reach this objective is to use some multi-criteria decision support by the choosing some troubles pipes for rehabilitation. Multi-criteria decision support methods are most applicable for a decision making by the choosing of optimal alternative of sewer pipe rehabilitation. The optimal alternative is represented as one or more pipes of sewer network. However, the user (expert) has to do the definitive decision.*

## I. MULTI-CRITERIA DECISION SYSTEMS

The multi-criteria decision support is the modelling of the decision-making situation. In every situation, the set of variations and set of criteria are defined. The criteria are helpful for evaluation of pipe condition and they are chose or used by the priority of the sewer network operator. The expression of the relation between the criteria is very important in this process.

## II. CRITERIA FOR THE CONDITION ASSESSMENT OF THE SEWER PIPES AND THEIR COMPUTATION

The extensive set of criteria is applicable for rehabilitation planning. Some criterion is the function of the cost, another one is depended on the pipe technical or hydraulic condition. The value of criterion can be expressed as a costs, risk or contribution to potentials problems in the area. We can consider the interest of sewer network operator, of customers or of another persons and the reducing of cost by the coincident rehabilitation of couple of pipes (water, sewer, gas, etc.).

## III. CRITERIA FOR THE SEWER NETWORKS

Some criteria are presented in the next part. It is possible to divide the criteria by they importance. At the Brno University, the questionnaire was done among the sewer networks operators in the Czech Republic for the determination of an importance of each criterion. Those criteria was used in CARE-S project and designed by the experts, for example [5]:

- Number of failures
- Hydraulic capacity
- Amount of ballast water
- Condition by the camera control
- Year of laid,
- Loading of pipe
- Chemical composition of waste water
- Pipe material
- Hydraulic condition
- Etc.

## IV. EVALUATION OF THE VARIANTS BY THE MULTI-CRITERIA METHODS

A lot of multi-criteria methods for evaluation of variants are available. Those methods have a general character, which is not depended on the content of the decision-making process. The most popular methods are:

- WSA (Weighted Sum Approach)
- TOPSIS (Technique for Order Preference by Similarity to Ideal Solution)
- ELECTRE methods (ELimination and Choice Expressing the REALity)

## V. MODIFIED CASE STUDY

The methodology “WSA” was used for the evaluation. An example for the sewer network is presented here. In this case, ten pipes were considered “Table

1”. For example, I have defined the following criteria:

- Number of failures – K1 [number of failures per km and year]
- Year of laid – K2 [year]
- Hydraulic capacity – K3 [filling level]
- Coordination with other network – K4 [the Next Building is planning or was done previously]

Pipe $a_i$	Criteria			
	K1	K2	K3	K4
1.	0,23	84	0,16	0
2.	1,86	73	0,55	1
3.	0,2	9	0,81	1
4.	0,64	83	0,71	0
5.	1,12	78	0,43	0,5
6.	0,56	39	0,32	1
7.	0,25	10	0,91	0
8.	0,43	11	0,86	0
9.	1,99	16	0,72	1
10.	0,78	1	0,44	0,5
<b>Weight <math>w_j</math></b>	<b>0,182</b>	<b>0,455</b>	<b>0,273</b>	<b>0,091</b>

Table 1: Input data

Pipe $a_i$	Normalized matrix of alternatives				u(alt.)
	K1	K2	K3	K4	
1.	0,017	1,000	0,000	1,000	<b>0,549</b>
2.	0,927	0,867	0,520	0,000	<b>0,705</b>
3.	0,000	0,096	0,867	0,000	<b>0,280</b>
4.	0,246	0,988	0,733	1,000	<b>0,785</b>
5.	0,514	0,928	0,360	0,500	<b>0,659</b>
6.	0,201	0,458	0,213	0,000	<b>0,303</b>
7.	0,028	0,108	1,000	1,000	<b>0,418</b>
8.	0,128	0,120	0,933	1,000	<b>0,424</b>
9.	1,000	0,181	0,747	0,000	<b>0,468</b>
10.	0,324	0,000	0,373	0,500	<b>0,206</b>
<b>Weight <math>w_j</math></b>	<b>0,182</b>	<b>0,455</b>	<b>0,273</b>	<b>0,091</b>	<b>1,000</b>

Table 2: Choice of right alternatives

The score was calculated for each pipe (value of the function  $u$ ) as a product sum of the normalized criteria values and their weights. The sorting of pipes is doing based on this function. In this case, the pipe with the higher value is preferred by the reconstruction. Its reconstruction is more suitable. Based on the “Table 2”, the pipes no. 4 is more suitable for the reconstruction.

## VI. CONCLUSIONS

The order of sewer network pipes, which can be determinate by the means of one of multi-criteria methods, is depended on the importance of each

criterion and on the used multi-criteria method. The using of more methods is eligible to check of the order sensitivity with regard to used methods. Only the variant, which is on first position by the means of the free method, is most favourable for rehabilitation.

## REFERENCES

- [1] Roy, B. Multicriteria Methodology for Decision Aiding, Note: Original version in French “Méthodologie multicritère d'aide à la décision, Economica”, Paris 1985.
- [2] Hwang, C.L. and Yoon, K. Multiple attribut decision making: Methods and applications. Springer-Verlag, Berlin 1981.
- [3] Rolf Baur, Raimund Herz and Ingo Kropp. Procedure for Choosing the Right Sewer Rehabilitation Technology, CARE-S (Computer Aided REhabilitation of Sewer networks), Report WP6, Dresden, December 2003.
- [4] Fiala, P., Jablonsky, J. and Manas, M. Vicekriterialni rozhodovani. VSE v Praze, 314 s, 1997, ISBN 80-7079-748-7.
- [5] Malanik, S., Nosek, R. and Raclavsky, J. Kriteria pro vyber optimalni strategie obnovy stokovych siti, 9. konference o bezvykopovych technologiich NO-DIG, p. 26 – 31, Znojmo 2004.

# Possibilities of waste raw materials – fly ash in special application in civil engineering

Pavla Matulova, Gabriela Michalcova, (Rostislav Drochytka)  
Institute of Technology of Building Materials and Components  
Brno University of Technology  
Brno, Czech Republic

Email: matulova.p@fce.vutbr.cz, michalcova.g@fce.vutbr.cz

**Abstract** — *This paper describes the special application of using fly ash in grouting materials, wall facings and in repair materials. Continuous expansion of industrial production in the recent past has resulted in a huge growth in production of waste materials. Large volumes of industrial waste lead to creation of various waste dumps and to their ecological unwholesomeness. For these reasons we constantly search for new methods of exploitation of waste raw materials. One of the advantages of these newly developed materials with fly ash is their low acquisition cost. Utilisation of fly ash as fillers in new progressive materials also represents a great benefit for our environment.*

## I. FLY ASH- DESCRIPTION OF APPLIED MATERIALS

The properties of the fly ash depend on the quality of fired fuel, on the combustion process and on the type of separators. The most appropriate fly ash is formed during the combustion of black coal and has the form of small glass balls. In the case of large scale sources the quality of the fly ash is comparatively stable.

The dominant components of the fly ash matrix are  $\text{SiO}_2$  and  $\text{Al}_2\text{O}_3$  in the ratio of about 2:1. These components form up to 80 % of the fly ash mass. The further important component is  $\text{Fe}_2\text{O}_3$  in average up to about 10 %. Iron can be present even in the form of  $\text{FeO}$ . The oxides  $\text{CaO}$ ,  $\text{MgO}$ ,  $\text{TiO}_2$ ,  $\text{K}_2\text{O}$  are present in the order of units under 5 %.

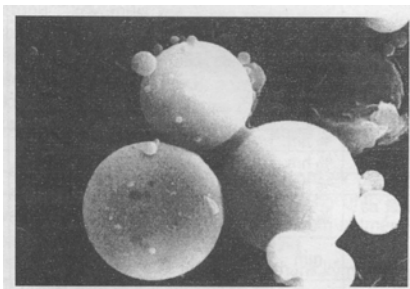


Figure 1: Optical microscope image shows fly ash (enlarged 15000x)

## II. POSSIBILITIES OF WASTE RAW MATERIALS APPLICATION IN GROUTING MATERIALS

Problem in foundation engineering is the unstable subsoil with low bearing capacity. The stabilization of geological subsoil by grouting mixtures, in places where the original subsoil doesn't have the demanded bearing capacity is a technology known already for more decades. It concerns the pumping process of liquid with changeable viscosity into the soil, into disintegrated soil or concrete with the aim to decrease the permeability. Clay-cement or purely cement suspensions were formerly used for this purpose. The endeavour or trend of the last years is the utilization of economically not demanding waste materials. This is the advantageous utilization of these materials exactly into grouting mixtures for the stabilization of subsoil or for filling of bulk caverns.

### A. METHOD OF REALIZED WORKS

Formulae were designed with the substitution of filler by 10 till 50% of waste materials. The reference mixture was the concentrate mixture (cement, bentonite, special admixtures) and quartz sand. We have performed the experimental verification of the partial substitution effect of filler by the grouting mixture. The fresh mixtures of all selected formulae were tested by following basic tests: Consistency of the mixture, initial and final setting time, bending strength on test pieces (40/40/160 mm), compression strength on test pieces (40/40/160 mm), volume mass, shrinkage during hardening on test pieces (40/40/160 mm). The filler (quartz sand) was substituted by fly ash.

### B. CONCLUSION

The grouting materials containing waste materials fulfil and in some properties significantly exceed the demanded values, expressed by the reference material. It was further proved that it is possible with the suitably selected substitution of the original filler by waste materials to manufacture grouting materials for utilization in practice which fulfil the given condi-

tions. The demanded minimum bending strength values (1-2 MPa) and the compression strength values (5-7 MPa) were exceeded in the case of all waste materials. The greatest bending strength achieved the mixture with the mixture with 40 % of fly ash. This is caused by the grain size composition of the filler (the nearer is this composition to the ideal grain size curve, the better strength values should show the formulae) and also by the perfect distribution of the grains (no sedimentation takes place).

### III. POSSIBILITIES OF WASTE RAW MATERIALS APPLICATION IN WALL FACINGS

At Institute of Technology of Building Materials and Components at Brno University of Technology we are developing new thin wall facings where the filler was substituted by fly ash. One of the most important characteristic of this material is absorbability. Formulae were designed with the substitution of filler by 10 till 50% of fly ash.

### IV. POSSIBILITIES OF WASTE RAW MATERIALS APPLICATION IN REPAIR MATERIALS

Repair materials are supposed to re-profile concrete structural elements into their original shape, or to renew or increase the thickness of the liner layer above reinforcement, or possibly to statically strengthen the structure. They primarily serve for renewal of durability of concrete elements and for reinstatement of their initial appearance.

Repair materials must satisfy in particular the following requirements: high adhesiveness to the basic material, good waterproofing and frost resistance properties, minimal volume change as consequences of changes in humidity and temperature, limited formation of shrinkage cracks, low modulus of elasticity, high compressive and tensile strength during bending conditions, resistance to aggressive media in relation to specific exposure conditions, etc.

#### A. METHOD OF REALIZED WORKS

First the mixes of repair materials with fly ash have been proposed and reference (waste free) mixes as proposed by Lena Chemical Ltd., Šternberk, Czech Republic, have been selected. Reference mixes and newly proposed mixes have been subjected to basic quality testing: cohesion to the base material, tensile strength during bending and compressive strength. Mixes suitable for further testing have been selected on the basis of those initial tests. Further supplementary testing has been carried out: water tightness, absorbability, wearability, frost resistance, modulus

of elasticity under conditions of bending, resistance to UV radiation, specific gravity, cohesion to wet base material and permeability for water vapour and carbon dioxide. Not all type of tests and requirements on quality of material for rehabilitation of concrete structures are mentioned in standards. The Association for Rehabilitation of Concrete Structures has published Technical Conditions for Rehabilitation of Concrete Structures; it describes types of tests, testing procedures and minimal required values for materials to be used in the field of rehabilitation of concrete structures. The publication replaces standards and all repair materials containing industrial waste products must comply with the requirements stated there.

#### B. CONCLUSION

Comparison of test results obtained from test specimens of individual mixtures and of the values as given in the publication Technical Conditions for Rehabilitation of Concrete Structures provides the finding that mixtures with fly ash satisfy, and sometimes even significantly exceed, the thus required values.

#### ACKNOWLEDGMENTS

The given problems are solved in the framework of the Grant Project no. 103/05/H044 called: "Stimulation of Doctorands Scientific Development in the Branch of Building-Materials Engineering" and in the framework of the research project MSM 0021630511 called: "Progressive Building Materials with Utilization of Secondary Raw Materials and their Effect on Service Life of Structures". And project Tandem č.FT-TA 2/076.

#### REFERENCES

- [1] Emmons, P.H., Drochytka, R., Jeřábek, Z. Rehabilitation and Maintenance of Concrete in Pictures. CERM, Brno, Czech Republic, 1999 (in Czech).
- [2] Drochytka, R., Dohnálek, J., Bydžovský, J., Pumpr, V. Technical Conditions for Rehabilitation of Concrete Structures. BEKROS, Brno, Czech Republic, 2003 (in Czech).
- [3] Smýkalová, R. Development of Grouting Materials with Utilization of Waste Raw Materials. Graduation Thesis, Brno UT, Czech Republic, 2005 (in Czech).
- [4] Michalcová, G. Modification of Epoxy Screed and Repair Materials with Waste Fillers. Graduation Thesis, Brno UT, Czech Republic, 2003 (in Czech).

# Mitigation of Energy Loss and CO<sub>2</sub> Emission from the Building Stock

Martin Mohapl and Petr Lizal (Faculty Mentor)

Faculty of civil engineering  
Brno university of technology  
Brno, Czech Republic

Email: mohapl@centrum.cz

**Abstract** — This article deals with impact of european EPB Directive (2002/91/EC). Overall energy performance improvements including better insulation, improved efficiency of heating and cooling systems and energy generation systems are key objective of the Directive. Minimized energy loss lead up to mitigation of CO<sub>2</sub> emission. The main energy saving potential lies in the existing building stock. Newly built houses are generally already built in compliance to national performance standard and therefore exhibit inherently small savings potential in CO<sub>2</sub> emissions. The article analyses energy losses of existing building stock.

## I. INTRODUCTION

From the 40% contribution made by the building sector towards end energy consumption in the EU, the EPB Directive (2002/91/EC) [2] aims to contribute to the Members States joint commitment under the Kyoto Protocol [1], an 8% reduction in greenhouse gas emission by 2010.

## II. ENERGY LOSS

Energy loss from the buildings depends on proportions of construction, shape of roof, format of built up area, etc. But generally ways of energy losses describes Figure 1.

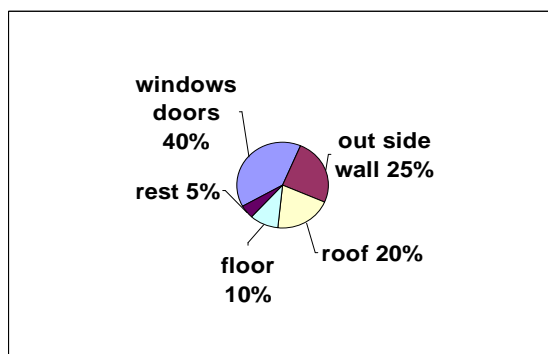


Figure 1: Energy loss

This loss must be met a energy for heating and cooling. The production of energy brings CO<sub>2</sub> emission. Value of CO<sub>2</sub> emission depends on source of energy.

Energy carrier	Emission factor [g/kWh]
Gas	202
Oil	266
Coal	338
Electricity	610
Wood	20
District heating (Czech Rep)	285

Table 1: Factors of different end-energy carriers[3]

## III. CO<sub>2</sub> EMISSION FROM THE BUILDING STOCK

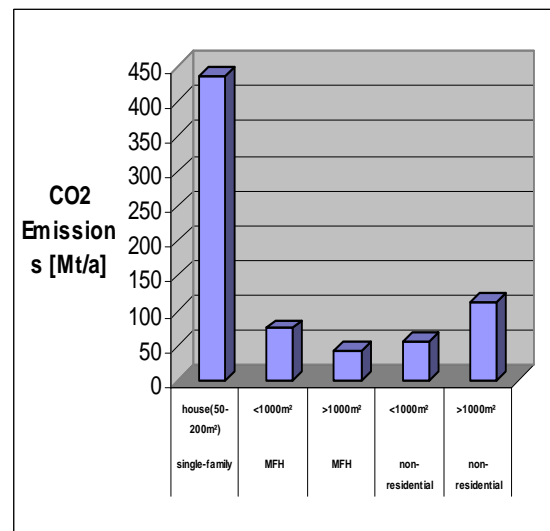


Figure 2: CO<sub>2</sub> emission of the European building stock 2002 [4]

#### IV. APPLIKATION OF EPB DIRECTIVE (2002/91/EC)

The EU Energy Performance of Buildings Directive came into force on 16 December 2002 and requires implementation in the legislation of the EU Members States by 4 January 2006. Four main elements define the requirements which need to be intergrated into national legislation:

- Establishment of a methodology for an interated calculation of the overall energy performance of buildings;
- Definition of minimum energy-efficiency requirements per Member State based on this methodology,
- Energy-efficiency certification of new and existing buildings;
- Regular inspection of heating and air-conditioning systems.

#### REFERENCES

- [1] Kyoto Protocol to the United Nations Framework Convention on Climate Change (1997)
- [2] EPB Directive (2002/91/EC)
- [3] Petersdorf Carsten, Cost-Effective Climate Protection in the Building Stock of the New EU Members States
- [4] Petersdorf Carsten, Boermans Thomas. Energy model Ecofys

# New Materials in Old Buildings - The Problem of Heat Flow and Vapour Diffusion through Walls (Facades)

Iva Muraj, M.Sc., Dipl.Eng.Arch. and Prof. Jasenka Bertol-Vrček, Ph.D., Dipl.Eng.Arch.  
Faculty of Architecture  
University of Zagreb  
Zagreb, Croatia  
Email: iva.muraj@arhitekt.hr

**Abstract** — *The renovation of old buildings and the preservation of protected historic buildings can provide sufficient savings in thermal energy consumption. Most of old houses were constructed without any thermal insulation. The greatest savings can be achieved by thermal renovation of the facades.*

*The renovation project of small “Sokol” gym hall built 1933 in Zagreb (designed by the Croatian architect Egon Steinmann) shows how the problem of heat flow and vapour diffusion through walls (facades) can easily be solved by adequate use of new materials.*

## I. INTRODUCTION

Architecture of 21<sup>st</sup> century has to give answers to some new requirements. It has to be technically correct; it has to maintain reasonable consumption and living standards. Responsibility became the key word in the architecture of the future if it wants to serve all the future generations. The employment of the most modern and ecologically acceptable techniques, materials and technologies that do not pollute the environment are needed. Science in sustainable architecture has achieved level which, when applied, can attain considerable contribution in decreasing emission of greenhouse gases. Some well-known facts are [1]:

- The building construction entails 40% of the total energy consumption
- Energy used for heating is accounted for 50-60% of total energy used in buildings
- Heat losses through windows and doors represent 70% of all thermal building losses
- Thermal insulation of the whole building envelope can reduce the energy consumption by 50-80%

Therefore priority is laid on renovation of existing buildings and implementing new systems such as implementing the insulating layer of outer walls.

## II. HEAT FLOW AND VAPOUR DIFFUSION IN OLD BUILDINGS

The starting point for this research project was the “Sokol” gym hall designed by Croatian architect Egon Steinmann (1901-1966) in the inner city of Zagreb (1933-1934). This small sports hall was built seventy years ago and until today it hasn't been adequately renovated and maintained. During this long period, it was exposed to a lot of controlled and uncontrolled renovation work. Today it serves University of Zagreb and its eight Faculties for student's physical education [2]. The compact building was built according to building structure achievements of Modernism. It consists of frame reinforced concrete loadbearing structure filled up with brick but without thermal protection. In winter time through walls and roof with outdated installations for heating and ventilation this building had great heat flow i.e. high heat loss.

Previous constant painting of the inner walls of the building could not have solved the condensation of water vapour (mould growth) in the upper parts of inner walls and at the side of reinforced concrete structure edges. Moisture in the construction led to damage to the building fabric and unhealthy use of the space. Condensation within the construction must be prevented [3].

Old buildings have little or even no thermal insulation, and there is great potential for energy savings. Buildings built before 1970s don't have any thermal insulation and even buildings completed before 1980s have poor thermal insulation. According to housing statistics data over 80% of existing buildings in Croatia have unsatisfactory thermal insulation.

## III. FAÇADE THERMAL RENOVATION

The goal set for the renovation was the preservation of historic building substance and equipping the

space in accordance with contemporary requirements. This renovation project was designed respecting various regulations and guidelines that insure the best building construction in terms of form, construction, building physics and economizing. Detailed analyses of existing architectural structure, calculation based on present day regulations and right application of materials enabled revival of this building.

Renovation planning project for this type of building is based on two basic principles of thermal renovation of the facades. Mainly, the rendered thermal insulation layer was attached to external structure of the basic gym hall volume. The protective layer consists of render applied to the insulation of expanded polystyrene, thickness: 8 cm. Achieved results are: brick wall (38 cm) U value was 0.96 W/m<sup>2</sup>K and new U value is 0.359 W/m<sup>2</sup>K; reinforced concrete wall (38 cm) U value was 1.65 W/m<sup>2</sup>K and new U value is 0.424 W/m<sup>2</sup>K.

On some parts of the building the thermal insulation was attached on inner surfaces of external structures. This principle is used only when outer changes are not allowed because of historical value of the building. In relation to building physics, extra solutions of the phenomenon of vapour diffusion were considered. The vapour barrier is integrated inside prior to fixing the expanded polystyrene in order to prevent condensation. Expanded polystyrene was produced 1954 by German chemical concern BASF under the protected name "Styropor®". It is organic, synthetic raw material, excellent thermal insulation, inexpensive and easy to be worked with mechanically.

Tendency is that the wall U value of 0.15 W/m<sup>2</sup>K should be standard for new construction in all European countries and possibly for existing buildings [4]. As compared to other European countries, Croatia has been several years behind the schedule producing national regulations but is accepting all European norms, which are to be adjusted to its legislation. The new Technical Regulation on thermal energy savings and thermal protection in buildings came into force July 2005 and its obligatory application starts July 2006. According to the new requirements /for heated buildings  $\geq 18^{\circ}\text{C}$ / the attainment of heat transmission coefficient for outer wall should be 0,80 W/m<sup>2</sup>K /min. thermal protection/ and  $U = 0,45 \text{ W/m}^2\text{K}$  /energy saving/ in Zagreb. Applying the new Technical Regulation, the expected thermal energy savings are estimated at about 30%. In order to attain a satisfactory heat loss limitation level thicker thermal insulation should be installed and optimum designing parameters should be applied [5].

#### IV. CONCLUSION

The primary goal of this research was the preservation of historic building and its adjustment to new requirements and today's needs. The problem of heat flow and vapour diffusion through walls (facades) is the key physical and structural problem of the inter war period buildings built mainly without thermal insulation. Technology and science development is producing materials with the most convenient characteristics, thickness, characteristics and way of building in, make a great contribution in building construction or renovation. With optimal renovation planning project building damage can be solved, wider damage can be prevented, greater savings attained in heating energy consumption and old buildings can be usable again.

The contribution of this work is to offer some of the techniques and some technical measures for renovation of old houses, reaching the level of a standard insulated house. A more widespread consciousness of the need for preservation measures to historic buildings and at the same time possible energy savings by renovation of existing buildings should become the main concern in Croatia.

#### REFERENCES

- [1] Z. Hrs Borkovic. VODIC kroz energetski efikasnu gradnju /GUIDE for Energy Efficient Building. Ministry of Environmental Protection, Physical Planning and Construction, Institute for physical planning; Institute Hrvoje Požar, Zagreb, 2005.
- [2] I. Muraj. Arhitektura moderne u djelu Eгона Steinmanna /Modern Architecture in the Work of Egon Steinmann. Master thesis, Faculty of Architecture, Zagreb, December 2004.
- [3] J. Bertol-Vrček and I. Muraj. The Impact of Design and Building Constructions Quality on Heat Loss. In Proceedings of the 4th International Conference "Technologies for Sustainable Development in Regions", pages 34-40, Prague, The Czech Republic, April 2004.
- [4] The Critical Importance of Building Insulation for the Environment. European Insulation Manufacturers Association, Brussels.
- [5] J. Bertol-Vrček and V. Duplancic and I. Muraj. Croatian Building Legislation with a Focus on Environmental Protection. In Proceedings of the International Conference on Industrial Pollution and Sustainable Development, pages 40-50, Maribor, Slovenia, December 2005.

# Ecodesign Decision Boxes for Environmentally Sound Product Development

Hesamedin Ostad Ahmad Ghorabi and Wolfgang Wimmer (Faculty Mentor)  
Institute for Engineering Design and Logistics Engineering  
Technical University of Vienna  
Vienna, Austria  
Email: ostad@ecodesign.at, wimmer@ecodesign.at

**Abstract** — Industry projects show that Life Cycle Thinking and the idea of ECODESIGN are still not well established among engineers in product development. Available tools such as the ECODESIGN Product, Investigation, Learning and Optimization Tool (PILOT) [Wimmer, Züst, Lee 2004] may help to implement ECODESIGN into product development considerations and to improve an already existing product. However, an application of those tools in the decisive early stages of the product development process remains difficult for design engineers.

A systematic tool called 'Ecodesign Decision Boxes' was developed for integrating the concept of ECODESIGN into product development in order to help engineers to develop an environmentally sound product which has an optimised environmental performance [Ostad Ahmad Ghorabi 2005].

## I. OBJECTIVE

According to [Luttropp 1999] around 30 aspects need to be addressed in the product development process. Some of these aspects are e.g. materials, reliability, quality or profit. The environmental aspect is also one of the aspects which have to be considered in product development.

The Ecodesign Decision Boxes were developed to give special attention to this part and aspect of the product development process and allow the implementation of environmental considerations into technical product designs and product development processes. Aim was to develop a tool that allows optimizing the entire product as well as tracking and controlling the influence on environmental aspects of a product along its life cycle phases. An overall evaluation of the environmental performance of the product design as well as a detailed view on the performance of each component, part and of each material used in the components should be assured.

## II. METHOD

For the development of a first version of the tool product data from a multinational company producing office chairs were taken into account.

At first, life cycle data for the product obtained in a Life Cycle Assessment (LCA) according to the EDIP method [Wenzel, Hauschild, Alting 1997] have been gathered and further processed to suit an application in Ecodesign Decision Boxes. Before an optimization of the environmental performance of a product can be achieved, it is necessary to get an overview of the current environmental performance of the product through its life cycle phases. This is done in the first step of the tool. In this step graphs based on LCA data for the assembled product are generated and displayed in a so-called 'Design Box'. With the help of the Design Box those components contributing most to the environmental impact of the product can be tracked. In a second step LCA-based graphs for the most relevant components can be generated in 'Component Boxes' where the environmental performance of the considered component can be tracked more detailed for all its life cycle phases. The Component Box allows identifying the most relevant materials with respect to their environmental performance. In a third step LCA-based graphs are generated for each material used in the components in a 'Material Box'. The procedure of the application of the Decision Boxes is demonstrated in Figure 1.

A Material Box shows the aggregated environmental impact per weight of a given material over a typical life cycle based on LCA results for the type of product the material is used for.

A Material Box for the three materials PA66, ASt35 and PP is shown in Figure 2. The characterized impact for Global Warming (char. impact for GW) is drawn against the weight of the material.

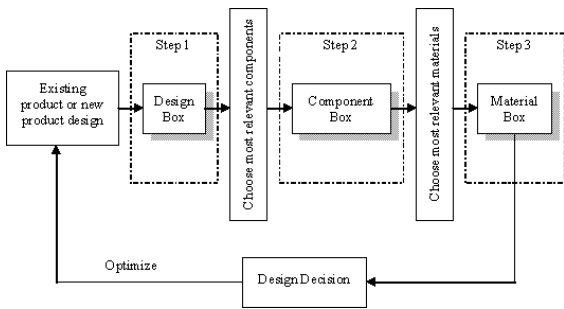


Figure 1: Optimizing a product in the design stage with Decision Boxes

The graphs contain life cycle data for the materials which are listed in Table 1.

MAT	PA66	ASt35	PP
PRO	Injection moulding	Cold trans-forming	Injection moulding
SUR	No treat-ment	Painted	No treat-ment
TRA	Lorry, 1000km	Lorry, 1000km	Lorry, 1000km
EOL	European Scenario	European Scenario	European Scenario

Table 1: Life cycle data for PA66, ASt35 and PP (MAT: material, PRO: production, SUR: surface, TRA: transport, EOL: end of Life)

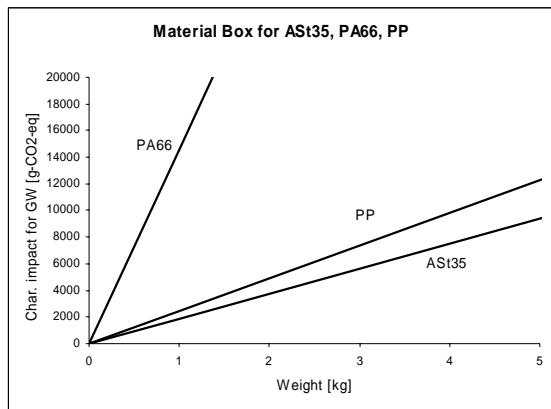


Figure 2: Material Box for ASt35, PA66, PP

Obviously the graph with the highest slope in Figure 2 (PA66) contributes most to environmental impact at low weight. Using PA66 in a part or component of a product influences the environmental performance of the component and also the entire product significantly.

On the one hand the introduced Design Box, Component Box and Material Box help to identify

environmentally most relevant design elements, e.g. materials or parts, on the other hand they help to make decisions for the optimization of the environmental performance of the product design.

The LCA-based graphs in the different boxes consider life cycles phases, e.g. extraction, processing, transport or end of life scenarios, of the specific material.

The proposed Ecodesign Decision Boxes allow tracking the environmental impact of a current design during early design stages and give opportunity to influence them if necessary. The product can easily be optimised by considering environmental aspects by the engineer in product development.

The application of this tool is easy since the engineer in product development does not need to know details about Life Cycle Assessment. A basic understanding of Life Cycle Thinking and of the interaction of environmental parameters and design parameters is sufficient.

First introduction of this tool in an office chair producing company already gave positive feedback and was well understood and appreciated.

The first version of the developed Ecodesign Decision Boxes is product type specific. The databases are developed for a certain product type, in this case office chairs, and even for certain technologies used in a certain company. The development of a complete database which is matter of further investigations should facilitate the use of the tool for different products.

## REFERENCES

- [1] W. Wimmer and R. Züst and K. Lee. Ecodesign Implementation – A Systematic Guidance on Integrating Environmental Considerations into Product Development, Springer, Netherlands, 2004.
- [2] H. Ostad Ahmad Ghorabi. Ecodesign Decision Boxes for a Systematic Integration of Environmental Considerations into the Product Development, Master Thesis, Institute for Engineering Design and Logistics Engineering, Vienna University of Technology, 2005.
- [3] C., Luttrupp. Eco-design in early product development, World Conference R99, Geneva, Switzerland, 1999
- [4] H. Wenzel and M. Hauschild and L. Alting. Environmental Assessment of Products, volume.1: Methodology, tools and case studies in product development, Chapman & Hall, London, UK, 1997.

# Photoacoustic Monitoring of CO<sub>2</sub> in Biogas Matrix Using a Quantum Cascade Laser

Wolfgang Ritter and Bernhard Lendl  
Institute of Chemical Technologies and Analytics  
Vienna University of Technology  
Vienna, Austria  
Email: w.ritter@tuwien.ac.at

**Abstract** — *The renewable energy source biogas gains in market importance. New developments promote the supply of biogas by the local gas distributor. Regulations about the composition of the supplied biogas ask for an appropriate quality control of the gas content.*

*This work demonstrates the outstanding capability of photoacoustic detection (PA) based on quantum cascade laser (QCL) for the in-line measurement of CO<sub>2</sub> in the difficult matrix biogas. Compared to standard techniques QCL-PA shows several distinct advantages as higher selectivity and faster response.*

## I. BIOGAS – A RENEWABLE ENERGY SOURCE

In the past decades, global energy consumption has exhibited a remarkable increase. Unlike natural gas, biogas (i.e. fermentation gas) is CO<sub>2</sub>-neutral [1]. Consequently, it helps to reduce the amount of greenhouse gases in the atmosphere when used as a substitute for fossil fuels [2]. Biogas consists of 50 – 70% methane, 25 – 45% carbon dioxide, 0 – 5% nitrogen, as well as small quantities of hydrogen sulphide and ammonia [3.] After the purification of the biogas for the achievement of natural gas quality, biogas can be inducted into the local gas supply system. However, a gas analysis has to be conducted beforehand. A market survey, also with regard to economic aspects, showed that in practice such an analysing system is not available yet.

## II. PHOTOACOUSTIC – AN INNOVATIVE DETECTION SCHEME

The high sensitive photoacoustic (PA) scheme is particularly attractive in combination with recently available compact QCL sources. The signal, which is recorded by a microphone, is directly proportional to the absorbed incident laser power [4]. Furthermore, the signal is recorded on a zero background. Photoacoustic sensors offer the advantage of a simple and robust setup, low maintenance and room temperature operation and compact size.

## III. EXPERIMENTAL – THE PROOF OF CONCEPT

In order to comply with the requirements of biogas analysis, a mobile prototype based on photo-acoustic laser spectroscopy has been developed [5]. As a light source, a Peltier-cooled quantum cascade laser, emitting at 4.29 μm, was chosen. The photoacoustic cell was adapted to the geometry of the laser beam and consists of a Helmholtz resonator. Carbon dioxide was used as a test-analyte to demonstrate the applicability as an online technique. Calibration was performed by measuring carbon dioxide concentrations ranging from 1 to 100 %vol., directly within the gas flow. The quality-factor (Q) was found to be 9 with a resonance frequency range from 1.6 to 2.8 kHz due to the variable gas composition. A detection limit of 250 ppmv CO<sub>2</sub> and a response time of 6 minutes were determined. Furthermore, the photoacoustic sensor was qualified for flow rates of up to 400 ml min<sup>-1</sup>. Field measurements at a pilot plant in St. Martin, Austria confirmed the road capability of the sensor in noisy surroundings.

The linear relationship between the PA signal and the reference concentration is shown in Figure 1. The evaluated concentration range is of high relevance for the control system of the purification plant (set point is 2.0 %vol). Reference analytic was realized with the commercial carbon dioxide analyzer NGA 2000 (Emerson AG, Switzerland).

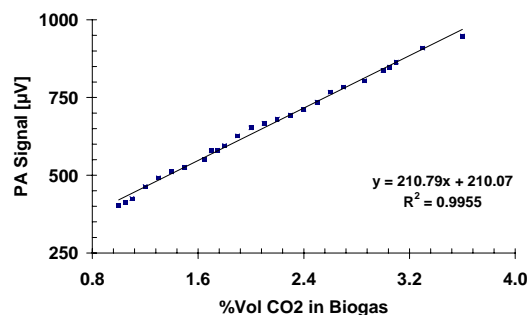


Figure 1: Measurements of CO<sub>2</sub> in Biogas

#### IV. CONCLUSIONS

This work shows the potential of a portable sensor system based on quantum cascade lasers for the detection of industrial relevant analytes in complex matrices such as biogas. It has been demonstrated that a continuous monitoring of the CO<sub>2</sub> concentration in biogas is possible directly in the gas flow. Carbon dioxide concentrations ranging from 1 to 100 % Vol are detectable with high temporal resolution. The sensor is fast enough to react on small changes in concentration and provide detailed information's to optimize the purification process.

Photoacoustic detection shows several distinct advantages such as higher selectivity, faster response, on-line analysis, and portability compared to standard technologies. The construction of the prototype was designed to enable a quick and easy exchange of the laser source. Thus, as a future prospective, other analytes could be detected in the biogas as well. This option is of particular relevance for the trace components ammonia and hydrogen sulphide.

#### ACKNOWLEDGMENTS

The authors gratefully acknowledge the contributions by Dr. C. Haisch, Prof. Dr. R. Nießner, Dr. M. Harasek and Dr. M. Schwarz.

#### REFERENCES

- [1] Österreichisches Bundesministerium für Land- und Forstwirtschaft. Strategie Österreichs zur Erreichung des Kyotos-Ziels - Klimastrategie 2008/2012. June 2002.
- [2] H. Tretter. Neue Optionen für die Nutzung von Biogas. 2003. Institut für Verfahrenstechnik, Umwelttechnik und Technische Biowissenschaften - Technische Universität Wien.
- [3] P. Weiland, Production and energetic use of biogas from energy crops and wastes in Germany. Applied Biochemistry and Biotechnology 109, pages 263-274. 2003.
- [4] H. A. Beck, R. Niessner and C. Haisch, Development and characterization of a mobile photoacoustic sensor for on-line soot emission monitoring in diesel exhaust gas. Analytical and Bioanalytical Chemistry 375, 1136-1143. 2003.
- [5] W. Ritter. Mobile photoakustische Analyse von Biogas mittels Quanten-Kaskaden-Laser. Institut für Chemische Technologien und Analytik der Technischen Universität Wien. 2005.

# Soil Conservation and Flood Protection in Loucka River Watershed

Aleksandra Sala, Miroslav Dumbrovský  
Institute of Landscape Water Management  
Brno University of Technology  
Brno, Czech Republic

Email: {sala.a,dumbrovsky}@fce.vutbr.cz

**Abstract** — *Frequently occurring regional rains, which affected small basins in recently years, invoke request of highest need of flood protection. This problem should be solved integrally and it should begin even in catchment's areas to decrease erosion effect and surface runoff respectively. This can be achieved via erosion control measures. The main goal of the measures is to decrease the peak discharge caused by precipitation and to retain the water in the basin. However, retention reservoirs management and increasing the river capacity are the next parts of the flood control of the same importance.*

## I. INTRODUCTION

Arable lands are the most affected by water erosion, where the overland flow from precipitation occurs on. Hence the attention must be focus on them in realization of integrated territory protection. Land use planning could be utilized, especially erosion and flood control measures through the Plan of common facilities, which can reduce surface run-off, remove or eliminate demanding effect of erosion and will be the most important part of rational organization and useful territory protection. The problem described above can happen even on other kind of land, like forest lands or build-up areas. All have to be incorporated into integrated territory protection

## II. METODOLOGY

The main idea of integrated territory protection is to create design of alternative data set of soil and water conservation and flood protection measures such as: changes in land-use, agro-technical, forest-technical, biotechnical measures and other. The multifunction measures can reduce overland flow, washing out, and sediment load transmission into water courses. It can also improve river basin retention capability and utilizing of precipitation water in separate part of catchment's area.

Optimal combination of alternative data set of conservation and flood protection measures must be found. As it was said not only arable land must be

consider. Runoff hydrographs, soil losses by erosion, damages in build-up area caused by surface run-off, economic detriments arise from realization of protective measures and costs which these measures take, have to be determined "Table 1".

Characteristics of variation - location I		Economic parameters [thousand of CZK]			
		Damages	Economic losses	Own expanses	Capital costs
without reservoir	Present State	252	346	0	0
	Non-row Crops	140	231	0	0
	Design	77	274	20	408
	Permanent grass land	9	692	0	0
with reservoir	Present State	215	346	0	0
	Non-row Crops	112	231	0	0
	Design	65	307	20	408
	Permanent grass land	0	692	0	0

Table 1: Characteristics of variation for location I

Alternative of hydro-technical structures on rivers and reservoirs water management measures, their cost functions, flood losses must be figured out in all parts of river.

With respect to the fact that it is necessary to find optimal dimensions for some of the system elements, there is usually a great number, in the case of a continuum approach to the solution, even an infinite number, of possible combinations. It is therefore necessary to use an optimization mathematical model to find the most suitable combination. This model was created on the basis of a mixed discrete programming and consists of three generally formulated partial models: a) a partial model of protective measures at individual sites of an interest territory; b) a partial model of a watercourse; c) a partial model of a reservoir. The optimization mathematical model is a system of equations which, model a given system behaviour. Each optimization scene is necessary to define one or more optimality criterions formulated as objective function.

While designing the optimization system in connection with the process of territory organisation a requirement of a maximal protection of inhabited and other areas with the exertion of minimal means was formulated for the solving process on the level of land adjustments as one of the suitable optimization criteria. It is a criterion consisting of three simultaneously operating partial economic, but simultaneously water-management and socially aimed in their impacts, criteria (all with the same significance 1:1:1):

- Minimization of the average annual damage
- Minimization of the average annual economic losses in the farming production
- Min. of the average annual own expenses

The mentioned methodology has been successfully tested on a real case study of Loucka river basin. There are some results hereafter.

### III. RESULTS AND CONCLUSION

As mentioned above and proved by results using erosion and flood protection measures in catchment's area substantially reduce surface run-off effects. Soil losses by erosion, run-off surface and transport sediment loads were significantly decreased and districted by means of complex protection and organization of landscape in catchment's area "Figure 1 and 2".

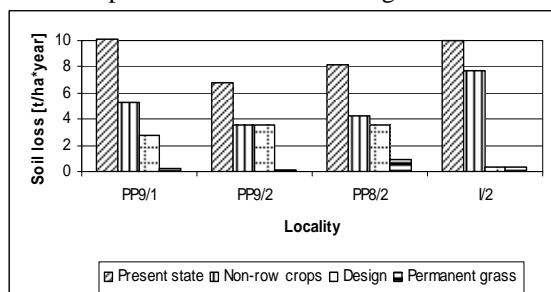


Figure 1: Soil loss for each variation

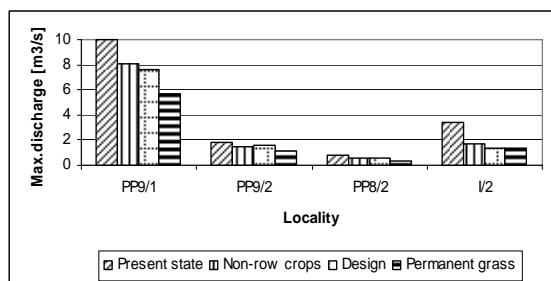


Figure 2: Peak discharge for each variation

All these adjustments at the same time mark down removal costs (mucking sediment load from rivers,

reservoirs), flood damage disposals or profit losses by unsuitable farming, top-soil and sub-soil degradation. Desirable impoundment of water in landscape is achieved in the same time.

An infinite quantum of optimal solutions can be found due to possibility of modelling of costs and efficiency of measures, because model allows changing of input criterions, requirements and circumstances. Thanks to this we can create characteristics of system and its behaviour in a different kind of scripts and make precisely decision "Table 2" (but on the other hand economically) about final erosion and flood protection measures in catchment's area.

Indicators		Variation			
		1	2	3	4
Objective function	[thousand of CZK]	386	752	814	913
damages		79	10	66	65
economic losses		287	742	470	511
own expenses		20	0	278	337
Capital costs	[mil CZK]	0.4	0	6.9	8.3
Soil loss	[t/ha*yr]	1.97	0	1.97	1.94
Peak discharge	[m³/s]	8.04	6.6	3	1.27

Table 2: Output variables for all alternatives of locations PP9/1 – I/2

A great advantage of the model lies in a general formulation of its components – partial models of protective measures at individual sites of the interest territory, water course and reservoir. This should enable its problem-free application for optimization design of integrated territory protection under any conditions and at any site.

### REFERENCES

- [1] S. Korsuň. Vytvoření a ověření modelu pro optimalizaci návrhu komplexní ochrany a organizace povodí, Final report of A01-NAZV-QC1292 BUT, Brno, 2002 .
- [2] M. Dumbrovsky et al. Optimization of the system of soil and water conservation for runoff minimizing in certain watershed in the process of land consolidation. (in Czech). Final report of research. NAZV-QC1292, Praha. 2003.
- [3] M. Janeček. Ochrana zemědělské půdy před erozí, ISBN-85866-85-8, ISV nakladatelství 2002

# Use of organomineral complex at remediation of contaminated soil

Zuzana Sejakova, Marianna Skokanová, Katarina Dercová  
Faculty of Chemical and Food Technology, Institute of Biotechnology and Food Technology,  
Department of Biochemical Technology  
Slovak University of Technology, Radlinskeho 9 Bratislava, Slovak Republic  
Email: {zuzana.sejakova}@stuba.sk

**Abstract** — *This contribution provides data on use of organomineral complex (OMC) to decontaminate chlorinated organic pollutants from soil. The key role in elimination of contaminants from the soil is played by a quality of organic matter/humic acids. Adsorption/desorption experiments with pentachlorophenol (PCP) were carried out for OMC on the basis of clay mineral (zeolite) and organic matter (humic acids). Sorption characteristics and biodegradation with bacterial isolate Comamonas testosteroni CCM 7350, of PCP were studied in real soil samples in three types of soil (chernozem, fluvisol, and regosol), with and without addition of OMC. Fast and effective adsorption and low desorption may serve as a pretreatment step of bioremediation technology for reducing PCP content in soil.*

## I. INTRODUCTION

Chlorophenols have been defined as dangerous pollutants due of their toxicity and persistence in environment. For these reasons, chlorophenols are listed in EC list of dangerous substances [1] and the US EPA list of priority pollutants [2]. Pentachlorophenol (PCP), the main component of wood preservative, is also a microbial breakdown product of the many pesticides commonly used in agriculture production [3].

Classical remediation technologies (such as incineration) are generally non-ecological and non-economical, alternative methods involving biodegradation by microbial populations have been developed. Degradation of PCP in soil is affected by organic matter concentration and composition, clay mineral content, and moisture content [4]. Some remediation technologies are mainly used at strongly contaminated locations. Predominant part of agricultural soil is not extremely contaminated. Soil is capable to partly eliminate contaminants, the key role is played by quality of organic matter mainly by humic acids (HAs). Their excellent sorption properties depend on their chemical structure and composition. In our experiment were used HAs isolated from lignite matrices. Lignite HAs contain 20 times higher content of organic carbon than agricultural soil.

The ability of soil to retain organic contaminants is attributed to adsorption phenomena and chemical reactions occurring on active surface of humic substances and mineral particles. The immobilization phenomena have several important consequences: (1) the amount of compound available to interact with biota is reduced; due to decreased bioavailability one can achieve lowering of toxicity; (2) the complexed products are less toxic than their parent compounds; and (3) binding restricts leaching of chemicals across the soil profile, thus preventing ground water contamination. It is possible to use the sorption properties of contaminant to the benefit of microorganisms. High influent concentration can be decreased to less toxic levels by adsorption to allow maximum degradation take a place.

Our work was focused on immobilization of PCP in organomineral complex particles. OMC was prepared by binding humic acid from lignite on zeolite at laboratory conditions and uses excellent sorption properties of the both component.

## II. RESULTS AND DISCUSSION

We have attempted to combine excellent sorption properties of both humic acid and zeolite and to develop a procedure for soil decontamination based on the application of OMC into soil. Adsorption/desorption experiments involving PCP were carried out with OMC prepared on the basis of clay mineral (zeolite) and organic matter (humic acids isolated from lignite) in three real exactly characterized soil samples (Chernozem, Fluvisol and Regosol) in the apparatuses enabling simultaneous monitoring of biodegradation, sorption and evaporation of organic aromatic chlorinated pollutants. Higher amount of HAs bound on zeolite enhances its potential to adsorb and retain PCP. Our previous study has confirmed that OMC containing cca. 4,3 mg HA/g of zeolite possesses the best retention ability towards PCP and represents optimal economic solution from the point of view of the technological preparation [6]. Adsorption of PCP was determined after 1 h of stirring the flasks on a rotary shaker. Desorption was determined after 24 h and carried out under the conditions of decreasing pH value 4 which simulated

acid rains that release of PCP from soil at real conditions. The best results – the highest adsorption and retention – were obtained in soil with addition of OMC as shown in Fig. 1. Soil with addition of pure zeolite showed values of PCP adsorption/desorption relation comparable to or slightly higher than that observed with the pure soil.

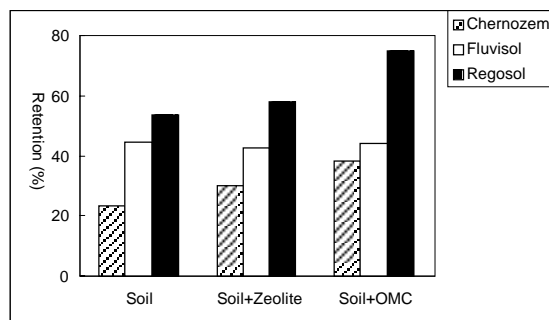


Fig. 1 Retention of PCP ( $10 \text{ mg.l}^{-1}$ ) by the selected soils.

Biodegradation of PCP in sterile soil with and without addition of OMC was studied at the initial concentrations of PCP 10, 50 and  $100 \text{ mg.kg}^{-1}$ . Soil samples were bioaugmented with a bacterial isolate *Comamonas testosteroni* ( $0,5 \text{ g.kg}^{-1}$ ) with ability to use phenol as a sole carbon source. The soil samples were analyzed after 7, 17 and 24 days, as example process of biodegradation in chernozem is shown on Fig. 2. In the series of experiment with three types of soil shown in biodegradation of PCP after 7 days was significantly lower in the samples with OMC than in soil without OMC. This implies partial adsorption of PCP on OMC and then decrease of its bioavailability. After 17 days, degradation has increased markedly in both samples, which suggested a release of PCP from the bound state.

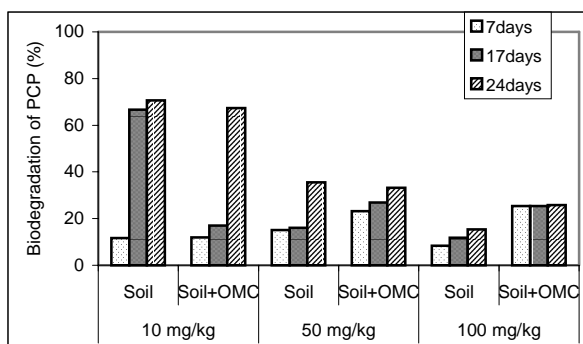


Fig. 2 Biodegradation of PCP in the Chernozem with and without addition of OMC

However, degradation was still lower in samples with addition of OMC. After 24 days, percentage of PCP degradation in soil with addition of OMC reached a value of PCP degradation in soil without

OMC. This observation indicates that the binding is reversible and the presence of microorganisms and under the conditions of acid pH a subsequent release of PCP for biodegradation occurs.

### III. CONCLUSION

According to our results, humic acid bound on zeolite appeared to be good trap of PCP with potential application in remediation technology. One can assume that fast and effective adsorption and low desorption may serve as remediation technology for reducing PCP content in soil and thus for reducing its initial high toxicity due to low bioavailability. Lower concentration of toxic pollutant will probably inhibit survival and degradative ability of bacterial strains present. Humic acids and zeolite are of natural origin and therefore suitable to be used in the environment and support natural ability of soil to eliminate contaminants.

### ACKNOWLEDGMENTS

Financial support from VEGA Grant Agency (Grant No.1/1309/04) is gratefully acknowledged

### REFERENCES

- [1] EPA Method 604, Phenols. Environmental Protection Agency, Part VIII, 40 CFT Part 136, Federal Registration, 58; 1984.
- [2] EPA Method 625, Base/neutral and acids. Environmental Protection Agency, Part VIII, 40 CFT Part Part 136, Federal Registration, 153; 1984
- [3] M. Häggblom, R. J. Valo.: In: (L. Young, C. Cerniglia, eds.) *Microbial Transformation and Degradation of Toxic Organic Chemicals*. Wiley-Liss., 89; 1995
- [4] G. Barančíková. Proceeding of VI. International FZK/TNO Conference: &contaminated Soil'98, p. 903. London 1998
- [5] G. Barančíková, M. Madaras, J. Makovníková, M. Klučáková, M. Pekař, K. Dercová. Possibility of use of organomineral complex at remediation of agricultural soil 3<sup>rd</sup> Agricultural days in Slovakia, Mojmirovce, In: *Book of the Conference Contributions*, J. Sabocká, P. Jambor (Eds.). Societas Pedologica Slovaca, SSCRI Bratislava, CD ROM, p. A4, 2004

# Life Cycle Assessment Case Study of Aluminium Production

Lenka Sencakova, Lucia Gdovicinova and Edita Vircikova (Faculty Mentor)  
Department of Integrated Management, Faculty of Metallurgy  
Technical University of Kosice  
Kosice, Slovakia  
Email: Lenka.Sencakova@tuke.sk  
Lucia.Gdovicinova@tuke.sk

**Abstract** — *Life Cycle Assessment is a scientific tool for evaluation of all environmental impacts (both positive and negative) of a product during its complete life cycle 'from cradle to grave' (mining and extraction of raw materials, fabrication, transportation, use and recycling/disposal, including energy and ancillary material supplies). The purpose of life cycle assessment is to define the scope of all environmental impacts associated with the product during its life cycle and to identify and reduce aspects with the most significant environmental impacts. The aim of this paper is to assess the environmental impacts of aluminium produced by electrolysis in production company in Slovakia and to propose some measures for improving the aluminium production life cycling.*

## I. INTRODUCTION

Life Cycle Assessment (LCA) is intended for broad use throughout the industry with a view to assess and stimulate environmental improvement in production processes and product development. Past experiences have shown that the review of LCA environmental aspects in production processes can lead to improvements in the production processes themselves. Typical LCA comprises the following steps:

1. Goal and Scope Definition - the goal definition describes the covered application, the reasons for carrying out the study, and the target audience. The scope is the detailed technical description of the "product system" under study
2. Life Cycle Inventory Analysis - comprises the environmental inputs and outputs compilation and quantification of the product system during its life cycle
3. Life Cycle Impact Assessment - the purpose of this stage is to understand and evaluate the

magnitude and significance of the potential environmental impacts of the product system

4. Interpretation - the conclusions and recommendations are derived from the findings of the life cycle inventory analysis and impact assessment in line with the defined goal and scope

Harmonised LCA approach is provided by International Standards ISO 14 040 (Principles and Framework), ISO 14 041 (Goal, Scope and Inventory Analysis), ISO 14 042 (Life Cycle, Impact Assessment), and ISO 14 043 (Life Cycle Interpretation).

The aim of life cycle impact assessment is to evaluate the significance of potential environmental impacts by assigning of the life cycle inventory analysis results to different impact categories (e.g. global warming, resource depletion, land use, etc.).

## II. DATA FOR ENVIRONMENTAL IMPACT ASSESSMENT

The primary aluminium production in this company includes the following unit processes: anode production (pre-baked anodes), electrolysis and casting.

For anode production, calcined petrol coke and the pitch are the basic material inputs, alumina and carbon in pre-baked anodes are the basic material inputs for electrolysis.

Aluminium is produced from alumina (aluminium oxide) by the Hall-Heroult electrolytic process that dissolves the alumina in a molten cryolite bath and passes current through this solution, thereby decomposing the alumina into aluminium and oxygen. Aluminium is tapped out of the reduction cell (pot) at daily intervals and the oxygen combines with the carbon of the anode to form carbon dioxide [1].

Aluminium produced by electrolysis is the basic material input for casting process. Material inputs for unit processes in this company are given in "Table 1" [2].

Material inputs [g/t Al]	Anode production	Electrolysis	Casting
Alumina		2118000	
Anode		517000	
Al <sub>2</sub> F <sub>3</sub>		14000	
Soda		2 000	
Calcined Petrol Coke	373570		
Pitch	82130		
Collar matter	8820		
Al			1000000
Chlorine			0,323
Refined salt			60600

Table 1: Material inputs in aluminium production

Specific aluminium production emissions are: Fluoride gaseous and fluoride particulates (primarily aluminium fluoride and cryolite), which arise from molten bath; CF<sub>4</sub> and C<sub>2</sub>F<sub>6</sub> (commonly reported as PFC) are gases generated with an uncontrolled anode overvoltage situation named „anode effect“; tars and PAH, which arise from anode consumption; particulates, sulphur dioxide and nitrogen oxide come typically from fuel combustion and carbon dioxide and carbon oxide. Wastes generated by this company are monitored in two categories:

- 1 Hazardous waste (60 183 g/t Al)
- 2 Other waste (147 408 g/t Al).

Value of air emissions from aluminium production in this company are given in “Table 2”.

Parameter [g/t Al]	Anode production	Electrolysis	Casting
HF	2,44	188,43	5,47
SO <sub>2</sub>	372,7	11387,34	2,56
NO <sub>x</sub>	163,23	3448,46	53,96
CO	3766,22	89169,78	10,06
C	0,48	0,25	7,26
F	0,01	42,7	0,43
Particulate	74,73	702,94	22,78
Tars	1275,75		

Table 2: Value of air emissions from aluminium production

For environmental impact assessment of aluminium production, method developed within the Danish programme “Environmental Design of Industrial Products” was applied. The following environmental impacts were evaluated:

1. Global warming
2. Photochemical ozone production
3. Acidification
4. Eutrophication
5. Hazardous waste
6. Other waste

### III. RESULTS AND DISCUSSIONS

Resulting from analysis, environment is most loaded by CO emissions and by hazardous wastes generated in this company. Hazardous waste and photochemical ozone production and acidification (caused by hazardous wastes generation and CO emissions) are the most significant environmental impact. Other waste generation is also very significant. In compare with these impacts, global warming and eutrophication are minor, but not negligible impacts.

Environmental impact can be often reduced only by more effectively utilization of material and energy inputs and by waste amount reducing. Air emissions should be also reduced.

The most air emissions and wastes arise from electrolysis. Hazardous waste from electrolysis is landfilled. An alternative hazardous waste disposal process should be found. It could be used for electric power generation in incineration plants. However, this solution is more expensive.

In this paper, the study is not complete. Environmental impacts from electric power generation, from material transportation to company and final product to customers should be also included, as well as the impacts from bauxite mining and from extraction of other material inputs.

### REFERENCES

- [1] Life cycle assessment of aluminium: Inventory data for the worldwide primary aluminium industry. International Aluminium Institute. March 2003.
- [2] J.Senková. Life cycle assessment of aluminium produced in Slovalco, Žiar nad Hronom. Diploma work, pages 50-51. Slovak technical university, Slovakia, 2004.

# Toxicity of Low-chlorinated Phenols and Pentachlorophenol (PCP)

Marianna Skokanova, Katarina Dercova and Zuzana Sejkova  
Faculty of Chemical and Food Technology, Department of Biochemical Technology  
Slovak University of Technology  
Bratislava, Slovak Republic  
Email: {marianna.skokanova}@stuba.sk

**Abstract** — Determination of toxicity of the chlorophenols and pentachlorophenol under laboratory conditions were studied. Different bacteria strains were used. It was found that toxicity of the chlorophenols depends not only on the number of chlorine atoms but also on their position on aromatic ring, and is structurally conditioned.

## I. INTRODUCTION

Chlorophenols have been defined as dangerous pollutants due to their toxicity and persistence in the environment. For these reasons, chlorophenols are listed in the EC list of dangerous substances [1] and the US EPA list of priority pollutants [2]. Soils contaminated with PCP are considered to be hazardous wastes. PCP is mainly used as a wood preservative, inhibitor in cooling towers, in adhesives, construction materials, paint and paper, as well as a pesticide and insecticide. It is also a microbial breakdown product of many pesticides commonly used in agriculture production [3]. It is toxic in low concentrations in both plants and animals and its effects are cumulative.

As a consequence of intensive use and due to the stability and sorption ability of molecule, it has become a progressively widespread contaminant in soil, sediments, and groundwater [4].

## II. EXPERIMENTAL DESIGN

**Chlorophenols (CP).** The objective of this work was to study toxicity and the other factors that predominantly influence biodegradation of phenol, selected low-chlorinated phenols (2-CP; 3-CP; 4-CP; 3,5-CP; 2,3-CP; 2,4-CP; 2,5-CP; 2,6-CP; 2,4,5-CP; 2,4,6-CP) and pentachlorophenol (PCP) shown in Fig.1. This information may be useful in the bioremediation technology of PCP-contaminated soil.

**Microorganisms (Fig. 2).** Toxicity of the above mentioned phenol and chlorinated phenols was determined in the presence of bacterial strains *Micrococcus varians* CCM 2253 (strain from the

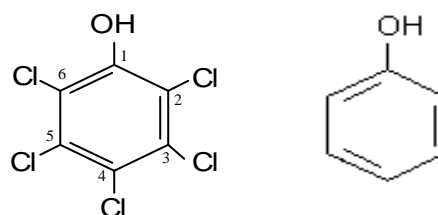


Figure 1: Structural formulas of pentachlorophenol (with numbered chlorine positions on aromatic ring) and phenol.

collection of microorganisms), *Alcaligenes xylosoxidans* (iso late from long-term contaminated soil), *Comamonas testosteroni* RF2 and its metabolic mutant VM (isolates from waste water treatment plant sludge, both fed in a laboratory bioreactor with phenol, the mutant obtained by adding 1 mg/l  $\text{NaN}_3$ ).

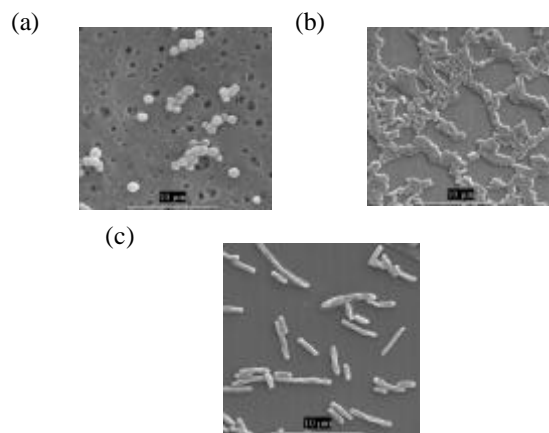


Figure 2: Tested bacteria strains (a – *Micrococcus varians*, b – *Alcaligenes xylosoxidans*, c – *Comamonas testosteroni*).

**Toxicity assay.** Determination of toxicity was based on inhibition of biomass growth in the presence of different concentrations of chlorinated phenols considered as growth inhibitors. Glucose was used as a carbon source.

Another method used to measure the toxicity of the phenols was a bioluminescence method LumisTox using a sensitive marine standard bacterial strain *Vibrio fischeri*. The method is based on the bioluminescence extinguishing.

ID<sub>50</sub> values were obtained in order to compare the used chlorophenols' toxicity effect on the tested bacteria strains as shown in Fig. 3.

### III. EXPERIMENTAL RESULTS

**Biomass growth inhibition method.** 2,4,5-CP showed the highest toxicity, while PCP and 3,5-CP revealed slightly lower values of toxicity. The other tested phenols were much less toxic. The most resistant strain to the tested chlorophenols was *Micrococcus varians*. *Comamonas testosteroni* VM demonstrated significantly lower resistance. Bacterial strains *Alcaligenes xylosoxidans* and *Comamonas testosteroni* RF2 (growth curves shown in Fig. 4) were the most sensitive.

**Bioluminescence method.** 3,5-CP and 2,6-CP showed the highest toxicity of all tested phenols. Our microorganisms revealed one order higher resistance than the standard strains.

### IV. CONCLUSIONS

The results obtained using the both methods (growth and bioluminescence inhibition) show that toxicity of chlorophenols depends not only on the number of substituents, but also on the substitution pattern, therefore toxicity is structurally dependent.

### ACKNOWLEDGEMENTS

Financial support from VEGA Grant Agency (Grant No.1/1309/04) is gratefully acknowledged.

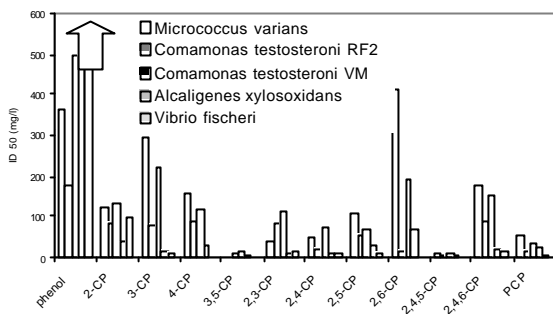


Figure 3: The ID<sub>50</sub> values of the selected chlorophenols in the presence of tested bacteria.

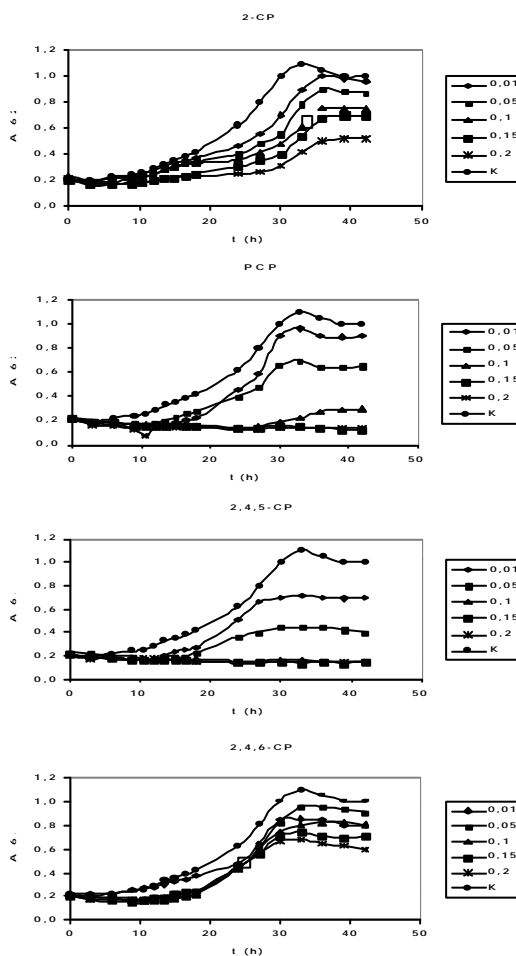


Figure 4: Growth curves of *Comamonas testosteroni* RF2 in the presence of selected chlorophenols (g/l).

### REFERENCES

- [1] EPA Method 604, Phenols. Environmental Protection Agency, Part VIII, 40 CFT Part 136, Federal Registration, 58,1984.
- [2] EPA Method 625, Base/neutral and acids. Environmental Protection Agency, Part VIII, 40 CFT Part 136, Federal Registration, 153, 1984.
- [3] M. Häggblom, R. J. Valo: In: (L. Young, C. Cerniglia, eds.) Microbial Transformation and Degradation of Toxic Organic Chemicals. Wiley – Liss. Inc., 89, 1995.
- [4] Männistö et al.: Water Res. 35, 2496, 2001.

# Applications of the data-driven modelling techniques in hydrology

Luka Stravs and Mitja Brilly  
Faculty of Civil and Geodetic Engineering  
University of Ljubljana  
Ljubljana, Slovenia  
Email: {LSTRAVS,MBRILLY}@fgg.uni-lj.si

**Abstract** — *New type of data-driven models like neural networks, fuzzy models and decision trees have recently emerged in the hydrological praxis. Applications of the machine learning methods for generation of the decision tree models in the field of hydrological modelling are presented in this paper. Very useful models were developed by combining the conceptual knowledge and the use of the machine learning methods. Usage of machine learning methods like decision trees for generation of structurally transparent and explanatory models from the data has offered great promise in helping scientists to uncover patterns hidden in their data.*

## I. INTRODUCTION

Hydrological modelling is a constantly evolving discipline in the field of hydrological science where different more or less successful approaches exist. Well known are conceptual models that are based on the prior theoretical knowledge of all the hydrological processes in the form of theoretically developed or empirical equations. Conceptual models require a lot of detailed data like river network, land cover and soil characteristics data or topographical maps which are often unavailable or not available at the time of model development. Empirical black box models simply connecting input and output have also been widely used in hydrology. On the other hand new type of data-driven models like neural networks, fuzzy models and decision trees have recently emerged in the hydrological praxis.

Successful applications of data-driven modelling techniques in modelling environmental processes like debris flows or floods are well known [2]. While usage of neural networks has already been widely researched [1], new emerging methods like decision trees, instance-based learning, fuzzy based systems or chaos theory have not gained so much attention in the field of environmental science yet.

## II. METHODS

Models generated with the machine learning methods are mostly used for forecasting & prediction and for extracting new knowledge about the observed proc-

esses. The basic idea of generating the decision tree models is to develop simple, transparent models that are easy to use and implement. By feeding the machine learning method with enough input and output data of the modelled process it can automatically learn the patterns underlying the modelled process and divide the input data (in machine learning theory called attributes) space into its subspaces where certain characteristic similarities or patterns exist.

The basic components of a decision tree are the decision nodes, branches and leaves. Results of the modelling are decision tree models, which are a way of representing a series of rules that lead to a class value, numerical value or linear equation, and are therefore classified into:

- classification trees with class values as leaves of the model;
- regression trees with constant numerical values as leaves of the model;
- model trees with linear equations as leaves of the model.

In our case we used the machine learning methods M5 and J4.8 as they are implemented in the WEKA system [3], developed at the University of Waikato, New Zealand, to generate decision tree models:

- to analyse the impact of reforestation on the water balance of the entire Dragonja River basin and learn more about climate and other factors influencing it (CASE #1);
- for the purpose of improvement and development of the long-term low flow forecasting at water stations located at various Sava River's tributaries (CASE #2) and
- for the purpose of the short-term flood forecasting at the Savinja River basin (CASE #3).

## III. RESULTS

### A. CASE #1

Decision tree models connecting some of the measured factors influencing the precipitation interception process in the Dragonja River basin and precipitation interception rate were developed.

Many interesting and useful details about the process of precipitation interception by the forest in the Dragonja River basin were found. In most cases, rainfall events with up to approximately 2.5 mm of rainfall contribute almost nothing to the recharge of groundwater at the Dragonja river basin and the Dragonja river discharge, with the exception of rainfall events longer than 1.67 hours and temperature lower than 14°C. The generated models also show that approximately 23 to 43% of the water at events with more than 2.5 mm of rainfall is intercepted by the forest as a direct consequence of natural reforestation in the last few decades.

Rainfall <= 2.5 :	
	Temperature <= 14.2 :
	EventDuration <= 1.67 : PI_percent = 81.2
	EventDuration > 1.67 : PI_percent = 47.2
	Temperature > 14.2 : PI_percent = 95.5
Rainfall > 2.5 :	
	Rainfall <= 7.5 : PI_percent = 42.8
	Rainfall > 7.5 : PI_percent = 23.2

Figure 1: Generated regression tree (M5 method) – pruned regression tree.

#### B. CASE #2

Models with variable (Table 1) and models with the constant recession coefficient were tested on the 2003 streamflow recession data (Figure 2).

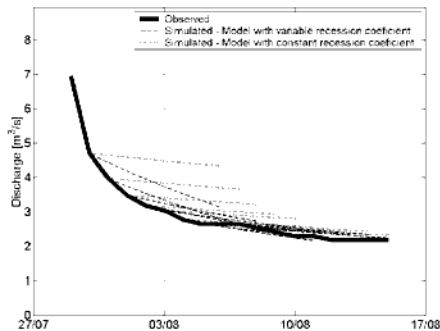


Figure 2: Verification and comparison of the models for the Radovna River.

Verification of the built low flow forecasting models with the variable recession coefficient showed really good accuracy (Figure 2), especially when compared to the accuracy of the models with the constant- or single-valued recession coefficient, where the variability of the factors influencing the streamflow recession is not captured.

Radovna – Gauging station Podhom	
dQ <= 0.207 :	
	dQ <= 0.123 :
	Qt <= 2.2 : <b>k = 0.00813</b>
	Qt > 2.2 : <b>k = 0.01730</b>
	dQ > 0.123 : <b>k = 0.02580</b>
dQ > 0.207 :	
	dQ <= 0.554 : <b>k = 0.03520</b>
	dQ > 0.554 : <b>k = 0.05770</b>

Table 1: Generated regression tree model of the recession coefficient for gauging stations Podhom.

#### IV. CONCLUSIONS

Applications of the machine learning methods for generation of the tree-like models in the field of hydrological modelling were shown. Very useful models were developed by combining the conceptual knowledge and the use of the machine learning methods.

Usage of data-driven modelling techniques in hydrology presents a very useful alternative to classic hydrological modelling, especially from the view of reducing man-power spent in the process of calibration of the hydrological model. After the data preparation process is done, training of the models is easy, fast and mostly depends on the modeller's choice of how complex versus how accurate model is wanted. From the built tree-like models' structure new knowledge about processes in the river basin can be extracted.

Usage of machine learning methods like decision trees for generation of structurally transparent and explanatory models from the data has offered great promise in helping scientists to uncover patterns hidden in their data. However, the development of models is only one of the steps in acquisition of new knowledge; the selection, collection and preparation of data, the control over the model development and the interpretation of the generated models by the scientists who understand the modelled processes are equally if not even more important.

#### REFERENCES

- [1] Govindaraju R.S. and Ramachandra Rao A. Artificial neural networks in hydrology. Kluwer Academic Publishers, Dordrecht, Netherlands, 2000.
- [2] Solomatine D.P. and Dulal K.N. Model trees as an alternative to neural networks in rainfall-runoff modeling, Hydrological Sciences Journal, 48 (3): 399–411, 2003.
- [3] Witten I. H. and Frank E. Data mining: Practical machine learning tools and techniques with java implementations. Morgan Kaufmann Publishers, San Francisco, USA, 2000.

# Life Cycle Assessment, Total Quality Management and Intelligent Metrology to support disassembly, recycling and re-use of parts from used electronic products

H. Tahirova, P.H. Osanna, N.M.Durakbasa  
Department for Interchangeable Manufacturing and Industrial Metrology  
Vienna University of Technology  
A-1040 Vienna, Austria  
alima\_th@yahoo.com, durakbasa@mail.ift.tuwien.ac.at

**Abstract** — *Important change of the environment, limited availability of natural resources and the increasing growth of waste require new concepts and strategies to recycle technical products as there are household instruments, consumer electronics and passenger cars -instead of land filling, burning or steel production a high potential of recycling is necessary. Environmental attributes are becoming a factor of growing importance at all stages of an electronic products life cycle from design to end-of-life. The European legislation has passed the directive on Waste of Electrical and Electronic Equipment (WEEE) to regulate their collection and appropriate end-of-life treatment. An economic, sustainable and ecological procedure is necessary to prepare and to refurbish products, therefore the disassembly is the first step of a high potential of recycling.*

## I. INTRODUCTION

Basic conditions for enterprises of almost all industries have significantly changed in the last years. Intensified competition and economical pressure force enterprises to critically analyse competition strategies and competition-critical success factors such as price, quality, capability characteristics, duration, service and image even more.

It is hard for consumer to differentiate products nowadays, while it was much simpler to select a product from certain product groups in the last decades.

Apart from the classical "product qualities", which differ very little from one competitor to another, the environment-oriented design of the product in the context of production, use and disposal is in the focus for last years. Consumers approach some products like electrical and electronic even more critically. Producers of electrical and electronic products are under pressure from consumers to have products that environmentally friendly and cause less pollution.

Currently disposal of electronic products is very important problem. Besides the "Directive of Waste from electronics and electrical equipment" (WEEE), which apart from the prohibition of certain substance contents (Pb, CD, Hg, halogens...), also regulates recycling

quota, there exist some other ways of utilization and disposal the waste already partly established on the market. The environmental profile of a product can substantially affect the procedures and the quality of the disposal. The evaluation with the help of the ecological balance, which is to take up the environmental effects of the entire life cycle of a product, is the method to be quantified as beneficial.

If the life cycle of a product is considered, then the requirements are resulted from the sum of the individual requirements of the each life cycle phases. While in the past frequently only the phases of development, production, distribution as well as use or service were considered, the current requirements increased from the complete view of the products up to their end of life.

This means additional consideration of the End of Life Phases: recycling and disassembly of the products as well as Redistribution and disposal. The disassembly takes a central position within recycling. The non destructive disassembly is to be regarded therefore as one of the most important goals for the reuse of electronic products. The increasing trend for mobile communication in the past years causes an increase of old mobile phones, which in turn should be professionally eliminated. Mobile telephones have an amazingly short life period. Presently there are already about 2000 different types of mobile phone world-wide.

Many components of mobile phone must be placed in a very small space which is very disassembly unfriendly. There are hardly very small screws gripping surfaces for disassembling of these components. Regulation of exact positions screw and snap connec-

tions is an important issue in disassembly of old mobile telephones.

In this case the coordinate measuring technique (KMT) is an important tool so that to get information about the condition of the products. With the help of KMT work pieces with complex geometrical characteristics can be measured with high precision. In this study using the coordinate measuring apparatus (KMG) in a Cartesian coordinate system points at the surface of a mobile telephone in the computer a numeric image of the work pieces is provided.

A goal of the current study is the creation basis for the flexible automation of the disassembly as contribution to the introduction of economical and ecological solutions for the disassembly.

## REFERENCES

- [1] A. Dinge.: Demontage komplexer Produkte in einer Kreislaufwirtschaft, Josef EUL Verlag, Lohmar-Köln, 2000
- [2] Directive 2002/96/EC of the European Parliament and of the council on waste electrical and electronic equipment (WEEE) of 27 January 2003.
- [3] Elektronikschrott-Recycling- Wirtschaftsfaktor oder Flop?, VDI-Berichte 1695, Tagung Frankfurt 17 Oktober 2002, Hrsg.: VDI-Kompetenzfeld Betrieblicher Umweltschutz und Umweltmanagement.- Düsseldorf: VDI Verlag, 2002
- [4] P.H. Osanna, H. Weseslindtner, M.N. Durakbasa, H. Tahirova, A. Afjeji-Sadat.: "TQM, LCA and Sustainability in European Industry Supported by Intelligent Flexible Disassembly and Recycling of Used Products" in Innovation- Technics- Education, BUDAPEST TECH, 2005, Vortrag; pages 312 - 318.
- [5] G. Kaufmann.: Möglichkeiten und Grenzen des Produktrecycling von dem Hintergrund einer ökologieorientierten Unternehmensführung, Verlag Dr. Kovac, Hamburg, 2002

# Giant Phospholipid Vesicles as a Possible Diagnostic System for the Study of Protein Interaction with Membranes

Jasna Urbanija and Veronika Kralj-Iglič  
Institute of Biophysics  
University of Ljubljana  
Ljubljana, Slovenia  
[jasna.urbanija@biofiz.mf.uni-lj.si](mailto:jasna.urbanija@biofiz.mf.uni-lj.si)

**Abstract**— *The aim of our study is to develop a simple diagnostic tool for detection of certain proteins in a human sera. Phospholipid vesicles are good approximation of real cell membranes, therefore interaction between them and certain proteins of interest (in our case different antibodies and beta2-glycoprotein1) could show the presence of these proteins in the sample. The interactions could be defined by observing the effect of proteins on the morphology and dynamics of vesicles.*

## INTRODUCTION:

Antiphospholipid syndrome (APS) [1] is an autoimmune disease characterized by thrombotic events and/or pregnancy morbidity. It is more common in women than in men [1]. The etiology and underlying mechanisms of APS are not yet understood, however, activation of the coagulation system is evident.

Antiphospholipid antibodies are present in the sera of patients with APS [1]. These antibodies were found to interact directly with anionic phospholipids constituting cell membranes (e.g. cardiolipin) or to bind to epitopes of plasma proteins – antigens, which form complexes with phospholipids [1,2]. The most common antigen for antiphospholipid antibodies is beta2-glycoprotein1 ( $\beta_2$ GP1) [1].

## STUDY OF INTERACTIONS :

A standard method of antiphospholipid antibodies characterization is ELISA test, a biochemical technique used in immunology to detect the presence in a sample of antibodies or antigens, by their interaction with a micro-titre plate. The accuracy of this method is limited since the configuration of molecules on the micro-titre plate differs considerably from their configuration in the membrane. It is of interest to develop a

well defined system that would resemble the native configuration of the molecules in the membrane. Phospholipid vesicles could represent such system as they form the base of biological membranes. Phospholipid vesicles can be produced in various sizes ranging from 50 nm (small) to 50  $\mu$ m (giant), various compositions of phospholipids and in well controlled environment. The interactions between vesicles and exogeneously added substances can be assessed by observing their effect on the morphology and dynamics of vesicles. Thereby, interactions between phospholipids, antibodies and antigens can be studied by their effect on the vesicles. This system thus represents a possible simple and inexpensive diagnostic tool to detect the presence of particular antibodies in the sample.

In order to propose improvements in the diagnostic procedure, phospholipid vesicles and their interactions with antibodies and antigens should be studied and the results compared with results obtained with existing diagnostic procedures. Here, we study the effect of the direct interactions between phospholipid vesicles, antiphospholipid antibodies and  $\beta_2$ GP1 (both dissolved in phosphate buffer saline) on morphology of giant phospholipid vesicles containing high weight proportion of cardiolipin.

## MATERIALS:

The vesicles were prepared in sugar solution by the electroformation method [3]. Monoclonal antibodies anti- $\beta_2$ GP1 Cof-22 were obtained from BALB/c mice immunized with human  $\beta_2$ GP1 [4] where recognizing domain III of  $\beta_2$ GP1 was dialyzed against phosphate buffer saline as described in [5]. Antiphospholipid antibodies of a single patient were contained in the immunoglobulin fractions (IgG fractions which however contain many different antibodies) and

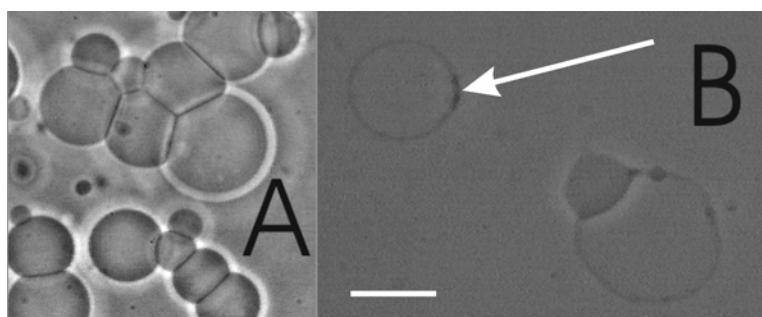


Figure 1: Giant phospholipid vesicles containing 40% weight fraction of cardiolipin after the addition of monoclonal antiphospholipid antibodies dissolved in phosphate buffer saline (A) and after simultaneous addition of the IgG fraction of the healthy person and  $\beta_2$ GP1 (B). The arrow indicates lateral segregation of the membrane constituents. Bar denotes 10  $\mu$ m.

dissolved in phosphate buffer saline [5]. For control, IgG fraction of a healthy person was dissolved in phosphate buffer saline [5].  $\beta_2$ GP1 was aliquoted and dissolved in phosphate buffer saline [6]. Vesicles were observed under optical microscope with the phase contrast optics and recorded with the video camera.

#### RESULTS:

We observed the following effects: adhesion of vesicles to the ground and to each other (Fig.1A,B), suppression of vesicle contour fluctuations, enhancement of the contrast of the vesicle contour (Fig.1A), permeabilisation of vesicle membrane to sugar resulting in disappearance of the contrast between the vesicle interior and exterior (Fig.1B), lateral segregation of the membrane constituents (Fig.1B, indicated by the white arrow) and bursts of vesicles.

These effects differed upon the content of the exogenously added substances (monoclonal antibodies, IgG fraction of healthy or diseased person,  $\beta_2$ GP1 or different combinations). Adhesion of vesicles is greatest with monoclonal antibodies (Figure1A), but weakens when monoclonal antibodies are added together with  $\beta_2$ GP1. Adhesion is much less pronounced with IgG fractions of healthy and diseased person, but increases when IgG fractions are added together with  $\beta_2$ GP1 (Figure1B). IgG fraction of a healthy person causes greater adhesion of vesicles to the ground and bursts of vesicles than IgG fraction of the diseased person. In all cases the fluctuations of the vesicles completely ceased, however, the change in fluctuations and contrast occurred faster with IgG fractions of the healthy person in comparison to IgG fraction of the diseased person. Segregation of the membrane constituents was

greatest with IgG fraction of the diseased person or its combination with  $\beta_2$ GP1.

#### CONCLUSIONS:

Our results indicate that antibodies and antigens may have an important role in the formation of complexes composed of cells, membrane fragments and proteins - complexes which are important in blood clot formation. Moreover, systematization of the method (e.g. possibility to analyze the fluctuation pattern) and control of the environment (such as temperature etc.) offer new possibilities in study of the interaction of proteins with biological membranes.

This work was done in collaboration with: A. Ambrožič, S. Čučnik, N. Tomšič, M. Lokar, B. Babnik, B. Rozman, A. Iglič

#### REFERENCES:

1. Mackworth-Young C., *Autoimmunity Reviews* **2006**, 5: 70-75
2. Alberts B.: *Molecular biology of the cell*, Garland Science **2002**
3. Angelova M. I., Soléau S., Meléard P., Faucon J. F., Bothorel P., *Prog. Colloid Polym. Sci.* **1992**, 89: 127-131
4. Polz, E. and Kostner, G. M., *FEBS Lett.* **1979**, 102: 183-186
5. Ambrožič A, Božič B, Kveder T, Majhenc J, Arrigler V, Svetina S, Rozman B., *Biochim. Biophys. Acta* **2005**, 1740: 38-44
6. McNally T., MacKie I. J., Isenberg D. A., Machin S. J., *Thromb Res* **1993**, 72:275-286

# Investigations at Industrial Wastewater Treatment Plants in Nicaragua

U. Wegricht, V. Parravicini, H. Kroiss (Faculty Mentor)  
Institute for Water Quality, Resources and Waste Management  
Vienna University of Technology  
Vienna, Austria

Email: {uwegircht, vparravi, hkroiss} @iwag.tuwien.ac.at

**Abstract** —*Nicaragua is one of the poorest countries in the tropical region of Central America. Until now only a small amount of waste water is being treated in this country and not a lot of investigation has been done on waste water treatment in tropical.*

*The aim of this project was to assess the efficiency of the WWTP of 3 different food industries and to develop a systematic approach to use while planning or optimising WWTP.*

*Not only technical issues were taken into account, but also social and climatic differences.*

## I. INTRODUCTION

In the period between March and August 2004 three wastewater treatment plants (WWTP) of different food industries in Nicaragua were investigated. The aim of the project was to assess the efficiency of the WWTP and to develop a systematic approach to use while planning or optimising WWTP. The most important aspect was to take into account the special requirements of WWTP in a tropical developing country like Nicaragua.

This study was realised as a master's thesis at "Proyecto ASTEC" in Nicaragua, which is a project of the EZA<sup>1</sup>, in cooperation with the Vienna University of Technology and the University of Natural Resources and Applied Life Sciences, Vienna.

## II. APPROACH

All over the world water issues as water supply, sewage disposal or wastewater treatment are getting increasingly important. Wastewater treatment is essential to maintain or restore a good water quality of lakes and rivers and as a consequence even the quality of the raw water for drinking water supply. This issue is even more important in a developing country like Nicaragua where a large amount of drinking water is taken directly from surface waters.

Since 2000 it is obligatory to treat industrial wastewater in Nicaragua. Like in most developing countries still only a small part of wastewater (approx. 20 %) is actually being treated in WWTP [1]. On the one hand building and operating WWTP strongly depends on available technology and financial resources, on the other hand social and cultural issues as e.g. the level of professional education must be taken into account.

Although size and technology of the WWTP and the composition of the wastewater were different in all three WWTP investigated, a comparison was possible since similar processes were applied in all of them: After a mechanical treatment, the wastewater was treated biologically in anaerobic bio filters and successively treated in an aerobic final step.

Difficulties and shortcomings in process, operation and maintenance were localised and analysed. As a result a systematic method was elaborated, which indicates the minimum of analytic monitoring and information on process parameters necessary for planning or analysing a WWTP, considering the limited laboratory and human resources of a developing country. Mass balances were used as a tool to check the data

## III. RESULTS

In all investigated WWTP 80-93 % of the organic carbon load was removed and the quality of the treated wastewater complied with the limits specified by the Nicaraguan Government. Figure 1 shows as an example the COD concentration in various measuring points at the WWTP of a brewery. The point number 6 in this figure marks the effluent of the WWTP. The continuous line indicates the Nicaraguan limits, whereas the dashed line shows the Austrian ones.

However it has to be considered that because of different reasons, like missing pumps or tubing and insufficient capacity, only 25-50 % of the wastewater generated in the industrial process was treated in the WWTP. The remaining wastewater was discharged untreated into the water body. [2]

---

<sup>1</sup> Austrian Development Cooperation

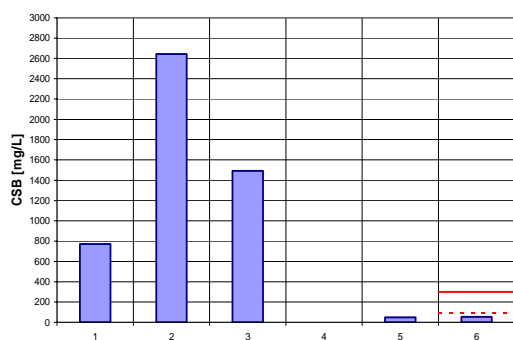


Figure 1: COD concentrations in various measuring points at the WWTP of a brewery

In two cases lack of maintenance was the reason that the maximum capacity was already reached due to plugged bio filters even though the hydraulic- and biochemical design load have not been reached yet. In one case the hydraulic inflow exceeded the design value.

Since the size of the investigated WWTP is in a range of 910-36.360 PE<sup>2</sup>, it is difficult to compare the costs considering the scale effect. The specific building costs were similar at all three WWTP and amounted to 6,2 to 7,4 €/PE\*a. The specific operating costs depended strongly on the size and how efficiently the capacity of the WWTP was used. They came up to 1,6 to 5,0 €/PE\*a. Biogas, produced in the anaerobic stage of the process, could bring a cost reduction up to 100 % of the operating costs.

Building and operating costs in Europe are about four times higher [3], but cannot easily be compared since processes, requirements on limits and climatic conditions are extremely different.

#### IV. RECOMMENDATION FOR FUTURE PLANNING AND OPERATION

Various defects and shortcomings regarding operation and efficiency were localised in almost all processes of the WWTP. Numerous improvements could easily be implemented with only little money. Other problems however result from bad design and the selection of treatment processes, which were not suitable as well as a low level of professional education and the low interest of industry owners and managers. The following list indicates some important points to be considered when planning a WWTP in Nicaragua.

- Because of low sludge generation, low energy input and the production of biogas, anaerobic

bio filters in tropical countries have many advantages. Nevertheless they require skilled operation and regular maintenance for efficient wastewater treatment.

- Construction and equipment of the WWTP must be suitable for the specific local climatic conditions. They should also be robust and easy to handle for operators.
- If possible construction material and equipment should come from the region where the WWTP is built to simplify maintenance.
- It is recommendable to involve operators of WWTP into the project as soon as possible. As the level of professional education is usually low in Nicaragua, it is essential to offer training in WWTP operation as well as monitoring and documentation.

#### V. CONCLUSION

Design, construction and operation of a WWTP in Nicaragua is not only a question of technology and financial resources, but also a social issue. After decades of dictatorship and civil war the population is only starting to realise their possibilities to take initiatives rather than to wait for orders. Structures are still hierarchic and education or professional development is not supported enough by the authorities.

All this leads to the point that not only the construction of WWTP and sewer systems is highly important, but also education and professional training of the people and helping them to find their possibilities and responsibilities.

#### REFERENCES

- [1] L. KORSACK, L.MORENO, Wastewater treatment in Nicaragua. In Proceedings of the 9<sup>th</sup> IWA specialized conference on Design, Operation and Economics of Large Wastewater Treatment Plants, pages 213-216, Prague, Czech Republic, September 2003
- [2] U.WEGRICHT, Effizienz und Nachhaltigkeit von industriellen Kläranlagen in Nicaragua, Vienna, Austria, March 2005
- [3] S. LINDTNER, O.NOWAK, H.KROISS; Benchmarking für Abwasserreinigungsanlagen, Wiener Mitteilungen, Band 176, Vienna, Austria, February 2002

<sup>2</sup>Population Equivalent; 1 PE = 110 g COD/d

# Development of an Online Tool for the Simulation of the Anaerobic Digestion Process

A. Wolfsberger, S. Beisteiner and P. Holubar (Faculty Mentor)  
Department of Biotechnology, Institute of Applied Microbiology  
University of Natural Resources and Applied Life Sciences Vienna  
Muthgasse 18, A-1190 Vienna, Austria  
Email: alexandra.wolfsberger@boku.ac.at

**Abstract** — *Anaerobic digestion (AD) of biomass is a rather complex process. To gain more insight into this bio-process, a deterministic software tool, a so called “Virtual Laboratory (VL)” was developed. This tool is based on the Anaerobic Digestion Model No.1 (ADM1). This AD model was adopted to meet the demands of modelling the biogas process using energy crops as substrate. The extension of the ADM1 covers the implementation of a second hydrolysis rate for carbohydrates and the sulphate reduction process.*

## I. INTRODUCTION

Anaerobic digestion of wastewater, organic wastes and biomass results in the formation of a useful end-product (biogas). Biogas is primarily composed of methane and carbon dioxide and can be processed to electrical energy and heat. Due to a special encouragement by the government, there is a proper boom of biogas-plant technology in Austria, in recent times. Most of these biogas plants are agricultural biogas plants and use energy crops, especially maize, as a renewable and sustainable substrate.

To integrate the energy production from biogas into the existing energy infrastructure, the AD of biomass has not only to be made economically attractive, but also certain problems have to be solved e.g. low methane content of the gas, self heating or odor problems.

It has been shown before ([1], [2], [3]) that it is possible to enhance the performance of a biogas plant with an advanced process control system. But to implement an effective control tool, a good knowledge of the AD-process itself is necessary.

Therefore a “Virtual Laboratory” (VL) – a software training tool – was developed. This tool is thought as an instrument to provide users the possibility to gain more insight into the biogas process. It should also support the daily work of researchers and engineers. The VL is planned to be online accessible to share common knowledge of the process. Basis of the VL is the Anaerobic Digestion Model No.1 (ADM1). The ADM1 is a mathematical model describing the AD process [4].

## II. MATERIALS AND METHODS

As the ADM1, most of the published anaerobic models are designed for the use of primary sludge or organic wastes ([5], [6]). As the use of crops in biogas plants becomes more important, subsequently a better adapted model for energy crops is necessary.

The original ADM1 is very general and keeps to the surface of the AD-process, although it provides a common basis for a broad range of different applications and supports further development. Information is missed in some areas: For example, no analysis and validation data of the suggested biological parameters exist, especially for different feeds and reactor designs. Moreover, little information is given on the changes of kinetics for different temperature ranges [4].

The modification of the model comprises the consideration of an increased solid and cellulose content of substrates and the sulphate reduction process (SRP). The implementation of the SRP was already shown by Strik (2004) [7]. The high solid input – usual for energy-crop biogas plants - is considered in the input and the high cellulose content is taken into account by a second hydrolysis rate (slow and fast degradable material). “Equation (1)” shows the extra process rate.

$$\rho_{20} = k_{hyd\_ch\_s} * X_{37} \quad (1)$$

Moreover, the parameters suggested by the IWA Task group are not fitting properly for the use of energy crops as substrate but for surplus sewage sludge. As a consequence the most important and sensitive parameters are experimentally estimated for different crops, particularly maize silage.

Data for the estimation of kinetic parameters, model calibration and validation are obtained on four 20 l lab-scale anaerobic completely stirred tank reactors (CSTR). Two of the reactors are operated mesophilically and two thermophilically. Two different kinds of substrates are used. First: a synthetic substrate, consisting mostly of flour and Peptone, representing the nutrient composition of maize silage. Second: grounded maize silage was used. In- and

output of the reactors are monitored both online and offline.

### III. RESULTS AND DISCUSSION

For model calibration the differential equation system of the adapted model is solved with a differential equation (DE) solver (ODE15s Solver from MATLAB®). The results are then compared with measured data. If necessary parameters are adjusted until the best fit is found. The adapted and calibrated model is then introduced in the VL.

A further output of the project is a European database on energy crops and also needed kinetic parameter for the model. This database is based on both literature data and also on experimental data. The database is implemented in the VL and provides a good basis to model different plant scenarios. For advanced users of the tool it is also possible to change model parameters or enlarge the database and so increase the capabilities of the tool. The database also potentiates to make useful simulation of the process without a high range of measurements.

The VL consists of different layers for substrate choice and characterization of the used reactor. After the selected case is modelled, the output of the model is presented in form of diagrams and tables (“Figure 1”).

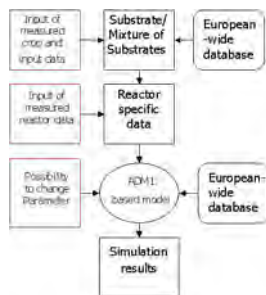


Figure 1: Structure of the VL

### IV. CONCLUSION

The ADM1 should serve, in an adjusted form, as basis for a VL. The adaptation covers the consideration of a high cellulose content, as energy crops are used as substrate and an extension for the sulfate reduction process [7].

Four completely stirred tank reactors were operated with maize silage. The results of several months of operation are used for model validation and calibration.

Result is an online tool that gives the possibility to gain first experiences with modelling and simulation of a complex biological process. It provides also a strong tool to impart knowledge about the AD process.

### ACKNOWLEDGMENTS

The project CROPGEN is funded by the European Commission on the project number: SDES6-CT-2004-502824. Special thanks goes to C. Rosen and U. Jeppsson for providing the SIMULINK® script of the original ADM1.

### REFERENCES

- [1] P. Holubar, L. Zani, M. Hager, W. Fröschl, Z. Radak and R. Braun. Advanced controlling of anaerobic digestion by means of hierarchical neural networks. *Water Research*, 36:2582–2588, 2002
- [2] P. Holubar, L. Zani, M. Hager, W. Fröschl, Z. Radak and Rudolf Braun. Start-up and recovery of a biogas-reactor using a hierarchical neural network-based control tool. *Journal of chemical technology and biotechnology*, 78:847–854, 2003
- [3] D.P.B.T.B. Strik, A.M. Domnanovich, L. Zani, R. Braun, P. Holubar. Prediction of Trace Compounds in Biogas from Anaerobic Digestion using the MATLAB® Neural Network Toolbox. *Environmental Modeling & Software*, 20:803-810, 2005
- [4] D.J. Batstone, J. Keller, I. Angelidaki, S.V. Kalyuzhnyi, S.G. Pavlostathis, A. Rozzi, W.T.M. Sanders, H. Siegrist, V.A. Vavilin. *The IWA Anaerobic Digestion Model No. 1 (ADM1)*. IWA Publishing, London, 2002
- [5] I. Angelidaki, L. Ellegaard and B.K. Ahring. A Mathematical Model for Dynamic Simulation of Anaerobic Digestion of Complex Substrates: Focusing on the Ammonia Inhibition. *Biotechnology and Bioengineering*, 42:159-166, 1993
- [6] H.Siegrist, D. Vogt, J.L. Garcia-Heras and W. Gujer. Mathematical Model for Meso- and Thermophilic Anaerobic Sewage Sludge Digestion. *Environmental Science and Technology*, 36:1113-1123, 2002
- [7] D.P.B.T.B. Strik. Modeling and Control of Hydrogen Sulphide and Ammonia in Biogas of Anaerobic Digestion towards Biogas usage in Fuel Cells. Dissertation, University of Natural Resources and Applied Life Science, Vienna, 2004

# Meanings in Urban Public Landscapes

Burcu Yigit Turan and Richard Stiles (Faculty Mentor)  
Department of Urban Design and Landscape Architecture  
Vienna University of Technology  
Vienna, Austria

Email: burcu@landscape.tuwien.ac.at, richard.stiles@tuwien.ac.at

**Abstract** — *The aim of this study is to explore the meanings of urban public landscapes, which is very important on people’s use of places and their development of identity over their use and personal representation, generating a new theoretical framework based on general issues and methods in the field of semiotics considering the physical and social characteristics of urban public landscape and topics in urban landscape research.*

*A model, which is the result of this analytical framework, is applied on urban public landscape bringing new interpretations of concepts from semiotics. The model of meaning formation in urban public landscape, and different types of textual and visual presentations for different urban landscape meanings constitutes the research results.*

## I. INTRODUCTION

Meaning, which is defined as “*the import of any signification*” and as “*the product or result of communication*” [1], has been generally taken as an issue by philosophy, linguistics, communication studies, sociology, literature, anthropology, and analytical psychology under the umbrella of semiotics [2, 3].

From landscape architectural point of view, meaning as a topic has been the subject of several studies in landscape research focusing on different aspects of human and landscape relationship over recent decades [4, 5, 6, 7]. Some of these studies concerning the meanings in landscapes focus on landscape structures altered by humans to explain the social structure and rituals of society as landscape meaning, while others searching for the values and thoughts of people relating to existing urban landscapes as landscape meanings.

In abstract terms, semiotics sees meaning as a product of a dynamic process of cycling systems of interacting elements. The primary message is sent by the author, which elicits from reactions by readers as seen in a summary model “Figure 1” [2,3]. The smallest meaningful unit in the message is called as “*morpheme*” [2].

Therefore, it is required to see the formation of meaning by evaluating these two aspects considering the interaction between them involving a large spec-

trum in factors required from discussions, terminologies, and models from semiotics to understand how meanings in urban public landscapes are produced, interact with people and cycle.

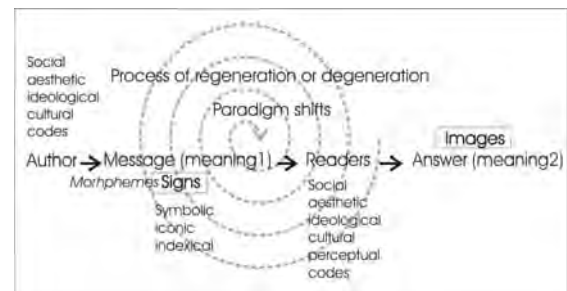


Figure 1: Process of meaning formation

Creation of first meaning, as a message in any form of object, is a work of a creator, who shapes the meaning with his/her social, aesthetic, cultural and ideological codes. The object (message) involves different elements, signs in different forms such as symbolic, iconic or indexical, as vehicles of meaning. When the message (first constructed meaning) is received by the readers, they produce their own meanings (images) based on their personal social, aesthetic, ideological, cultural and perceptual codes as reflections. These meanings of authors and readers interacting start a process of meaning formation, which may include regenerations and degenerations through the paradigm shifts in codes of social structure in society, ideology and aesthetics “Figure 1” [1, 2, 3, 8]. This process of shifts in codes is called codification [2].

## II. TRANSFER OF THEORY: CONSTRUCTION OF A NEW THEORY? REFLECTIONS OF SEMIOTICS ON LANDSCAPE

Urban public landscapes, with their material aspects of functions, design styles, specialized spaces, symbols and aesthetics are mostly a sphere, where the city authorities and landscape architects stress their ideological and aesthetic tendencies as the authors of the projected meanings. The users of the urban landscapes in front of the projected constructions of

meanings in urban public landscapes generate their own reflected meanings as images related to their basic ideological tendencies, cultures, values, beliefs, aesthetic preferences, and social characteristics. Some of the users accept and agree with the messages sent by the urban public landscape producers, while they are rejected by others. This reaction of acceptance and refusal is reflected in the decision of the use, benefit and represent or not to use, benefit and represent by the public. Also people, who do not have certain perspective on their ideology and social life, adopt the meanings as their own personal meanings, reshaping their life style according to the projected urban public landscapes. Within the paradigm changes and interactions, urban public landscapes evolve with their new physical infrastructures, new locations or new reacted meanings into the same physical infrastructures and involve some people, while exclude others [5, 7, 9].

The suggested typologies of morphemes and signs in urban public landscapes considering the physical characteristics include monumental trees, plain grass surfaces, meandering paths, statues of people or things, squares, play grounds, advertisement signs, buildings and many other recreational functions and structures. The functional assets and aesthetic language of the urban public landscape are shaped by city authority and landscape architect can be evaluated also in terms of ideological and aesthetic codes. For instance, in modernist paradigm, with the rise of idea of welfare state and the role of city municipality for the public interest, had taken sport areas in their functional program, in the meanwhile constructivist aesthetic had become codes for urban public landscapes in the beginning of 20<sup>th</sup> century. The images generated by people through the perceptions as reacted meanings for those urban public landscapes can be exposed from old pictures, historical narratives, poems, movies and diaries. For the contemporary reacted meanings for urban public landscapes, the method is the field research including site observations, interviews and questionnaires.

Different meanings projected for urban public landscapes by city authority and landscape architect can be classified visually, based on physical analysis for exposing the different typologies. Different meanings generated by users can be visualized with representative images and personal meaning maps.

### III. CONCLUSION: TOWARDS A PROFESSIONAL STRATEGY

Many policies, especially in European context, for the urban environments, have suggested inclusive civic urban public landscapes, where every citizen can use, benefit and enjoy from the urban land-

scape, and represent his/her own personality, and interact with each other in a free, peaceful and plural atmosphere. For the public interest, within this analytical framework of meaning formation and new terminology for the exposition for the meanings of urban public landscapes, the landscape architect as a professional is able to question his/her social, ideological, and aesthetical stand point in the creation of urban public landscapes in relation to the social, ideological, aesthetic, cultural and perceptual codes in the society, and reflect this data as input for defunct urban public landscapes for regeneration diminishing the physical obstacles and producing new creative languages of design with the deconstructed existing morphemes and newly designed morphemes with the aim of social inclusion and maximum benefit from urban public landscapes for people.

### REFERENCES

- [1] T. O'Sullivan, J. Hartley, D. Saunders and J. Fiske. *Key Concepts in Communication*. Methuen, London, 1983:182.
- [2] D. Chandler. *Semiotics: The Basics*. Routledge, London, Second Edition, 2003.
- [3] D. Sless. *In Search of Semiotics*. Barnes & Nobles Books, First Edition, USA, 1986.
- [4] M. Treib. *Must Landscape Mean?* (1995). In *Theory in Landscape Architecture: A Reader*, Edited by S. Swaffield, pages 89-101, University of Pennsylvania Press, Philadelphia, 2002.
- [5] R. Thayer. *Three Dimensions of Meaning* (1994). In *Theory in Landscape Architecture: A Reader*, Edited by S. Swaffield, pages 104-108, University of Pennsylvania Press, Philadelphia, 2002.
- [6] M. Francis and R. T. Hester. *The Meaning of Gardens: Idea, Place and Action*. The MIT Press, Cambridge, Second Print, 1991.
- [7] L. Tyrväinen, K. Mäkinen, J. Schipperijn and H. Silvennoinen. *Mapping Social Values and Meanings of Green Areas in Helsinki, Finland*. University of Helsinki, Department of Forest Ecology. Electronic publications, <http://www.fsl.dk/euforic/nbw.htm>, 2004.
- [8] C.K. Ogden and I.A. Richards. *The Meaning of Meaning*. Routledge and Kegan Paul, London, 1968.
- [9] B. Yigit Turan and R. Stiles. *Planning the Urban Landscape in Ankara: Changes of Meaning: The Period between 1920s-2000s*. In *Proceedings of ECLAS (European Council of Landscape Architecture Schools) Conference "Landscape Change"*, pages 152-163, Ankara, 2005.

# Interactions of Halide Ions with Aqueous Ammonia under Ultraviolet Irradiation with Low Pressure Mercury Lamps

Beckles Yvette and Diyamandoglu Vasil (Faculty Mentor)  
The City College of New York  
City University of New York  
New York, U.S.A.  
Email: {ybeckles,vasil}@ce.ccny.cuny.edu

**Abstract** — *The interactions of chloride (Cl<sup>-</sup>) bromide (Br<sup>-</sup>) and iodide (I<sup>-</sup>) ions with ammonia (NH<sub>3</sub>), under UV irradiation from low-pressure mercury vapour lamps were investigated. The findings revealed that Br<sup>-</sup> and Cl<sup>-</sup> promote ammonia photo-oxidation at all pH levels. Protons were released during NH<sub>3</sub> photo-oxidation while the halide ion concentrations remained unchanged. Nitrite (NO<sub>2</sub><sup>-</sup>) and nitrate (NO<sub>3</sub><sup>-</sup>) were produced with the yield being dependent on the initial pH of the irradiating solution. The extent to which NH<sub>3</sub> photo-oxidation occurred in the presence of halide ions was found to be dependent on the type and concentration of the halide ion, as well as the initial solution pH.*

## I. INTRODUCTION

Ultraviolet (UV) irradiation with low-pressure (LP) mercury vapour lamps is widely used in drinking water and wastewater disinfection. The effectiveness of LP lamps in advanced oxidation processes (i.e. removal of *N*-nitrosodimethylamine from water) has also been demonstrated (Lee et al, 2005). Studies on the chemical transformations occurring when common water constituents are exposed to UV light are limited. Such studies are important for effective UV process control. This study specifically addresses the interactions that occur between halide ions (namely chloride (Cl<sup>-</sup>), bromide (Br<sup>-</sup>) and iodide (I<sup>-</sup>)) and ammonia in water when irradiated with low-pressure mercury vapour lamps.

Cl<sup>-</sup> and Br<sup>-</sup> ions are prevalent in source waters used for drinking water, with Cl<sup>-</sup> being the most abundant. Significant quantities of Cl<sup>-</sup> are also found in some wastewaters. Major products formed in the photo-oxidation of ammonia under UV irradiation are nitrite (NO<sub>2</sub><sup>-</sup>) and nitrate (NO<sub>3</sub><sup>-</sup>) (Wang et al, 1994). In acidic solutions, pH 1– 6 both UV irradiation and a photo-catalyst are required to affect ammonia photo-oxidation with NO<sub>3</sub><sup>-</sup> formed as the final stable product. Under basic pH (8 – 12) ammonia photo-oxidation proceeds without the use of a photo-catalyst with NO<sub>2</sub><sup>-</sup> as the major end product.

## II. METHODS

The photoreactions were conducted in a well-mixed 5-L glass reactor equipped with temperature control and containing four low-pressure mercury vapour lamps (ACE, Model 12128, 3.5 W) with combined light intensity of 5.27 x 10<sup>-6</sup> Einstein/litre-second. Solution pH and dissolved oxygen were measured using an Ingold oxygen sensor and pH electrode (Mettler Toledo Process Analytical, Inc., Wilmington, MA) recorded at one-minute intervals.

Known concentrations of the sodium salts of the ions (Aldrich Chemical Company) were spiked into Milli-Q water up to a total volume of 5 litres and the solutions were irradiated. All experiments were conducted at a controlled temperature of 20°C. A DX500 (Dionex Corporation, Sunnyvale, CA) dual channel ion chromatography system (Dionex Ionpac AG9-HC and AS9-HC, 4mm) was used to determine time dependent concentrations of the anions.

## III. RESULTS AND DISCUSSION

### A. AMMONIA PHOTO-OXIDATION ENHANCED BY THE PRESENCE OF HALIDE IONS

When aqueous ammonia solutions were irradiated in the presence and absence of Cl<sup>-</sup> and Br<sup>-</sup> ions, NH<sub>3</sub> photo-oxidation occurred more rapidly in the presence of the halide ions. The extent to which NH<sub>3</sub> photo-oxidation is augmented by the presence of halide ions was found to be dependent on the type and concentration of the halide ion, as well as the initial pH of the irradiating solution, as illustrated in Figure 1. Ammonia solutions were irradiated in the presence of various halide concentrations at initial solution pH of 10 and 8. At pH 10, the rate of NH<sub>3</sub> oxidation increased in the presence of Cl<sup>-</sup> = 0.28 and 0.56 mM (10 and 20 mg/L respectively) and Br<sup>-</sup> = 0.06 mM (5 mg/L) over NH<sub>3</sub> oxidation without halide ions. At Cl<sup>-</sup> = 0.28 mM and Br<sup>-</sup> = 0.06 mM the increase in the rate of NH<sub>3</sub> oxidation was comparable. In addi-

tion, at  $\text{Br}^- = 0.03 \text{ mM}$  (2.2 mg/L) no increase in the rate of  $\text{NH}_3$  oxidation at pH 10 was observed, but at pH 8 there was a noticeable increase in the rate of  $\text{NH}_3$  oxidation for the same  $\text{Br}^-$  concentration of 0.03 mM over  $\text{NH}_3$  oxidation without halide ions at initial solution pH 8.

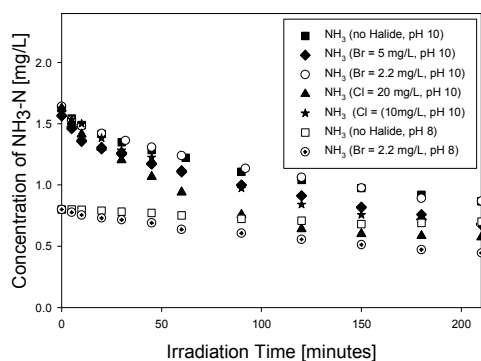


Figure 1. Comparison of  $\text{NH}_3$  Decay with Varying Halide ion Concentrations

#### B. INFLUENCE OF INITIAL SOLUTION PH AND HALIDE ION/AMMONIA CONCENTRATION RATIO ON THE REACTION PRODUCTS

In the presence of  $\text{Cl}^-$  and  $\text{Br}^-$  ammonia photo-oxidation proceeded only slightly in acidic solutions but more extensively in basic solutions. However, in the presence of  $\text{I}^-$  (see Figure 2) in acidic solutions,  $\text{NH}_3$  oxidation was inhibited and the pH of the irradiating solution increased. In basic solutions  $\text{NH}_3$  oxidation occurred in the presence of all the halides, and protons were generated as observed by a depression of the solution pH. When  $\text{NH}_3$  oxidation occurred it was also observed that the halide ion concentrations remained unchanged during the course of the reaction.

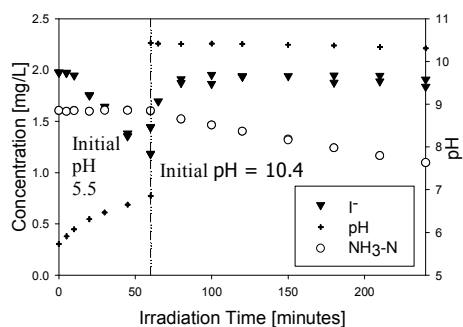


Figure 2.  $\text{I}^- = 0.016 \text{ mM}$  (2.0 mg/L) and  $\text{NH}_3\text{-N} = 0.114 \text{ mM}$  (1.6 mg/L)

It is proposed that this phenomenon occurred as a result of electrons ( $e^-$ ) being generated during  $\text{NH}_3$  oxidation. Irradiating  $\text{NH}_3$  in the presence of  $\text{I}^-$  in acidic solution (pH = 5.6) resulted in a depletion of  $\text{I}^-$  concentration. However when the pH of the irradiating solution was adjusted to basic (pH = 10.4) the concentration of  $\text{I}^-$  reverted to its original value.

Depending on the halide ion to ammonia concentration ratio,  $\text{NH}_3$  oxidation in basic solutions may proceed to such an extent that the pH is eventually depressed with prolonged irradiation and the  $\text{NO}_2^-$  formed is readily converted to  $\text{NO}_3^-$ . In the absence of halide ions,  $\text{NO}_2^-$  remains as the major reaction product. Figure 3 depicts the reaction kinetics for an aqueous ammonia solution containing  $\text{Cl}^- = 0.56 \text{ mM}$  (20 mg/L) and  $\text{NH}_3\text{-N} = 0.114 \text{ mM}$  (1.6 mg/L) at pH = 10. At this halide ion/ammonia concentration ratio, ammonia decay was rapid during the initial stages of the irradiation causing an ultimate drop in the solution pH. As the pH declined during the irradiation, the nitrite formed was converted to nitrate.

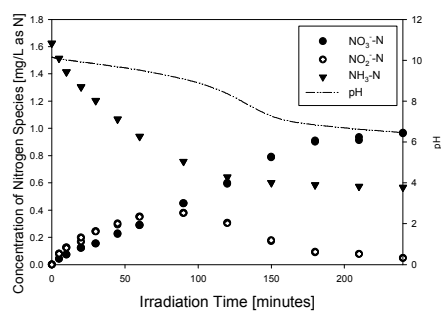


Figure 3. Irradiation of  $\text{Cl}^- = 0.56 \text{ mM}$  (20 mg/L) and  $\text{NH}_3\text{-N} = 0.114 \text{ mM}$  (1.6 mg/L)

#### REFERENCES

- [1] C. Lee, W. Choi, Y. G. Kim and J. Yoon. UV Photolytic Mechanisms of *N*-Nitrosodimethylamine in Water: Dual Pathways to Methylamine versus Dimethylamine. *Environmental Science and Technology*, 39(7) : 2101-2106, July 2005.
- [2] A. Wang, J. Edwards and J. Davies. Photooxidation of Aqueous Ammonia With Titania-Based Heterogeneous Catalysts. *Solar Energy*, 52 (6): 459-466, June 1994.

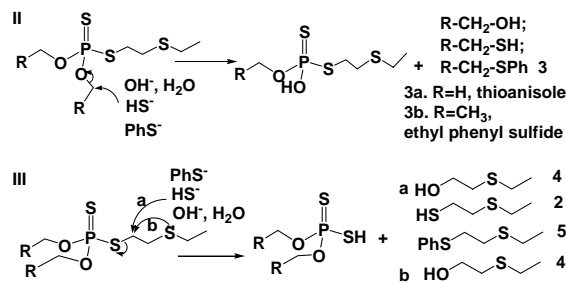
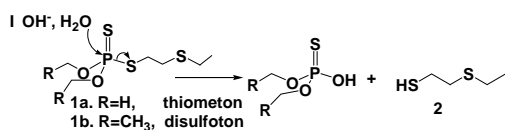
# The Role of Reduced Sulfur Species in the Degradation of Thiometon and Disulfoton in Stimulated Coastal Environments

Qiu Gan and Urs Jans (Faculty Mentor)  
 Department of Chemistry  
 The City College of New York  
 New York, United States  
 Email: qgan@sci.cuny.edu

**Abstract** — Reactions of thiometon and its ethyl analog, disulfoton, with reduced sulfur species (e.g. bisulfide ( $HS^-$ ), polysulfides ( $S_n^{2-}$ ), thiophenolate ( $PhS^-$ ), thiosulfate ( $S_2O_3^{2-}$ )) were examined in well-defined aqueous solutions under anoxic conditions. Experiments at 25 °C demonstrated that  $HS^-$ ,  $S_n^{2-}$ ,  $PhS^-$  and  $S_2O_3^{2-}$  promoted the degradation of thiometon to great extent while only  $S_n^{2-}$  and  $PhS^-$  showed a small accelerating effect in the degradation of disulfoton. The reactivity of the reduced sulfur species decreased in the following order  $S_n^{2-} > PhS^- > HS^- > S_2O_3^{2-}$ . Transformation products were confirmed by standards or characterized by GC-MS. The results illustrate that multiple pathways occur in reactions with reduced sulfur species, among which the nucleophilic attack at alkoxy group was the predominant pathway.

## I. INTRODUCTION

Esters and thioesters of phosphoric acid and thiophosphoric acid are widely applied as pesticides in agricultural and urban environments, taking advantage of their inhibitory action on cholinesterase. [1] Organophosphorus pesticides (Ops) are among EPA's highest priority for review under FQPA due to the influence on function of nervous system. Thiometon and disulfoton (Scheme 1) enter the environment primarily during their uses in agriculture and domestics, which result in the release into sensitive coastal environments such as estuaries, salt marshes and sediments. Anoxic conditions are prevalent in such environments and relative high concentrations of reduced sulfur species are reported. [2] Reduced sulfur species are versatile environmental "reagents" capable of reacting with many pollutants. The possible mechanisms of reaction of thiometon and disulfoton with sulfur species were proposed based on the report by wanner: [3]



Scheme 1 Possible Mechanisms of the reaction of thiometon and disulfoton in pH buffer containing reduced sulfur species.

## II. EXPERIMENTAL

All reaction solutions were prepared in an anaerobic chamber (5%  $H_2$ , 95%  $N_2$ ). Reactions were initiated by spiking the stock solution of pesticides into the preequilibrated pH buffer containing reduced sulfur species. Reaction mixtures were maintained anoxic and incubated in a water bath at selected temperature. The kinetics was monitored by extracting aliquots (1 mL) of the reaction mixture with 1 mL ethyl acetate throughout the experiments. The resulting extracts were subjected to GC/FID or GC/MS analysis. Reaction kinetics were determined assuming a pseudo-first-order reaction model.

## III. RESULT AND DISCUSSION

Hydrolysis is a major removal process for Ops in the aqueous system. Hydrolysis of thiometon and disulfoton were investigated in aqueous solution at pH 9.20, 50 mM borate buffer or phosphate buffer, 100 mM NaCl or  $NaClO_4$  and 5% methanol at 25 °C (Figure 1). The influence of chlorine ion could be explored by comparing the experiments with NaCl and  $NaClO_4$ . The degradation of thiometon yielded 2-(ethylthio)ethyl disulfide, dimer of 2-(ethylthio)ethanethiol (2, Scheme 1), which accounted for ~70% of the loss of thiometon and resulted from the attack on the central phosphorus atom (Pathway I) and quantified with the standard prepared in our lab. At the same time, a small amount of 2-(ethylthio)ethanol (4, Scheme1) was

detected as another degradation product, which result from the intramolecular and/or intermolecular nucleophilic attack at the carbon of 2-(ethylthio)ethyl group (Pathway III) and accounted for only ~10% loss of thiometon. Hydrolysis of disulfoton is much slower than thiometon. No accelerating effect of  $\text{Cl}^-$  on the disappearance of disulfoton was observed at 25 °C. Accelerating effect of  $\text{Cl}^-$  may result from a nucleophilic attack of  $\text{Cl}^-$  at alkoxy groups.

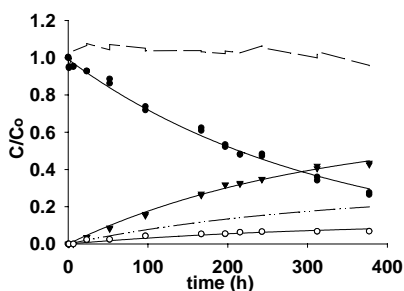


Figure 1 Hydrolysis of thiometon at pH 9.20 (50 mM borate buffer, 100 mM NaCl, and 5% methanol) at 25 °C, indicating the degradation of thiometon (●), the formation of 2-(ethylthio)ethanethiol (▼), the accelerating effect from  $\text{Cl}^-$  (— · — ·), the formation of 2-(ethylthio)ethanol (○) and the mass balance (—).

Product identification is a very important tool for the elucidation of reaction mechanisms. In the reaction of thiometon with bisulfide, a faster formation of 2-(ethylthio)ethyl disulfide was observed. (Figure 2(a)), which imply that  $\text{HS}^-$  attacked at 2-(ethylthio)ethyl group (Pathway III(a)). Another reason for the increase in  $k_{obs}$  might be the nucleophilic attack of  $\text{HS}^-$  at methoxy group (Pathway II), which was confirmed by the detection of thioanisole (3a, Scheme 1) in the reactions of thiometon with  $\text{PhS}^-$ . Another degradation product, 2-(ethylthio)ethylthio phenyl sulfide (5, Scheme 1) was detected in the reactions of thiometon with  $\text{PhS}^-$  (Figure 3). The formation of 2-(ethylthio)ethyl phenyl sulfide may be attributed to the nucleophilic attack of  $\text{PhS}^-$  at 2-(ethylthio)ethyl group (Pathway III(a)), which is consistent with the nucleophilic attack of  $\text{HS}^-$  at 2-(ethylthio)ethyl group in the reaction with bisulfide.

Reactions were monitored at varying concentration of reduced sulfur species. Linear regression of the corrected observed rate constants for hydrolysis and reduced sulfur concentration would give the second-order rate constants (Figure 2b), which are summarized in Table 1. The reaction with thiometon is much faster than disulfoton. The reactivity decreases in the following order  $\text{S}_n^{2-} > \text{PhS}^- > \text{HS}^- > \text{S}_2\text{O}_3^{2-}$ .

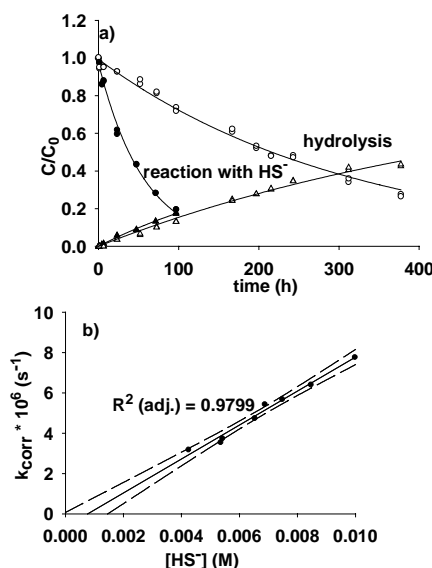


Figure 2. a) Degradation of thiometon at pH 9.20, 5.43 mM  $[\text{H}_2\text{S}]_T$  and hydrolysis at pH 9.20, at 50 mM borate buffer, 100 mM NaCl, and 5% methanol) at 25 °C, indicating the degradation of thiometon(●), the formation of 2-(ethylthio)ethanethiol (▲). b) Plot of  $k_{corr}$  versus  $[\text{HS}^-]$  for the reaction of thiometon with bisulfide

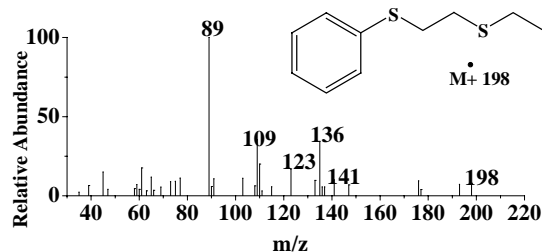


TABLE 1. Second-order Rate Constants ( $\text{M}^{-1} \text{s}^{-1}$ ) in for Reaction of Thiometon (1a) and Disulfoton (1b) with Reduced Sulfide Species at 25 °C

Ops	$k''_{\text{HS}^-}$	$k''_{\text{PhS}^-}$	$k''_{\text{S}_n^{2-}}$	$k''_{\text{S}_2\text{O}_3^{2-}}$
1a	$8.4 \times 10^{-4}$	$2.1 \times 10^{-3}$	$6.4 \times 10^{-3}$	$7.1 \times 10^{-4}$
1b	Too small	$8.4 \times 10^{-5}$	$1.1 \times 10^{-4}$	Too small

## REFERENCES

- [1] Coats, J.R. *Chemtech* **1993**, 23, 25-29.
- [2] Boulegue, J.; Lord, C.J.; Church, T.M. *Geochim. Cosmochim. Acta* **1982**, 46, 453-464.
- [3] Wanner, O.; Egli, T.; Fleischmann, T.; Lanz, K.; Reichert, P.; Schwarzenbach, R.P. *Environ. Sci. & Technol.* **1989**, 23, 1232-1242

# Characterization of Biomass Burning: Fourier Transform Infrared Analysis of North American Woods and Vegetation Combustion Products

Diomaris Padilla and Dr. Jeffrey Steiner (Faculty Mentor)  
The City University of New York  
The City College- Earth and Atmospheric Sciences  
New York, United States  
**Email:** [dpadilla@sci.ccny.cuny.edu](mailto:dpadilla@sci.ccny.cuny.edu)

**Abstract** — *The Fourier Transform Infrared Spectroscopic (FTIR) examination of the combustion products of forest materials were used to detect biomass burning for satellite remote sensing. Combustion of conifer and deciduous woods and lumber in a Meeker burner flame at temperatures of up to 900 °C produces a cluster of broad distinct peaks throughout the wavenumber spectrum (400 to 4000 cm<sup>-1</sup>). Distinct bands are located near: 400-700, 1500-1700, 2200-2400 and 3300-3600 cm<sup>-1</sup> and vary in intensity with an average difference of 47 percent between the highest and lowest absorbing species. Spectral band differences of 10 percent are within the range of modern satellite spectrometers, and support the argument that band differences can be used to discriminate between various types of vegetation.*

## I. INTRODUCTION

There is a growing interest in the relationship of present and predicted biomass burning to climate change models [1]. Projections indicate that the use of primitive cooking fires, burning of waste products, and land clearings will escalate throughout the third world, forcing intensified amounts of pollutants into the atmosphere [2]. Consequently, the characterization of the reflectance and absorption properties of these combustion aerosols will provide important information to atmospheric modellers.

The goal of this research is to correlate specific carbon by-products to sets of wood products attempting to link specific by-products to specific subsets of wood and vegetation. These associations can contribute to detecting differences between the smoke produced by different species, as well as to possible differences between dried lumber products (building materials and therefore building fires) and non-dried vegetation. A secondary goal is to make

correlations between carbon by-products of green wood smoke versus dry wood smoke. In addition, these correlations will be supported by scanning electron microscope and energy dispersive analyses that attempt to correlate the trace metal chemistry of the smoke products to different source materials and, or specific temperature ranges.

## II. RESULTS

Combustion of conifer *Pinus Strobus* (White Pine) and deciduous *Pterocarpus Dalbergiodes* (Purple Heart wood), *Prunus Serotina* (Cherry), *Acer Rubrum* (Red Maple), *Fragrans Nigra* (Eastern Black Walnut), *Fraxinus Americana* (American Ash), *Betula Papyrifera* (Birch), *Querus Alba* (White Oak) and *Querus Rubra* (Red Oak) lumber, in a Meeker burner flame at temperatures of up to 900 °C produces a cluster of broad distinct peaks throughout the wavenumber spectrum (400 to 4000 cm<sup>-1</sup>). The distinct bands are located near the wave numbers: 400-700, 1500-1700, 2200-2400 and 3300-3600 cm<sup>-1</sup> and vary in intensity with an average difference, between the highest and lowest absorbing species, of 47 percent. Spectral band differences of 10 percent are within the range of modern satellite spectrometers, and support the argument that band differences can be used to discriminate between various types of vegetation.

A similar examination of soot and smoke derived from the leaves and branches of the conifer *Pinus Strobus* (White Pine) and deciduous *Querus Alba* (White Oak), *Querus Rubra* (Red Oak), *Liquidambar Styraciflua* (Sweetgum), *Acer Rubrum* (Red Maple) and *Tilea Americana* (American Basswood) at combustion temperatures of 400 to 900 °C produce a similar broad spectrum with a shift in peak location occurring in peaks below 1700 wavenumbers.

The new peaks occur near the wavenumbers 1438-1444 and 875 and 713  $\text{cm}^{-1}$ . This noted shift in wavenumber location may be indicative of a fingerprint region for green woods distinguishable from lumber through characteristic biomass suites.

Distinctions using temperature variations were also made during the burning of green woods. Results show that the spectra of low temperature smoldered aerosols, occurring near 400 to 450  $^{\circ}\text{C}$ , may be distinguished from higher temperature soot aerosols that occur above 600  $^{\circ}\text{C}$ . Key differences were spotted at peak wavenumbers 2348-2372, where changes of polarity were found. At this location the high temperature carbon-oxygen 2348 mode is the product of 5 individual combustion experiments, each of which is scanned 64 separate times. The negative peak is discernable in all cases. This suggests that peak inversions of the carbon-oxygen mode can be used to distinguish high vs. low energy burning conditions. Heightened absorbance intensities were also noted throughout the wavenumber spectrum at an increase of 50 percent when comparing readings of lower temperature generated soot and smoke to that of higher temperature generated material.

Analysis of the combusted leaf, branch, bark and various crown assemblages, are performed on a LEO scanning electron microscope with a Princeton Gamma-tech Energy Dispersive Analyzer with Spirit software (SEM/EDS). KBr preparations are coated with gold (KBr-Au), to estimate the percentage of carbon in soot particles, and separately with graphite (KBr-C) to detect light elements. Comparisons of six lumber and six vegetation products by KBr-C analysis show that Pine lumber soot is enriched in iron (to 3%), phosphorus (to 3%) and nitrogen (to 16%) relative to Pine vegetation that is characterized by up to 2% of oxygen, nitrogen and phosphorus as well as 3% of sulphur and 1% each of iron and sodium. Further KBr-C analysis found that all lumber and vegetation combustion materials contained iron in amounts ranging from 3% to 1%, the higher amount of iron found mostly in lumber samples. The KBr-Au determinations show that soot particles comprise 70 to 80% carbon by weight. SEM/EDS yield comparable morphological and geochemical parameters. These observations suggest the possibility of establishing biomass reduction markers using a ratio method.

Conclusively, the FTIR spectra for the combustion products of lumber and green wood have been shown to be relatively unique for the

woods. In particular, the green wood information forms a complex array of data that can be organized on the basis of the position of a given absorption band occupying a set of bands in the interval of 900 to 400 wavenumbers thereby giving evidence of spectral signatures per sample species. Furthermore, the differences exhibited between lumber and green wood absorbance's are an indication that much of the tree chemistry is retained in the inner and outer bark portions of the tree. The magnitude of the vibrational response suggests that the FTIR differences can be recorded by satellite platforms. The SEM/EDS information demonstrates that the aerosol chemistry of the solid aerosol particulates can be used in combination with the FTIR to strengthen the definition of the combustion products. The SEM/EDS data are equally suggestive of the possibility that the chemistry of the smoke can be used to differentiate between deciduous and conifer forest combustion products.

## REFERENCES

- [ 1 ] Kuhlbusch, T. A. J. (1998). Black Carbon and the Carbon Cycle, *Science*, 280, 1903-1904.
- [ 2 ] Crutzen, P. J. and M. O. Andreae (1990), Biomass Burning in the Tropics: Impact on Atmospheric Chemistry and Biogeochemical Cycles, *Science*, 250, 1669-1678.

# Multi-Scale Modeling of H<sub>2</sub> Storage in Clathrates

Prasad Yedlapalli and Jae W. Lee

Department of Chemical Engineering,

The City College of the City University of New York

New York, United States of America

Email: {prasad, lee} @chemail.engr.cuny.cuny.edu

**Abstract** — *Structure II (sII) hydrogen gas hydrates stably encage two and four hydrogen molecules in the small and large cavities, respectively. By treating two hydrogen molecules or four hydrogen molecules as one rigid body cluster, we determine ab initio binding energies between water molecules and hydrogen clusters at the MP2 level with the 6-31++G (2d, 2p) basis set. These binding energies will be used to determine the parameters of the Exp-6 potential function from which the smooth cell potential and the Langmuir constant of each cluster are calculated. Then, the dissociation pressure is determined using the Zele-Lee-Holder cell distortion model.*

## I. INTRODUCTION

Gas hydrates are crystalline compounds, also known as clathrates. The H<sub>2</sub> molecules are entrapped in a cage like structure of hydrogen bonded water molecules. Their general formula is M<sub>n</sub>(H<sub>2</sub>O)<sub>p</sub> where M: Gas, n : number of gas molecules, p: number of water molecules. The unit cell is comprised of small and large cavities. The design of gas hydrate storage systems needs an accurate prediction of dissociation pressures with temperature.

The dissociation pressures are generally predicted using van der Waals and Platteeuw theory [1]. It is applicable to singly occupied cavities. This model can not be directly applied to H<sub>2</sub> gas hydrates. Multiple H<sub>2</sub> occupancies in one water cavity are handled by assuming that bi hydrogen and tetra hydrogen molecule clusters are single cluster molecules. *Ab initio* calculations are performed for determining binary interaction potential of one H<sub>2</sub> cluster with one water molecule for various inter molecular distances and various spatial cluster configurations using GAMESS [2, 3]. The interaction energies are fit to various forms: Exp 6, Lennard-Jones and Kihara. The best fit form, Exp-6, is used to calculate the Langmuir constant. At equilibrium, the chemical potential of water in liquid / ice phase will be equal to that of water in hydrate

phase. The other phase present is the gas phase. The reference chemical potential will be adjusted, if necessary, to get close agreement between the experimental dissociation pressure and the calculated dissociation pressure using a cell distortion model [4]. This model can be used to explore the possibility of producing low-pressure H<sub>2</sub> hydrates with possible promoters such as tetrahydrofuran [5], propylene oxide, etc.

## II. AB INITIO CALCULATIONS

To calculate binding energies between the hydrogen clusters (bi-hydrogen or tetra-hydrogen cluster) and one water molecule, the *ab initio* second-order Möller-Plesset (MP2) calculations will be performed using the GAMESS program. The basis set of 6-31++G(2d,2p) is used for the calculations. The distances between hydrogen molecules are selected as 2.58 Å for the bi-hydrogen cluster and 2.90 Å for the tetra-hydrogen cluster. These two hydrogen clusters are assumed to be rigid bodies in the calculations. By varying the distance (*r*) between the water molecule and the hydrogen clusters, the binding energies can be calculated. Then the angle averaged binding energies  $\langle \Delta E_{cp}(r) \rangle$  are fit to Exp-6 form [3].

$$\langle \Delta E_{cp}(r) \rangle = \frac{\epsilon}{\alpha - 6} [6 \exp(\alpha(1 - \frac{r}{r_m})) - \alpha (\frac{r_m}{r})^6] \quad (1)$$

The curve fitting results are shown in Table 1.

### A. CALCULATION OF LANGMUIR CONSTANT

With the smooth cell potential  $\langle W(R) \rangle$  [3], the Langmuir constant for gas molecule *j* in a cavity of type *i* is determined by taking a volume integral.

$$C_{ij} = \frac{4\pi}{kT} \int_0^a \exp\left(-\frac{\langle W(R) \rangle}{kT}\right) R^2 dR \quad (2)$$

Where *a* is the cavity radius.

### III. WATER CHEMICAL POTENTIALS IN THE WATER AND HYDRATE PHASES

By the use of the chemical potential of the theoretical empty hydrate lattice,  $\mu^\beta$ , as the reference state (273.15 K and zero pressure), the equilibrium equation becomes

$$\Delta\mu_w^\alpha = \Delta\mu_w^H \quad (3)$$

Where  $\Delta\mu_w^\alpha = \mu^\beta - \mu_w^\alpha$  and  $\Delta\mu_w^H = \mu^\beta - \mu_w^H$ . The statistical thermodynamic model for the hydrate phase as stated by van der Waals and Platteeuw is

$$\frac{\Delta\mu_w^H}{RT} = -\sum_{i=1}^2 v_i \ln(1 - \sum \theta_{ij}) \quad (4)$$

where  $v_i$  is the number of  $i$ -type cavities per water molecule and  $\theta_{ij}$  is the fractional occupancy of  $i$ -type cavities with  $j$ -type molecules. The fractional occupancy is expressed as

$$\theta_{ij} = \frac{C_{ij} f_j}{(1 + \sum_j C_{ij} f_j)} \quad (5)$$

where  $f_j$  is the fugacity of the gas. Peng-Robinson's correlation is used for the calculation of the fugacity in this work. The model developed by Holder et al. [6] is used to predict the chemical potential of water in the aqueous phase that is in equilibrium with the hydrates. The model is given as

$$\frac{\Delta\mu_w^\alpha}{RT} = \frac{\Delta\mu_w^0}{RT_0} - \int_{T_0}^T \frac{\Delta h_w}{RT^2} dT + \int_0^P \frac{\Delta V_w}{RT} dP - \ln \gamma_w X_w \quad (6)$$

Table 2 shows the calculated reference chemical potential difference, reference enthalpy difference, and two cavity radii by using the cavity distortion model. These values, along with the pair potential parameters in Table 1, allow us to predict dissociation pressures over a wide range of temperatures as shown in Figure 1.

Interaction pair	2H <sub>2</sub> - H <sub>2</sub> O	4H <sub>2</sub> - H <sub>2</sub> O
$\epsilon$ , J/mol	694.70	674.9456
$\alpha$	4.0434	4.2628
$r_m$ , Å	3.28	4.0418

Table 1: Exp-6 Curve Fitting Results

$\Delta\mu_w^0$ (J/mol)	1486.49
$\Delta h_w^0$ (J/mol)	693.66
Small cavity radius (Å)	3.89
Large cavity radius (Å)	4.73

Table 2: Reference Parameters and Optimized Cavity Radii of H<sub>2</sub> Hydrates

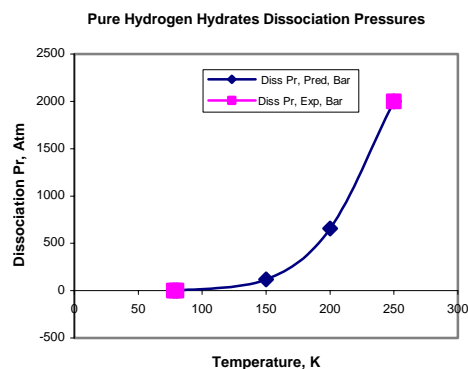


Figure 1: Pure H<sub>2</sub> Hydrates Dissociation pressures with temperature

### REFERENCES

- [1] van der Waals, J. H.; Platteeuw, J. C. *Adv. Chem. Phys.* **1959**, 2, 1.
- [2] Cao, Z.; Tester, J. W.; Trout, B. L. *J. Chem. Phys.* **2001**, 115, 2250.
- [3] Lee, J.W., Yedlapalli, P., and Lee, S. *J. Phys. Chem. B*, 110, 5, 2332 - 2337, 2006
- [4] Zele, S. R.; Lee, S.-Y.; Holder, G. D. *J. Phys. Chem. B* **1999**, 43, 10250.
- [5] Florusse, L. J.; Peters, C. J.; Schoonman, J.; Hester, K. C.; Koh, C. A.; Dec, S. F.; Marsh, K. N.; Sloan, E. D. *Science* **2004**, 306, 469.
- [6] Holder, G. D.; Corbin, G.; Papadopoulos, K. D. *Ind. Eng. Chem. Fundam.* **1980**, 19, 282.

# Amplification of small electric fields in neurons; implications for environmental risks

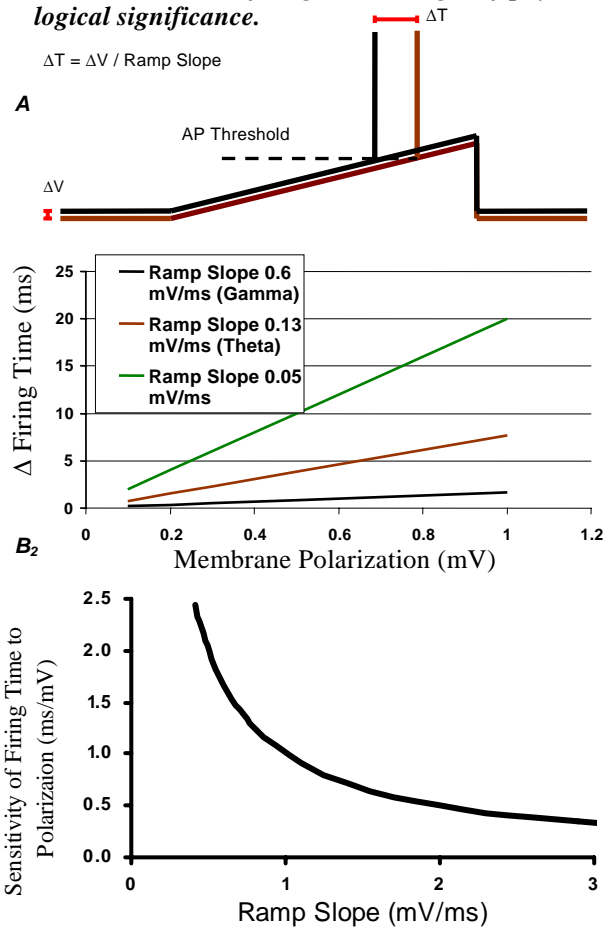
Thomas Radman (Student), Lucas Parra, Marom Bikson (Faculty Mentors)  
 Grove School of Engineering, Department of Biomedical Engineering  
 The City College of The City University of New York  
 Manhattan, USA  
 Email: tradman00@ccny.cuny.edu

**Abstract** — *It is well established that electric fields can modulate brain function. However, many aspects of the interaction of electric fields with nervous tissue remain unclear; in particular the mechanisms by which small electric fields modulate nervous system function need to be quantified. The study of how electric fields affect brain function is important for several reasons. First, these studies directly address concerns about the potential risks of human exposure to environmental electro-magnetic fields such as those generated by power-lines and mobile phones. Second, these studies provide insight into the mechanisms by which electric fields generated by the brain itself (as are manifest in the EEG) could 'feedback' unto the brain and modulate brain function. Lastly, they have practical application in the design of electrical brain stimulation devices for the treatment of neurological diseases (e.g. Deep Brain Stimulation).*

Here we demonstrate a novel mechanism by which single cells in the brain 'amplify' very small electric fields. Small electric fields, such as those commonly found in urban environments will polarize neurons by only a small amount; for this reason small electric fields have previously been considered ineffective/safe. However, we propose the effects of electric fields when coupled with a depolarizing ramp input (typical of cellular communication), can affect the timing of firing threshold crossing. This process results from the non-linear properties of brain cells as illustrated in Figure 1. The amplified change in timing ( $\Delta T$ ) is inversely proportional to ramp slope and directly proportional to the amount of polarization ( $\Delta V$ ):  $\Delta T = \Delta V / (\text{ramp slope})$ .

Figure 1: Schematics of the novel proposed mechanism for field amplification. A) A *small membrane polarization ( $\Delta V$ ) due to an extracellular field can significantly effect the firing time of a neuron ( $\Delta T$ ) in response to a depolarizing (synaptic) ramp. B<sub>1</sub>) Predicted relationship between change in firing time and initial membrane*

*polarization for three different ramp slopes. Note that for each ramp slope the relationship between firing time ( $\Delta T$ ) and polarization ( $\Delta V$ ) is linear; moreover, the slope of this relationship is inversely related to the ramp slope. The change in timing for any given membrane polarization increases (is 'amplified') as the slope of the ramp is decreased. B<sub>2</sub>) The inverse relationship between the ramp slope and the sensitivity to membrane polarization can then be summarized in a single plot. Note that a polarization of 1 mV, as is expected from in vivo extracellular fields (see text), will result in firing time changes of physiological significance.*

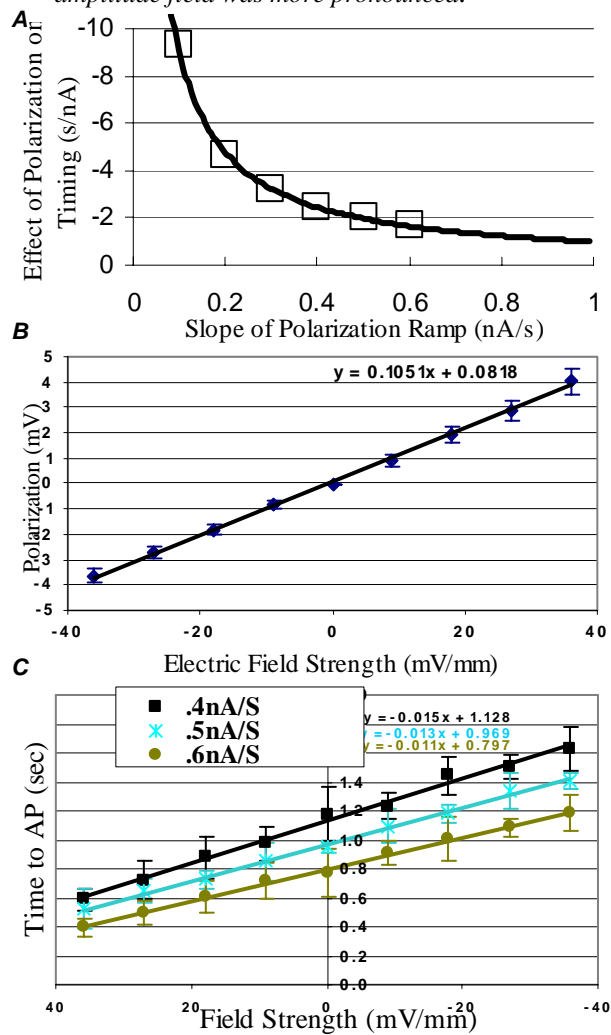


The novel single neuron amplification mechanism was validated in hippocampal slices. CA1 Pyramidal neurons were slightly polarized by varied levels of holding current and their firing time in response to depolarizing ramps were measured. For each ramp, we determined the change in firing time resulting from a change in holding current. Hyper-polarization of the neuron with an increasingly negative holding current, incrementally delayed action potential firing time in response to a ramp. The change in timing increased linearly with the holding current and inversely with ramp slope (Figure 2A). These results show that the membrane dynamics of real CA1 pyramidal neurons support the novel single neuron amplification mechanism proposed above (compare with Figure 1B<sub>2</sub>)

In separate experiments, electric fields were generated across tissue and the resting potential of a single neuron was monitored. Application of a constant uniform field induced a membrane polarization. The polarization of the neuron was dependent on the direction of the field (Figure 2B). The magnitude of the polarization was a linear function of field strength. The steady-state sensitivity (coupling strength) of neurons ranged from 0.06 to 0.22 mV per 1 mV/mm applied uniform field ( $n=21$ ). The applied field could significantly modulate the firing latency of single neurons to intracellular current injection (Figure 2C). Fields inducing membrane hyperpolarization delayed action potential initiation while fields inducing membrane depolarization had the opposite effect (Figure 2B). These results demonstrate the profound effect even a small field-induced polarization can have on spike timing. Moreover, the relationship between AP timing and depolarizing ramp slope, predicted above and demonstrated for changes in intracellular holding current (Figure 1), is shown to be valid for polarization by extracellular fields (Figure 2A,C).

**Figure 2:** CA1 pyramidal neuron action potential timing in response to ramp stimulation, effect of applied fields on neuronal polarization (A) *Open squares:* For each ramp, the resulting calculated slope (in s/nA) was plotted against the slope of the injected depolarizing ramp (nA/s). *Line:* Result of

simulation using integrate-and-fire neurons (see 1.B2). (B) Application of a uniform field caused the polarization of a CA1 pyramidal neuron; the magnitude of the polarization was linearly related to the amplitude of the electric field. (C) The neuron was depolarized with intracellular current ramps of three slopes during application of uniform fields. Uniform fields caused a change in action potential firing time. Note that for lower amplitude current ramps, the effect of any given amplitude field was more pronounced.



These results demonstrate our hypothesis for magnification of the effect of small electric fields through changes in the timing of action potentials. These results are particularly relevant for situations in which small electric fields are manifest in the brain (e.g. environmental fields). Fields previously considered too small to have an affect on physiology, must now be considered.

# Developing a Remotely Sensed Rainfall Retrieval Algorithm using Multi-Spectral Information

Cecilia Hernandez, Shayesteh Mahani, and Reza Khanbilvardi  
Department of Civil Engineering  
The City College of the City University of New York  
New York, USA  
Email: {chernandez-aldarondo}@gc.cuny.edu

**Abstract** — *Improving infrared-based rainfall retrieval algorithms using satellite-based multi-spectral infrared (IR) and microwave (MW) is the main objective of this study. A multi-sensor algorithm based on an artificial neural networks system is in development for estimating more accurate rainfall using cloud-top IR brightness temperature from the Geostationary Operational Environmental Satellite (GOES) in conjunction with microwave from the Advanced Microwave Sounding Unit (AMSU). Combining both sources of information is expected to improve the accuracy of rainfall estimates because IR sees only the cloud top and MW inside it.*

## I. INTRODUCTION

Estimating accurate precipitation from remote sensing information is still a challenge, particularly, for remote and mountainous regions where ground-based gauge networks and radar coverage are not available. This study attempt to develop a multi-sensor algorithm based on an artificial neural networks system which can facilitate the rain rates estimates on those areas. The idea is to use a combination of remotely sensed infrared from the Geostationary Operational Environmental Satellite (GOES) with microwave from the Advanced Microwave Sounding Unit (AMSU) using the feature that infrared provides brightness temperature only from the cloud top, but microwave spectrum can penetrate deeper and provide some properties from inside the clouds. Therefore, using multi-sensor IR and MW information is expected to improve the accuracy of precipitation estimates.

## II. BACKGROUND

Previous investigations had developed algorithms to estimate rain rates using different model inputs. There exists a variety of algorithms that only uses infrared to estimate rainfall in real time, like Hydro-Estimator (HE), Auto-Estimator (AE), Precipitation Estimation from Remote Sensing Information using an Artificial Neural Networks

(PERSIANN), and the GOES Multi-Spectral Rainfall Algorithm (GMSRA). In addition to IR, HE, AE and GMSRA use physical parameters obtained from the Eta Model in addition to IR to adjust rainfall estimates according to atmosphere conditions. Additionally, AE use radar to discriminate cirrus from raining clouds [1], and, GMSRA uses a set of thresholds between all the five GOES channels [2].

There are algorithms that only use satellite-based microwave such as: the Special Sensor Microwave/Imager (SSM/I), Tropical Rainfall Measuring Mission (TRMM) and AMSU-B. MW-based algorithms tend to underestimate warm precipitation, and IR based algorithms has the tendency to overestimate, mostly over land, for the reason that infrared cannot provide information from inside cloud physics which are required for estimating accurate rainfall amount. Therefore, most researchers are trying to add microwave to infrared for rainfall estimation. For instance, the MW-IR Blended algorithm uses relationship between MW rainfall estimates and IR brightness temperature and the modified version of the PERSIANN model is trained using microwave-based rainfall. Other algorithms are combination of existing operational algorithms like the regression technique of the Self-Calibrating Multivariate Precipitation Retrieval (SCaMPR), which uses GMSRA, AE, and SSM/I algorithms [3].

The main difference between those algorithms and the one that is in development in this study is the input data as well as the model structure. Most of the mentioned algorithms that use cloud top brightness temperature from GOES are physical based model or use operational microwave rainfall estimates for model calibration

## III. METHODOLOGY

For this study, an artificial neural network system is applied to develop a model to estimate rainfall at  $0.25^\circ \times 0.25^\circ$  resolution. IR cloud top brightness temperature from GOES 10, channel 4

(10.7  $\mu\text{m}$ ), and microwave limb corrected brightness temperature from AMSU 89 and/or 150 GHz were selected as model inputs because they are more correlated with rainfall. NEXRAD stage IV rainfall data, radar measurement calibrated against rain gauge observation, is used to train and validate the ANN model. The study area is located in western United States, between latitudes 32° N to 42° N, and longitudes 100° W to 110° W (Figure 1). Warm season storms in summer 2004 were selected as the warm season to be studied.

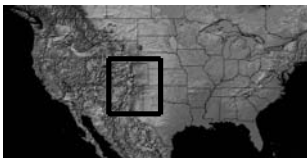


Figure 1: Study Area

#### IV. RESULTS AND DISCUSSION

Study of the various parameters of the ANN model is ongoing, such as training and minimizing the errors of the networks. The following results are from the best ANN obtained so far, using backpropagation and adaptive learning with two inputs, two hidden layers with 12 neurons in each one, and one output of rainfall estimates.

Figure 2 shows the relationships between model rainfall estimates obtained from IR data and rainfall observation with an average correlation coefficient about 0.51, for the calibration case. Figure 3 and 4 show the model estimates vs. observations, for the calibration case, using combination of MW and IR with average correlation coefficient of about 0.61 (about 0.63 for using AMSU-89 GHz and 0.59 using -150 GHz). Therefore, the combination of MW and IR can improve the IR-based rainfall estimates. However, the mentioned ANN network did not work well for validation case and should be modified.

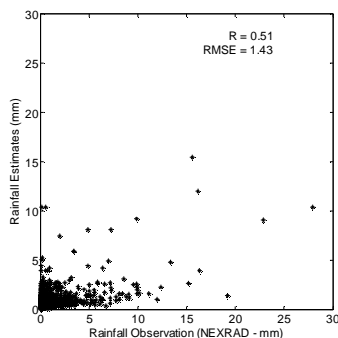


Figure 2: Scatterplot of model rainfall estimates vs. rainfall observation using only IR

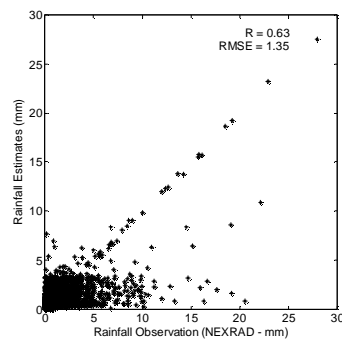


Figure 3: Scatterplot of model rainfall estimates vs. rainfall observation using IR+MW (89 GHz)

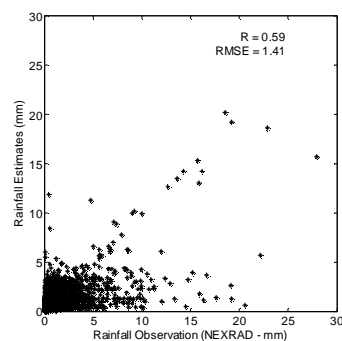


Figure 4: Scatterplot of model rainfall estimates vs. rainfall observation using IR+MW (150 GHz)

#### ACKNOWLEDGMENTS

The National Oceanic and Atmospheric Administration-Cooperative Remote Sensing Science and Technology Center (NOAA-CREST) support this work. The authors would like to thank Ralph Ferraro and Robert Kuligowski from NOAA, for their valuable cooperation and providing the data.

#### REFERENCES

- [1] Vicente, G. A., R. Scofield, and W. P. Menzel, 1998: The operational GOES infrared rainfall estimation technique. *Bull. Amer. Meteor. Soc.*, 79, 1883-1898.
- [2] Ba, M., and A. Gruber, 2001: GOES Multispectral Rainfall Algorithm (GMSRA), *J. Appl. Meteor.*, 40, 1500-1514.
- [3] Kuligowski, R. J., 2002: A self-calibrating GOES rainfall algorithm for short-term rainfall estimates. *Hydrometeor.*, 3, 112-130.

# Multi-Spectral Remotely Sensed Snowfall Rate Estimation

Yajaira A. Mejia (Student)

Shayesteh Mahani and Reza Khanbilvardi (Faculty Mentors)

Department of Civil Engineering, NOAA-CREST

The City College of The University of New York (CUNY)

New York, USA

Email: {yajaira, mahani, rk}@ce.ccny.cuny.edu

**Abstract** — *In the last three decades, remote sensing has rapidly explored various fields of applications. One of the challenges is application of remote sensing for estimating global precipitation (rainfall/snowfall) particularly over regions where traditional observation technique cannot cover. In this project, satellite based multi-spectral cloud information is used for snowfall rate estimation. The developed model uses cloud-top infrared (IR) from the Geostationary Operational Environmental Satellites (GOES) in conjunction with microwave (MW) spectral bands from Advanced Microwave Sounding Units (AMSU). Ground surface information and also some meteorological information are combined with remote sensing data, to improve snowfall detection and estimation. An artificial neural network (ANN) system is used in this study.*

## I. INTRODUCTION

Precipitation, (rainfall/snowfall), is a key factor required for hydrological, hydro-climatological and meteorological models applied for flood and weather forecasting, climate change predicting, water resource management and many other applications. Snowfall estimates are also used to update existing Snow Water Equivalent (SWE) required for different scientific communities such as: River Forecast Centers (“RFCs”) and Weather Forecast Offices (“WFOs”). SWE is the major source of water supply in the most parts of the world, particularly in the western and southwestern of United States. Furthermore, traditional ground-based techniques can only provide snowfall depth observations over specific stations, while there is no gridded based measuring system.

This study aims to develop an artificial neural network-based algorithm for estimating snowfall rate from satellite-based cloud observations. Most of research groups are working on developing remotely sense based model to recognize snow covered areas and estimate snow depth. For instance, researches at the University of Arizona

use conceptual models [1]. In this study, snowfall estimates are obtained using remotely sensed microwave and infrared observation data. Real time snowfall estimation will allow us to improve runoff predicting and flash flood forecasting.

## STUDY AREA AND TIME

The study area is selected over the western United States, with longitude from 109W to 114W and latitude from 42N to 47N. More accurate snowfall information is very important for the most water related applications. The study time is December 12-13, and 27-29, 2003.

## II. METHODOLOGY

In order to estimate snowfall depth from satellite IR imagery a methodology was developed. It is based on two steps:

### FIRST STEP: SNOWFALL DETECTION

In this study, ground surface temperature is used for recognition of snowfall area. The assumption is that if the maximum daily temperature is less than zero degrees Celsius then the pixel is classified as only snowy pixel, but if it is above zero, then the pixel is classified as rainy or mixed snow-rain pixel during that day. Figure 1 shows the snow level (frozen layer), which distinguishes the snowy area (above this level) from the rainy area. The frozen layer is selected at the level that the maximum daily temperature is equal to 0° Celsius.

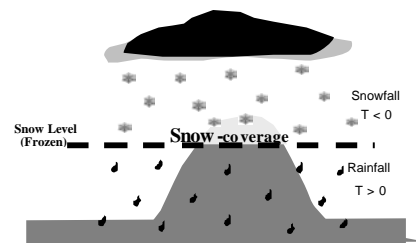


Figure 1: Snowfall Detection (frozen layer)

## SECOND STEP : SNOWFALL RATE ESTIMATION

An Artificial Neural Network (ANN) technique is selected to derive the relationship between inputs (multi-sensor information) and snowfall rate.

Multi-sensor information from three different sources has been used in this study. They included satellite-based IR from Geostationary Operational Environmental Satellites (GOES), spectral band observation that provides cloud top brightness temperature ( $T_b$ ) and MW from Advance Microwave Sounding Unit (AMSU) that can penetrate inside clouds. Ground-based information such as: topography (DEM) and temperature, because snowfall amount varies at different surface temperature and elevation. Atmospheric information, such as air temperature, relative humidity and wind speed at 700 mb level were also used.

For training the model, SWE information from SNOTEL stations was used. The assumption is, if the maximum daily surface temperature is less than  $0^{\circ}\text{C}$ , the difference between SWE from the same and the previous day would be equal to snowfall rate during that day.

## III. RESULTS AND DISCUSSION

The relationships between snowfall rates from model vs. ground based information are illustrated and discussed in this section.

Snowfall estimates using only GOES-IR data show very poor correlation with the ground-based observations (Figure 2), with  $CC = 0.39$ .

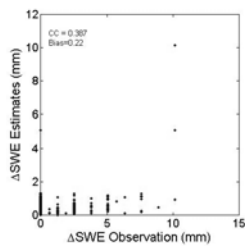


Figure 2: Using IR as input to estimate snowfall.

Infrared-based model snowfall rate estimates have been improved by adding MW at 89GHz ( $MW_{89}$ ) and/or MW at 150GHz ( $MW_{150}$ ) to IR. Improvement of IR-based model estimates using combination of IR and  $MW_{89}$ , with  $CC = 0.58$ , is demonstrated in Figure 3. And, using IR in conjunction with  $MW_{150}$  could also improve IR-based estimates with  $CC = 0.61$  (Figure 4), even more than using IR+ $MW_{89}$ . Figure 5 illustrates that using combination of both MW spectrum with IR could increase the correlation between model estimates and observation up to 0.69.

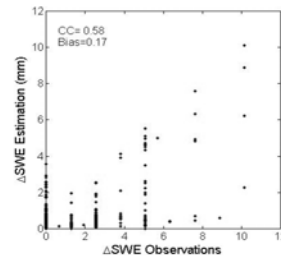


Figure 3: Using IR and  $MW_{89}$  as model input

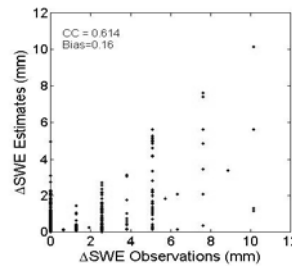


Figure 4: Using IR and  $MW_{150}$  as model input

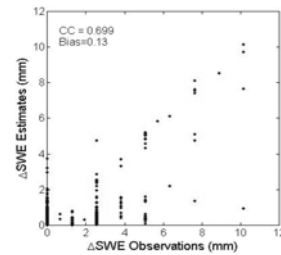


Figure 5: Using IR,  $MW_{150}$ , and  $MW_{89}$  as input

## IV. CONCLUSIONS

- Adding microwave cloud information to infrared as model input can improve snowfall estimates.
- Microwave at higher frequency is more sensitive to snowfall rate.

## V. ACKNOWLEDGMENTS

This work was supported by National Oceanic Atmospheric Administration, Cooperative Remote Sensing Science and Technology Center (NOAA-CREST). I would also like to thank Ralph Ferraro from NOAA-NESDIS for his valuable support.

## VI. REFERENCES

- [1] Roger C. Bales and Robert F. Harrington, Recent progress in snow hydrology, the Department of Hydrology and Water Resources at the University of Arizona, 1995.

# Concentration and Chiral Signatures of Chlordane in Surficial Sediments from Long Island Sound

Lijia Yang<sup>1</sup>, Xiqing Li<sup>1</sup>, Youxian Wu<sup>1</sup>, Michael Melcer<sup>2</sup>, Pengfei Zhang<sup>1</sup>, Urs Jans<sup>1</sup>

<sup>1</sup> City College of New York of CUNY

<sup>2</sup> U.S. Merchant Marine Academy  
New York, U.S.A.

Email: [lyang001@sci.ccny.cuny.edu](mailto:lyang001@sci.ccny.cuny.edu)

**Abstract** — Long Island Sound (LIS) is one of the largest estuarine systems on the Atlantic coast of the U.S. The Sound, however, has been contaminated with various pollutants, including organochlorine pesticides such as chlordane. The concentrations of chlordane and other organochlorine pesticides were determined by GC-ECD and the enantiomeric fractions (EFs) of chlordane were determined by GC-MS with negative chemical ionization. The results show that chlordane and other organochlorine pesticide are still widely present at these sites, with concentrations in the range of 0.04–30 ng/g sediment. The EFs of chlordane in the surficial sediments are close to that of a racemic standard, suggesting that bio-selective degradation was not the key mechanism for the attenuation of chlordane in the surficial sediments.

## I. INTRODUCTION

Long Island Sound (LIS) is one of the largest estuarine systems on the Atlantic coast of the U.S., ranked 4th in population (over 6 million) and 10th in population density among U.S. estuarine drainage areas. It provides vital transportation and rich fishing and shell-fishing grounds for commercial interests. The Sound, however, has been contaminated with various pollutants, including organochlorine pesticides such as chlordane. The contamination and declining environmental quality directly threatens the regional fishing and shell-fishing industry. Information on the fate of organochlorine pesticides in the sediments is, therefore, of direct practical importance. The structure of *trans*-chlordane and *cis*-chlordane is shown in Figure 1.

Chiral compounds are generally produced as racemic mixtures that contain equal amount of (+) and (–) enantiomers. The chiral signature is often described by the enantiomeric fraction (EF), defined as:

$$EF = \frac{C_+}{C_+ + C_-} = \frac{C_+}{C}$$

where  $C_+$  and  $C_-$  are the concentrations of the (+) and (–) enantiomers, and  $C$  is the total concentration of

the two enantiomers. Physical or chemical breakdown do not change the racemic signature of chiral compounds.[1] In contrast, microbial degradation and biological metabolism may be enantioselective and therefore change the chiral signature.[2]

The objectives of the project are to: (1) determine chlordane concentration decline in surficial sediments from Long Island Sound (LIS); (2) elucidate the mechanisms that may have caused the chlordane concentration decline in LIS sediments; and (3) examine the chiral signature of chlordane residues in the LIS sediments to assess the significance of microbial degradation on chlordane removal.

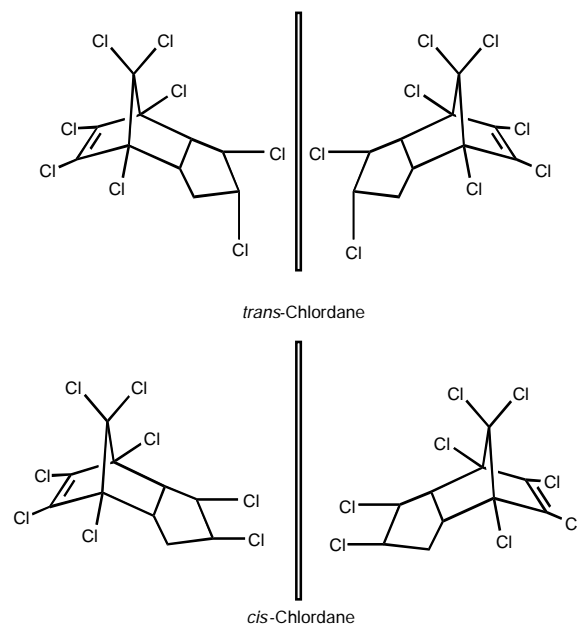


Figure 1: Chiral structures of chlordane.

## II. EXPERIMENTAL METHODS

We visited 10 sites in LIS that were established by the National Oceanic and Atmospheric Administration's National Status and Trends (NS&T) Program. The sediment sampling sites are shown in Figure 2.

We took surficial sediments in these sites, and took sediment cores at four sites: LIMB, LILN, LITN, LIHH. Surficial sediment samples contain only the top 1-cm of sediment within the area of the grab jaws and 50-cm long core sediments were taken from each of the four sites.

Chlordane and other compounds are extracted from the sediment by Soxhlet extraction. In order to remove interferences and sulfur in the Soxhlet extract, Florisil cleanup and sulfur cleanup procedures were employed.

Quantitative analysis of the organochlorine pesticides in sediments was accomplished by gas chromatography with an electron capture detector (GC-ECD). A DB-5 capillary column of 30 m × 0.25 mm × 1 μm was employed; chiral signature of chlordane in the sediment samples were determined by GC-MS in the negative ionization mode (GC-NIMS). A Betadex120 column of 30m × 0.25mm × 0.25 μm was used; m/z 410, 412 was used for selected ion monitoring mode.



Figure 2: Sampling sites of sediment in LIS.

### III. RESULTS AND DISCUSSION

*Trans*-chlordane(TC) and *cis*-chlordane (CC) were determined by GC-ECD, and the concentrations results are shown in Table 1. The chiral signature analysis gave the EF values for surficial sediments that are listed in Table 2.

From the surficial sediments results we can see that chlordane and other PBTs are still widely present in the LIS surficial sediments almost 20 years after its ban; Manhasset Bay and Little Neck Bay which are close to high population density area are the most contaminated area; the EF values of the surficial sediments are close to racemic which indicate no enantiomer selective degradation like biodegradation; racemic in surficial sediments indicate racemic sources, house foundation sources, for example.

Site	TC ng/g dry wt.	CC ng/g dry wt.
LIHR	0.05	1.82
LISI	0.34	0.41
LIHU	0.04	6.48
LIMR	0.41	1.99
LIHH	1.57	2.58
LITN	4.02	4.88
LILN	7.98	21.33
LIMB	13.13	29.63

Table 1: Chlordane concentration of LIS surficial sediments.

Site	EF (CC)	Stdev	EF (TC)	Stdev
LIHR	BD		0.55	0.04
LISI	0.61	0.07	0.49	0.02
LIHU	0.57	0.05	0.49	0.03
LIMR	0.52	0.03	0.49	0.02
LIHH	0.52	0.04	0.51	0.03
LITN	0.52	0.02	0.50	0.01
LILN	0.52	0.01	0.50	0.01
LIMB	0.51	0.01	0.50	0.01

Table 2: EF values of LIS surficial sediments.

### ACKNOWLEDGMENTS

- Dr. Gunner Lauenstein-NOAA
- Captain Timothy Tisch -USMMA
- USMMA water front
- Richard R Rendigs and Dann Blackwood-USGS
- Drs. Terry F. Bidleman and Tom Harner-Environment Canada
- U.S. EPA, Grant# : RD-83221501-0

### REFERENCES

- [1] Buser, H.R., and M.D. Mueller. 1993. Enantioselective determination of chlordane components, metabolites, and photoconversion products in environmental samples using chiral high-resolution GC-MS. *Environ. Sci. Technol.* 27: 1211-1220.
- [2] Harner, T. K. Wiberg, and R. Norstrom. 2000. Enantiomer fractions are preferred to enantiomer ratios for describing chiral signatures in environmental analysis. *Environ. Sci. Technol.* 34: 218-220.

# Analysis of Polar Organic Compounds in Aerosols

Barbara Rollinger, Heidi Bauer, Petra Kotianova, Christoph Schmidl,  
Yo Abe and Hans Puxbaum (Faculty Mentor)  
Institute for Chemical Technologies and Analytics  
Vienna University of Technology  
Vienna, Austria  
Email: [brolling@pop.tuwien.ac.at](mailto:brolling@pop.tuwien.ac.at)

## I. INTRODUCTION

Natural and man-made sources produce aerosols, which are mixed in the atmosphere. The contribution of individual sources to the air pollution is appreciated by determination of compounds which are typical for sources, so called markers. The markers are metals, ions, inorganic or organic compounds. Our interest is focused on polar organic compounds.

Polar organic compounds play an important role in aerosol analyses. They serve as markers of different aerosol sources:

1. resin acids for soft wood burning
2. syringol for hard wood burning
3. monocarboxylic acids (MCA) for the vegetative detritus
4. 9-Hexadecenoic acid and particulate nonanal for cooking
5. dicarboxylic acids (DCA) predicate the amount of secondary built aerosol.

## II. ANALYTICAL PROCEDURE

The analytical procedure was developed for determination of polar organic compounds in the atmospheric aerosols and several aerosol sources. The polar compounds were extracted with the mixture of methanol and acetone from a filter under ultrasonic agitation. Consequently, the organic acids are derivatised to the methyl esters. The target analytes were then extracted to cyclohexane and determined with GC-MS.

Gas chromatographic measurements were performed on HP-5890 connected to a mass selective detector HP-5971A (70eV). The experiments were performed on a capillary column HP-5 MS (30 m x 0.25 mm I.D. x 0.25  $\mu$ m film thickness). The injection was done with an autosampler GC-PAL.

## III. MOTIVATION OF REALISATION

This work is part of the AQUELLA and AQUELLIS projects. The goal of these projects is the make up of a source model for particulate matter in the atmosphere. Therefore it is necessary to analyse source samples and ambient air samples. It is performed to find out the biggest producers of the atmospheric aerosols and subsequently to prevent exceeding the legal limits of PM10 concentrations in the air (50 $\mu$ g/m<sup>3</sup> daily mean).

## IV. RESULTS

In present work data from source samples (cooking, wood combustion) and ambient air samples will be presented. Ambient air samples come from three Austrian cities (Graz, Salzburg Wien). It will be shown that the city aerosol exhibits the same composition in the three towns, although they all have different geographically and meteorological situations.



**Symposium 4**

**Science and Technology**



# Finite Mixture Model Diagnostics Using the Parametric Bootstrap

Bettina Grün

Department of Statistics & Prob. Theory  
Vienna University of Technology  
Vienna, Austria

Email: Bettina.Gruen@ci.tuwien.ac.at

Friedrich Leisch

Department of Statistics  
University of Munich  
Munich, Germany

Email: Friedrich.Leisch@stat.uni-muenchen.de

**Abstract** — *Finite mixture models are a popular tool for modelling unobserved heterogeneity. As these models are in general very complex, it is essential to have suitable methods for model diagnostics which allow e.g. to check for model identifiability, model fit and possible model restrictions. In this paper we propose to use the parametric bootstrap for model diagnostics and to visualize the bootstrap results using parallel coordinate plots. The application of the proposed methods is illustrated using an artificial example.*

## I. INTRODUCTION

This paper outlines the use of the parametric bootstrap for finite mixture model diagnostics as a special case of the general framework presented in [1], which encompasses different resampling methods.

## II. FINITE MIXTURE MODELS

The finite mixture models considered in this paper are given by

$$H(y|\mathbf{x}, \Theta) = \sum_{k=1}^K \pi_k F(y|\mathbf{x}, \boldsymbol{\vartheta}_k)$$

where  $H$  is the mixture distribution,  $\mathbf{x}$  is an optional vector of regressors,  $y$  the vector of responses,  $K$  the number of components,  $F$  the component distribution function,  $\boldsymbol{\vartheta}_k$  the component specific parameters and  $\pi_k$  the subcomponent probabilities.  $\Theta$  is the vector of all parameters with  $\Theta \in \Omega$ , where  $\Omega$  denotes the space of admissible parameters for  $K$ -component mixtures. The restrictions on the parameters are

- $0 < \pi_k \leq 1, \forall k = 1, \dots, K,$
- $\sum_{k=1}^K \pi_k = 1,$  and
- $\boldsymbol{\vartheta}_k \neq \boldsymbol{\vartheta}_l, \forall l \neq k$  with  $l, k \in \{1, \dots, K\}.$

Given the number of components  $K$  and the component distribution function  $F$ ,  $\mathcal{A}_K = \mathcal{A}_K(F, \Omega)$  denotes the set of all finite mixture models with  $K$  components and mixture distributions of form  $H(\cdot|\cdot, \Theta)$

In a frequentist framework the Expectation-Maximization (EM) algorithm is the most popular method to determine the model  $a(\mathcal{X}_N) \in \mathcal{A}_K$  with the maximum likelihood. As the EM algorithm might be trapped in a local optimum, it is in general recommended to choose the best solution of several

runs with different starting values in order to detect the global maximum.

## III. MODEL DIAGNOSTICS USING RESAMPLING METHODS

Resampling methods are already a popular technique for model diagnostics of linear and generalized linear models. The use of the parametric bootstrap for finite mixture models has been proposed for

- determining the number of components [2, 3]
- estimating standard deviations [4] and
- checking for identifiability problems [5].

The parametric bootstrap procedure can be outlined by:

1. Estimate  $\hat{a}(\mathcal{X}_N) \in \mathcal{A}_K$  and determine a corresponding parameterization  $\hat{\Theta} \in \Omega.$
2. Sample  $B$  bootstrap samples  $\mathcal{X}_N^b$  ( $b = 1, \dots, B$ ) independently with the parametric bootstrap:  $\mathcal{X}_N^b \sim \hat{a}(\mathcal{X}_N).$
3. Fit models to the bootstrap samples using the EM algorithm with either
  - (a) random initialization:  $\hat{a}^b(\mathcal{X}_N^b) \in \mathcal{A}_{K_0}$  with possibly  $K_0 \neq K,$  or
  - (b) initialization in  $\hat{\Theta}$ :  $\hat{a}^b(\mathcal{X}_N^b, \hat{\Theta}) \in \mathcal{A}_{K_0}$  with  $K_0 = K.$

Depending on whether global or local characteristics of the fitted model are analyzed either random initialization or initialization in the solution is used. Random initialization introduces the problem of *label switching* which has already received some attention in Bayesian analysis and which makes it necessary to suitably relabel the components before making component-specific analyses.

## IV. VISUALIZATION

Parallel coordinate plots are a visualization technique for hyperdimensional data [6]. For visualizing the bootstrap results the data used are the parameter estimates of each component of the models fitted to each bootstrap sample. This visualization technique can be enhanced by

- adding the confidence intervals for the parameter estimates derived using standard asymptotic theory and

- using different colors or line types for each of the components after appropriate relabelling, e.g. by imposing an ordering constraint on one of the parameters.

## V. EXAMPLE

All computations are done in R [7] using package **flexmix** [8]. For illustration we use an artificial example of a finite mixture of Gaussian regression models which is not identifiable due to intra-component label switching [9]. It is assumed that the following mixture distribution consisting of three components has been fitted to a sample with 50 observations for each value of  $x$  where  $x$  is a binary variable with values  $\{0, 1\}$ :

$$\begin{aligned} \text{Class 1: } & \pi_1 = 0.45, y = x + \epsilon \\ \text{Class 2: } & \pi_2 = 0.45, y = 2 + x + \epsilon \\ \text{Class 3: } & \pi_3 = 0.10, y = -2 + \epsilon \end{aligned}$$

with  $\epsilon \sim N(0, 0.1)$ .

The parametric bootstrap procedure is applied to this model with  $B = 200$ . As identifiability problems are investigated, the EM algorithm is randomly initialized and the best solution of 5 repetitions is reported. The fitted parameters are visualized in Figure 1. It can clearly be seen that the estimated parameters cluster around three distinct values for the coefficient of the intercept, while they cluster around a single point for  $\sigma$ . The identifiability problem is indicated by the different bundles which connect the estimates of the coefficients of the intercept to those of  $x$ .

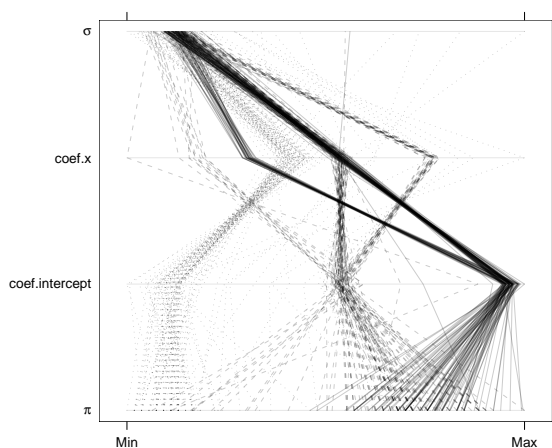


Figure 1: Parallel coordinate plot of the parameters fitted to 200 parametric bootstrap samples. The line types are according to an ordering constraint on the intercept.

## VI. CONCLUSIONS & FUTURE WORK

The presented procedure is based on resampling methods and can be seen as complementary to methods using standard asymptotic theory. In order to facilitate the interpretation of the results a visualization method is proposed which uses parallel coordinate plots.

In the future these methods shall be implemented by extending the R package **flexmix**. As **flexmix** allows the user to easily extend available functionality and develop new mixture models, the diagnostic tools can be used for all these models as this approach is general enough to be applied to different kinds of mixture models.

## ACKNOWLEDGMENTS

This research was supported by the Austrian Academy of Sciences (ÖAW) through a DOC-FORTE scholarship and the Austrian Science Foundation (FWF) under grant P17382.

## REFERENCES

- [1] B. Grün and F. Leisch. Finite mixture model diagnostics using resampling methods. Unpublished manuscript, 2005.
- [2] G. J. McLachlan. On bootstrapping the likelihood ratio test statistic for the number of components in a normal mixture. *Journal of the Royal Statistical Society C*, 36(3):318–324, 1987.
- [3] Z. D. Feng and C. E. McCulloch. Using bootstrap likelihood ratios in finite mixture models. *Journal of the Royal Statistical Society B*, 58(3):609–617, 1996.
- [4] K. E. Basford, D. R. Greenway, G. J. McLachlan, and D. Peel. Standard errors of fitted means under normal mixture model. *Computational Statistics*, 12:1–17, 1997.
- [5] B. Grün and F. Leisch. Bootstrapping finite mixture models. In Jaromir Antoch, editor, *Compstat 2004 — Proceedings in Computational Statistics*, pages 1115–1122. Physica Verlag, Heidelberg, 2004.
- [6] E. J. Wegman. Hyperdimensional data analysis using parallel coordinates. *Journal of the American Statistical Association*, 85:664–675, 1990.
- [7] R Development Core Team. *R: A language and environment for statistical computing*. R Foundation for Statistical Computing, Vienna, Austria, 2005. ISBN 3-900051-07-0.
- [8] F. Leisch. FlexMix: A general framework for finite mixture models and latent class regression in R. *Journal of Statistical Software*, 11(8), 2004.
- [9] C. Hennig. Identifiability of models for clusterwise linear regression. *Journal of Classification*, 17:273–296, 2000.

# Electrophysiological Monitoring of Membrane Capacitance Changes in Cell-Attached Mammalian Lactotrophs

Jernej Jorgačevski<sup>1</sup>, Matjaž Stenovec<sup>2</sup>, Marko Kreft<sup>2</sup>, Robert Zorec<sup>1,2</sup>

<sup>1</sup>Laboratory of Neuroendocrinology - Molecular Cell Physiology, Institute of Pathophysiology, Medical School, University of Ljubljana, 1000 Ljubljana, Slovenia

<sup>2</sup>Celica Biomedical Sciences Center, Stegne 21, 1000 Ljubljana, Slovenia

E-mail: jernej.jorgacevski@mf.uni-lj.si

E-mail: robert.zorec@mf.uni-lj.si

**Abstract** — *Prolactin is a protein hormone, synthesized and secreted from the lactotrophs. Among prolactin functions, we find the participation in osmo-regulation in lower vertebrates. Since today it has not been studied whether mammalian lactotrophs response directly to aniso-osmotic conditions. We therefore used the cell-attached patch-clamp technique to monitor discrete changes in membrane capacitance in isolated rat lactotrophs at normal and hypo-osmotic conditions. Our data confirm that discrete changes in membrane capacitance very likely represent fusion-fission of prolactin-containing secretory vesicles with the plasma membrane and that hypo-tonicity increases the probability of vesicle fusion with the plasma membrane.*

## I. INTRODUCTION

Prolactin is a protein hormone, synthesized and secreted from cells of the anterior pituitary gland, the lactotrophs. Over 300 different functions of prolactin have been reported, among which also the participation in osmo-regulation in lower vertebrates [1]. However, whether aniso-osmotic conditions affect the secretory activity of mammalian lactotrophs is yet unclear.

## II. METHODS

We used the cell-attached patch-clamp technique to monitor discrete changes in membrane capacitance ( $C_m$ ) in isolated rat lactotrophs, prepared as primary cultures. Since biological membranes behave like electrical capacitors,  $C_m$  is directly proportional to membrane surface area, which is changing due to fusion and fission events. Therefore, by using the cell-attached patch-clamp technique, we monitored

discrete changes in  $C_m$  in isolated rat lactotrophs at normal and hypo-osmotic conditions [2].

## III. RESULTS

We measured the incidence of elementary events of fusion of prolactin-containing secretory vesicles with the plasma membrane at normal and hypo-osmotic conditions. Out of 29 patches with a total recording time of 4.1 h, we recorded discrete  $C_m$  elementary events in 13 patches. In all patches that exhibited  $C_m$  steps we observed that an up-step was followed by a down-step with the same amplitude within less than 1 s. Together they represent transient fusion event, also known as "kiss and run" exocytosis, where after the vesicle fusion with plasma membrane the fusion pore reverses, vesicle integrity is reformed and partial release of vesicle content is achieved [3].

The amplitude of events was 0.8 – 6.0 fF, which agrees well with the size of prolactin-containing vesicles in lactotrophs [4]. While the average amplitude of elementary events increased slightly following the addition of hypo-osmotic medium, no change in the average fusion pore dwell time has been noticed. However, the probability of occurrence of elementary events increased in 8 of 13 patches following the hypo-osmotic shock.

## IV. SUMMARY

Our data show that discrete changes in  $C_m$  very likely represent fusion-fission of prolactin-containing secretory vesicles with the plasma membrane and that hypo-tonicity increases the probability of vesicle fusion with the plasma membrane.

## REFERENCES

- [1] M. E. Freeman, B. Kanyicska, A. Lerant, and G. Nagy. Prolactin: structure, function, and regulation of secretion. *Physiological Reviews*, 80(4):1524–1631, October 2000.
- [2] E. Neher and A. Marty. Discrete changes of cell membrane capacitance observed under conditions of enhanced secretion in bovine adrenal chromaffin cells. *Proc. Natl. Acad. Sci. U.S.A.*, 79:6712–6716, November 1982.
- [3] M. Stenovec, M. Kreft, I. Poberaj, W. J. Betz and R. Zorec. Slow spontaneous secretion from single large dense-core vesicles monitored in neuroendocrine cells. *FASEB J.*, 18:1270–1272, August 2004.
- [4] R. Zorec, S. K. Sikdar and W. T. Mason. Increased cytosolic calcium stimulates exocytosis in bovine lactotrophs. Direct evidence from changes in membrane capacitance. *J. Gen. Physiol.*, 97:473–497, March 1991.

# Methods from SPM family

Jaroslav Kala

Doctorate Degree Programme (2)

Dept. of Physics, Faculty of Electrical Engineering and Communication,

Brno University of Technology, Czech Republic

E-mail: xkalaj00@stud.feec.vutbr.cz

Supervised by: Doc. Ing. Lubomír Grmela, CSc.

**Abstract** -*The defectoscopy went through a huge improvement during last century. Until recently the word “nanotechnology” was only music of the future or hot object of the Sci-Fi discussions. In the present, thanks to many methods, we can observe tested items on the atomic level and herewith defectoscopy obtains new proportion. For better examination of the sample is good to use several methods of defectoscopy. These methods can offer us different view on the tested surface of the object and on its local characteristics. The poster describes two methods from SPM (Scanning Probe Microscopy) family and their junction. First part is dealing with common description of STM (Scanning Tunneling Microscopy) method and its advantages and disadvantages. Two modes of TS 3130 modified STM are described. The 3D processing and its benefit for defectoscopy and SPM methods are studied. The details of SNOM (Scanning Near-field Optical Microscopy) method, its advantages and disadvantages in the local nondestructive measurement are also presented.*

## I. SCANNING TUNNELING MICROSCOPY

STM belongs to the group of devices with a raster probe known as SPM (Scanning Probe Microscope). These microscopes work in this way: the surface of the object is scanned by the help of thin mechanical probe, which is proceeding very closely to the surface and the signal acquired from particular point forms subsequently whole picture of the object. The carrier of the information can be electric current or voltage, respectively [1].

STM uses a tunnel effect, which is coming up when an electric charge breaches the air barrier. The electric charge breaches the barrier even if the distance sample-tip is very low (a few nanometers). Therefore we need to place the probe very close to the object. When electric current breaches the barrier the magnitude of this current can be read and compile one point of the image.

Example of the STM microscopes is TS 3130 instrument made by TESCAN Brno Company. TS 3130 can operate in two modes, constant current mode and constant height mode [2].

## II. SCANNING NEAR FIELD OPTICAL MICROSCOPY

The significance of SNOM is that it allows a spatial resolution with more than an order of magnitude improvement over the best conventional optical methods, including laser scanning confocal microscopy. Although optical characterization is the most widespread method to analyze materials from biology to the semiconductor industry [3], it suffers from one inherent problem: the diffraction limit provides a spatial resolution limit of about half of the wavelength of light. Thus, features smaller than 250 nm can not be imaged or spectrally characterized with visible light. SNOM combines scanning probe microscopy instrumentation with optical microscopy and spectroscopy to provide optical characterization with, in some cases, 15 nm lateral resolution by using a visible light. The technique employs a sharpened optical fiber [4] that is coated with metal such that a small aperture (approximately 25 nm diameter) is formed at the tip of the fiber. This aperture serves to illuminate a small spot on the sample which is much smaller than the conventional diffraction limit. The sample is then scanned beneath the tip and the image is formed in the same fashion that a dot matrix printer prints a picture.

This method offers the use of a very small light source as the imaging mechanism, by using a point-like light source with a diameter much smaller than the wavelength of light. To reach the resolution better than diffraction limit is necessary to lighten the sample from vicinity, often only a few nm. Thereby will be frustrated so-called “near-field”. Instruments of the SNOM method can operate in two principal modes, reflection and transmission mode.

### III. CONCLUSION

There is a possibility to join STM and SNOM method. By creating of the instrument, which can use SNOM and STM at the same time, it is possible through one scanning process to obtain two images of the tested material and use all advantages of both methods. Thanks to similarity of both methods, it is possible to use only one probe for either side. If the scanning probe is coated by metal or another conductive material, there is a possibility to use it for STM and SNOM simultaneously.

Movement of the sample below the probe performs a piezo-nanomanipulator. Both methods need to use nanomanipulator, which is a crucial component for STM and SNOM set-up. The instrument combining both methods can be used in nondestructive testing. The goal of this design is to obtain cheaper and simpler system.

#### ACKNOWLEDGEMENT

This research has been supported by the Czech Ministry of Education in the frame of MSM 0021630503 Research Intention MIKROSYN New Trends in Microelectronic System and Nanotechnologies.

#### REFERENCE

- [1] Bonnell, D.A.: Scanning Tunneling Microscopy and Spectroscopy, VCH Publishers, New York, 1993, ISBN 0-89573-768-X.
- [2] Kala, J.: Scanning Tunnelling Microscopy, Workshop NDT 2004, Brno University of Technology, p. 75-79, ISBN 80-7204-371-4.
- [3] TOMÁNEK, P., BENEŠOVÁ, M., DOBIS, P., KOŠTÁLOVÁ, D., GRMELA, L. KAWATA, S., Near-field optical diagnostics of carrier dynamics in semiconductor with superresolution, Phys. Low-Dim. Struct., 2003, No. 3-4, pp. 131-138.
- [4] TOMANEK,P., Fiber tips for reflection scanning near-field optical microscopy, in:D.W.Pohl, D.Courjon (Eds): Near Field Optics, p. 295-302, Kluwer Academic Publishers, Dordrecht, 1993.

# Constructional and Architectural Analysis of Great Moravian Masonry Buildings

Ing. Lubor Kalousek (Doc. Ing. Milan Vlček, CSc.)  
Faculty of Civil Engineering, Institute of Building Structures  
Brno University of Technology  
Brno, Czech Republic  
Email: lubor.kalousek@centrum.cz

**Abstract** — *This contribution is aimed at the constructional and architectural analysis of Great Moravian Masonry churches with a rectangular chancel which could be connected with what is known as “Irish-Scots” architecture.*

*Although only ground plans and some structural components of these buildings have been preserved in the region of the Czech Republic, we can carry out their hypothetical reconstruction with the use of modern scientific methods. In this context there has been a very important recent occurrence; the recent research into St Margita Antiochijska’s Church in the village of Kopčany in the Slovak Republic. This church is considered to be the oldest existing sacred building in Central Europe.*

## I. INTRODUCTION

Great Moravia was a nation which was located in the present territory of the Czech and Slovak Republics from 833 to 905-8 AD. The oldest Great Moravian masonry churches were built perhaps at the beginning of the ninth century, and the main building activity was in the second half of the ninth century. To this day only fragments of foundations have been preserved, giving an idea of buildings’ ground plans, and various architectural and structural components.

We suppose that there were two important types of architecture which could have influenced Great Moravian buildings:

- Byzantine architecture
- “Irish-Scots” (or West European) architecture

To this day about 20 to 24 church fragments have been found. The only existing complete Great Moravian church is St Margita’s Church in the village of Kopčany in the Slovak Republic.

## II. ANALYSIS OF MASONRY CHURCHES

### A. TYPOLOGY AND ARCHITECTURE

As an example we can introduce the church in the village of Modrá in the Czech Republic “Figure 1”.

This Great Moravian church with a rectangular nave and near right-angled chancel is considered to be an example of the genuine type of Celtic insular church from the period of the eighth century [1].

This church had internal nave dimensions (7.5 x 5.6m) almost equal to the double of its internal chancel dimensions without a triumphant arch (3.8 x 2.8m). Its longitudinal axis was oriented from west to east.

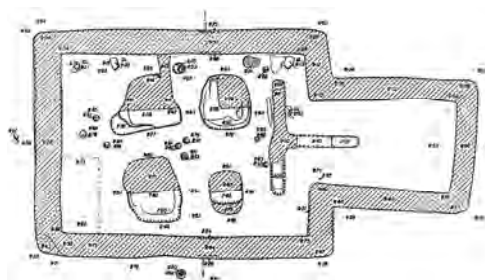


Figure 1: Ground plan of the church in the village of Modrá near Velehrad (CZ) [1]

### B. BUILDING CONSTRUCTION ANALYSIS

In connection with recent research we can present the following technical data about the chosen structures [2, 3]:

- The foundations were built of stone and lime mortar. Their width was about 600 – 740mm (= 2-2½ Roman feet, 1 Roman foot is 295.7mm).
- Vertical bearing walls were built of stone (e.g. sandstone) bonded with lime mortar, sometimes with an admixture of brick shards. The brickwork sometimes contained Roman bricks.
- Floors were made of clay or lime mortar poured on a gravel layer. The floor covering was often made of stone tiles.
- The brickwork was often plastered with a lime plaster which was sometimes covered by paint or internal wall paintings.

- The sloping roof was supported by a roof frame. Its pitch was about 35-40°. St Margita's Church roof has a slope of about 52°. Roofing was made of shingles or thatches or it was consisted of roofing tiles of Roman character, e.g. pantiles.

### C. ST MARGITA'S CHURCH IN KOPČANY

This building "Figure 2" is the only preserved Great Moravian church in existence and it was built at the earliest in the beginning of the tenth century. It has a near right-angled chancel and a rectangular nave which was formerly connected with an antechapel. The internal dimensions of the nave are about 4.9 x 3.8m, and the chancel is about 2.5 x 2m. The design of this church comes from Carolingian cultural influence, which was spread by the Salzburg archbishopric (e.g. St Kilian's church in Höxteri from 780-800AD).

Its brickwork is made of quarry sandstone and some limestone which is bonded by lime mortar. The longitudinal bearing walls are not vertical, but are sloped into the nave. The height of the bearing walls of the nave is about 6m and in the chamber it is about 5.1m. The brickwork was simply daubed on two sides with the lime mortar which poured out from the bricks' mortar joints. The authentic cylindrical vault in the chamber is very interesting too. The nave ceiling was made up of a cylindrical vault or there was a roof truss with a view to a garret. There are two well-preserved authentic window-holes in the northern frontage. There were made with the help of arch centering. The windows have a semicircular funicular arch with a triangle keystone and near-perpendicular window lining.

Over the course of time, some modifications have been made to this church, for example: the rebuilding of the southern frontage windows in the middle of the thirteenth century, portal modification in the sixteenth century, and baroque conversion in the seventeenth century. Even so, it is believed that 80% of the total mass of the church is authentic. [4]



Figure 2: St Margita's Church in Kopčany (SK).  
View of the north-eastern frontage.

At the present time an archeological survey is still being carried out which will certainly bring a substantial quantity of new knowledge to clarify the many problems connected with the hypothetical reconstructions of Great Moravian churches.

### III. CONCLUSION

According to the basic information presented here it is noticeable that we have certain data for research and for the following reconstruction of the above-ground parts of buildings. Although there are a lot of experts from various fields, who have been interested in this problem for a very long time, there are still plenty of underlying questions which we can not satisfactorily answer.

Among key questions requiring consideration:

- The heights and widths of bearing walls.
- The conceivable dimensions and shapes of gaps which could be made in bearing walls.
- The type of nave and chancel ceiling (e.g. vault, joisted ceiling or opening to roof truss).
- The type of roofing in connection with roof slope and the type of roof covering used.
- The validity of the modular system and the mutual ratio of dimensions. Using a Roman foot (= 0,2957m) as a basic measure.
- Analogy between the chosen Great Moravian churches and examples of so-called "Irish-Scots" architecture which have been preserved in Western Europe and in the United Kingdom.

Specific hypothetical models have been made in the past, but they have not taken note of real conditions satisfactorily, particularly the static and constructional aspects. There is therefore space for civil engineers, who can make, with the help of archaeologists, real models with consideration given to the real behaviour of buildings.

### REFERENCES

- [1] J. Cibulka. Velkomoravský kostel v Modré u Velehradu a začátky křesťanství na Moravě, Nakladatelství Československé akademie věd, Praha, Czech Republic, 1958
- [2] L. Galuška and M. Vaškových. Památník Velké Moravy, Slovákcké muzeum, Uherské Hradiště, Czech Republic, 2002.
- [3] J. Klouda. Dissertation Thesis, Brno University of technology, Brno, CZ, 2005.
- [4] <http://obnova.sk/article.php?sid=1467>

# Integrated map of construction processes

Kozák Peter (PhD student)

Institute of construction technology and construction materials

Technical University of Košice

Košice, Slovakia

Email: peter.kozak@azet.sk

**Abstract** — *These days, an extremely accent is putted on efficient and quality of construction. There is a demand for new management tools in all production areas of construction. Effectivity growth of construction processes, in perception of integrated management systems in the field of construction, also depends from new management tools. These tools have the duty to preserve complex quality of keeping work at desired level. That tool can be an integrated management subsystem of construction processes, where a graphic representation of this tool is presented with integrated map of construction processes.*

*The paper deals with depiction of integrated management subsystem of construction processes model, whose basis is the integrated map of construction processes.*

## I. INTRODUCTION

With introduction of management systems in the field of quality, health and safety protection and environment protection at construction, a production of new management tools is connected. These tools have to be managed effectively and have to support management systems in the organization. With the introduction of management systems came the idea to integrate the common elements in the separate management systems (subsystems) and the creation of common Integrated management system for every field. The result is the integrated management system, which in my field of study compounds areas of quality, health and safety and environment. With the existence of integrated management system, also management tools must exist. At the organization level, the management system is presented with the organization politics, a reference manual, directives, management process documentation, management of records and the like. The firms have perfectly elaborated these management systems.

Construction product in contractor organizations is a structure. The structure is made out of organization residence, at the construction site. The problem of many construction firms is to bring the management system to the level of the structure, and give it into

workers disposal, which are the main value of construction process in the final product – the structure.

## II. INTEGRATED MANAGEMENT SUBSYSTEM OF CONSTRUCTION PROCESS

The solution of this problem can be a new management tool – integrated management subsystem of construction processes. The aim of such system is to integrate all fields of the system (quality of processes and products, health and safety at work, protection of environment) in construction, but also to provide the workers with needed information at right time. The result is a harmony in construction, work effectivity and contractors satisfaction.

The basis of integrated management subsystem of construction processes is integrated map of construction processes. The map introduces graphical treatment of the system. There are specified individual elements of the system, reciprocal connections and converts between elements, the outputs from the system are in form of documents and records.

## III. INTEGRATED MAP OF CONSTRUCTION PROCESSES

The aim of the map of construction processes is graphically to explain to the user, the model of the system. The map represents the whole composition of the system and his whole functionality.

The map consists of several records, which represent independent data group. The structure of map comes from an integrated card of construction process, where are analyzed constituent quality factors of construction process (people, material, machines, regulators, actions, environment, time and surroundings). The quality factors, which create the construction process, represent aspects (influence on quality, health and safety protection, environment protection), which affect construction process. The consequence of the aspects is the influence in constituent fields. This influence has impact at constituent and ultimate result of the structure. The aim of the tool is to show the possible aspects and:

- to define the field of their constitution,

- to define the impact of the aspect in constituent field.
- to evaluate aspect, and to try to remove his impact, or to moderate the impact,
- to define the synergy of effects, causing the impacts in construction process.

After analyzing the aspects, it is necessary to monitor and to check their impact in constituent fields. The QES (Quality – Environment – Health and Safety) plan was developed for the supervision. The QES is an innovative element in plans for managing the projects. Its main aim is to manage and to control inconvenient impacts from constituent factors in the fields of quality, health and safety and environment, as their compound effects. The constitution of impact prevention expects the notification, the advisement and the education of workers for actual aspects and their impacts in the constituent fields.

The QES plan is a component of the system, and his model is an element of integrated map of construction processes. For creation of QES plan it is needed more information, which is entered in the records.

The outputs in the map are indicated for the aspect measurement stage, as for the construction processes control stage. The outputs are used for:

- aspects assessment and impacts valuation for quality, occupational health and safety and environment protection at building site,
- risk valuation and risk management at building site, arising from executed operations and products,
- progress assessment for construction processes,
- request identification and accessing of regulations and other request associated with quality, occupational health and safety and environment protection at building site and their continuous actualization,
- measurable index/characteristic assessment, and their impact manage from other operations utilization,
- responsibility identification for individual construction processes/construction operations,
- training and education, considering to required specialized capability of employees,
- coincidence monitoring of transmitted operations and progress with construction regulations request,
- transmitted processes control.

#### IV. CONCLUSION

The Integrated map of construction processes is possible to use as a foundation for the creation of a database system, which increase efficiency of the data work in the field of the construction process managing. The aim is to simplify and to streamline the work with the construction documentation and to manage the construction processes, as for as the continuous evaluation of each construction process.

#### ACKNOWLEDGMENTS

The article is a component of the project solution VEGA nr. 1/1221/04. - Integrated management system in construction.

#### REFERENCES

- [1] Ďurica,T.: Quality in construction process; pg. 382 ; Elfa s.r.o. ; Košice; Slovakia; 2001
- [2] Kozák,P.: Integrated card of construction process; In.: Proceeding of the Conference - JUNIORSTAV 2006; Technical university, Brno – Faculty of Civil engineering; pg. 215-218; Brno; January 2006
- [3] Kozlovská,M. Kozák,P.: Analysis of Integrated management systems structure as a foundation for IMS tools creation; In.: Proceeding of the IV scientific - technical Conference with international presence; Technical University of Košice; Faculty of Civil engineering; pg. 113-118; Copy-center Košice; April 2005

# Quantum cascade laser dynamics probed by broad-band Terahertz pulses

Josef Kröll and Karl Unterrainer  
Photonics Institute  
Vienna University of Technology  
Vienna, Austria  
Email: josef.kroell@tuwien.ac.at

**Abstract** — *In this contribution we present unique THz time-domain measurements of quantum cascade lasers. By coupling externally generated broad-band THz pulses into the laser structure, the processes within the active zone of the laser can be probed. Compared to Fourier transform infrared spectroscopy parameters like absorption, reduced losses and amplification can directly be measured in time-domain and distinguished. This gives information regarding the energy, dynamics and coherence of optical transitions in such structures.*

## I. INTRODUCTION

In recent years Terahertz (THz) technology has been successfully developed to a state of the art tool in physics, chemistry and medicine [1]. The outstanding properties of this particular part of the electromagnetic spectrum (0.1-10 THz) makes it to one of the most promising frequency bands for future applications. Moreover, the non-ionizing property of THz radiation and the possibility of performing contactless measurement makes it a good alternative to x-rays.

A very promising device for science and commercial applications is the THz quantum cascade laser (QCL) [2]. Such devices can be designed to the required wavelengths and show extremely high output powers compared to their size. Until now their properties have only been measured in terms of output power, wavelength and spectral line width of the emission. However, there is still a lack of additional information about the internal processes of such structures. Especially the internal dynamics of QCLs are of great interest and cannot be accessed by measurement methods performed in frequency-domain like standard Fourier transform infrared spectroscopy. A promising technique to obtain the needed data is Terahertz time-domain spectroscopy (THz-TDS) [1]. Such measurements performed in time-domain allow determining the properties and dynamics of such semiconductor devices by optical probing of the electrically driven active zone.

## II. EXPERIMENTAL SETUP

A THz-TDS system with a femtosecond pulse laser source is used to generate the THz radiation. The laser provides pulses with a length of 85 fs centered at a wavelength of 820 nm. The THz pulses generated with a photo-conductive switch are guided through the QCL and detected with an electro-optic sensor made of 300  $\mu\text{m}$  thick gallium-phosphide. The sensor is coated with an ultra-thin metallic layer which acts as anti-reflection coating [3] and allows to reach a spectral sensing bandwidth of 7 THz with a signal-to-noise ratio of more than 60 dB.

The THz-QCL used in this report is a unipolar GaAs/AlGaAs heterostructure with a bound-to-continuum intersubband lasing transition [4]. The QCL's threshold current density for lasing is below 150 A/cm<sup>2</sup> and the emission line (Figure 1) is centered at a frequency of 2.87 THz ( $\lambda \sim 105 \mu\text{m}$ ).

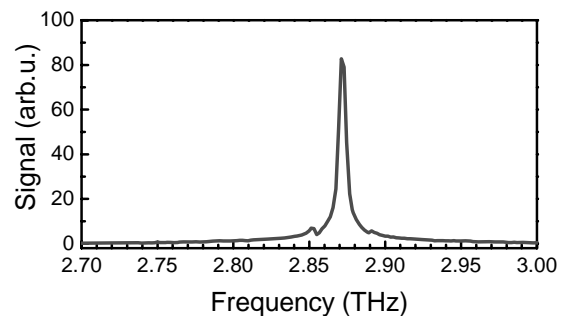


Figure 1: Emission spectrum of the THz-QCL.

The structure was processed into a 2 mm long ridge laser with a width of 170  $\mu\text{m}$ . Since the wavelength of used the THz radiation is larger ( $\sim 60\text{--}600 \mu\text{m}$ ) than the cross-section of the waveguide (170x12  $\mu\text{m}$ ) special coupling optics were employed (Figure 2). The THz beam is primarily focused by a parabolic mirror and a spherical silicon lens in close proximity to the laser ridge facet. In addition an aperture is used to avoid beam parts bypassing the chosen laser structure. For suppressing background noise and measuring directly the interaction of THz pulses with the QCL modulation spectroscopy was applied.

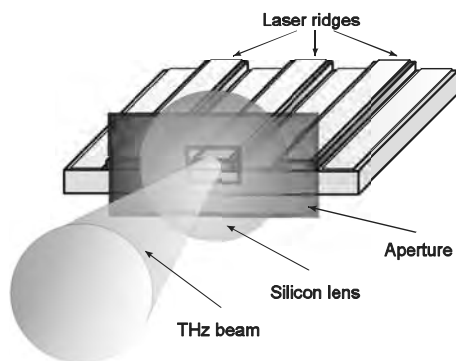


Figure 2: THz-QCL with incoupling optics.

### III. RESULTS

Without activating the laser structure no modulation in the probe signal can be observed. But by activating the laser and increasing the current through it an inversion of population of the lasing transitions in the active zone is built up. If then externally generated THz seed pulses are coupled to the waveguide they initiate a coherent emission. This makes it possible to sense directly the QCL's electric field of the output emission in time-domain and so the internal dynamics of the laser. In Figure 3 the transmitted and the modulation signal is shown. During the time when the probe pulse passes the laser's cavity oscillations build up and persist for more than 10 ps. The spectrum of those oscillations shows various features. The peak intensity correlates with the QCL's lasing line of 2.87 THz and shows the gain bandwidth of the device which is about 0.3 THz. The region around 1.2 THz is most likely related to reduced losses in the biased injector and the charge carriers in the active zone.

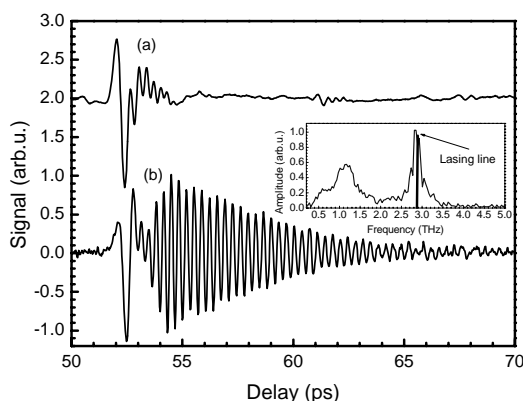


Figure 3: (a) THz-TDS seed pulse and (b) modulation signal through the QCL (inset: spectrum of the modulation signal).

In Figure 4 the current dependency of the modulation signal and the output power is shown. The amplitude of the observed oscillations starts to increase before the driving current reaches the lasing threshold level. This indicates that the oscillations follow the gain of the device. This observation stands in a good agreement with the theory because the lasing on-set condition ( $\text{gain} > \text{losses}$ ) is not essential for obtaining a modulation signal which just probes the active zone. This information allows us in future experiments to get first-time insight in the real-time processes in the starting laser. This would lead to a better understanding of the involved physics and the knowledge needed for fundamental improvements of quantum-cascade based devices.

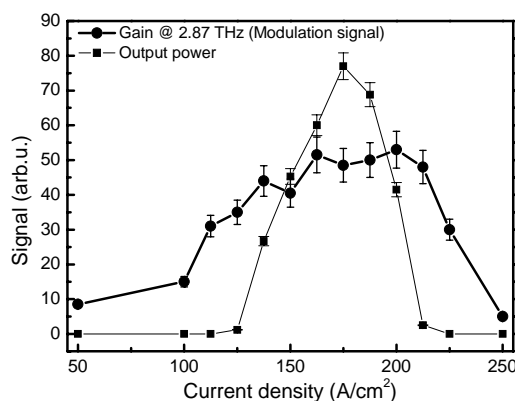


Figure 4: Current dependency of the QCL output power and the gain.

### ACKNOWLEDGMENTS

The author acknowledge support from the Austrian Fond zur Förderung der wissenschaftlichen Forschung (SFB-ADLIS) and from the EU project Ter-aNova (IST-511415). Special thanks to Juraj Darmo (TU-Wien), Thales R&T and University Paris 7.

### REFERENCES

- [1] D. Mittleman, Sensing with terahertz radiation (Springer, New York 2003).
- [2] R. Koehler, A. Tredicucci, et al. "Terahertz semiconductor-heterostructure laser," *Nature*, vol. 417, p. 156, 2002.
- [3] J. Kröll, J. Darmo, and K. Unterrainer "High performance electro-optic detector," *Electron. Lett.*, vol. 40, no. 12, 2004.
- [4] J. Alton, et al. "Buried waveguides in terahertz quantum cascade lasers based on two-dimensional surface Plasmon modes," *Appl. Phys. Lett.*, vol. 86, p. 71109, 2005.

# CO<sub>2</sub> Separation by Chemical Looping Combustion – Modelling Results

Luisser Markus and Hermann Hofbauer (Faculty Mentor)  
Institute of Chemical Engineering  
Vienna University of Technology  
Vienna, Austria  
Email: mluisser@mail.zserv.tuwien.ac.at

**Abstract** — *Chemical-looping combustion is one of the principal ways of removing CO<sub>2</sub> from fossil fuel burning. A mathematical model for the simulation of the fuel reactor was developed and implemented as computer program. For a selected number of determinative system parameters, simulations of the system were conducted. The influence of the parameters on the gas and solid conversion is shown from the start of the operation of a unit until gas and solid conversion reach their dynamic equilibrium.*

## I. INTRODUCTION

In principal there exist four different pathways for CO<sub>2</sub> separation from fossil-fuel-powered plants; *post-combustion capture*, where the CO<sub>2</sub> is removed from the flue gas, *pre-combustion capture*, where the fuel is converted to hydrogen by a reforming process before burning it, *oxy firing* which uses pure oxygen to burn the fuel and lastly *chemical-looping*, where oxygen is transported to the fuel via a metal carrier.

Chemical-looping is the youngest [1] of these methods and has the potential to become an important tool for cost-efficient climate protection to which Austria committed with the signing of the Kyoto Protocol [2].

An oxygen carrier is used in a circulating fluidised bed to burn the fuel (CH<sub>4</sub> in this work) without contact to air, so that the flue gas consists only of carbon dioxide and water (see Figure 1). The latter can be easily condensed to obtain pure CO<sub>2</sub> for further processing (e.g. sequestration).

As oxygen carrier serves a metal (Fe, Ni, Cu are the most promising) that can be enhanced by a harder support material to increase the life expectancy and decrease the costs of the method.

The carrier is oxidised in a fast fluidized bed and then transported into a bubbling bed reactor where it is reduced with the fuel. The oxygen-depleted carrier is transported back into the first reactor to undergo another cycle.

The fuel reactor of a chemical looping system is a critical part for the optimization of the process. Using a mathematical model of the reactor, a simulation program allows cheap, fast and efficient optimisation.

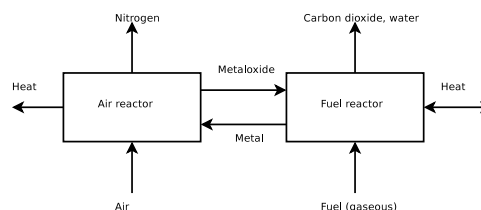


Figure 1: Basic scheme of the chemical looping process.

## II. MODEL DESCRIPTION

The fuel reactor model is based on a modified version of the two-phase theory [3]. Especially the rate of reaction is critical for the model because in general it will not be of first order with respect to the conversion of the solids (see Eq. 1).

$$\frac{dX}{dt} = r_i (1 - X)^{n_{\text{Conv}}} C^{n_i} \quad (1)$$

Therefore the reaction rate cannot be represented properly by a mean conversion of solids within the bed. In addition, particles in different oxidation states can be found simultaneously in the bed. At a distinct level in the bed, particles in a certain oxidation state may be reduced whereas particles in another oxidation state may be oxidised at the same time for thermodynamic reasons.

In order to allow proper reaction rate calculations, the particles are divided into a given number of conversion classes of a specific conversion  $X_k$  and a certain class width  $\Delta X$ . Each class is related with their mass fraction  $E(X_k)$ . This technique has been demonstrated by Thurnhofer [4].

$$E(X_k) = \frac{n_k}{\sum_{i=1}^N n_i} \left( \Delta X = \frac{1}{N} \right) \quad (2)$$

Since the modified two phase theory provides information on how fluidised bed characteristics change over the height of the reactor (see Figure 2), the model is capable of predicting the change of the gas conversion over the height of the reactor. Since this information is only very difficult to obtain by experimental work, the modelling is an interesting possibility to conduct fast and cost efficient optimisation and scale-up work on the reactor.

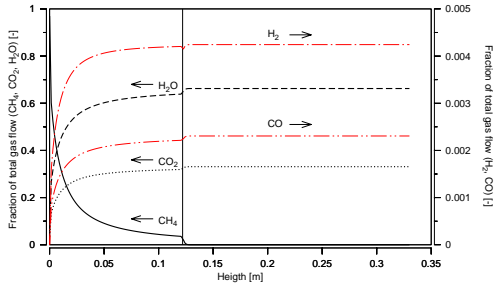


Figure 2: Predicted change of gas concentrations over the reactor height for the basic operation case (see Table 1).

Model Parameter	Value
Fuel flow (100 % CH <sub>4</sub> ) [Nm <sup>3</sup> /h]	1
Reactor temperature [K]	1123.15
Reactor pressure [Pa]	1.01 · 10 <sup>5</sup>
Oxygen carrier [-]	Ni (Al <sub>2</sub> O <sub>3</sub> )
Fraction of active carrier [-]	0.4
Bed material mass flow [kg s <sup>-1</sup> ]	0.06
Particle diameter [m]	1.35 · 10 <sup>-4</sup>
Apparent particle density [kg/m <sup>3</sup> ]	3.45 · 10 <sup>3</sup>

Table 1: Basic model simulation parameters.

### III. RESULTS AND DISCUSSION

Figures 3 and 4 show some results of the parameter study. While Figure 3 shows variations (Table 2) of the entire bed material across different simulations, Figure 4 shows the equilibration of the oxidation state at the begin of the operation. The oxygen loaded bed material is reduced by the fuel and a certain part of the material is constantly replaced with fresh unspent particles from the air reactor.

Parameter	Values				
Temperature $T$ [K]	1073	1098	<b>1123</b>	1148	1173
Fuel Flow $\dot{V}_F$ [Nm <sup>3</sup> /h]	0.50	0.75	<b>1.00</b>	1.25	1.50
Solid Fl. $\dot{M}$ [10 <sup>-2</sup> kg/s]	3.15	4.73	<b>6.30</b>	7.88	9.45
Bed height $H_b$ [m]	0.06	0.09	<b>0.12</b>	0.15	0.18
Part. diam. $d_p$ [10 <sup>-4</sup> m]	0.68	1.01	<b>1.35</b>	1.69	2.03

Table 2: Parameter variations. The parameter value of the base case is printed in bold.

### IV. CONCLUSION

The method has been demonstrated in principle and the measurements conducted during the operation of a hot laboratory-scale unit prove in accordance with the model calculations that the gas concentrations at the exit are chemically equilibrated [5].

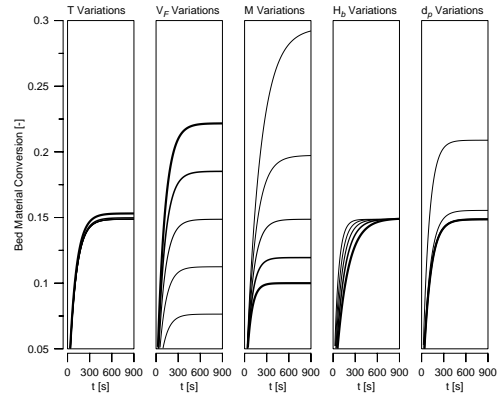


Figure 3: Mean solid conversion versus time for all conducted simulations. The lines become thicker with increasing parameter (see Table 2).

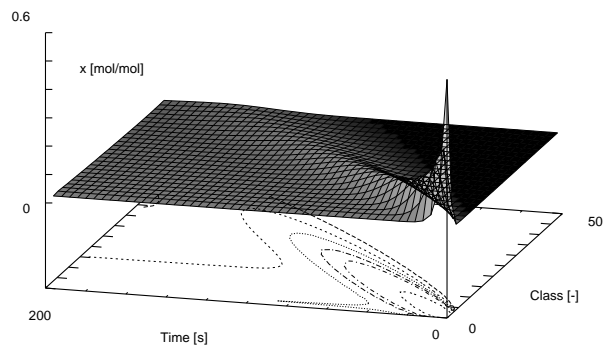


Figure 4: Three dimensional view of solid fractions versus time and conversion classes.

### REFERENCES

- [1] Horst Richter and Karl Knoche. Reversibility of combustion processes. ACS Symposium Series 235, ACS, Thayer School of Engineering, Dartmouth College, Hanover, NH 03755, 1983.
- [2] UN Framework Convention on Climate Change. Kyoto protocol to the united nations framework convention on climate change, December 1997.
- [3] F. Johnsson, S. Andersson, and Bo Leckner. Expansion of a freely bubbling fluidized bed. *Powder Technology*, pages 117–123, 1991.
- [4] Albin Bernd Ansgar Thurnhofer. *Memory-Effekte von Eisenerzen bei hohen Drücken und Temperaturen*. PhD thesis, Vienna University of Technology, Getreidemarkt 9/166, 1060 Wien, April 2004.
- [5] Anders Lyngfelt, Bernhard Kronberger, Juan Adanez, Jean-Xavier Morin, and Paul Hurst. The GRACE project. development of oxygen carrier particles for chemical-looping combustion. design and operation of a 10 kW chemical-looping combustor. In *GHGT7*, 2004. Vancouver, Canada.

# Propagation of High Power Laser Pulses through Hollow Core Photonic Band Gap Fiber

F. Orban<sup>1</sup>, H. Kofler<sup>1</sup>, A. B. Fedotov<sup>2</sup>, A. M. Zheltikov<sup>2</sup> and E. Wintner<sup>1</sup>

<sup>1</sup>Photonics Institute

Vienna University of Technology

A-1040 Vienna, Austria

<sup>2</sup>Physics Department, International Laser Center

M.V. Lomonosov Moscow State University

119899 Moscow, Russia

Email: mail@filip-orban.net

**Abstract** — *For many medical and technical applications the delivery of high power laser pulses is necessary. Beside the possibility of transmission without destruction of such laser pulses through a single optical fiber, the spatial shape of the output beam is of great importance, because the transmitted beam needs to be focused again. Only hollow core photonic band gap fiber showed the potential to provide those desired and optimum properties. Additionally, the hollow core can be evacuated to prevent the formation of plasma, which inevitably would lead to destruction of the optical fiber.*

## I. INTRODUCTION

The laser-induced damage threshold (LIDT) of silica is the common limitation why standard optical fibers cannot be used for delivery of high power laser pulses. That constraining threshold damage fluence lies at around 100 J/cm<sup>2</sup> for 10 ns pulse duration. For precise and tight focusing only a high quality beam can be used. Such a beam consisting merely of the fundamental mode at the optical fiber output can be provided only by conventional single-mode fibers or by hollow core photonic band gap (PBG) fibers, single-mode fibers, however, are constrained by LIDT. Large core or multimode silica fibers are in principle able to transmit high power laser pulses but only with poor quality at their output. Hollow core fibers have been shown to guide high intensity laser pulses as well, but facing the same problem of low quality beam output like the multimode fibers. For tight focusing a beam of quality close to the diffraction limit  $M^2 \approx 1$  is required. To overcome both limitations of conventional and hollow optical fibers the hollow core PBG fiber was developed. The structure comprises the hollow core and a two-dimensional photonic crystal around the core, which provides spatial filtering and thus allows to obtain a high quality beam at the output of the fiber by monomode propagation also for rather large diameters up to 20  $\mu\text{m}$ . PBG fibers are specially manufactured for a certain wavelength or a narrow band of wavelengths due to the photonic crystal type periodic struc-

ture. Worth mentioning are the comparable high losses of PBG fibers by reason of an other guiding principle than the conventional optical fibers used in telecommunications, which employ the principle of total internal reflection. The photonic crystal structure forms a narrow-band dielectric mirror and thus the guiding in PBG fibers is based upon multiple interface reflections, which introduce greater losses along the transmission path.

## II. EXPERIMENTAL DETAILS

The PBG fiber used in the experiments has in the middle a hollow core with a diameter of 15  $\mu\text{m}$  and a surrounding 7-layer photonic band gap structure (see Figure 1a). Furthermore, the PBG fiber is designed for a laser emission wavelength of 1060 nm, at which the attenuation reaches its minimum of 60 dB/km. The length of the fiber in our experiments was 2 - 3 cm. Nanosecond laser pulses have been shown to be the best solution for laser ignition of gases [1]. A fortiori a flashlamp-pumped passively Q-switched Nd:YAG laser at a wavelength of 1064 nm was used as a source of high power laser pulses, producing 5 ns and 10 ns short pulses at a maximum energy of 30 mJ with adjustable repetition rate up to 50 Hz. The beam quality of the laser was approximately  $M^2 \approx 1.54$ .

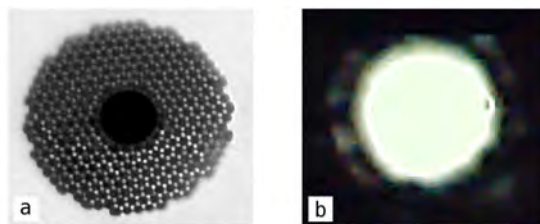


Figure 1: (a) Cross section of the fiber (b) Single mode pattern at the output

The incoming beam was focused into the core of the fiber by using single aspherical lens with focal length 11 mm, which was fixed on a three dimensional micropositioning stage. In contrast to the focusing lens, the fiber

was fixed on the movable part of that stage, so that precise adjusting could be accomplished. One of the most important steps in the experiments is to couple the laser beam correctly and efficiently into the hollow core of the fiber. Visualisation of the coupling process was performed with the help of a CCD camera. A beam optimally adjusted into the middle of the hollow core yielded minimum attenuation of the fiber and allowed to take pictures of single mode patterns as it can be seen on the Figure 1b.

### III. RESULTS

To examine if the coupling procedure was successful the input and output energies were measured and then the coupling and transmission efficiency was calculated, which lies at a value of approximately 80%. Certainly, this value is strongly dependent on the surface quality of the fiber. Due to non-availability of a conventional cleaver designed specially for the hollow core PBG fiber, cleaving was done by hand, so the surface quality was directly related to the results and thus could be determined by the energy measurements as well.

The first goal of the performed experiments was to find out the threshold energy under normal pressure conditions. It was determined, that the breakdown occurred at higher pulse energies than  $610 \mu\text{J}$  when using 10 ns pulses and above  $260 \mu\text{J}$  when using 5 ns pulses. This corresponds to flux of  $330 \text{ Jcm}^{-2}$ , which is three times higher than the LIDT of bulk silica. It should be pointed out that using this fiber as a device for the delivery of high peak power laser pulses for the purpose of igniting gas mixtures in internal combustion engines, the repetition rate was set to 12.5 Hz to simulate the authentic conditions. To reach the threshold intensity for being able to ignite every type of common gases at pressures, which can prevail in such combustion chambers, an energy of 10 mJ per pulse is needed. This results in increase of intensity which leads to air-breakdown by forming plasma sparks causing inevitable damage to the fiber. Solely the evacuation of the hollow core allows to overcome this barrier, because the threshold intensity of air-breakdown increases with decreasing pressure. Hence 10 mJ can be reached at a pressure of 1.5 mbar [2].

The Figure 2 below shows the results of output energy from the fiber versus the reduction of pressure in the vacuum chamber. Evacuation down to 300 mbar could be done up till now and led to increased breakdown threshold, which rose from  $610 \mu\text{J}$  to 1.067 mJ and consequentially nearly doubled.

### IV. CONCLUSION

These experiments were focused on the background of applications for laser ignition in internal combustion engines. As a consequence, investigations concentrated

on optical and mechanical material properties of hollow core PBG fibers using nanosecond laser pulses. It can be expected that using an inert gas like He or Ar in the vacuum chamber also allows to increase the threshold energy because of the higher optical breakdown properties of these gases. An energy flux of  $660 \text{ Jcm}^{-2}$  at 450 mbar looks promising so that further evacuation can lead to envisaged applications in field of laser ignition. This fiber might provide a tool to transmit high power ultra-short laser pulses down to fs duration, being e.g. important for medical applications, as it has been shown earlier with ps pulses [3].

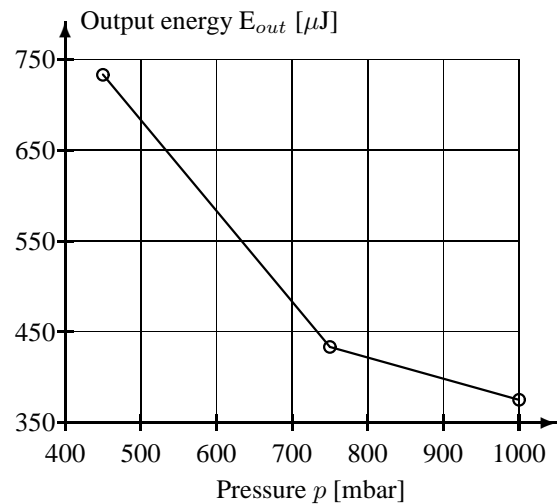


Figure 2: Output energy in respect to pressure.

### ACKNOWLEDGMENTS

This study was supported in part by Austrian Academic Exchange Service (ÖAD) and by A3 Austrian Advanced Automotive Technology Program.

### REFERENCES

- [1] S. H. Chan. Transport Phenomena in Combustion. In *Proceedings of the 8th International Symposium on Transport Phenomena in Combustion (ISTP-VIII)*, pages 176-184, San Francisco, California, July 1995.
- [2] P. Chylek, M. A. Jarzembski, V. Srivastava and R. G. Pinnick. Pressure dependence of the laser-induced breakdown thresholds of gases and droplets. *Applied Optics*, 29(15):2303-2306, May 1990.
- [3] S. O. Konorov, V. P. Mitrokhin, A. B. Fedotov, D. A. Sidorov-Biryukov, V. I. Beloglazov, N. B. Skibina, E. Wintner, M. Scalora and A. M. Zheltikov. Hollow-core photonic-crystal fibres for laser dentistry. *Physics in Medicine and Biology*, 49(7):1359-1368, March 2004.

# Voltammetry of immobilised microparticles-characteristics of different powder materials electrodisolution

Lubomir Pikna , Ladislav Lux  
Department of Chemistry, Faculty of Metallurgy  
Technical University in Kosice  
Kosice, Slovakia

E-mail: [Lubomir.Pikna@tuke.sk](mailto:Lubomir.Pikna@tuke.sk), [Ladislav.Lux@tuke.sk](mailto:Ladislav.Lux@tuke.sk)

**Abstract** – Voltammetry of immobilised microparticles (VIM) is electrochemical method, which has been used for studying a number of chemical compounds reviewed in [1]. The aim of present work was to use VIM method for study of different powder materials immobilized at the surface of working electrode. Voltammetric, chronoamperometric and chronopotentiometric measurements of iron powder, chalcopyrite ( $\text{CuFeS}_2$ ) and hematite ( $\alpha\text{-Fe}_2\text{O}_3$ ) were realized in electrolytes with different composition and various pH. Influence of the mean particle size, electrolyte pH, electrolyte composition and scan rate to anodic oxidation or cathodic reduction processes were examined.

## INTRODUCTION

Electrochemical analytical techniques [1] belong among characterization methods of well-defined specificity. While the more traditional methods of elemental and phase analysis (chemical or microprobe analysis, Xray diffraction and spectral techniques) can be used universally for almost any solid, electroanalysis can be applied only in certain cases. But if applicable, electrochemical investigation of powdered material can bring more detailed information on the investigated compounds.

Voltammetry of immobilized microparticles (VIM) is a convenient method for electrochemical study of powder materials such as organic compounds (indigo, acridine, quinhydrone) [2], oxides of iron [3], manganese [4] and chromium [5], metal sulphides and many other materials [6], including Fe powder [7].

The method described enables immobilization of powder particles onto the surface of paraffin-impregnated graphite or other suitable electrode material and application of such prepared electrode for study of powder properties. VIM is useful, fast and handy method for studying powder materials. The method requires no complicated instrumentation and can be used in less sophisticated laboratories.

The aim of this work was to show several examples of powder electroanalysis of different powder materials immobilized at the surface of working graphite electrode.

Influence of the mean particle size, electrolyte pH, electrolyte composition and scan rate to anodic oxidation or cathodic reduction processes was examined. In the present work, the quantitative aspects of voltammetry of immobilized microparticles (electrode surface covering, repeatability of immobilization) were also investigated.

## EXPERIMENTAL

Working electrode was obtained by mechanical deposition of samples on the surface of paraffin impregnated spectral graphite rod. Electrochemical measurements (cyclic voltammetry, chronoamperometry and chronopotentiometry) were done in a common three-electrode cell with above described working electrode, saturated calomel reference electrode (SCE) and platinum plate as auxiliary electrode. Measurements were performed with a PC-controlled potentiostat ECASTAT 110 PS (Istran, Bratislava, Slovakia).

Voltammetric, chronoamperometric and chronopotentiometric measurements of iron powder, chalcopyrite ( $\text{CuFeS}_2$ ) and hematite ( $\alpha\text{-Fe}_2\text{O}_3$ ) were realized in electrolytes with different composition and various pH. Iron powder was studied in 1 M acetate buffer with 1 M KCl (1 M total acetate, acetic acid to sodium acetate ratio 1:1, pH~4.5). For chalcopyrite 0.5 M HCl + 3 M NaCl with addition of  $\text{CuCl}_2$  solution was used and finally 1 M acetate buffer for studying of hematite. The solution of supporting electrolytes was prior to experiment deaerated with  $\text{N}_2$  and  $\text{N}_2$  atmosphere was kept over the solution during measurements.

Particles size: Fe powder < 45  $\mu\text{m}$ , and 63-100  $\mu\text{m}$   
 $\text{CuFeS}_2$  <73  $\mu\text{m}$  and  $\alpha\text{-Fe}_2\text{O}_3$  <10  $\mu\text{m}$ .

## RESULTS AND DISCUSSION

Potential of anodic as well as cathodic peak is influenced with particle size and with scan rate of voltammetric measurements. The influence of mean particle size on voltammetric peak potential was studied with iron powder. Figure 1 shows anodic dissolution voltammograms of two different iron

powder fractions. Peak potential shifts to more positive potential with increasing of particle size.

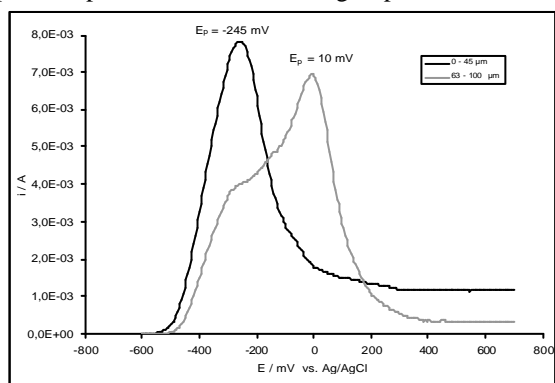


Figure 1: Dependence of  $E_p$  on particle size

Volatmmetric peak potential of hematite reductive dissolution depends on scan rate and a shift from -250 mV to -550 mV for scan rates  $0.2 \text{ mV s}^{-1}$  to  $50 \text{ mV s}^{-1}$  can be observed. Because the scan rate and particle size are factors, which affect peak potential significantly, for qualitative analysis only curves registered for the same scan rates and approximately equivalent powder fractions can be evaluated.

Cyclic voltammetry was also used to studying the electrochemical behaviour of powdered chalcopyrite mineral in dilute hydrochloric acid.

Figure 2 represents cyclic voltammogram of chalcopyrite electrodisolution. As scan proceeds to more negative potential, a cathodic peak C1 appears. This peak means iron (II) ions reduction in chalcopyrite lattice, because it does not appear in the second scan, and was not found in voltammograms registered with CuS and Cu<sub>2</sub>S powder.

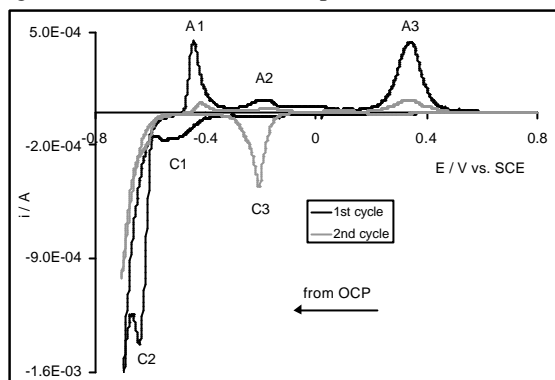
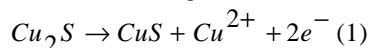


Figure 2 Cyclic voltammogram of chalcopyrite

Reduced iron is oxidized in A1 like active dissolution together with copper, and in A3 like transpassive dissolution together with chalcocite to covellite oxidation according to reaction (1).



Current peaks A1, A2, A3 and C2, C3 could be assigned to oxidation or reduction of chalcopyrite

intermediates like chalcocite and covellite. Cathodic current peak C3 reflects the reduction of copper (II) into covellite (CuS), and C2 could be reduction to copper. Statistical evaluation of immobilization process was performed with chronopotentiometric and chronoamperometric measurement of anodic dissolution of iron powder. Relative standard deviation for immobilization process obtained from chronoamperometric experiments differs from 2.0% to 7.2%, average is 4.3%. Repeatability of immobilization for chronopotentiometry differs from 5.2% to 18%, and, average is around 13% [9]. Chronoamperometric measurements are influenced with factors, which may misrepresent the results, and therefore can be stated that correctness of chronopotentiometry is better for evaluating of immobilization process, at least with respect to the quantity of immobilized material.

#### ACKNOWLEDGEMENT

This work was supported by APVT grant No.20-009404, and Grant Agency of the Slovak Republic VEGA, project No. 1/1108/04.

#### REFERENCES

- [1] Scholz F. and Meyer B., Voltammetry of solid microparticles immobilized on electrode surfaces In: *Electroanalytical Chemistry, a Series of Advances, vol. 20* (Bard A.J., Ed.) Marcel Dekker, Inc., New York pages 1-86, 1998
- [2] Komorsky-Lovric Š., Mirceski V., Scholz F., Voltammetry of organic microparticles, *Mikrochim. Acta*, 132:67-77, 1999
- [3] Grygar T., Bezdicka P., Doménech-Carbó A., Hradil D., Marken F., Pikna L., Cepriá G., Voltammetric analysis of iron oxide pigments, *Analyst*, 127:1100-1107, 2002
- [4] Bakardjieva S., Bezdicka P., Grygar T., Vorm P., Reductive dissolution of microparticulate manganese oxides, *J. Solid State Electrochem.*, 4:306-313, 2000
- [5] Grygar T., Bezdicka P., Electrochemical dissolution of Cr<sup>III</sup> and Cr<sup>VI</sup> oxides, *J. Solid State Electrochem.*, 3:31-38, 1998
- [6] Grygar T., Marken F., Schröder, Scholz F., Electrochemical analysis of solids, *Coll. Czech. Chem. Commun.*, 2:67, 2002
- [7] Gálová M., Grygar T., Pikna L., Lux L., Electrochemical study on the reactivity of Fe powders. *Chem. Anal. (Warsaw)*, 48(2):293-303, 2003

# A Two-dimensional Mathematical Hydraulic Model of a Hydro Power Structures Operation

Tanja Prešeren and Franci Steinman  
Faculty of Civil and Geodetic Engineering  
University of Ljubljana  
Ljubljana, Slovenia

Email: tanja.preseren@fgg.uni-lj.si, franci.steinman@fgg.uni-lj.si

**Abstract** — *In the last few years the operation of the hydro power plant has lead to an unwanted deposition of sediments in the downstream river reach. To solve the problem or at least to mitigate the inconvenient state the experiments on a physical model took place in the hydraulic institute of water structures and water management in Graz. This paper presents a two-dimensional numerical model of a river reach Salzach that has been made a few years later after the physical model has been built.*

## I. INTRODUCTION

Physical and mathematical hydraulic models are commonly used during design stages in order to solve the pretentiousness of planning a hydro power structure and to optimize and ensure a safe operation.

In the last few years the operation of the hydro power structure St. Veit has caused an increased sediment deposition in the downstream reach. This is inconvenient in view of water energy exploitation and in view of river morphology.

To answer the questions relating to river hydraulics the experiments on a physical model took place in the hydraulic institute of water structures and water management in Graz. The aim of the research was to find the measures which would reduce the process of sediment deposition in order to decrease the extent of expensive maintenance.

In the framework of the presented work a two-dimensional numerical model of a river reach Salzach has been made with an interface SMS and with a hydraulic modelling system FESWMS.

## II. THE MATHEMATICAL MODEL

### A. FINITE ELEMENT NETWORK

The numerical model consists of 42 polygons and is composed of approximately 40 000 finite elements. The hydraulic values have been calculated in almost 100 000 points (nodes). "Figure 1" shows the finite element mesh respectively the upstream section of a model.



Figure 1: Upstream section of a two-dimensional mathematical model - finite element network

### B. MODELLING HYDRO POWER STRUCTURE

The modelling of the hydro power structure's operational conditions presented a special challenge.

Although FESWMS places special emphasis on modelling flow trough (along) hydraulic structures (e.g. highway river crossings) where complex hydraulic conditions exist turbine outflow had to be modelled by implementing an innovative approach. Use of "enabled" finite elements and exceeded roughness (Manning's value) in the turbine polygons provided increased outflow velocities and a sufficient difference between upstream and downstream water elevation.

### C. BOUNDARY CONDITIONS

The mathematical model dealt with the hydraulic conditions in several different hydrological and operational situations. As an upstream boundary condition different discharges was set in different flow simulations: mean discharge and discharges with 1, 5, 30 and 100 year flood return period:

$$- Q_{mean} = 88.8 \text{ m}^3/\text{s},$$

- $Q_1 = 220 \text{ m}^3/\text{s}$ ,
- $Q_5 = 472 \text{ m}^3/\text{s}$ ,
- $Q_{30} = 650 \text{ m}^3/\text{s}$ ,
- $Q_{100} = 767 \text{ m}^3/\text{s}$ .

As a downstream boundary condition water elevation was set.

Also different operational situations were used. E.g. in some simulations all the gates were shut down and both of the turbines were in operation, in some simulations only one gate was opened etc.

#### D. RESULTS

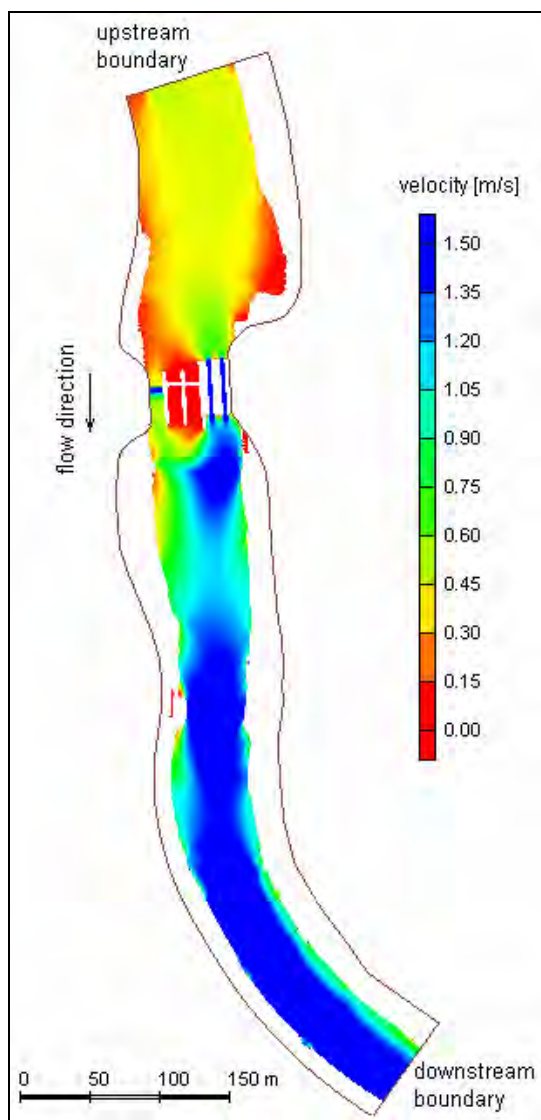


Figure 2: Velocities: both turbines are in operation, only the third gates are opened

The results obtained with mathematical model were sets of velocities, water depth and water height. "Figure 2" shows the results of a simulation of a flood with one year return period when only one gates are opened both turbines are in operation.

The study was also supposed to deal with the sediment transport. Since the program does not provide the necessary function, these calculations have not been done yet.

### III. CONCLUSIONS

The comparison between water station level calculated by a two-dimensional mathematical model and the results obtained by the physical model showed that the water slope of the mathematical model is greater than the one given by the physical model. The measurements of water surface were not obtained for the period before the bed-form changes took place. The physical model on the other hand has been made with lower friction without the usual procedure of gluing small particles that provide an operational roughness, since the main focus of the research was on the sediment transport process.

Therefore at this stage of the research it is difficult to evaluate the accuracy of the results obtained with the two-dimensional mathematical model, but the undertaken analysis represents a solid basis for further research.

### REFERENCES

- [1] T. Prešeren. Hidravlično modeliranje obratovanja hidroenergetskega objekta. Univerza v Ljubljani, Fakulteta za gradbeništvo in geodezijo, Ljubljana, May 2005.
- [2] H. Chanson. The Hydraulics of Open Channel Flow. Hodder Headline, London, 1999.
- [3] G. L. Morris, J. Fan. Reservoir Sedimentation Handbook. McGraw-Hill, New York, 1997.
- [4] Salzach Kraftwerk St. Veit, Geschiebetrift im Unterwasser, Hydraulischer Modellversuch. Hermann Grenn Laboratorium, Technische Universität Graz, Institut für Wasserbau und Wasserwirtschaft, Graz, 2003.
- [5] SMS Surface Water Modeling System Tutorials. Brigham Young University - Environmental Modeling Research Laboratory, Provo, 2002.
- [6] User's Manual for FESWMS Flo2DH. Office of Research, Development, and Technology; Federal Highway Administration, Georgetown Pike, 2002.
- [7] C. T. Yang. Sediment Transport: Theory and Practice. McGraw-Hill Companies, Inc., New York, 1996.

# Readiness for Adoption of eInvoicing service

Kornélia Pupáková  
Department of Applied Informatics and Process Control  
Technical University of Košice  
Košice, Slovakia  
Email: kornelia.pupakova@tuke.sk

**Abstract** - *Many companies realized that making business in nowadays condition of preferring Internet applications and approaches of Information Technologies developments is no longer the same as it used to be. There is a need for re-design of companies' business processes and implementation of newly improved application into company's internal information systems. Actual trends are more oriented towards the usability of Information Systems with the support of Information and Communication Technologies in every-day business processes. This fact requires an implementation of new ICT into the internal information systems of companies, through which company provides services or products. There is a need for new service development and further deployment.*

*Based on several researches done in the area of adoption of eBusiness solutions, my main focus will be given to the small and medium-sized enterprises (SMEs). The main goal of my research will be discovering the state of the SMEs' readiness for the adoption of the eBusiness solutions, mostly preferring the usage of electronic applications within financial business transactions. Financial management processes are not always the greatest interest of managers, but the benefits gained through the adoption can be massive [1].*

*Within the scope of my research I would like to focus on the level of "European SMEs' readiness" for adoption of eInvoicing service in several regions of Finland and connect Finland in the "e-Invoicing way" with Sweden, Denmark and some other EU countries (The Netherlands, Belgium, Slovakia, Slovenia, Czech Republic).*

## I. E-INVOICING SERVICE

The service to be presented is an e-Invoicing service for cost-efficient and paperless method of processing invoices. The e-Invoicing Service suits both SMEs and other organizations that issue invoices for goods, services and all other types of expenses.

The purpose of e-Invoicing is to achieve cost savings both for the seller and the buyer by reducing the cost of dealing with invoices. By converting financial transactions from paper invoices into e-Invoices will increase the efficiency of information and payment flows as well as reduce the administration burden related to the current paper work.

## II. RESEARCH SEQUENCES

Research bases on the theory of the innovation adoption [2]. It is important to that the technological uncertainty of particular innovation is reduced due to the fact that most of the companies are trying to avoid very complicated technologies.

At the same time, the Roger's theory of diffusion is applied. Diffusion of particular innovation means its dissemination and acceptance of the technology by market, in our case by the SMEs. The rate of such a adoption is influenced by several variables, where one of them is the achievement of the critical mass of adopters. Based on previously carried out research, the overall adoption of any eBusiness solution was growing exponentially when the main obstacles of only 20% of the SMEs as the critical mass amount were removed.

To be able to deploy the usability of e-Invoicing service in order to carry out a successful implementation, it must follow a stepwise process.

### A. PRE-PHASE

The empirical part of my study discusses the adoption of electronic invoicing by SMEs. Data will be collected with a mail survey for detection of the current situation of using the eInvoicing service within SMEs. The aim of the survey is to try to answer the question of how long it will take to the companies to adopt this service, and if they decide for non-adoptions, what are the reasons.

### B. COMPANIES' READINESS

The users' acceptance of the e-Invoicing Service plays an essential role for its success. Initial factor for the deployment of the eInvoicing service is the motivation and capability of SMEs. It is important to

find out the stage of their “readiness” for converting the paper invoicing into e-Invoicing.

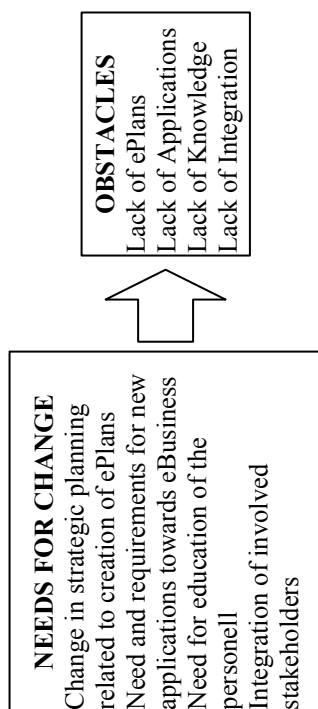


Figure 1. The main obstacles for the adoption of the e-Invoicing service

Companies willing to convert their invoices must also adjust the core business processes. These core business processes are:

- CRM – Customer Relationship Management
- SCM – Supply Chain Management
- ERP – Enterprise Resource Planning

#### C. CREATION OF CHANNELS

By using an example of an already running e-Invoicing service in Finland is simple to be deployment by following the steps for the tests of interoperability between participating and involved stakeholders: banks, operators, SMEs and financial management (FM) applications creators.

The main issue to be dealt with is the creation of communicating channels, of which functionality will be tested be following this sequences:

1. The agreement between banks (and operators) provides the background for the testing and know-how transfer
2. The interoperable e-Invoicing service between banks and operators is mutually tested
3. The integration of this FM application to the e-Invoicing service

4. The SME’s selection of the e-Invoicing service alternative and e-Invoicing agreement between the bank and SME is done
  - a. The Net-banking agreement between the bank and SME
  - b. The File Transfer agreement between the bank and SME
5. The sellers and the buyers are trained to the use of e-Invoicing
6. The e-Invoices are sent and received between SMEs and their big clients in real-life

#### D. TESTING OF INTEROPERABILITY

The interoperability testing will be studied between banks, between operators, between banks and operators. The main focus will be given to the existing cooperation (interoperability) channels.

The players as well as the functionality of created channels are needed for the regional as well as for the cross-regional

#### REFERENCES

- [1] United Nations Economic Commission for Europe- Electronic invoicing project update, Geneva, April 2005
- [2] Edelmann Jan, Pulli Hennariina, Sintonen Sanna – Impact of Knowledge on Adoption of e-invoicing, ISPIM 2005

# Hyperpolarized xenon in 4.7 T NMR system

Jan Rychnovský<sup>(1,2)</sup>, Zdeněk Buchta<sup>(1,3)</sup> and Karel Bartušek<sup>(1)</sup>, Josef Lazar<sup>(1)</sup>

<sup>(1)</sup>Institute of Scientific Instruments, Academy of Sciences of Czech Republic

<sup>(2)</sup>Department of Electrotechnology, Faculty of Electrical Engineering and Communication,  
Brno University of Technology

<sup>(3)</sup>Institute of Physical Engineering, Faculty of Mechanical Engineering,  
Brno University of Technology

Brno, Czech Republic

Email: jerycho@isibrno.cz

**Abstract** — We present the first experimental results of  $^{129}\text{Xe}$  hyperpolarization obtained by 4.7 T NMR system and high power semiconductor laser with reduced emission linewidth. The hyperpolarization process was based on the spin exchange collision technique between  $^{129}\text{Xe}$  atoms and optically pumped Rb atoms. The amplification of the  $^{129}\text{Xe}$  spectral line amplitude about 400 times was achieved. Furthermore, the influence of the optical pumping duration to the  $^{129}\text{Xe}$  spectral line amplitude was surveyed.

## I. INTRODUCTION

The hyperpolarized xenon  $^{129}\text{Xe}$  plays major role in the study of microporous materials like zeolites. The study and application is based on the chemical shift in xenon gas. At very low hyperpolarized xenon pressures and at the room temperature, the chemical shift is sensitive to the interaction of xenon atoms with the walls. It leads to the study of microporous materials [1].

The production of HpG, predominantly the xenon  $^{129}\text{Xe}$  became attractive for its potential applications in medicine as well. The powerful technique of MRI of human body has a limited ability to examine organs with low water content and/or with air spaces, such as colon or lungs. An introduction of a highly contrasting ingredient would significantly extend its potential. Gaseous xenon is normally not present in the body, so the experiments do not suffer from unwanted background signals. More, the hyperpolarized xenon acts as a non-radioactive source of very strong NMR signal, which can even lead to introduction of specialized simple MRI apparatuses with significantly less powerful magnets. These applications show that HpG may become a useful tool for non-invasive investigation of human lung ventilation, giving access to static imaging during breathhold, dynamics of inspiration/expiration, and functional imaging.

## II. EXPERIMENTAL ARRANGEMENT

The experimental arrangement consists of two crucial parts.

The first one is commercially available 4.7 T NMR system. It is used for  $^{129}\text{Xe}$  spectral line detection and as a source of the homogeneous 16 mT magnetic field too. The homogeneous magnetic field splits the Rb energy levels to two sublevels. For optical pumping is used the circularly polarized laser radiation, which excite Rb atoms with defined magnetic spin. The source of the laser radiation is the second one of the two mentioned crucial parts of presented arrangement. The main component of the laser system is a high-power laser diode S- $\lambda$ -3000C-200-H (Coherent). The maximum output CW power is approximately 3 W and the central wavelength is about 797 nm at the temperature 25°C. Due to the efficiency of the Rb atoms optical pumping process, the laser diode emission linewidth had to be reduced. To achieve the laser diode emission linewidth reduction, a diffraction grating was used [2]. It was applied in Littrow configuration as a wavelength selective feedback. With experimental setup we were able to reduce the laser diode emission linewidth more then 10 times, from 1000 GHz to 69 GHz full width at half maximum. The power loss was 49%, from 3.14 W to 1.60 W.

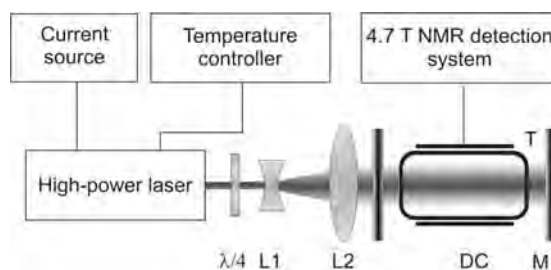


Figure 1: Experimental arrangement.  $\lambda/4$  is a retardation quarter-wave plate, L1 and L2 is an optical telescope, DC is detection coil, T is a target cell and M is 4.7 T magnet.

### III. EXPERIMENT

The target cell used for measurement was a simple cylinder 9.2 cm long. The cell is made of borosilicate glass with flat windows. It was enclosed in a teflon box to allow thermostating by a hot-air flow. The box with target cell was placed in front of the 4.7 T NMR system in homogeneous 16 mT magnetic field.

A small amount of Rb was moved into the cell under vacuum conditions. Before the cell sealing, it was filled by the mixture of xenon  $^{129}\text{Xe}$  (100 kPa) and nitrogen  $\text{N}_2$  (200 kPa). The target cell was heated to  $100^\circ\text{C}$  and the Rb vapor was optically pumped for 30 minutes. Then, the target cell was placed into the 4.7 T NMR system to obtain  $^{129}\text{Xe}$  spectral line.

### IV. EXPERIMENTAL RESULTS

The spectral line of  $^{129}\text{Xe}$  in natural state is shown in Figure 2. The spectral line of the hyperpolarized  $^{129}\text{Xe}$  is shown in Figure 3. The amplification of the spectral line amplitude is about 400 times.

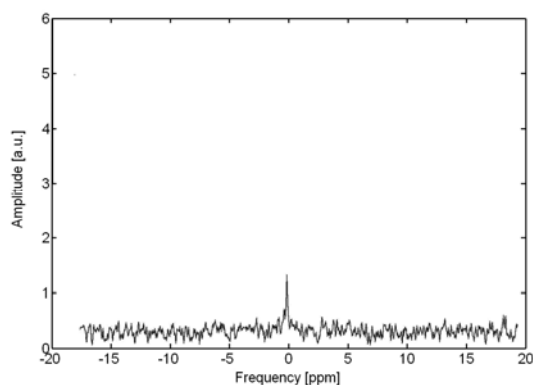


Figure 2: Spectral line of  $^{129}\text{Xe}$  in natural state

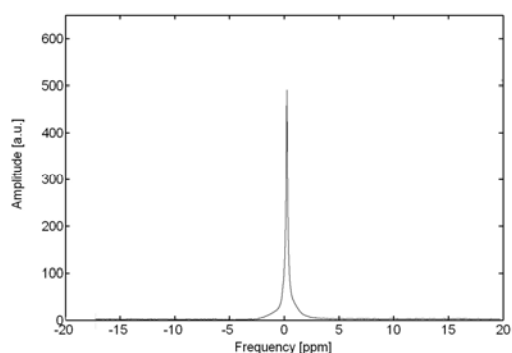


Figure 3: Spectral line of  $^{129}\text{Xe}$  in hyperpolarized state

The influence of the optical pumping duration to the  $^{129}\text{Xe}$  spectral line amplitude is shown in Figure 4. Relaxation time  $T_1$  is 26.9 minutes for natural state and 27.6 minutes for hyperpolarized state under given conditions.

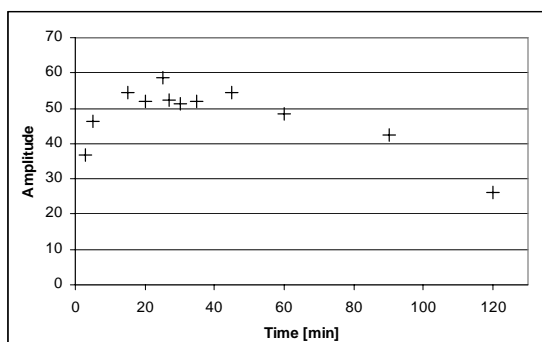


Figure 4: Dependence of amplitude of hyperpolarized xenon spectral line on duration of laser optical pumping

### V. CONCLUSION

We realized the experimental arrangement for  $^{129}\text{Xe}$  hyperpolarization consists of 4.7 T NMR system and high-power laser system. We obtained the  $^{129}\text{Xe}$  spectral line for natural and hyperpolarized state. The amplification of the spectral line amplitude is about 400 times. The influence of the optical pumping duration to the  $^{129}\text{Xe}$  spectral line amplitude was surveyed.

We realized the special laser system for Rb optical pumping [2]. The emission linewidth was reduced from 1 THz to 69 GHz with a half of the total optical power loss.

### ACKNOWLEDGMENTS

This work was supported by the Grant Agency of the Academy of Sciences of the Czech Republic, project No.: IAA 10653303 and by the Grant Agency of the Czech Republic, project No.: GA102/04/2109.

### REFERENCES

- [1] A. M. Oros and N. J. Shah, Hyperpolarized xenon in NMR a MRI, Physics in Medicine and Biology, vol. 49, pp. 105-153, 2004
- [2] Z. Buchta, J. Rychnovský, J. Lazar, Optical pumping of Rb by Ti:Sa laser and high-power LD, Journal of materials science: Materials in electronics Iss. 1, vol. 8, 2006

# Measurement infiltration in terrain on non-saturated streaming waters

Sedlackova Radovana (Miroslav Dumbrovsky)  
Institute of Landscape Water Management  
University of Technology  
Brno, Czech Republic

Email: {sedlackova.r , dumbrovsky.m}@fce.vutbr.cz

**Abstract** — *Water erosion is a wide spread phenomena in Czech Republic . In recent years interest in conservation tillage systems has increased in response to the need to limit erosion and promote water conservation*

*This Paper analyses efficiency of some erosion control measures of agronomic and technical nature is evaluated in view of their possible impact on landscape water regime and their contribution to the ecological stability of the landscape. Presented report brings an actual view on use of minimal soil cultivation from aspect of soil properties and contribution from standpoit water- management function protection against water erosion and also examine, how these technologies influence hydraulic and hydropedologic characteristics of soil profiles mainly infiltration rate of soil and other physical parameters.*

Assignment of other hydropedologic characteristics proceed also according to in common use methodist whose is defined in a book [3].

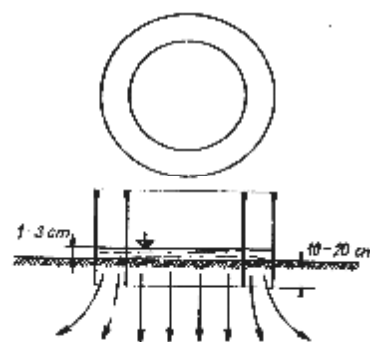


Figure 1: Sounding system

## I. INTRODUCTION

In the locality of Studená in Southern Bohemia proceed measurement infiltration capacity soils and her influence on hydraulic and hydropedologic characteristics soil enviroment. This properties were measured variable on two different agricultural lands, which that differs vary technologic process in a way ploughing.

A long-term field trial was conducted at Studená to determine some parameters of soil physical and hydropedology properties in soil profiles to 0,10 0,20 and 0,30 m depth under minimum tillage system There were observed the main physical soil parameters, namely:

- Specific and volume mass
- Maximum capillary capacity
- Porosity etc.

## II. METHODS

On determination infiltration rate of soil was used Double-ring method, which is described in a book [3] and gauging ring charactered Figure 1.

## III. RESULTS AND DISCUSSION

In phase from June to August 2005 were effected 3 infiltration tests in terrain. Out of him follows, that quantity suck up waters at point application ploughing is c. 3,30 l and seep rate attempt is  $v_{t1} = 4,47 \text{ mm} \cdot \text{min}^{-1}$  during the first minute. After 10 min is quantity soak into waters 5,6 l and seep rate is  $v_{t10} = 0,98 \text{ mm} \cdot \text{min}^{-1}$ . But then no - ploughing technology are record somewhat different. Results show a decrease infiltration capacity and soil increase water quantity

As for the specific mass by working minimal soil processing is biggest accretion notching of the zone 0,2 - 0,3 m in the subsoil layers. Compare to that no-ploughing technology embodies globally average increase which can be detector bigger quality of soil organic matter.

Volume mass reduced is again globally at average higher near soil protection technology. Tendency hereof indices would had grow up direction deep, but owing to transformation and accumulation in profile can be this tendency substantial disturbed.

At comparison actual moisture coming-out expressively better values near no-ploughing technology neat metering 16.6.2005 ( 64,15 % vol. , by topsoil.), when acknowledges better water storage

capillary, indeed and attached classical technologies this value was at 19.08.2005 quite higher in the zone 0,1m ( 36,50% vol.).

Situation about total porosity is kindles with minimal cultivation at the depth to the 0,1 m, compared to convectional tillage which shows on mature soil structure in topsoil by soil conservation technology.

Try to valorize soil-moisture constant like retention water capacity, absorbability or full water capacity and maximum capillary capacity, find out, that values e.g . near absorbability under - riding funds porosity, even in all cases metering are these values much higher namely in both collation technology.

In concrete conditions then size infiltration rate of soil and seep rate is considerably dependent into a kind of surface, or finds-if on surface crust, in the even of classical ploughing, which is for water very little for permeable and happens to undesirable surface runoff and production erosion, or is it surface softened whic is while using soil protection technology.

#### IV. SUMMARY AND CONCLUSION

Experimental results document a significant influence of soil loosening especially on an increase in the infiltration capacity of soil, leading to a decrease in the depth of surface runoff.

Emphasis is put on handling with post-harvest remainders in system of soil cultivation without plowing effect of non-traditional technologies onto soil physical properties and soil organic matter, because this faces to improvement infiltration rate of soil at rainstorms and to dispraise areal surface runoff.

For responsible evaluation however is tracked period too short and repetition rate small, nevertheless project will go on and experiment will pecify.

#### REFERENCES

- [1] J. Drbal., *Praktikum meliorační pedologie*. Praha: SPN, 1971
- [2]. M. Stach , et al . *Ochranné zpracování půdy z hlediska půdních vlastností, zaplevelení porostů, produkce plodin, energetické a ekonomické náročnosti. Závěrečná výzkumná zpráva projektu EP 7228 NAZV*.
- [3] J.Šálek. *Praktikum vodohospodářské pedologie*. Praha: SPN, 1978.
- [4] Materials provided to company STAGRA spol . s r. o. Studená and HORSCH.

- [5] R. Loch and I.Fole. *Measurement of aggregate breakdown under rain comparison with test of water stability and relationship with field measurement of infiltration*. Aust.J.Soil. Res.,1994

- [6] Research Institute for Soil and Water Conservation Praha. *Scientific studies 12*, 2001.

# Secondary Frequency Standard for Experimental Satellite

Jiri Spacek and Miroslav Kasal  
Institute of Radio Electronics  
Brno University of Technology  
Brno, Czech Republic

Email: xspace07@stud.feec.vutbr.cz, kasal@feec.vutbr.cz

**Abstract** — This paper deals with the design, construction and measurement of the 5 MHz PLL oscillator. The oscillator will serve as a secondary frequency standard onboard an experimental communication satellite. The experimental satellite has an ultra-stable 5 MHz oscillator (USO). USO has excellent output signal parameters. Reliability is an essential requirement for USO. For this reason, the USO needs a back up. The described secondary frequency standard based on VCXO that can be locked to USO by phase-locked loop (if USO signal exists) has been selected as the optimal arrangement for this purpose.

## I. INTRODUCTION

Satellite has experimental communication equipment, which is synchronized by onboard ultra-stable 5 MHz oscillator (USO). USO has excellent frequency accuracy as well as long term frequency stability and very low phase noise, respectively. However, essential requirement for USO is reliability. For this reason the USO needs a back up. Well performed free running VCXO that can be locked to USO by phase lock loop (if USO signal exists) has been selected as optimal arrangement for this purpose.

If the USO is operational, then the phase locked loop is active and VCXO is synchronized by USO signal. If the USO is out of order, then the phase locked loop is inactive and VCXO runs free at frequency of 5 MHz quartz.

## II. LAYOUT

The block diagram of the PLL oscillator is given in Figure 1.

Input signal from USO is formed by Schmitt trigger inverter. Next circuit detects the USO signal. If this signal is detected then the PLL is active.

When USO signal is not detected a constant voltage for VCXO's tuning input is supplied by a mode detector (VCXO operates in free running mode).

Output level of described oscillator is +3 dBm in all cases, independent on level of USO signal.

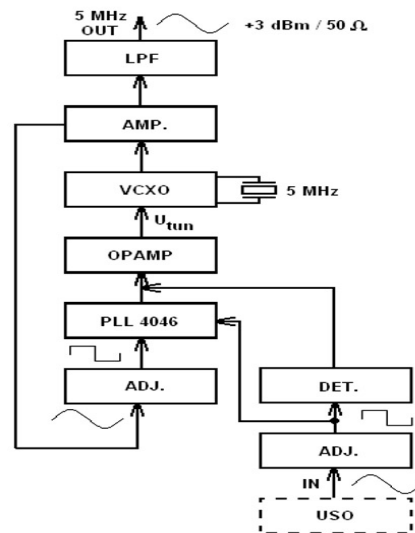


Figure 1: Block diagram of the secondary frequency standard

The circuit of oscillator is build into metal shielding box with dimensions 60 x 48 x 23 mm. Connection to other outside circuits of this box - ports IN and OUT - is done by the SMA connectors.

## III. MEASUREMENTS

The described back up oscillator has been measured as follows: the output frequency for free running mode is 4.999982 MHz. Lock-in range is between 4.99938 MHz and 5.00105 MHz.

The phase noise of free running VCXO output signal is better than -104.5 dBc@100Hz. In the lock-in state, the value of phase noise is better than -103.1 dBc@100Hz.

At present, the described secondary frequency standard is under pre-launch tests.

## REFERENCES

- [1] U. L. Rohde Microwave and wireless synthesizers - Theory and design, John Wiley & Sons, Inc., 1997.
- [2] 74HC/HCT4046A, Datasheet.



# High Performance Concrete Bridge Superstructure Composed of Precast Prestressed Girders and Cast-in-situ Slab

Karel Tesar (PhD student) and Prof. Jiri Strasky (Faculty Mentor)  
 Institute of concrete and masonry structures  
 Brno University of Technology  
 Brno, Czech Republic  
 Email: karel.jr@tesar.cz

**Abstract** — This paper is focused on a study of load bearing structure of a continuous composite concrete bridge composed of precast prestressed T-shaped girders and cast-in-situ slab. At present, an effort is made to use high performance concrete (HPC) in bridge engineering field. Application of HPC in comparison to standard structural concrete enables for the same bridge span to decrease structural height and to increase distance between girders, which becomes cost-effective and material saving solution. The paper presents optimization of above mentioned type of bridge superstructure and shows possibilities of solving the problem by means of FEM programme Nexis32 (ESA-Prima Win). For detailed analysis, construction stages module with utilization of prestressing module and time dependent analysis (TDA) was used.

formwork usually employed in prefabrication of such girders from structural concrete – see Figure 3.

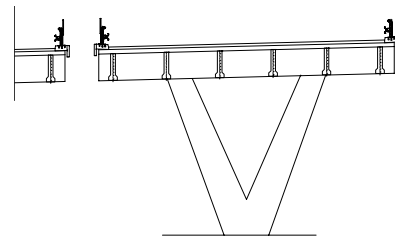


Figure 2: Transverse view

Cast-in-situ reinforced concrete slab was designed from HPC C55/67. The deck slab stiffens the structure, distributes a wheel load and resists longitudinal and transverse compression stresses caused both by global and local bending. A composite action of the prefabricated girders with cast-in-situ slab is guaranteed by shear reinforcement connectors.

## I. INTRODUCTION

The Composite Concrete Bridge composed of Precast Prestressed T-shaped Girders with Cast-In-Situ Slab was developed for medium span bridges of spans from 25 to 40 m. The bridge width, number of precast girders and their axial distance and height depend on the span length and loading. For optimization, a typical three span motorway bridge was chosen with individual spans 27 + 42 + 27 m – see Figure 1. Inner width between road barriers was taken 15.5 m and the superstructure width (i.e. the width of the cast-in-situ slab) was taken 16.6 m – see Figure 2.

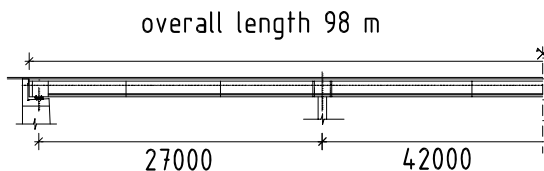


Figure 1: Longitudinal view

Precast prestressed concrete girders were designed from HPC C60/75. Shape of the cross section and their height resulted from demand to use existing

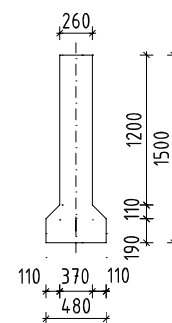


Figure 3: Girder cross section

Superstructure of the bridge is supported by elastomer sliding bearings on the edge abutments, which allows for movements caused by external and time dependent loading. Intermediate V-shaped piers are framed into superstructure, which gives statically indeterminate action and therefore better distribution of load and stresses around the whole structure.

## II. STRUCTURAL TYPE DEVELOPMENT

The development of the system was done in several steps. At first, axial distance of the girders and the slab height were optimized by using influence lines of the transverse transfer of load on a simplified space computational model. Final axial distance of **3.0 m** between girders was chosen from particular distances 1.7 m, 1.9 m, 2.1 m, 2.3 m, 2.5 m, 3.0 m, 3.65 m and 3.75 m, where for each axial distance 3 alternatives of the slab height (0.18 m, 0.20 m and 0.22 m) were considered, resulting in final value of **0.2 m**.

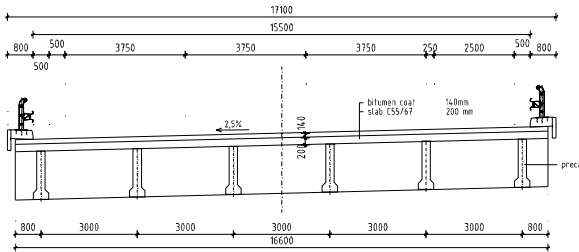


Figure 4: Final girder layout

For the final arrangement of the structure (see Figure 4) was performed very detailed finite element analysis, where the structure was modelled as a space structure that corresponds with the designed shape as well as with proposed construction technique (see Figure 5 and 6).

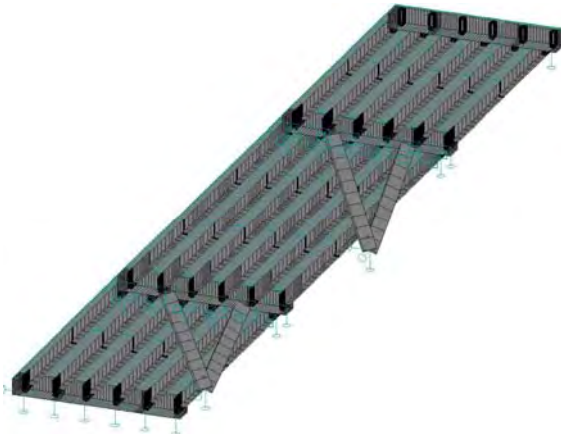


Figure 5: 3D - model

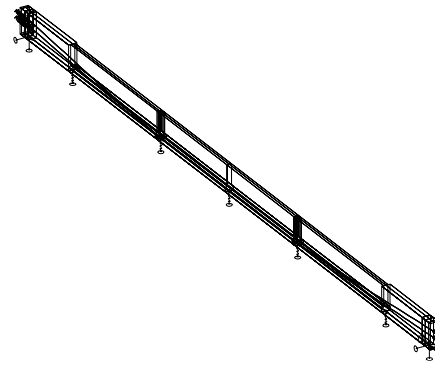


Figure 6: 3D – model of 1 girder

As one of the “construction time saving” requirements was to avoid intermediate erection supports except those near-by the piers, an optimization of girder prestressing in individual construction phases had to be carried out, using the module for prestressing and construction stages accommodated in the Nexis FEM computational programme. For optimized prestressing, individual modules were analysed for a redistribution of stresses resulting from creep and shrinkage of concrete during time.

## III. CONCLUSIONS

Above studied superstructure was checked in every important section, which finally showed that the HPC concrete was reasonably used to capture all of the stresses produced inside the structure during the lifetime period of the bridge, with benefits stated in abstract. Nevertheless, the analysis revealed that for some parts of construction stages a nonlinear analysis is necessary. Special attention then has to be paid to the action of the slab over the intermediate piers and its representation in analysis model.

## ACKNOWLEDGMENTS

The author would like to thank his supervisor, Prof. Jiri Strasky, for his leadership during the PhD study.

## REFERENCES

- [1] Journal BETON, Zavádění EN 1992: “Navrhování betonových konstrukcí do praxe”, 1/2003.

# Erbium Laser Decontamination of Dental Titanium Implants

A.Yousif, M. Strassl, Ernst Wintner

Photonics Institute,

Vienna University of Technology

A-1040 Vienna, Austria

Email: ayousif@mail.zserv.tuwien.ac.at

**Abstract** — *The purpose of this study is to evaluate laser treatment for the decontamination of titanium implant surfaces (titanium plasma sprayed TPS) by employing pulses in the range of microseconds generated by an Er,Cr:YSGG laser system with different settings. Precise surface characterization is done by means of scanning electron microscopy.*

## I. INTRODUCTION

Several studies have already demonstrated the bactericidal effect of high-power microsecond pulse laser irradiation on contaminated dental implant surfaces. Conventionally, the laser energy is specifically absorbed by water molecules which cause water-rich tissue to be preferentially vaporized. In bacterial cytoplasm this effect causes cell lysis [1, 2]. Current goals of dental therapy include the development of easy to fabricate and implantable prosthetic fixture to aid in replacing missing or extracted teeth. The presence of bacteria on the implant surfaces may result in an inflammation of the peri-implant mucosa, and, if left untreated, it may lead to a progressive destruction of the bone supporting the implant, representing periimplantitis. Based on the literature, studies of the efficiency of surgical lasers as a method of decontamination of different implant surfaces showed a clear dependence on laser intensity [3]. The Er:YAG lasers are recommended when following the aspect that they do not exert a negative impact on the implant surface. In this context, this laser causes the least amount of heating in the bone tissue surrounding the implant resulting from the heat conduction through the implant material.

## II. EXPERIMENTAL DETAILS

In the experiments, the Er,Cr:YSGG Waterlase™ laser (wavelength 2.78  $\mu\text{m}$ , fixed repetition rate 20Hz, maximum pulse energy 300mJ, pulse duration about 50-80 $\mu\text{s}$ ) was used with manual handling to proceed in a similar way to the dentist's work in the clinic. The radiation was delivered by a slightly conical sapphire tip (tapered from 600 to 400  $\mu\text{m}$ , Type "G6") for the treatment of clean and contaminated titanium

plasma-sprayed implants (TPS) fabricated by Straumann AG. The settings used for the power investigations were 17 steps from 0.5 W to 4.5 W with a step size of 0.25 W (representing pulse energies of 25 mJ to 225 mJ in steps of 12.5 mJ). The irradiation was performed one time without water spray cooling and one time with water spray cooling (panel setting 5-85% water, 15-95% air). The irradiation time was 1 s per spot. The uncontaminated sample was used to test the impact of the laser radiation on the surface for different power settings to find parameters not affecting the metal surface of the implant. The contaminated samples afterwards were used to test these power settings for removal of remaining tissue. The power settings for the contaminated samples was 1.5 W; 1.75 W and 2 W without water spray and later on 1.25 W with water spray.

## III. RESULTS

Our results showed no significant damage effect on the clean implants irradiated with water spray in all the investigated setting as shown in Figure 1 and 2. The same was achieved for the contaminated implants irradiated with 1.5 and 1.75 W according to environmental scanning electron microscope (ESEM) examination depicted in Figure 3 and 4. The uncontaminated samples treated without water cooling showed surface melting even at the lowest power settings and crack formation for higher settings. These results indicate the possibility of less thermal effect on the implant and bone surfaces by cooling which will be evaluated carefully in the temperature measurement experiment under preparation.

## IV. CONCLUSION AND OUTLOOK

Irradiation of the clean implants with water/air cooling setting causes no surface damage with no molten areas surrounding the irradiated spot. The same results can be obtained for the contaminated implants. The laser beam interacts with the contamination layers on the base of linear absorption inducing the deposition of heat which causes their removal. Temperature measurement during laser irradiation in the vicinity of the implant is important in order to

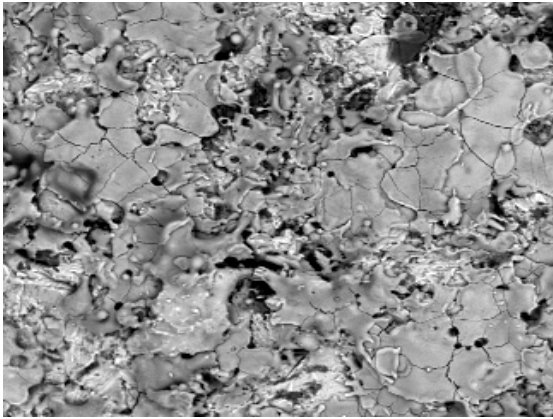


Figure 1: The clean implant surface before laser irradiation, 250x under ESEM.

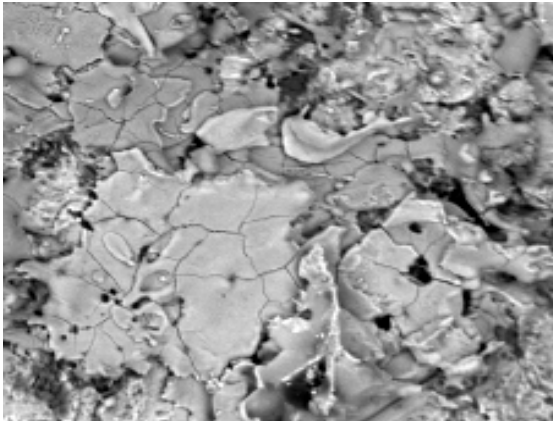


Figure 2: The same implant surface after laser irradiation with no modification ,no significant damage, 250x under ESEM.

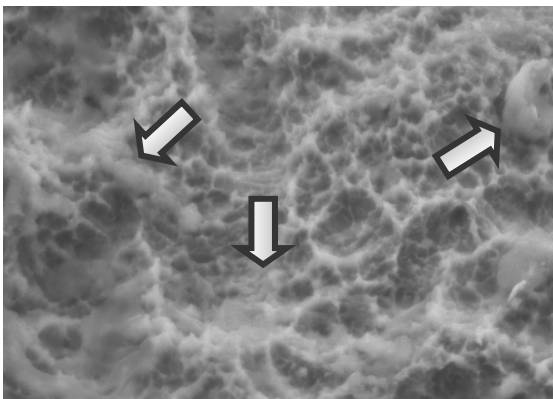


Figure 3: Surface of a contaminated implants before laser irradiation. The organic contaminations easily can be recognized by their smooth structure, 250x under ESEM.

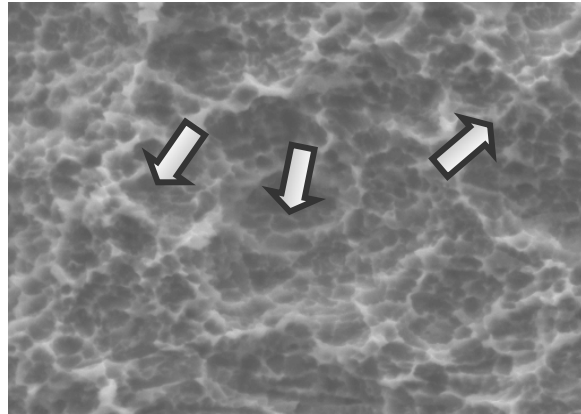


Figure 4: No surface modification, no molten zones could be found at a power setting of 1.25 W with water spray cooling, 250x under ESEM.

estimate any possible thermal damage to the adjacent retaining bone structures. Scanned ultra- short laser pulses (USLPs) may provide a technically superior solution in implant decontamination by reducing the heat and avoiding any expected damages to the treated surfaces.

#### ACKNOWLEDGMENTS

We would like to thank Prof. J.Wernisch, Vienna University of Technoloy for the ESEM examinations and Dr. Leon Verhagen, Lichtenvoorde, Netherlands for providing the implants and his scientific cooperation.

#### REFERENCES

- [1] T. Kato, H. Kusakari and E. Hoshino. Bactericidal efficacy of carbon dioxide laser against bacterial contaminated titanium implant and subsequent cellular adhesion to irradiated area. *Laser Surg. Med.* 23: 299-309, 1998.
- [2] S. Judson, R. B. Hickey, M. J. O'Neal, S. L. Scheidt, D. T. Strong and T. E. Van Dyke. Microbiologic Characterization of Ligature-Induced Periimplantitis in the Microswin Model. *Cli. Oral Implant Res.*, 11: 93-98, 2000.
- [3] J. Mouhyi, L. Sennerby and Van Reck. The soft tissue response to contaminated and cleaned titanium surfaces using CO<sub>2</sub> laser, citric acid and hydrogen peroxide. An experimental study in the rat abdominal wall. *J.Periodontal*, 62(9), September 1991.

# Simulation of indoor climate of a dwelling heated by convection and radiation

Ondřej Šikula and Günter Gebauer  
Institute of Building Services  
University of technology  
Brno, Czech Republic  
Email: sikula.o@fce.vutbr.cz

**Abstract** — *Some of the important parameters of the indoor climate in a dwelling are the distribution of air temperatures and surface temperatures of the internal structures. The actual CFD (Computational Fluid Dynamics) calculation by computer software FLUENT is based on a numerical solution of differential equations which describe fluid flow, heat convection and heat transfer by radiation. These differential equations are solved by numerical control - volumes method. The results can be considered trustworthy only if proper models of turbulence and radiation are used. Suitable turbulence models are RNG  $k-\epsilon$  model and RSM (Reynolds Stress Model). Suitable radiation models are then DO (Discrete Ordinates) and DTRM (Discrete Transfer Radiation Model).*

- Heat transfer by radiation is carried out by long and short wave lengths corresponding to surface temperatures of walls and Sun
- The airflow velocity in the room heated by the heating element is low
- The airflow can be in individual parts of the room laminar, transition or turbulent

For simulation of turbulent flow with low airflow velocity and low-Reynolds-number are appropriate RNG  $k-\epsilon$ , and RSM models [2].

The optical thickness  $aL$  is a good indicator for radiation model choice ( $a$  is a gas absorption coefficient and  $L$  is appropriate length scale) [3]. For inside air  $aL < 1$  and suitable radiation models are S2S, DO and DTRM.

## I. INTRODUCTION

The article presents the experience acquired by the simulation of the airflow and the distribution of temperatures in a dwelling room heated by a radiator in the computer program FLUENT. The work compares results of CFD simulation with the measuring of temperatures, velocities and heat output of the radiator in this room. The goal of the paper is finding out turbulence and radiation models which could describe both heat transfer mechanisms in the room.

## II. ANALYSIS

While choosing the physical-mathematical model is very important to define correctly its characteristic properties and neglect the minor ones. Presumptions for the calculation in case of the room heated by the heating element by convection and radiation are as follows:

- The solution must be generally three-dimensional
- Internal surfaces in the room can be assumed as grey, mat emitters
- The absorption of thermal radiation of the inside air can be neglected

### A. EXAMPLE

The actual solution was based on the simplified geometry of the room; boundary conditions correspond to stationary conditions in winter time (1<sup>st</sup> March, 1p.m. GMT).

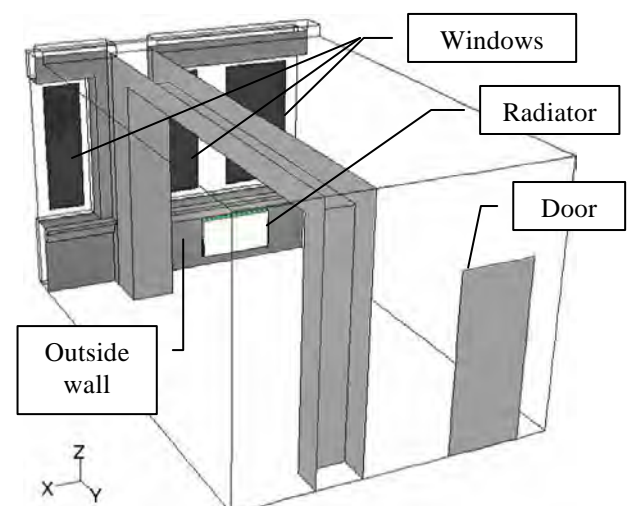


Figure 1: Geometry

The main evaluated variants are in the Table 1.

Variant	Flow	Long-wave radiation	Sun radiation
A	laminar	no	no
B	turbulent	no	no
C	turbulent	yes	no
D	turbulent	yes	yes

Table 1: Variants

### III. RESULTS

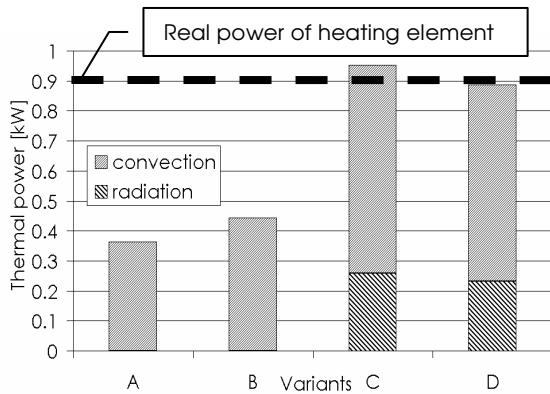


Figure 2: Thermal power of the heating element

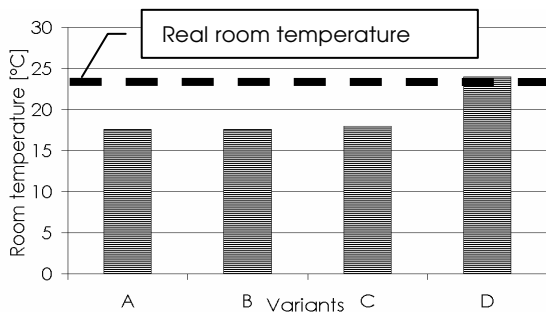


Figure 3: Average room temperature

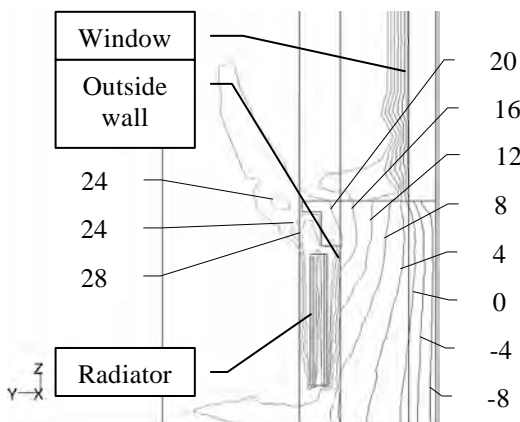


Figure 3: Temperatures – variant A

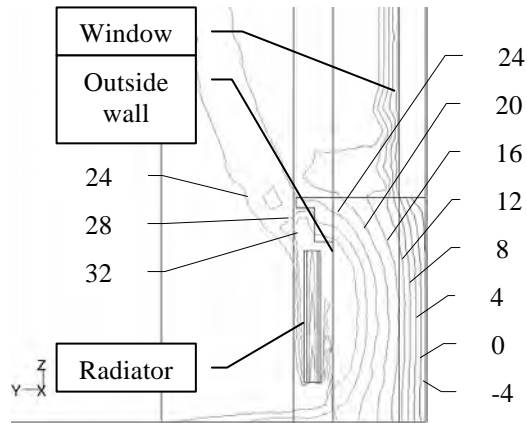


Figure 4: Temperatures – variant C

### IV. CONCLUSIONS

Achieved results show acceptable models for the solution of the problem. Suitable turbulence models are RNG k- $\epsilon$ , model and RSM (Reynolds Stress Model). Suitable radiation models are DO (Discrete Ordinates) and DTRM (Discrete Transfer Radiation Model). The radiation model S2S (Surface – to – Surface) proved to be very computationally demanding and therefore less convenient.

### ACKNOWLEDGMENTS

The numerical calculations in Fluent software were performed in conjunction with the company Sobriety Ltd.

### REFERENCES

- [1] O. Šikula and K. Ponweiser. Modelling of heat transfer in the field of technical facility equipment and calculation using modern techniques. Civil Engineering Journal Stavební obzor 4/2006, pages 6, Prague, Czech Republic, March 2006.
- [2] M. Kozubková and S. Drábková. Numerické modelování proudění, Ostrava, Czech Republic, 2003.
- [3] FLUENT User's Guide, February 2003.

# Hyperglycemia Induced Adenosine Tri-phosphate Depletion and Endothelial Cell Dysfunction

Stewart Russell and David Rumschitzki  
Grove School of Engineering, Department of Biomedical Engineering  
The City College of the City University of New York  
United States of America  
Email: rus9750@me.ccny.cuny.edu

**Abstract:** Cell dysfunction is the underlying cause of diabetic complications. Cells such as the renal epithelium, retinal ganglion, peripheral neurons, and vascular endothelium are found to dysfunction through a variety of altered genetic, structural, and protein-mediated functions. High glucose levels have been correlated to the incidence of diabetic retinopathy, neuropathy, nephropathy, and atherosclerosis. High glucose levels have also been correlated to an increase in the activity of Poly(ADP-ribose) polymerase (PARP), which is known to deplete intracellular Adenosine Triphosphate (ATP). Our results show that ATP depletion may be a critical intermediate step between the activity of high-glucose induced PARP activation and cellular dysfunction in diabetes.

## I. INTRODUCTION

Cell dysfunction is the underlying cause of diabetic complications. Cells such as the renal epithelium, retinal ganglion, peripheral neurons, and vascular endothelium are found to dysfunction through a variety of altered genetic, structural, and protein-mediated functions. High glucose levels have been correlated to the incidence of diabetic retinopathy, neuropathy, nephropathy, microvascular complications, and atherosclerosis.

Four models of the pathogenesis of diabetic complications have been described. These include Aldose Reductase pathway (AR), formation of reactive oxygen species (ROS), the accumulation of advanced glycation end-products (AGE), and inappropriate activation of protein kinase C (PKC).

Brownlee et al (2005) have proposed a unifying mechanism for the activation of the molecular pathways of cell dysfunction in diabetes. Elevated levels of ROS have been found to decrease the activity of the key glycolytic enzyme glyceraldehydes-3 phosphate dehydrogenase (GAPDH) by modifying the enzyme with ADP-ribose [1]. The increased activity of PARP that causes modification of GAPDH itself comes from ROS damage to DNA. PARP is known to be a large

consumer of ATP [2]. The activation of PARP by radiation or chemotherapy, and subsequent ATP depletion, has been generally accepted as an important step in the pathway to killing of resting lymphocytes [3]. ATP is a staple of cancer therapy [4]. We propose that the effect of the unifying mechanism proposed by Brownlee *et al* is to lower ATP levels in the cell by activation of PARP and inhibition of GAPDH, thereby causing ATP depletion induced cell dysfunction and apoptosis. Consistent with this hypothesis, clinical data show some types of cancer are less likely in people with unregulated diabetes [5, 6]

## II. RESULTS

We measured rates of apoptosis, a known contributor to endothelial permeability, and also directly measured tight junction integrity, by measurement of volume flow rate through cultured monolayers. Data from a series of experiments revealed a correlation between increased glucose, intracellular ATP concentration, apoptosis and permeability.

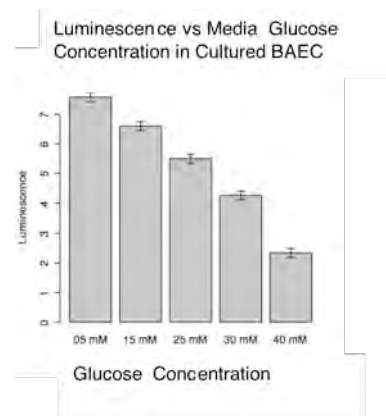


Figure 1) Decrease in luminescence as a function of increased glucose concentration. Arbitrary normalized luminescence data shows a decrease in ATP content in higher glucose concentration culture media, compared to normal (5mM).

In preliminary experiments, Bovine Aortic Endothelial Cells (BAEC) (Vectec) were grown in 8 different glucose concentrations, from 5mM to 40mM. Detection of intracellular ATP by the firefly luciferase-luciferin reaction showed a monotonic decrease of ATP with increasing glucose concentration, as shown in Figure 1. Previous studies have showed ATP depletion and PARP activation in diabetes, but did not reveal a functional relationship to high glucose

In measurements of apoptosis, data showed an increase in apoptosis with increasing glucose concentration in the media. This is in agreement with the results of Ho et al 2000. When our apoptosis data is reparameterized in terms of reduced ATP depletion, using the results from our ATP experiments, apoptosis results are also in agreement with Lieberthal 1998, as shown in Figure 2. Significantly, ATP levels decreased more than apoptosis increased, indicating ATP depletion is not only a function of a decreasing number of live cells.

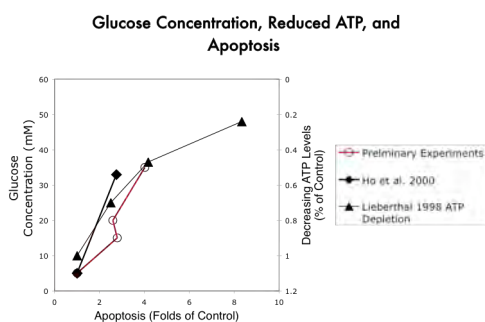


Figure 2) Apoptosis as a function of ATP depletion or High Glucose. Preliminary results plotted with similar experimental results of Ho et al, Lieberthal et al.

In direct measurements of permeability, monolayers were grown in high or low glucose on filters, and placed into an apparatus to measure water flux through the layer in response to an applied pressure gradient. Our data revealed an increase in permeability with increasing glucose concentration as shown in figure 3.

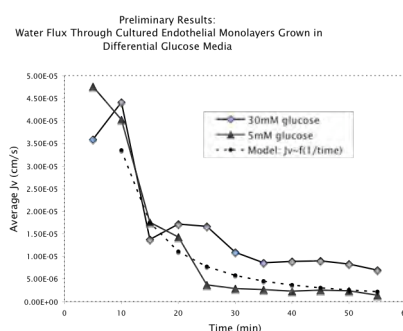


Figure 3) Increased water flux in high glucose cultured monolayers

### III. CONCLUSION

Our results show that ATP depletion may be a critical intermediate step between the activity of high-glucose induced PARP activation and cellular dysfunction in diabetes.

### IV. REFERENCES

1. Du, X., T. Matsumura, D. Edelstein, L. Rossetti, Z. Zsengeller, C. Szabo, and M. Brownlee, *Inhibition of GAPDH activity by poly(ADP-ribose) polymerase activates three major pathways of hyperglycemic damage in endothelial cells.* J Clin Invest, 2003. **112**(7): p. 1049-57.
2. Martin, D.S. and G.K. Schwartz, *Chemotherapeutically induced DNA damage, ATP depletion, and the apoptotic biochemical cascade.* Oncol Res, 1997. **9**(1): p. 1-5.
3. Pettitt, A.R., A.R. Clarke, J.C. Cawley, and S.D. Griffiths, *Purine analogues kill resting lymphocytes by p53-dependent and -independent mechanisms.* Br J Haematol, 1999. **105**(4): p. 986-8.
4. Martin, D.S., J.R. Bertino, and J.A. Koutcher, *ATP depletion + pyrimidine depletion can markedly enhance cancer therapy: fresh insight for a new approach.* Cancer Res, 2000. **60**(24): p. 6776-83.
5. Nerlich, A.G., H.G. Hagedorn, M. Boheim, and E.D. Schleicher, *Patients with diabetes-induced microangiopathy show a reduced frequency of carcinomas.* In Vivo, 1998. **12**(6): p. 667-70.
6. Weiderpass, E., W. Ye, H. Vainio, R. Kaaks, and H.O. Adami, *Reduced risk of prostate cancer among patients with diabetes mellitus.* Int J Cancer, 2002. **102**(3): p. 258-61.

# Retinal Vascular Permeability in Diabetes

Sandra V. Lopez and John M. Tarbell (Faculty Mentor)

Wallace H. Coulter Laboratory

City College of New York

New York, USA

Email: vero\_lo@yahoo.com

**Abstract** — *Diabetic retinopathy is the most common microvascular complication of diabetes mellitus, despite of many years of research it continues to constitute the major cause of blindness in adults. This research aims to understand the molecular mechanisms by which the Blood Retinal Barrier (BRB) is regulated. In order to do so, we have measured the transport of solutes from the luminal to the apical side through monolayers of Bovine Retinal Endothelial Cells (BRECS). The average diffusive permeabilities to TAMRA (466.92 Da), Dextran (70 KDa) and Di-LDL (200,000 KDa) were found to be  $1.36 \times 10^{-5}$ ,  $1.29 \times 10^{-6}$  and  $4.37 \times 10^{-7}$  cm/s respectively. The average effective permeabilities (i.e. diffusive and convective transport) after two hours of convection were found to be  $7.34 \times 10^{-6}$ ,  $2.72 \times 10^{-6}$  and  $6.95 \times 10^{-7}$  cm/s respectively.*

## I. INTRODUCTION

The inner BRB is formed by complex tight junctions (TJ) of the retinal vascular endothelial cells to restrict the transport between the circulating blood and neural retina. The transporters at the inner BRB have an essential role in supplying nutrients to the retina and in the efflux of neurotransmitter metabolites from the retina to maintain neural functions. Understanding the molecular mechanisms by which transport across the BRB is regulated is a key step to find improved means to control vascular permeability and loss of vision in persons with diabetic retinopathy. To elucidate the transport properties of the endothelium of the retina, we have designed an in-vitro experiment based on previous studies in the laboratory [1-5]. Confluent monolayers of BREC are placed in a sealed chamber with controlled physiological temperature and pH to measure the solute permeability of the monolayer to three different size solutes: TAMRA (466.92 Da), Dextran (70 KDa) and Di-LDL (200,000 KDa). Two kinds of permeability were recorded, Pd or the permeability in the absence of a pressure gradient across the monolayer (during one hour) and Pe or the permeability when the monolayer was subjected to a pressure gradient of 10 cm H<sub>2</sub>O that caused water to

flow across the monolayer from the luminal to the abluminal side (during 2 hours). The water flux across the monolayer (Jv/A) was recorded following the protocol of previous experiments done in our laboratory.

## II. CHEMICALS AND CELL CULTURE

Frozen vials were thawed and placed in T-75 flasks to be grown in MCDB-131 media with 10%FBS, 10 ng/mL EGF, 0.2mg/mL EndoGro, 0.09 mg/mL Heparin and 1% antibiotic/antimycotic. Cells were plated at a density of  $3.0 \times 10^5$  cells/cm<sup>2</sup> onto Transwell polycarbonate filters (0.4 um pore size, 24.5 mm diameter), previously coated with fibronectin. When the monolayer reached confluency, about 2 to 3 days after plating, transport experiments were run using MCDB-131-1%BSA as experimental media.

## III. MEASUREMENT OF WATER FLUX AND SOLUTE PERMEABILITY

The measurement of water and solute flux was made as in previous experiments, basically, a fluorescent detection system, integrated with a bubble tracker allowed for the real time measurement of solute and water going across the cell monolayers. The diffusive permeability (Pd) was averaged over the first 15 minutes to obtain the initial Pd and the last 15 minutes to obtain the final Pd. The same was done to obtain the effective permeability (Pe) during the first 15 minutes of convective flux and the final 15 minutes.

## IV. RESULTS

The average diffusive permeabilities to TAMRA (466.92 Da), Dextran (70 KDa) and Di-LDL (200,000 KDa) were found to be  $1.36 \times 10^{-5}$ ,  $1.29 \times 10^{-6}$  and  $4.37 \times 10^{-7}$  cm/s respectively. The average effective permeabilities (i.e. diffusive and convective) as soon as a 10 cm H<sub>2</sub>O pressure gradient was applied to the monolayers were found to be  $1.43 \times 10^{-5}$ ,

$8.40 \times 10^{-6}$  and  $2.04 \times 10^{-6}$  cm/s respectively. After having the monolayers at this pressure gradient for two hours, the effective permeability was measured again and the permeabilities were found to decrease to  $7.34 \times 10^{-6}$ ,  $2.72 \times 10^{-6}$  and  $6.95 \times 10^{-7}$  cm/s for TAMRA, 70KDa-Dextran and Di-LDL respectively.

As seen in Figure 1, the diffusive permeability of TAMRA is almost 10 times that of the 70KDa Dextran and 30 times that of Di-LDL, and the effective permeability of TAMRA is around 2 times that of the 70KDa Dextran and 9 times that of Di-LDL. Both the diffusive and the effective permeability decreased for TAMRA, but only the effective one for Dextran and Di-LDL.

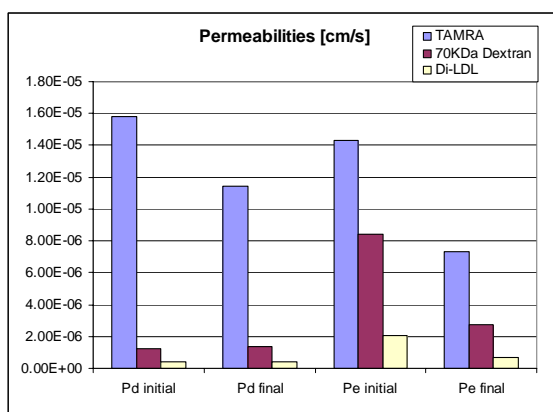


Figure 1: Comparative Permeabilities

## V. FUTURE WORK

The permeability values of the intact endothelial monolayer have been established. In the future these values will be compared to values obtained when using diabetes induced monolayers to try to elucidate how and how much these properties are altered during the disease

## ACKNOWLEDGMENTS

Dr. Antonetti, Dr. Gardner and Ellen Wolpert from the Milton S. Hershey Medical Center at Penn State College U.S.A.

## REFERENCES

[1] DA Antonetti, AJ Barber, S Khin, E Lieth, JM Tarbell and TW Gardner. Vascular permeability in experimental diabetes is associated with reduced endothelial occludin content: vascular endothelial growth factor decreases occludin in retinal endothelial cells. Penn State Retina Research Group. *Diabetes*,47(12):1953-9 December 1998.

[2] L DeMaio, DA Antonetti, RC Jr Scaduto, TW Gardner and JM Tarbell. VEGF increases paracellular transport without altering the solvent-drag reflection coefficient. *Microvasc Res*. 68(3):295-302, November 2004.

[3] L DeMaio, JM Tarbell, RC Jr Scaduto, DA Antonetti, and TW Gardner. A transmural pressure gradient induces mechanical and biological adaptive responses in endothelial cells. *Am J Physiol Heart Circ Physiol*. 286(2):H731-41. February 2004

[4] S Lakshminarayanan, JM Tarbell and TW Gardner. Effect of VEGF on retinal microvascular endothelial hydraulic conductivity: the role of NO. *Invest Ophthalmol Vis Sci*. 41(13):4256-61. December 2000.

[5] S Lakshminarayanan, JM Tarbell and TW Gardner. Effect of shear stress on the hydraulic conductivity of cultured bovine retinal microvascular endothelial cell monolayers. *Curr Eye Res*. 21(6):944-51. December 2000.

# ***In vitro* study of LDL transport through endothelial monolayers under convective conditions**

Limary M. Cancel<sup>1,2</sup>, Andrew W. Fitting<sup>3</sup> and John M. Tarbell<sup>1</sup> (Faculty Mentor)

<sup>1</sup>Department of Biomedical Engineering  
Grove School of Engineering  
The City College of New York  
New York, NY, USA

<sup>2</sup>The Graduate Center  
The City University of New York  
New York, NY, USA

<sup>3</sup>Department of Chemical Engineering  
The Pennsylvania State University  
State College, PA, USA

Email: limarycancel@yahoo.com

**Abstract** — *It is difficult to assess the transport pathways that carry low density lipoprotein (LDL) into the artery wall in vivo, and there has been no previous in vitro study that examined transendothelial transport under physiologically relevant pressurized (convective) conditions. Therefore, we measured water, albumin, and LDL fluxes across bovine aortic endothelial cell (BAEC) monolayers in vitro and determined the relative contributions of vesicles, paracellular transport through breaks in the tight junction, and “leaky” junctions associated with dying or dividing cells. To further explore the leaky junction pathway, TNF $\alpha$  and cycloheximide were used to induce apoptosis on BAEC monolayers and the fluxes of water and LDL were measured.*

## I. INTRODUCTION

The inner lining of all blood vessels is a single layer of endothelial cells which provides the most immediate barrier to transport from the lumen to the underlying tissue. Areas of the vasculature that have increased LDL wall permeability may develop fatty streaks. These streaks can later grow into larger, calcified plaques that inhibit blood flow which may potentially be deadly. Therefore, it is critical that the pathways that LDL takes to cross the endothelial barrier be well understood. Previous *in vitro* studies have focused on the uptake and metabolism of LDL by endothelial cells via receptor-mediated processes. Other studies have shown that cells in a state of turnover can allow large macromolecules, including LDL and albumin, to cross the endothelium through so-called “leaky junctions”. Little work has probed the transport of LDL across cultured endothelial

monolayers that may serve as models for understanding and controlling transendothelial transport of LDL.

## II. METHODS

BAECs were plated onto porous, polyester filters in Transwell supports. Macromolecule flux ( $J_s$ ) was measured using an automated fluorometer system and water flux ( $J_v$ ) measurements were recorded using a bubble tracker system previously developed in our laboratory[1]. Each convective transport experiment consisted of data collection under diffusive conditions for one hour, followed by application of a 10-cm H<sub>2</sub>O pressure differential and data collection for one hour, and finally two additional hours of data collection under diffusive conditions. During the pressurized period,  $J_v$  values were recorded along with the solute permeability data. The macromolecules used were human LDL tagged with 1,1'-dioctadecyl - 3,3,3',3'-tetramethylindocarbocyanine perchlorate (DiI-LDL) and albumin tagged with tetramethylrhodamine (Albumin-TMR).

To determine the contribution of vesicular transport, cells were fixed with 1% paraformaldehyde and the diffusive permeability was measured. In addition, to assess the role that receptors play in LDL transport, the cells were incubated with a 50-fold excess of untagged, native LDL and the permeability was measured.

BAEC monolayers were treated with TNF $\alpha$  (20ng/mL) and cycloheximide (3 $\mu$ g/mL) for 3.5 hours to induce an elevated rate of apoptosis. The rates of apoptosis for control and treated monolayers were measured with an annexin V/PI apoptosis

assay. TNF $\alpha$ /cycloheximide treated cells were used in transport experiments to determine the effect of treatment on permeability.

### III. RESULTS

The diffusive permeability ( $P_o$ ) of LDL was  $1.7 \times 10^{-7}$  cm/s. This was reduced to  $0.69 \times 10^{-7}$  in fixed monolayers. Saturation of the LDL receptor with untagged, native LDL reduced the diffusive permeability by 2.27-fold which was not significantly different from the 2.46-fold reduction obtained in fixed monolayers. The diffusive permeability of albumin was  $2.9 \times 10^{-6}$  cm/s and it was reduced to  $1.8 \times 10^{-6}$  after fixation. Under convective conditions the average  $J_v$  was  $5.39 \times 10^{-6}$  cm/s, the apparent permeability ( $P_e$ ) of LDL increased by a factor of 6.38 from diffusive control, and the apparent permeability of albumin increased by a factor of 1.98 from diffusive control.

BAEC monolayers had a baseline apoptosis rate of 0.14%. TNF $\alpha$ /cycloheximide treated monolayers had an apoptosis rate of 3.3%, a 24-fold increase over baseline. This resulted in a 2.7-fold increase in LDL permeability, and a 2.8-fold increase in water flux.

### IV. DISCUSSION

The diffusive, convective and vesicular transport data obtained was used to fit a three pore model to determine the relative contributions of the vesicle, break in the tight junction, and "leaky" junction pathways to the overall transport of water, albumin and LDL under convective conditions. The model assumes that the 3 pathways are arranged in parallel and that the convective-diffusive permeability coefficient for each solute in each pathway is described by the equations[2]:

$$P_e = P_o Z + (1 - \sigma_s) J_v \quad (1)$$

$$Z = N_{Pe} / [\exp(N_{Pe}) - 1] \quad (2)$$

where  $\sigma_s$  is the reflection coefficient and  $N_{Pe}$  is the Peclet number. The model predicts that the break in the tight junction is the dominant pathway for water (77.7%) and albumin (53%), while most of the LDL (90.9%) is carried through the "leaky" junction. The vesicular pathway accounts for 20 and 9.1% of the transport of albumin and LDL, respectively.

This study was the first to quantify transendothelial transport of LDL *in vitro* under pressurized conditions, simulating the convectively dominated transport that arises in arteries *in vivo*. Our results are consistent with *in vivo* observations[3-6] indicating that leaky junctions, not vesicles, provide the dominant pathway for LDL uptake by arteries. The experiments using the apoptosis inducers TNF $\alpha$ /cycloheximide support the hypothesis that

apoptosis rates dictate, at least in part, the permeability of the endothelium to LDL and demonstrate the potential of manipulating endothelial monolayer permeability by altering the rate of apoptosis pharmacologically.

### REFERENCES

- [1] H Sill, YS Chang, JR Artman, JA Frangos, TM Hollis, JM Tarbell. Shear Stress Increases Hydraulic Conductivity of Cultured Endothelial Monolayers. *American Journal of Physiology*, 268(2 Pt 2):H535-543, 1995.
- [2] FE Curry, WL Joyner, JC Rutledge. Graded Modulation of Frog Microvessel Permeability to Albumin Using Ionophore A23187. *American Journal of Physiology*, 258:H587-H598, 1990.
- [3] S-J Lin, K-M Jan, G Schuessler, S Weinbaum, S Chien. Enhanced Macromolecular Permeability of Aortic Endothelial Cells in Association with Mitosis. *Atherosclerosis*, 73:223-232, 1988.
- [4] S-J Lin, K-M Jan, S Chien. Role of Dying Endothelial Cells in Transendothelial Macromolecular Transport. *Arteriosclerosis*, 10:703-709, 1990.
- [5] S-J Lin, K-M Jan, S Weinbaum, S Chien. Transendothelial Transport of Low Density Lipoprotein in Association with Cell Mitosis in Rat Aorta. *Arteriosclerosis*, 9:230-236, 1989.
- [6] S Weinbaum, G Tzeghai, P Ganatos, R Pfeffer, S Chien. Effect of Cell Turnover and Leaky Junctions on Arterial Macromolecular Transport. *American Journal of Physiology*, 248:H945-H958, 1985.

# The Effect of Chronic Hypertension on the Filtration Properties of Intact and Denuded Vessels

Tieuvi Nguyen and David Rumschitzki  
Grove School of Engineering  
The City College of the City University of New York  
New York, USA  
Email: Tieuvi@gmail.com

**Abstract** — Hypertension has long been recognized as a major risk factor in atherosclerosis, but the mechanism behind this effect is not yet completely understood. In this study we investigate the influences of chronic hypertension and of endothelial removal on the fluid filtration properties of the rat aorta. Thoracic aortas from spontaneously hypertensive (SHR) and Wistar Kyoto (WKY) rats were excised under pressure and cannulated with a 4% bovine serum albumin (BSA) solution. The hydraulic conductivity ( $L_p$ ) of each vessel was calculated at five different pressures. Our preliminary data suggests that ultrastructural changes in the SHR aorta cause an increase in resistance to transmural flow, and that the percent effect of the endothelial removal in SHR vessels were less than normotensive WKY.

## I. INTRODUCTION

Although hypertension has been identified as a major risk factor in the progression of atherosclerosis, the mechanism behind this effect is not completely understood. In this study we investigate the influences of chronic hypertension and of endothelial removal on the fluid filtration properties of the rat aorta. It is well documented that atherosclerosis is triggered by the entry of macromolecules including low density lipoprotein (LDL) cholesterol into the blood vessel wall [1]. Previous models have shown that this transport is convection dominated and, as such, the nature of water transport plays a central role in the lipid accumulation process [2, 3]. We shall measure the hydraulic conductivity ( $L_p$ ) of both intact and denuded aortas as a function of transmural pressure (DP) *ex-vivo* on the same vessels. We hypothesize that the increase in vessel wall thickness due to hypertension will result in greater resistance to transmural water flow and an ultimate reduction in overall  $L_p$ .

## II. METHODS

Thoracic aortas from spontaneously hypertensive (SHR) and Wistar Kyoto (WKY) rats were excised under pressure and cannulated with a 4% bovine serum albumin (BSA) solution containing  $10^{-3}$  M  $\text{NaNO}_3$  to reduce smooth muscle cell contraction. The transmural fluid flux ( $J_v$ ) was dynamically monitored and recorded using a spectrophotometer tracking system and the hydraulic conductivity ( $L_p$ ) of each vessel was calculated at five different pressures. The same vessels were then mechanically denuded and  $L_p$ -values were re-measured at the same pressures. As is standard in the field, one assumes that  $L_p$  adds like linear capacitances in series [4]. Therefore, we can calculate the resistance ( $1/L_p$ ) of each blood vessel layer by the following relationship:

$$\frac{1}{L_{p_i}} = \frac{1}{L_{p_{e+i}}} + \frac{1}{L_{p_{m+i}}} \quad (1)$$

where  $L_{p_i}$  is the total hydraulic conductivity of an intact vessel,  $L_{p_{e+i}}$  is contribution of the endothelium and intima, and  $L_{p_{m+i}}$  represents the hydraulic conductivity of the media and internal elastic lamina (IEL) following vessel denudation.

## III. RESULTS

Intact vessels for both WKY and SHR showed no significant change in  $L_p$ -value with increasing transmural pressure. This trend was also observed in denuded vessels (Figure 1). Similarly, the effect of chronic hypertension did not result in significant changes in  $L_p$  in both intact and denuded vessels ( $P > 0.05$ ). However, the effect of the endothelium to overall resistance appears to be more pronounced in the WKY vessels than in the SHR. Upon denudation  $L_p$ -values increased an average of 33.2% across the entire pressure range for WKY vessels compared to only 13.9% for SHR. The average  $L_{p_{e+i}}$  for SHR was calculated to be 65% greater than for normotensive WKY vessels.

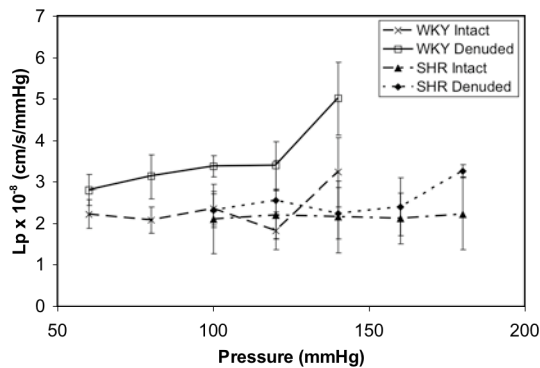


Figure 1: Summary of hydraulic conductivity ( $L_p$ ) results for WKY and SHR intact and denuded vessels. Mean  $L_p$ -values reported as Mean  $\pm$  S.D.

#### IV. DISCUSSION

Histological results indicate that the wall of blood vessels subjected to chronic hypertension is markedly thicker than those subjected to normal pressure conditions. Intuitively, one would expect that this ultrastructural difference would result in an increase in the vessels resistance to transmural fluid flow; however, our results showed that this is not the case. Upon removal of the endothelium we were able to delineate the contribution of the endothelium to the overall fluid flux was much more pronounced in hypertensive vessels. The source of this increased endothelial permeability is not yet completely known.

To this point we assumed that the transport of water across the endothelium was attributed to tight junctions, both normal and those which are transiently *leaky* due to apoptosis or mitosis. Another possibility results from work done in our lab by J. Toussaint who showed, for the first time, the existence of the ubiquitous water channel aquaporin-1 (AQP1) on the surface of rat aortic endothelial cells. We hypothesize that water transport is not just a passive response to transmural pressure and osmotic pressure differences, but rather is partially due to transport through AQP1 channels. Pilot studies repeating  $L_p$ -measurements, as those carried out above, with the additional presence of the aquaporin blocker solution mercuric chloride ( $HgCl_2$ ) suggest that the fractional contribution of AQP protein channels to overall water transport is 27% and 57% to the endothelial  $L_p$  at  $P = 60$ mmHg.

#### ACKNOWLEDGMENTS

The authors would like to thank Dr. Kung-Ming Jan for his advisement on this project. This research was funded by the National Institutes of Health grant 41459-0004.

#### REFERENCES

- [1] Ross R. The pathogenesis of atherosclerosis: a perspective for the 1990s. *Nature* 1993;362:801.
- [2] Yuan F, Chien S, Weinbaum S. A new view of convective-diffusive transport processes in the arterial intima. *J Biomech Eng* 1991;113:314.
- [3] Huang Y, Rumschitzki D, Chien S, Weinbaum S. A fiber matrix model for the growth of macromolecular leakage spots in the arterial intima. *J Biomech Eng* 1994;116:430.
- [4] Tedgui A, Lever MJ. Filtration through damaged and undamaged rabbit thoracic aorta. *Am J Physiol* 1984;247:H784.

# Time-sliced imaging and Monte Carlo simulation study of ex vivo cancerous and normal breast tissues

M. Alrubaiee, M. Xu, S. K. Gayen and R. R. Alfano

Institute for Ultrafast Spectroscopy and Lasers, Physics Department

The City College of New York and the Graduate School of the City University of New York,  
138th Street at Convent Avenue, New York, NY 10031

Email: [malrub@sci.ccnycuny.edu](mailto:malrub@sci.ccnycuny.edu)

**Abstract** — *Normal and cancerous ex vivo breast tissue samples were investigated optically using time-resolved transillumination measurements. The samples were illuminated using 800 nm, 120 fs, 1 kHz repetition rate pulses from a Ti: sapphire laser system. A sequence of two-dimensional time-sliced images were recorded using an ultrafast gated camera system. Images recorded with earlier arriving light highlighted cancerous region while, those recorded with later arriving light highlighted normal tissues. Temporal intensity profiles of the images were analyzed using Monte Carlo simulation of light transport through tissues. The results show a significant difference in transport length between cancerous and normal tissues. The technique provides a mean for noninvasive evaluation of normal and cancerous tissues.*

## I. INTRODUCTION

Near-infrared (NIR) imaging and spectroscopy is being actively pursued for developing a noninvasive modality for detection and diagnosis of breast cancer.[1] Light propagation in biological tissues is governed by tissue optical properties that include the anisotropy factor ( $g$ ), scattering coefficient ( $\mu_s$ ) and absorption coefficient ( $\mu_a$ ). Estimation of the optical properties is complicated due to variations in the cell shape and size, the index of refraction, and boundary conditions. [2-3]

It has been demonstrated that time-sliced transillumination imaging approaches can distinguish normal and cancerous thin (<10-mm) ex vivo breast tissue specimens. [4] However, a quantitative approach to extract optical parameters has not yet been well developed. Optical characterization of breast tissue in the past decade has focused on applying the Radiative Transport equation (RTE) or its diffusion approximation (DA) to fit experimental data. In this paper we introduce a method for retrieving the transport length  $l_t$ , and absorption length  $l_a$ , from a sequence of time-sliced 2-D images using a Monte

Carlo simulation (MCS) approach. The MCS approach assumes a random walk of photons, takes the detector-gate resolution into account, and assumes a fixed value for  $g$  to extract  $l_a$  and  $l_t$

## II. MONTE CARLO SIMULATION APPROACH

Measurement of the time-resolved profile of light transmission through a thin layer (<5-mm) of biological samples provides an accurate approach to determine the optical properties ( $\mu_a$  and reduced scattering coefficient,  $\mu_s = ((1-g) \mu_s)$  of the sample. We fit the measured time-resolved light transmission to a Monte Carlo model of light propagation in turbid media. The Monte Carlo simulation (MCS) assumed a Henyey-Greenstein phase function [5] and a fixed  $g = 0.9$  for the samples investigated. The MCS follows a random walk of  $10^4$  photons, chosen as a compromise between CPU time and acceptable least error. In the fitting procedure, the  $l_t$  is scanned through a range of 0.4-mm to 1.2-mm and the absorption coefficient is varied until a least error for each  $l_t$  is reached. The accuracy of fitted  $l_t$  and  $l_a$  is better than 0.01mm.

## III. METHODS AND MATERIALS

Experimental arrangement for time-sliced imaging, shown schematically in Fig.1, made use of approximately 120-fs duration, 1 kHz repetition-rate, 800-nm pulses from a Ti:sapphire laser and amplifier system [4] for sample illumination. A 200-mW beam was expanded using a beam expander and an aperture selected a 3-cm diameter central part to illuminate the sample. An ultrafast gated intensified camera system (UGICS) recorded 2-D images using ~80 picosecond-duration slices of light transmitted through the sample. The time gate position could be varied over 20 nanosecond intervals in step sizes of 25ps-2ns. The breast tissue samples comprising normal and invasive ductal carcinoma (IDC) used in

the study were obtained from the National Disease Research Interchange (NDRI) and Memorial Sloan Kettering Cancer Center (MSKCC). The samples were placed between two thin microscope slides and slightly compressed to assure uniform thickness. Table I shows a list of the samples used.

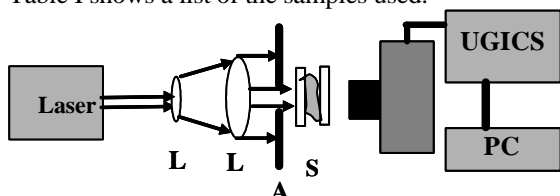


Fig. 1 Schematic of experiment setup (L) lens, (A) aperture, (S) sample, and (PC) computer

#### IV. RESULT

A sequence of time-sliced 2-D images of samples #1 and sample #2 are shown in Fig. 2(a) and 2(b), respectively. As can be seen, early-light images highlight cancerous regions, while image recorded with late-arriving light accentuate normal regions. These results indicate that cancerous tissue is less scattering than normal tissue ( $l_t$  cancer  $>$   $l_t$  normal). For a quantitative comparison, we retrieve the  $l_t$  values using the MCS approach. We integrated the same normal and the same cancerous region of each time-sliced image and plotted this intensity versus time to generate respective temporal profiles. Then we ran MCS for the known thickness and  $g = 0.9$  and an input of  $10^4$  photons. Table I shows the retrieved transport length  $l_t$  and absorption length  $l_a$  for various samples.

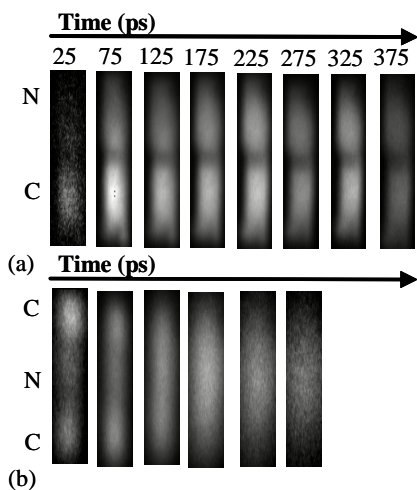


Fig. 2 Time-slice images of (a) sample #1 and (b) sample #2. Normal (N), and Cancerous (C)

The transport length had consistently higher values for the cancer region than the normal region for all samples. The results provide a quantitative validation

that cancerous tissues are less scattering than normal, assuming the  $g$  values are the same. The NIR time-sliced imaging, combined with MCS analysis, has a potential for improving optical breast tomography.

Sample #	Thickness (mm)	Tissue	$l_t$ (mm)		$l_a$ (mm)	
			Normal	Cancer	Normal	Cancer
1	~10	IDC	0.7	1	22.3	26.5
2	~5	IDC	0.65	0.85	34.6	33
3	~5	IDC	0.65	0.85	47.6	38.9
4	~5	IDC	0.63	0.78	20.5	14.5

Table I Transport length  $l_t$  and absorption length  $l_a$  of various tissue specimens using the MCS approach

#### REFERENCES

- [1] R. R. Alfano Guest Editor, "Advances in Optical Breast Imaging," Technology in Cancer Research and Treatment 4 (2005, special issue).
- [2] A. Ishimaru, "Wave Propagation and Scattering in Random Media" (Academic, New York, 1978)
- [3] Bevilacqua F, Marquet P, Coquoz O and Depeursinge "Role of tissue structure in photon migration through breast tissues," Appl. Opt. 36, 44-48, (1997).
- [4] M. Alrubaiee, S. K. Gayen, J. A. Koutcher, and R. R. Alfano, "Spectral and Temporal Near-Infrared Imaging of Ex Vivo Cancerous and Normal Human Breast Tissues," Technology in Cancer Research and Treatment 4 (2005).
- [5] S. Jacques, C. Alter, and S. Prahl, "Angular dependence of HeNe laser light scattering by human dermis," Lasers in the Life Sciences, 1, 309-333, (1987).

# Partial Characterization of Blm10p, an Activator of the Nuclear 20S Core Proteasome, that Functions in the Relief of Oxidative Stress in *Saccharomyces cerevisiae*

Leah D. Pride<sup>1</sup> and Carol Wood Moore, Ph.D<sup>2</sup> (Faculty Mentor)  
The City College of New York (City University of New York)<sup>1</sup>  
Sophie Davis School of Biomedical Education (City University of New York)<sup>2</sup>  
New York, NY 10031, United States  
{Pride, Moore}@sci.ccny.cuny.edu

**Abstract** — This paper focuses on the partial functional characterization of *Blm10p*, an activator of the nuclear 20S core proteasomal subunit. The *BLM10* gene was isolated in this laboratory as a multi-copy suppressor of the extreme DNA damage and hypersensitivity to lethal effects of oxidative agents (e.g. bleomycin) conferred by the *blm3-1* mutation of *Saccharomyces cerevisiae* (baker's yeast). Results have shown that *Blm10p* is widely conserved and localizes throughout the cell cycle in the nucleus, similar to the human PA200 homolog. The protein is not essential for viability in the absence of oxidative agents. In the presence of several drugs, the protein becomes essential for cell survival and the protection of DNA. *Blm10* is part of an extensive protein network, which links the 26S proteasome to DNA repair.

## I. INTRODUCTION

The *blm3-1* mutation of *Saccharomyces cerevisiae* conveys hypersensitivity to the anticancer drug, bleomycin (BM), or structurally related phleomycin, (PM). The *BLM10* gene was cloned as a multi-copy suppressor of the *blm3-1* mutation by functional complementation [1]. BM, in the presence of oxygen and Fe(II), cleaves DNA through a method involving the formation of free radicals [2] causing DNA damage. The drug also damages the cell wall and plasma membrane in *S. cerevisiae* [3], facilitating uptake of the drug into the cell. After BM uptake, the drug concentrates into the vacuoles of yeast where it is degraded [4], or is degraded by bleomycin hydrolase [5]. Though well studied, these pathways do not suggest how BM/PM becomes detoxified in the nucleus.

## II. CHARACTERIZATION OF THE BLM10 PROTEIN (BLM10P)

The *BLM10* sequence encodes a protein of 2143 amino acids. Our studies showed that wild type *Blm10* localized to the nucleus of *S. cerevisiae* and

remained in the nucleus throughout the cell cycle (Figure 1).

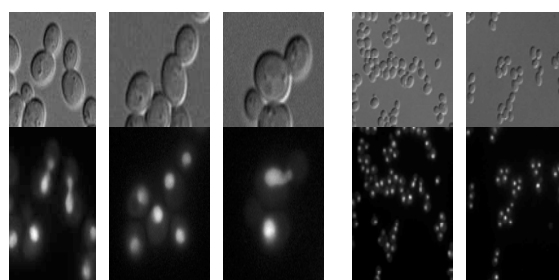


Figure 1: Nuclear localization of YFP-Blm10p is shown here in full images. Fluorescence microscopy was carried out in collaboration with The National Center for Research Resources' Yeast Resource Center at the University of Washington in Seattle.

Figure 2 clearly demonstrates that *Blm10p* (*BLM10/BLM10*) confers resistance against oxidative damage. However, when the gene is deleted in the cells, they are unable to maintain the integrity of their DNA and they experience increased killing. When treating the *blm10Δ/blm10Δ* cells with lower doses of PM, it is quite clear that the strain is capable of maintaining chromosomal structure as low as 0.001 μg/ml phleomycin and as high as 0.1 μg/ml phleomycin (data not shown). These results show the importance of *Blm10p* in protecting against DNA damage and killing.

While in the nucleus, *Blm10p* has been shown to cap and activate the 20S catalytic core particle of the 26S proteasome [6] in a manner that does not require the activity of ATPase for proteasomal cleavage [7]. The 20S subunit is primarily found in the nucleus of yeast, consistent with the nuclear localization of *Blm10p*. The finding that *Blm10p* participates in the capping and activation of the 20S core particle of the proteasome, and that these activities are independent of energy, combined with our oxidative damage and sensitivity data, leads to the possibility of a novel detoxification pathway in which the activated *Blm10p*-20S core

particle complex is directly involved in degrading BM/PM, or other oxidative agents, upon entry into the nucleus.

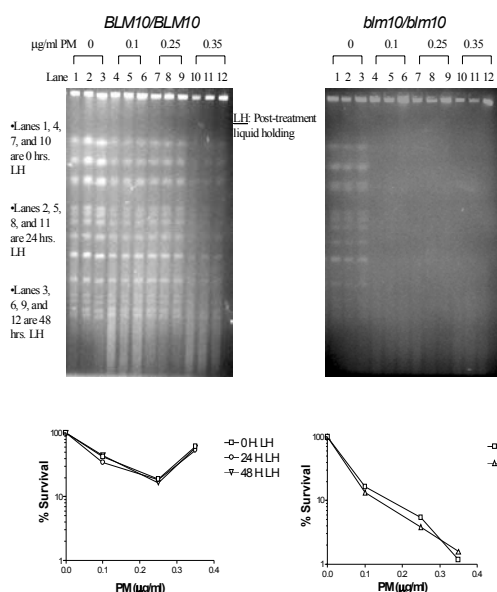


Figure 2: Homozygous *BLM10* deletion diploids (*blm10Δ/blm10Δ*) are hypersensitive to DNA damage and killing by the BM-PM family of DNA damaging agents, as shown using pulsed field gel electrophoresis and measurements of survival.

### III. PROPOSED BLM10 PROTEIN NETWORK

Blm10 is an energy-independent 20S proteasomal activator, not requiring ATPases and ubiquitinated substrates. Using MALDI-TOF mass spectroscopy to identify baited protein complexes, all of the proteins found to associate with Blm10p are located in the nucleus. Gavin *et al* [8] and Ho *et al* [9] determined that Blm10 interacts with two proteins associated with the 20S core particle of the 26S proteasome (Sc11 and Pre8), and two proteins associated with the non-homologous end joining/histone remodeling pathway (Sir4 and Zds2). These primary interactions yield a complex 26S proteasome-DNA repair protein network surrounding Blm10p (Figure 3). The relationship between DNA repair and Blm10 activation of the 20S core particle activation is currently being studied.

### ACKNOWLEDGEMENTS

The authors would like to acknowledge the research efforts of Dr. Kevin Doherty, Dr. Ajay Pramanik, Mr. Ronald Charles, and Mr. James Lukose. Support for this presentation was graciously provided by City College and Sophie Davis School of Biomedical Education (CUNY).

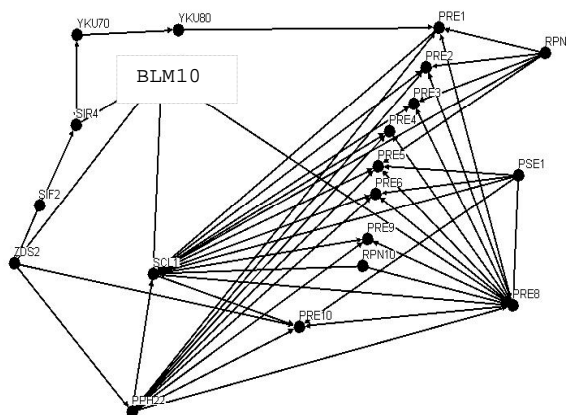


Figure 3: YEAST GRID database used to determine Blm10 interacting proteins.

### REFERENCES

- [1] D.E. Febres, A. Pramanik, M. Caton, K. Doherty, J. McKoy, E. Garcia, W. Alejo and C.W. Moore. The novel *BLM3* gene encodes a protein that protects against lethal effects of oxidative damage. *Cell. Mol. Biol. (Noisy-le-grand)*, 47:1149-1162, 2001.
- [2] R.M Burger. Cleavage of nucleic acids by bleomycin. *Chem. Rev.*, 98:1153-1170, 1998.
- [3] C.W. Moore, R. Del Valle J.F. Mc.Koy, A. Pramanik and R.E. Gordon. Lesions and preferential initial localization of [S-methyl-3H]bleomycin A2 on *Saccharomyces cerevisiae* cell walls and membranes. *Antimicrob Agents Chemother*, 36:2497-2505, 1992.
- [4] M. Aouida, A. Leduc, H. Wang and D. Ramotar. Characterization of a transport and detoxification pathway for the antitumour drug bleomycin in *Saccharomyces cerevisiae*. *Biochem J.* 384:47-58, 2004.
- [5] H. Xu and S. Johnston. Yeast bleomycin hydrolase is a DNA-binding cysteine protease. Identification, purification, biochemical characterization. *J. Biol Chem*, 19;269(33):21177-21183, 1994.
- [6] M. Schmidt, W. Haas, B. Crosas, P. Santamaria, S. Gygi, T. Walz and D. Finley. The HEAT repeat protein Blm10 regulates the yeast proteasome by capping the core particle. *Nat Struct Mol Biol.*, 12(4):294-303, 2005.
- [7] V. Ustrell, L. Hoffman, G. Pratt and M. Rechsteiner. PA200, a nuclear proteasome activator involved in DNA repair. *EMBO J.*, 21:3516-3525, 2002.
- [8] A. Gavin *et al*. Functional organization of the yeast proteome by systematic analysis of protein complexes. *Nature*, 415(6868):141-147, 2001.
- [9] Y. Ho *et al*. Systematic identification of protein complexes in *S. cerevisiae* by mass spectrometry. *Nature*;415:180-183, 2001.

# Hall effect induced by microwave field in two dimensional electron gas with static vortex: A semi-classical approach

Hsuan-Yeh Chang and David Schmeltzer (Faculty Mentor)

Physics Department

City College of the City University of New York

New York, NY, USA

Email: hsuanyeh@yahoo.com, david@sci.ccny.cuny.edu

**Abstract** — *A new mechanism for inducing a Hall voltage on a confined two-dimensional electron gas having an circular insulating region is proposed. The electron wave function vanishes at the insulating region, which is described by a static vortex of radius  $D$ . By applying an external microwave to the system, the time average of the response gives rise to a Hall voltage. This phenomena can be used to convert a microwave field into a power source.*

## I. INTRODUCTION

Conventionally, a Hall voltage is generated in response to an external magnetic field applied to a sample. Recently, the possibility of generating D.C. (time-independent) voltage in one-dimensional structure in response to an A.C. (time-dependent) voltage is proposed [1, 2, 3, 4, 5]. In addition, a spin-Hall current can also be generated on a two-dimensional electron gas (2DEG) [6] as a result of the Aharonov-Casher spin-orbit effect [7, 8]. Related phenomena, such as zero resistance states, have also been observed [9] when a microwave field is applied to a GaAs quantum dot in an external magnetic field.

We will show that a D.C. Hall voltage can be generated in the *absence* of a *magnetic field* when one applies a *microwave* field (time-dependent electric field) to a confined two-dimensional electron gas which contains an *insulating region*. Since the electronic wave function vanishes in the insulating region, we are allowed to describe it effectively as a localized vortex. Therefore, we consider the 2DEG of size  $L \times L$  as being confined by a harmonic oscillator potential  $V_c(\vec{r})$  with a classical turning point  $L_F$ , where  $L \simeq L_F$ . The confined 2DEG is hereinafter referred to as a quantum dot. In this paper, we consider the insulating region as a circle centered at  $\vec{R}$  with radius  $D$ . This effect can be used to convert microwave field into a D.C. power source and might have important applications in the field of communications.

## II. MODEL HAMILTONIAN

We will now build a model which describes the physics of a high mobility 2DEG GaAs quantum dot. A typical high mobility quantum dot has an electronic density of  $n \simeq 10^{15}m^{-2}$ , a Fermi energy of  $E_F \simeq 0.01eV$  and a

Fermi temperature of  $T_F \simeq 120K$ . This corresponds to a Fermi wavelength  $\lambda_F \simeq 0.5 \times 10^{-7}m$ . For high mobility GaAs, the typical scattering time is  $\tau \simeq 10^{-11}sec$  which corresponds to the mean free path  $\ell = v_F\tau$ . Since the ratio between the mean free path and the Fermi wavelength is  $\frac{\ell}{\lambda_F} = \frac{v_F\tau}{\lambda_F} = \frac{\hbar\tau}{\lambda_F^2 m} \simeq 30$ , which is much larger than one, we can neglect the multiple scattering effects. When the thermal length is comparable with the size of the system  $L \simeq \lambda_{thermal} = (\frac{T_F}{T})^{1/2}\lambda_F$ , one obtains a ballistic system with negligible multiple scattering.

The quantum dot of size  $L \times L$  with an insulating region is described by the following model Hamiltonian:

$$\hat{H} = \frac{\hbar^2}{2m} \vec{K}^2 + V_c(\vec{r}) + U_I(\vec{r}) \quad (1)$$

where  $V_c(\vec{r})$  is the confining potential and  $U_I(\vec{r})$  is an infinite potential which gives rise to a vanishing electron wave function in the insulating region. The confining potential is given by a harmonic oscillator potential

$$V_c(\vec{r}) = \frac{m\omega_0^2}{2} \vec{r}^2 \quad (2)$$

which has a ‘‘classical turning point’’  $L_F$  determined by the condition  $\frac{m\omega_0^2 L_F^2}{2} = E_F$ . This condition describes the effective physics of a free electron gas of size  $L \leq L_F$ . By demanding that the classical turning point  $L_F$  is of the order of thermal wavelength  $L_F \simeq \lambda_{thermal}$ , one can determine the confining frequency as  $\omega_0 = 2\pi f_0 = \frac{\hbar}{m} (\frac{T}{T_F}) \frac{1}{\lambda_F}$ . For this condition, we obtain a ballistic regime where  $L < L_F \sim 10^{-7} - 10^{-6}m$ ,  $T \sim 1 - 10K$ ,  $f_0 \simeq 1 - 10 GHz$  and  $\tau \simeq 10^{-11}sec$ . In order to observe quantum scattering effects caused by the insulating region of radius ‘‘ $D$ ,’’ we require that the wavelength  $\lambda_F$  obeys the condition  $D > \lambda_F \simeq 0.5 \times 10^{-7}m$ . (For  $D < \lambda_F$ , the electrons are not diffracted by the insulating region.) Based on these requirements, we will investigate a 2DEG with the parabolic potential given in eq. (2), which provides the confining length of size  $L$ .

The effect of the insulating region of radius ‘‘ $D$ ’’ is described by a potential  $U_I(\vec{r})$ , which will ultimately cause the electronic wave function  $\Phi(\vec{r}; \vec{R})$  to vanish at the circular region  $|\vec{r} - \vec{R}| \leq D$ . We describe the vanishing of

wave function by considering it effectively as a localized vortex centered at  $\vec{r} = \vec{R}$  [10]. We can parametrize the wave function  $\Phi(\vec{r}; \vec{R})$  as

$$\Phi(\vec{r}; \vec{R}) = \frac{|\vec{r} - \vec{R}|}{D} e^{i\theta(\vec{r}, \vec{R})} \psi(\vec{r}) \quad (3)$$

for  $|\vec{r} - \vec{R}| \leq D$ , and

$$\Phi(\vec{r}; \vec{R}) = e^{i\theta(\vec{r}, \vec{R})} \psi(\vec{r}) \quad (4)$$

for  $|\vec{r} - \vec{R}| > D$ . The wave function  $\psi(\vec{r})$  is a regular function and  $\theta(\vec{r}; \vec{R})$  is a multivalued function.

With the help of the above gauge transformation of wave function, we obtain

$$e^{-i\theta(\vec{r}; \vec{R})} \hat{H} \Phi(\vec{r}; \vec{R}) \xrightarrow{|\vec{r} - \vec{R}| > D} H(\vec{\Pi}, \vec{r}) \psi(\vec{r}) \quad (5)$$

where  $H(\vec{\Pi}, \vec{r})$  is the transformed Hamiltonian and  $\vec{\Pi}$  is the kinetic momentum. The Hamiltonian  $\hat{H}$  given in eq. (1) are thus replaced by the transformed Hamiltonian

$$H = \frac{\hbar^2}{2m} \vec{\Pi}^2 + V_c(\vec{r}) \quad (6)$$

where  $\vec{\Pi} = \vec{K} - \vec{\partial}\theta(\vec{r}; \vec{R})$  is the kinetic momentum [11]. The derivative of the multivalued phase  $\theta(\vec{r}; \vec{R})$  determines the vector potential  $\vec{A}(\vec{r}; \vec{R}) = \vec{\partial}\theta(\vec{r}; \vec{R})$ . As a result of this gauge transformation, the kinetic momenta no longer commute with each other. The kinetic momentum obeys the commutation relation

$$[\Pi_1(\vec{r}), \Pi_2(\vec{r})] = i\vec{B}(\vec{r}) \quad (7)$$

where  $\vec{B}(\vec{r}) = \epsilon_{ij} \partial_i A_j$  represents a localized magnetic field,  $i, j = 1, 2$ ,  $\epsilon_{ii} = 0$  and  $\epsilon_{12} = -\epsilon_{21} = 1$ . The localized magnetic field  $\vec{B}(\vec{r})$  in eq. (7) is non-zero only for  $|\vec{r} - \vec{R}| \leq D$ . A good approximation to the vortex solution given in ref. [10] would be to use a delta function with a finite width  $D$ , which can be replaced by a step function.

### III. EQUATION OF MOTION

For the remaining part of this paper, we will solve our model using Heisenberg's equation of motion formalism. For simplicity, we first introduce a dimensionless time  $s = \omega_0 t$  and a dimensionless coupling constant  $\gamma = \frac{\hbar\omega_0}{m\omega_0^2 D^2} < 1$ . Based on the Hamiltonian given in eq. (6), we obtain from the Heisenberg's equation of motion, i.e.  $\dot{\Pi}_i = \frac{1}{i\hbar} [\Pi_i, H(\vec{\Pi}, \vec{r})]$ , that the kinetic momentum  $\Pi_{i,H}(t)$  in the Heisenberg representation obeys the following differential equation:

$$\left(\frac{d^2}{ds^2} + 1\right) \Pi_{i,H}(s) + \epsilon_{ij} \frac{\gamma}{2} \frac{d}{ds} \{\vec{B}(\vec{r}_H(s)), \Pi_{j,H}(s)\}_+ = 0 \quad (8)$$

The notation  $\{A, B\}_+ = AB + BA$  represents the anti-symmetric combination. The solution of eq. (8) is given as a power series in the coupling constant  $\gamma$

$$\Pi_{i,H}(s) = \Pi_{i,H}^{(0)}(s) + \gamma \Pi_{i,H}^{(1)}(s) + \dots \quad (9)$$

where  $\Pi_{i,H}^{(0)}(s)$  is the solution of free harmonic oscillator with the initial condition  $\Pi_{i,H}^{(0)}(0) = K_i$ ,  $i = 1, 2$  and  $\Pi_{i,H}^{(1)}(s)$  represents the first order term in the coupling constant  $\gamma$ .

### IV. RESPONSE TO THE EXTERNAL MICROWAVE FIELD

We shall now investigate the response of the quantum dot having a vortex localized at  $\vec{R} = (R_1, R_2)$  due to an external microwave field. The external microwave potential is given by

$$H_{ext} = -er_2 E_2(t) \quad (10)$$

for  $t \geq 0$  where  $E_2(t) = E_0 \cos(\omega t + \alpha(t))$  is the microwave field with an amplitude  $E_0$ , " $\omega$ " is the microwave frequency, and  $\alpha(t)$  is the phase. The coherency of the microwave source is characterized by  $\langle \alpha(t)\alpha(t') \rangle \simeq \alpha_0 e^{-|t-t'|/2\Delta^2}$ . For  $\Delta|t-t'| \geq 2\pi$ , the microwave radiation is described by a random phase  $0 \leq \alpha < 2\pi$ .

The response of the kinetic momentum and coordinate due to the external microwave field are defined as the differences between two Heisenberg representations, namely the one induced by the external microwave potential, and the one in the absence of the external microwave potential. Therefore, we can write the response of the kinetic momentum as

$$\delta \vec{\Pi}_{ext}(t) = \vec{\Pi}_{ext}(t) - \vec{\Pi}_H(t) \quad (11)$$

and

$$\delta \vec{r}_{ext}(t) = \vec{r}_{ext}(t) - \vec{r}_H(t) \quad (12)$$

where

$$\vec{\Pi}_{ext}(t) = e^{\frac{i}{\hbar} \int_0^t dt' (H + H_{ext}(t'))} \vec{\Pi}(0) e^{-\frac{i}{\hbar} \int_0^t dt' (H + H_{ext}(t'))} \quad (13)$$

and

$$\vec{\Pi}_H(t) = e^{\frac{i}{\hbar} H t} \vec{\Pi}(0) e^{-\frac{i}{\hbar} H t}. \quad (14)$$

Similarly, the response of the coordinate is written as

$$\delta \vec{r}_{ext}(t) = \vec{r}_{ext}(t) - \vec{r}_H(t) \quad (15)$$

where

$$\vec{r}_{ext}(t) = e^{\frac{i}{\hbar} \int_0^t dt' (H + H_{ext}(t'))} \vec{r}(0) e^{-\frac{i}{\hbar} \int_0^t dt' (H + H_{ext}(t'))} \quad (16)$$

and

$$\vec{r}_H(t) = e^{\frac{i}{\hbar} H t} \vec{r}(0) e^{-\frac{i}{\hbar} H t}. \quad (17)$$

As a result, we obtain the differential equation for the shifted momentum  $\delta\vec{\Pi}_{ext}(s)$ ,

$$\begin{aligned} & \left(\frac{d^2}{ds^2} + 1\right)\delta\Pi_{i,ext}(s) \\ & + \epsilon_{ij} \frac{\gamma}{2} \frac{d}{ds} \left[ \{\bar{B}(\vec{r}_{ext}(s)), \Pi_{j,ext}(s)\}_+ \right. \\ & \quad \left. - \{\bar{B}(\vec{r}_H(s)), \Pi_{j,H}(s)\}_+ \right] \\ & = -\frac{1}{\omega_0\tau} \frac{d}{ds} \delta\Pi_{i,ext}(s) - \frac{e}{\hbar\omega_0} \frac{d}{ds} (E_2(s)) \delta_{i,2} \end{aligned} \quad (18)$$

where  $E_2(s) = E_0 \cos((\omega/\omega_0)s + \alpha)$ . The shifted coordinate  $\delta\vec{r}_{ext}(s)$  is given by integrating the shifted momentum  $\delta\vec{\Pi}_{ext}(s)$  over the dimensionless time  $s$ , namely

$$\delta\vec{r}_{i,ext}(s) = \frac{\hbar}{m\omega_0} \int_0^s ds' \delta\Pi_{i,ext}(s'). \quad (19)$$

In eq. (18), we have introduced the single particle *relaxation time*  $\tau$  caused by impurity scattering (see the first term on the left side given by  $\frac{1}{\omega_0\tau} \frac{d}{ds} \delta\Pi_{i,ext}(s)$ ).

Following the same spirit as described in section III., we can solve eq. (18) as power series in  $\gamma$  and compute the time-independent momentum deviation from equilibrium induced by the microwave field. The presence of such a static shift in the momentum is an indication of a steady state D.C. current. For  $\gamma < 1$  and a weak microwave amplitude  $E_0$ , we can solve eq. (18) as power series in  $\gamma$

$$\begin{aligned} \delta\Pi_{i,ext}(s) = & \{\delta_{i,1}[\gamma\delta\Pi_{1,ext}^{(1)} + \gamma^3\delta\Pi_{1,ext}^{(3)} + \dots] \\ & + \delta_{i,2}[\delta\Pi_{2,ext}^{(0)} + \gamma^2\delta\Pi_{2,ext}^{(2)} + \dots]\}. \end{aligned} \quad (20)$$

The solution of  $\delta\Pi_{i,ext}(s)$  has two parts, namely a D.C. (time-independent) part and an A.C. (time-dependent) part.

The zeroth order solution used to generate the series are given by

$$\delta\Pi_{1,ext}^{(0)}(s) = 0 \quad (21)$$

and

$$\delta\Pi_{2,ext}^{(0)}(s) = A_{2,ext}^{(0)} \sin\left[\left(\frac{\omega}{\omega_0}\right)s + \varphi + \alpha\right] \quad (22)$$

where  $\tan \varphi = \frac{\omega/\tau}{\omega^2 - \omega_0^2}$  and  $A_{2,ext}^{(0)} = -\frac{eE_0\tau(\omega/\omega_0)}{\hbar\omega_0} \sin \varphi$ .

The first order term in  $\gamma$  is given by  $\delta\Pi_{1,ext}^{(1)}(s)$ , the D.C. (time-independent) component of which is defined as

$$\delta\Pi_{1,D.C.}^{(1)} = \frac{1}{2\pi} \int_0^{2\pi} \delta\Pi_{1,ext}^{(1)}(s') ds'. \quad (23)$$

By iterating eq. (18), we can obtain a geometric series in  $\gamma$  for the shifted momenta  $\delta\Pi_{1,D.C.}$  and  $\delta\Pi_{2,D.C.}$  in the  $i = 1$  and the  $i = 2$  directions, respectively.

## V. COMPUTATION OF CURRENT

In the semi-classical approximation, the induced current density  $J_1(\vec{r})$  in the  $i = 1$  direction is defined as a weighted integral over the shifted momentum  $\delta\Pi_{1,D.C.}(\vec{\Pi}, \vec{r})$ , namely

$$J_1(\vec{r}) = \frac{e\hbar}{m} \int \frac{d^2\Pi}{(2\pi)^2} \delta\Pi_{1,D.C.}(\vec{\Pi}, \vec{r}) f_{F.D.}[H(\vec{\Pi}, \vec{r}) - E_F], \quad (24)$$

where  $f_{F.D.}[H(\vec{\Pi}, \vec{r}) - E_F]$  is the Fermi-Dirac occupation function. The current in the  $i = 1$  direction is given by

$$I_1 = \frac{1}{L} \int_{-L/2}^{L/2} \int_{-L/2}^{L/2} d^2r J_1(\vec{r}) \quad (25)$$

where  $L \times L$  is the size of the quantum dot. The result given in eq. (25) is the current in  $i = 1$  direction when two edges of the sample at  $x = -L/2$  to  $x = L/2$  are connected.

The application of a microwave field in the  $i = 2$  direction induces a D.C. voltage in the  $i = 1$  direction. This voltage is obtained from the shifted momentum  $\delta\Pi_{1,D.C.}$ . We obtain the induced electric field  $E_{1,D.C.}$  using the relation  $E_{1,D.C.} \simeq \delta\Pi_{1,D.C.}(\frac{\hbar}{e\tau})$ , from which we obtain the voltage

$$V_{1,D.C.} = \int_{-L/2}^{L/2} dx E_{1,D.C.} \simeq E_{1,D.C.} L. \quad (26)$$

This voltage satisfies the equation that  $V_{1,D.C.} = I_1/\sigma$ , where  $I_1$  is the current in the  $i = 1$  direction and  $\sigma = \frac{ne^2\tau}{m}$  is the conductivity of the sample. The microwave field is expressed in terms of an R.M.S. (effective) voltage  $V_{R.M.S.} = E_0 L/\sqrt{2}$  which allows us to define a dimensionless voltage induced in the  $i = 1$  direction

$$v_{1,D.C.} = \frac{V_{1,D.C.}}{V_{R.M.S.}} = \left(\frac{D}{L}\right)^2 \gamma G(\varphi, \alpha, E_0) \quad (27)$$

where

$$G(\varphi, \alpha, E_0) \equiv G^{(1)}(\varphi, \alpha) + G^{(2)}(\varphi, E_0) \quad (28)$$

and

$$G^{(1)}(\varphi, \alpha) \simeq -\frac{\sin \varphi \cos(\varphi + \alpha)}{1 - (\gamma \sin \varphi)^2} \quad (29)$$

$$G^{(2)}(\varphi, E_0) = \frac{1}{2} \left(\frac{\omega}{\omega_0}\right)^2 \left(\frac{E_0}{E_{int}}\right) \sin^2 \varphi \quad (30)$$

where  $E_0/E_{int} \ll 1$ . Here  $E_{int} \equiv \frac{\hbar}{e\tau < R >}$  is the internal electric field. Using typical values of  $\gamma = \frac{\hbar\omega_0}{m\omega_0^2 D^2} \simeq 0.7$ ,  $D$  and  $L$ , we obtain that the amplitude of the dimensionless voltage  $v_{1,D.C.}$  (the rectification efficiency) given by  $\sqrt{2}(\frac{D}{L})^2 \gamma$  takes values in the range of  $0.01 - 0.001$ , making it possible to be used as a D.C. voltage source.

## VI. RESULTS AND CONCLUSIONS

According to the result of the dimensionless voltage given in eq. (27), we can analyze the function  $G(\varphi, \alpha, E_0)$  for different cases.

- a) *The coherent case.* For this case we take  $\alpha \simeq 0$  and find that the function  $G^{(1)}(\varphi, \alpha)$  changes sign for  $\omega \simeq \omega_0$  and vanishes in the limits  $\omega \rightarrow 0$  and  $\omega \rightarrow \infty$ . When  $\omega \simeq 0.9\omega_0$  and  $\omega \simeq 1.1\omega_0$ , the function reaches the maximum.
- b) *The incoherent case.* For this situation, the first term  $\frac{1}{2\pi} \int_0^{2\pi} d\alpha G^{(1)}(\varphi, \alpha) = 0$  and we are left with  $G^{(2)}(\varphi, E_0) \geq 0$  which vanishes like  $\frac{1}{2} \left(\frac{E_0}{E_{int}}\right) \left(\frac{1}{\omega_0\tau}\right) \left(\frac{\omega}{\omega_0}\right)^3$  for  $\omega \rightarrow 0$  and saturates to  $\frac{1}{2} \left(\frac{E_0}{E_{int}}\right) \left(\frac{1}{\omega_0\tau}\right)$  for  $\omega \rightarrow \infty$  and reaches the maximum at  $\omega = \omega_0$ .

At present time, there is no clear experiment with which we can compare our theory. Recently, an experiment which contains insulating disks in a 2DEG quantum dot [12] shows a resonance behavior as a function of an external magnetic field. We have used this data (see figure 3 of ref. [12]) which shows that at *zero magnetic field* the Hall voltage changes sign as a function of the microwave frequency. We have used figure 4 in ref. [12] to extract the behavior of the voltage as a function of  $\frac{\omega}{\omega_0}$  for zero magnetic field. Figure 3 in ref. [12] shows clearly that the voltage at zero magnetic field *changes sign* when the microwave frequency varies between 1.46 GHz to 34 GHz and vanishes at 17.41 GHz! This experimental behavior agrees qualitatively with our result once we take  $\omega_0 = 17.41 \text{ GHz}$  with  $\frac{1.46}{17.41} \leq x = \frac{\omega}{\omega_0} \leq \frac{34}{17.41}$ .

To conclude, we have considered in this paper a confined 2DEG in the presence of a localized insulating region. The insulating region, which causes the electronic wave function to vanish, is described effectively as a static vortex. By applying a microwave field to the sample, a D.C. Hall voltage is obtained. This phenomena can be used to convert a microwave field into a D.C. power source.

## ACKNOWLEDGMENTS

The authors would like to thank V. N. Muthukumar for valuable comments and Jingqiao Zhang for communicating with us their experimental results of ref. [12].

## REFERENCES

- [1] D. Schmeltzer. Tunnelling between two luttinger liquids induced by a driving field. *Physical Review Letters*, 85:4132, 2000.
- [2] P. W. Brouwer. Scattering approach to parametric pumping. *Physical Review B*, 58:R10135, 1998.
- [3] L. DiCarlo, C.M. Marcus, and J.S. Harris Jr. Photocurrent, rectification, and magnetic field symme-

try of induced current through quantum dots. *Physical Review Letters*, 91:246804, 2003.

- [4] D. J. Thouless. Quantization of particle transport. *Physical Review B*, 27:6083, 1983.
- [5] D.E. Feldman, S. Scheidl, and V.M Vinokur. Rectification in luttinger liquids. *Physical Review Letters*, 94:186809, 2005.
- [6] R. Winkler. *Spin-orbit coupling effects in two-dimensional electron and hole systems*, volume 191. Springer Tracts in Modern Physics, 2002.
- [7] Y. Aharonov and A. Casher. Topological quantum effects for newtral particles. *Physical Review Letters*, 53:319, 1984.
- [8] B. Reznik and Y. Aharonov. Question of the non-locality of the aharonov-casher effect. *Physical Review D*, 40:4178, 2005.
- [9] R. G. Mani, J. H. Smet, Klaus von Klitzing, V. Narayamurty, W. B. Johnsona, and V. Umansky. Zero resistance states induced by electromagnetic wave excitation in gaas/algaas heterostructures. *Nature*, 420:646, 2002.
- [10] Zyun F. Ezawa. *Quantum Hall Effect*. World Scientific, 2000.
- [11] Landau and Lifshitz. *Statistical Physics part 2*. Pergamon Press, 1981.
- [12] Jingqiao Zhang et.al. Directed electron transport through ballistic quantum dot under microwave radiation. *Cond-Mat/0504087*.

# Surface Enhance Raman Spectroscopy (SERS) As Sensing Method for Biomolecules on MBE-Grown Quantum Dots

Richard Livingstone and John Lombardi  
City College of New York  
New York,  
NY,10031 USA  
Email: livingstonerm@aol.com

**Abstract** — *Using Surface Enhance Raman Spectroscopy (SERS) technique, we have observed bio-molecules at extremely low concentration, adsorbed on self-organized II-VI semiconductor quantum dots, grown by molecular beam epitaxy (1).*

*The samples were grown on InP substrates with ZnCdMgSe barriers, and involve hemi-ellipsoidal dots of CdSe assembled above a thin wetting layer. Excitation at 488nm produces intense Raman spectra of adenine, tryptophan and tyrosine, when adsorbed on these structures. Examination of individual Raman frequencies provides information as to the mode of attachment of the molecules to the CdSe surface. These results demonstrate that the CdSe quantum dot system provides a high degree of molecular specificity and large Raman enhancement factor, enabling sensitive detection and identification of biological molecules.*

## I. INTRODUCTION

Raman spectroscopy has been found to present considerable advantages in probing molecules of biological interest. The advantages of Raman spectroscopy over other detection methods include the ability to explore molecules in aqueous media, high resolution, high specificity, and non-destructive effects on the sample, allowing *in situ* detection and characterization. These advantages encourage the search for ways to construct optical devices for use as probes for sensing instruments, which are sensitive to extremely small quantities of biologically important molecules. The high resolution and specificity of Raman signals are of considerable advantage in designing such probes<sup>2,3</sup>. Furthermore, the technique of Molecular Beam Epitaxy (MBE) presents a means of construction and testing of solid-state surfaces, which are precisely controlled during fabrication and have high quality surface features. This makes them ideal for research into prototypes for

sensitive devices for detection of molecular species. In this article we explore the feasibility of utilizing enhanced Raman spectra of molecules adsorbed on the surface of MBE-grown semiconductor quantum dots for bio-sensing devices.

## II. EXPERIMENTAL

**Molecular beam epitaxial growth.** Self-assembled CdSe/CdZnSeMg quantum dots (QDs) samples grown by molecular beam epitaxy (MBE) on InP (001) substrates were utilized. The quantum-dots nanostructures were not covered with a cap-layer. These samples were grown in an ultrahigh vacuum (UHV) Riber system. Samples were removed from the chamber immediately following the QD formation. To slow a possible ripening effect, the samples were immediately immersed in liquid nitrogen after the growth and kept in this condition until the moment of taking the surface topography or Raman spectra.

**Atomic force microscopy (AFM).** Atomic Force Microscope (AFM) images were recorded in non-contact mode using a ThermoMicroscopes Explorer™ system (Veeco Instruments, Santa Barbara, CA, USA), operated in air and at room temperature. The processing was conducted using the SPMLab software.

**Raman Spectroscopy.** To obtain the adsorption of biological molecules, the quantum-dots samples were immersed in stock solution of tryptophan, adenine or tyrosine prepared at 0.01 M concentration, for 20 minutes. At the end of these treatments, the samples were subjected to a short ultrasonic agitation in order to remove excess species, so that only adsorbed species were left on the surfaces.

The Raman experiments were performed at room temperature in air. The excitation light was the 488 nm line of an Argon ion laser. Typical power levels at the sample were 30 mW.

### III. RESULTS

Figure 1 shows a representative AFM image of the quantum dot sample before adsorption of molecules. The surface quantum dot density is  $7 \times 10^8 \text{ cm}^{-2}$  and height distribution shows an approximately Gaussian lineshape with  $4.5 \pm 0.5 \text{ nm}$  being the most abundant value. The average radius of the QDs base is  $47 \text{ nm}$ .

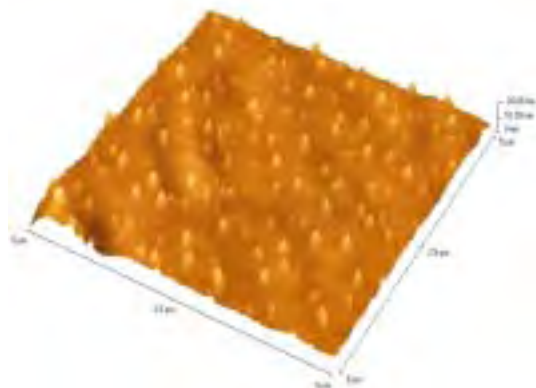


Figure 1 AFM of CdSe/CdZnSeMg quantum dots.

In figure 2 we show the ex-situ Raman spectrum from CdSe/CdZnSeMg quantum dots after the immersion in liquid tryptophan and the following sonication. We also measured the Raman spectrum of solid tryptophan and observed a close resemblance between this spectrum and that in Fig. 2. This suggests that the Raman bands measured on the semiconductor nanostructure originate from tryptophan molecules adsorbed on it and we are able to observe them because they are enhanced from the SERS effect.

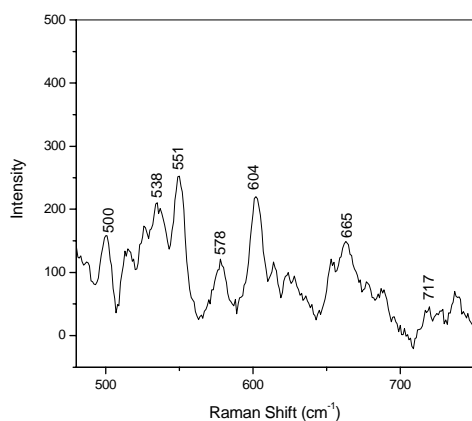


Figure 2. SERS spectrum of Tryptophan molecules adsorbed on CdSe/CdZnSeMg quantum dots.

Details of band positions and tentative mode assignments are tabulated in Table 1 together with our Raman data (at 488 nm) on solid tryptophan. Some of the other lines present in the figure are due to the underlying semiconductor structure, and

since some coincide with expected molecular lines, it is likely the latter are obscured in this spectrum.

Modes <sup>a</sup>	SERS (488nm) from Trypt on Quantum Dots <sup>b</sup>	Raman (488nm) from Trypt solid <sup>c</sup>
$\beta\text{-CO}_2^-$	500	
	529	
def. R,r	538	
$\beta\text{-NH(r)}$	551	562
$\beta\text{-NH(r)}$	578	580
$\beta\text{-CH}$	604	608
	665	
def. r,R	717	716

**Table 1.** Vibrations of Tryptophan (Trypt) in various systems (in wavenumber/ $\text{cm}^{-1}$ ). R-benzene ring, r-pyrrole ring, v-stretch,  $\beta$ -bend

### VI. CONCLUSION

We have demonstrated that MBE-grown quantum dots can be used as a surface for considerable enhancement of the Raman signal from molecules of biological interest. The signal is unique to the particular molecule, and is sensitive to extremely small quantities of the adsorbate. The high sensitivity, molecular specificity and non-destructive nature of this procedure encourages us to consider the possibility that such systems could be utilized to fabricate devices to be used as biosensors.

### ACKNOWLEDGEMENTS

This work was supported by the National Science Foundation under Cooperative Agreement No. RII-9353488, grant No. CHE-0091362 and grant number ECS0217646 and by the City University of New York PSC-BHE Faculty Research Award Program

### REFERENCES

- (1) Quagliano, Lucia G., *J. Am. Chem. Soc* 126 (2004) 7393
- (2) Colvin, V. L.; Schlamp, M.C.; Alivisatos, A. P., *Nature*, (1994) 370, 354
- (3) Cao, C.; Jin, R.; Mirkin, C. A., *Science* (2002) 297, 1536-1762

# Calculated proton uptake on anaerobic reduction of cytochrome c oxidase and quinol oxidase using MCCE

Jun Zhang, Yifan Song and Marilyn Gunner  
 City College of New York & Graduate Center  
 City University of New York  
 New York City USA  
 Email: junzhang@sci.ccny.cuny.edu

**Abstract** — *Using the continuum model MCCE program, the proton transfer behaviour in the binuclear centre of Cytochrome C oxidase and Quinol Oxidase are studied. Based on the calculation from OOOO, OORR and RRRR states, a proton is bound to CuB site in the fully oxidized state, and 2.5 uptake protons per 4 electrons in fully reduced binuclear centre are calculated, which agree with experiments.*

## INTRODUCTION

Cytochrome *c* oxidase and Quinol oxidase are the terminal electron acceptor in the electron transfer chain. These transmembrane proteins build an electrochemical gradient using chemical energy from the reduction of O<sub>2</sub>. The mechanism of action of this large complex is still an active research topic. The understanding of the electron transfer chain will be very helpful for the people looking for new energy resources. Ionization states of all residues were calculated with Multi-Conformation Continuum Electrostatics method (MCCE) in several anaerobic oxidase redox states ranging from fully oxidized to fully reduced. One longstanding problem is how proton uptake is coupled to the reduction of the active site binuclear center (BNC). The BNC has 2 cofactors: Heme a<sub>3</sub> and CuB. If the protein needs to maintain electroneutrality, then two protons will be bound when the BNC is reduced by 2 electrons in the reductive half of the reaction cycle. The effective pK<sub>a</sub>s of ionizable residues around the BNC are evaluated. At pH 7, only a hydroxide coordinated to CuB shifts its pK<sub>a</sub> from below 7 to above 7, and so picks up a proton when Heme a<sub>3</sub> and CuB are reduced. Glu I-286, Tyr I-288, His I-334 and a second hydroxide on Heme a<sub>3</sub> all have pK<sub>a</sub>s above 7 in all redox states. Thus, they are protonated and cannot serve as proton acceptors. The propionic acids near the BNC are deprotonated with pK<sub>a</sub>s well below 7. They are well stabilized in their anionic state and do not bind a proton upon BNC reduction. This suggests electroneutrality in the BNC is not maintained during the anaerobic reduction. Proton

uptake on reduction of CuA, Heme a, Heme a<sub>3</sub>, and CuB show 2.5 protons bound per 4 electrons, in agreement with prior experiments in Cytochrome *c* oxidase. One proton is bound by a hydroxyl group in the BNC, the rest to groups far from the BNC. The electrochemical midpoint potential (E<sub>m</sub>) of Heme a is calculated in the fully oxidized protein, and with one or two electrons in the BNC. The E<sub>m</sub> of Heme a shifts down when the BNC is reduced, which agrees with prior experiments. If the BNC reduction is electroneutral, then Heme a E<sub>m</sub> is independent of the BNC redox state. This work is confirmed while computing Cytochrome *c* oxidase and Quinol oxidase using MCCE program.

## TABLES

Cytochrome c oxidase	OO OO	RO OO	OR OO	OO OR	OR OR	OO RR	RR RR
OH-HEME a <sub>3</sub>	13.3	13.7	15.0	5.6	8.1	18.8	19.9
OH- CUB	-9.8	-9.5	-8.2	25.0	13.8	18.7	20.6

Table1. Calculated pK<sub>7</sub> in cytochrome *c* oxidase using MCCE program. Free energy terms expressed in MCCE program are in equation 1.

In equation 2, pK<sub>7</sub> describes the protonation free energy from zero at PH 7. (The cofactor states are in the order CuA; Heme a; Heme a<sub>3</sub>;CuB)

Ubiquinol Oxidase	OOO	OOR	ROR	ORR	RRR
OH-HEME a3	13.7	13.0	12.9	19.3	20.5
OH- CUB	-0.5	17.9	18.4	14.4	15.2

Table2. Calculated  $pK'$  in cytochrome c oxidase using MCCE program. (The cofactor states are in the order Heme b; Heme O3;CuB)

#### EQUATIONS:

$$DG = 2.3RT(7 - pK_{a,sol}) - (DDG_{rxn} + DG_{pol} + DG_{res,7}^{mfe}) \quad (1)$$

$$pK_7' = 7 - \frac{DG_7}{RT} \quad (2)$$

#### REFERENCES

- [1] Gunner M.R., Alexov E. 2000. A pragmatic approach to structure based calculation of coupled proton and electron transfer in proteins. *Biochim. Biophys. Acta* 1458:63-87.
- [2] Song, Y. Michonova-Alexova, E. Gunner, M.R. Calculated proton uptake on anaerobic reduction of cytochrome c oxidase: Is the reaction electroneutral? Accepted for publication in *Biochemistry* pending minor revisions.
- [3] Song Y., Mao, J., Gunner M.R. Electrostatic environment of hemes in proteins:  $pK_a$ s of hydroxyl ligands. *Biochemistry*. Accepted for publication in *Biochemistry* pending minor revisions.
- [4] Abramson, J., Riistama, S., Larsson, G., Jasaitis, A., Svensson-Ek, M., Laakkonen, L., Puustinen, A., Iwata, S., Wikstrom, M. The structure of the ubiquinol oxidase from *Escherichia coli* and its ubiquinone binding site. *Nat.Struct.Biol.* v7 pp.910-917, 2000
- [5] Svensson-Ek, M., Abramson, J., Larsson, G., Tornroth, S., Brzezinski, P., and Iwata, S. (2002) The X-ray crystal structures of wild-type and EQ(I-286) mutant cytochrome c oxidases from *Rhodobacter sphaeroides*, *J Mol Biol* 321, 329-339.
- [6] Mao, J., Hauser, K., and Gunner, M. R. (2003) How cytochromes with different folds control heme redox potentials, *Biochemistry* 42, 9829-9840.
- [7] Brzezinski, P. (2004) Redox-driven membrane-bound proton pumps, *Trends Biochem. Sci.* 29, 380-387.
- [8] Ferguson-Miller, S., and Babcock, G. T. (1996) Heme/copper terminal oxidases, *Chem. Rev.* 96, 2889-2907.
- [9] Ruitenber, M., Kannt, A., Bamberg, E., Ludwig, B., Michel, H., and Fendler, K. (2000) Single electron reduction of the oxidized state is coupled to proton uptake via the K pathway in *Paracoccus denitrificans* cytochrome c oxidase. *Proc. Natl. Acad. Sci. U.S.A.* 97, 4632-4636.
- [10] Gunner, M. R., and Honig, B. (1991) Electrostatic control of midpoint potentials in the cytochrome subunit of the *Rhodospseudomonas viridis* reaction center, *Proc. Natl. Acad. Sci. USA* 88, 9151-9155.
- [11] Michel, H. (1998) The mechanism of proton pumping by cytochrome c oxidase, *Proc Natl Acad Sci U S A* 95, 12819-12824.

# Author's Index

- Abe, Yo, 297  
Albeseder, Daniel, 83  
Alexy, Pavol, 143, 157  
Alfano, R. R., 343  
Alrubaiee, M., 343  
Andrade, Rui, 215  
Andreev, Alexey, 191  
Andrews, Aaron Maxwell, 91, 171  
Andrijasevic, Daniela, 89  
Armengaud, Eric, 11  
Austerer, Max, 169
- Bajwa, Hassan, 87  
Bakoš, Dušan, 103, 185  
Barančok, Drahoslav, 165, 187  
Barinka, Radim, 127  
Bartušek, Karel, 323  
Batista, Carlos A. Silvera, 197  
Bauer, Heidi, 215, 223, 241, 243, 297  
Beckles, Yvette, 281  
Beisteiner, Susanne, 217, 277  
Bellušová, Denisa, 101, 181  
Benz, Alexander, 91  
Bertol-Vrček, Jasenka, 255  
Bikson, Marom, 289  
Bjegovic, Dubravka, 175  
Blaha, Martin, 123  
Bleyer, Michael, 61  
Block, Karin A., 207  
Bogatin, Sonja, 3  
Borsig, Eberhard, 179  
Brenner, Werner, 89, 97  
Brilly, Mitja, 269  
Bubeníková, Silvia, 103, 185
- Buchner, Christoph, 221  
Buchta, Zdeněk, 323  
Bugaj, Peter, 143, 157
- Cancel, Limary, 339  
Caseiro, Alexandre, 215, 223  
Černáková, Ludmila, 147  
Cernoch, Pavel, 95  
Češka, Milan, 49  
Chang, Hsuan-Yeh, 347  
Chen, Xinghao, 87  
Chodák, Ivan, 143  
Čík, Gabriel, 243  
Círák, Július, 165, 187  
Cvetanovic, Aleksandra, 97
- Džubera, Jakub, 7  
Degischer, Hans Peter, 149  
Delvai, Martin, 27  
Denn, Morton M., 199, 201  
Dercová, Katarina, 263, 267  
Detter, Helmut, 97  
Diyamandoglu, Vasil, 281  
Drochytka, Rostislav, 237, 251  
Dulíková, Mária, 167  
Dumbrovský, Miroslav, 261, 325  
Žuračka, Miroslav, 143  
Durakbasa, Numan Muhammet, 29, 271
- Edtmaier, Christian, 135  
El Salloum, Christian, 9  
Elmenreich, Wilfried, 33, 35, 41, 53, 67  
Erler, Jens, 179  
Fürnsinn, Stefan, 227

Fasching, Gernot, 91  
 Feckova, Zuzana, 107  
 Fedotov, Andrey B., 315  
 Fedra, Zbyněk, 13  
 Feichtner, Helmut, 225  
 Feldgitscher, Claudia, 105  
 Feng, Chun-Min, 193  
 Feranc, Jozef, 143  
 Fitting, Andrew, 339  
 Foppe, Karl, 3  
 Foret, Rudolf, 189  
 Foret, Zdeněk, 109  
 Frank, Andrew, 17  
 Frank, Andrew U., 79  
 Fridrichova, Marcela, 159  
 Fritscher, Christina, 131  
 Frk, Martin, 111  
 Fuger, René, 113  
 Fuleová, Veronika, 157  
  
 Gan, Qiu, 283  
 Gayen, S. K., 343  
 Gdovicinova, Lucia, 265  
 Gebauer, Günter, 333  
 Gelautz, Margrit, 61  
 Ghorabi, Hesamedin Ostad Ahmad, 257  
 Golka, Sebastian, 169  
 Goyal, Rajesh, 201  
 Grün, Bettina, 301  
 Granzer, Wolfgang, 15  
 Grum, Eva, 17  
 Gunner, Marilyn, 353  
  
 Hähndel, Andreas, 209  
 Hála, Ondřej, 19  
 Hamza, Fatmir, 115  
 Handl, Thomas, 23  
 Handler, Markus, 229  
 Hanus, Stanislav, 65  
 Hanzlíková, Klára, 117  
 Hašková, Lea, 231  
 Haslinger, Stefan, 119  
  
 Havranek, Jan, 69, 121  
 Hefner, Stepan, 123  
 Hefty, Ján, 21  
 Hein, Sonja, 217  
 Hell, Johannes, 119  
 Hengstberger, Florian, 125  
 Hernandez, Cecilia, 291  
 Heželová, Mária, 233  
 Hladik, Jiri, 127  
 Hlavinec, Petr, 249  
 Hofbauer, Hermann, 225, 227, 239, 313  
 Holubar, Peter, 217, 277  
 Homa, Johannes, 129  
 Hrčka, Michal, 21  
 Hrdý, Radim, 139  
 Hubálek, Jaromír, 139  
 Hudec, Ivan, 101, 181  
  
 Inführ, Robert, 131  
 Ingolic, Elisabeth, 183  
 Ivanovici, Sorin, 133  
  
 Jadlovský, Ján, 25  
 Janhsen, Thomas, 135  
 Jans, Urs, 283, 295  
 Jaroš, Lubomír, 235  
 Jasenovec, Lubomír, 25  
 Jeitler, Marcus, 27  
 Jirak, Josef, 95  
 Jorgačevski, Jernej, 303  
  
 Kahsay, Gebremeskel, 29  
 Kaiser, Bertrand, 173  
 Kala, Jaroslav, 305  
 Kalousek, Lubor, 307  
 Kalova, Veronika, 237  
 Kamenský, Jozef, 231  
 Kandl, Susanne, 31  
 Karvaš, Anton, 143  
 Kasal, Miroslav, 327  
 Kasper-Giebl, Anne, 215, 223  
 Kastner, Wolfgang, 15, 59

Kaushal, Priyanka, 239  
 Khanbilvardi, Reza, 291, 293  
 Khunová, Viera, 137  
 Kickelbick, Guido, 105, 115, 133, 163  
 Kirner, Raimund, 31  
 Kladeková, Daniela, 233  
 Klatzer, Barbara, 241  
 Klimová, Daniela, 137  
 Klingler, Gernot, 33  
 Klosová, Kateřina, 139  
 Kocian, Martin, 141  
 Kofler, Heinrich, 315  
 Kogoj, Dušan, 3  
 Kohout, Jan, 117  
 Kopetz, Hermann, 9, 55, 63, 73  
 Kosel, Franc, 161  
 Köbler, Alexander, 33, 35  
 Kotianová, Petra, 243, 297  
 Kowach, Glen, 193  
 Kozák, Peter, 309  
 Kozelj, Daniel, 245  
 Kralj-Iglič, Veronika, 273  
 Kramárova, Zuzana, 143  
 Kramer, Felix, 37  
 Kreft, Marko, 303  
 Krejza, Ondřej, 145  
 Kretzschmar, Ilona, 197  
 Krištofič, Michal, 167  
 Krivak, Petr, 39  
 Kroiss, Helmut, 275  
 Kröll, Josef, 311  
 Krywult, Stefan, 41  
 Kucera, Tomas, 247  
 Kuiper, Andy, 43  
 Kuna, Ladislav, 131  
 Kunovská, Katarína, 147  
 Kyselá, Gabriela, 101  
  
 Lacík, Igor, 103  
 Laimer, Johann, 119  
 Lakkundi, Vishwas, 45  
  
 Lasagni, Andrés, 151  
 Lasagni, Fernando Adrián, 149  
 Laschober, Stefan, 153  
 Lazar, Josef, 323  
 Lee, Jae W., 287  
 Leisch, Friedrich, 301  
 Lendl, Bernhard, 259  
 Li, Xiqing, 295  
 Lichtenegger, Helga, 131  
 Limbeck, Andreas, 229  
 Lin, Feng-Bao, 195, 205  
 Lis, Fátima Bertrán de, 219  
 Liska, Robert, 131, 173  
 Livingstone, Richard, 351  
 Lizal, Petr, 253  
 Lombardi, John, 351  
 Lopez, Sandra V., 337  
 Lu, Hong, 211  
 Lugstein, Alois, 171  
 Luisser, Markus, 313  
 Lukáč, Pavol, 137  
 Lux, Ladislav, 107, 233, 317  
  
 Macalik, Michal, 155  
 Magerl, Gottfried, 71  
 Mahani, Shayesteh, 291, 293  
 Majzner, Jiri, 69  
 Malanik, Stanislav, 249  
 Marsalek, Roman, 45  
 Matsché, Norbert, 219  
 Matulova, Pavla, 251  
 Mejia, Yajaira, 293  
 Melcer, Michael, 295  
 Michalcova, Gabriela, 251  
 Mohapl, Martin, 253  
 Mohn, Peter, 177  
 Moore, Carol Wood, 345  
 Moser, Heinrich, 47  
 Mücklich, Frank, 151  
 Muelhaupt, Ralf, 179  
 Muraj, Iva, 255

Nahálková, Anna, 157  
 Nguyen, Tieuvi, 341  
 Nikolics, Johann, 89  
 Novosad, Petr, 49  
 Novotny, Vit, 85  
  
 Ocenasek, Pavel, 51  
 Orban, Filip, 315  
 Osanna, Peter Herbert, 29, 271  
 Ostradecky, Ivo, 159  
  
 Padilla, Diomaris, 285  
 Parra, Lucas, 289  
 Parravicini, Vanessa, 275  
 Paukovits, Christian, 53  
 Paulitsch, Harald, 55  
 Pflügl, Christan, 169  
 Pikna, Lubomir, 317  
 Pio, Casimiro, 215, 223  
 Pirochta, Ondřej, 57  
 Praus, Fritz, 59  
 Prešeren, Tanja, 319  
 Pride, Leah D., 345  
 Prokeš, Aleš, 7, 57  
 Pukšič, Andrej, 161  
 Pupáková, Kornélia, 321  
 Puxbaum, Hans, 215, 223, 229, 241, 243,  
 297  
  
 Radman, Thomas, 289  
 Radosch, Hans-Joachim, 209  
 Reichhold, Alexander, 225  
 Reichl, Christoph, 221  
 Rhemann, Christoph, 61  
 Říčný, Václav, 19  
 Rill, Christoph, 163  
 Ritter, Wolfgang, 259  
 Roch, Tomas, 91, 171  
 Rollinger, Barbara, 297  
 Röschlová, Jana, 165, 187  
 Rosenberg, Erwin, 153  
 Rous, Mohammad Abu, 183  
  
 Rumpler, Bernhard, 63  
 Rumschitzki, David, 335, 341  
 Russell, Stewart, 335  
 Růžička, Zdeněk, 65  
 Ryba, Jozef, 167  
 Rychnovský, Jan, 323  
  
 Sala, Aleksandra, 261  
 Saracevic, Ernis, 219  
 Schörgendorfer, Angela, 67  
 Schartner, Stephan, 169  
 Schmeltzer, David, 347  
 Schmid, Ulrich, 47, 75  
 Schmidl, Christoph, 297  
 Schmidt, Volker, 131  
 Schramböck, Matthias, 171  
 Schrenk, Werner, 91, 169, 171  
 Schuster, K. Christian, 183  
 Schuster, Monika, 173  
 Šebesta, Vladimír, 13  
 Sedlackova, Radovana, 325  
 Sedlak, Petr, 69, 121  
 Sedlarikova, Marie, 155  
 Sejakova, Zuzana, 263, 267  
 Sencakova, Lenka, 265  
 Serdar, Marijana, 175  
 Shklyaeva, Anna, 85  
 Sieberer, Martin, 177  
 Sigmund, Milan, 43  
 Šikula, Ondřej, 333  
 Sikula, Josef, 69, 123  
 Silveira, Daniel, 71  
 Singh, John Paul Bir, 199  
 Skokanová, Marianna, 263, 267  
 Škrovanová, Lubica, 179  
 Smrčka, Aleš, 93  
 Song, Yifan, 353  
 Spacek, Jiri, 327  
 Špirk, Eugen, 143  
 Stampfl, Jürgen, 129, 131, 173  
 Starý, Miloš, 235

Steiner, Jeffrey C., 207, 285  
 Steinhammer, Klaus, 73  
 Steininger, Andreas, 11, 23, 77, 81  
 Steinman, Franci, 245, 319  
 Stenovec, Matjaž, 303  
 Stiles, Richard, 279  
 Stipanovic, Irina, 175  
 Stráník, Rostislav, 111  
 Stráský, Jiří, 329  
 Strasser, Gottfried, 91, 169, 171  
 Strassl, Martin, 331  
 Stratil, Hannes, 75  
 Stravs, Luka, 269  
 Šuri, Peter, 143  
 Sveda, Miroslav, 51  
 Szendiuch, Ivan, 127  
  
 Tahirova, Halima, 271  
 Tamargo, Maria C., 211  
 Tarbell, John, 339  
 Tarbell, John M., 337  
 Tesař, Karel, 329  
 Tuhovcak, Ladislav, 247  
 Tummeltshammer, Peter, 77  
 Turan, Burcu Yigit, 279  
 Turecek, Claudia, 173  
 Twaroch, Florian A., 79  
  
 Unterrainer, Karl, 91, 311  
 Urbanija, Jasna, 273  
 Ůrögiová, Eva, 101, 181  
  
 Vajda, Ján, 165, 187  
 Vana, Norbert, 221  
 Vančo, Marek, 165, 187  
 Varga, Christian, 81  
 Varga, Franz, 173  
 Varga, Ksenija, 183  
 Vassová, Iveta, 167  
 Věchet, Stanislav, 117  
 Vircikova, Edita, 265  
 Vlček, Milan, 307  
  
 Vodná, Lucia, 103, 185  
 Vondrák, Jiří, 141, 145  
  
 Wang, Xiaojun, 205  
 Waubke, Holger, 37  
 Weber, Harald W., 113, 125  
 Wegracht, Ulrike, 275  
 Weis, Martin, 165, 187  
 Widder, Josef, 83  
 Wilfert, Otakar, 39  
 Wimmer, Wolfgang, 257  
 Wintner, Ernst, 315, 331  
 Wolfsberger, Alexandra, 217, 277  
 Wu, Youxian, 295  
  
 Xu, M., 343  
  
 Yang, Lijia, 295  
 Yedlapalli, Prasad, 287  
 Yousif, Ariej, 331  
 Yu, Zhonghua, 203  
  
 Zajacek, Jiri, 191  
 Zbiral, Hannes, 229  
 Zeng, Fei, 195  
 Zhang, Jun, 353  
 Zhang, Li, 203  
 Zhang, Pengfei, 295  
 Zheltikov, Aleksey M., 315  
 Zlámal, Bronislav, 189  
 Zobl, Reinhard, 91  
 Zorec, Robert, 303

ISBN 3-902463-05-8

Technische Universität Wien

Karlsplatz 13 | A-1040 Wien

Tel. +43/(0)1/58801-0 | Fax +43/(0)1/58801-41099